Inamuddin · Rajender Boddula ·
Abdullah M. Asiri *Editors*

Methods for Electrocatalysis

Advanced Materials and Allied Applications

Springer

Methods for Electrocatalysis

Inamuddin · Rajender Boddula ·
Abdullah M. Asiri
Editors

Methods for Electrocatalysis

Advanced Materials and Allied Applications

Springer

Editors
Inamuddin
Department of Chemistry
Faculty of Science
King Abdulaziz University
Jeddah, Saudi Arabia

Department of Applied Chemistry
Faculty of Engineering and Technology
Aligarh Muslim University
Aligarh, India

Abdullah M. Asiri
Department of Chemistry
King Abdulaziz University
Jeddah, Saudi Arabia

Rajender Boddula
Cas Key Laboratory of Nanosystem
and Hierarchical Fabrication
Beijing, China

ISBN 978-3-030-27160-2 ISBN 978-3-030-27161-9 (eBook)
https://doi.org/10.1007/978-3-030-27161-9

This Springer imprint is published by the registered company Springer Nature Switzerland AG
The registered company address is: Gewerbestrasse 11, 6330 Cham, Switzerland

Contents

Earth Abundant Electrocatalyst

Kartick Chandra Majhi, Paramita Karfa and Rashmi Madhuri

Abstract Altering/replacing the rare elements and noble metal like platinum (Pt), iridium (Ir) and ruthenium (Ru) with the earth abundant materials towards the energy devices have extended a lot of attention for the improvement of efficient electrocatalyst. In this chapter, we have focused on the earth abundant electrocatalysts primarily used for overall water splitting, oxygen reduction reaction (ORR) in fuel cells, O_2C reduction, N_2 reduction and detection of pollutants in water samples. The problem related to the non-noble metals electrocatalysts are their poor electrocatalytic activity, restricted active sites and also small mass transport properties. However, recent studies show that earth abundant materials can be a suitable/efficient candidate for these applications with optimized composition and nano-scale particle size, which will definitely accelerate their catalytic activity. In this chapter, we have focused on all these aspects of earth abundant electrocatalysts (EAEs) and discussed their future perspectives also.

Keywords Electrocatalyst · Earth abundant · Overall water splitting · Oxygen reduction reaction · Carbon dioxide reduction · Nitrogen dioxide reduction

1 Introduction

Electrocatalysts are one type of catalysts, which involves in electrochemical reactions. Electrocatalysts can enhance the electrochemical reactions rate, without altering the electrocatalyst or catalyst remains intact. At the time of electrochemical reaction the rate electron transfer between the electrode and reactants accelerated with electrocatalyst, which lead to required lower onset potential values. A better electrocatalyst can always have lower overpotential in electrochemical reactions.

With the increase of worldwide population and growing industrialization lead to depletion of fossil fuels and crisis of energy is the major concerns in future. Year to year the energy consumption largely increased collected from United States Energy

K. C. Majhi (✉) · P. Karfa · R. Madhuri
Department of Chemistry, Indian Institute of Technology (Indian School of Mines) Dhanbad, Dhanbad, Jharkhand 826004, India
e-mail: kcmajhi1995@gmail.com

Inamuddin et al. (eds.), *Methods for Electrocatalysis*,
https://doi.org/10.1007/978-3-030-27161-9_1

Information Administration (EIA). For instance, whole world energy consumption will be 549, 629 and 815 quadrillion British thermal units (Btu) in the year of 2012, 2020 and 2024, respectively [16]. It means, the consumption of energy will increase 48% in the year of 2024 than 2102. But the 78% energy consumption will be derived from different fossil resources like coal, natural gas, liquid fuels etc. Consumption of fossils release some harmful gas like CO_2, SO_x and NO_x, which affect the environment. For instance, in the year of 2012, worldwide CO_2 emission was 32.2 billion metric tons, whereas in 2040, it will be predicted to be 43.2 billion metric tons known from International Energy Outlook 2016 (IEO2016). Therefore, from 2012 to 2040 the CO_2 may increase 34% [16]. For that reason, making the world green and improving the sustainable and renewable energy technologies for the future, we need the safe alternatives, which is not an easy task.

Earth abundant electrocatalytic energy storage and conversion has been the most effective and freshest pathways to convert the form of energy mainly electrical energy into chemical energy or vice versa and store the energy [30, 38, 73]. Several electrochemical reactions like overall water splitting which consists hydrogen evolution reaction (HER) at cathode and oxygen evolution reaction (OER) at anode for conversion of energy and another important reactions like oxygen reduction reaction (ORR) function in fuel cell. The complete water decomposed is the combination of HER and OER, which can enable to convert the electrical energy to hydrogen [83]. Moreover, hydrogen is a suitable candidate as energy carrier, which can effectively transfer the chemical energy into the electrical energy in fuels cells, simultaneously, water is formed as a byproduct [56, 104]. On the other way, coupling of OER and ORR, enable for energy conversion i.e. chemical energy into electrical energy, which is used in metal-ion batteries [5, 62, 66]. However, in HER process two electrons transfer is observed, which is kinetically possible but in OER and ORR multi electrons are required (like four electrons for OER) to carry out the reactions and it is kinetically slow, which requires large overpotential to success the reaction, which is the disadvantages towards their practical applications or industrial applications.

To enhance the reactions rate of OER and ORR a suitable catalyst is required. Till date, the highly effective catalyst for ORR/HER is platinum (Pt), for OER RuO_2 and IrO_2 are well known. However, due to the RuO_2, IrO_2 electrode materials are unstable in alkaline and acidic medium these catalysts have some limitations. Moreover, RuO_2 and IrO_2, itself get oxidized to RuO_4 and IrO_3, respectively, and also these are low abundant, have scarcity and high cost. This is the reason the researcher pressing to investigate the highly effective, suitable and benchmark electrocatalysts to enhance the electrochemical performance towards OER, ORR and HER. Other than these, earth abundant materials came up as replacement and suitable candidate for OER, HER and ORR than noble metal-based catalysts. This is mainly due to some distinctive chemical properties and physical properties mainly mechanical, thermal stability and good electrical conductivity [19, 20, 43, 99]. Other than energy storage and conversion the earth abundant electrocatalyst have been also used for the reduction of inactive trivial molecules like O_2C and N_2 into carbon monoxide, ammonia, methane, methanol and ethylene with high conversion value.

Earth abundant materials have been broadly studied last few years ago as electrocatalyst for OER, HER and ORR. In general, the electrocatalysts involves three steps, (1) mass diffusion, (2) surface interaction and (3) electron transfer. To obtain the maximum catalytic activity of electrocatalyst must possesses above mentioned steps. The earth abundant materials are the efficient candidate for electrocatalyst owing to their small particle size with good surface morphology, abundant, inexpensive, have large surface area and possess synergic effect [78].

2 Role of Earth Abundant Electrocatalyst (EAEs) Towards Various Applications

In overall water splitting have been consists two cell reactions HER and OER, on other hand OER and ORR have been plays in metal air batteries. Prior to discussing the role of earth abundant catalysts in electrochemical reactions. In the next section, we have discussed the fundamentals of some popular reactions like OER, HER and ORR.

2.1 Role of EAEs Towards Hydrogen Evolution Reaction (HER)

Hydrogen evolution reaction is the important half-cell reaction of water splitting take place in both the acidic and alkaline medium at cathode. The reaction of water splitting can be represented by reaction (1).

$$2H_2O \rightarrow 2H_2 + O_2 \tag{1}$$

Water electrolysis is the only method, which offered high purity hydrogen gas without emission of any harmful toxic reagents to the environment [44]. The HER in acidic and basic condition are represented by reaction (2) and (3), respectively.

$$2H^+ + 2e^- \rightarrow H_2 \quad Acidic\,condition \tag{2}$$

$$2H_2O + 2e^- \rightarrow 2OH^- + H_2 \quad Basic\,condition \tag{3}$$

The reaction mechanism steps of HER in acidic and basic condition are different and the reaction steps are depicted in the following equation (M indicates the available active site of the catalyst). From the literature study, the most common accepted mechanisms consist of two steps such as Volmer–Heyrovsky steps and Volmer–Tafel steps [34]. In Volmer step i.e. first step, the proton adsorbed on the catalyst surface (shown in Eq. 4). The second step i.e. Tafel step, consist of self-combination of

adsorbed hydrogen atom (M-H_{ads}), shown in Eq. (5) or the Heyrovsky step combination of hydrogen ion and M-H_{ads} to form hydrogen by one electron transfer (shown in Eq. 6).

The HER mechanism steps in acidic condition

$$Volmer\ step\text{: } M + H^+ + e^- \rightarrow M - H_{ads} \tag{4}$$

$$Tafel\ step\text{: } 2M - H_{ads} \rightarrow H_2 \tag{5}$$

$$Heyrovsky\ step\text{: } M - H_{ads} + H^+ + e^- \rightarrow H_2 \tag{6}$$

Similarly, the mechanism step of HER in alkaline condition also consists of two mechanisms, which is Volmer–Tafel and Volmer–Heyrovsky steps [22]. But in alkaline condition, in the first step i.e. Volmer step, water molecule dissociate in presence of catalyst to form M-H_{ads} (shown in Eq. 7). In second step hydrogen gas is formed by two-ways, (a) self-combination of M-H_{ads} (Tafel step, shown in Eq. 8) and (b) combination of water and M-H_{ads} by electron transfer (Heyrovsky step, shown in Eq. 9). The Gibbs free energy (ΔG) of M-H_{ads} is almost low value i.e. zero, if this value is too high or too low, which directly affect the adsorption or desorption steps [46].

The HER mechanism steps in basic condition:

$$Volmer\ step - water\ dissociation\text{: } M + 2H_2O + 2e^- \rightarrow 2M - H_{ads} + 2OH^- \tag{7}$$

$$Tafel\ step\text{: } 2M - H_{ads} \rightarrow H_2 \tag{8}$$

$$Heyrovsky\ step\text{: } H_2O + M - H_{ads} + e^- \rightarrow H_2 + OH^- \tag{9}$$

Determination of rate determine step is solely depends upon the Tafel slope value. Based on the Tafel slope value, the Tafel slope value of each mechanism steps such as, Heyrovsky, Tafel steps and Volmer are 30, 40 and 120 mV/dec, respectively [45]. Platinum and its analogue have been widely used as HER catalyst with higher catalytic activity and low overpotential [1] but it's has some limitation such as low abundance and high cost. This is why, researcher try to explore the suitable inexpensive, stable, good electrocatalyst. Recently, earth abundant materials have been widely studied as an electrocatalyst for HER due to their eco-friendly nature, less expense, higher activity. In the next section, we have discussed the role of earth catalysts in HER.

2.1.1 Monometallic EAEs for HER

In 2015, Zhang et al. has developed polymorphic cobalt diselenide, $CoSe_2$ through electrodeposition at 300 °C towards HER in acidic condition [95]. They found outstanding performance of catalysts with little overpotential and low Tafel slope – 70 mV@ten mA/cm^2 and 30 mV/decade respectively. In 2017, another research group has developed bi anionic monometallic, CoPS through chemical vapor transport for HER in acidic condition [80]. Authors have studied theoretical and experimental aspects of CoPS and found (111) facet has higher catalytic activity than that of (100) facet. The overpotential of (111) facet has low overpotential than (100), and Tafel slope of (111) and (100) facet were found 86 and 109 mV/decade, respectively. In the same year (2017), Wu et al. has synthesized iron phosphosulfide anchored with carbon nanotube (CNT) nanoparticles for HER where 0.5 M H_2SO_4 used as an electrolyte [82]. The synthesized system offered small overpotential 260 mV and little Tafel slope. In the year of 2019, Zhang and co-workers has first time developed nickel sulfide boron via electrodeposition method towards hydrogen evolution reaction in pH 14 [81]. The developed system offered little onset potential, low overpotential and also low Tafel slope 0.027 V, 240 mV@ten mA/cm^2 and 140.7 mV/decade respectively. The earth abundant $Ni_{0.85}Se$ have been used as an electrocatalyst for HER in acidic condition by Yu et al. [90]. The prepared $Ni_{0.85}Se$ offers low overpotential of -275 mV@30 mA/cm^2 and very low Tafel slope of 49.3 mV/decade. In 2017, Qi et al. has synthesized rhenium diselenide, $ReSe_2$ and ReS_2 through nucleation method designed for hydrogen evolution reaction in pH 14 [65]. The prepared $ReSe_2$ and ReS_2 nanoparticles has offered low overpotential 300 mV@8 mA/cm^2 and 300 mV@3 mA/cm^2 respectively and their corresponding small Tafel slope 67.5 and 143.3 mV/decade respectively. The field emission scanning electron microscope (FESEM) of $ReSe_2$ and polarization curve of $ReSe_2$ and ReS_2 are shown in Fig. 1 [65].

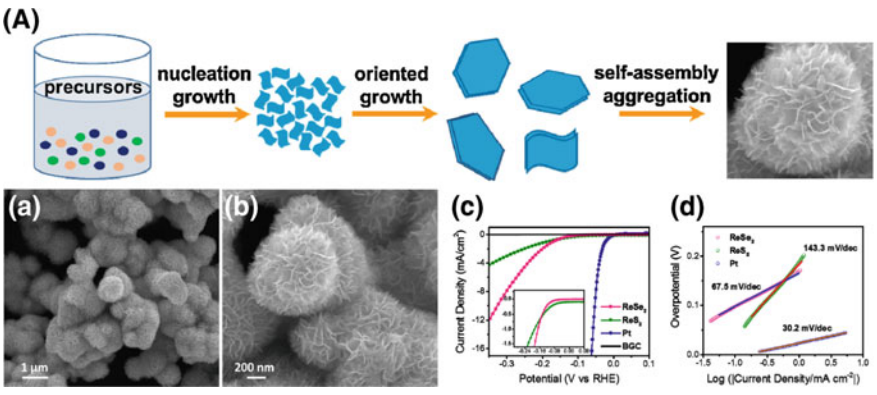

Fig. 1 Schematic representation showing synthesis of $ReSe_2$ (**A**). FESEM images of $ReSe_2$ (**a**, **b**), LSV polarization curve (**c**) and Tafel plot (**d**) of $ReSe_2$ for HER in 0.5 M H_2SO_4. Permission taken from [65]

Role of monometallic earth abundant electrocatalyst for complete water splitting i.e. combination of HER and OER is also reported in the literature. For example, in 2019, Lu et al. have synthesized cobalt phosphide grown on nitrogen graphene nanosheets by simple hydrothermal method followed by phosphorization for bifunctional OER and HER in acidic and alkaline medium [55]. The synthesized cobalt phosphide grown on nitrogen graphene nanosheets have displayed outstanding performance towards HER and exhibited little onset potential of −0.087 V and small Tafel slope 63.8 mV/dec in acidic medium and −0.114 V and 59.6 mV/dec in alkaline medium. It also showed the excellent performance of catalysts towards OER with low onset potential 1.48 V, overpotential potential and Tafel slope were 354 mV@ten mA/cm^2 and 63.8 mV/dec respectively with long term stability for OER as well as HER in both the medium (acidic and alkaline).

2.1.2 Bimetallic EAEs for HER

Recently, earth abundant materials have been greatly explored as an electrocatalyst for HER due to their have admirable electrical conductivity, great melting point, high corrosion resistance, and high stability. In 2019, He et al. have first time synthesized one-dimensional iron-tungsten carbide nanorods reduced graphene oxide, Fe_3W_3C NRs/RGO for HER [29]. Fe_3W_3C NRs/RGO revealed outstanding HER performance with almost zero onset potential like platinum and little Tafel slope 50 mV/decade. Hierarchical microsphere molybdenum nickel porous nanosheets exhibited outstanding performance towards HER in 1.0 M KOH developed by Yang et al. [89]. Molybdenum nickel porous nanosheets offered small onset potential, overpotential and Tafel slope −0.007 mV, 72 mV@ten mA/cm^2 and 36.6 mV/decade respectively. In 2019, Abdullah et al. successfully synthesized earth abundant nickel doped cobalt hollow nanoparticles via facile ultrasonic-assisted chemical reduction method for HER in 1.0 M potassium phosphate buffer (pH = 7) [2]. The synthesized nanoparticles employed very outstanding performance towards HER with minor overpotential 41 mV to drive the current density ten mA/cm^2 and Tafel slope 35 mV/decade, which is found stable up to 20 h. Liu and co-workers have synthesized tungsten disulfide-tungsten (WS_2/W) heterojunction using bottom up approach via simple ultra-sonication method and employed as an electrocatalyst for HER [47]. WS_2/W offered small onset overpotential 30 mV, little overpotential 108 mV to drive the 10 mA/cm^2 and low Tafel slope 81.4 mV/decade. Hou et al. [31] has developed $NiSe_2$–$Ni_{0.85}Se$ and wrapped by reduced graphene oxide by hydrothermal method and employed as an electrocatalyst for HER with highly durable 18 h [31]. It has low onset potential (−175 mV), overpotential (240 mV@ten mA/cm^2) and Tafel slope (31.3 mV/decade). In 2018, Choi and co-workers have synthesized sulfur doped in nickel cobalt, NiCo on carbon quantum dot via simple hydrothermal method for hydrogen evolution reaction [4]. It has low overpotential and Tafel slope 232 mV@ten mA/cm^2 and 80.2 mV/decade respectively with highly stable up to 20 h without changing the current density. In 2017, Cao et al. has developed first time the MoS_2/Ni_3S_2 nanocomposite grown on nickel foam via hydrothermal method

for [12]. They found small onset potential (145 mV), little overpotential (76 mV) and small Tafel slope (56 mV/decade), stable up to 24 h. The admirable electrocatalytic activity of the prepared nanocomposite can be described on the basis of their synergistic effect, electrical coupling between Ni, MoS_2, and Ni_3S_2, the super hydrophilic interface, and large active edge sites. In 2019, Chen et al. has first time developed a composite of CoP_3 and CoMoP nanosheet array through hydrothermal method and studied the catalytic activity towards HER [36]. They found low overpotential 125 and little Tafel slope 61.1 mV/decade. In addition, some of the earth abundant electrocatalyst towards HER in acidic and alkaline medium is portrayed in Table 1.

2.2 Role of EAEs Towards Oxygen Evolution Reaction (OER)

Oxygen evolution reaction is another half-cell reaction of water electrolysis, chemical reaction of OER is as follows: $2H_2O \rightarrow O_2 + 4H^+ + 4e^-$, therefore for the formation of O=O, required four electrons. This is the reason the OER is kinetically sluggish and to enhance the OER activity a selective suitable catalyst has been required. The thermodynamic potential for H_2O decomposed is 1.23 V, but in practical some extra potential needed to success the reaction (oxygen evolution) called overpotential. The reaction mechanism of OER is greatly affect by the pH of the medium. Therefore, the OER mechanism is different for acidic and basic medium. Till date the exact mechanism is still under debate. But all the proposed mechanism proceeds through the same intermediate like FO and F–OH (where, F represents the active site of catalyst). The most accepted mechanism for OER in acidic and basic medium is presented below in following equation.

Probable mechanism for OER in acidic condition:

$$F + H_2O \rightarrow F - OH_{ads} + H^+ + e^- \tag{10}$$

$$F - OH_{ads} + OH^- \rightarrow F - O_{ads} + H_2O + e^- \tag{11}$$

$$F - OH_{ads} + F - OH_{ads} \rightarrow 2F + O_2 \tag{12}$$

Or

$$F - OH_{ads} + H_2O \rightarrow F - OOH_{ads} + H^+ + e^- \tag{13}$$

$$F - OOH_{ads} + H_2O \rightarrow F + O_2 + H^+ + e^- \tag{14}$$

Possible mechanism for OER under aqueous basic condition:

$$F + OH^- \rightarrow F - OH_{ads} + H^+ + e^- \tag{15}$$

Table 1 Some of the reported efficient earth abundant electrocatalysts for HER in acidic and alkaline medium

S. No.	Earth abundant catalyst	Synthesis method	Medium/electrolyte	Overpotential (mV)@10 mA/cm^2	Tafel slope (mV/dec)	References
1.	Ni_2P	–	0.5 M H_2SO_4	130@20 mA/cm^2	46	Popczun et al. [64]
2.	MoP	–	0.5 M H_2SO_4	117	–	Kibsgaard and Jaramillo [40]
	MoPS			90		
3.	Mo	Sintering	0.5 M H_2SO_4	441	92	Xiao et al. [85]
	MoP			–	147	
	Mo_3P			–	54	
4.	NiS_2	Thermal sulfidation	0.5 M H_2SO_4	230@1 mA/cm^2	48.8	Faber et al. [21]
	FeS_2			217@1 mA/cm^2	56.4	
	CoS_2			128@1 mA/cm^2	52	
	PyS_2			196@1 mA/cm^2	58.7	
	$Co_{0.59}Ni_{0.41}S_2$			170@1 mA/cm^2	50	
	$Fe_{0.48}Co_{0.52}S_2$			143@1 mA/cm^2	47.5	
5.	Cu_2MoS_4	Precipitation	–	135@0.04 mA/cm^2	95	Tran et al. [77]

(continued)

Table 1 (continued)

S. No.	Earth abundant catalyst	Synthesis method	Medium/electrolyte	Overpotential (mV)@10 mA/cm^2	Tafel slope (mV/dec)	References
6.	CoP	–	0.5 M H_2SO_4	75	50	Callejas et al. [11]
	Co_2P			95	45	
7.	WS_2	CVD[a]	0.5 M H_2SO_4	Onset potential: −0.2 V Overpotential: 142	70	Lukowski et al. [57]
8.	$NiSe_2$	–	0.5 M H_2SO_4	57	43	Zhou et al. [102]
9.	$CoSe_2$	Solvothermal	–	Onset potential: −0.126 V Overpotential: 250@60 mA/cm^2	31.6	Yu et al. [91]
10.	MoO_2/-Mo_2C	Hydrothermal	1.0 M KOH	100	50	Zinola et al. [103]
			0.5 M H_2SO_4	152	65	
11.	Hollow prisms $CoMoS_3$	Precipitation	0.5 M H_2SO_4	171	56.9	Yu et al. [93]
12.	CoS_2@MoS_2 nanoarray	Hydrothermal	0.5 M H_2SO_4	68	57.3	Zhang et al. [96]
	CoS_2 nanopyramid array			83	66.5	
	MoS_2 nanosheet array			115	47.1	
13.	$FeCo_2S_4$ grown on nickel foam	Hydrothermal	1.0 M KOH	131	52	Gong et al. [25]

[a]Chemical vapor deposition

$$F - OH_{ads} + OH^- \rightarrow F - O_{ads} + H_2O + e^- \quad (16)$$

$$F - OH_{ads} + F - OH_{ads} \rightarrow 2F + O_2 \quad (18)$$

$$F - OH_{ads} + OH^- \rightarrow F - OOH_{ads} + e^- \quad (19)$$

$$F - OOH_{ads} + OH^- \rightarrow F + O_2 + H_2O\ (l) + e^- \quad (20)$$

The hydroxyl ion from water molecule adsorbed on the active site of catalyst (represented as F) to form F–OH_{ads}. Two way the oxygen can formed (a) self-combination of F–OH_{ads} (shown in Eq. (12) for acidic condition and Eq. (18) for basic condition, (b) formation of another intermediate F–OOH_{ads} from F–OH_{ads} (shown in Eqs. (13) and (19) for acidic and basic condition, respectively) followed to produce oxygen (shown in Eqs. (14) and (20) for acidic and basic condition, respectively).

From the OER mechanism (discussed above), it is very clear that catalyst plays vital role in each step. The well-known state of the art noble metal such as platinum, iridium dioxide and ruthenium dioxide have been used as an effective catalyst for OER with small onset potential as well as small overpotential [44]. But these electrocatalysts have some limitation for the industrial application, because of low stability in acidic and basic condition (itself oxidized), high cost, and scarcity [44]. Presently, developing the efficient expensive stable electrocatalysts have been great challenging task for researcher. The earth abundant materials have been broadly explored for OER, due to high abundance, low cost, stability under acidic and basic condition and offered benchmark performance towards OER with small overpotential.

2.2.1 Monometallic EAEs for OER

Last few years, different monometallic based earth abundant materials have been widely used for OER in alkaline medium. In 2014, Tian et al. have synthesized cobalt phosphide with nanowire morphology developed on carbon cloth, CoP/CC using hydrothermal process towards OER in pH 14 [75]. The synthesized CoP/CC exhibited benchmark performance towards electrocatalytic activity with overpotential and Tafel slope of 67 mV and 51 mV/decade respectively. In 2018, Marje et al. was first time synthesized by hydrous pyrophosphate $Ni_2P_2O_7.8H_2O$ by chemical bath deposition method for OER in pH 14 [60]. The prepared $Ni_2P_2O_7.8H_2O$ offered outstanding performance with low overpotential 239@ten mA/cm^2 and 308 mV@25 mA/cm^2. They have found low Tafel slope of 51.5 mV/decade with higher stability of 9 h. Jiang et al. [37] first time prepared nickel phosphorous (Ni–P) films by electrodeposited method and studied OER activity [37]. Ni–P films exhibited good OER performance in alkaline condition with pH 14 with overpotential and Tafel slope 344 mV and 49 mV/decade respectively. Nickel selenide, $NiSe_2$ employed good electrocatalyst

for OER in pH 14 reported by Cai et al. [10, 12]. $NiSe_2$ exhibited outstanding performance with overpotential, Tafel slope 299 mV and 68 mV/decade respectively. In the year of 2017, Babar et al. was reported oxidized nickel oxide, NiO used as electrocatalyst towards OER in pH 14 [6]. NiO shows excellent performance for OER with overpotential and Tafel slope 310 mV@ten mA/cm^2 and 54 mV/decade respectively and good durability 24 h. Guo et al. [28] have prepared cobalt sulfide grown on nickel foam (CoS/NF) by hydrothermal process for OER [28]. CoS/NF revealed overpotential and Tafel slope were 297 mV@ten mA/cm^2 and 106 mV/decade respectively and stable up to 40 h without degradation. In [84], Xiang and co-workers developed 2D nickel thiophosphate, $NiPS_3$ nanosheets by simple hydrothermal method and studied electrochemical performance towards OER [7]. Catalysts has shown overpotential and Tafel slope 320 mV and 51 mV/decade respectively and highly stable up to 36 h. Liu et al. (2019) have synthesized $NiPS_3$ nanosheets by chemical vapor deposition (CVD) process towards OER [52]. The prepared $NiPS_3$ nanosheets exhibited remarkable electrocatalytic performance with low overpotential and Tafel slope 320 mV and 51 mV/decade in alkaline medium. The schematic representation, FESEM images and polarization curve of $NiPS_3$ nanosheets are shown in Figs. 2 and 3 (Permission from Liu et al. [52]).

2.2.2 Bimetallic EAEs for OER

Recently, bimetallic based earth abundant electrocatalyst have also been greatly used in OER. Some of the recently reported earth abundant materials used as an electrocatalyst for OER discussed in this section. In the year of 2017, Zhang et al. has first time synthesized earth abundant $MnCo_2S_4$ nanowire array grown on titanium mesh by sulfurization method for OER in basic condition [100]. The bimetallic sulfide $MnCo_2S_4$ nanowire array exhibited benchmark performance for OER with low overpotential 325 mV@50 mA/cm^2 and great turnover frequency (TOF) 0.81 mol O_2 per second. The electrocatalyst also offered a Tafel slope 115 mv/decade with higher stability 100 h. The higher catalytic activity of nanowire array due to higher number of exposed active sites [50]. Nsanzimana et al. [63] has prepared trimetallic boride, $FeCo_{2.3}NiB$ with particle size 30–40 nm for OER as an electrocatalyst [63]. Trimetallic boride electrocatalyst materials offered admirable electrocatalytic performance with onset potential and overpotential 1.46 V and 274 mV@10 mA/cm^2 respectively. They have also found the prepared catalyst was highly stable up to 10 h and offered small Tafel slope 38 mV/dec. The excellent catalytic activity towards OER, owing to the formation of distinctive amorphous multimetal-metalloid complex nanostructure. In the year of 2018, Lin et al. have synthesized $CaCo_2O_4$ nanoplate by simple sol-gel method and studied electrocatalytic activity for OER [51]. The synthesized bimetallic oxide offered low overpotential and Tafel slope were 371 mV@ten mA/cm^2 and 71 mV/decade respectively. The excellent performance, owing to the distinctive electronic structure obtained from Ca and Co, improved the electrical conductivity. Teng and co-workers have synthesized $MoCoO_4$ different shaped like nanorods and nanosheets by simple hydrothermal method and used it towards OER [54]. They

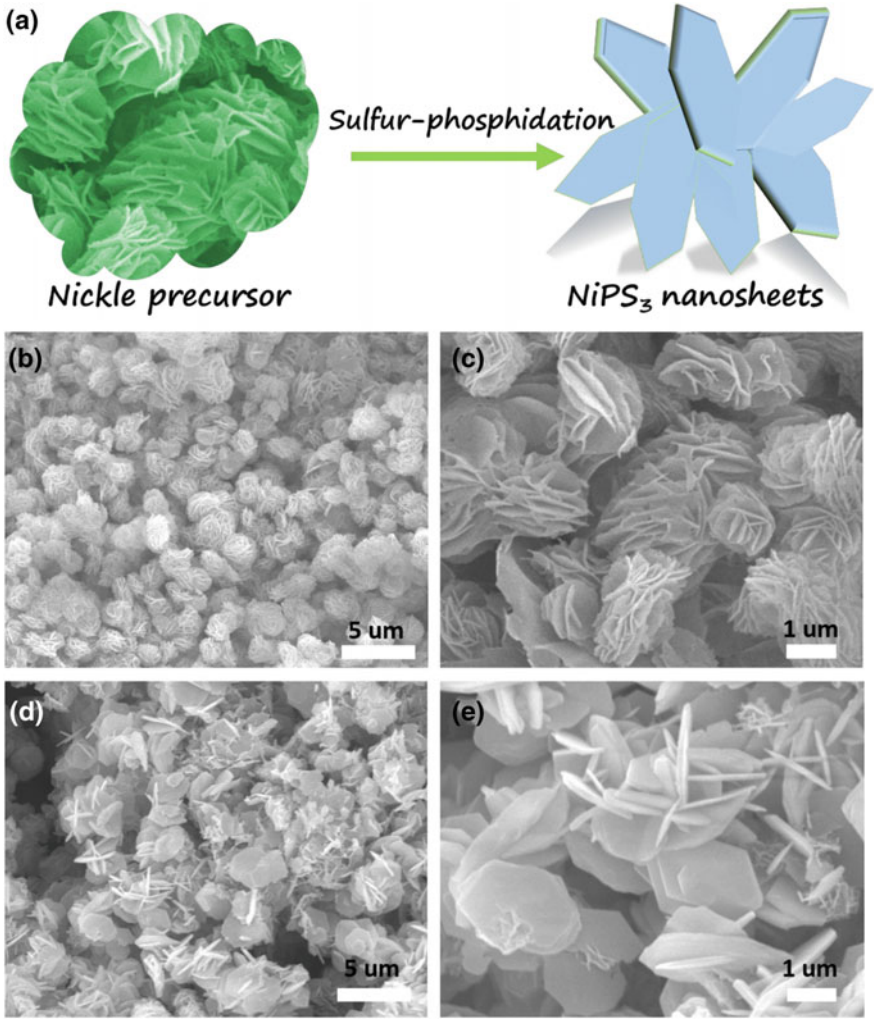

Fig. 2 **a** Schematic representation showing synthesis of $NiPS_3$ nanosheets. **b–e** FESEM images of $NiPS_3$ nanosheets in different magnification. Permission taken from Liu et al. [52]

have found that nanorods of $MoCoO_4$ has seven-time greater surface area (49.3 m^2/g) than nanosheets (7 m^2/g) and 5.7 times higher current density (8.93 mA/cm^2) than nanosheets shaped bimetallic nanomaterials (1.56 mA/cm^2) at potential 550 mV. The obtained Tafel slope were found 72 and 98 mV/dec for nanorods and nanosheets of $MoCoO_4$, respectively. In 2015, Kargar et al. has first time developed $CoFe_2O_4$ grown on three dimensional carbon fiber papers (CFPs) by hydrothermal method employed as an electrocatalyst for OER [39]. They have found low overpotential (378 mV) and Tafel slope (73 mV/decade). In 2018, Akbar et al. has synthesized nickel cobalt selenide, $NiCoSe_2$ grown on 3D nickel foam through electrodeposition method [3].

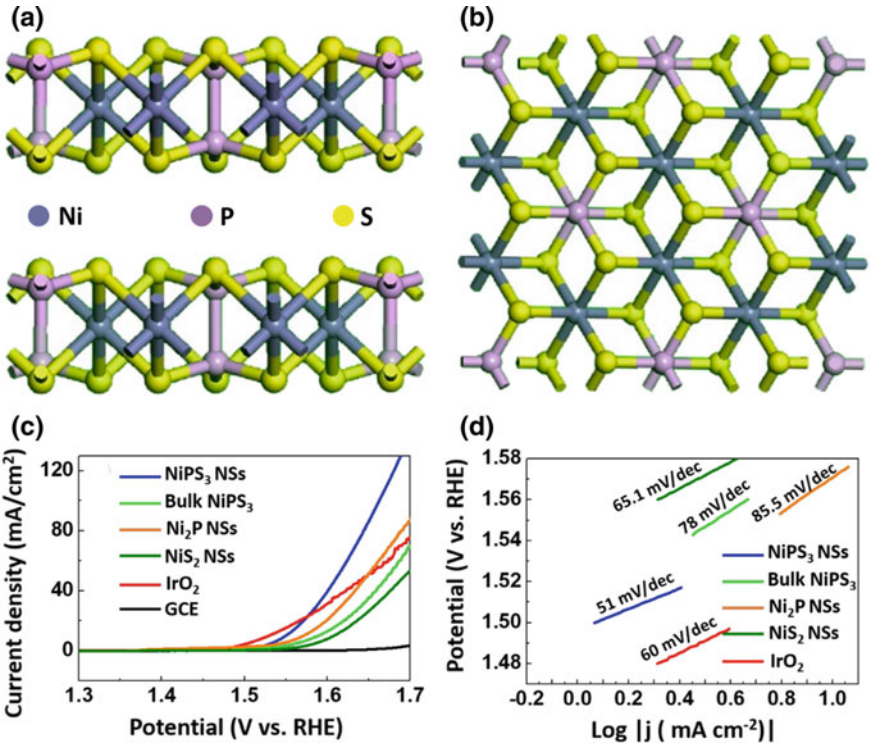

Fig. 3 Different crystal structure of $NiPS_3$ (**a**, **b**), LSV polarization curve (**c**) and Tafel plot (**d**) of synthesized electrocatalysts for OER in 1.0 M KOH. Permission taken from Liu et al. [52]

The prepared $NiCoSe_2$/3D NF offered outstanding performance with small overpotential and Tafel slope 183 mV@ten mA/cm^2 and 97 mV/decade respectively with long term stable up to 50 h. In 2019, Tran et al. was first time prepared NiCoP via simple hydrothermal method and studied for overall water splitting [76]. The synthesized earth abundant material has offered excellent activity for both HER and OER in alkaline medium. The obtained overpotential were 57 mV for HER and 330 mV for OER. The synthesized materials also offered little Tafel slope 170 mV/decade for HER and 113 mV/decade for OER. The water splitting by electrochemically is depicted in Fig. 4 [25, 76]. Moreover, some of the reported efficient earth abundant electrocatalyst for OER in acidic and basic medium is summarized in Table 2.

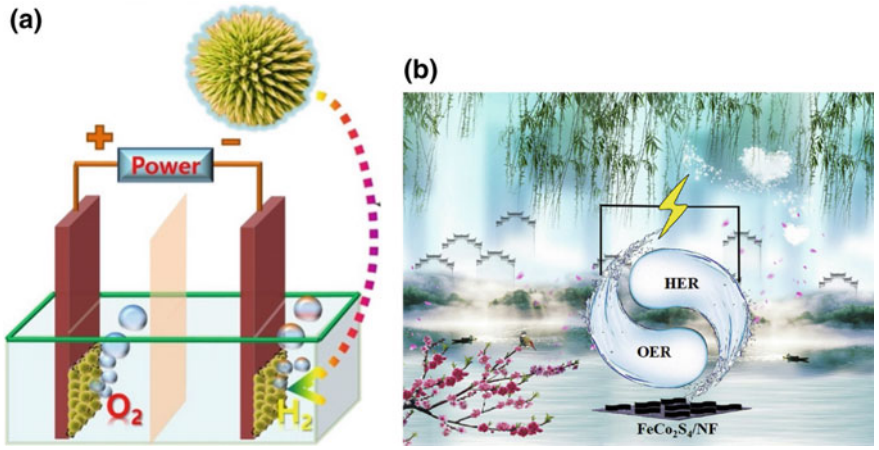

Fig. 4 **a** Schematic representation showing overall water splitting using two electrode system in presence of earth abundant electrocatalyst and **b** graphical presentation showing role of $FeCo_2S_4$/NF electrode as high-performance electrocatalyst for water splitting under electrochemical reaction conditions. Permission taken from [25, 76]

2.3 Role of EAEs Towards Oxygen Reduction Reaction (ORR)

ORR is the key reaction related to energy conversion, fuel cell, and metal-ion batteries [23, 24]. Similar to OER, ORR also have slow reaction kinetics. To succeed the reaction high overpotential is needed, which is the limitation for the practical applications of fuel cells. The most common efficient platinum and platinum-based materials are the best candidate for ORR, which offers low overpotential and oxygen reduced via four electron transfer reaction. But disadvantage of these catalyst is their expensive nature, scarcity and poor stability for prolonged period of time and working conditions [15, 94]. In order to resolve these problems, the earth abundant materials are the best candidate for ORR in both alkaline and acidic medium. Earth abundant catalysts are most abundant materials, which have high electrical conductivity, durability, inexpensive, and non-toxicity. The proper mechanism of the ORR is still under study but the probable mechanism of ORR is solely depending upon the adsorption of oxygen over catalyst surface. The oxygen molecule can be reduced by two pathways: (a) straight $4e^-$ transfer and (b) two step $2e^-$ pathways.

(A) **Straight $4e^-$ transfer path**

In this pathway, the oxygen molecule can reduce directly via four electron transfer process. The oxygen molecule is reduced into two molecules of water in acidic condition via four electron transfer (shown in Eq. 21), but in alkaline condition oxygen is reduced into four hydroxyl ions (displayed in Eq. 22). The reduction of oxygen in acidic and basic condition is depicted in the following equation:

Table 2 Some of the reported earth abundant electrocatalysts for OER in different concentration of KOH solution

S. No.	Earth abundant catalyst	Synthesis method	KOH concentration (M)	Overpotential (mV)[a]	Tafel slope (mV/dec)	References
1	ZIF@LDH@Ni-foam-600	Electrodeposition	1.0	318	97	Tang et al. [74]
	ZIF@LDH@Ni-foam				185	
2	CoFe LDH@Ni foam	–	1.0	260	47	Liu et al. [53]
3	$NiCo_2S_4$/NW/NF	Hydrothermal	1.0	260	40.1	Sivanantham et al. [71]
	Ni_3S_2/NF			300	51	
	$NiCo_2S_4$/NF			330	66.9	
	$NiCo_2S_4$			350	74.5	
4	$Ni_{0.5}Co_{0.5}$/nitrogen-doped carbon	–	1.0	300	68	Bayatsarmadi et al. [9]
	$Ni_{0.5}Co_{0.5}$			380	91.6	
5	$CoMoO_4$-$Ni(OH)_2$/NF nanosheet	Hydrothermal Calcination Electrodeposition	1.0	349@100 mA/cm^2	67.6	Xu et al. [87]
6	MnVOx@N-rGO	Hydrothermal Calcination	0.1	440	66.6	Xing et al.[86]

(continued)

Table 2 (continued)

S. No.	Earth abundant catalyst	Synthesis method	KOH concentration (M)	Overpotential (mV)[a]	Tafel slope (mV/dec)	References
7	NiCo-LDH@HOS/NS/NF	Hydrothermal	0.1	293	72	Xing et al. [84]
8	$NiPS_3$	–	1.0	437@20 mA/cm^2	73	Song et al. [72]
	$FePS_3$			–	419	
	$Ni_{0.95}Fe_{0.05}PS_3$			359@20 mA/cm^2	87	
	$Ni_{0.90}Fe_{0.10}PS_3$			329@20 mA/cm^2	69	
	$Ni_{0.85}Fe_{0.15}PS_3$			356@20 mA/cm^2	101	
9	$FeCo_2S_4$/NF/NS	Hydrothermal	0.1	270@50 mA/cm^2	59	Hu et al. [32]
	$FeCo_2O_4$/NF/NS			350@50 mA/cm^2	79	
10	3D $NiCoSe_2$/NF	Electrodeposition	1.0	183	97	Akbar et al. [3]
	NF			–	185	

[a] @10 mA/cm^2

N.B ZIF@LDH@NF-zeolitic imidazolate framework@layered double hydroxide@nickel foam; *LDH* layered double hydroxides; *NW* nanowire; *NF* nickel foam; *NS* nanosheets; *HOS* hydroxysulfide

$$O_2 + 2H_2O + 4e^- \rightarrow 4OH^- \quad (basic\ condition) \tag{21}$$

$$O_2 + 4H^+ + 4e^- \rightarrow 2H_2O \quad (acidic\ condition) \tag{22}$$

(B) **Two step two electron transfer path**

In this pathway, the two intermediate H_2O_2 and OOH are produced from oxygen reduction in acidic and alkaline condition, respectively (presented in Eqs. 23–26) [92, 97].

$$Acidic\ condition: O_2 + 4H^+ + 4e^- \rightarrow H_2O_2 \tag{23}$$

$$Acidic\ condition: H_2O_2 + 2H^+ + 4e^- \rightarrow 2H_2O \tag{24}$$

$$Basic\ condition: O_2 + H_2O + 2e^- \rightarrow OOH^- + OH^- \tag{25}$$

$$Basic\ condition: OOH^- + H_2O + 2e^- \rightarrow 3OH^- \tag{26}$$

Moreover, the two step two electrons pathway offered the lower onset potential than four electron transfer pathway. That is why, the two step two electrons have been used in fuel cells with high efficiency.

In this section, we have summarized few previously reported earth abundant electrocatalyst for ORR. In 2018, Xue et al. has developed cerium lanthanum carbide, $CeLa_2C_x$-NC for ORR in alkaline medium [88]. In 2018, Zhang et al. developed bamboo like nitrogen doped carbon nanotubes by simple single pyrolysis method for ORR [98]. They have found that oxygen has been reduced by four electron transfer pathways with smaller Tafel slope 57.5 mV/decade in comparison to standard commercial Pt/C i.e. 72.8 mV/decade. In 2015, Nguyen et al. has successfully synthesized cobalt phosphide, Co_2P and employed it as electrocatalyst for ORR [18]. In 2018, Xing et al. has successfully synthesized $[Mn_4V_4O_{17}(OAc)_3]_3$ developed on reduced graphene oxide by simple hydrothermal process and applied it as a bifunctional catalyst of OER and ORR [86]. They have found excellent performance of bifunctional catalyst towards ORR and HER with long period of durability [86]. They have also calculated the number of electrons required during the reduction of oxygen by Koutecky-Levich equation i.e. two to three, at all potentials. This information confirms that oxygen molecule can reduced via two step two electron pathway with the intermediate OOH^-. Zhao and Chen [101] has used carbon doped born nitride nanosheet as an electrocatalyst ORR and showed excellent performance [101]. In 2014, Ma et al. has successfully prepared sulfur doped graphene and used as an electrocatalyst for ORR and revealed excellent catalytic activity [58]. In 2016, Masud and Nath has developed durable, efficient Co_7Se_8 for ORR [61].

2.4 Role of EAEs Towards Carbon Dioxide Reduction Reaction

In the last few decades, the carbon dioxide reduction by electrocatalysis have been attracted attention of researchers owing to its used fuels and removing the harmful impact of CO_2. The oxidation sate of carbon atom in CO_2 is four i.e. stable. Therefore, the reduction of CO_2 demands large overpotential, due to stable oxidation state of carbon and presence of stable double bond of carbon oxygen [78]. The development of suitable efficient electrocatalysts have been required for the CO_2 reduction, although it is challenging. In this section we will summarize recently published earth abundant electrocatalyst for CO_2 reduction. The mechanism of CO_2 reduction in presence of catalyst consists of three steps. In first step, CO_2 molecules adsorbed on the catalyst surface, in second step electron and or proton transfer occurred followed by formation of intermediate and last step is the formation of different products after desorption from the catalyst surface. The formation of different products from CO_2 by reduction is shown in Eqs. (27–33) and each steps of CO_2 is described in Fig. 5 [17].

$$O_2C + 2H^+ + 2e^- \rightarrow HCOOH \tag{27}$$

$$O_2C + 2H^+ + 2e^- \rightarrow OC + OH_2 \tag{28}$$

$$O_2C + 4H^+ + 4e^- \rightarrow HCHO \tag{29}$$

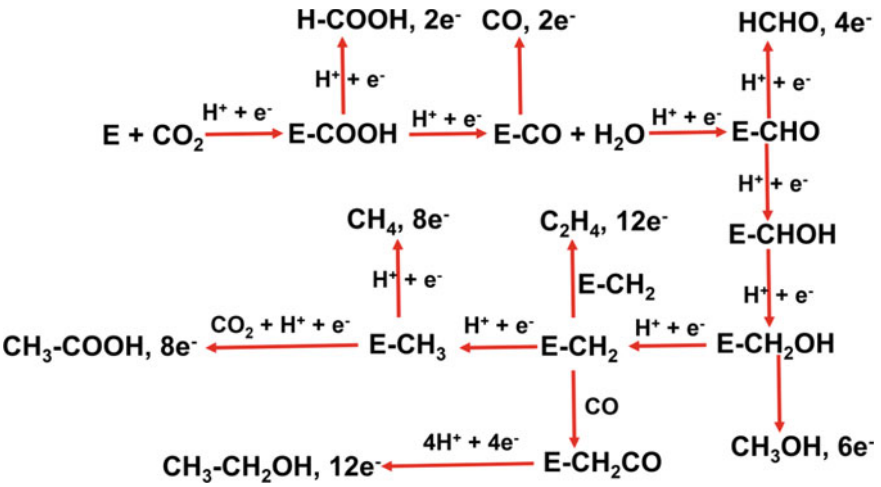

Fig. 5 Steps involved in carbon dioxide (CO_2) reduction reaction. Reproduced with permission taken from [17]

$$O_2C + 6H^+ + 6e^- \rightarrow H_3C - OH + OH_2 \quad (30)$$

$$O_2C + 8H^+ + 8e^- \rightarrow H_4C + OH_2 \quad (31)$$

$$2O_2C + 12H^+ + 12e^- \rightarrow H_5C_2 - OH + 3OH_2 \quad (32)$$

$$2O_2C + 12H^+ + 12e^- \rightarrow H_4C_2 + 4OH_2 \quad (33)$$

In 2018, Hu et al. has first time developed earth-abundant transition metal nitrogen doped porous carbon electrocatalysts (L–N–C, where L=Ni, Fe and Co) using silica template for the carbon dioxide to carbon monoxide [33]. They have found that electrocatalytic activity of nickel and iron, nitrogen doped carbon materials are high compared to cobalt with maximum faradic efficiency of 93%. In 2017, Gratzel and co-workers have successfully synthesized SnO_2 deposited on copper oxide, CuO and employed for the formation of CO from CO_2 with efficiency of 13.4% [68]. In 2014, earth abundant copper gold nanoalloys, $Cu_{63.9}Au_{36.1}$ on nanoporous copper films were prepared through electrodeposition method using copper films as a template for the reduction of CO_2 to CH_3–OH and C_2H_5–OH [35]. The prepared electrocatalyst offered excellent performance with faraday efficiency of 15.9 and 12.5% for methanol and ethanol, respectively. In 2014, Manthiram et al. has developed copper nanoparticles and employed it for the reduction of CO_2 to CH_4 [59]. They have found faraday efficiency of 80% at potential −1.25 V.

2.5 Role of EAEs Towards Nitrogen Reduction Reaction

Currently, reduction of N_2 by electrocatalysis using catalyst have become very popular. Nitrogen is one of the most abundant elements in atmosphere and most inert also [13, 70]. The production of ammonia from nitrogen by reduction has been widely used in fertilizer and industrial applications. The reduction of nitrogen is most difficult than the carbon dioxide reduction, due to presence of three covalent bond between nitrogen atoms, which have high bond energy of 941 kJ/mol and therefore very difficult to perform. For the reduction of nitrogen suitable electrocatalyst is must require and in order to develop the suitable electrocatalyst, earth abundant materials are found as good candidate [78].

The most accepted mechanism of nitrogen reduction contains associative and dissociative path [74]. Firstly, the nitrogen molecules are adsorbed on the catalyst surface and secondly the nitrogen adsorbed catalyst is dissociating the triple bond of N-N followed by hydrogenation. The mechanism of nitrogen reduction is shown in Fig. 6 [70]. As for example, production of ammonia from nitrogen in presence of iron catalyst at ambient temperature and pressure is called Haber Bosch process. In 2018, Shen et al. has first time used Fe_2O_3-carbon nanotube (CNT) as an electrocatalyst

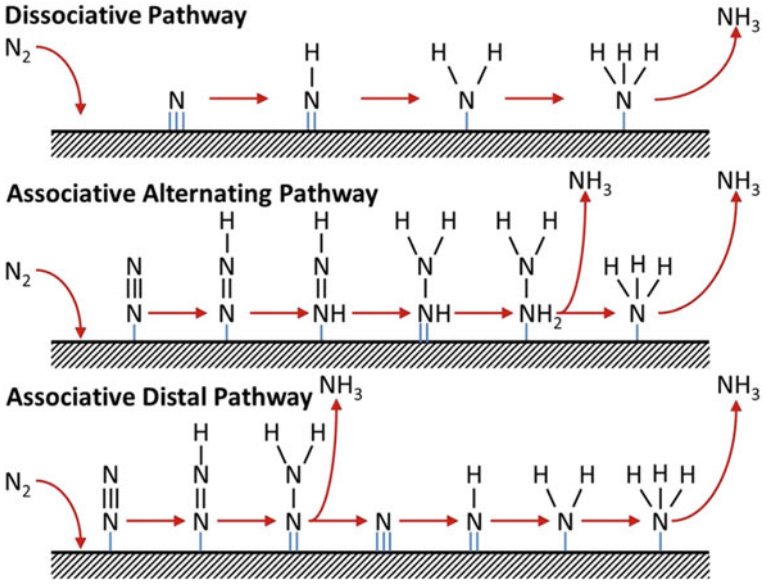

Fig. 6 Schematic illustration showing nitrogen (N_2) reduction reaction. Permission taken from [70]

for the preparation of ammonia from nitrogen reduction with Faraday efficiency of 95.1% [14]. Han and co-workers have developed nickel wire as an electrocatalyst and 0.1 M LiCl/ethylenediamine electrolyte for the reduction of nitrogen with Faraday efficiency of 17.2% [42]. This catalyst offered the ammonia with yield of 7.73×10^7 mol/L, after one hour of electrolysis at a cell voltage of 1800 mV. Li et al. has first time reported the ruthenium nanocluster on gallium nitride nanowires for the production of ammonia from nitrogen reduction [48]. In 2016, Kim et al. has employed a porous nickel foam and used it for nitrogen reduction with the solution of water and 2-propanol at ambient condition [41]. The reported electrocatalyst offered a current efficiency of 0.89% and a rate of 1.54×10^{11} mol/s and 0.5 mA/cm^2 of catalytic current for NH_3 production.

2.6 Role of EAEs in Detection of Toxic Elements

In recent time, the tremendous increase of the pollutants in the water resources has gained attention of scientists working in the field of clean water technology. Therefore, the detection of toxic elements in water samples have become very important. Electrochemical treatment has been one of the most important technique using earth abundant electrocatalyst. For instance, in 2019, Balasubramanian et al. has first time successfully prepared $CoMnO_3$ nanosheets through co-precipitation method

and used for the detection of 4-nitrophenol (4-NP) in water sample [8]. The prepared $CoMnO_3$ nanosheets electrocatalyst offered excellent electrocatalytic activity with large sensitivity of 2.458 $\mu A\ \mu M^{-1}\ cm^{-2}$, linear range up to 249 μM and low limit of detection (LOD) 10 nM. In 2015, Shahid et al. has first time synthesized different morphologies like nanowires, nanoflowers, nanobundles, nanocubes, and nanoplates of CO_3O_4 via facile hydrothermal technique and used for the detection or reduction of 4-NP through electrochemical process, where CO_3O_4 was used as an electrocatalyst [69]. They have observed that the nanocubes morphology offered remarkable catalytic performance for the detection or reduction of 4-NP with limit of detection (LOD) = 0.93 μM than other morphology. In 2014, Wu et al. has successfully synthesized α-MnO_2 nanotubes via facile hydrothermal process and studied for the detection of 4-NP [79]. The prepared catalyst has shown remarkable performance with great sensitivity of 19.18 $mA\ mM^{-1}\ cm^{-2}$ and LOD of 0.1 mM.

2.7 *Role of EAEs in Proton Exchange Membrane (PEM)*

Fuel cell is one type of electrochemical devices, which can played the hydrogen energy source coming from fuel is converted into the electrical energy using atmospheric oxygen as an oxidant. Fuel cells are largely depends on the electrolyte and it can be classified according to the electrolyte. The typical design of fuel cell is depicted in Fig. 7. In 1960, proton exchange membrane for water electrolysis (PEM WE) or polymer electrolyte membrane was first time developed [26, 27, 67, 105]. Among them only proton-exchange membrane (PEM) fuel cell is widely used. Due to the use of quasi solid electrolyte, PEM fuel cell has gained more attraction. It is used in transportation and portable power application etc. PEM fuel cells have some advantages like can be operated at low temperature to high temperature i.e. 90 °C, have compact design, and easy in operation. In the fuel cell, the key role of membrane is to carry the proton or hydrogen ion from anode to cathode. The fuel and

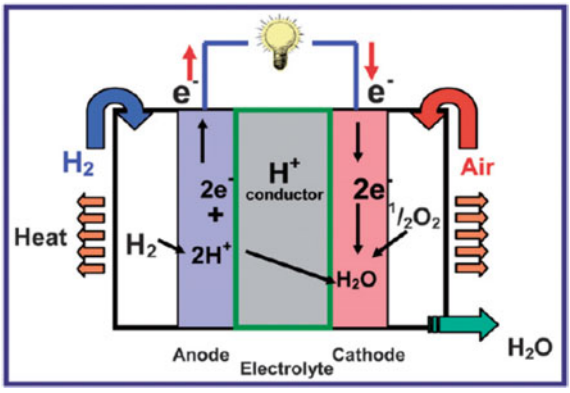

Fig. 7 Schematic representation of proton exchange membrane (PEM) based fuel cell. Taken from [105]

oxidant are provided from external devices and the system is continued until the fuel or oxidants get exhausted. The schematic representation of proton exchange membrane (PEM) fuel cells is depicted in Fig. 7. At anode the hydrogen obtained from fuel is decomposed to form positively charged H^+ and negatively charge electron, followed by the H^+ ion passage via the polymer electrolyte membrane to the cathode of the fuel cell. At cathode, H^+ combines with reduced oxygen to form H_2O as a byproduct. Moreover, the decomposition of hydrogen required a suitable catalyst, on the other hand the decomposition of strongly bonded oxygen or reduction of oxygen is too difficult. Till date, platinum is the best catalyst but it have some limitation like low abundance, high cost and scarcity. Therefore, worldwide researcher tries to investigate the alternative way or catalysts in place of platinum.

Earth abundant materials are the effective materials to carry out the above mentioned electrochemical reaction (ORR) with high electrocatlytic activity. As we know, earth abundant electrocatlysts have numerous benefits like inexpensive, high activity, high abundance and non-toxicity. For instance, in 2018, Li et al. have first time synthesized Mn–N–C via two step doping adsorption technique for ORR in fuel cells [49]. They have studied the mechanism of ORR and found oxygen is reduced via four electrons transfer pathway.

3 Conclusion and Future Prospects

In this chapter, we have summarized the role of electrocatalyst specially earth abundant electrocatalyst in the various field like energy storage and conversion, detection of toxic elements etc. The earth abundant electrocatalyst plays key role with remarkable electrocatalytic performance and long term stability. Earth abundant materials used as electrocatalysts have some advantages over the novel metal electrocatalysts, because earth abundant materials are inexpensive, have high electrical conductivity, non-toxic in nature, most abundant and possess large biocompatibility. Now a day's, wide number of earth abundant electrocatlysts have been synthesized through different synthesis strategies. The catalytic activity of earth abundant materials depends on following properties, which are summarized below. Electrocatalytic activity of earth abundant materials are largely depends on their:

(A) Composition;
(B) Shape or morphology;
(C) Size of the particles;
(D) Covalent or ionic nature;
(E) Preparation method used for the synthesis;
(F) Synthesis condition like temperature, nature of the solvent etc.

Although the earth abundant materials exhibited remarkable electrocatalytic performance but they needs some modifications in future to improve their electrocatalytic activity. For example, the stability of the catalyst is not so good, therefore the development of some potent stabilizer or stabilizing agents are strongly needed to

improve their electrocatalytic activity. Adding some doping agent may also enhance their catalytic activity. For instance bimetallic earth abundant nano-electrocatalysts have large electrocatalytic activity than the monometallic electrocatalysts. Moreover, constant studies are very much required for the improvement of more efficient and stable earth abundant electrocatalysts with wider and practical applications.

Author Declaration Mr. Majhi has given the major contribution in writing this book chapter along with drawing the Figures and Tables, taking the copyright permission etc.

References

1. Abbas MA, Bang JH (2015) Rising again: opportunities and challenges for platinum-free electrocatalysts. Chem Mater 27(21):7218–7235
2. Abdullah MI, Hameed A, Zhang N, Ma M (2019) Nickel doped cobalt-hollow nanoparticles as an efficient electrocatalyst for hydrogen evolution from neutral water. Int J Hydrog Energy
3. Akbar K, Jeon JH, Kim M, Jeong J, Yi Y, Chun SH (2018) Bifunctional electrodeposited 3D $NiCoSe_2$/nickle foam electrocatalysts for its applications in enhanced oxygen evolution reaction and for hydrazine oxidation. ACS Sustain Chem Eng 6(6):7735–7742
4. Ali Y, Nguyen VT, Nguyen NA, Shin S, Choi HS (2019) Transition-metal-based NiCoS/C-dot nanoflower as a stable electrocatalyst for hydrogen evolution reaction. Int J Hydrogen Energy 44(16):8214–8222
5. Appel AM, Bercaw JE, Bocarsly AB, Dobbek H, DuBois DL, Dupuis M, Ferry JG, Fujita E, Hille R, Kenis PJ, Kerfeld CA (2013) Frontiers, opportunities, and challenges in biochemical and chemical catalysis of CO_2 fixation. Chem Rev 113(8):6621–6658
6. Babar PT, Lokhande AC, Gang MG, Pawar BS, Pawar SM, Kim JH (2018) Thermally oxidized porous NiO as an efficient oxygen evolution reaction (OER) electrocatalyst for electrochemical water splitting application. J Ind Eng Chem 60:493–497
7. Bai L, Wen X, Guan J (2019) Amorphous FeCoNi oxide for oxygen evolution reaction. Mater Today Energy 12:311–317
8. Balasubramanian P, Balamurugan TST, Chen SM, Chen TW (2019) Simplistic synthesis of ultrafine $CoMnO_3$ nanosheets: an excellent electrocatalyst for highly sensitive detection of toxic 4-nitrophenol in environmental water samples. J Hazard Mater 361:123–133
9. Bayatsarmadi B, Zheng Y, Russo V, Ge L, Casari CS, Qiao SZ (2016) Highly active nickel–cobalt/nanocarbon thin films as efficient water splitting electrodes. Nanoscale 8(43):18507–18515
10. Cai C, Mi Y, Han S, Wang Q, Liu W, Wu X, Zheng Z, Xia X, Qiao L, Zhou W, Zu X (2019) Engineering ordered dendrite-like nickel selenide as electrocatalyst. Electrochim Acta 295:92–98
11. Callejas JF, Read CG, Popczun EJ, McEnaney JM, Schaak RE (2015) Nanostructured Co_2P electrocatalyst for the hydrogen evolution reaction and direct comparison with morphologically equivalent CoP. Chem Mater 27(10):3769–3774
12. Cao J, Zhou J, Zhang Y, Wang Y, Liu X (2018) Dominating role of aligned MoS_2/Ni_3S_2 nanoarrays supported on three-dimensional Ni foam with hydrophilic interface for highly enhanced hydrogen evolution reaction. ACS Appl Mater Interfaces 10(2):1752–1760
13. Cao N, Zheng G (2018) Aqueous electrocatalytic N_2 reduction under ambient conditions. Nano Res 11(6):2992–3008
14. Chen S, Perathoner S, Ampelli C, Mebrahtu C, Su D, Centi G (2017) Electrocatalytic synthesis of ammonia at room temperature and atmospheric pressure from water and nitrogen on a carbon-nanotube-based electrocatalyst. Angew Chem Int Ed 56(10):2699–2703

15. Chen Z, Higgins D, Chen Z (2010) Nitrogen doped carbon nanotubes and their impact on the oxygen reduction reaction in fuel cells. Carbon 48(11):3057–3065
16. Conti J, Holtberg P, Diefenderfer J, LaRose A, Turnure JT, Westfall L (2016) International energy outlook 2016 with projections to 2040 (No. DOE/EIA-0484 (2016)). USDOE Energy Information Administration (EIA), Washington, DC, USA. Office of Energy Analysis
17. Cui H, Guo Y, Guo L, Wang L, Zhou Z, Peng Z (2018) Heteroatom-doped carbon materials and their composites as electrocatalysts for CO_2 reduction. J Mater Chem A 6(39):18782–18793
18. Doan-Nguyen VV, Zhang S, Trigg EB, Agarwal R, Li J, Su D, Winey KI, Murray CB (2015) Synthesis and X-ray characterization of cobalt phosphide (Co_2P) nanorods for the oxygen reduction reaction. ACS Nano 9(8):8108–8115
19. Dong Y, Hu M, Zhang Z, Zapien JA, Wang X, Lee JM (2018) Hierarchical self-assembled Bi 2 S 3 hollow nanotubes coated with sulfur-doped amorphous carbon as advanced anode materials for lithium ion batteries. Nanoscale 10(28):13343–13350
20. Dong Y, Yang S, Zhang Z, Lee JM, Zapien JA (2018) Enhanced electrochemical performance of lithium ion batteries using Sb_2S_3 nanorods wrapped in graphene nanosheets as anode materials. Nanoscale 10(7):3159–3165
21. Faber MS, Lukowski MA, Ding Q, Kaiser NS, Jin S (2014) Earth-abundant metal pyrites (FeS_2, CoS_2, NiS_2, and their alloys) for highly efficient hydrogen evolution and polysulfide reduction electrocatalysis. J Phys Chem C 118(37):21347–21356
22. Fu G, Lee JM (2019) Ternary metal sulfides for electrocatalytic energy conversion. J Mater Chem A 7(16):9386–9405
23. Fu G, Jiang X, Chen Y, Xu L, Sun D, Lee JM, Tang Y (2018) Robust bifunctional oxygen electrocatalyst with a "rigid and flexible" structure for air-cathodes. NPG Asia Mater 10(7):618
24. Fu G, Yan X, Chen Y, Xu L, Sun D, Lee JM, Tang Y (2018) Boosting bifunctional oxygen electrocatalysis with 3D graphene aerogel-supported Ni/MnO particles. Adv Mater 30(5):1704609
25. Gong Y, Pan H, Xu Z, Yang Z, Lin Y, Wang J (2018) Crossed $FeCo_2S_4$ nanosheet arrays grown on 3D nickel foam as high-efficient electrocatalyst for overall water splitting. Int J Hydrogen Energy 43(36):17259–17264
26. Grubb WT, Niedrach LW (1960) Batteries with Solid Ion-exchange membrane electrolytes II. Low-temperature hydrogen-oxygen fuel cells. J Electrochem Soc 107(2):131–135
27. Grubb WT (1959) Batteries with solid ion exchange electrolytes I. Secondary cells employing metal electrodes. J Electrochem Soc 106(4):275–278
28. Guo P, Wu YX, Lau WM, Liu H, Liu LM (2017) CoS nanosheet arrays grown on nickel foam as an excellent OER catalyst. J Alloy Compd 723:772–778
29. He C, Bo T, Wang B, Tao J (2019) RGO induced one-dimensional bimetallic carbide nanorods: an efficient and pH-universal hydrogen evolution reaction electrocatalyst. Nano Energy
30. Hong WT, Risch M, Stoerzinger KA, Grimaud A, Suntivich J, Shao-Horn Y (2015) Toward the rational design of non-precious transition metal oxides for oxygen electrocatalysis. Energy Environ Sci 8(5):1404–1427
31. Hou W, He J, Yu B, Lu Y, Zhang W, Chen Y (2018) One-pot synthesis of graphene-wrapped $NiSe_2Ni_{0.85}Se$ hollow microspheres as superior and stable electrocatalyst for hydrogen evolution reaction. Electrochim Acta 291:242–248
32. Hu J, Ou Y, Li Y, Gao D, Zhang Y, Xiao P (2018) $FeCo_2S_4$ nanosheet arrays supported on Ni foam: an efficient and durable bifunctional electrocatalyst for overall water-splitting. ACS Sustain Chem Eng 6(9):11724–11733
33. Hu XM, Hval HH, Bjerglund ET, Dalgaard KJ, Madsen MR, Pohl MM, Welter E, Lamagni P, Buhl KB, Bremholm M, Beller M (2018) Selective CO_2 reduction to CO in water using earth-abundant metal and nitrogen-doped carbon electrocatalysts. ACS Catal 8(7):6255–6264
34. Jayabal S, Saranya G, Wu J, Liu Y, Geng D, Meng X (2017) Understanding the high-electrocatalytic performance of two-dimensional MoS_2 nanosheets and their composite materials. J Mater Chem A 5(47):24540–24563

35. Jia F, Yu X, Zhang L (2014) Enhanced selectivity for the electrochemical reduction of CO_2 to alcohols in aqueous solution with nanostructured Cu–Au alloy as catalyst. J Power Sources 252:85–89
36. Jiang D, Xu Y, Yang R, Li D, Meng S, Chen M (2019) CoP_3/CoMoP heterogeneous nanosheet arrays as robust electrocatalyst for pH-universal hydrogen evolution reaction. ACS Sustain Chem Eng
37. Jiang N, You B, Sheng M, Sun Y (2016) Bifunctionality and mechanism of electrodeposited nickel–phosphorous films for efficient overall water splitting. ChemCatChem 8(1):106–112
38. Jiao Y, Zheng Y, Jaroniec M, Qiao SZ (2015) Design of electrocatalysts for oxygen-and hydrogen-involving energy conversion reactions. Chem Soc Rev 44(8):2060–2086
39. Kargar A, Yavuz S, Kim TK, Liu CH, Kuru C, Rustomji CS, Jin S, Bandaru PR (2015) Solution-processed $CoFe_2O_4$ nanoparticles on 3D carbon fiber papers for durable oxygen evolution reaction. ACS Appl Mater Interfaces 7(32):17851–17856
40. Kibsgaard J, Jaramillo TF (2014) Molybdenum phosphosulfide: an active, acid-stable, earth-abundant catalyst for the hydrogen evolution reaction. Angew Chem Int Ed 53(52):14433–14437
41. Kim K, Lee N, Yoo CY, Kim JN, Yoon HC, Han JI (2016) Communication—electrochemical reduction of nitrogen to ammonia in 2-propanol under ambient temperature and pressure. J Electrochem Soc 163(7):F610–F612
42. Kim K, Yoo CY, Kim JN, Yoon HC, Han JI (2016) Electrochemical synthesis of ammonia from water and nitrogen in ethylenediamine under ambient temperature and pressure. J Electrochem Soc 163(14):F1523–F1526
43. Kulkarni P, Nataraj SK, Balakrishna RG, Nagaraju DH, Reddy MV (2017) Nanostructured binary and ternary metal sulfides: synthesis methods and their application in energy conversion and storage devices. J Mater Chem A 5(42):22040–22094
44. Lee J, Jeong B, Ocon JD (2013) Oxygen electrocatalysis in chemical energy conversion and storage technologies. Curr Appl Phys 13(2):309–321
45. Li A, Sun Y, Yao T, Han H (2018) Earth-abundant transition-metal-based electrocatalysts for water electrolysis to produce renewable hydrogen. Chem A Eur J 24(69):18334–18355
46. Li H, Tsai C, Koh AL, Cai L, Contryman AW, Fragapane AH, Zhao J, Han HS, Manoharan HC, Abild-Pedersen F, Norskov JK (2016) Activating and optimizing MoS_2 basal planes for hydrogen evolution through the formation of strained sulphur vacancies. Nat Mater 15(1):48
47. Li J, Hong W, Jian C, Cai Q, Liu W (2019) Seamless tungsten disulfide-tungsten heterojunction with abundant exposed active sites for efficient hydrogen evolution. Appl Catal B 244:320–326
48. Li L, Wang Y, Vanka S, Mu X, Mi Z, Li CJ (2017) Nitrogen photofixation over III-nitride nanowires assisted by ruthenium clusters of low atomicity. Angew Chem Int Ed 56(30):8701–8705
49. Li J, Chen M, Cullen DA, Hwang S, Wang M, Li B, Liu K, Karakalos S, Lucero M, Zhang H, Lei C (2018) Atomically dispersed manganese catalysts for oxygen reduction in proton-exchange membrane fuel cells. Nat Catal 1(12):935
50. Liang Y, Liu Q, Luo Y, Sun X, He Y, Asiri AM (2016) $Zn_{0.76}Co_{0.24}S/CoS_2$ nanowires array for efficient electrochemical splitting of water. Electrochim Acta 190:360–364
51. Lin X, Zhou J, Zheng D, Guan C, Xiao G, Chen N, Liu Q, Bao H, Wang JQ (2019) Rational synthesis of $CaCo_2O_4$ nanoplate as an earth-abundant electrocatalyst for oxygen evolution reaction. J Energy Chem 31:125–131
52. Liu P, Ali RN, Li J, Hu G, Zhu X, Lu Y, Xiang B (2019) Self-reconstruction in 2D nickel thiophosphate nanosheets to boost oxygen evolution reaction. Appl Surf Sci 484:54–61
53. Liu PF, Yang S, Zhang B, Yang HG (2016) Defect-rich ultrathin cobalt–iron layered double hydroxide for electrochemical overall water splitting. ACS Appl Mater Interfaces 8(50):34474–34481
54. Liu Z, Yuan C, Teng F (2019) Crystal facets-predominated oxygen evolution reaction activity of earth abundant $CoMoO_4$ electrocatalyst. J Alloy Compd 781:460–466
55. Lu Y, Hou W, Yang D, Chen Y (2019) CoP nanosheets in-situ grown on N-doped graphene as an efficient and stable bifunctional electrocatalyst for hydrogen and oxygen evolution reactions. Electrochim Acta 307:543–552

56. Lubitz W, Tumas W (2007) Hydrogen: an overview
57. Lukowski MA, Daniel AS, English CR, Meng F, Forticaux A, Hamers RJ, Jin S (2014) Highly active hydrogen evolution catalysis from metallic WS_2 nanosheets. Energy Environ Sci 7(8):2608–2613
58. Ma Z, Dou S, Shen A, Tao L, Dai L, Wang S (2015) Sulfur-doped graphene derived from cycled lithium-sulfur batteries as a metal-free electrocatalyst for the oxygen reduction reaction. Angew Chem Int Ed 54(6):1888–1892
59. Manthiram K, Beberwyck BJ, Alivisatos AP (2014) Enhanced electrochemical methanation of carbon dioxide with a dispersible nanoscale copper catalyst. J Am Chem Soc 136(38):13319–13325
60. Marje SJ, Katkar PK, Kale SB, Lokhande AC, Lokhande CD, Patil UM (2019) Effect of phosphate variation on morphology and electrocatalytic activity (OER) of hydrous nickel pyrophosphate thin films. J Alloy Compd 779:49–58
61. Masud J, Nath M (2016) Co_7Se_8 nanostructures as catalysts for oxygen reduction reaction with high methanol tolerance. ACS Energy Lett 1(1):27–31
62. McKone JR, Lewis NS, Gray HB (2013) Will solar-driven water-splitting devices see the light of day? Chem Mater 26(1):407–414
63. Nsanzimana JMV, Peng Y, Xu YY, Thia L, Wang C, Xia BY, Wang X (2018) An efficient and earth-abundant oxygen-evolving electrocatalyst based on amorphous metal borides. Adv Energy Mater 8(1):1701475
64. Popczun EJ, McKone JR, Read CG, Biacchi AJ, Wiltrout AM, Lewis NS, Schaak RE (2013) Nanostructured nickel phosphide as an electrocatalyst for the hydrogen evolution reaction. J Am Chem Soc 135(25):9267–9270
65. Qi F, Wang X, Zheng B, Chen Y, Yu B, Zhou J, He J, Li P, Zhang W, Li Y (2017) Self-assembled chrysanthemum-like microspheres constructed by few-layer $ReSe_2$ nanosheets as a highly efficient and stable electrocatalyst for hydrogen evolution reaction. Electrochim Acta 224:593–599
66. Roy SC, Varghese OK, Paulose M, Grimes CA (2010) Toward solar fuels: photocatalytic conversion of carbon dioxide to hydrocarbons. ACS Nano 4(3):1259–1278
67. Russell JH, Nuttall LJ, Fickett AP (1973) Hydrogen generation by solid polymer electrolyte water electrolysis. Am Chem Soc Div Fuel Chem Prepr 18:24–40
68. Schreier M, Heroguel F, Steier L, Ahmad S, Luterbacher JS, Mayer MT, Luo J, Gratzel M (2017) Solar conversion of CO_2 to CO using Earth-abundant electrocatalysts prepared by atomic layer modification of CuO. Nat Energy 2(7):17087
69. Shahid MM, Rameshkumar P, Huang NM (2015) Morphology dependent electrocatalytic properties of hydrothermally synthesized cobalt oxide nanostructures. Ceram Int 41(10):13210–13217
70. Shipman MA, Symes MD (2017) Recent progress towards the electrosynthesis of ammonia from sustainable resources. Catal Today 286:57–68
71. Sivanantham A, Ganesan P, Shanmugam S (2016) Hierarchical $NiCo_2S_4$ nanowire arrays supported on Ni foam: an efficient and durable bifunctional electrocatalyst for oxygen and hydrogen evolution reactions. Adv Func Mater 26(26):4661–4672
72. Song B, Li K, Yin Y, Wu T, Dang L, Cabaan-Acevedo M, Han J, Gao T, Wang X, Zhang Z, Schmidt JR (2017) Tuning mixed nickel iron phosphosulfide nanosheet electrocatalysts for enhanced hydrogen and oxygen evolution. ACS Catal 7(12):8549–8557
73. Stamenkovic VR, Strmcnik D, Lopes PP, Markovic NM (2017) Energy and fuels from electrochemical interfaces. Nat Mater 16(1):57
74. Tang Y, Fang X, Zhang X, Fernandes G, Yan Y, Yan D, Xiang X, He J (2017) Space-confined earth-abundant bifunctional electrocatalyst for high-efficiency water splitting. ACS Appl Mater Interfaces 9(42):36762–36771
75. Tian J, Liu Q, Asiri AM, Sun X (2014) Self-supported nanoporous cobalt phosphide nanowire arrays: an efficient 3D hydrogen-evolving cathode over the wide range of pH 0–14. J Am Chem Soc 136(21):7587–7590

76. Tran DT, Le HT, Kim NH, Lee JH (2019) Hierarchically porous nickel-cobalt phosphide nanoneedle arrays loaded micro-carbon spheres as an advanced electrocatalyst for overall water splitting application. Appl Catal B Environ
77. Tran PD, Nguyen M, Pramana SS, Bhattacharjee A, Chiam SY, Fize J, Field MJ, Artero V, Wong LH, Loo J, Barber J (2012) Copper molybdenum sulfide: a new efficient electrocatalyst for hydrogen production from water. Energy Environ Sci 5(10):8912–8916
78. Wang Q, Lei Y, Wang D, Li Y (2019) Defect engineering in earth-abundant electrocatalysts for CO_2 and N_2 reduction. Energy Environ Sci
79. Wu J, Wang Q, Umar A, Sun S, Huang L, Wang J, Gao Y (2014) Highly sensitive p-nitrophenol chemical sensor based on crystalline α-MnO_2 nanotubes. New J Chem 38(9):4420–4426
80. Wu T, Stone ML, Shearer MJ, Stolt MJ, Guzei IA, Hamers RJ, Lu R, Deng K, Jin S, Schmidt JR (2018) Crystallographic facet dependence of the hydrogen evolution reaction on CoPS: theory and experiments. ACS Catal 8(2):1143–1152
81. Wu Y, Gao Y, He H, Zhang P (2019) Novel electrocatalyst of nickel sulfide boron coating for hydrogen evolution reaction in alkaline solution. Appl Surf Sci
82. Wu Z, Li X, Liu W, Zhong Y, Gan Q, Li X, Wang H (2017) Materials chemistry of iron phosphosulfide nanoparticles: synthesis, solid state chemistry, surface structure, and electrocatalysis for the hydrogen evolution reaction. ACS Catal 7(6):4026–4032
83. Xia B, Yan Y, Wang X, Lou XWD (2014) Recent progress on graphene-based hybrid electrocatalysts. Mater Horiz 1(4):379–399
84. Xiang K, Guo J, Xu J, Qu T, Zhang Y, Chen S, Hao P, Li M, Xie M, Guo X, Ding W (2018) Surface sulfurization of NiCo-layered double hydroxide nanosheets enable superior and durable oxygen evolution electrocatalysis. ACS Appl Energy Mater 1(8):4040–4049
85. Xiao P, Sk MA, Thia L, Ge X, Lim RJ, Wang JY, Lim KH, Wang X (2014) Molybdenum phosphide as an efficient electrocatalyst for the hydrogen evolution reaction. Energy Environ Sci 7(8):2624–2629
86. Xing X, Liu R, Cao K, Kaiser U, Zhang G, Streb C (2018) Manganese vanadium oxide–N-doped reduced graphene oxide composites as oxygen reduction and oxygen evolution electrocatalysts. ACS Appl Mater Interfaces 10(51):44511–44517
87. Xu Y, Xie L, Li D, Yang R, Jiang D, Chen M (2018) Engineering $Ni(OH)_2$ nanosheet on $CoMoO_4$ nanoplate array as efficient electrocatalyst for oxygen evolution reaction. ACS Sustain Chem Eng 6(12):16086–16095
88. Xue S, Wang W, Song J, Tao P, Wang P, Lei Z (2018) Facile fabricate stable rare-earth bimetallic carbide as electrocatalyst for active oxygen reduction reaction. J Taiwan Inst Chem Eng 84:93–100
89. Yang L, Zeng L, Liu H, Deng Y, Zhou Z, Yu J, Liu H, Zhou W (2019) Hierarchical microsphere of MoNi porous nanosheets as electrocatalyst and cocatalyst for hydrogen evolution reaction. Appl Catal B 249:98–105
90. Yu B, Hu Y, Qi F, Wang X, Zheng B, Liu K, Zhang W, Li Y, Chen Y (2017) Nanocrystalline $Ni_{0.85}Se$ as efficient non-noble-metal electrocatalyst for hydrogen evolution reaction. Electrochim Acta 242:25–30
91. Yu B, Qi F, Zheng B, Zhou J, Chen Y (2018) One-pot synthesis of self-assembled coral-like hierarchical architecture constructed by polymorphic $CoSe_2$ nanocrystals as superior electrocatalyst for hydrogen evolution reaction. Electrochim Acta 277:161–167
92. Yu L, Pan X, Cao X, Hu P, Bao X (2011) Oxygen reduction reaction mechanism on nitrogen-doped graphene: a density functional theory study. J Catal 282(1):183–190
93. Yu L, Xia BY, Wang X, Lou XW (2016) General formation of M-MoS_3 (M=Co, Ni) hollow structures with enhanced electrocatalytic activity for hydrogen evolution. Adv Mater 28(1):92–97
94. Zhang C, Hao R, Liao H, Hou Y (2013) Synthesis of amino-functionalized graphene as metal-free catalyst and exploration of the roles of various nitrogen states in oxygen reduction reaction. Nano Energy 2(1):88–97
95. Zhang H, Li Y, Xu T, Wang J, Huo Z, Wan P, Sun X (2015) Amorphous Co-doped MoS_2 nanosheet coated metallic CoS_2 nanocubes as an excellent electrocatalyst for hydrogen evolution. J Mater Chem A 3(29):15020–15023

96. Zhang H, Yang B, Wu X, Li Z, Lei L, Zhang X (2015) Polymorphic $CoSe_2$ with mixed orthorhombic and cubic phases for highly efficient hydrogen evolution reaction. ACS Appl Mater Interfaces 7(3):1772–1779
97. Zhang L, Xia Z (2011) Mechanisms of oxygen reduction reaction on nitrogen-doped graphene for fuel cells. J Phys Chem C 115(22):11170–11176
98. Zhang M, Gao J, Hong W, Wang X, Tian Q, An Z, Wang L, Yao H, Liu Y, Zhao X, Qiu H (2019) Bimetallic Mn and Co encased within bamboo-like N-doped carbon nanotubes as efficient oxygen reduction reaction electrocatalysts. J Colloid Interface Sci 537:238–246
99. Zhang X, Si C, Guo X, Kong R, Qu F (2017) A $MnCo_2S_4$ nanowire array as an earth-abundant electrocatalyst for an efficient oxygen evolution reaction under alkaline conditions. J Mater Chem A 5(33):17211–17215
100. Zhang Y, Zhou Q, Zhu J, Yan Q, Dou SX, Sun W (2017) Nanostructured metal chalcogenides for energy storage and electrocatalysis. Adv Funct Mater 27(35):1702317
101. Zhao J, Chen Z (2015) Carbon-doped boron nitride nanosheet: an efficient metal-free electrocatalyst for the oxygen reduction reaction. J Phys Chem C 119(47):26348–26354
102. Zhou H, Yu F, Liu Y, Sun J, Zhu Z, He R, Bao J, Goddard WA, Chen S, Ren Z (2017) Outstanding hydrogen evolution reaction catalyzed by porous nickel diselenide electrocatalysts. Energy Environ Sci 10(6):1487–1492
103. Zinola CF, Martins ME, Tejera EP, Neves NP (2012) Electrocatalysis: fundamentals and applications. Int J Electrochem 2012
104. Zou X, Zhang Y (2015) Noble metal-free hydrogen evolution catalysts for water splitting. Chem Soc Rev 44(15):5148–5180
105. Zuo Z, Fu Y, Manthiram A (2012) Novel blend membranes based on acid-base interactions for fuel cells. Polymers 4(4):1627–1644

Metal–Organic Frameworks for Electrocatalysis

Muhammad Usman and Qi-Long Zhu

Abstract Metal–organic frameworks (MOFs) have recently become prospective materials for electrocatalysis. MOFs constructed via coordination chemistry of inorganic metal nodes and organic ligands, possess the exclusive features over traditional inorganic or organic materials, which include ultrahigh porosity, large surface areas, structural tunability and high stability. Based on these features, MOFs are already being applied in storage and separation, catalysis, optoelectronics, drug delivery and biomedical imaging. Particularly, with the advantageous feature, MOFs have potential to work as efficient electrocatalysts for a variety of redox reactions, such as hydrogen evolution reaction (HER), oxygen reduction reaction (ORR), oxygen evolution reaction (OER), etc. In this chapter, a discussion has been presented on MOFs, their composites, MOF-derived carbon materials and their performance as electrocatalysts. This chapter will inspire new research direction regarding the development of advanced electrocatalytic materials using MOFs.

Keywords Metal–organic frameworks · Coordination polymers · Electrocatalysts · Electrochemistry

Abbreviations

HER	Hydrogen evolution reaction
OER	Oxygen evolution reaction
ORR	Oxygen reduction reaction
CO_2RR	Carbon dioxide reduction reaction
MOFs	Metal–organic frameworks
PCPs	Porous coordination polymers
ZIFs	Zeolitic imidazolate frameworks
CPE	Controlled-potential electrolysis

M. Usman · Q.-L. Zhu (✉)
State Key Laboratory of Structural Chemistry, Fujian Institute of Research on the Structure of Matter (FJIRSM), Chinese Academy of Sciences (CAS), Fuzhou 350002, China
e-mail: qlzhu@fjirsm.ac.cn

Inamuddin et al. (eds.), *Methods for Electrocatalysis*,
https://doi.org/10.1007/978-3-030-27161-9_2

DMF	Dimethylformamide
DEF	Diethylformamide
GC	Glassy carbon
CV	Cyclic voltammetry
TS	Tafel slope
TON	Turnover number
BHT	Benzenehexathiol
TOF	Turnover frequency
MoS_X	Molybdenum polysulfide
POMs	Poly oxometalates
OFP	Open-framework polyoxometalate
POMOFs	POM-based metal-organic frameworks
TBA	Tetrabutylammonium ion
BDC	1,4-benzene-dicarboxylate
BTB	Benzenetribenzoate
BTC	1,3,5-benzenetricarboxylate
H_4dcpa	4,5-di(4′-carboxylphenyl)phthalic acid
azene	(*E*)-1,2-di(pyridin-4-yl)diazene
4,4′-bpy	4,4′-bipyridine
2,2′-bpy	2,2′-bipyridine
H_2adip	Adipic acid
5-H_2bdc	5-nitroisophthalic acid
Im	Imidazolate
mim	2-methylimidazolate
bim	Benzimidazolate
H_2bbta	1H,5H-benzo(1,2-d:4,5-d′)bistriazole
H_2TCPP	4,4′,4″,4‴-(porphyrin-5,10,15,20-tetrayl)tetrabenzoate
BHT	Benzenehexathiol
tht	Triphenylene-2,3,6,7,10,11-hexathiolate
HITP	2,3,6,7,10,11-hexaiminotriphenylene
tpy	2,2′:6′,2″-terpyridine
H_2dcbpy	2,2′-bipyridine-5,5′-dicarboxylic acid
H_2bpdc	4,4′-biphenyldicarboxylic acid
ade	Adenine
TBA	Tetrabutylammonium
BPT	[1,1′-biphenyl]-3,4′,5-tricarboxylate
trim	1,3,5-benzenetricarboxylate
biphen	4,4′-biphenyldicarboxylate
tbapy	1,3,6,8-tetrakis (p-benzoate) pyrene
Ted	Triethylene-diamine
PB	Phosphate buffer
FTO	Fluorine-doped tin oxide
NF	Nickel form
NFF	NiFe alloy foam
GO	Graphene oxide

GA	Graphene aerogel
CNTs	Carbon nanotubes
NPs	Nanoparticles
NGO	Nitrogen-doped graphene oxide
DHT	Dihydroxyterephthalate
RDE	Rotating-disk electrode
NCNHP	N-doped carbon hollow polyhedron
LDH	Layered double hydroxide
SURMOF	Surface-mounted metal–organic framework
SURMOFD	Surface-mounted metal–organic frameworks derivative

1 Introduction of Metal–Organic Frameworks (MOFs)

Metal–organic frameworks (MOFs) are constructed through coordination bonds via highly organized metal nodes and organic linkers, [1] which results into the formation of highly-order crystalline frameworks with ultrahigh porosity, large surface areas, unique host-guest dynamics, thermal stability and mechanical flexibility, etc. [2]. Owing to these structural and functional properties, MOFs have been widely used for many applications such as storage and separation, water purification, optoelectronics, proton conduction, dielectrics, drug delivery, chemical sensors and biomedical applications [3, 4]. Beside these traditional applications, there is a huge scope for utilization of MOFs into wider industrial applications. Generally, MOFs are constructed through self-assembly of metal nodes/clusters and organic ligands in certain solvents as shown in Fig. 1 [5], forming one-, two- and three-dimensional periodic frameworks with permanent porosity. The structural geometry of MOFs depends upon the coordination numbers and orientation of binding sites of metal and the organic ligands as demonstrated in Fig. 2 [6, 7]. For example, a hexagonal diamondoid network will be formed from linear bifunctional ligands via coordination with metal nodes of tetrahedral geometry. Similarly, a octahedral network will be generated from the metal nodes with octahedral geometry [8].

With their ultrahigh surface areas of more than even 10,000 $m^2\ g^{-1}$ and pore sizes of greater than 10 nm, MOFs are regarded as superior materials than the commercially available porous materials like activated carbon [8–10]. For instance, the isoreticular series of MOF-74, which are constructed with numbers of phenylene rings (I) as linkers, have the pore apertures of up to 98 angstroms (IRMOF74-XI) [11]. There is substantial research on the synthesis of novel MOFs and more than 30,000 MOFs have been reported with a variety of shapes, structures and applications. Some examples of porous MOFs are shown here in Fig. 3 [12].

MOFs possess high surface areas and abundant active sites, which recently expands their applications towards electrochemistry. However, the low charge transfer in MOFs is a big hurdle to use them in electrical energy related applications. MOFs generally have very low conductivity less than 10^{-10} S/cm [13]. The low electrical

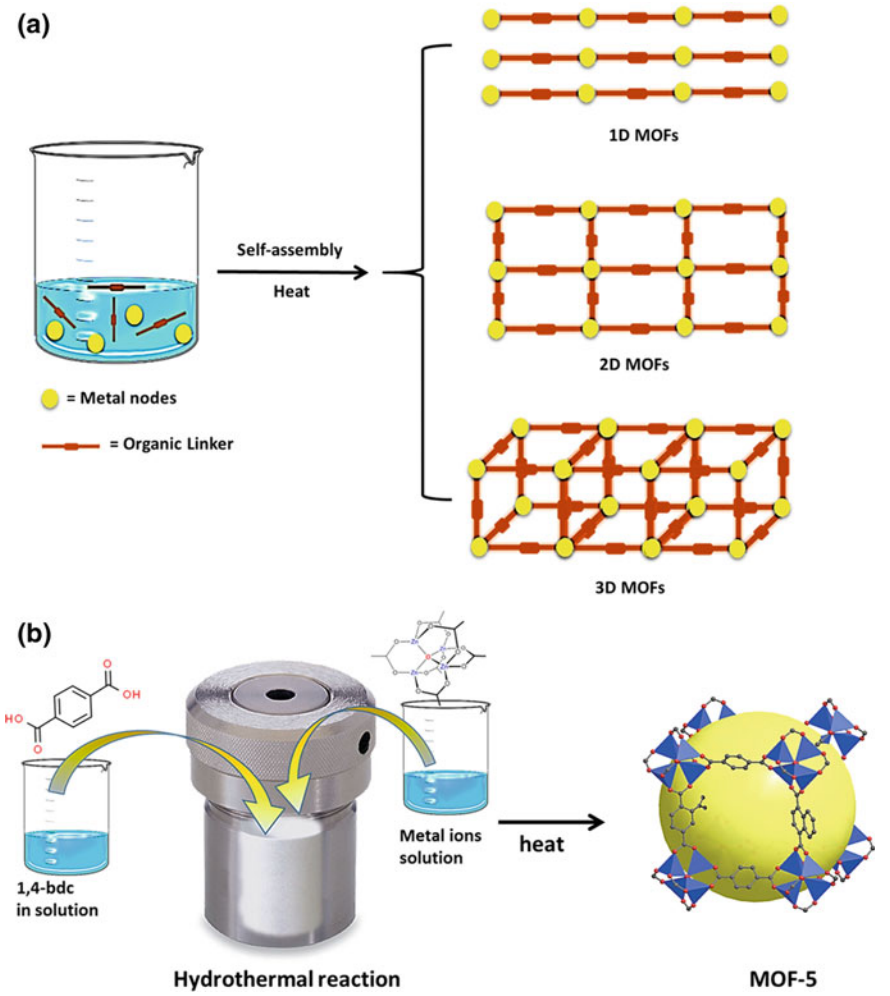

Fig. 1 **a** Generic scheme for the preparation of 1D, 2D and 3D MOFs. **b** Preparation scheme for MOF-5 via hydrothermal process

conductivity of MOFs is due to maximum use of carboxylic linkers in their synthesis [14]. The electronegativity of the oxygen atom is higher, which requires higher voltage to pass the electrons through the linker. Poor overlap of oxygen with the metal d-orbitals is also responsible for the low charge transfer in MOFs. In addition to their key structural features such as high surface areas, good stability, abundant active sites, it is important to understand charge transfer in MOFs, which will help to expand the applications of MOFs towards electrochemistry. The recent progress of electrically conductive MOFs that can enable the great enhancement in the conductivity for their application in the field of electrocatalysis. Given that the electrical

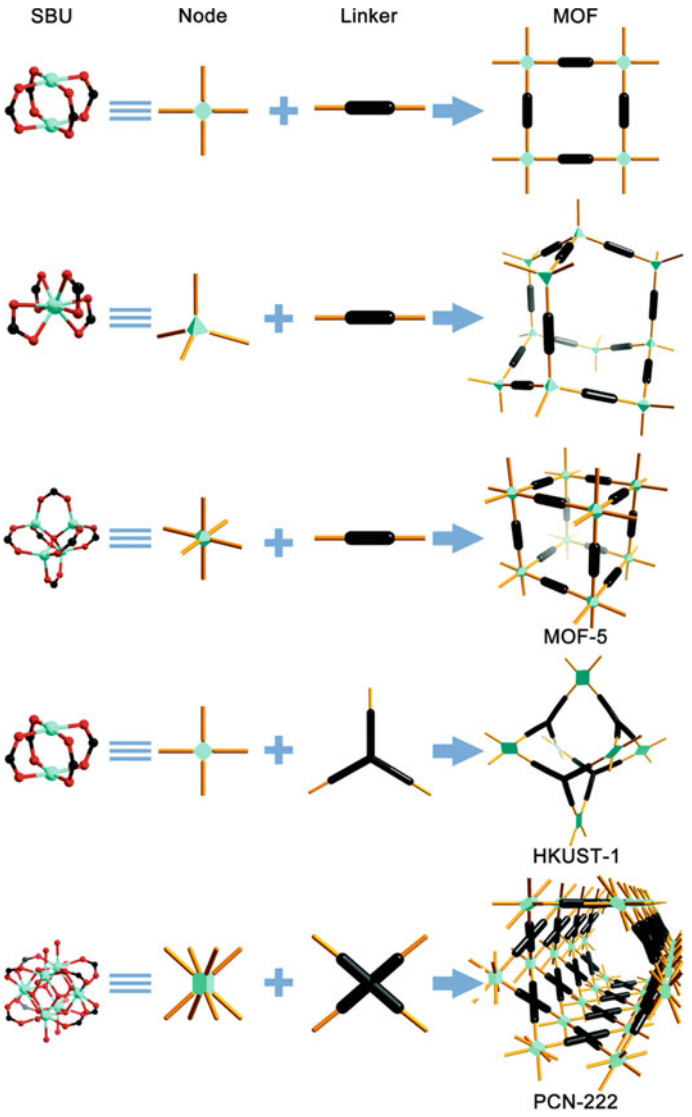

Fig. 2 Coordination geometries of some representative MOFs from metal nodes and organic linkers [6]. Reprinted with permission from Ref. [6]. Copyright@2014 Royal Society of Chemistry

properties of the MOFs can be regulated by the structural tunability, post-synthesis modifications, host and guest chemistry within the frameworks, the solvent molecules and their interactions, and the cooperation of conducting molecules/particles, MOFs will offer a promising opportunity for being used as industrially vital energy storage/generation materials. The abundant functionality, high surface areas, ease of tunability of crystal structures, and modification on functional groups mark MOFs

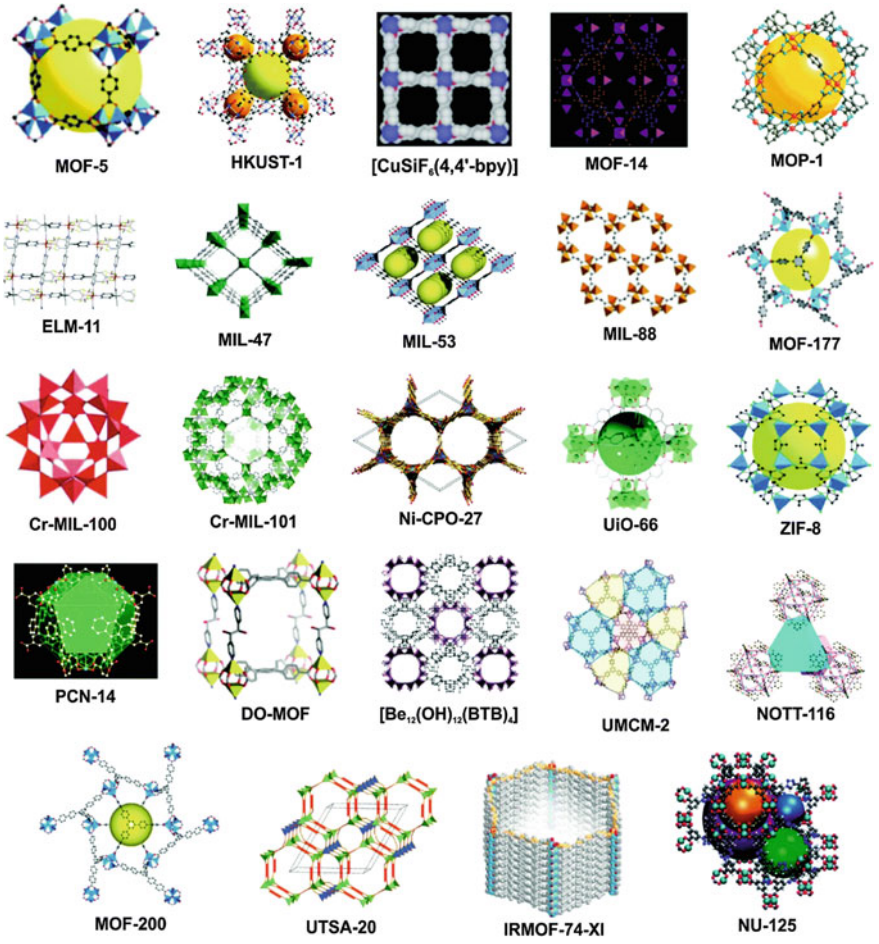

Fig. 3 Crystal structures of some famous MOFs with high porosity and surface areas [12]. Reprinted with permission from Ref. [12]. Copyright@2015 Royal Society of Chemistry

highly useful as compared with other inorganic and organic materials for designing efficient electrocatalysts. However, the study of the charge transfer behaviors of MOFs is still in its preliminary stage and additional studies will be needed [15, 16]. Scientists have reported on developing MOFs that show intrinsic conductivity. High conductivity was investigated for thin films composed of [Ni_3(2,3,6,7,10,11-hexaiminotriphenylene)$_2$], which can be utilized as electrocatalysts for ORR [17–20]. Recently, a highly conductive Cu-based MOF [Cu_2(6-Hmna)(6-mn)·NH_4]$_n$ (Hmna = mercaptonicotinic acid, 6-mn = 6-mercaptonicotinate) has been reported, which consists of a 2D (Cu–S)$_n$ plane and shows conductivity of 10.96 S cm^{-1} for its single crystal measurements [21]. Metal centres with the higher charge density (Cu and Fe etc.), electron enriched organic linkers and charge transfer mechanisms could be the

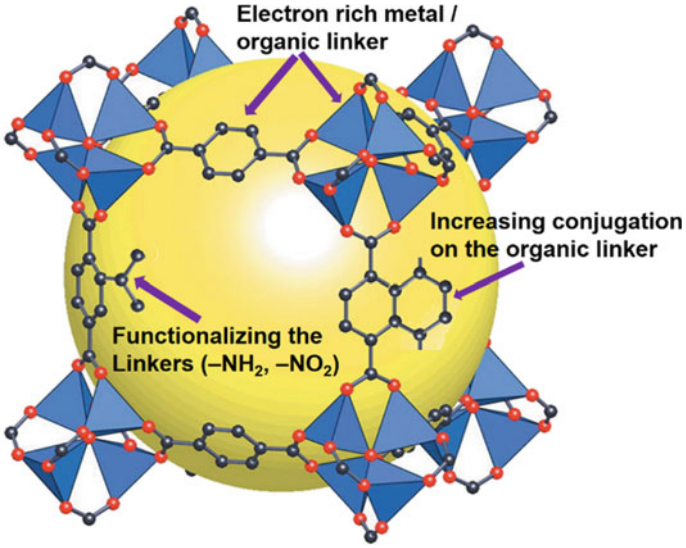

Fig. 4 Proposed mechanisms for bandgap engineering for MOF-5 with bandgap of 3.4 eV to improve electrical conductivity [16, 22]. Reprinted with permission from Ref. [22]. Copyright@2016 John Wiley and Sons

factors for increasing the electrical conductivity of these MOFs. Therefore, electrical conductivity of MOFs can be improved by three ways as follows: (i) growing the conjugation on the organic molecule, (ii) choosing electron-enrich metals and organic linkers, and (iii) functionalizing organic linkers with nitro, sulfide and amino groups (Fig. 4) [22].

2 MOFs for Electrocatalysis

With the increasing consciences on climate change and development of renewable energy sources, the investigation on effectual electrochemistry in electrolytic cells, batteries, supercapacitors, and fuel cells have been accelerated in modern times [23]. Electrochemical devices comprise of various type of electrochemical reactions, including HER, ORR, OER, carbon CO_2RR, metal ions redox reactions, etc. [24]. However, improving the efficiency and performance of electrochemical devices is a challenging task. Most of devices involving these half reactions need extra potentials to operate due to the slow reaction kinetics of these mechanisms. In efforts to improve the rate of electrochemical reactions, highly efficient and selective catalysts are required and their electrochemical performance is dependent on the sample amount. To meet the requirement of high catalytic activity and selectivity, MOFs with their ultrahigh surface areas and a number of active centers are among the promising candidates for the future of electrocatalysis.

Based on current progress, MOFs can be helpful as electrocatalysts in the process of energy generation with high activity and multi-dimensional designing. Some pristine MOFs have been used as electrocatalysts for different electrocatalytic reactions. However, the electrocatalytic performances of pristine MOFs are sometime limited by their insufficient conductivity. In order to overcome the low charge transfer in porous MOFs, several methods have been adopted such as compositing with inorganic/organic materials, carbonization of MOFs, etc. (Fig. 5) [4, 25, 26]. Particularly, pyrolysis of MOFs to form MOF-derived carbon materials is one of the most successful strategies, where the organic linkers are decomposed to give graphitic carbon materials while metal nodes generate active metal sites in different forms [27]. In this technique, MOFs are regarded as precursors for designing various nanostructures to achieve desired functionality. In this regard, the MOFs with different metals such as Co, Zn and Fe and amino-functionalized ligands are widely used as they can produce heteroatom/metal-doped carbons, which are suitable for catalytic activity [28–30].

Porous MOFs, their composites and MOF-derived materials provide an opportunity for electrochemical applications to improve diverse electrochemical reactions. Recent progresses in exploring MOFs and MOF-based materials as electrocatalysts for HER, ORR, OER, and so on, are discussed in detail in this chapter. Research articles appeared on electrocatalytic MOFs are significantly increasing with every passing years (Chart 1). This chapter provides a literature summary of recent progresses on (i) pristine MOFs as electrocatalysts, (ii) MOF composites as electrocatalysts and (iii) MOF-derived materials as electrocatalysts (Fig. 5).

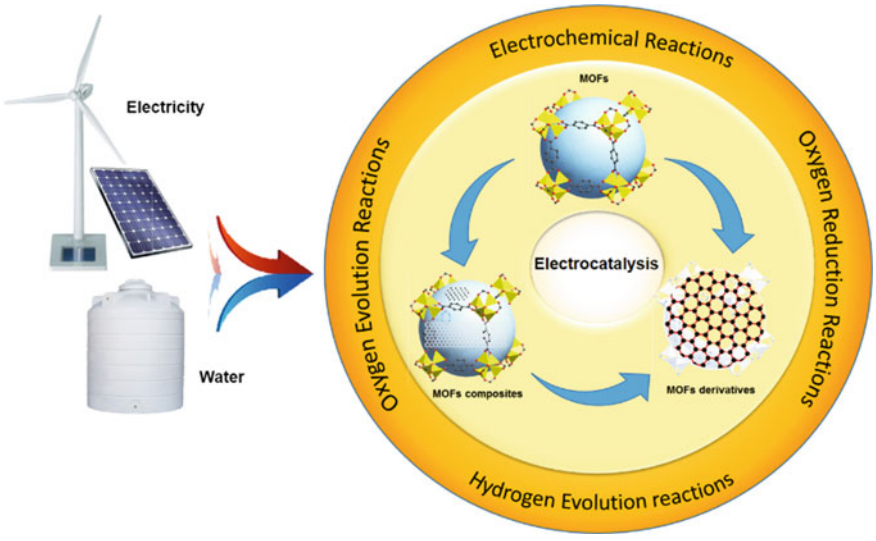

Fig. 5 MOFs as electrocatalysts are divided into three categories. (i) Pristine MOFs, (ii) MOFs composites, and (iii) MOFs derivatives

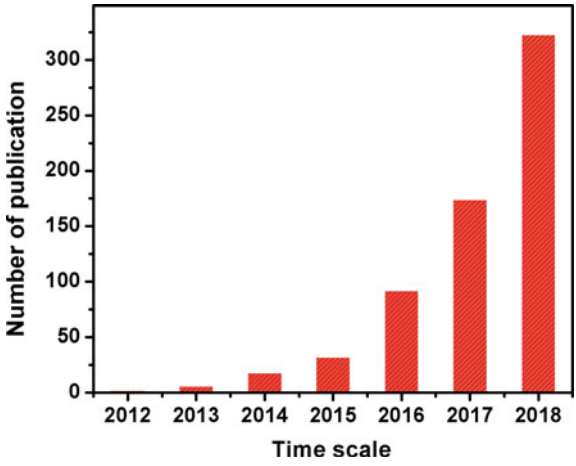

Chart 1 Progress on publications of MOFs and their applications for electrocatalysis with respect to time (data obtained from the ISI Web of Science)

2.1 Pristine MOFs as Electrocatalysts

MOFs have been regarded as alternative materials for traditional inorganic 2D and 3D materials for many applications [31]. MOF materials possess heterogeneous nature, better carrier mobility, high stability, and good surface/volume ratio, which allow to use them for electrocatalysis and batteries. With a mass of active metal sites, porous MOFs have been investigated for their electrocatalytic performance for HER, OER, ORR, and other electrochemical reactions. MOF-5, $[Zn_4O(BDC)_3]$, which is one of the most commonly known MOFs, also called IRMOF-1, was synthesized in ionic liquid system and used as catalyst for HER in 2014 by Liang et al. [32]. Carbon paste electrodes modified with MOF-5(IL) for CV measurements in 1 M dm^{-3} H_2SO_4 solution indicated that MOF-5(IL) is suitable to catalyze HER. Co-based MOFs, 2D $[Co_4L_2(4,4'\text{-bpy})(H_2O)_6]\cdot 3.5\,H_2O$ and 3D $[Co_2(dcpa)(azene)(H_2O)_3]\cdot DMF$ constructed with multicarboxylate ligands have also been studied for water splitting, which showed high catalytic performance for the generation of H_2 as well as O_2 from H_2O with high current density and low overpotentials [33]. Two Co-based MOFs, $[Co(L)_{0.5}(adip)]$ and $[Co_2(L)_2(5\text{-bdc})_2(H_2O)_2\cdot H_2O]$ were founded to exhibit electrocatalytic activities for OER. These MOFs were designed using two ligand system, where the second ligands was 1,4-bis(3-pyridylaminomethyl)benzene (L) [34]. When the MOF-modified electrodes were utilized, a quasi-reversible redox peak with a less potential ($\eta = 0.46$ V; +1.05 V vs. SCE) was detected for $[Co(L)_{0.5}(adip)]$, as compared with the water-containing $[Co_2(L)_2(5\text{-bdc})_2(H_2O)_2\cdot H_2O]$ ($\eta = +0.81$ V; +1.4 V vs. SCE). Two Co-based MOFs having different coordination bonding of water molecules in the structures were compared based on their HER performance and found that the coordination of solvent molecules in MOF is highly significant to tune the electrocatalytic properties [35].

ZIF series of porous MOFs are well-known for their structural tunability, easy synthesis, and large surface areas, which have structural anatomy similar to Si–O–Si

with angle of $\theta = 145°$, leading to the bridges in the form of M–Im–M framework (M = Zn or Co) [36]. High chemical and thermal stability of ZIFs and their structural tunability have potential to produce large number of structures and morphologies to get desired functionality or properties. Post-modifications such as plasma etching on (Co)ZIF-67 can also generate more coordinately unsaturated metal sites in ZIF-67, which improved its electrocatalytic performance [37]. Wang and co-workers have investigated Co-ZIF-9 [$Co(bim)_2$] for its OER catalytic activity in a various pH solutions [38]. The theoretical investigation have also been performed using DFT, which revealed that the water was adsorbed firstly at catalyst [Co-ZIF-9], directing H to C atom (C–H = 2.11 Å), and the longer distance of H–O was observed at tradition state while the C–H bond distance was decreased. The DFT study on Co-ZIF-9 revealed that not only active metal site but also the ligands (benzimidazole) played a significant role as proton acceptors during the proton-coupled electron transfer process during OER.

Effect of different metal sites of MOFs on electrocatalytic activity have also been investigated by Wang et al. [39]. A series of isostructural compounds, i.e., a Ni MOF [$Ni_3(btc)_2(H_2O)_3$], a Fe MOF [$Fe_3(btc)_2(H_2O)_3$] and a mixed metal MOF [$Fe_{0.23}Ni_{2.77}(btc)_2(H_2O)_3$], have been synthesized using different metal clusters and their OER performance and alkaline stability were compared (Fig. 6). The thin films of these MOFs have been deposited on Ni foams via electrochemical deposition and it was found that the mix metal compound [$Fe_{0.23}Ni_{2.77}(btc)_2(H_2O)_3$] exhibited outstanding OER performance with less overpotential of $\eta_{10} = 270$ mV and higher current density, as compared with other mononuclear counterparts in their study.

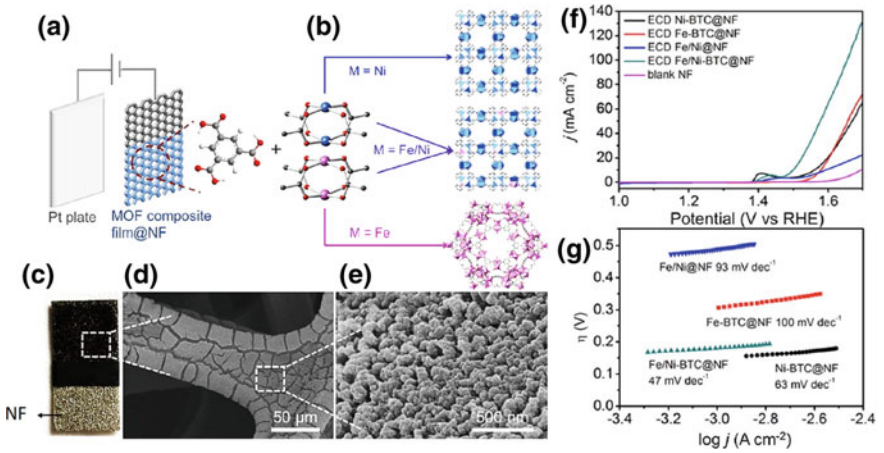

Fig. 6 **a** electrochemical setup with two electrodes having MOF deposited on nikal foam and Pt. **b** Synthetic scheme and crystal structures of [$M(btc)_2$] (M = Fe_3, Ni_3 and $Fe_{0.23}Ni_{2.77}$). **c** Optical and (d, e) SEM images of Fe/Ni-BTC@NF. **f** Linear sweep voltammetry data and **g** Tafel plots for [$M(btc)_2$] measured at 1 mV s^{-1}. Reprinted with permission from Ref. [39]. Copyright 2016@American Chemical Society

Su and coworkers have also reported the crystal engineering of a Fe and Co containing electrocatalytic MOF to achieve excellent OER activity [40]. Strong binding interactions among the catalyst and adsorbate in the bimetallic MOFs as compared with monometallic MOFs resulted in the better catalytic performance of the bimetallic MOFs. Series of bimetallic MOFs have been reported, which exhibited much better electrocatalytic performance over the isostructural monometallic MOFs [41, 42]. Beside bimetallic electrocatalytic MOFs, there are also trimetallic MOFs (e.g., Fe/Ni/Co(Mn)-MIL-53), which exhibited excellent OER activity at an optimized composition of metals [43].

Chen and coworkers reported a Co-based MOF, $[Co_2(\mu\text{-}OH)_2(bbta)]$ (MAF-X27-OH), which exhibited excellent performance as inorganic OER catalysts with an overpotential $\eta_{10} = 292$ mV in basic solution (Fig. 7) [44]. In addition, MAF-X27-Cl showed excellent chemical stability in 0.001 M HCl as well as 1.0 M KOH solution for a period of 7 days. It was found that the active metal sites and hydroxide ligands in the MOF played significant role in creating low-energy intraframework coupling pathways.

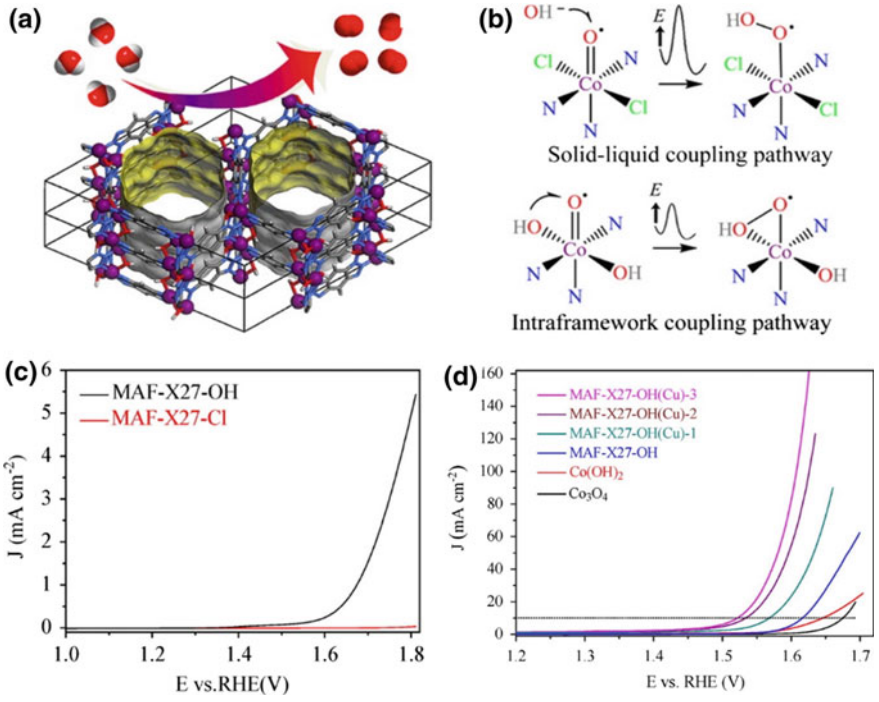

Fig. 7 **a** Crystal structure of a 3D MAF-X27-OH. **b** Solid–liquid and Intraframework coupling pathways. **c** Linear sweep voltammetry curves in neutral solution. **d** Linear sweep voltammetry plots for different samples and their comparison at pH = 10. Reprinted with permission from Ref. [44]. Copyright 2016@American Chemical Society

Mao and coworkers have designed Cu-BTC and Cu-bipy-BTC, and reported their electrocatalytic properties [45]. This study indicated that these Cu-based MOFs were useful in catalyzing ORR via four-electron reduction pathways. Cu-MOF-modified glassy carbon (GC) electrodes have been designed and their cyclic voltammetry (CV) data were recorded in 0.10 M phosphate buffer solution. Redox reactions of CuII/I in these MOF resulted in electrochemical activity with well-defined redox peaks at a potential of −0.10 V versus Ag/AgCl. The electrocatalytic behavior of Cu-bipy-BTC modified electrode for ORR was much stable as compared with Cu-BTC modified one. Considering the stability issue, a highly robust heterogeneous catalyst PCN223-Fe was designed via reaction of Zr6 oxo clusters and Fe(III) porphyrin ligand and the resulted product was grown on a conductive FTO substrate, which was further utilized as working electrode for ORR in 0.1 M $LiClO_4$/DMF [46]. A bifunctional catalytic Fe-based MOF has also been prepared by Yin and coworkers, which not only showed excellent ORR but also displayed remarkable activity for OER in an alkaline solution [47]. The catalytic process adopted a two electron pathway at potentials from −0.30 to −0.50 V versus Ag/AgCl and then shifted to four-electron pathway from −0.50 to −0.95 V versus Ag/AgCl.

Due to the conducting nature of Cu ions, Cu-based MOFs have also been widely reported for electrocatalytic HER, OER and ORR. In addition, there are some MOFs that are reported for electrocatalytic CO_2RR. $[Cu_3(btc)_2(H_2O)_3]$ and $[Cu_2(ade)_2((CH_3)_2COO)_2]$ have been studied as effective catalysts for CO_2RR to MeOH and EtOH in bicarbonates [48]. A porphyrin-based MOF $[Al_2(OH)_2$Co-TCPP] has also shown outstanding catalytic properties for CO_2 reduction to CO in aqueous electrolytes with CO selectivity of 76%, TON of 1400 and stable electrolysis for 7 h [49].

Most of the MOFs reported for high porosity possess 3D crystal structures. However, 2D MOFs have the following advantages over traditional electrocatalysts and 3D MOF electrocatalysts. (i) They possess uniform arrangement of the active sites in hexagonal networks; (ii) catalytically active centers can be more exposed in 2D MOFs; (iii) these catalytic active sites can remain active in aqueous solutions due their immobilization with solid-state materials. In order to utilize 2D MOFs for the reduction of water, Marinescu and coworkers have reported on the formation of 2D cobalt dithiolene films (MOS-1 and MOS-2) using bht, a trinucleating conjugated ligand, and cobalt(II) salt via a liquid–liquid interfacial method [50]. MOS-1 $[H_3(Co_3^{III}(bht)_2)]$ and MOS-2 $[H_3(Co_3^{III}(tht)_2)]$ showed excellent HER performance with maximum conductivity ($\sigma = 10^{-6}$ S cm^{-1}) for MOS-1 (Fig. 8). Square planar coordination geometry of 2-connected metal nodes and 3-connected organic linkers results into the formation of honeycomb-like 2D sheets with a thickness of 360 nm. When the pH value of the buffer solution decreased, the current intensity tended to increase. Under aqueous conditions with a very low value of pH = 1.3, the MOS-1 and MOS-2 electrodes showed the overpotentials of $\eta_{10} = 0.34$ and 0.53 V, respectively (Fig. 8e, f). Similarly, 2D supramolecular nickel bis(dithiolene) complexes in the form of layered sheets (0.7–0.9 nm) has also been reported for their outstanding electrocatalytic activities for HER with η_{10} of 333 mV and Tafel slope of 80.5 mV dec^{-1} [51]. $[Ni_3(HITP)_2]$ is a well-known conducting MOF, which is

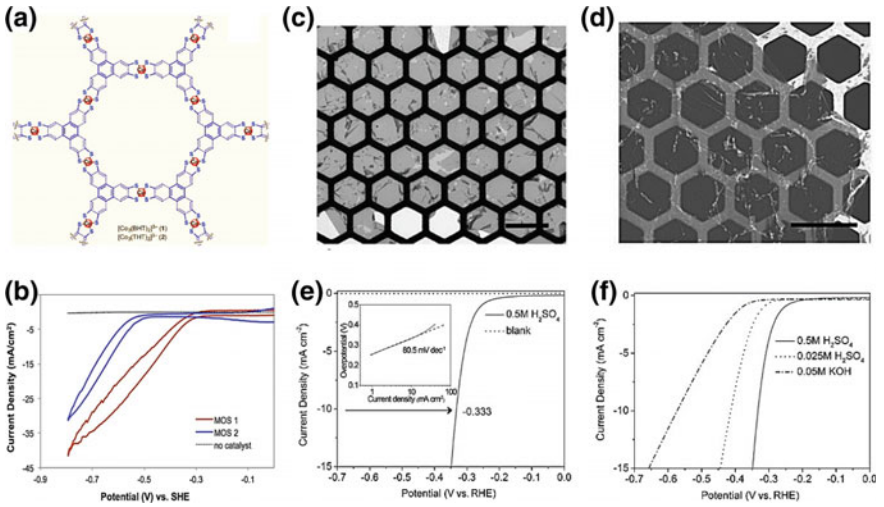

Fig. 8 **a** A schematic design of the honeycomb-like net of cobalt dithiolene framworks. **b** Polarization data of MOS-1, MOS-2 and the blank samples in H_2SO_4 solution (pH = 1.3) at scan rate of 100 mV s^{-1}. Reprinted with permission from Ref. [51]. Copyright@2015 John Wiley and Sons. **c** TEM and **d** SEM images of layered-sheets of nickel bis(dithiolene) compounds. **e** Linear sweep voltammetry curves of nickel bis(dithiolene)-coated electrodes and blank GC-RDE in 0.5 M H_2SO_4 solution (Tafel plot (80.5 mV dec^{-1}) is shown in inset). **f** Polarization curves in different concentration of acidic and basic solutions (H_2SO_4 and KOH) at 10 mV^{-1} scan rate. Reprinted with permission from Ref. [50]. Copyright@2015 American Chemical Society

among the highest electrical conductive MOFs. Owing to a number of the highly active square planar Ni–N_4 sites, it has been recently reported for its functions as a tunable electrocatalyst for ORR in alkaline solution, with a η_{10} of 0.18 V and good stability [20].

In short, the exposed electrocatalytic active sites and high active site density endow 2D and 3D MOFs with efficient activities for electrocatalysis. Recently reported pristine MOFs as electrocatalysts for HER, OER and ORR are listed in Table 1.

2.2 MOF Composites as Electrocatalysts

2.2.1 Molecular Catalyst@MOF Composites

With advantage of the highly porous structures of MOFs, catalytically active molecules could be integrated into the pores of MOFs to form novel catalysts, which possess the properties of heterogeneous MOFs and the catalytic properties of the guest molecules. The high exposure of active sites owing to the large surface areas of MOFs could lead to high catalytic activity and stability. A MOF composite

Table 1 Examples of pristine MOFs as electrocatalysts for HER, OER and ORR

MOFs	Short names	Electrochemical reactions (electrolyte)	η10 (mV) versus RHE	TS (mV dec^{-1})	References
$Na_3[Co_3(bht)_2]$	MOS-1	HER (0.05 M H_2SO_4)	340	NA	[50]
$H_3[Co_3(tht)_2]$	MOS-2	HER (0.05 M H_2SO_4)	530	NA	[50]
$H_3[Ni_3(tht)_2]$Cal	THT-Ni	HER (0.5 M H_2SO_4)	333	80.5	[51]
$H_3[Co_3(tht)(tha)]$Cal	THTA-Co single-layer	HER (0.5 M H_2SO_4)	283.0 ± 1.5	71.0 ± 1.1	[52]
$H_3[Co_3(tht)(tha)]$Cal	THTA-Co	HER (0.5 M H_2SO_4)	332.0 ± 1.8	87.0 ± 1.1	[52]
$H_3[Ni_3(tht)(tha)]$Cal	THTA-Ni single-layer	HER (0.5 M H_2SO_4)	315.0 ± 1.7	76.0 ± 1.0	[52]
$H_3[Co_3(tht)_2]$	THT-Co single-layer	HER (0.5 M H_2SO_4)	323.0 ± 2.0	82.0 ± 1.2	[52]
$H_3[Co_3(tht)_2]$	THT-Co	HER (0.5 M H_2SO_4)	495.0 ± 1.8	157 ± 1.2	[52]
$[Cu_3(btc)_2(H_2O)_3]$	HKUST-1	HER (0.5 M H_2SO_4)	691	127	[53]
$[Co_2(\mu\text{-}OH)_2(btta)]$	MAF-X27-OH	OER (1 M KOH)	387	66	[44]
$[Co_2(\mu\text{-}OH)_2(btta)]$	MAF-X27-OH	OER (1 M KOH)	292	88	[44]
$[K(H_2O)_2Co_3(cit)(Hcit)]$	USTA-16	OER (1 M KOH)	408	77	[54]
$[Co(bim)_2]$	Co-ZIF-9	OER (0.1 M KOH)	510 (1 mA cm^{-2})	93	[38]
$[Fe_{0.23}Ni_{2.77}(btc)_2]$	Ni/Fe-BTC	OER (0.1 M KOH)	270	43	[39]
[Co(bdc)]	CoBDC	OER (0.1 M KOH)	490	48.8	[55]
$[Co(mim)_2]$	ZIF-67	OER (0.1 M KOH)	443 (4 mA cm^{-2})	NA	[56]
$[Co(mim)_2]$	ZIF-67	OER (0.1 M KOH)	450	102	[57]
$[Co_2(\mu\text{-}OH)_2(btta)]$	MAF-X27-OH	OER (1.0 M PB)	489	127	[44]

(continued)

Table 1 (continued)

MOFs	Short names	Electrochemical reactions (electrolyte)	$\eta 10$ (mV) versus RHE	TS (mV dec^{-1})	References
$[Co_2(dobdc)(H_2O)_2]$	MOF-74-Co	OER (0.1 M PB)	492	129	[58]
$[Co(mim)_2]$	ZIF-67	OER (0.1 M PB)	525	125	[58]
$[Co(mim)_2]$	ZIF-67	OER (0.1 M PB)	581	NA	[56]
$[Co_2(ptbc)_4]$	NA	OER (0.2 M PB)	671	NA	[59]
$[Pb_2(H_2tcpp)]$	PbTCPP	OER (0.2 M PB)	NA	126	[60]
$[Cu_2(OH)(bpy)_2(btc)_3]$	NA	ORR (0.1 M PB)	3.8 (0.40 V)	NA	[45]
$[Al_2(OH)_2(Co(tcpp))]$	Co-Al-PMOF	ORR (0.1 M H_2SO_4)	2.9 (0.55 V)	NA	[61]
$[Zr_6(\mu_3\text{-}O)_4(\mu_3\text{-}OH)_4(Fe(tcpp))_3Cl_3]$	PCN-223-Fe	ORR (DMF)	3.2 (−0.65 vs. SHE)	NA	[46]
$[Ni_3(tha)_2]$	NA	ORR (0.1 M KOH)	2.25 (0.77 V)	−128	[20]
$[Cu_3(btc)_2(H_2O)_3]$	HKUST-1	ORR (0.1 KOH)	1.74 (0.77 V)	NA	[62]
$[Co(mim)_2]$	ZIF-67	ORR (0.1 M KOH)	NA	−50	[57]
$[Fe_3F(H_2O)_2O(btc)_2])$	MIL-100(Fe)	ORR (0.1 M KOH)	2.1 (0.47 V)	−137	[47]
$[Cr_3F(H_2O)_2O(btc)_2]\cdot[Co(salen)]$	Co-salen@MIL-100(Cr)	ORR (0.1 M PB)	3.84	NA	[63]

$(MoS_x)_y$/UiO-66-NH_2 ($y = 1$–6) has been reported where the HER activity of molybdenum polysulfide (MoS_x) combined high chemical stability of UiO-66-NH_2 resulted in novel HER catalysts [64]. MOF composite with MoS_x exhibited excellent HER activity with $E_{onset} = 125$ mV, Tafel slope = 59 mV dec^{-1}, $\eta_{10} = 200$ mV and TOF = 1.28 s^{-1}. It was highly stable even after 5000 cycles of CV. Dong and coworkers have synthesized a series of 2D MOFs and furthermore the metal dithiolene-diamine (MS_2N_2), metal bis(dithiolene) (MS_4), and metal bis(diamine) (MN_4) complexes were integrated into the hexagonal networks of these 2D MOFs [52]. These highly active molecular sites in the 2D MOFs are suitable for electrocatalytic H_2 production. It can be seen that the catalytic activities of the complexes followed by the order of $CoS_2N_2 > NiS_2N_2 > CoS_4$ and the protonation step took place at the M–N sites of the MS_2N_2 based compounds. Hence, highly order arrangement of the active sites is highly important to deliver the electrocatalytic performance.

Integration of electrocatalytic metal-containing molecules into the pores of the MOFs is a quite successful technique, which can balance the charge in the MOFs via redox hopping and support to get desired catalytic properties. Combining the catalytic activity of metal complexes with advantageous properties of MOFs can be useful for high performance electrocatalysis. A molecular water oxidation catalyst, $[Ru(tpy)(dcbpy)(OH_2)](ClO_4)_2$, has been integrated into the well-known porous MOF, $[Zr_6O_4(OH)_4(bpdc)_6]$ (UiO-67), grown on the surface of FTO, by post-synthetic ligand exchange (Fig. 9) [65]. The resulting UiO-67-[$RuOH_2$]@FTO as a new OER electrocatalyst can oxide water at 1.5 V versus Ag/AgCl with a current density of 11.5 μA cm^{-2}. It was found that the intrinsic UiO-67 show poor OER activity ($\eta = 766$ mV at a current density of 0.05 mA cm^{-2}, pH = 8.4); however, after integration of the Ru-complex into this MOF, the current density was enhanced to 0.5 mA cm^{-2} at $\eta = 766$ mV (Fig. 9). This study also indicates that the MOF supports are able to stabilize the structure of Ru-based catalysts. Then, a similar result was reported in 2016, where $Ru(tpy)(dcbpy)OH_2]^{2+}$ has been integrated to thin films of UiO-67 to form the Ru-UiO-67 electrocatalyst, which oxidized H_2O with a TOF of 0.2 ± 0.1 s^{-1} at 1.71 V versus NHE in solution of pH = 7 [66].

MOF-based composite $[Cr_3F(H_2O)_2O(BTC)_2]$·[Co(salen)] (Cr-MIL-100·Co-salen) has also been reported for its excellent ORR performance. The composite consist of highly porous Cr-MIL-100 and a Co(II) complex [63]. The 3D Cr-MIL-100, with the pore window diameters of 4.8×5.8 $Å^2$ and 8.6×8.6 $Å^2$ and incredibly large internal pores (25 and 29 Å), can incorporate Co-salen ($15.3 \times 9.2 \times 5.0$ $Å^3$) inside its pores via the synthetic approach called “ship in a bottle”. GC electrode modified Co-salen@Cr-MIL-100 has been investigated for the ORR performance in PB electrolyte of pH = 6.84. The results of CV indicated sharp peak at potential of 0.39 V versus RHE, which was assigned to O_2 reduction. The composite had good reproducibility of CV data for 50 cycles and was stable for 24 h in a buffer solution of pH = 7.

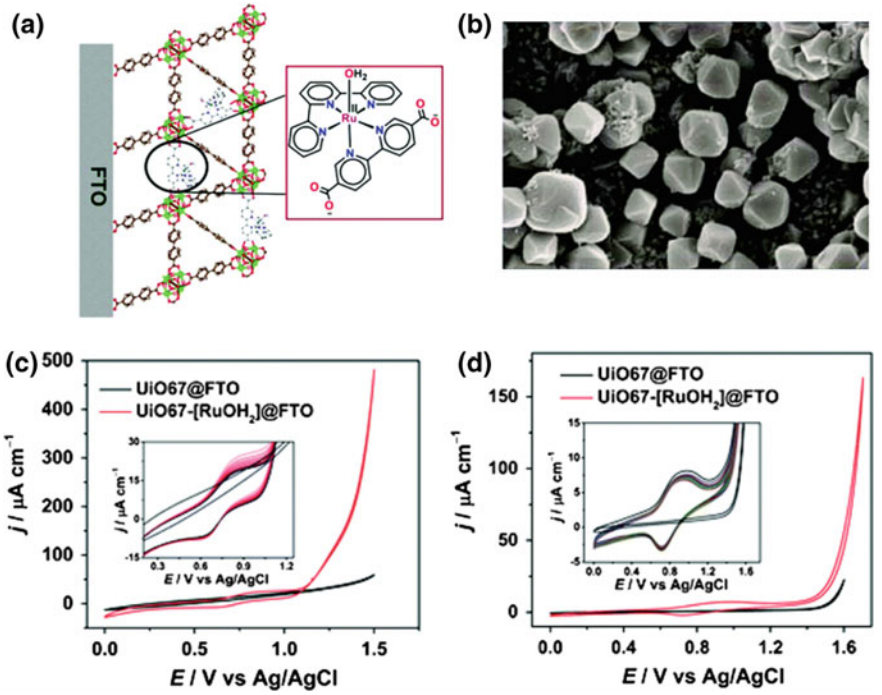

Fig. 9 **a** Representation of Ru-UiO-67 deposited on FTO electrode and its symmetric unit. **b** SEM image of Ru-UiO-67. CV plots of UiO-67 and Ru-UiO-67@FTO in **c** pH = 8.4 and **d** pH = 6.2. Region of the RuIII/II coupling is shown in inset of **c**, **d**. Reprinted with permission from Ref. [65]. Copyright@2017 Royal Society of Chemistry

2.2.2 POM@MOF Composites

Anionic metal-oxide clusters of metals from d-block, called polyoxometalates (POMs) are emerged as novel multifunctional materials with advantageous electrocatalytic properties [67]. Incorporation of POMs into highly porous MOFs with high surface areas can greatly increase the dispersion of POMs. In addition, high thermal stability, recyclability and easy structural tunability are the significant advantages of POM-based MOF materials as heterogeneous catalysts with enriched catalytic properties. Three different types of POM@MOF composite materials can be prepared which includes (i) POMs as nodes directly connecting with organic linkers, (ii) POMs inside the pores of MOFs and (iii) porous POM-pillared coordination polymers (Fig. 10a).

There are several reports on POM-based MOFs for the electrochemical applications particularly for HER [51, 52, 68, 69]. Dolbecq and coworkers presented that MOFs constituted using POMs could inherits catalytic properties of POMs and will be useful for electrochemical reactions [68]. They reported the designing of a POM-based MOF using ε-Keggin Zn building blocks. It was found that the POM-based

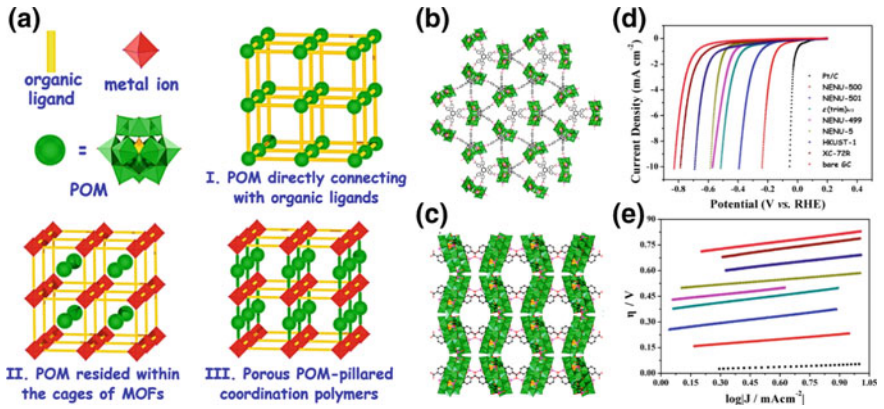

Fig. 10 **a** Possible construction of different types of POM@MOF composites. **b** Crystal structure of (**b**) NENU-500 and (**c**) NENU-501. **c** Comparison of linear sweep voltammetry plots of different materials. **d** Tafel plots for NENU-500, NENU-501 and related compounds after coating on electrodes in acidic solution. Reprinted with permission from Ref. [53]. Copyright@2015 American Chemical Society

materials displayed excellent catalytic behavior for HER with a high TOF (6.7 s^{-1}) at $\eta = 200$ mV in aqueous solution. CPE measurements at $E = -0.2$ V versus RHE indicated 95% higher FE and a large TOF (6.7 s^{-1}). Bonding the redox activity of POMs and porous MOFs, Lan, Zhou and coworkers have also reported the POM-based MOFs, NENU-500 ($[TBA]_3[\varepsilon\text{-}PMo_8^{V}Mo_4^{VI}O_{36}(OH)_4Zn_4][BTB]_{4/3}\cdot x$Guest) and NENU-501 ($[TBA]_3[\varepsilon\text{-}PMo_8^{V}Mo_4^{VI}O_{37}(OH)_3Zn_4][BPT]$, as efficient electrocatalysts for HER (Fig. 10b–e) [53]. NENU-500 exhibited outstanding performance for HER in acidic solution (Fig. 10d, e). Owing to its high stability, large porosity, and abundant active sites, NENU-500 is recognized for its best electrocatalytic performance for HER performance among all MOFs. The current studies on POM-based MOFs demonstrate that with high porosity and stability, these materials have a lot of opportunities as hydrogen-evolving electrocatalysts with outstanding activity.

Mixed-valent $[\varepsilon\text{-}PMo_8^{V}Mo_4^{VI}O_{40}Zn_4]$ (εZn) Keggin units have also been reported for their HER catalytic performance [70]. The POM-based MOFs were designed using metallic cations $[M(bpy)_3]^{2+}$ (M = Co, Ru) and tritopic/ditopic organic linkers. Their electrocatalytic HER performance was measured in 0.1 M H_2SO_4 (pH = 1.0) aqueous solution. Reduction of protons was found to be responsible for this catalytic activity at potentials below −0.6 V versus Ag/AgCl. From this study, it can be concluded that the existence of monovalent cations such as TBA^+ or PPh_4^+ in POM-based MOFs resulted in better catalytic properties of these compounds as compared with the bigger divalent counterions like $[M(bpy)_3]^{2+}$ (M = Ru, Co). However, the dimension of crystal structure and the nature of POM unit did not affect much on electrocatalytic properties.

2.2.3 Graphene/Carbon@MOF Composites

MOFs are known as low conducting materials; hence, to overcome this disadvantage of MOFs, researcher have designed their composite with highly conducting materials such as graphene, which can improve the conductivity of MOFs and further expand their applications as electrocatalysts. In efforts to enhance the conductivity of pristine MOFs, a Cu-MOF composite with GO, (GO *X* wt%) Cu-MOF, was reported as catalyst for HER, OER and ORR. The catalytic activity of the composite materials with various GO weight% in the MOF was investigated [71]. The Cu-MOF composite with 8 wt% GO exhibited excellent catalytic performance for different electrochemical reactions and better stability in acid media as compare to intrinsic MOF.

Nitrogen doped graphene and other carbon materials with their high electrical conductivity are well-known for non-Pt-based ORR catalysts [72]. Combining their high conductivity feature with porosity of MOFs is quite successful for improving electrocatalytic properties. Hence, the ZIF-67/N-doped carbon composites in different ratios have been investigated for ORR performance in 0.1 M KOH with *n* value of ~4 (0.55 V vs. RHE). CPE indicated that the ZIF-67/N-doped carbon with 2:1 ratio have good stability for more than 10,000 s [57].

2.2.4 Metal-Based NP@MOF Composites

MOFs with a large number of nanopores can also be used as templates for hosting metal-based NPs [73, 74], which could be used as efficient electrocatalysts [75]. Hupp and coworkers presented NU-1000 ($[Zr_6(\mu_3\text{-}OH)_8(OH)_8(tbapy)_2]$) as scaffolds for designing Ni–S rods with higher surface area, which exhibited improved electrocatalytic activity for HER in comparison to MOF-free Ni–S [76]. NU-1000 thin films were synthesized on FTO using hydrothermal process, and Ni–S were then fabricated at the end terminals of the NU-1000 nanorods via electrodeposition, leading to the NU-1000/Ni–S composite on electrode surface. By integrating with MOFs, the active surface area of the metal-sulfide based catalyst was enhanced, which improved the catalytic activity. Suh and coworkers have designed CuS NPs within HKUST-1 ($[Cu_3(BTC)_2{\cdot}(H_2O)_3]$), which showed the excellent ORR activity in an alkaline solution (Fig. 11) [62]. With the increase of Cu–S content in the MOF, the conductivity was found to be enhanced significantly. This new composite material that consists of 28 wt% Cu–S NPs in MOF template showed the onset potential of 0.91 V versus RHE via four electron transfer pathways (Fig. 11b, c). Metal oxide NPs can also be embedded in the MOFs, which can prevent them to aggregate during the chemical processing and hence improve their catalytic activities as well as stability in the framework. Yin and coworkers have prepared a ε-MnO_2@Fe-MOF composite, in which nanorod particles of ε-MnO_2 were embedded separately on the surface of a Fe-MOF template [77]. With improved structural morphology, this ε-MnO_2@Fe-MOF composite showed remarkable ORR electrocatalytic activity and good stability in an alkaline solution as compare to the intrinsic ε-MnO_2.

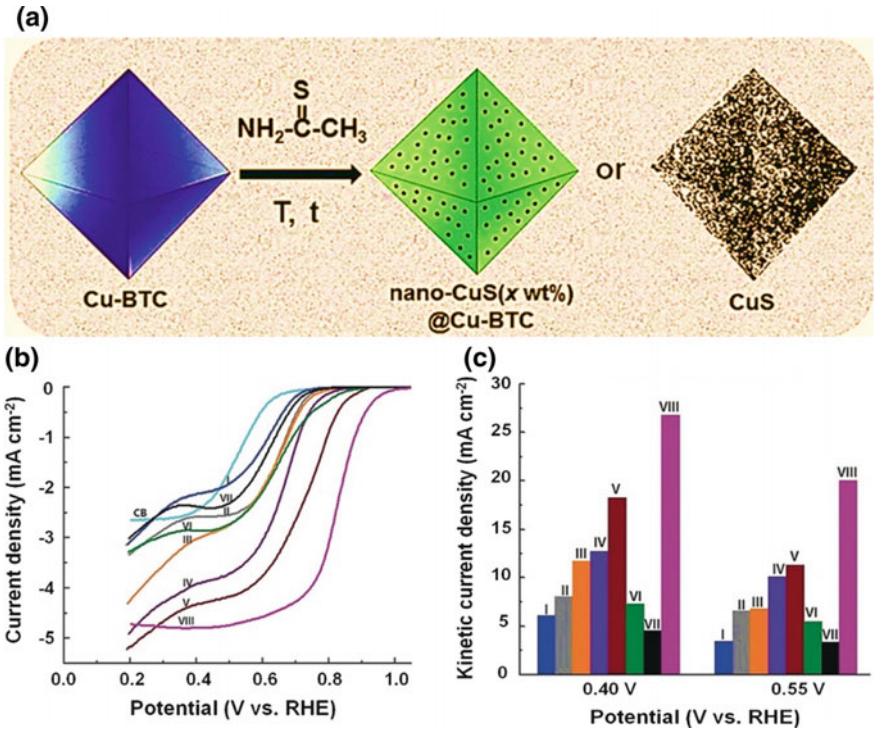

Fig. 11 **a** Synthetic scheme of nanosized-CuS(*x* wt%)@Cu-BTC and nano-CuS(99 wt%). **b** Linear sweep voltammetry curves for composites I–VIII in 0.1 M KOH at scan rate of 10 mV s^{-1}. **c** Kinetic current density measured at 0.40 and 0.55 V versus RHE. I = Cu-BTC, II = (1.4 wt%)nano-CuS@Cu-BTC, III = (5.3 wt%)nano-CuS@Cu-BTC, IV = (8.8 wt%)nano-CuS@Cu-BTC, V = (28 wt%)nano-CuS@Cu-BTC, VI = (56 wt%)@nano-CuSCu-BTC, VII = (99 wt%) nano-CuSand VIII = Pt/C. Reprinted with permission from Ref. [62]. Copyright 2016 John Wiley and Sons

2.2.5 MOF Grown on Substrates

Integration of catalytic functional materials into MOFs have been extensively reported with improved catalytic performances. However, for practical applications of MOFs and their composites as electrodes, it is needed to fabricate them in the form of uniform membranes. Uniform growth of MOFs into a thin film can not only improve the charger transfer but also expose more active metal sites, and hence MOFs in form of thin films or sheet could exhibit the better catalytic activity. In this regard, there are few examples, where MOFs have been grown either on a particular substrate or utilized as the self-supported electrode materials for electrocatalysis. In 2016, Tang and coworkers have reported ultrathin nanosheets of NiCo-based bimetallic MOF on the surface of copper foam, which showed improved OER activity due to high conductive nature of copper form as compared to glassy carbon electrodes [78]. Zhao and coworkers have also reported ultrathin MOFs array grown on different

substrates (e.g., nickel form (NF), glassy carbon (GC), etc.) which displayed good catalytic activities for both the OER and HER [79]. The electrical conductivity of ultrathin MOF nansheets grown on the surface of NF was investigated, which was significantly higher than bulk MOF material and was the main contributor towards high catalytic performance of the ultrathin MOFs array. Recently, Fischer and coworkers have reported the growth of surface-mounted MOF (SURMOF) thin films directly on electrode via layer-by-layer deposition [80]. These SURMOF films and their derivatives (SURMOFD) showed an excellent mass activity of 2.5 mA μg^{-1} at $\eta = 300$ mV for OER with high stability (100 h). The catalytic performance of SURMOFD was found to be highly reliant on thickness and shape of the MOF films. Approach to control the thickness and morphology of self-supported MOF composite electrodes was also reported, where a NiFe alloy foam (NFF) has been used as a substrate as well as metal source (Fig. 12a) [81]. Ni(Fe)-MOF nanosheets with ultralow thickness of ~1.5 nm have been constructed on the surface of NFF as self-supported NiFe-NFF electrode, which showed outstanding OER properties with current densities of 10 and 100 mA cm^{-2} at overpotentials of 227 and 253 mV, respectively (Fig. 12b, c).

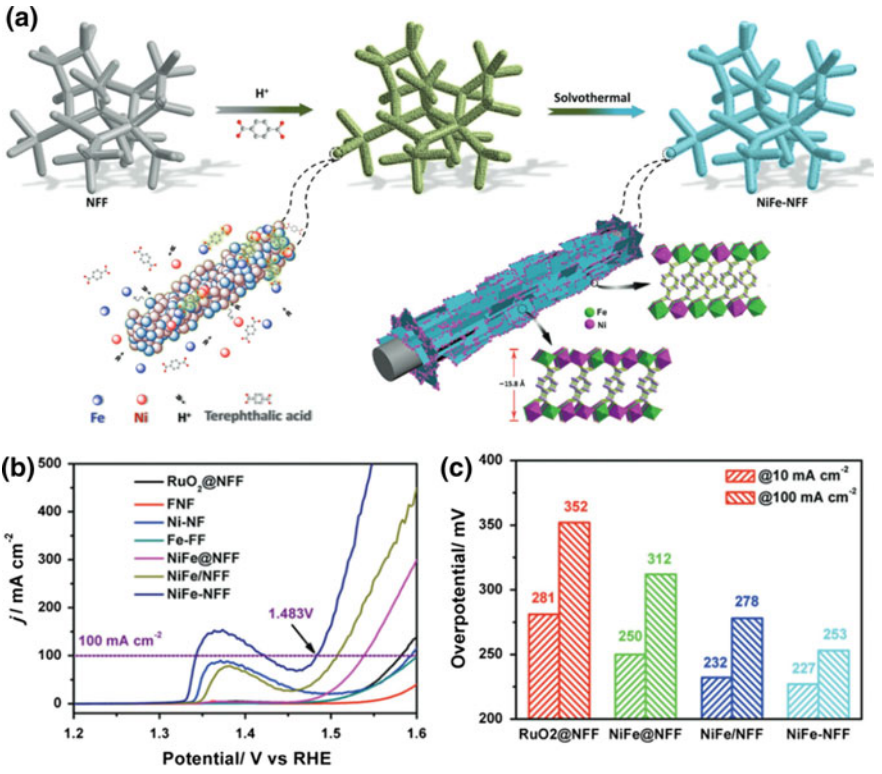

Fig. 12 **a** Illustration for the preparation of the free-standing NiFe-NFF electrode. **b** LSV plots and **c** the overpotentials and current density relation for the electrodes. Reprinted with permission from Ref. [81]. Copyright 2016 John Wiley and Sons

Outstanding electrocatalytic performance of the NiFe-NFF electrodes was due to the nanoarchitecture of MOF composite, which provided additional active metal sites, Ni and Fe interactions and improved conductivity.

Lu and coworkers have reported a bimetallic MOF, which displayed superior catalytic activity for water splitting after its fabrication on the surface of NF [82]. MIL-53(FeNi) grown on NF have also showed excellent catalytic activity for OER in 1 M KOH with the current density of 50 mA cm^{-2} at $\eta = 233$ mV and Tafel slope = 31.3 mV dec^{-1} [83]. The 3D NF is one of the suitable materials for electrocatalysis due to its high porosity, high conductivity and mechanical strength. The growth of MOFs on NF is a quite successful technique to develop binder-free 3D electrodes, which not only increases the charge transfer in MOF/NF, but also improves mechanical stability. Besides, NF provides extra Ni metal center, which increases the number of active metal cites on bimetallic MOFs [83].

In short, the integration of MOFs and other functional materials could combine the characteristics and advantages of them, providing great potential for electrocatalytic applications. A list of different MOF composites for HER, OER and ORR applications is given in Table 2.

2.3 MOF-Derived Materials as Electrocatalysts

Although intrinsic MOFs exhibit excellent electrocatalytic activities; however, their low electrical conductivity and poor stability in acidic/basic media prompt researchers to search for alternative routes to use MOFs. Hence, since the first study in the synthesis of porous carbons from MOFs reported by Xu et al. [88], the pyrolysis of MOFs at high temperature provides an effective way to obtain MOF-derived materials for efficient electrocatalytic applications. Generally, two kinds of carbon-based materials, i.e., pure porous carbons and carbon composite materials, can be derived from MOFs depending on pyrolysis conditions. Carbon-based materials derived from MOFs usually have the advantageous features of high porosity and surface areas, appropriate doping of nitrogen and/or metal-based components, more catalytically active sites and efficient electron transfer paths. Numerous MOF-derived materials have been reported for their excellent catalytic performance as electrocatalysts (Table 3). The electrocatalytic properties of MOF-derived materials are highly dependent on the pyrolysis conditions, including heating temperature, holding time, and gas flow etc.

Pyrolysis of ZIF-8, a MOF known for its high thermal stability and surface area, produced a high N-doped carbon material with N of 8.4%, while not compromising on surface area and porosity [89]. Pyrolyzed ZIF-8 showed an excellent HER activity at cathodic polarization treatment for 6 h in 0.5 M H_2SO_4 solution. Nanosized FeCo alloy embedded in N-doped graphene derived from a Co–Fe containing MOF as stable HER catalyst were reported by Chen and coworkers in 2015 [90]. Electrochemical study revealed that this MOF-derived hybrid material displayed the excellent HER activity with an overpotential of $\eta_{10} = -0.262$ V versus RHE

Table 2 Examples of MOF composite materials as electrocatalysts for HER, OER and ORR

Catalysts	Short names	Electrochemical reactions (electrolyte)	η10 (mV) versus RHE	TS (mV dec^{-1})	References
$(tba)_3[(PMo_{12}O_{36}(OH)_4Zn_4)(btc)_{4/3}]$	$\varepsilon(btc)_{4/3}$	HER (1 M LiCl/HCl)	99 (7 μA cm_{-2})	NA	[68]
$(tba)_3[(PMo_{12}O_{36}(OH)_4Zn_4)(btc)_{4/3}]$	$\varepsilon(btc)_{4/3}$	HER (0.5 M H_2SO_4)	515	142	[53]
$(tba)_3[(PMo_{12}O_{36}(OH)_4Zn_4\}(btb)_{4/3}]$	NENU-500	HER (0.5 M H_2SO_4)	237	96	[53]
$(tba)_3[(PMo_{12}O_{37}(OH)_3Zn_4)(bpt)]$	NENU-501	HER (0.5 M H_2SO_4)	392	137	[53]
$(tma)_2[Cu_2(btc)_{4/3}(H_2O)_2]_6[HPMo_{12}O_{40}]$	NENU-5	HER (0.5 M H_2SO_4)	858	94	[53]
$(bta)_2[Co(bpy)_3][PMo_{12}O_{37}(OH)_3Zn_4](btb)_{4/3}$	$[Co\text{-}\varepsilon(btb)_{4/3}]$	HER (0.5 M H_2SO_4)	419	NA	[70]
$[Ru(bpy)_3]_4[PMo_{12}O_{38}(OH)_2Zn_4]_2(btc)_2$	$[Ru\text{-}\varepsilon_2(btc)_2]$	HER (0.5 M H_2SO_4)	617	NA	[70]
$[Ru(bpy)_3]_3[PMo_{12}O_{37}(OH)_3Zn_4Cl]_2(bpdc)_2$	$[Ru\text{-}\varepsilon_2(bpdc)_2]$	HER (0.5 M H_2SO_4)	337	NA	[70]
$[Zr_6(\mu_3\text{-}OH)_8(OH)_8(tbapy)_2)]$/Ni–S	NU-1000/Ni–S	HER (0.5 M H_2SO_4)	238	182	[76]
$(MoSx)_5/[Zr_6(\mu_3\text{-}O)_4(\mu_3\text{-}OH)_4](anbdc)_6]$	$(MoSx)_5$/UiO-66-NH_2	HER (0.5 M H_2SO_4)	200	59	[64]
$GO/[Cu_2(bdc)_2(ted)_2]$	GO/Cu-MOF	HER (0.5 M H_2SO_4)	159	84	[71]

(continued)

Table 2 (continued)

Catalysts	Short names	Electrochemical reactions (electrolyte)	η10 (mV) versus RHE	TS (mV dec^{-1})	References
GO/$H_3[Co_3(tht)(tha)]$	GO/THTA-Co	HER (0.5 M H_2SO_4)	230 ± 2.2	70 ± 1.4	[52]
$[Fe_{1.84}Co_{1.16}F(H_2O)_2O(btc)_2]$	Co/MIL-100(Fe)	OER (0.1 M KOH)	734 (5 mA cm_{-2})	NA	[84]
$[Zr_6(\mu_3\text{-}O)_6(\mu_3\text{-}OH)_4](bpdc)_{5.61}[Ru(tpy)(dcbpy)(OH_2)]_{0.39}](ClO_4)_{0.78}$	UiO-67-[$RuOH_2$]	OER (1 M KNO_3)	818 (0.15 mA cm_{-2})	NA	[65]
$[Cr_3F(H_2O)_2O(btc)_2]$·[Co(salen)]	Co-salen@MIL-100(Cr)	ORR (0.1 M PB)	3.84	NA	[63]
(Co species)@$[Cr_3F(H_2O)_2O(bdc)_3]$	Co/MIL-101(Cr)-R	ORR (0.1 M KOH)	3.9	−107	[85]
G-py/$[Zr_6(\mu_3\text{-}OH)_8(OH)_8(Fe(tcpp))C_{12}]$	G-py/PCN-222	ORR (0.5 M H_2SO_4)	NA	NA	[86]
GO(8 wt%)/$[Cu_2(bdc)_2(ted)_2]$	GO(8 wt%)/Cu-MOF	ORR (0.5 M H_2SO_4)	NA	−69	[71]
ε-MnO_2/$[Fe_3F(H_2O)_2O(btc)_2]$)	ε-MnO_2/MIL-100(Fe)	ORR (0.1 M KOH)	3.8 (0.55 V)	−117	[77]
CuS(28 wt%)/$[Cu_3(btc)_2(H_2O)_3]$	CuS(28 wt%)/HKUST-1	ORR (0.1 M KOH)	3.82 (0.55 V)	−NA	[62]
rGO/$[Cu_2(tmbdi)(H_2O)_2]$	rGO/NPC-4	ORR (0.1 M PB)	1.8 (0.67 V), 3.2 (0.37 V)	NA	[87]

Table 3 Examples of MOF-derived materials as electrocatalysts for HER, OER and ORR

MOF derivatives	Short names	Electrochemical reactions (electrolyte)	η10 (mV) versus RHE	TS (mV dec^{-1})	References
$CoSe_2$ nanoparticles anchored on carbon fibers	ZIF-67	HER (1 M KOH)	95	52	[117]
Hollow CoS_2 nanotube arrays	ZIF-L(Co)	HER (1 M KOH)	193	88	[118]
Ni–Co bimetal phosphide nanotubes	MOF-74	HER (1 M KOH)	129	52	[119]
RuCo@N-doped C	$Co_3[Co(CN)_6]_2$ Prussian blue analogue	HER (1 M KOH)	28	31	[120]
N-Doped C@Co–N-doped C core–shell nanocages	ZIF-8@ZIF67	OER (0.1 M KOH)	410	91	[121]
Hollow Co_3O_4 nanospheres in N-doped C	ZIF-L(Co)	OER (1 M KOH)	352	N/A	[122]
Ni–Co bimetal phosphide nanotubes	MOF-74	OER (1 M KOH)	245	61	[119]
Hollow CoS_2 nanotube arrays	ZIF-L(Co)	OER (1 M KOH)	276	81	[118]
$CoSe_2$ nanoparticles anchored on carbon fibers	ZIF-67	OER (1 M KOH)	297	41	[117]
N-Doped C nanotube frameworks	ZIF-67	OER (0.1 M KOH)	370	93	[123]
N-Doped C nanotube frameworks	ZIF-67	ORR (0.1 M KOH)	N/A	64	[123]
Hollow Co_3O_4 nanospheres in N-doped C	ZIF-L(Co)	ORR (1 M KOH)	N/A	51	[122]
Co single atoms on N-doped C	Bimetallic Zn/Co-MOF (ZIF-8/67)	ORR (0.1 M KOH)	N/A	75	[124]

(continued)

Table 3 (continued)

MOF derivatives	Short names	Electrochemical reactions (electrolyte)	η10 (mV) versus RHE	TS (mV dec^{-1})	References
Honeycomb-like carbon-based framework	CoAl-LDH@ZIF-67	ORR (0.1 M KOH)	N/A	63	[125]
N-Doped C@Co–N-doped C core–shell nanocages	ZIF-8@ZIF67	ORR (0.1 M KOH)	N/A	51	[121]

and high stability even for more than 10 000 cycles. Benefited from the high thermal stability, Co-based ZIF-67 is also one of the most commonly used MOFs for preparing various electrocatalysts. Xia and coworkers have also reported the HER catalytic activity of cobalt NPs inserted in a nitrogen-doped carbon material, attained by low-temperature pyrolysis of ZIF-67, with $\eta_{10} = 0.339$ V versus RHE and Tafel slope = 119 mV dec^{-1} [91]. Careful control of the pyrolysis of MOFs can even get the desired catalytic materials with intriguing morphologies. Chen and coworkers reported the carbonization-oxidation-selenylation process of ZIF-67 to design $CoSe_2$ nanoparticles integrated in defect carbon nanotubes ($CoSe_2$@DC), which displayed outstanding HER catalytic performance (Fig. 13) [92].

The pyrolysis of ZIF-67, PEG-2000, urea and boric acid, followed by phosphidation resulted in the formation of CoP@BCN-1 nanotubes, which exhibited excellent

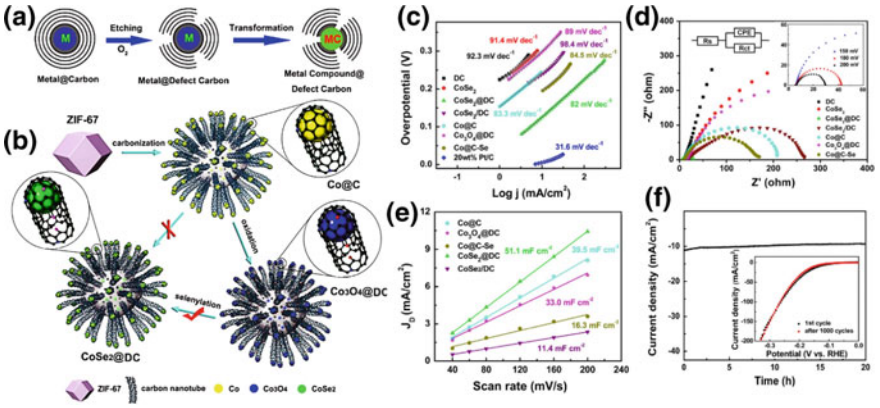

Fig. 13 **a** Designing methods for the metal compound @ carbon via oxidation. **b** Systematic preparation of $CoSe_2$@DC. **c** Tafel plots of inorganic materials and derived materials. **d** Nyquist plots of the various compounds coated on electrodes (Circuit diagram and Nyquist plots of $CoSe_2$@DC-modified electrodes is shown in inset). **e** Capacitive current versus scan rate. **f** Chronoamperometric behavior (polarization curves in inset) for $CoSe_2$@DC. Reprinted with permission from Ref. [92]. Copyright@2016 Elsevier

electrocatalytic activity for HER in 1 M KOH (alkaline; pH = 13.9), 0.5 M H_2SO_4 (acidic; pH = 0.3) and 1 M phosphate (neutral; pH = 7) solutions [93]. With more active sites in CoP@BCN-1 nanotubes, ZIF-derived electrocatalysts showed lower overpotentials of 87, 215, and 122 mV in acidic, basic and neutral buffer solutions, respectively. Cobalt-nitrogen-doped graphene aerogel (Co–N–GA) electrocatalyst was also investigated by the pyrolysis of the MOFs@GA composite, which was synthesized by the reaction of Co(ii) ions on graphene oxide (GO) sheets and 5-amino-1*H*-tetrazol [94]. Co–N–GA inherited the highly ordered porosity from MOF, which led to its superior electrocatalytic performance as compared to other non-noble metal HER catalysts.

ZIFs have been extensively utilized for the derivation of carbon-based materials. However, many carboxylate linker-based MOFs have also been pyrolyzed to form metal-doped carbon-based materials. Lee and coworkers have reported the pyrolysis of a 2D sheet structured Co-based MOF and hexamethylenetetramine at 650 °C in argon atmosphere, which resulted in the development of 2D layers of Co/N-carbon [95]. This composite showed quite good HER catalytic performance with a low overpotential of $\eta_{10} = 103$ mV versus RHE, high-cycle durability and stability. Beside Co-based MOF, Wang and coworkers have investigated a Ni-containing MOF, $[Ni_2(BDC)_2Ted]$, to derive carbon materials, which can show electrocatalytic activity for HER [96]. Nanoparticles of Ni with surface nitridation on the carbon sheets derived from the Ni-based MOF were mainly responsible for improving the HER catalytic performance. In a two-step process, N-doped graphene oxide/nickel sulfide (NGO/Ni_7S_6) composite nanosheets resulted from the pyrolysis of Ni-MOF-74 possessed highly order porosity, nitrogen contents, accessible nickel active sites, good mass transfer, and high stability against corrosion, showing excellent HER performance [97].

In Sect. 2.2.3, it has been reported that the combination of MOFs and graphene is useful to improve the overall electrical conductivity for prompting their electrocatalytic performance. Alternatively, graphitic carbon with uniform metallic nanoparticles can be obtained upon the pyrolysis of a MOF in an inert atmosphere, which could be used as efficient electrocatalysts [98]. Jiang and coworkers have reported the Ni@graphene derived from a Ni-based MOF, which exhibited tremendous catalytic activity in a 1.0 M KOH solution [99]. This MOF derived Ni-based electrocatalysts with excellent HER as well as ORR performance represents an ideal material to be used for water splitting. ZIF-8 nanocrystals fabricated on GO (ZIF-8@GO) were treated at 900 °C to design N-doped porous carbon@graphene (N-PC@G) with high porosity (1094.3 $m^2\ g^{-1}$), micro- and mesopores, appropriate N content, and high degree of graphitization [100]. This N-PC@G-0.02 exhibited tremendous electrocatalytic activity for ORR and high stability.

The conditions of pyrolysis or thermal treatment are significantly important for the final state of the metals in the derived materials and their morphologies. For instance, nanoporous carbon–cobalt oxide hybrids have been reported, which were obtained by the pyrolysis of a cobalt-based ZIF-9 in two-step process as shown in Fig. 14 [101]. The transformation of cobalt to cobalt oxide was highly dependent on the conditions of thermal treatment. Despite the lower surface area, the Z9-800-250

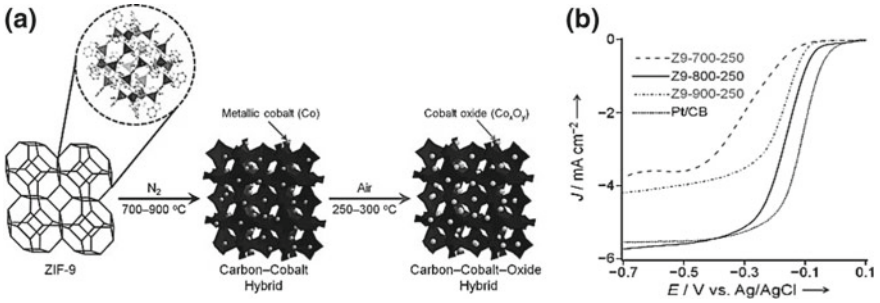

Fig. 14 **a** Schematic illustrations for the preparation of carbon–cobalt oxide composites via 2-step thermal processing of ZIF-9. **b** Polarization plot for ORR of different electrodes modified with Z9-900-250, Z9-800-250, Z9-700-250 and Pt/CB at 2000 rpm and 5 mV s^{-1}. Reprinted with permission from Ref. [101]. Copyright@2014 John Wiley and Sons

sample exhibited improved electrocatalytic performance for ORR as compared to the Z9-900-250 sample, which is due to better conversion rate of metallic cobalt to cobalt oxide for Z9-800-250. Shape and size of the parental MOFs are also important to get the derived porous materials with desired nanoscale morphologies and optimized functionality. Co NP-contained nitrogen-doped carbon polyhedrons were prepared from ZIF-67, where the derived materials preserved the size and morphology of the parental MOF [102]. The nano-sized MOF derived materials exhibited improved performance towards ORR in acidic solution as compared with those derived from large-sized MOF precursors.

Bimetallic MOFs are also good candidates for the design of high-performance ORR electrocatalysts. The pyrolysis of the Zn–Co bimetallic MOF afforded the Co–N–C electrocatalyst with high porosity (~500 m^2 g^{-1}), orderly-distributed Co NPs (~9.5 nm), and appropriate N contents (8.5%) [103]. The catalytic properties of this porous Co–N–C polyhedron electrocatalysts have been tested in different buffer solutions and found that it exhibited good catalytic activity and stability, comparable to the well-known commercial ORR catalytic Pt/C, as shown in Fig. 15. MOF-derived Co,N-doped carbons have also been synthesized via a mesoporous silica ($mSiO_2$)-protected calcination method [104]. Zn–Co bimetallic ZIF NPs were coated with $mSiO_2$ and treated at 900 °C. Outer coating of mesoporous silica prevented the aggregation of Co,N-doped carbon material particles and the $mSiO_2$ was finally removed by chemical wet etching. This MOF-derived material exhibited excellent catalytic activity for ORR in alkaline solution.

Beside metal/metal oxide NP-embedded carbon materials, there are also many reports on the preparation and electrocatalytic properties of MOF-derived metal phosphides, sulfides, and so on. Zhu et al. have constructed the N and S dual-doped honeycomb-like porous carbons immobilizing cobalt sulfide nanoparticles (Co_9S_8@CNS*T*) from a MOF, which exhibited excellent catalytic performance for ORR (Fig. 16) [105]. The unique structural and doping properties with increased accessible active sites with synergetic interactions and enhanced mass transport of

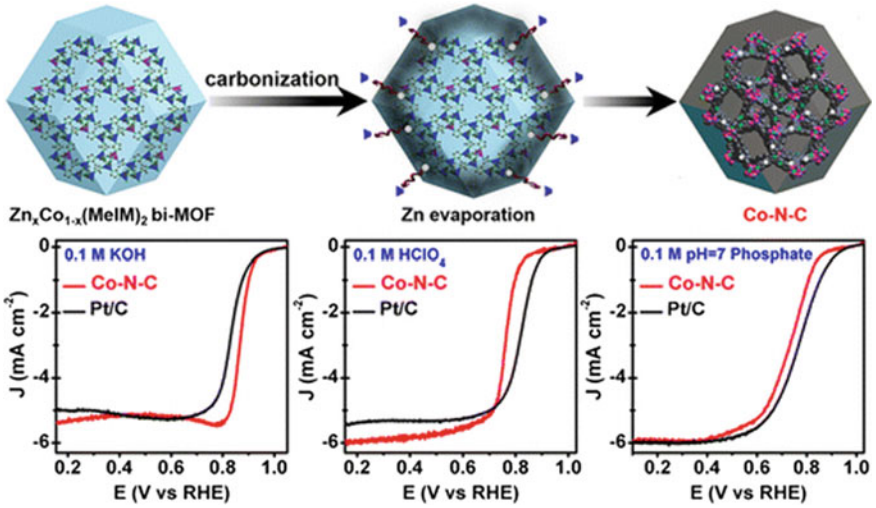

Fig. 15 Schematic preparation of Co–N–C via carbonization without any post-treatment. MOF-derived Co–N–C exhibited excellent ORR activity that is comparable and much stable than Pt/C in different electrolytes. Reproduced with permission from Ref. [103]. Copyright@2015 American Chemical Society

oxygen and electrolyte in this open nanostructure led to notably superior ORR catalytic activity and long-term stability under alkaline conditions. The pyrolysis of core–shell ZIF-8@ZIF-67 material resulted in the generation of CNTs on the top of a polyhedron, which was further treated by oxidation–phosphidation process to form CoP NPs integrated in N-doped carbon hollow polyhedra (NCNHP) [106]. The resulting CoP/NCNHP was used for water splitting, with excellent bifunctional catalytic properties. Ni–Co–P/C nanoboxes were derived from ZIF-67 following several steps [107]. The reaction of ZIF-67 nanocubes prepared by a surfactant-supported method with $Ni(NO_3)_2$ resulted in the formation of Ni–Co LDH on the surface of ZIF-67 nanocubes (ZIF-67@LDH nanoboxes), which were subsequently treated with NaH_2PO_2 to form Ni–Co P/C catalyst. This bimetallic phosphide catalyst exhibited excellent OER activity. With the advantage of higher contact area on electrode, the nanobox like hollow architectures of bimetallic phosphide derived from MOFs afforded better OER performance as compared with the bulk counterpart. Similarly, mix-metal nanocages (Ni–Co based Prussian blue analogue) have also been derived from MOFs, which possessed huge electrolyte/electrode contact area and hence showed good OER activity [108].

Pyrolysis of MOFs can result in the formation of the derivates in the form of either single metal atom doped or metal derivative doped carbon materials. Recently, single-atom catalysts have been widely used due to the fine dispersion of single metal active sites. There are several methods to achieve such dispersed single atom active sites on the support materials, such as metals trapped on N-doped carbon materials [109]. Metal nodes and organic linkers are periodically arranged in the

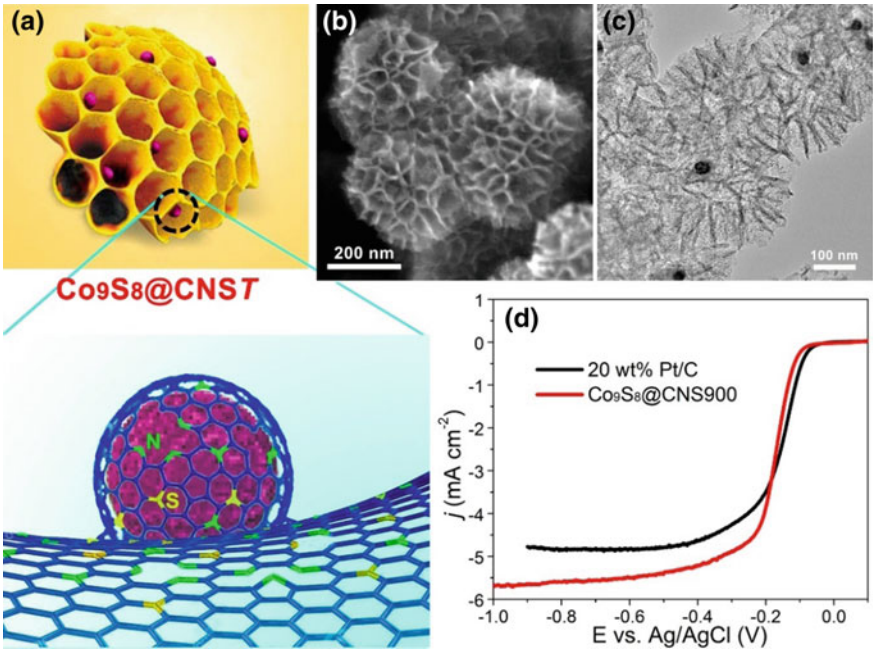

Fig. 16 **a** Illustration of the honeycomb-like porous structure of Co_9S_8@CNS*T* catalysts; **b** SEM and **c** TEM images of Co_9S_8@CNS900; **d** ORR catalytic properties of Co_9S_8@CNS900 and commercial 20 wt% Pt/C catalyst. Reproduced with permission from Ref. [105]. Copyright@2016 John Wiley and Sons

MOFs, which provides an opportunity to further treat them in order to design such a catalyst, where the active sites are single atomically distributed (called a single metal atom-doped carbon) [110]. Pyrolysis of MOFs can form a single metal atom-doped carbon materials (M–N–C) as excellent catalytic properties [111]. Li and coworkers have synthesized a N-doped single-atom carbon catalyst for ORR, from a bimetallic Zn/Co-based MOF [112]. Addition of Zn ions in precursor resulted in the formation of long-distance dispersion of Co ions, stabilized by N (derived after pyrolysis of MOF). Similarly, a N-doped Fe-single-atom porous catalyst, derived from a MOF composite has also been reported with a unique hierarchical structure having macro-, messo- and microspores [113]. This Fe/N-GPC electrocatalyst was prepared by the pyrolysis of FeD@MIL-101-NH_2 composite and showed outstanding catalytic performance for ORR in alkaline solution, owing to the more accessible active sites and the mass diffusion (Fig. 17). A similar ORR catalyst (Fe/N-GPC) was also designed by the pyrolysis of core-shell $Fe(acac)_3$@ZIF-8. Pyrolysis at 800 °C provided the N-doped carbon, while single Fe atoms dispersed on N was achieved from $Fe(acac)_3$ [114]. A mixed metals based carbon catalyst [CoFe@C], prepared by the one-step pyrolysis of dual metal-doped Zn-MOF, exhibited excellent ORR performance due to periodically dispersion of Co and Fe on porous carbon [115, 116]. Recent studies showed that

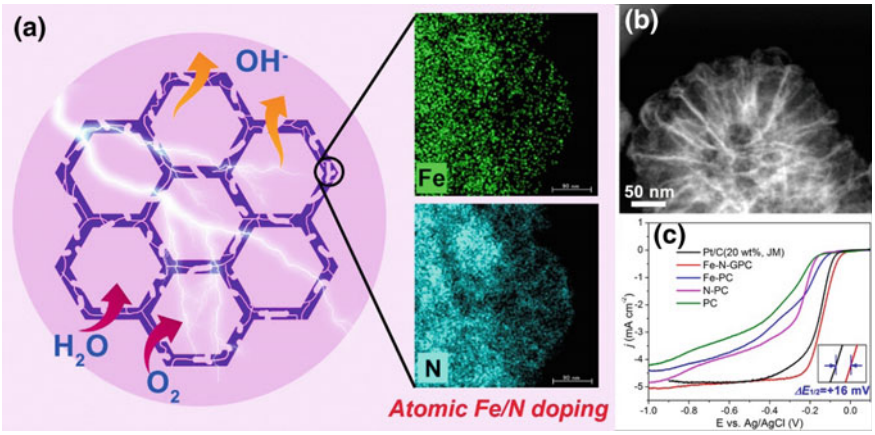

Fig. 17 **a** Illustration of the hierarchical porous Fe/N-GPC catalysts with atomic Fe and N doping; **b** TEM images of Fe/N-GPC; **c** ORR catalytic properties of Fe/N-GPC, comparative samples and 20 wt% Pt/C catalyst. Reproduced with permission from Ref. [113]. Copyright@2017 American Chemical Society

the single metal atom-doped carbon materials derived from MOFs have significant superior performance as catalysts over traditional metals.

3 Conclusion

In this chapter, we have discussed various MOFs, their composites and MOF-derived materials as catalysts various electrochemical reactions, including HER, OER, ORR and other redox reactions. MOFs with their advantageous features such as ultrahigh porosity, large surface areas and structural tunability have significant applications in redox chemistry. However, their low stability and conductivity are the negative factors, which should be controlled in order to improve their electrocatalytic properties. In order to improve the catalytic behaviors, MOFs are composited with conducting materials like graphene, metal NPs, metal oxides/sulfides and so on, which not only enhances their electrical conductivity but also gives additional electrocatalytic features. The unique morphologies and ultrahigh surface areas of MOFs further prompted researchers to pyrolyze them to drive carbon-based materials, which can inherit MOFs' high surface areas and morphologies and perform better electrocatalytic activity and stability than the original MOFs. A series of MOFs, their composites, and MOF-derived materials are discussed here for their electrocatalytic applications. Nonetheless, further investigations are still essential in the field of MOF electrocatalysts. Crystal design and structural morphologies, theoretical simulations, and computational studies should be further performed, which could help to optimize and evaluate their electrochemical properties.

References

1. Furukawa H, Cordova KE, O'Keeffe M, Yaghi OM (2013) The chemistry and applications of metal-organic frameworks. Science 341:1230444
2. Schröder M (2010) Functional metal-organic frameworks: gas storage, separation and catalysis, 1st edn. Springer, Berlin
3. Kirchon A, Feng L, Drake HF, Joseph EA, Zhou H-C (2018) From fundamentals to applications: a toolbox for robust and multifunctional MOF materials. Chem Soc Rev 47:8611–8638
4. Wang H, Zhu Q-L, Zou R, Xu Q (2017) Metal-organic frameworks for energy applications. Chem 2:52–80
5. Zhou HC, Kitagawa S (2014) Metal-organic frameworks (MOFs). Chem Soc Rev 43:5415–5418
6. Lu W, Wei Z, Gu Z-Y, Liu T-F, Park J, Park J, Tian J, Zhang M, Zhang Q, Gentle T III, Bosch M, Zhou H-C (2014) Tuning the structure and function of metal–organic frameworks via linker design. Chem Soc Rev 43:5561–5593
7. Deria P, Mondloch JE, Karagiaridi O, Bury W, Hupp JT, Farha OK (2014) Beyond post-synthesis modification: evolution of metal–organic frameworks via building block replacement. Chem Soc Rev 43:5896–5912
8. Farha OK, Wilmer CE, Eryazici I, Hauser BG, Parilla PA, O'Neill K, Sarjeant AA, Nguyen ST, Snurr RQ, Hupp JT (2012) Designing higher surface area metal-organic frameworks: are triple bonds better than phenyls? J Am Chem Soc 134:9860–9863
9. Hendon CH, Rieth AJ, Korzyński MD, Dincă M (2017) Grand challenges and future opportunities for metal-organic frameworks. ACS Cent Sci 3:554–563
10. Farha OK, Eryazici I, Jeong NC, Hauser BG, Wilmer CE, Sarjeant AA, Snurr RQ, Nguyen ST, Yazaydın AÖ, Hupp JT (2012) Metal-organic framework materials with ultrahigh surface areas: is the sky the limit? J Am Chem Soc 134:15016–15021
11. Deng H, Grunder S, Cordova KE, Valente C, Furukawa H, Hmadeh M, Gándara F, Whalley AC, Liu Z, Asahina S, Kazumori H, O'Keeffe M, Terasaki O, Stoddart JF, Yaghi OM (2012) Large-pore apertures in a series of metal-organic frameworks. Science 336:1018
12. Silva P, Vilela SMF, Tomé JPC, Almeida Paz FA (2015) Multifunctional metal–organic frameworks: from academia to industrial applications. Chem Soc Rev 44:6774–6803
13. Kobayashi Y, Jacobs B, Allendorf MD, Long JR (2010) Conductivity, doping, and redox chemistry of a microporous dithiolene-based metal–organic framework. Chem Mater 22:4120–4122
14. Hendon CH, Tiana D, Walsh A (2012) Conductive metal–organic frameworks and networks: fact or fantasy? Phys Chem Chem Phys 14:13120–13132
15. Stavila V, Talin AA, Allendorf MD (2014) MOF-based electronic and opto-electronic devices. Chem Soc Rev 43:5994–6010
16. Silva CG, Corma A, García H (2010) Metal–organic frameworks as semiconductors. J Mater Chem 20:3141–3156
17. Talin AA, Centrone A, Ford AC, Foster ME, Stavila V, Haney P, Kinney RA, Szalai V, El Gabaly F, Yoon HP, Léonard F, Allendorf MD (2014) Tunable electrical conductivity in metal-organic framework thin-film devices. Science 343:66
18. Sheberla D, Bachman JC, Elias JS, Sun C-J, Shao-Horn Y, Dincă M (2016) Conductive MOF electrodes for stable supercapacitors with high areal capacitance. Nat Mater 16:220
19. Sheberla D, Sun L, Blood-Forsythe MA, Er S, Wade CR, Brozek CK, Aspuru-Guzik A, Dincă M (2014) High electrical conductivity in Ni_3(2,3,6,7,10,11-hexaiminotriphenylene)$_2$, a semiconducting metal-organic graphene analogue. J Am Chem Soc 136:8859–8862
20. Miner EM, Fukushima T, Sheberla D, Sun L, Surendranath Y, Dincă M (2016) Electrochemical oxygen reduction catalysed by Ni_3(hexaiminotriphenylene)$_2$. Nat Commun 7:10942
21. Pathak A, Shen J-W, Usman M, Wei L-F, Mendiratta S, Chang Y-S, Sainbileg B, Ngue C-M, Chen R-S, Hayashi M, Luo T-T, Chen F-R, Chen K-H, Tseng T-W, Chen L-C, Lu K-L

(2019) Integration of a (–Cu–S–)$_n$ plane in a metal–organic framework affords high electrical conductivity. Nat Commun 10:1721
22. Usman M, Mendiratta S, Lu K-L (2017) Semiconductor metal-organic frameworks: future low-bandgap materials. Adv Mater 29:1605071
23. Sivula K, van de Krol R (2016) Semiconducting materials for photoelectrochemical energy conversion. Nat Rev Mater 1:15010
24. Turner JA (2004) Sustainable hydrogen production. Science 305:972
25. Guan BY, Yu L, Lou XW (2016) A dual-metal–organic-framework derived electrocatalyst for oxygen reduction. Energy Environ Sci 9:3092–3096
26. Petit C, Bandosz TJ (2009) MOF–graphite oxide composites: combining the uniqueness of graphene layers and metal-organic frameworks. Adv Mater 21:4753–4757
27. Dang S, Zhu Q-L, Xu Q (2017) Nanomaterials derived from metal–organic frameworks. Nat Rev Mater 3:17075
28. Xu L, Wang X, Chai L, Li T-T, Hu Y, Qian J, Huang S (2019) Co_3O_4-anchored MWCNTs network derived from metal–organic frameworks as efficient OER electrocatalysts. Mater Lett
29. Zhang H, Hwang S, Wang M, Feng Z, Karakalos S, Luo L, Qiao Z, Xie X, Wang C, Su D, Shao Y, Wu G (2017) Single atomic iron catalysts for oxygen reduction in acidic media: particle size control and thermal activation. J Am Chem Soc 139:14143–14149
30. Zhu Q-L, Xu Q (2014) Metal–organic framework composites. Chem Soc Rev 43:5468–5512
31. Ko M, Mendecki L, Mirica KA (2018) Conductive two-dimensional metal–organic frameworks as multifunctional materials. Chem Commun 54:7873–7891
32. Yang HM, Song XL, Yang TL, Liang ZH, Fan CM, Hao XG (2014) Electrochemical synthesis of flower shaped morphology MOFs in an ionic liquid system and their electrocatalytic application to the hydrogen evolution reaction. RSC Adv 4:15720–15726
33. Gong Y, Hao Z, Meng J, Shi H, Jiang P, Zhang M, Lin J (2014) Two Co^{II} metal-organic frameworks based on a multicarboxylate ligand as electrocatalysts for water splitting. ChemPlusChem 79:266–277
34. Gong Y, Shi H-F, Hao Z, Sun J-L, Lin J-H (2013) Two novel Co(ii) coordination polymers based on 1,4-bis(3-pyridylaminomethyl)benzene as electrocatalysts for oxygen evolution from water. Dalton Trans 42:12252–12259
35. Wu Y-P, Zhou W, Zhao J, Dong W-W, Lan Y-Q, Li D-S, Sun C, Bu X (2017) Surfactant-assisted phase-selective synthesis of new cobalt MOFs and their efficient electrocatalytic hydrogen evolution reaction. Angew Chem Int Ed 56:13001–13005
36. Phan A, Doonan CJ, Uribe-Romo FJ, Knobler CB, O'Keeffe M, Yaghi OM (2010) Synthesis, structure, and carbon dioxide capture properties of zeolitic imidazolate frameworks. Acc Chem Res 43:58–67
37. Tao L, Lin C-Y, Dou S, Feng S, Chen D, Liu D, Huo J, Xia Z, Wang S (2017) Creating coordinatively unsaturated metal sites in metal-organic-frameworks as efficient electrocatalysts for the oxygen evolution reaction: insights into the active centers. Nano Energy 41:417–425
38. Wang S, Hou Y, Lin S, Wang X (2014) Water oxidation electrocatalysis by a zeolitic imidazolate framework. Nanoscale 6:9930–9934
39. Wang L, Wu Y, Cao R, Ren L, Chen M, Feng X, Zhou J, Wang B (2016) Fe/Ni metal-organic frameworks and their binder-free thin films for efficient oxygen evolution with low overpotential. ACS Appl Mater Interfaces 8:16736–16743
40. Xue Z, Li Y, Zhang Y, Geng W, Jia B, Tang J, Bao S, Wang H-P, Fan Y, Wei Z-W, Zhang Z, Ke Z, Li G, Su C-Y (2018) Modulating electronic structure of metal-organic framework for efficient electrocatalytic oxygen evolution. Adv Energy Mater 8:1801564
41. Wang X-L, Dong L-Z, Qiao M, Tang Y-J, Liu J, Li Y, Li S-L, Su J-X, Lan Y-Q (2018) Exploring the performance improvement of the oxygen evolution reaction in a stable bimetal-organic framework system. Angew Chem Int Ed 57:9660–9664
42. Zhou W, Huang D-D, Wu Y-P, Zhao J, Wu T, Zhang J, Li D-S, Sun C, Feng P, Bu X (2019) Stable hierarchical bimetal-organic nanostructures as high performance electrocatalysts for the oxygen evolution reaction. Angew Chem Int Ed 58:4227–4231

43. Li F-L, Shao Q, Huang X, Lang J-P (2018) Nanoscale trimetallic metal-organic frameworks enable efficient oxygen evolution electrocatalysis. Angew Chem Int Ed 57:1888–1892
44. Lu X-F, Liao P-Q, Wang J-W, Wu J-X, Chen X-W, He C-T, Zhang J-P, Li G-R, Chen X-M (2016) An alkaline-stable, metal hydroxide mimicking metal-organic framework for efficient electrocatalytic oxygen evolution. J Am Chem Soc 138:8336–8339
45. Mao J, Yang L, Yu P, Wei X, Mao L (2012) Electrocatalytic four-electron reduction of oxygen with Copper (II)-based metal-organic frameworks. Electrochem Commun 19:29–31
46. Usov PM, Huffman B, Epley CC, Kessinger MC, Zhu J, Maza WA, Morris AJ (2017) Study of electrocatalytic properties of metal-organic framework PCN-223 for the oxygen reduction reaction. ACS Appl Mater Interfaces 9:33539–33543
47. Song G, Wang Z, Wang L, Li G, Huang M, Yin F (2014) Preparation of MOF(Fe) and its catalytic activity for oxygen reduction reaction in an alkaline electrolyte. Chin J Catal 35:185–195
48. Albo J, Vallejo D, Beobide G, Castillo O, Castaño P, Irabien A (2017) Copper-based metal-organic porous materials for CO_2 electrocatalytic reduction to alcohols. ChemSusChem 10:1100–1109
49. Kornienko N, Zhao Y, Kley CS, Zhu C, Kim D, Lin S, Chang CJ, Yaghi OM, Yang P (2015) Metal-organic frameworks for electrocatalytic reduction of carbon dioxide. J Am Chem Soc 137:14129–14135
50. Clough AJ, Yoo JW, Mecklenburg MH, Marinescu SC (2015) Two-dimensional metal-organic surfaces for efficient hydrogen evolution from water. J Am Chem Soc 137:118–121
51. Dong R, Pfeffermann M, Liang H, Zheng Z, Zhu X, Zhang J, Feng X (2015) Large-area, free-standing, two-dimensional supramolecular polymer single-layer sheets for highly efficient electrocatalytic hydrogen evolution. Angew Chem Int Ed 54:12058–12063
52. Dong R, Zheng Z, Tranca DC, Zhang J, Chandrasekhar N, Liu S, Zhuang X, Seifert G, Feng X (2017) Immobilizing molecular metal dithiolene–diamine complexes on 2D metal–organic frameworks for electrocatalytic H_2 production. Chem-A Eur J 23:2255–2260
53. Qin J-S, Du D-Y, Guan W, Bo X-J, Li Y-F, Guo L-P, Su Z-M, Wang Y-Y, Lan Y-Q, Zhou H-C (2015) Ultrastable polymolybdate-based metal-organic frameworks as highly active electrocatalysts for hydrogen generation from water. J Am Chem Soc 137:7169–7177
54. Jiang J, Huang L, Liu X, Ai L (2017) Bioinspired cobalt-citrate metal–organic framework as an efficient electrocatalyst for water oxidation. ACS Appl Mater Interfaces 9:7193–7201
55. Zhao L, Dong B, Li S, Zhou L, Lai L, Wang Z, Zhao S, Han M, Gao K, Lu M, Xie X, Chen B, Liu Z, Wang X, Zhang H, Li H, Liu J, Zhang H, Huang X, Huang W (2017) Interdiffusion reaction-assisted hybridization of two-dimensional metal-organic frameworks and $Ti_3C_2T_x$ nanosheets for electrocatalytic oxygen evolution. ACS Nano 11:5800–5807
56. Xu Q, Li H, Yue F, Chi L, Wang J (2016) Nanoscale cobalt metal–organic framework as a catalyst for visible light-driven and electrocatalytic water oxidation. New J Chem 40:3032–3035
57. Wang H, Yin F-X, Chen B-H, He X-B, Lv P-L, Ye C-Y, Liu D-J (2017) ZIF-67 incorporated with carbon derived from pomelo peels: a highly efficient bifunctional catalyst for oxygen reduction/evolution reactions. Appl Catal B 205:55–67
58. Shen J-Q, Liao P-Q, Zhou D-D, He C-T, Wu J-X, Zhang W-X, Zhang J-P, Chen X-M (2017) Modular and stepwise synthesis of a hybrid metal-organic framework for efficient electrocatalytic oxygen evolution. J Am Chem Soc 139:1778–1781
59. Gong Y, Shi H-F, Jiang P-G, Hua W, Lin J-H (2014) Metal(II)-induced coordination polymer based on 4-(5-(Pyridin-4-yl)-4H-1,2,4-triazol-3-yl)benzoate as an electrocatalyst for water splitting. Cryst Growth Des 14:649–657
60. Dai F, Fan W, Bi J, Jiang P, Liu D, Zhang X, Lin H, Gong C, Wang R, Zhang L, Sun D (2016) A lead–porphyrin metal–organic framework: gas adsorption properties and electrocatalytic activity for water oxidation. Dalton Trans 45:61–65
61. Lions M, Tommasino JB, Chattot R, Abeykoon B, Guillou N, Devic T, Demessence A, Cardenas L, Maillard F, Fateeva A (2017) Insights into the mechanism of electrocatalysis of the oxygen reduction reaction by a porphyrinic metal organic framework. Chem Commun 53:6496–6499

62. Cho K, Han S-H, Suh MP (2016) Copper-organic framework fabricated with CuS nanoparticles: synthesis, electrical conductivity, and electrocatalytic activities for oxygen reduction reaction. Angew Chem Int Ed 55:15301–15305
63. Miao P, Li G, Zhang G, Lu H (2014) Co(II)-salen complex encapsulated into MIL-100(Cr) for electrocatalytic reduction of oxygen. J Energy Chem 23:507–512
64. Dai X, Liu M, Li Z, Jin A, Ma Y, Huang X, Sun H, Wang H, Zhang X (2016) Molybdenum polysulfide anchored on porous Zr-metal organic framework to enhance the performance of hydrogen evolution reaction. J Phys Chem C 120:12539–12548
65. Johnson BA, Bhunia A, Ott S (2017) Electrocatalytic water oxidation by a molecular catalyst incorporated into a metal–organic framework thin film. Dalton Trans 46:1382–1388
66. Lin S, Pineda-Galvan Y, Maza WA, Epley CC, Zhu J, Kessinger MC, Pushkar Y, Morris AJ (2017) Electrochemical water oxidation by a catalyst-modified metal-organic framework thin film. ChemSusChem 10:514–522
67. Khan MI, Swenson LS (2013) Open-framework hybrid materials and composites from polyoxometalates (Chap. 2). In: New and future developments in catalysis. Elsevier Science
68. Nohra B, El Moll H, Rodriguez Albelo LM, Mialane P, Marrot J, Mellot-Draznieks C, O'Keeffe M, Ngo Biboum R, Lemaire J, Keita B, Nadjo L, Dolbecq A (2011) Polyoxometalate-based metal organic frameworks (POMOFs): structural trends, energetics, and high electrocatalytic efficiency for hydrogen evolution reaction. J Am Chem Soc 133:13363–13374
69. Du D-Y, Qin J-S, Li S-L, Su Z-M, Lan Y-Q (2014) Recent advances in porous polyoxometalate-based metal–organic framework materials. Chem Soc Rev 43:4615–4632
70. Salomon W, Paille G, Gomez-Mingot M, Mialane P, Marrot J, Roch-Marchal C, Nocton G, Mellot-Draznieks C, Fontecave M, Dolbecq A (2017) Effect of cations on the structure and electrocatalytic response of polyoxometalate-based coordination polymers. Cryst Growth Des 17:1600–1609
71. Jahan M, Liu Z, Loh KP (2013) A graphene oxide and copper-centered metal organic framework composite as a tri-functional catalyst for HER, OER, and ORR. Adv Funct Mater 23:5363–5372
72. Nie Y, Li L, Wei Z (2015) Recent advancements in Pt and Pt-free catalysts for oxygen reduction reaction. Chem Soc Rev 44:2168–2201
73. Zhu Q-L, Li J, Xu Q (2013) Immobilizing metal nanoparticles to metal-organic frameworks with size and location control for optimizing catalytic performance. J Am Chem Soc 135:10210–10213
74. Zhu Q-L, Xu Q (2016) Immobilization of ultrafine metal nanoparticles to high-surface-area materials and their catalytic applications. Chem 1:220–245
75. Guo J, Zhang X, Sun Y, Tang L, Liu Q, Zhang X (2017) Loading Pt nanoparticles on metal-organic frameworks for improved oxygen evolution. ACS Sustain Chem Eng 5:11577–11583
76. Hod I, Deria P, Bury W, Mondloch JE, Kung C-W, So M, Sampson MD, Peters AW, Kubiak CP, Farha OK, Hupp JT (2015) A porous proton-relaying metal-organic framework material that accelerates electrochemical hydrogen evolution. Nat Commun 6:8304
77. Wang H, Yin F, Chen B, Li G (2015) Synthesis of an ε-MnO_2/metal–organic-framework composite and its electrocatalysis towards oxygen reduction reaction in an alkaline electrolyte. J Mater Chem A 3:16168–16176
78. Zhao S, Wang Y, Dong J, He C-T, Yin H, An P, Zhao K, Zhang X, Gao C, Zhang L, Lv J, Wang J, Zhang J, Khattak AM, Khan NA, Wei Z, Zhang J, Liu S, Zhao H, Tang Z (2016) Ultrathin metal–organic framework nanosheets for electrocatalytic oxygen evolution. Nat Energy 1:16184
79. Duan J, Chen S, Zhao C (2017) Ultrathin metal-organic framework array for efficient electrocatalytic water splitting. Nat Commun 8:15341
80. Li W, Watzele S, El-Sayed HA, Liang Y, Kieslich G, Bandarenka AS, Rodewald K, Rieger B, Fischer RA (2019) Unprecedented high oxygen evolution activity of electrocatalysts derived from surface-mounted metal-organic frameworks. J Am Chem Soc 141:5926–5933

81. Cao C, Ma D-D, Xu Q, Wu X-T, Zhu Q-L (2019) Semisacrificial template growth of self-supporting MOF nanocomposite electrode for efficient electrocatalytic water oxidation. Adv Funct Mater 29:1807418
82. Senthil Raja D, Chuah X-F, Lu S-Y (2018) In situ grown bimetallic MOF-based composite as highly efficient bifunctional electrocatalyst for overall water splitting with ultrastability at high current densities. Adv Energy Mater 8:1801065
83. Sun F, Wang G, Ding Y, Wang C, Yuan B, Lin Y (2018) NiFe-based metal-organic framework nanosheets directly supported on nickel foam acting as robust electrodes for electrochemical oxygen evolution reaction. Adv Energy Mater 8:1800584
84. Wang H, Yin F, Li G, Chen B, Wang Z (2014) Preparation, characterization and bifunctional catalytic properties of MOF(Fe/Co) catalyst for oxygen reduction/evolution reactions in alkaline electrolyte. Int J Hydrogen Energy 39:16179–16186
85. He X, Yin F, Li G (2015) A Co/metal–organic-framework bifunctional electrocatalyst: the effect of the surface cobalt oxidation state on oxygen evolution/reduction reactions in an alkaline electrolyte. Int J Hydrogen Energy 40:9713–9722
86. Sohrabi S, Dehghanpour S, Ghalkhani M (2016) Three-dimensional metal-organic framework graphene nanocomposite as a highly efficient and stable electrocatalyst for the oxygen reduction reaction in acidic media. ChemCatChem 8:2356–2366
87. Jiang M, Li L, Zhu D, Zhang H, Zhao X (2014) Oxygen reduction in the nanocage of metal–organic frameworks with an electron transfer mediator. J Mater Chem A 2:5323–5329
88. Liu B, Shioyama H, Akita T, Xu Q (2008) Metal-organic framework as a template for porous carbon synthesis. J Am Chem Soc 130:5390–5391
89. Lei Y, Wei L, Zhai S, Wang Y, Karahan HE, Chen X, Zhou Z, Wang C, Sui X, Chen Y (2018) Metal-free bifunctional carbon electrocatalysts derived from zeolitic imidazolate frameworks for efficient water splitting. Mater Chem Front 2:102–111
90. Yang Y, Lun Z, Xia G, Zheng F, He M, Chen Q (2015) Non-precious alloy encapsulated in nitrogen-doped graphene layers derived from MOFs as an active and durable hydrogen evolution reaction catalyst. Energy Environ Sci 8:3563–3571
91. Zheng F, Xia H, Xu S, Wang R, Zhang Y (2016) Facile synthesis of MOF-derived ultrafine Co nanocrystals embedded in a nitrogen-doped carbon matrix for the hydrogen evolution reaction. RSC Adv 6:71767–71772
92. Zhou W, Lu J, Zhou K, Yang L, Ke Y, Tang Z, Chen S (2016) $CoSe_2$ nanoparticles embedded defective carbon nanotubes derived from MOFs as efficient electrocatalyst for hydrogen evolution reaction. Nano Energy 28:143–150
93. Tabassum H, Guo W, Meng W, Mahmood A, Zhao R, Wang Q, Zou R (2017) Metal-organic frameworks derived cobalt phosphide architecture encapsulated into B/N Co-doped graphene nanotubes for all pH value electrochemical hydrogen evolution. Adv Energy Mater 7:1601671
94. Zhu Z, Yang Y, Guan Y, Xue J, Cui L (2016) Construction of a cobalt-embedded nitrogen-doped carbon material with the desired porosity derived from the confined growth of MOFs within graphene aerogels as a superior catalyst towards HER and ORR. J Mater Chem A 4:15536–15545
95. Huang T, Chen Y, Lee J-M (2017) Two-dimensional cobalt/N-doped carbon hybrid structure derived from metal-organic frameworks as efficient electrocatalysts for hydrogen evolution. ACS Sustain Chem Eng 5:5646–5650
96. Wang T, Zhou Q, Wang X, Zheng J, Li X (2015) MOF-derived surface modified Ni nanoparticles as an efficient catalyst for the hydrogen evolution reaction. J Mater Chem A 3:16435–16439
97. Jayaramulu K, Masa J, Tomanec O, Peeters D, Ranc V, Schneemann A, Zboril R, Schuhmann W, Fischer RA (2017) Electrocatalysis: nanoporous nitrogen-doped graphene oxide/nickel sulfide composite sheets derived from a metal-organic framework as an efficient electrocatalyst for hydrogen and oxygen evolution. Adv Funct Mater 27:1700451
98. Higgins D, Zamani P, Yu A, Chen Z (2016) The application of graphene and its composites in oxygen reduction electrocatalysis: a perspective and review of recent progress. Energy Environ Sci 9:357–390

99. Ai L, Tian T, Jiang J (2017) Ultrathin graphene layers encapsulating nickel nanoparticles derived metal-organic frameworks for highly efficient electrocatalytic hydrogen and oxygen evolution reactions. ACS Sustain Chem Eng 5:4771–4777
100. Liu S, Zhang H, Zhao Q, Zhang X, Liu R, Ge X, Wang G, Zhao H, Cai W (2016) Metal-organic framework derived nitrogen-doped porous carbon@graphene sandwich-like structured composites as bifunctional electrocatalysts for oxygen reduction and evolution reactions. Carbon 106:74–83
101. Chaikittisilp W, Torad NL, Li C, Imura M, Suzuki N, Ishihara S, Ariga K, Yamauchi Y (2014) Synthesis of nanoporous carbon–cobalt-oxide hybrid electrocatalysts by thermal conversion of metal–organic frameworks. Chem A Eur J 20:4217–4221
102. Xia W, Zhu J, Guo W, An L, Xia D, Zou R (2014) Well-defined carbon polyhedrons prepared from nano metal–organic frameworks for oxygen reduction. J Mater Chem A 2:11606–11613
103. You B, Jiang N, Sheng M, Drisdell WS, Yano J, Sun Y (2015) Bimetal-organic framework self-adjusted synthesis of support-free nonprecious electrocatalysts for efficient oxygen reduction. ACS Catal 5:7068–7076
104. Shang L, Yu H, Huang X, Bian T, Shi R, Zhao Y, Waterhouse GIN, Wu L-Z, Tung C-H, Zhang T (2016) Well-dispersed ZIF-derived Co, N-Co-doped carbon nanoframes through mesoporous-silica-protected calcination as efficient oxygen reduction electrocatalysts. Adv Mater 28:1668–1674
105. Zhu Q-L, Xia W, Akita T, Zou R, Xu Q (2016) Metal-organic framework-derived honeycomb-like open porous nanostructures as precious-metal-free catalysts for highly efficient oxygen electroreduction. Adv Mater 28:6391–6398
106. Pan Y, Sun K, Liu S, Cao X, Wu K, Cheong W-C, Chen Z, Wang Y, Li Y, Liu Y, Wang D, Peng Q, Chen C, Li Y (2018) Core-shell ZIF-8@ZIF-67-derived CoP nanoparticle-embedded N-doped carbon nanotube hollow polyhedron for efficient overall water splitting. J Am Chem Soc 140:2610–2618
107. He P, Yu X-Y, Lou XW (2017) Carbon-incorporated nickel-cobalt mixed metal phosphide nanoboxes with enhanced electrocatalytic activity for oxygen evolution. Angew Chem Int Ed 56:3897–3900
108. Han L, Yu X-Y, Lou XW (2016) Formation of Prussian-blue-analog nanocages via a direct etching method and their conversion into Ni–Co-mixed oxide for enhanced oxygen evolution. Adv Mater 28:4601–4605
109. Qu Y, Li Z, Chen W, Lin Y, Yuan T, Yang Z, Zhao C, Wang J, Zhao C, Wang X, Zhou F, Zhuang Z, Wu Y, Li Y (2018) Direct transformation of bulk copper into copper single sites via emitting and trapping of atoms. Nat Catal 1:781–786
110. Wang X, Chen W, Zhang L, Yao T, Liu W, Lin Y, Ju H, Dong J, Zheng L, Yan W, Zheng X, Li Z, Wang X, Yang J, He D, Wang Y, Deng Z, Wu Y, Li Y (2017) Uncoordinated amine groups of metal-organic frameworks to anchor single Ru sites as chemoselective catalysts toward the hydrogenation of quinoline. J Am Chem Soc 139:9419–9422
111. Yang Q, Yang C-C, Lin C-H, Jiang H-L (2019) Metal–organic-framework-derived hollow N-doped porous carbon with ultrahigh concentrations of single Zn atoms for efficient carbon dioxide conversion. Angew Chem Int Ed 58:3511–3515
112. Ma S, Goenaga GA, Call AV, Liu D-J (2011) Cobalt imidazolate framework as precursor for oxygen reduction reaction electrocatalysts. Chem A Eur J 17:2063–2067
113. Zhu Q-L, Xia W, Zheng L-R, Zou R, Liu Z, Xu Q (2017) Atomically dispersed Fe/N-doped hierarchical carbon architectures derived from a metal-organic framework composite for extremely efficient electrocatalysis. ACS Energy Lett 2:504–511
114. Chen Y, Ji S, Wang Y, Dong J, Chen W, Li Z, Shen R, Zheng L, Zhuang Z, Wang D, Li Y (2017) Isolated single iron atoms anchored on N-doped porous carbon as an efficient electrocatalyst for the oxygen reduction reaction. Angew Chem Int Ed 56:6937–6941
115. Zhao R, Liang Z, Gao S, Yang C, Zhu B, Zhao J, Qu C, Zou R, Xu Q (2019) Puffing up energetic metal-organic frameworks to large carbon networks with hierarchical porosity and atomically dispersed metal sites. Angew Chem Int Ed 58:1975–1979

116. Wang J, Huang Z, Liu W, Chang C, Tang H, Li Z, Chen W, Jia C, Yao T, Wei S, Wu Y, Li Y (2017) Design of N-coordinated dual-metal sites: a stable and active Pt-free catalyst for acidic oxygen reduction reaction. J Am Chem Soc 139:17281–17284
117. Sun C, Dong Q, Yang J, Dai Z, Lin J, Chen P, Huang W, Dong X (2016) Metal–organic framework derived $CoSe_2$ nanoparticles anchored on carbon fibers as bifunctional electrocatalysts for efficient overall water splitting. Nano Res 9:2234–2243
118. Guan C, Liu X, Elshahawy AM, Zhang H, Wu H, Pennycook SJ, Wang J (2017) Metal–organic framework derived hollow CoS_2 nanotube arrays: an efficient bifunctional electrocatalyst for overall water splitting. Nanoscale Horiz 2:342–348
119. Yan L, Cao L, Dai P, Gu X, Liu D, Li L, Wang Y, Zhao X (2017) Metal-organic frameworks derived nanotube of nickel-cobalt bimetal phosphides as highly efficient electrocatalysts for overall water splitting. Adv Funct Mater 27:1703455
120. Su J, Yang Y, Xia G, Chen J, Jiang P, Chen Q (2017) Ruthenium-cobalt nanoalloys encapsulated in nitrogen-doped graphene as active electrocatalysts for producing hydrogen in alkaline media. Nat Commun 8:14969
121. Liu S, Wang Z, Zhou S, Yu F, Yu M, Chiang C-Y, Zhou W, Zhao J, Qiu J (2017) Metal–organic-framework-derived hybrid carbon nanocages as a bifunctional electrocatalyst for oxygen reduction and evolution. Adv Mater 29:1700874
122. Guan C, Sumboja A, Wu H, Ren W, Liu X, Zhang H, Liu Z, Cheng C, Pennycook SJ, Wang J (2017) Hollow Co_3O_4 nanosphere embedded in carbon arrays for stable and flexible solid-state zinc-air batteries. Adv Mater 29:1704117
123. Xia BY, Yan Y, Li N, Wu HB, Lou XW, Wang X (2016) A metal–organic framework-derived bifunctional oxygen electrocatalyst. Nat Energy 1:15006
124. Li W-J, Liu J, Sun Z-H, Liu T-F, Lü J, Gao S-Y, He C, Cao R, Luo J-H (2016) Integration of metal-organic frameworks into an electrochemical dielectric thin film for electronic applications. Nat Commun 7:11830
125. Li Z, Shao M, Zhou L, Zhang R, Zhang C, Wei M, Evans DG, Duan X (2016) Directed growth of metal-organic frameworks and their derived carbon-based network for efficient electrocatalytic oxygen reduction. Adv Mater 28:2337–2344

Single-Atom Electrocatalysts for Water Splitting

Robson R. Guimaraes, Josue M. Gonçalves, Olle Björneholm, C. Moyses Araujo, Arnaldo Naves de Brito and Koiti Araki

Abstract The amount of energy that has being required to keep the well-being of our society is increasing continuously imposing an urgent need for renewable and less pollutant alternative energy sources to fossil fuels, whose consumption in internal combustion engines and electric power plants are responsible for unprecedented atmospheric pollution, particularly concentrated in large cities. Another consequence seems to be the general increase of temperature of the planet leading to climate changes and catastrophic extreme events. Thus, the possibility of reserves depletion and global environmental issues associated with its use are prompting the search for clean renewable energy sources, as well as the development of efficient and more robust energy storage systems. The most promising one for such a purpose is based on the splitting of water in a photosynthetic system to store the energy of Sun as hydrogen and oxygen. In order to realize such a technology, new more efficient electrocatalysts for oxygen and hydrogen evolution reaction based on single-atom catalysts, especially designed to exploit the maximum potentiality of the elements, are being developed, fueled by increasingly powerful theoretical modelling and characterization tools, thus paving broad roads towards a bright and sustainable society. The main advancements for preparation and characterization of such novel strategic materials are considered in this account. Furthermore, atomic scale modelling based on density functional theory is also discussed in the context of the unique electronic

R. R. Guimaraes · J. M. Gonçalves · K. Araki (✉)
Department of Fundamental Chemistry, Institute of Chemistry, University of Sao Paulo, Av. Lineu Prestes 748, Butanta, Sao Paulo, SP 05508-000, Brazil
e-mail: koiaraki@iq.usp.br

O. Björneholm
Molecular and Condensed Matter Physics Division, Department of Physics and Astronomy, Uppsala University, Box 516 75120 Uppsala, Sweden

C. Moyses Araujo
Materials Theory Division, Department of Physics and Astronomy, Uppsala University, Box 516 75120 Uppsala, Sweden

A. N. de Brito
Institute of Physics "Gleb Wataghin", State University of Campinas, Campinas, SP 13083-859, Brazil

Inamuddin et al. (eds.), *Methods for Electrocatalysis*,
https://doi.org/10.1007/978-3-030-27161-9_3

structure that leads to superior catalytic activity, highlighting its potential to advance this important scientific field.

Keywords Single-atom catalyst · Water splitting · Oxygen evolution reaction · Hydrogen evolution reaction · Synthesis · Theoretical modelling

List of Abbreviations

ADF	Angular dark-field
ALD	Atomic layer deposition
CNT	Carbon nanotube
CoSSPIL	Co-single-site polymerized ionic liquid
CVD	Chemical vapor deposition
DFT	Density functional theory
EDX	Energy-dispersive X-ray spectroscopy
EELS	Electron energy-loss spectroscopy
EXAFS	Extended X-ray absorption fine structure
FePc	Iron (II) phthalocyanine
g-C_3N_4	Graphitic carbon nitrides
HAADF	High angle angular dark-field
HER	Hydrogen evolution reaction
ILs	Ionic liquids
LDHs	Lamellar double hydroxides
LSV	Linear-sweep voltammograms
MOFs	Metal-organic frameworks
M-NHGF	3d metals embedded in nitrogen-doped holey graphene frameworks
NEXAFS	Near Edge X-Ray Absorption Fine Structure
NPs	Nanoparticles
np-G	Nanoporous graphene
RHE	Reversible hydrogen electrode
SAC	Sigle-Atom Catalyst
SCE	Saturated calomel electrode
STEM	Scanning transmission electron microscopy
SWCT	Single-wall carbon nanotubes
TEM	Transmission electron microscopy
OER	Oxygen Evolution Reaction
XANES	X-ray absorption near-edge structure
XPS	X-ray photoelectron spectroscopy
ZIF	Zeolitic imidazole framework
Pd-NRs	Pd-nanorings

1 Introduction

There is a consensus that technological, economical, and social development are strongly dependent on sustainable energy sources, alternative to fossil fuels responsible for the green-house effect and global warming, as well as unacceptable imbalance in the environment that can be responsible for large-scale disasters in near future. Among the alternatives, water splitting has attracted large interest due to the possibility of producing high energy hydrogen and oxygen gas molecules that can then be recombined regenerating water while generating energy, for example in fuel cells, in an environmentally benign closed cycle.

Among the possibilities, the electrolysis of water (Fig. 1) is the most promising process [1] but the electricity must come ideally from clean and inexhaustible primary source such as from the Sun, directly as light, or as wind, waves, and hydroelectric energy, as well as geothermal sources, instead of from fossil fuels. In that process, water is reduced and oxidized respectively to hydrogen (Hydrogen Evolution Reaction, HER) and oxygen (Oxygen Evolution Reaction, OER), in alkaline or acidic conditions, as shown in Scheme 1. However, despite the apparent simplicity, that reaction is plagued by quite high overpotentials, particularly the OER involving $4H^+$ and $4e^-$, and the formation of an O=O bond. In fact, this has been the bottle neck for the development of more efficient fuel cells and water splitting systems, demonstrating the relevance of electrocatalysts with lower overpotentials and high current efficiency.

Another fundamental question come from the fact that HER and OER are coupled together and must take place in the same electrolyte solution, implying that the electrode materials for both processes must be stable at the operation conditions. Generally, the cathode and the anode are separated by an ionic conducting membrane avoiding the diffusion of H_2 into O_2 gas, and the charge build-up during the electrolysis by allowing the exchange of ions in between the anodic and cathodic

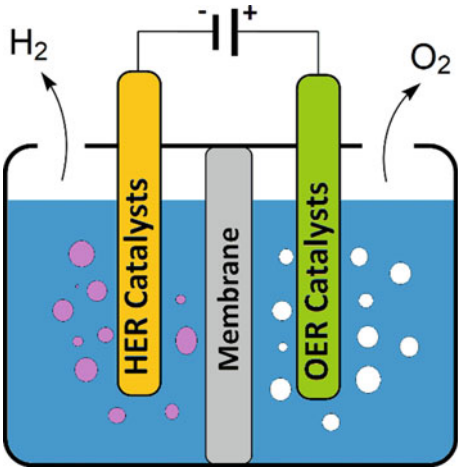

Fig. 1 Illustration showing a typical water splitting system constituted by two electrodes and a ion transport membrane. The negative and positive electrodes are made of a HER and OER catalyst respectively

Scheme 1 Water splitting reaction in acidic and alkaline conditions

Acidic condition

$$\text{HER:} \quad 2H^+ + 2e^- \longrightarrow H_2 \qquad E^0 = -1.23\ \text{V}$$

$$\text{OER:} \quad H_2O \longrightarrow \tfrac{1}{2}O_2 + 2H^+ + 2e^- \qquad E^0 = 0.00\ \text{V}$$

$$H_2O \longrightarrow H_2 + \tfrac{1}{2}O_2 \qquad E^0 = -1.23\ \text{V}$$

Alkaline condition

$$\text{HER:} \quad 2H_2O + 2e^- \longrightarrow H_2 + 2OH^- \qquad E^0 = -0.40\ \text{V}$$

$$\text{OER:} \quad 2OH^- \longrightarrow \tfrac{1}{2}O_2 + H_2O + 2e^- \qquad E^0 = -0.83\ \text{V}$$

$$H_2O \longrightarrow H_2 + \tfrac{1}{2}O_2 \qquad E^0 = -1.23\ \text{V}$$

chambers. The reduction of water takes place in the negatively polarized electrode made of, or coated with a suitable HER catalyst, generally based on platinum. The complementary oxidation reaction must take place in the positively polarized electrode made of, or covered with an efficient OER catalyst generally based on iridium oxide (IrO_2) and ruthenium oxide (RuO_2) [2].

The strategic relevance of water splitting catalysts have prompted researchers to test and seek for new materials with high activity as well as chemical and mechanical stability. Miles and Thomason demonstrated in 1976 that the catalytic activity in 0.1 M H_2SO_4, at 80 °C [3] is dependent on the metal element (Fig. 2). The best

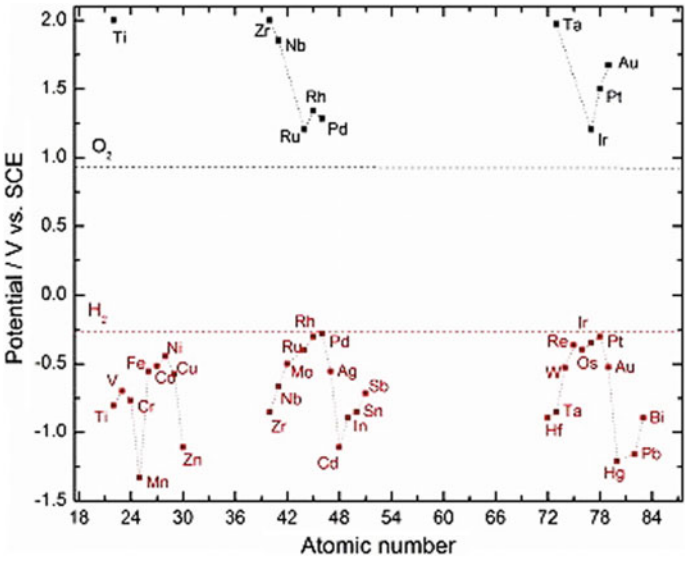

Fig. 2 Plot of potential (*vs.* SCE) at current density of 2 mA cm^{-2} in 0.1 M H_2SO_4 at 80 °C, determined by cyclic voltammetry at $v = 50$ mV s^{-1}, as a function of the atomic number of the metallic elements. Figure reproduced from [5] with permission of Elsevier

electrocatalysts for HER were found to be Pd > Pt ≈ Rh > Ir > Re > Os ≈ Ru > Ni, whereas the best ones for OER are Ir ≈ Ru > Pd > Rh > Pt > Au > Nb.

However, all metallic catalysts for water oxidation has the disadvantage to be unstable and been more or less easily converted to the respective oxides in operation conditions, where the chemical stability tend to be inversely proportional to the activity of the metallic material [4]. Accordingly, the development of new more chemically and mechanically resistant but highly active materials such as the metal oxides became of strategic relevance.

Among all metallic oxides, RuO_2 is the one commonly employed in OER given its high catalytic activity and low overpotentials in acidic and alkaline conditions [6], as well as high conductivity of the single crystals of about 10^4 cm^{-1} Ω^{-1} [7]. However, it is not immune to corrosion in acidic solutions and anodic potentials above 1.4 V (SCE) due to the formation of soluble oxides such as RuO_4 [8]. A generally used alternative is IrO_2, an oxide of a less abundant element exhibiting larger overpotentials but significantly larger stability in acidic solution (up to 2.0 V). New mixed ruthenium and iridium oxide catalysts and Ru-Ir metal alloys [9–12] with enhanced stability have being developed, but the use of noble metals for OER and HER increase the operation cost decreasing the competitiveness of the technology. Thus, it is of uttermost relevance finding low cost and highly efficient and stable alternative materials to make water splitting a widely used technology.

In this context, metal oxides/hydroxides of more abundant elements have been explored as both, HER and OER catalysts. The most commonly explored materials for the reduction reaction are based on iron, nickel, copper, cobalt, molybdenum and tungsten since exhibit quite high electrocatalytic activity and are much more abundant than platinum, the standard catalyst. In fact, sulfides, carbides, nitrides, selenides and phosphides of those metal elements have been investigated as hydrogen evolution catalysts [13, 14]. On the other hand, oxides/hydroxides of nickel, cobalt and manganese have being studied as catalysts for the oxygen evolution reaction showing much lower performance than noble metals such as Ir and Ru [15–17], but that have been significantly improved in the last five years. In addition, carbon materials such as graphene [18, 19], carbon nanotubes (CNT) [20], nanographite [21], fullerenes [22] and carbon hybrid materials [23] have evolved as excellent alternatives exhibiting good catalytic activity and very high stability at water splitting operation conditions. They have additional interesting properties such as high electric conductivity and mechanical resistance, high surface area and adsorption capacity, and can have high concentrations of functional groups to anchor other catalysts. Accordingly, they can be excellent building-blocks and co-catalysts for the development of hybrid and composite nanomaterials with interesting synergic effects.

Despite all those possibilities, the quest for HER and OER catalysts that can fulfill all the stringent requirements for real application are on the way, and precious metal are still being largely in use. However, in the beginning of this decade the concept of "Single-Atom Catalyst", SAC, was put forward opening wide new perspectives for the area as discussed now on.

2 Single-Atom Catalysts (SACs)

Molecular homogeneous catalysts tend to exhibit larger catalytic activity as compared with the solid-state materials since each of them presents an available active site. In contrast, only the sites on the particle surface are available for reaction in solid state catalysts. Accordingly, they are always prepared in such a way to maximize the surface area creating the highest as possible concentration of active sites, generally metal ions with open coordination sites, or highly acidic sites. In this context, minimizing the particles sizes is a very efficient strategy since the amount of such defects is inversely proportional to the square of radius, if spherical particles are considered. Accordingly, researches were focused on minimizing the size of the catalytic active particles as much as possible, if possible down to or below nanometer size.

However, such a focus was completely changed in 2003 when Fu, Saltsburg and Flytzani-Stephanopoulos [24] reported the successful preparation of a catalyst for water-gas shift reaction based on CeO_2 nanoparticles (NPs) but with gold and platinum deposited on the surface. The NPs were previously doped with La_2O_3 generating oxygen atom vacancies increasing their thermal stability, and subsequently treated with $HAuCl_4$ and H_2PtCl_4 solution. Interestingly enough, the material with less than 1 wt% of Au enhanced in 2 orders of magnitude the water-gas shift reaction, exhibiting a catalytic activity comparable to the commercial $Cu–ZnO–Al_2O_3$ (G-66A) catalyst. And, surprisingly, the $Au^{+1,+3}$ species, and $Pt^{+2,+4}$ in the case of the platinum derivative, were found to be responsible for such an impressive activity, after their removal with sodium cyanide and analyses. This achievement demonstrated that it is possible to use minimum amounts of precious metals to get new economically more attractive and environmentally more friendly high-performance catalysts.

The term "Single-Atom Catalyst" was coined and first introduced by Zhang and collaborators [25] in 2011 when they reported the preparation of Pt_1/FeO_x, a material constituted by iron oxide nanocrystals with single Pt atoms anchored on the surface by coprecipitation, under rigorous pH and temperature control. They realized a material with 0.17 wt% of Pt attached to surface defects of FeO_x nanoparticles exhibiting specific reaction rates for CO reduction by H_2 as high as 0.435 $mol_{CO}\ h^{-1}\ g_{Pt}^{-1}$, twice as large as compared with the standard Au/Fe_2O_3 catalyst. The characterization by atomic resolution high-angle annular dark-field and sub-ångström-resolution aberration-corrected scanning transmission electron microscopy (HAADF-STEM, Fig. 3a, b) clearly revealed the presence of single Pt atoms (white circles) homogeneously dispersed on the iron oxide surface.

The crystallochemical nature of the Pt atoms on the FeO_x nanoparticles surface was determined by extended X-ray absorption fine structure (EXAFS) using materials with increasing concentrations of Pt, that showed peaks at ~1.7 Å and ~2.5 Å, respectively assigned to Pt–O and Pt–Pt bond distances (Fig. 3c). Nevertheless, the material with 0.17 wt% of Pt exhibited only the Pt–O peak as expected for the presence of single Pt atoms attached to the iron oxide surface. In contrast, both peaks were found in the material with 2.5 wt% of Pt clearly indicating the presence of small

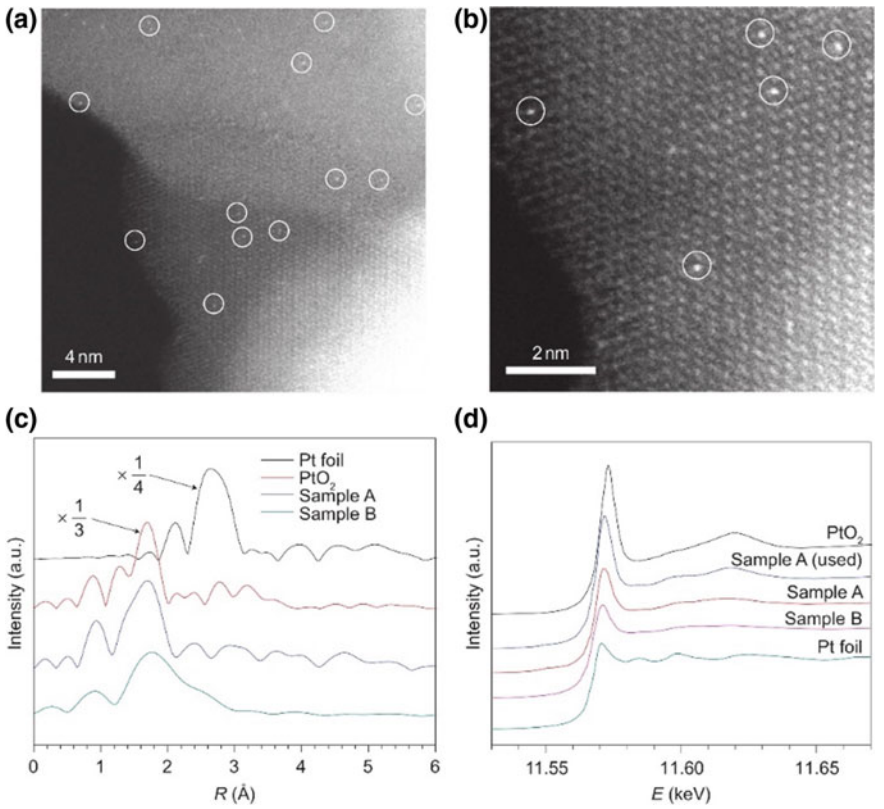

Fig. 3 **a**, **b** HAADF-STEM images of sample A. In sample A, Pt single atoms (white circles) are uniformly dispersed on the FeO_x support (**a**) and occupy exactly the positions of the Fe atoms (**b**). Examination of different regions reveals that only single Pt atoms are present in samples A and B X-ray absorption spectra, as shown in (**c**). The k3-weighted Fourier transform spectra from EXAFS. $\Delta k = 2.8–10.0$ Å^{-1} was used for samples A and B, but $\Delta k = 2.8–13.8$ Å^{-1} was used for Pt foil and PtO_2. The peaks at ~1.7 Å in the first shell of samples A and B are fitted to the Pt–O contribution from the interaction between Pt and the FeO_x support, and the very weak peaks at ~2.5 Å in the second shell are fitted to the Pt–Fe coordination in sample A and the Pt–Pt coordination in sample B, respectively. **d** The normalized XANES spectra at the Pt L_3 edge of sample A, sample B, PtO_2 and Pt foil. The data show a decreasing trend in the white-line intensities: PtO_2 > sample A (used) > sample A > sample B > Pt foil, which indicates that the Pt single atoms in sample A carry positive charges and were oxidized further during the reaction. a.u. = arbitrary units. Figure reproduced from [25] with permission of Springer Nature

Pt clusters in addition to isolated Pt atoms. In addition, normalized X-ray absorption near-edge structure (XANES) spectra of samples A and B presented peaks at 11.57 keV, similar to those found in PtO_2 and metal Pt standards (Fig. 3d), respectively indicated the predominance of Pt cations in the first and Pt^0 on the sample with 2.5 wt% Pt. Complimentary theoretical DFT study confirmed the high catalytic activity of Pt_1/FeO_x and the stabilization, as well as decrease of CO adsorption energy

and the activation energy for reduction of CO induced by electron-transfer from the Pt atoms to the iron oxide.

Accordingly, single-atom catalysts can be defined as materials containing isolated metal atoms directly bond on a suitable supporting material that are responsible for the catalytic effect. This can be any suitable material including metals (Fig. 4b), metal oxides (Fig. 4a), or even carbon-based materials such as graphene (Fig. 4c). Clearly, SACs are distinct materials when, for example, compared with hybrid materials or functionalized nanoparticles such as titanium dioxide with ruthenium complexes anchored on the surface [26] where two types of compounds can be easily distinguished. In SACs, the metal atoms can be sitting on specific coordination sites but that are part of the supporting material structure rather than distinct entities.

When a bulk material is ground forming smaller and smaller particles, for example microparticles, then nanoparticles, clusters, sub-nanoclusters and finally single-atoms, the surface area is increased in many orders of magnitude, greatly increasing the surface free-energy (Fig. 4d). Accordingly, single atoms have a strong tendency to form bonds and aggregates, that should be carefully controlled in order to realize materials with maximum concentration of active sites, overcoming the strong metal-metal interactions. Thus, the metal atoms must be bond strongly enough on the supporting material to stabilize and avoid the formation of clusters, demonstrating the fundamental relevance of choosing a suitable material to get durable SACs. In

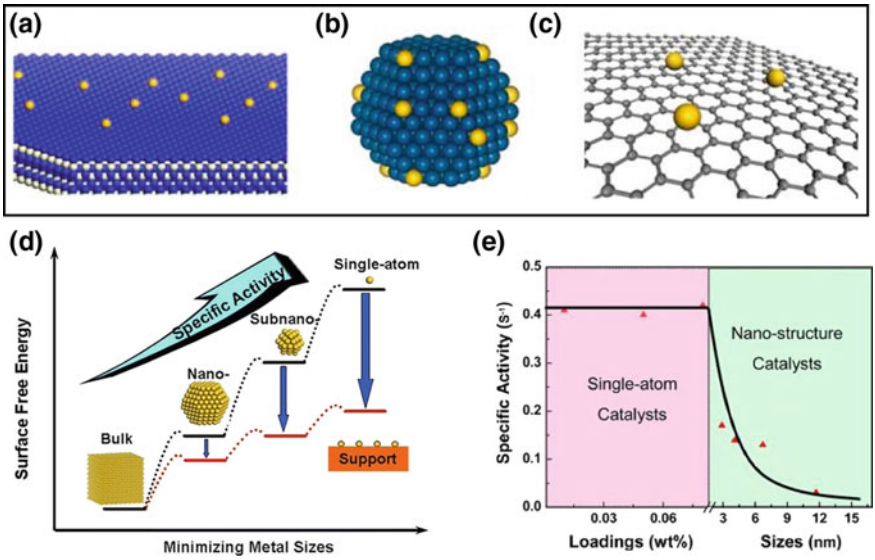

Fig. 4 Schematic diagrams illustrating different types of SACs: Metal single atoms anchored to **a** metal oxide and **b** metal surfaces, and **c** graphene. Schematic illustration showing the surface free energy and specific activity per metal atom as a function of metal particle size and the effect of the support on the stability of single-atoms (**d**). Specific activity as a function of metal loadings/sizes (**e**). Panel (a–e): Figure adapted and reproduced from [27] with permission of American Chemical Society

fact, this interaction must be accurately controlled since the presence of open coordination sites is responsible for the strong metal-adsorbate/metal-substrate interactions [27] leading to activation of the substrates in the catalytic processes. By using such a strategy for the design and preparation of the catalyst material, it is possible to make all metal atoms catalytically active, in contrast with conventional nanostructured materials in which only a fraction of them will be actually available for reaction. This can be easily confirmed by the increasing specific activity of nanostructured catalysts when the particles size is decreased, as depicted in Fig. 4e, since more and more non-accessible sites are exposed and activated as a function of the surface area. Of course, this tendency reaches a maximum when all active sites are exposed and available, exactly like in homogeneous catalysts. In this way, single-atom catalysts have properties resembling homogeneous molecular catalysts such as very high specific activity and well-defined local structures, combined with the robustness of heterogeneous catalysts, and the advantage of using all noble metal atoms as catalytic active sites, thus increasing performance and lowering the production cost.

The features described above justify the great technologic, scientific and economic expectations on SACs, and the number of related articles is increasing exponentially (Fig. 5), reflecting the high relevance and increasing interest for that kind of materials. In fact, we are experiencing the beginning of a revolution on the design, as well as preparation and characterization methods of catalytic materials, which may open up whole new perspectives for the comprehension of the phenomena controlling the interaction of molecules and their activation for chemical transformations. For example, we foresee a great impact of SACs for energy generation, for example in water splitting and artificial photosynthesis, where increasingly efficient catalysts for both, hydrogen and oxygen evolution reaction, are of uttermost relevance. The development of oxidation catalysts enabling efficient and durable fuel cells based in methanol, ethanol, formic acid and eventually glycerol also should bring great technologic and economic impact. The atomic scale modelling based on density

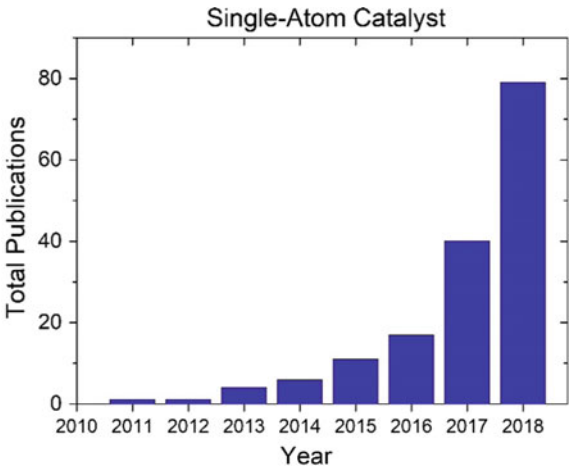

Fig. 5 Number of publications on single-atom catalysts in the last eight years (there is no publications previous to 2011). *Source* Web of Science-Clarivate Analytics

functional theory brings a great deal of opportunities in this area. Assessment of the thermodynamics of metal-metal and metal-substrate interactions can be achieved unveiling the tendency for the formation of inactive metal clusters, which in turn can guide the experimental activities [28]. The methodology, actually, allows the screening in a large materials-library to explore novel substrates. Furthermore, such theoretical framework has the potential to shed light on the reaction mechanisms providing accurate estimate of the reaction intermediates' energetics [29, 30], as well as fundamental understanding of the electronic structure on the metal center establishing the structure-activity relationships. Finally, joint theory-experiment studies involving X-ray spectroscopy can be a powerful tool to disentangle the effects of the metal centers and of the substrates [31].

In short, this chapter will be focused on the recent advances on single-atom catalysts for electrochemical water splitting, more specifically, for HER and OER, particularly the type of materials, preparation methods and strategies used to get materials with stabilized isolated highly catalytic active metal atom sites. In other words, we would like to provide readers with an account on the state of the arts on SACs, considering them not only from the experimental point of view but also relying on theoretical modelling and calculations in order to answer key questions such as: Which are the relevant parameters for building efficient SACs for water splitting? Which are the most interesting substrates and bonding strategies to get isolated active atoms or sites on the surface? Which are the techniques that we can relying on to characterize SACs? Which are the theoretical models that we can rely on to model SACs?

3 Density Functional Theory

The density functional theory (DFT) has become a powerful approach to solve the many-electrons problem in atoms, molecules and solids unveiling their fundamental properties. DFT has been particularly successful in the field of catalysis (both homogeneous and heterogeneous) because it provides a reliable way to access the energetics of the reaction intermediates establishing the structure-properties-activity relationships [32].

The DFT is based on two theorems established by Hohenberg and Kohn (HK) [33]. The first one states that for any system of interacting electrons in an external potential $V_{ext}(r)$, there is a one-to-one correspondence between the potential and the ground-state electron density $\rho_0(r)$. As a consequence, the ground-state expectation value of any observable can be written as a unique functional of the ground-state density $\rho_0(r)$. It implies that by knowing the ground-state particle density it is possible to reconstruct the system Hamiltonian and, by solving the Schrödinger equation, to calculate the many-body wave function. Therefore, all observable quantities can be obtained in a unique way from the density, which thus contain as much information as the wave function does.

The second theorem states that for any external potential applied to an interacting electron system, it is possible to define an universal total energy functional of the electron density, which is written such as

$$E[\rho(r)] = E_{HK}(\rho(r)) + \int V_{ext}(r)\rho(r)dr \tag{1}$$

where the first term on the right-hand side includes all internal energies of the interacting electron system and is independent of any particular external potential configuration, i.e. it is universal. The second part of this theorem states that this functional has a global minimum that corresponds to the exact ground-state total energy of the interacting system, E_0, and, among all possible energies, the one that minimize this functional is the ground-state electron density ρ_0(r). This result provides a clue in finding a way to replace the original formulation of the many-body problem by something that is more easily treatable.

This has been achieved by Kohn and Sham (K-S) who have developed a framework to apply those theorems to practical systems [34]. The main idea consists in replacing the interacting many-body problem by a corresponding non-interacting electron system in an appropriate external potential and having the same density. Applying this concept in the minimization scheme of the functional in Eq. (1) leads to the Schrödinger-like equation:

$$\left[-\frac{1}{2}\nabla^2 + V_{eff}(r)\right]\psi(r) = \epsilon\psi(r) \tag{2}$$

with the following effective potential

$$V_{eff}(r) = V_{ext} + \int \frac{\rho(r')}{|r - r'|}dr' + V_{xc} \tag{3}$$

where all exchange and correlation interactions are included in the term V_{xc}, which is viewed as an external potential acting on the auxiliary non-interacting electron system. Assuming that such exchange-correlation potential is known, the exact ground-state density and energy of the many-body electron problem can be found by solving the single-particle K-S Eq. (2) self-consistently.

The main challenge in the implementation of DFT is actually to find a good approximation for the exchange-correlation potential. The first approximation already proposed by Kohn and Sham is the so-called local density approximation (LDA) [34]. The only information needed in the implementation of LDA is the exchange-correlation energy of the homogeneous electron gas as a function of density. The LDA is expected to work well for systems with a slowly varying density, as for instance the nearly-free electron metals. Surprisingly, it also appears to be successful for many other systems including semiconductors and insulators. However, further improvements are still required.

A natural way to improve the LDA is to consider the exchange-correlation energy density not only depending on the density $\rho(r)$ but also on its gradient $\nabla\rho(r)$. This is implemented through an approach called generalized gradient approximation (GGA). The most widely used parameterizations for the GGA-functional are those obtained by Becke (B88) [35], by Perdew and Wang (PW91) [36], by Perdew, Burke and Enzerhof (PBE) [37]. More recent developments of the exchange-correlation functionals include, besides the electron density and its gradient, the Kohn-Sham orbital kinetic energy. These new functionals are termed meta-GGA as for instance the one developed by Tao, Perdew, Staroverov and Scuseria (TPSS) [38].

Another relevant aspect on the implementation of DFT is the expansion of the K-S wave function in term of appropriate basis functions. For solids, interfaces and surfaces the electronic structure calculations and geometry optimizations can be carried out using for instance the projector augmented wave (PAW) method [39]. This method has become very popular because it allows us to perform accurate calculations in relatively large systems. This is relevant to investigate the energetics and reaction pathways in the single-atom catalysis problem. One of the popular software that contains the implementation of PAW method is the Vienna ab initio simulation package (VASP) [40]. In a nutshell, the PAW method is an all-electron frozen core method, which combines the features of both the ultra-soft pseudopotentials [41] and augmented plane wave methods [42]. For atoms and molecules, instead of plane-waves based basis set, it is more efficient to use only localized atomic orbital like basis functions, which can be for instance of Gaussian form, Slater-type orbitals or numerical radial atomic like orbitals [43].

As mentioned above this density functional theory framework has been successfully applied to many catalysis related problems. One important feature here is the fact that DFT can estimate well the adsorption energies of different intermediate species, on the catalysts' surface, along the reaction pathways. Then, it is possible to assess the electronic structure modifications and stablish its relationship with the catalytic activity. It is usually very hard to obtain such information experimentally, which would require sophisticated *in operando* spectroscopy techniques. In particular, for the single-atom catalysis DFT modelling is an important tool to estimate the energetics of the metal adsorption on different supports facilitating the screening over a wide number of metallic systems. Through these calculations one can figure out whether or not the metal atoms will tend to form clusters or stay bound to the support.

One recent study has benchmarked the performance of different DFT based methods on the study of oxygen reduction reaction (ORR) catalyzed by Cu atoms supported on covalent triazine framework [44]. The results indicate that accurate methods are needed in the calculations of the electronic structure. Another aspect that turned out to be important in the DFT modelling of SAC problem is how to treat the solid-liquid interface. Hybrid approaches combining continuous dielectric medium and explicit descriptions of liquid molecules are providing the best descriptions.

4 Typical Preparation Methods

Single-atom catalysts are being prepared by deposition methods allowing fine control on that process and stabilization of high energy atoms/ions on the surface of suitable supports. Atoms and ions can be very reactive species such that they must be kept securely in place to avoid any further agglomeration/decomposition process. This can be achieved by generation of specific strongly binding sites capable to inhibit their diffusion, approach and collision, responsible for the formation of clusters and nanoparticles. Three are the main strategies that are being used for that purpose: (a) high-vacuum deposition, (b) wet-chemical route, and (c) high-temperature pyrolysis techniques.

Among the high-vacuum deposition techniques the atomic layer deposition, ALD, [45] is commonly used. In this method, chemical precursors in gas phase are sequentially deposited on a surface forming well organized atomic monolayers, thus allowing the precise control of their distribution even at sub-monolayer conditions. The first step of the deposition process generally is the reaction of an organometallic precursor A with the active sites on the substrate surface (red circles), where some of the metal-ligand bonds are replaced by metal-substrate bonds (Fig. 6a, b); and the excess is purged away by an inert gas flux and/or high vacuum (Fig. 6c). The second step aims the substitution of the still remaining ligands of the metal precursor A (blue circles) by injection of a second precursor B containing the binding/bridging atom, activating and making them prone to react again with the organometallic precursor (Fig. 6d). An atomic monolayer is generated on the substrate (Fig. 6e) after removal of the excess of B and reaction by-products. Such ALD cycle can be repeated as many time as necessary for the preparation of atomic multilayers in a controlled way, and is being commonly used for preparation of single atom catalysts [46–48]. The method is slow and expensive but allow unmatched control of the deposition process.

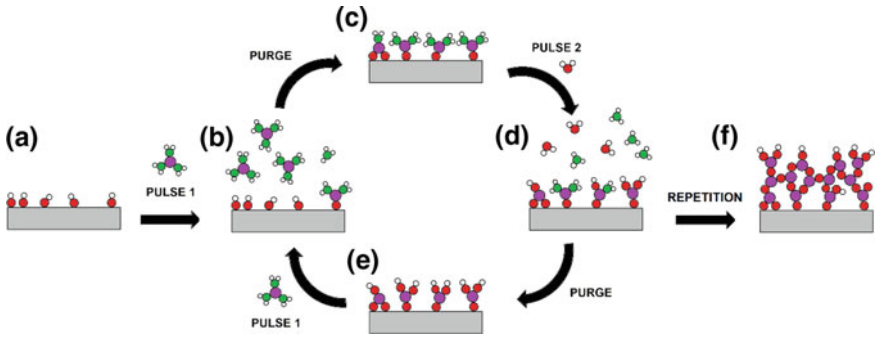

Fig. 6 Representation of film deposition by ALD method. The scheme shows **a** the substrate with reactive sites, **b** a pulse of the metallic precursor and formation of active sites reaction byproducts, **c** the purging of byproducts and unreacted precursor, **d** pulse of the second precursor, **e** purge of byproducts and second precursor, and **f** film resulting from several ALD cycles

The wet-chemical route is a simple deposition process that do not require sophisticated specialized apparatus. Typically, the single atomic species are bound onto the substrate mediated by a liquid phase. In this way, the substrate is impregnated by the metallic precursors during the synthetic process (one-pot chemical method), or after preparation by further precipitation or electrodeposition step. For example, Deng et al. [49] prepared MoS_2 nanosheets with single platinum atoms deposited on the surface by one-pot chemical method. This was achieved by dissolving the molybdenum precursor, $(NH_4)_2\ Mo_7O_{24}{\cdot}4H_2O$, and small amounts of H_2PtCl_6 complex (Mo/Pt molar ratio ~60) in water, adding CS_2 and heating the mixture in an autoclave at 400 °C for 4 h for hydrothermal growth of MoS_2. Tavakkoli et al. [50] prepared a SAC by electroplating Pt-atoms on SWNT deposited on glassy carbon working electrodes by cyclic voltammetry in H_2SO_4 solution, using a conventional three electrodes arrangement, with RHE as reference and a Pt foil as counter electrode. In each voltammetric cycle, the Pt^{2+} and Pt^{4+} ions released into the electrolyte solution upon oxidation of the platinum counter electrode was deposited on the SWNT in a more or less controlled way.

High-temperature pyrolysis is another simple method that has being largely utilized for preparation of carbon-based single-atom catalysts. Generally, metal precursors such as metal-organic frameworks (MOFs) and transition metal macrocycles [51] are adsorbed on conducting polymers and carbon materials, or incorporated in carbon material precursors, and submitted to high temperatures. In this way, a carbon matrix can be doped with single metal atoms, or it can be bound in strongly coordinating heteroatom-doped carbon sites as reported by Chen et al. [52]. They prepared a SAC by pyrolysis of a mixture of Na_2MoO_4, chitosan, SiO_2 and acetic acid, after drying at 80 °C and homogenization. The thermal process was carried out at 750 °C for 3 h, under argon atmosphere, in order to generate a graphitic carbon material, that was treated with 5 wt% HF solution for 4 h to get a N-doped graphene with dispersed molybdenum atoms.

5 Characterization Techniques

5.1 Synchrotron-Based Techniques as Ultimate Tools for SACs Characterization

A synchrotron radiation source is an accelerator of charged particles in which packages of electrons can be accelerated to extremely high energies and injected in circular path called storage ring. In this path synchronized electric fields are applied to control the kinetic energy, while synchronized magnetic fields are used to change direction periodically such that they move in a closed path. Photons are emitted in ≈60 pico-second pulses when the electrons bunches are accelerated changing direction generating beamlines of well-defined energy (from IR to hard X-rays) and polarization, that will be used in the stations where the experiments are carried out.

Each beamline surrounding the storage ring is designed for use with a specific technique or a particular type of research. The machine operates day and night, with periodic short and long shutdowns for maintenance.

The development of more advanced synchrotron facilities (MAX IV in Lund/Sweden and Sirius in Campinas/Brazil, also known as 4th generation synchrotrons) based on Multi-Bend Achromat technology [53], will be pushing the performance of spectroscopic techniques to frontiers beyond our imagination in the next years. The new machines can deliver highly coherent and focused beams (down to 1 nm diameter) with ultra-high power making possible not only single point analysis and single particle X-ray diffraction [54], but fast imaging of samples. These imaging are based not just on conventional spectroscopic and diffraction techniques such as XAS, XPS, XES and XRD, but also on techniques exploiting the very high coherence of those light sources.

5.2 X-Ray Photoelectron Spectroscopy (XPS)

X-ray photoelectron spectroscopy (XPS) is a surface-sensitive quantitative spectroscopic technique with chemical selectivity, providing information on e.g. elemental composition, and the electronic structure including oxidation states and local bonding [55]. The sample is irradiated with photons of a selected energy hν from e.g. a synchrotron, and electrons are emitted with kinetic energies E_{kin}, measured by an electron spectrometer, see Fig. 7. Together this yield the sample-specific electron binding energy, $E_B = h\nu - (E_{kin} + \Phi)$, where Φ is connected to the work function, i.e. the energy required to withdraw the bound electron entirely from the atom or

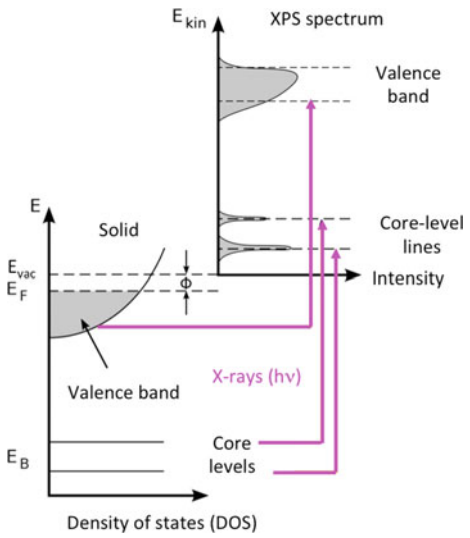

Fig. 7 Schematic illustration showing the correlation of materials energy levels with their respective XPS spectrum

surface. This provides information about the occupied electronic structure of the sample, as shown in Fig. 7.

The electron binding energy spectrum can conceptually be divided in two parts, the valence levels and the core levels. The valence level spectrum can, to a first approximation, be regarded as a function of the occupied molecular orbitals or valence bands depending on the type of sample, which is often used for band-mapping of solids. In contrast to the valence levels, the core levels in adjacent atoms do not overlap/combine significantly and remain essentially atomic-like and localized in a molecule or a solid. The core-level spectrum is relatively insensitive to the chemical environment and will thus provide information about the elemental composition of the sample. The core-level binding energies are however affected by the valence electronic structure and the local surroundings of the ionized atoms, an effect called the chemical shift. This provides information about e.g. oxidation states and local bonding environment.

One key feature of XPS is its surface sensitivity, which is related to the short inelastic mean free-path of electrons in matter. Traditionally this has meant that XPS has been carried out in ultra-high vacuum conditions, both to ensure that the surfaces remain uncontaminated and to allow outgoing electrons to reach the electron spectrometer. This has changed recently with the development of "ambient pressure" XPS, which will enable measurements under local pressures in the order of the room-temperature water vapor pressure [56–60]. This is based on differentially pumped electron lenses in combination with very finely focused X-rays, allowing a very short path of the outgoing electrons through the surrounding gas. "Ambient pressure" XPS was started already at 3rd generation synchrotrons, and the better-focused X-rays from 4th generation synchrotrons will provide greatly improved opportunities to study the gas-solid interface. Another interesting type of systems is solid-liquid interfaces, which can now also be studied with "ambient pressure" XPS using rapidly developing methods such as "dip and pull" [61]. Another exciting development is the liquid micro-jet [62, 63], in which a liquid is pushed through a thin nozzle with a diameter in the order of 5–20 μm into the vacuum, where it forms a jet, which is intersected by the X-rays shortly after the nozzle opening. The liquid micro-jet has opened up for XPS studies of aqueous solutions of inorganic ions, organic molecules and biomolecules, including studies of composition, structure and X-ray induced processes in both surface and bulk [64–70]. Yet another method relevant to the single atom catalyst is the possibility to apply XPS to free-standing nanoparticles (down to single atoms) isolated in vacuum utilizing an insertion device called aerodynamic lens [71, 72]. This method allows the quantum confinement effect on the electronic wave function to be probed. Knowledge of isolated properties may be a critical step to understand these systems when seating in a surface.

5.2.1 X-Ray Absorption Spectroscopy

Each element exhibits an X-ray absorption profile with characteristic binding energy that remains more or less unchanged whatever the material in which it is found.

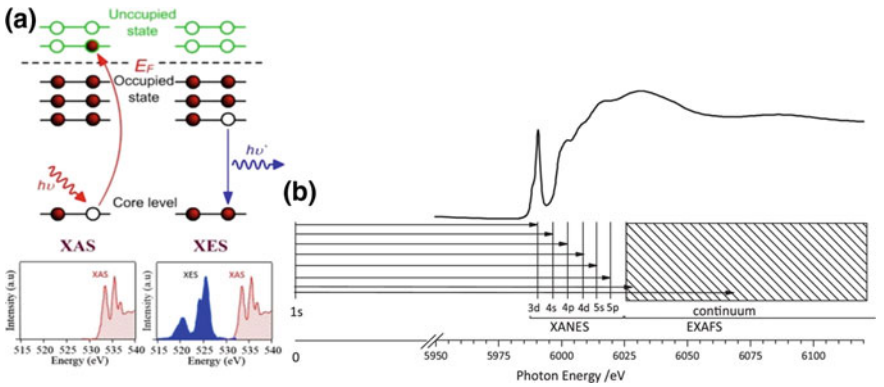

Fig. 8 **a** Basics of soft X-ray absorption (XAS) and emission (XES) spectroscopies and their corresponding experimental spectra. **b** Schematic diagram of the electronic transitions occurring at the Cr K-edge in CrO_2Cl_2. Panel (a): Figure adapted from [76] with permission of the John Wiley and Sons. Panel (b): Figure adapted from [75] with permission of Elsevier

However, is shifted depending on the oxidation state and the chemical group, or influenced/split by spin-orbit coupling, being a convenient technique to get structural information of the substrate, as well as of the isolated atoms constituting single-atom catalysts. In addition, it is relevant to note that the techniques based on X-ray absorption were greatly benefited by the technologic advancements in the last decades and wider access to high intensity and focused beam sources attainable only in synchrotron facilities [73, 74].

The X-ray absorption and X-ray emission spectroscopy are related techniques since the high-energy X-ray photons that are absorbed by inner core electrons promoting them to higher energy unoccupied orbitals, also generates vacant inner orbitals, as shown in Fig. 8a. However, those electrons are well shielded by the outer shell electrons and are less sensitive to the bonding environment, such that the absorption edge is dependent on and specific of each of the elements [75]; but still valuable chemical information about the local structure at the atomic/molecular level can be obtained [76]. The spectrum can be divided according to the energy relative to the absorption edge defining two techniques XANES (X-Ray Absorption Near Edge Structure) or NEXAFS (Near Edge X-Ray Absorption Fine Structure), and EXAFS (Extended X-Ray Absorption Fine Structure), see Fig. 8b. The first one is related to the spectroscopic profile near the absorption edge until up to 40 eV, that provides information specifically on the local electronic structure of the elements. A photoelectron in this region can travel longer distances while being scattered several times (multi-scattering), thus carrying information about the symmetry and chemical properties. The formal valence of the absorbing atom, the hybridization and local atomic arrangement can be obtained from XANES spectrum. On the other hand, EXAFS is the spectrum in the energy region beyond XANES. That photoelectrons have a much shorter free mean path and are only subjected to a single dispersion event, thus providing detailed structural information about the neighborhood of selected atoms.

In other words, EXAFS is the technique of choice to get structural information of the absorbing atom up to 10 Å [75] such as the coordination number, the nature of neighbor atoms, the bond length and the degree of the local structural disorder [76].

The quest for the ideal electrocatalyst has fueled the development of in situ and *in operando* X-ray absorption spectroscopy (XAS) techniques [77, 78] since they are essential to monitor the reaction intermediates and their actual oxidation states, the active site geometries, and the synergic effects involving the species present in the catalyst in the active state during the electrocatalytic process, with time resolution of milliseconds [79]. Nevertheless, such measurements must be complemented by imaging techniques, especially by high-resolution electron microscopy techniques to confirm the distribution of atoms and morphology of SACs, as discussed below.

5.2.2 Scanning Transmission Electron Microscopy for Atomic-Resolution Studies

Transmission electron microscopy and associated techniques evolved greatly in the last decades and reached resolution in the sub-angstrom scale, becoming indispensable for the characterization and quality control of SACs [80, 81]. In fact, aberration-corrected scanning transmission electron microscopy (STEM) associated with spectroscopic techniques such as electron energy-loss spectroscopy (EELS) and X-ray energy dispersive spectroscopy (EDX), as well as electron diffraction techniques, is a powerful technique for physico-chemical characterization of nanomaterials. A scheme showing the interaction of the accelerated electron beam with the sample and the associated techniques is shown in Fig. 9a. The electron beam is focused on the sample surface and moved in order to scan the sample providing valuable information point by point, by using each of the angular detectors to collect the scattered electron in a synchronized manner. In this way, the sample is imaged as a function of the collection angle providing complementary images based on different contrast mechanisms [82].

For example, extremely important structural information is given by the angular dark-field (ADF) detectors, especially by the one at high angle (HAADF). The HAADF images are generated mainly by Rutherford electron dispersion by atoms and is also denominated image by Z contrast (where Z is the atomic number of an element) since the scattering angle is approximately a linear function of Z^2 [82]. Fei et al. [81] used this technique to confirm the morphology of Co-NG nanosheets. Several bright spots corresponding to cobalt atoms, the heavy atom in this case, can be seen in the HAADF images (Fig. 9b), clearly demonstrating their distribution on the graphene surface. Each of those round bright spots is 2–3 nm large as expected for individual isolated Co atoms. When the image was magnified further (Fig. 9c), it was possible to see that each one of those atoms is localized in between the light C, N and/or O atoms, thanks to the excellent contrast in Z achieved.

The combination of imaging and spectroscopic mapping techniques that can be found in electronic microscopes can give even more precise information. The interaction of the electron beam with sample can generate electrons as a function of

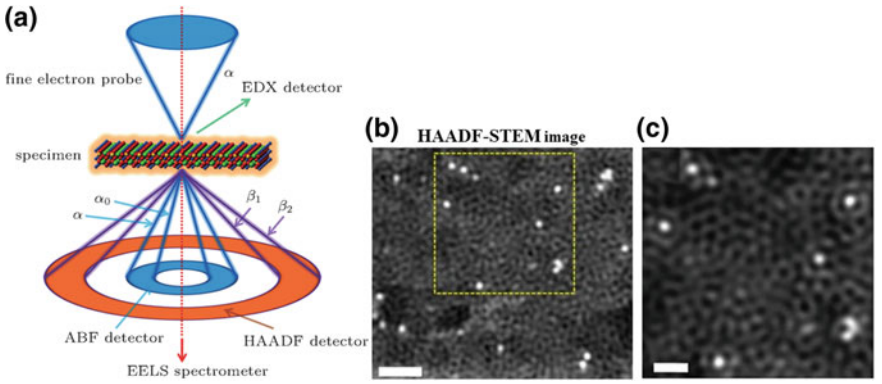

Fig. 9 **a** Schematic diagram of the common imaging and spectrum modes in an STEM, composed of annular dark-field (ADF) or high-angle annular dark-field (HAADF) images (depending on the inner angle β_1), bright-field (BF) or angular bright-field (ABF) image (depending on the inner angle α_0), electron energy-loss spectroscopy (EELS) and X-ray energy dispersive spectroscopy (EDX). **b** HAADF-STEM image of a Co-NG, showing many Co atoms well-dispersed on the carbon matrix. Scale bar, 1 nm. **c** The enlarged view of the selected area in B. Scale bar, 0.5 nm. Panel (a): Figure adapted from [82] with permission of IOP Publishing Ltd. Panel (b–c): Figure adapted from [81] with permission of Nature Publishing Group

the energy lost in the inelastic collisions. Such EELS data can provide information about the chemical bonds, valence and coordination state, analogous to that obtained by XAS but with much larger spatial resolution [82]. In addition, the characteristic X-ray photons that are also produced can be used to identify the elements constituting the material by energy-dispersive X-ray spectroscopy (EDS). This technique is especially suited for the identification of heavy elements. In short, the combination of spectroscopic techniques with STEM is a formidable tool to characterize the chemical and electronic structure of materials, in particular of SACs.

6 Hydrogen Evolution Reaction (HER)

The hydrogen evolution reaction is relatively simple than OER and the mechanism consists of two elemental steps, the adsorption of H^+ generating the activated intermediate species H^* followed by the formation of H_2 upon encounter of two H^*, or reaction with H^+ in solution. The rate determining step is controlled by the adsorption/desorption equilibrium of H^+ generating H^* on the surface of the catalyst, whose energies can be optimized in order to get moderate energy barriers. The best condition was found to be achieved when the free energy of adsorption of H^* ($\Delta G_H°$) is near zero.

In the last five years, MoS_2 is been extensively studied for the development of HER catalysts where the catalytic activity has been mainly assigned to the interaction of the S-atoms in the edge sites with H^+, whose $\Delta G_H° \sim 0.1$ eV [83, 84]. In addition,

many efforts have been carried out to improve the activity by anchoring metal atoms in its surface, noble rare metal and transition metal atoms.

One of the first works on water splitting based on materials containing single metal atoms was reported by Deng and collaborators [49], who prepared a catalyst by dispersing platinum atoms on MoS_2 nanosheets (Pt-MoS_2). The TEM images (Fig. 10a) clearly show the formation of nanosheet tactoids with interplanar distance of 0.62 nm correspondent to the (002) plane of MoS_2. The HAADF-STEM images shown in Fig. 10b–d revealed the presence of uniformly distributed single Pt atoms occupying Mo sites in the nanosheet structure. Accordingly, the Pt atoms are stabilized by Pt–S bonds that inhibits their diffusion and formation of clusters/nanoparticles with Pt–Pt bonds in the Pt-MoS_2 material, as confirmed by EXAFS analyses (Fig. 10e). The XANES peak at the Pt L_3-edge of MoS_2 (Fig. 10f) is more intense and shifted to higher energies than in 40% Pt/C and Pt foil, indicating a higher positive character on the Pt atoms as expected for the transfer of electronic density to the S atom of MoS_2.

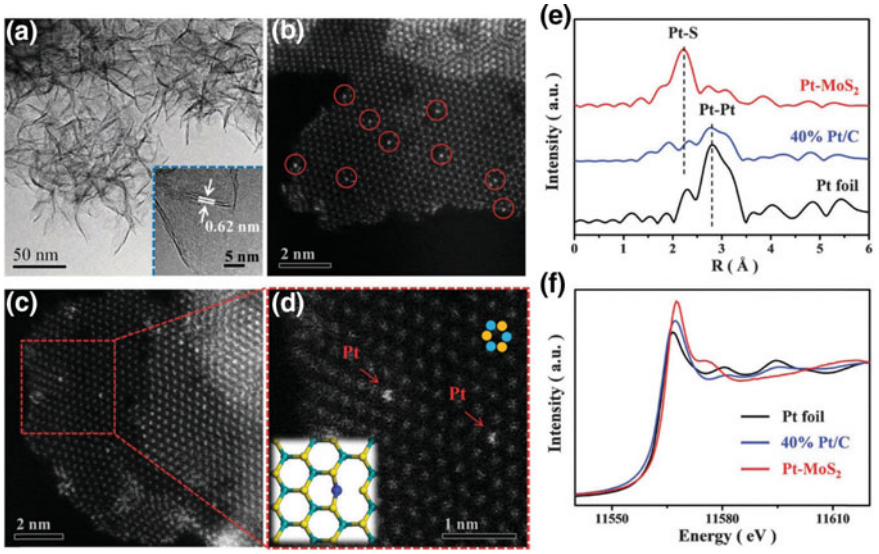

Fig. 10 **a** TEM image of Pt–MoS_2 with the inset showing a typical MoS_2 layer distance of 0.62 nm. **b**, **c** HAADF-STEM images of Pt–MoS_2 showing that single Pt atoms (marked by red circles in (**b**)) are uniformly dispersed in the 2D MoS_2 plane. **d** Magnified domain with red dashed rectangle in (**c**) showing a honeycomb arrangement of MoS_2, and single Pt atoms occupying the exact positions of the Mo atoms in the structure (marked by red arrows). The bottom inset shows the simulated configuration of Pt–MoS_2. The green, yellow and blue balls represent Mo, S and Pt, respectively. **e** The k^2-weighted EXAFS spectra of Pt–MoS_2 in comparison to Pt foil and commercial 40 wt% Pt/C. **f** The normalized Pt L_3-edge XANES spectra of Pt–MoS_2 in comparison to Pt foil and commercial 40 wt% Pt/C. Panel (a–f): Figure adapted and reproduced from [49] with permission of RSC Publishing

The electrocatalytic performance of Pt-MoS_2 for HER was studied by registering the polarization curves of three modified electrodes in 0.1 M H_2SO_4 solution. A significant reduction of overpotential of 60 mV at current density of 10 mA cm^{-2}, and of the Tafel slope from 98 to 96 mV dec^{-1} as compared with pure MoS_2, was measured indicating a material with higher catalytic activity for hydrogen evolution reaction.

Many efforts have been carried out using computational simulation in order to understand the effect of the metal ion substitution on the MoS_2 layered structure. Thus, in addition to the work of Deng and co-authors [49] on Pt-MoS_2 described above, DFT calculations showed that the substitution of some Mo atom in the MoS_2 structure by V, Ti, Fe, Mn, Cr, Mo and W led to preferential formation of hexa-coordinated sites with S-atoms. In contrast, Pt, Ag, Pd, Zn, Au, Co, Cu and Ni formed tetra-coordinated sites with S-atoms in the MoS_2 structure. In addition, the current exchange density (i_0) and $\Delta G_H°$ measured for the S-atoms around the Pt-atom sites in Pt-MoS_2 indicated that $\Delta G_H \sim 0$ as shown in the volcano curve shown in Fig. 11. This finding is consistent with the hypothesis that the H* adsorption energy is being modulated by the Pt-atoms, demonstrating to be a promising approach to enhance the activity of MoS_2 nanosheets, and to generate new alternative materials for water splitting. In other words, the implantation of tiny amounts of transition metal atoms in the MoS_2 structure, thus activating a larger number of S-atoms, was shown to be a good strategy for the development of HER catalysts with enhanced activity.

However, this type of material is better described as doped MoS_2 materials rather than single atom catalysts where the catalytic active sites must be provided by the single atoms dispersed on a matrix. We described in detail such doped material in

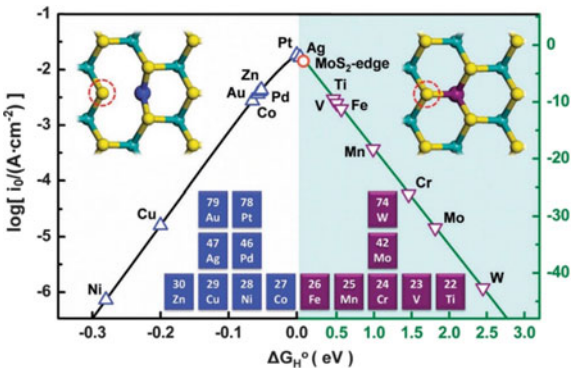

Fig. 11 The relation between current ($\log(i_0)$) and $\Delta G_H°$ presents a volcano shape. Two different scales were adopted for the left and right sides of the volcano plot for better visualization. The inserted graphs point to different configurations of doped MoS_2 as coordinated with four (left) and six (right) S atoms. The adsorption sites for H atoms are marked by the red dashed circles. The studied metal atoms are indicated in the "Periodic Table" shown in the bottom. Green balls: Mo; yellow balls: S; blue and purple balls: doped metal atoms. Figure adapted and reproduced from [49] with permission of RSC Publishing.

order to make clear the difference with SACs, but now on the attention will be focused only in this type of materials.

In 2016, Cheng et al. [46] reported on a N-doped graphene with Pt-atoms deposited on the surface by atomic layer deposition (ALD), exhibiting surprising 37 folds larger specific catalytic activity as compared to commercial Pt/C catalyst. The platinum deposition was achieved using methylcyclopentadienyl-trimethylplatinum ($MeCpPtMe_3$) as precursor, controlling the ALD reactor chamber temperature in 250 °C. The temperature of $MeCpPtMe_3$ was kept at 65 °C and injected in one second cycles while O_2 and N_2 was injected respectively in 5 and 20 s cycles. The size and surface concentration of Pt-clusters and Pt-atoms on N-doped graphene was controlled by the number of ALD cycles, as shown in Fig. 12a, b. In fact, more or less uniformly dispersed Pt-atoms and small amounts of Pt-clusters (bright spots) can be observed in the ADF STEM images of the sample prepared upon deposition of 50 ALD cycles (ALD50Pt/NGN). As expected, larger number of Pt nanoparticles and clusters were found in the sample prepared upon 100 ALD cycles (Fig. 12c, d) showing the effect of deposition cycles on the size and distribution of particles on the graphene surface. And, the normalized XANES spectra of ALD50Pt/NGN, ALD100Pt/NGN, Pt/C and Pt foil at Pt L_3- and L_2-edge are shown respectively in Fig. 12e, f. The intensity of the response at both edges was larger for the first one indicating a larger concentration of positively charged atoms than in ALD100Pt/NGN and Pt/C materials, as expected for a single Pt-atom catalyst with strong interaction with N-doped graphene used as support.

The catalytic activity of those catalysts was characterized based on their linear sweep voltammetry polarization curves in 0.5 M H_2SO_4 solution. The ALD50Pt/NGN sample presented lower overpotential for HER (Fig. 12g) exhibiting a mass activity (10.1 A mg^{-1}) respectively 4.8 and 37.4 times larger than ALD100Pt/NGN (2.12 A mg^{-1}) and Pt/C (0.27 A mg^{-1}), at an applied overpotential of just 0.05 V (Fig. 12h). The work of Cheng et al. [46] was supported by DFT calculations demonstrating that single Pt-atoms on N-doped graphene has higher density of unoccupied 3d states. According with the authors, these results are due to the transfer of electronic density from the Pt-atoms to the nitrogen atoms in the graphene support thus enhancing the catalytic activity of that material.

Other reports were published describing the preparation of HER catalysts by incorporation of Pt-atoms on carbon materials. Tavakkoli et al. [50] deposited 0.19–0.75% of Pt-atoms in single-wall carbon nanotubes (SWNT) getting a material as active as commercial Pt/C. The activated carbon materials were characterized by HAADF-STEM clearly showing a dispersion of platinum single-atoms, nanoparticles and clusters on SWNT. The electrochemical characterization for HER performance along 400 cycles was consistent with an overpotential of 27 mV at 10 mA cm^{-2}, and a Tafel slope of 38 mV dec^{-1}. This study was also supported by theoretical DFT calculations where the adsorption free energy of H^* (ΔG_H^0) on several configurations, and Pt–Pt distances considering two Pt-atoms adsorbed on the SWNT surface, were calculated. For example, a ΔG_H^0 of −0.3 eV was found when the two Pt-atoms was sitting on the same six membered aromatic C-atom ring, whereas that tended to zero when the Pt–Pt distance was increased. This finding supported a higher HER

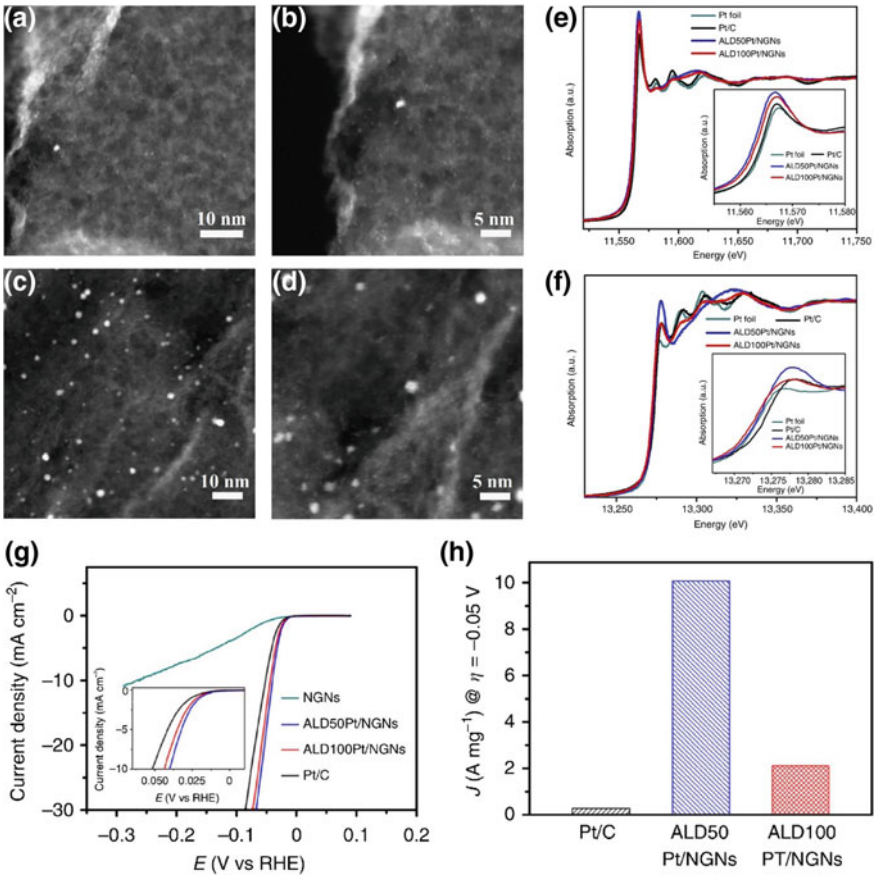

Fig. 12 ADF STEM images of ALDPt/NGNs samples with **a**, **b** 50 and **c**, **d** 100 ALD cycles. Scale bars, 10 nm (**a**, **c**) and 5 nm (**b**, **d**). **e** The normalized XANES spectra at the Pt L_3-edge of the ALDPt/NGNs, Pt/C catalysts and Pt foil. The inset shows the enlarged spectra at the Pt L_3-edge. **f** The normalized XANES spectra at the Pt L_2-edge of ALDPt/NGNs, Pt/C catalysts and Pt foil. The inset shows the enlarged spectra at the Pt L_2-edge. **g** The HER polarization curves for ALDPt/NGNs and Pt/C catalysts were acquired by linear sweep voltammetry with a scan rate of 2 mV s^{-1} in 0.5 M H_2SO_4 at room temperature. N_2 was purged before the measurements. The inset shows the enlarged curves at the onset potential region of the HER for the different catalysts. **h** Mass activity at 0.05 V (*vs*. RHE) of the ALDPt/NGNs and the Pt/C catalysts for the HER. Panel (a–h): Figure adapted and reproduced from [46] with permission of Springer Nature

catalytic activity for the material with single Pt-atoms homogeneously dispersed on the SWNT surface.

More recently, Zhang et al. [90] reported a single atom catalyst (Pt@PCM) based on Pt-atoms dispersed on a N-doped porous carbon matrix prepared from a nanocomposite constituted by polymerized dopamine and polystyrene-block-poly(ethylene oxide). The nanocomposite was treated with a H_2PtCl_6 solution for 4 h, at 50 °C, and

pyrolyzed to get a Pt@PCM catalyst with 0.53 wt% of Pt. The HER performance was determined in acidic and alkaline conditions by linear sweep voltammetry. The catalyst exhibited an overpotential of 105 mV in 0.5 M H_2SO_4 and 139 mV in 1 M KOH solution, at current density of 10 mA cm^{-2}, and Tafel slope respectively of 65.3 and 73.6 mV dec^{-1}.

Strategies for the dispersion of atoms of two metallic elements on conducting supports have been successfully realized and exploited for the development of SACs for HER. Zeng et al. [85] reported on materials with Pt-atoms bound to Fe–N_4 units by an oxygen molecule bridge generating Pt_1–O_2–Fe_1–N_4 sites dispersed on a carbon support denominated "single-atom to single-atom" catalyst. The Fe–N–C precursor catalyst was prepared by homogenization of a mixture of a zeolitic imidazole framework (ZIF-8), 1,10-phenantroline and iron acetate, followed by heat treatment in Ar/NH_3 atmosphere. Then, Pt-atoms were incorporated by interaction with a H_2PtCl_6 solution under stirring for 60 min at room temperature, and then at 70 °C for 8 h to get the Pt_1@Fe–N–C(w/heating) precursor. Finally, this was thoroughly washed and heated at 450 °C for 2 h in argon atmosphere to produce the Pt_1@Fe–N–C catalyst. A control material was also prepared by adsorbing Pt-atoms on carbonized ZIF-8 and 1,10-phenanthroline denominated Pt_1@C.

The HAADF-STEM images of those materials (Fig. 13a) presented about 0.3 nm large bright spots homogeneously dispersed on the carbon matrix, as expected for the formation of Pt_1–O_2–Fe_1–N_4 sites. Two possible configurations for the Pt_1@Fe–N–C active sites (Fig. 13b) were proposed based on previous works and X-ray absorption spectroscopy studies. The EXAFS spectra of the Fe and Pt sites shown in Figs. 13c and 4d were compared with Fe_2O_3, Fe foil, iron(II) phthalocyanine (FePc), Fe–N–C precursor, Pt foil, PtO_2 and Pt_1@C samples. Peaks consistent with Fe–O and Fe–N bonds, but with no Fe–Fe bonds were observed in the Fe absorption region of Pt1@Fe–N–C and Fe–N–C indicating the formation of atomic iron sites. Analogously, no peak corresponding to Pt–Pt bond was found in the Pt region of Pt_1@Fe–N–C (Fig. 13d), suggesting the presence of single platinum atoms but no clusters or nanoparticles dispersed on the carbon support. And, the heat treatment at 450 °C for 2 h led to the formation of stronger Pt–O bonds, as confirmed by the shift of the R = 1.9 Å peak assigned to 2O ∗ Pt bond in Pt_1@Fe–N–C (w/o heating) to R = 1.6 Å in Pt_1@Fe–N–C. The electrochemical performance of this material for HER was evaluated by the polarization curves in 0.5 M H_2SO_4 solution, where the overpotential at 10 mA cm^{-2}, $\eta_{10} = 60$ mV, and a Tafel slope of 42 mV dec^{-1} were found (Fig. 13e, f). These results are better than of Pt@C ($\eta_{10} = 89$ mV and Tafel slope = 51 mV dec^{-1}) and Fe–N–C ($\eta_{10} = 130$ mV and Tafel slope = 89 mV dec^{-1}). The H^* adsorption energies on the active sites $\Delta G_H°$ of Pt_1@Fe–N–C (0.16 eV), Pt_1@C (0.24 eV) and Fe–N–C (0.65 eV) were evaluated by DFT calculations, confirming the larger catalytic activity of the first one.

Chao et al. [86] prepared a HER catalyst based on Pt–Cu sites dispersed on ultrathin Pd-nanorings (Pd-NRs) containing only 1.5 atom% of Pt, prepared by a two-steps process. First, copper was deposited on Pd-NRs by mixing with a $CuCl_2 \cdot H_2O$ solution in the presence of CO as reducing agent, and the resulting material was impregnated with H_2PtCl_6 and ultrasonicated for 45 min. The structure of the resultant material

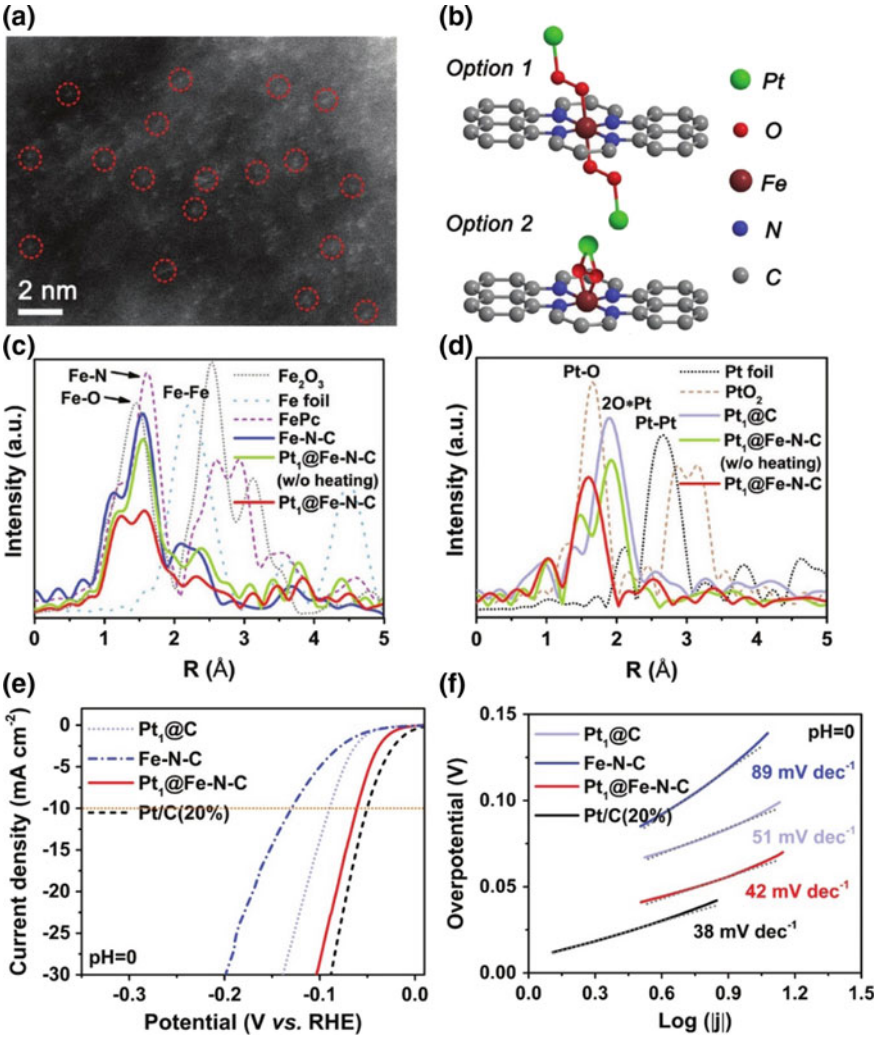

Fig. 13 **a** HADDF-STEM image of Pt_1@Fe–N–C catalyst. **b** Proposed schematic diagram of Pt_1–O_2–Fe_1–N_4–C_{12} as the active moiety of Pt_1@Fe–N–C. **c** Magnitudes of k^3-weighted Fourier-transformed EXAFS data of Fe in Fe–N–C, Pt_1@Fe–N–C (w/o heating) and Pt_1@Fe–N–C as compared to FePc, Fe_2O_3, and Fe foil references. **d** Fourier-transformed EXAFS data of Pt in the catalysts and PtO_2 and Pt foil reference materials. **e** HER polarization curves and **f** Tafel plots of Fe–N–C, Pt_1@Fe–N–C, Pt_1@C, and Pt/C (20 wt%) as reference catalyst measured in 0.5 M H_2SO_4. Panel (a–f): Figure adapted and reproduced from [85] with permission of John Wiley and Sons

was confirmed by EXAFS where intense peaks assigned to the Pt–Cu, Pt–Pd and Cu–Pd bonds were observed, whereas no peak associated to Pt–Pt and Cu–Cu bonds could be observed. The activity of this SAC was comparable to that of Pt/C with η_{10} = 30 mV and Tafel slope = 25 mV dec^{-1} in 0.5 M H_2SO_4, with a mass activity of 3002 A $g^{-1}_{(Pd+Pt)}$, twice as large than for Pt/C (1325 A g^{-1}_{Pt}).

Platinum is being the metallic element of choice given its high catalytic activity as compared with other elements. However, it is rare and quite expensive such that more abundant non-precious elements have been pursued as alternatives for the development of conventional heterogeneous catalysts, and single-atom catalysts also. In this context, Fei et al. [81] reported a catalyst based on cobalt atoms dispersed on N-doped graphene oxide (GO) named Co-NG, prepared by a simple and scalable freeze-dry method from an aqueous graphene oxide suspension (Fig. 14a). $CoCl_2{\cdot}6H_2O$ was added into the mixture, homogenized and freeze dried for 24 h, and submitted to heat treatment at 750 °C for 1 h in an argon/ammonia atmosphere, strongly bonding 0.57 wt% of cobalt on that carbon material. HADAAF-STEM images showed bright 2–3 Å large dots, that were assigned to single Co-atoms surrounded by C, N, and/or O atoms of N-doped graphene, homogeneously distributed on the surface (Fig. 14b, c). This material was much more active for HER than N-doped graphene itself decreasing the onset potential from 475 to 147 mV (A = 10 mA cm^{-2}), and the Tafel slope from 117 to 82 mV dec^{-1}, in 0.5 M H_2SO_4 solution (Fig. 14d, e).

Liang et al. [87] reported a similar carbon material based on single Co-atoms prepared by pyrolysis of a composite precursor containing cobalt tetramethoxyphenylporphyrin, vitamin B12 and cobalt/o-phenylenediamine, where silica nanoparticles were added as templates to increase the porosity of the resultant material. The incorporation of additional N- and Co-atoms on the carbon material generating the CoN_x/C catalyst, decreased the overpotential η_{10} to 133 mV and Tafel slope to 30 mV dec^{-1} in 0.5 M H_2SO_4 solution, generating a much more active material than the previous one.

On the other hand, Qiu et al. [88] successfully realized the insertion of individual Ni-atoms on nanoporous graphene (np-G) by chemical vapor deposition (CVD) method, followed by treatment with 2 M HCl solution for 4, 6 and 9 h to dissolve the excess of nickel. The material was characterized by TEM and HAADF-STEM imaging that revealed the 3D structure of the carbon material on the top of which 1–3 nm diameter dark spots assigned to small amounts Ni clusters can be observed (Fig. 15a), as well as large amounts of bright spots corresponding to single Ni-atoms sitting in between aromatic six membered rings of graphene (Fig. 15b). The polarization curves of the materials obtained upon treatment with HCl solution as a function of time was compared with that of rGO and platinum (Fig. 15c, d). The best result was obtained for the np-G/Ni with 6 h treatment which presented η_{10} = 190 mV and Tafel slope of 45 mV dec^{-1}.

The ΔG_{H^*} values were calculated by DFT considering Ni-atoms localized in the center of an aromatic six membered carbon ring of graphene (Ni_{ab}/G), or substituting a C-atom of an aromatic ring (Ni_{sub}/C) (Fig. 15e), or sitting on a defect site of a ring (Ni_{def}/C). The first one resulted in positive ΔG_{H^*} values suggesting Ni-atom should not adsorb on graphene (Fig. 15f), whereas the last one gave negative values in the

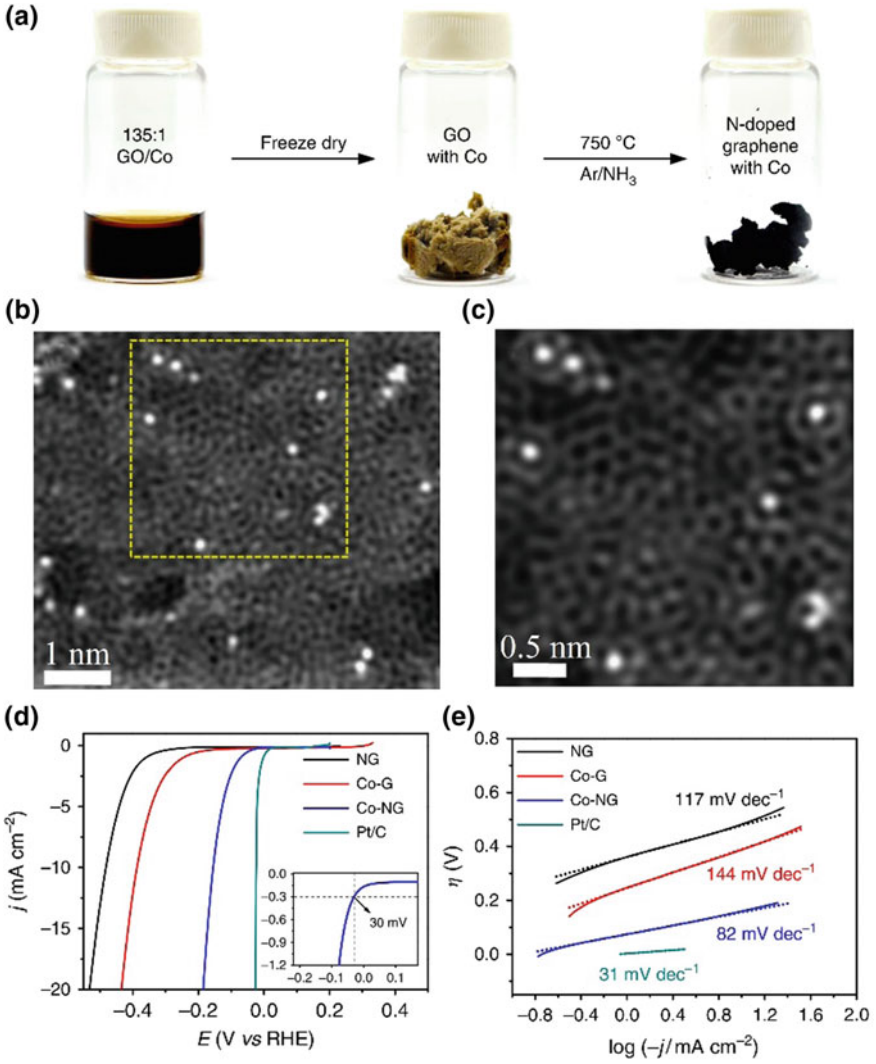

Fig. 14 **a** Schematic illustration of the synthetic procedure of the Co-NG catalyst. **b** HAADF-STEM image of the Co-NG, showing many Co atoms well-dispersed in the carbon matrix. Scale bar, 1 nm. **c** Enlarged view of the selected area in (**b**), scale bar = 0.5 nm. **d** Linear-sweep voltammograms (LSV) of NG, Co–G, Co–NG and Pt/C in 0.5 M H_2SO_4, at scan rate of 2 mV s^{-1}. Inset: enlarged view of the LSV for the Co–NG near the onset region is shown. **e** Tafel plots of the polarization curves in (**a**). Panel (a–e): Figure adapted and reproduced from [81] with permission of Springer Nature

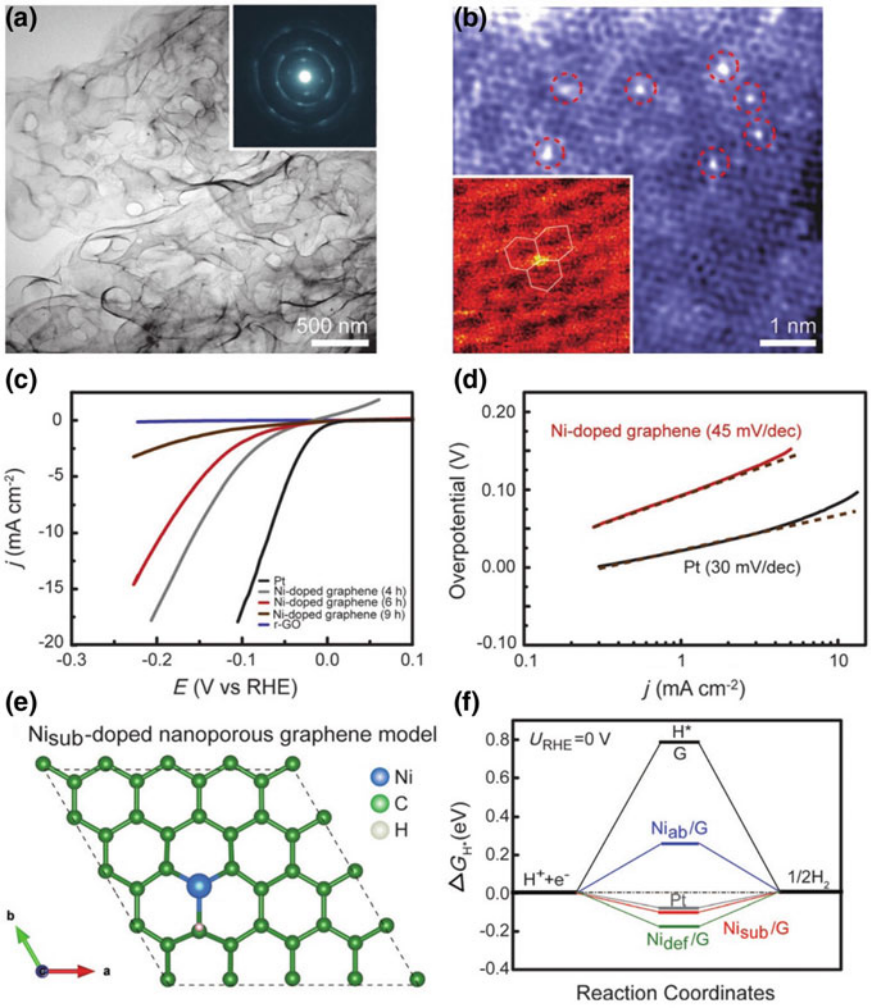

Fig. 15 **a** TEM image of Ni-doped np-G. Inset: SAED pattern. **b** HAADF-STEM image of Ni-doped graphene. Inset: Enlarged HAADF-STEM image (red circle) showing a substitutional Ni-atom (bright orange spot) occupying a carbon site in the graphene lattice (white lines). **c** Polarization curves of Ni-doped graphene samples after different Ni dissolution periods (4, 6, and 9 h) along with those of Pt and reduced graphene oxide (r-GO) electrodes for comparison. **d** Tafel plots of Ni-doped graphene (6 h dissolution) and Pt. **e** Hydrogen adsorption sites and configuration of the Ni_{sub}/G model with $\Delta G_{H^*} = -0.10$ eV and **f** calculated Gibbs free energy diagram of the HER at equilibrium potential for a Pt catalyst and Ni-doped graphene (Ni_{ab}/G, Ni_{sub}/G, and Ni_{def}/G) samples. The free energies for hydrogen adsorption on pristine graphene and Pt metal are plotted for comparison, with $\Delta G_{H^*} = 0.79$ and 0.09 eV, respectively. Panel (a–f): Figure adapted and reproduced from [88] with permission of John Wiley and Sons

−0.26 to −0.40 eV range depending on the nature of the structural defect. In fact, among the three possibilities described above, the most active nickel sites were shown to be the Ni_{sub}/C with ΔG_{H^*} of −0.10 eV, a value similar to that found for some Pt catalysts, that should account for most of the catalytic activity of np-G/Ni SAC.

A successful preparation of a nickel SAC by heat treatment of a metal-organic framework (MOF) prepared by reaction of $NiCO_3$ and $Ni(OH)_2$ nickel precursors with L-aspartic acid and 4,4′-bipyridine was presented by Fan et al. [89]. The MOF was carbonized at 700 °C in N_2 atmosphere and then treated with concentrated HCl and ultrasonication to get the A–Ni–C catalyst with 80 wt% of nickel dispersed as individual Ni-atoms and 20 wt% as clusters on a carbon material. The performance as HER catalyst evaluated by linear sweep voltammetry was carried out in 0.5 M H_2SO_4 solution giving a $\eta_{10} = 34$ mV and Tafel slope = 41 mV dec^{-1}, a result comparable with commercial Pt/C catalyst.

Strategies for the dispersion of atoms of two metallic elements on conducting supports have been successfully realized and exploited for the development of SACs for HER. Chen and collaborators [52] dispersed molybdenum instead of Pt and Ni atoms on N-doped graphene to prepare a new single-atom catalyst denominated $Mo_1N_1C_2$. The presence of Mo-atoms dispersed on N-doped carbon was monitored by STEM using a machine equipped with a spherical aberration corrector probe. The characterization of $Mo_1N_1C_2$ by FT-EXAFS spectroscopy at the Mo K-edge showed peaks at 1.3 Å consistent with Mo–N and Mo–C bonds, while no peaks could be assigned to Mo–Mo bonds, as expected for the absence of Mo nanoparticles and clusters. The polarization curves in 0.1 M KOH solution resulted in $\eta_{10} = 132$ mV and Tafel slope = 90 mV dec^{-1}. The ΔG_{H^*} value (0.082 eV) determined by DFT was positive but very close to zero, thus explaining the good catalytic activity of $Mo_1N_1C_2$ as HER catalyst (Table 1).

7 Oxygen Evolution Reaction (OER)

As discussed previously, finding high performance and robust electrocatalysts to boost the kinetics of the intrinsically slow and highly demanding oxygen evolution reaction, especially based on more abundant and cheap transition metal elements, is one of the biggest challenges for the development of alternative energy storage and energy conversion devices. The sluggishness of that reaction is mainly consequence of the four proton coupled electron-transfer processes [80] that can be summarized by the elemental steps, where * refers to the catalyst [91]. In fact, many materials were developed and tested as OER catalysts including some based on single-atoms as discussed below.

Table 1 Activity parameters of recently reported single atom catalyst for HER: pH condition, onset potential, Tafel slope and overpotential at 10 mA cm^{-2}

Atom sites	Support	η_{10} (mV vs. RHE)	Onset potential (mV vs. RHE)	Tafel slope (mV dec^{-1})	Exp. condition	References
Pt[a]	MoS_2 nanosheet	–	~150	96	0.1 M H_2SO_4	[49]
Pt	N-doped graphene	–	~40	29	0.5 M H_2SO_4	[46]
Pt	Single-walled CNT	27	–	38	0.5 M H_2SO_4	[50]
Pt	Porous carbon matrix	105	–	65.3	0.5 M H_2SO_4	[90]
Pt–O_2–Fe–N_4	Carbon support	60	–	42	0.5 M H_2SO_4	[85]
Cu–Pt	Pd nanoring	22.8	–	25	0.5 M H_2SO_4	[86]
Co	N-doped graphene	–	~147	82	0.5 M H_2SO_4	[81]
CoN_x	Carbon Support	133	–	75	0.5 M H_2SO_4	[87]
Ni	Graphene		~190	45	0.5 M H_2SO_4	[88]
Ni	Graphitized carbon	34		41	0.5 M H_2SO_4	[89]
Mo	N-doped carbon	132	–	90	0.1 M KOH	[52]

[a]Pt is a dopant of MoS_2 and not the catalytic active site

$$
\begin{aligned}
H_2O + * &\longrightarrow OH^* + H^+ + e^- \\
OH^* &\longrightarrow O^* + H^+ + e^- \\
O^* + H_2O &\longrightarrow OOH^* + H^+ + e^- \\
OOH^* &\longrightarrow O_2 + H^+ + e^- \\
\hline
2H_2O &\longrightarrow O_2 + 4H^+ + 4e^-
\end{aligned}
$$

In order to increase the conductivity and activate single metal catalysts for oxygen evolution reaction, strongly acidic or alkaline electrolytes are generally used. However, in such conditions, metal oxides generally are not stable enough and don't have high enough electric conductivity for practical applications. Accordingly, a strong tendency of using more conducting, mechanically and chemically stable carbon

materials such as graphitic materials, carbon nanotubes and graphene as anchoring substrates has been observed.

For example, Fei et al. [92] developed a rational strategy for preparation of a series of SACs characterized by the presence of single metal atom sites incorporated on N-doped graphene (Fig. 16a). Such materials where successfully analyzed by EXAFS and XANES spectroscopy and imaged by STEM (Fig. 16b–d) which demonstrated unequivocally the presence of graphitic carbon nitride M–N_4C_4 sites, where M=Ni, Fe, and Co. Such finding allowed a thorough study by density functional theory (DFT) in order to better understand the structure and activity correlation of the active sites in various electronic configurations. The catalytic properties (Fig. 16e, f) and the mechanistic pathways of such M–NHGF (3d metals embedded in nitrogen-doped holey graphene frameworks) materials for OER were shown to be strongly dependent on the *d*-orbital electronic configuration, and followed the tendency Ni–NHGF > Co–NHGF > Fe–NHGF. The respective linear sweep voltammograms were fully consistent with the theoretical calculation results since Ni–NHGF in fact exhibited an excellent catalytic activity and stability. At this point, it is relevant to remember that similar tendency was found for the respective metal oxides and hydroxides [93] when tested for OER (Ni > Co > Fe).

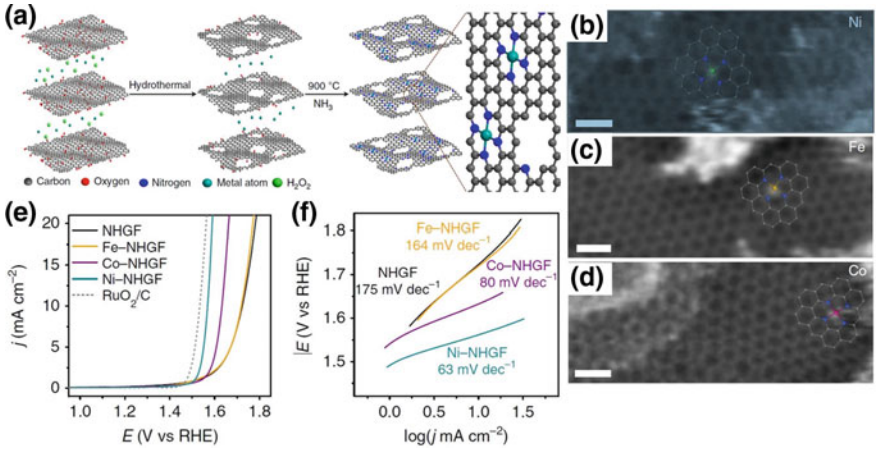

Fig. 16 The preparation route of M–NHGFs. (**a**) The graphene oxide solution in the presence of H_2O_2 and metal precursors was hydrothermally treated to form a 3D graphene hydrogel. After freeze drying the hydrogel, a thermal annealing process in NH_3 atmosphere was used to further reduce the graphene and incorporate N-dopants into the 2D graphene lattice. High-resolution TEM images enabled the direct visualization of the Ni (**b**), Fe (**c**) and Co (**d**) atoms embedded in the 2D graphene lattice. Scale bars, 0.5 nm. The bright region at the top part of (**d**) is attributed to out-of-focus thick graphene layers or non-planar flakes. **e** OER activity evaluated by LSV in 1 M KOH solution at a scan rate of 5 mV s^{-1} for NHGF, Fe–NHGF, Co–NHGF and Ni–NHGF along with RuO_2/C catalyst as reference. The data are presented with current–resistance (iR) correction. **f** Tafel plots of the catalysts shown in (**e**). Panel (a–f): Figure adapted from [92] with permission of Nature Publishing Group

Interesting results were found by Liu et al. [94] using graphitic carbon nitride (g-C_3N_4) materials showing layered structure and appropriate band-gap as substrate. A high temperature polymerization method was employed to prepare carbon nanotubes covered-up with g-C_3N_4, and Ni- and/or Fe-atoms were incorporated in its tri-s-triazine sites to generate Metal-N_x structures (Fig. 17a). The presence of such structures was probed by HAADF-STEM technique with sub-angstrom resolution, whose image showed homogeneously dispersed 1–2 Å large bright spots corresponding to isolated Ni- and Fe-atoms on the carbon matrix (Fig. 17b), but also small amounts of clusters. The variation of the signal intensity was analyzed confirming that the metal atoms are isolated and ~0.46 nm apart, separated by the lighter elements (Fig. 17c).

The bimetallic catalyst NiFe@g-C_3N_4/CNT was designed and tested, exhibiting a much better performance (η_{10} = 326 mV and Tafel slope = 67 mV dec^{-1}) for OER than the monometallic Ni@g-C_3N_4/CNT and Fe@g-C_3N_4/CNT catalysts (Fig. 17d, e). In addition, synchrotron-based X-ray absorption spectroscopy measurements revealed that the electronic structure of the Ni- and Fe-atoms were significantly modified in the bimetallic catalyst. Most notably, the Ni-atom was found in a much higher oxidation state when in the presence of iron, contributing directly to the enhanced OER activity of the material. However, it also become clear the significant role of the porous structure, and of the electrical conductivity and good contact between CNT and g-C_3N_4, for the performance of the nanostructured material. In fact, a clear and singular synergic effect was found in NiFe@g-C_3N_4/CNT which presented a much better performance than the Co-atom based SAC Co@g-C_3N_4/CNT reported by Zheng et al. [95].

Several Co-atom based SACs were prepared and extensively studied as OER catalysts, using doped graphene [96, 97] and carbon fibers [98], as well as carbon materials obtained by high temperature carbonization of MOFs [99], as substrates to anchor metal atoms. For example, Ding et al. [100] developed an easily scalable and simple strategy to get SACs by covering CNTs with polymerized ILs containing dispersed cobalt atoms in it (Fig. 18a), in this way combining the known property of ionic liquids (ILs) to enhance the catalytic performance.

The cobalt was bound by the reaction of $CoCO_3$ with the sulfate groups of the IL precursor forming a salt, and this was strongly adsorbed on single graphene sheets through the imidazolium moieties (energy of physisorption as high as 230 kJ mol^{-1}). In this way, isolated cobalt atoms can be distributed on CNT, as shown in the dark-field STEM (ADF-STEM) of Fig. 18b as small bright spots. The Co-atoms was colored pink in the expanded Fig. 18c to improve their visualization, and the LSV polarization curves are shown in Fig. 18d. The much higher activity of the CoSSPIL/CNT catalyst (Co-single-site polymerized ionic liquid/carbon nanotube) than Co_3O_4/CNT and $CoCO_3$ was assigned to a larger surface concentration and dispersion of Co-atoms making then more available for catalytic processes despite the much lower cobalt content in it.

Recently, we reviewed on the most recent advancements on OER electrocatalysts [101] based on coordination compounds, as well as on transition metal oxides and hydroxides and their composites. In this context, the bimetallic and trimetallic

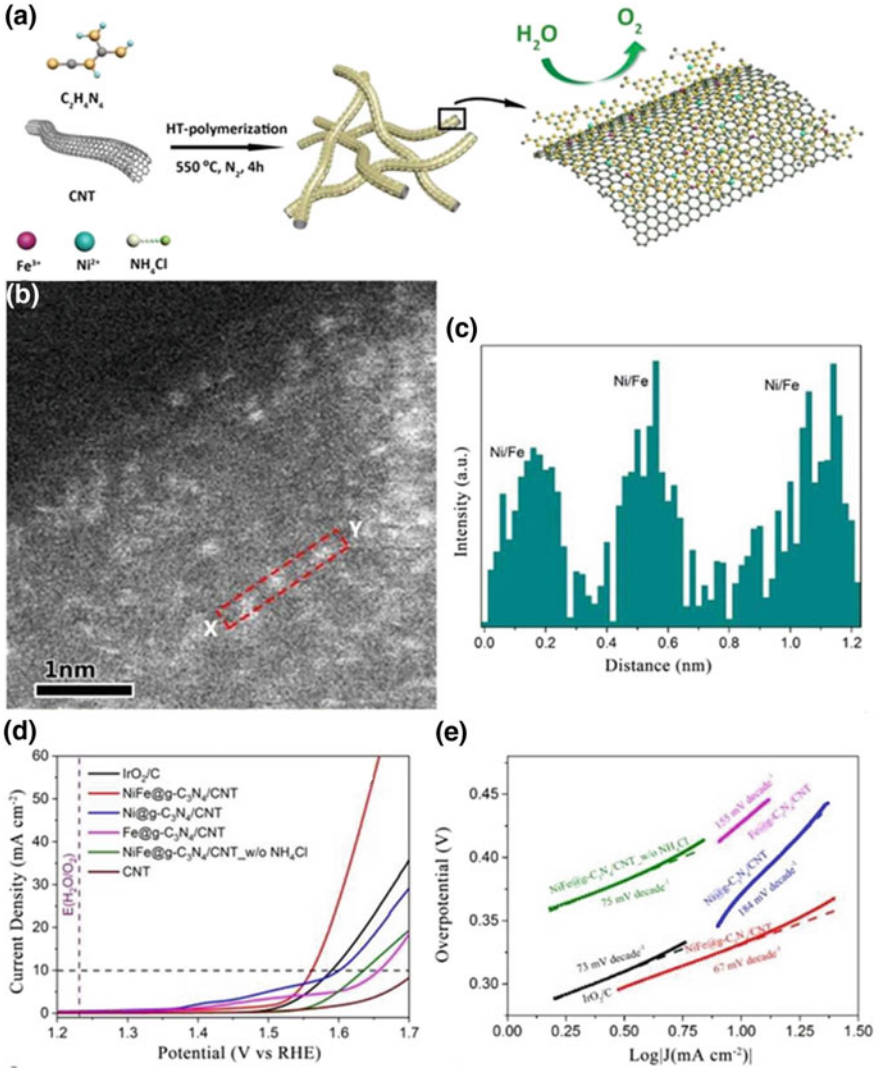

Fig. 17 **a** Schematic illustration of the fabrication of rationally designed NiFe@g-C_3N_4/CNT hybrid via a NH_4Cl-templated pyrolysis method, at high temperature (HT). **b** Magnified HAADF-STEM image and the corresponding intensity profiles along the X-Y lines (marked in red rectangle). **c** EDS mapping for Fe (blue), Ni (yellow), N (green) and C (red). **d** Polarization curves of NiFe@g-C_3N_4/CNT, Ni@g-C_3N_4/CNT, Fe@g-C_3N_4/CNT, NiFe@g-C_3N_4/CNT w/ NH_4Cl and IrO_2/C, respectively; and **e** the corresponding Tafel plots. The dashed line was fitted by the linear equation, $\eta = b(\log j) + a$. Panel (a–e): Figure adapted from [94] with permission of the Royal Society of Chemistry

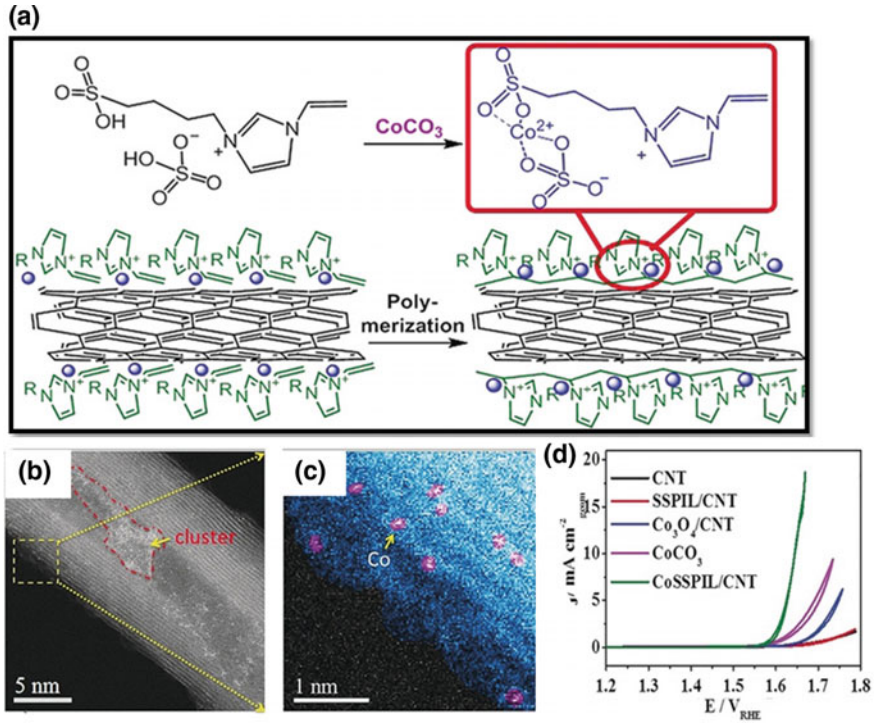

Fig. 18 **a** Schematic illustration of the preparation of the CoSSPIL/CNT (Co-single-site polymerized ionic liquid/carbon nanotube). H_2O and CO_2 are byproducts of the reaction between the SSIL and $CoCO_3$. The blue spheres represent single Co species. The image is not drawn to scale, and is only intended to show the cations on the CNT before and after polymerization. **b**, **c** ADF-STEM images of the CoSSPIL/CNT where a small amount of Co cluster were deposited on the CNT (red circles) in addition to separated metal atoms. **d** CV of the different samples normalized to the geometric area of the active electrode. Panel (a–d): Figure adapted from [100] with permission of the John Wiley and Sons

hydroxides, also known as lamellar double hydroxides (LDHs), were found to be the materials with the highest catalytic activity for OER, particularly when constituted by transition metal elements with one electron in e_g orbitals. Such a tendency seems to be general and intrinsic of the transition metal elements and the electronic configuration in the catalytic active species, such that similar behavior can be found for the respective single-atom catalysts using such materials as anchoring substrate, as shown in Table 2.

In this context, Zhang et al. [102] reported an easy method for preparation of self-assembled hierarchical structures of CoIr-x materials with high catalytic activity in neutral and alkaline conditions, consisting of flexible nanosheets of cobalt hydroxide covered with Ir-atoms. The Ir-atoms found on the top of ultra-thin α-$Co(OH)_2$ nanoribbons are bound to adjacent Co-atoms. In fact, the HAADF-STEM images revealed that the bright spots corresponding to Ir-atoms are uniformly bound in the

Table 2 Activity parameters of recently reported SACs based OER: experimental pH condition, onset potential, Tafel slope and overpotential at 10 mA cm^{-2} η_{10}

Single atom catalyst active site	Anchoring substrate	η_{10} (mV vs. RHE)	Onset potential (V vs. RHE)	Tafel slope (mV dec^{-1})	Exp. condition	References
Fe-N_x	N and S decorated carbon layer	370	–	82.0	0.1 M KOH	[104]
Ni-NHGF (Ni)	N-doped graphene	331	1.43	63.0	1.0 M KOH	[92]
Co-NHGF (Co)	N-doped graphene	402	–	80.0	1.0 M KOH	[92]
Fe-NHGF (Fe)	N-doped graphene	488	–	164.0	1.0 M KOH	[92]
Fe@g-C_3N_4/CNT (Fe)	Graphitic carbon nitride/CNT	>326	–	155.0	1.0 M KOH	[94]
Ni@g-C_3N_4/CNT (Ni)	Graphitic carbon nitride/CNT	>326	–	184.0	1.0 M KOH	[94]
NiFe@g-C_3N_4/CNT (NiFe)	Graphitic carbon nitride/CNT	326	~1.50	67.0	1.0 M KOH	[94]
Co@g-C_3N_4/CNT	g-C_3N_4/CNT	380	~1.50	68.4	1.0 M KOH	[95]
CUMESs-ZIF-67 (Co)	Zeolitic imidazole framework	410	~1.50	158.1	0.5 M KOH	[99]
SNG-Co^{2+} (Co^{2+})	S, N, O-doped Graphene	300–350	–	62.0	1.0 M KOH	[96]
SG-Co^{2+} (Co^{2+})	S, N, O-doped Graphene	320–350	–	62.0	1.0 M KOH	[96]
NG-Co^{2+} (Co^{2+})	N, O-doped Graphene	350	–	76.0	1.0 M KOH	[96]
OG-Co^{2+} (Co^{2+})	O-doped Graphene	400	–	65.0	1.0 M KOH	[96]
Pt/NiO (Pt and Ni)	NiO	358	–	33.0	1.0 M KOH	[105]
CoIr-*x*	$Co(OH)_2$	373	~1.56[a]	117.5	1.0 M KOH	[102]
[s]Au-NiFe-LDH (Au, Ni and Fe)	NiFe-LDH	237	~1.45[a]	~37.0[a]	1.0 M KOH	[103]
Pt_1@Fe–N–C (Pt)	Carbon support	310	1.33	62.0	0.1 M KOH	[85]

(continued)

Table 2 (continued)

Single atom catalyst active site	Anchoring substrate	η_{10} (mV vs. RHE)	Onset potential (V vs. RHE)	Tafel slope (mV dec^{-1})	Exp. condition	References
CoSSPIL/CNT (Co)	Carbon nanotubes	410	~1.58[a]	42.1	0.1 M KOH	[100]
CoN_4/NG (Co)	N-doped graphitic nanosheet	380	~1.50	81.0	0.1 M KOH	[97]
Ni-CN-200 (Ni)	g-C_3N_4	<350[a]	1.54	60.0	1.0 M KOH	[106]

Graphitic carbon nitride (g-C_3N_4) framework, carbon fibers network, and carbon cloth (CNW/CC)
[a]Approximate values by authors

hierarchical structure of CoIr-0.2 (Fig. 19a, b) and can be divided in two types: isolated Ir-atoms and clusters (marked in Fig. 19b). The first one can maximize the exposed surface area of the active sites as they bind onto the Co-atoms of the α-$Co(OH)_2$ nanosheets forming Co–Ir sites.

The optimized material containing 9.7 wt% of Ir showed high OER catalytic efficiency and presented η_{10} of 373 mV (Fig. 19c) and Tafel slope of 117.5 mV dec^{-1} (Fig. 19d) in 1.0 M phosphate buffer, surpassing the performance of commercial IrO_2 catalysts. Relevant information about the used catalyst was obtained by synchrotron-based X-ray absorption spectroscopy. The high applied potentials during the OER process generated in situ the catalytically active species, more specifically high valence cobalt oxide-hydroxide (β-CoOOH) species and low coordination high valence iridium species, responsible for the catalytic performance of the material. Thus, this work is highly relevant not only because describe the development of a new type of OER catalyst but also because provide excellent structural and spectroscopic characterization results for identification of the actual active sites.

As discussed above, transition metal hydroxides can be excellent substrates for anchoring transition metal atoms for preparation of SACs, since they can provide interaction/anchoring sites for the isolated transition metal atoms, tuning their electronic properties and enhancing the activity, but also providing additional catalytic active sites for OER. In fact, even better performances were measured when bimetallic LDH were used for the preparation of SACs, as recently reported by Zhang et al. [103], suggesting that this probably will be a major strategy for realization of more advanced and efficient electrocatalysts for OER. Isolated Au-atoms were deposited on NiFe-LDH generating materials denominated ^{S}Au/NiFe-LDH (TEM and HAADF-STEM images shown in Fig. 20a, b), and used to demonstrate why the LDH based materials are highly catalytic active. In addition, explains the possible reasons for the six fold enhancement of the catalytic activity by incorporation of 0.4 wt% of ^{S}Au, decreasing the overpotential to 0.21 V (Fig. 20d, e), improving the OER activity while lowering the Au consumption. This material exhibited a much faster kinetics as confirmed by the low Tafel slope and larger turnover frequency

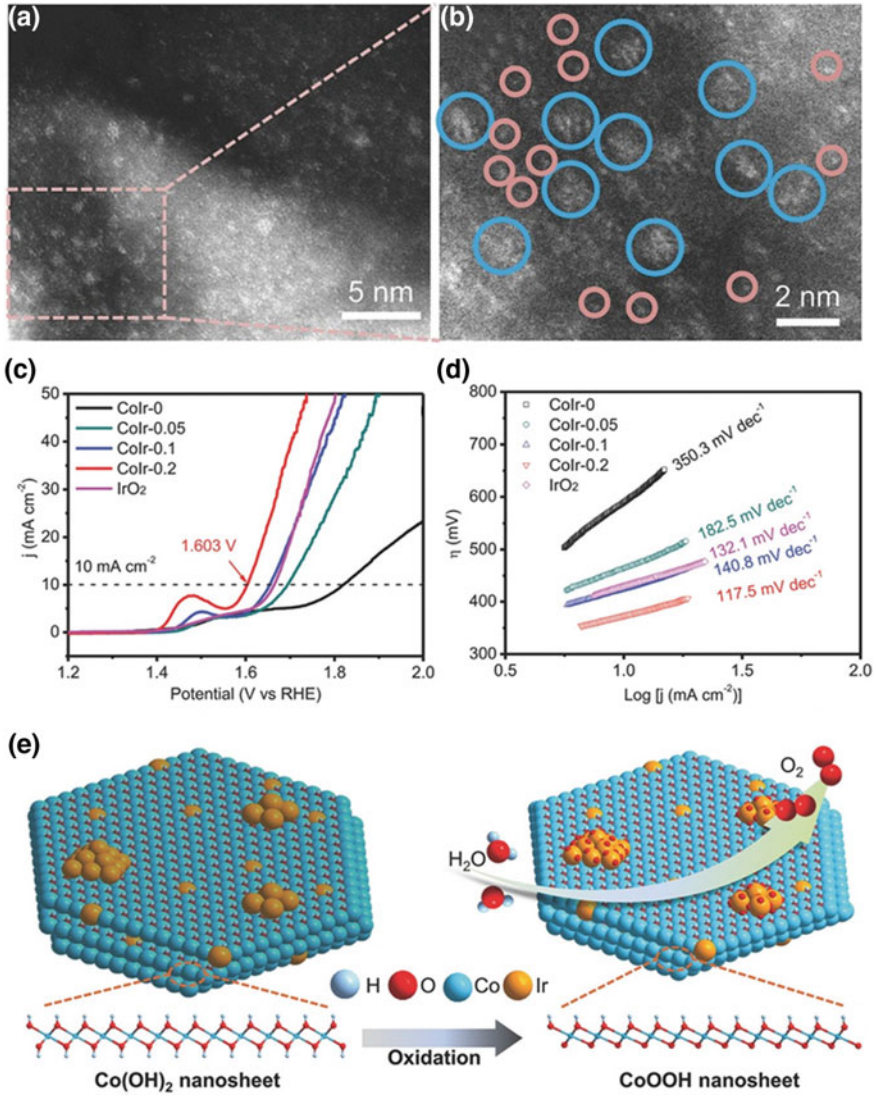

Fig. 19 **a**, **b** HAADF-STEM images of CoIr-0.2 with clusters of Ir marked as blue circles and single atoms of Ir highlighted as pink circles. **c** The iR corrected LSV curves and **d** the corresponding Tafel plots of CoIr-x and IrO_2 samples in 1.0 M PBS. **e** Scheme depicting the mechanism of OER on CoIr-0.2 surface and the transformation of α-$Co(OH)_2$ to β-CoOOH phase. Panel (a–e): Figure adapted from [102] with permission of the John Wiley and Sons

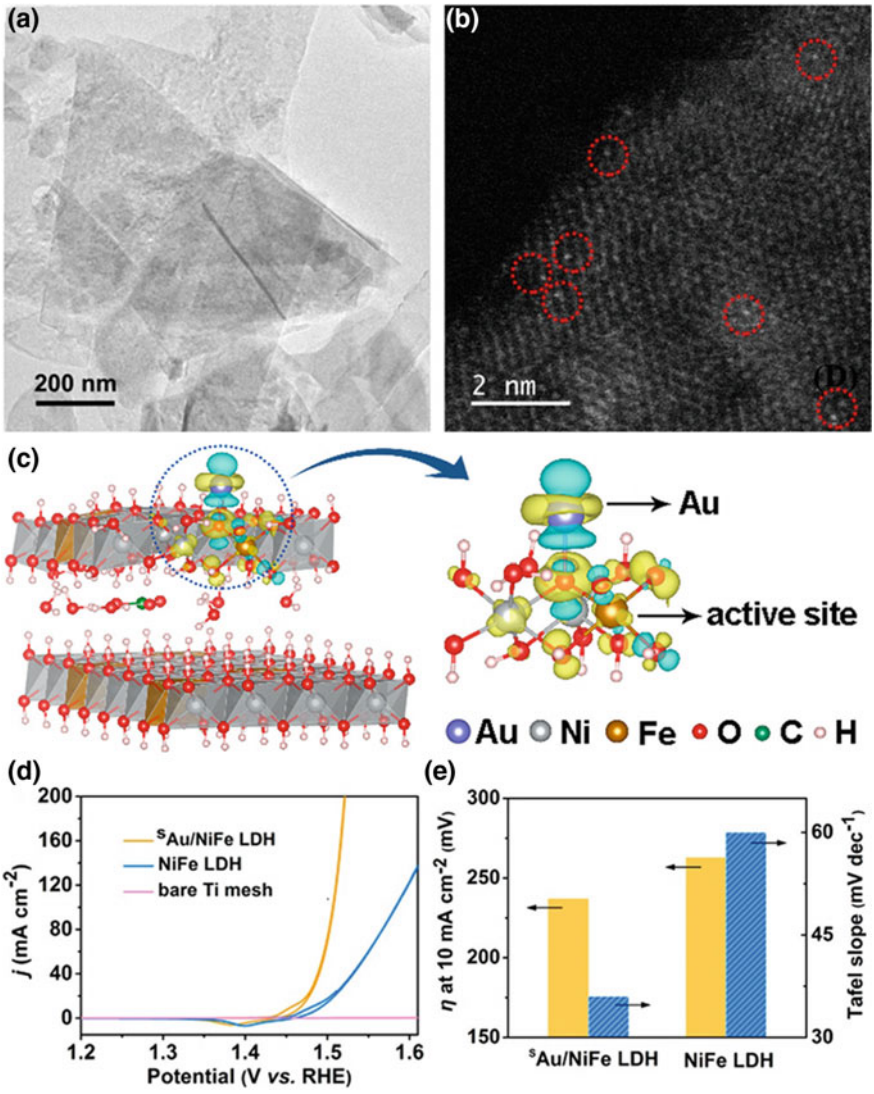

Fig. 20 **a** TEM and **b** HAADF-STEM images of ^{S}Au/NiFe LDH. **c** Differential charge densities of NiFe-LDH with and without Au-atom when one O-atom is adsorbed on the Fe site. Iso-surface value is 0.004 eÅ^{-3}. Yellow and blue contours represent electron accumulation and depletion, respectively. **d** Cyclic voltammetry (CV) curves of ^{S}Au/NiFe-LDH, pure NiFe-LDH and bare Ti mesh in 1 M KOH. **e** Overpotential (η_{10}) at 10 mA cm^{-2} (left) and Tafel slope (right) for ^{S}Au/NiFe-LDH and pure NiFe-LDH

(Fig. 20e). The enhanced activity of ^{S}Au/NiFe-LDH was found to be dependent on the synergic contributions of the two components leading to a charge redistribution responsible for the activation of the iron sites, as well as the presence of single Au-atoms anchored on the NiFe hydroxide and stabilized by the CO_3^{2-} ions and H_2O molecules in the interlamellar space of LDH (Fig. 20c).

8 Perspectives

The concept of single-atom catalysts is revolutionary in the sense that maximizes the specific activity of an element while bringing fundamental characteristics of homogeneous catalysts into heterogeneous catalysts, minimizing the consumption of rare elements. A great impact of SACs for energy generation in near future is foreseeing, for example by providing the catalysts for water splitting and artificial photosynthesis, whose realization depend on highly efficient materials for both, hydrogen and oxygen evolution reactions, greatly impacting economically and technologically our society. In fact, we are just experiencing the beginning of a revolution on the design and production of catalysts, which is being powered by the development of new, more precise and fast characterization tools and methods, concomitantly with an explosion on the theoretical calculation methods, that are opening whole new perspectives for the detailed and systematic comprehension of the interaction of molecules and catalytic active sites for chemical transformations. Such more detailed structure and properties correlation data have been used in the search of new support/single-atom pairs, aiming at adequate adsorption free energies with values near zero to go beyond the top of volcano shaped $\log(i_0)$ versus $\Delta G°$ diagrams. Another key aspect is the search for non-noble elements with as high as activity and stability as alternatives for noble metals, decreasing the pressure on natural resources.

Among the several possible substrates for preparation of SACs, carbon materials such as graphitic materials, carbon nanotubes and graphene derivatives has been explored with great interest as substrates for deposition of single-atoms sites because of their high conductivity allied to excellent mechanical and chemical properties, that have been combined in a synergic way to produce better and better electrocatalysts. In addition, their inherent catalytic activity has been largely improved by doping with nitrogen generating N-doped graphene and graphitic carbon nitrides ($g\text{-}C_3N_4$), materials with improved electronic and coordination properties. Nevertheless, the most efficient OER catalysts were prepared by combining the good electrocatalytic properties of transition metal hydroxides/oxides with that of single metal atoms, particularly Ni, Fe and Co.

Similar tendency of boiling activity could also be observed for HER materials in which carbon material substrates also play a very special role, but now a great deal of attention is being focused on MoS_2 based SACs where clearly charge-transfer interactions from de isolated atoms to the support material are fundamental for the electrocatalytic activity. Among the elements, platinum continue to be the king of

mountain but clearly there are lots of efforts focused on the quest for non-noble metal alternatives, such as nickel and cobalt based electrocatalysts.

Finally, it should be highlighted that theory-experiment joint studies would significantly advance these important fields of catalysis and energy science. The development of *in operando* X-ray spectroscopy based on synchrotron radiation along with first-principles calculations of the corresponding spectra will unveil the underlying mechanisms of the SAC reactions. Here, the contributions from the adsorbed metal atoms and the substrates can be disentangled. Furthermore, the thermodynamics of the metal adsorption and of the reaction mechanisms can be assessed through similar theoretical framework (most of them based on DFT). The stabilization of the reaction intermediates and kinetic barriers can be estimated in a wider range of compounds avoiding waste of sophisticated experimental resources. Furthermore, a great deal of excitement is coming with the development of high-throughput screening methods interplayed with artificial intelligence. Using appropriate descriptors for the respective reactions a large materials-library can be explored proposing novel catalysts that can be synthesized.

References

1. You B, Sun YJ (2018) Innovative strategies for electrocatalytic water splitting. Acc Chem Res 51(7):1571–1580
2. Zhu YP, Guo CX, Zheng Y, Qiao SZ (2017) Surface and interface engineering of noble-metal-free electrocatalysts for efficient energy conversion processes. Acc Chem Res 50(4):915–923
3. Miles MH, Thomason MA (1976) Periodic variations of overvoltages for water electrolysis in acid solutions from cyclic voltammetric studies. J Electrochem Soc 123(10):1459–1461
4. Jiao Y, Zheng Y, Jaroniec MT, Qiao SZ (2015) Design of electrocatalysts for oxygen- and hydrogen-involving energy conversion reactions. Chem Soc Rev 44(8):2060–2086
5. Carmo M, Fritz DL, Mergel J, Stolten D (2013) A comprehensive review on PEM water electrolysis. Int J Hydrogen Energy 38(12):4901–4934
6. Frydendal R, Paoli EA, Knudsen BP, Wickman B, Malacrida P, Stephens IEL, Chorkendorff I (2014) Benchmarking the stability of oxygen evolution reaction catalysts: the importance of monitoring mass losses. ChemElectroChem 1(12):2075–2081
7. Galizzioli D, Tantardini F, Trasatti S (1974) Ruthenium dioxide: a new electrode material. I. Behaviour in acid solutions of inert electrolytes. J Appl Electrochem 4(1):57–67
8. Kötz R, Stucki S, Scherson D, Kolb DM (1984) In-situ identification of RuO4 as the corrosion product during oxygen evolution on ruthenium in acid media. J Electroanal Chem Interfacial Electrochem 172(1):211–219
9. Mamaca N, Mayousse E, Arrii-Clacens S, Napporn TW, Servat K, Guillet N, Kokoh KB (2012) Electrochemical activity of ruthenium and iridium based catalysts for oxygen evolution reaction. Appl Catal B 111–112:376–380
10. Li G, Li S, Ge J, Liu C, Xing W (2017) Discontinuously covered IrO_2–RuO_2@Ru electrocatalysts for the oxygen evolution reaction: how high activity and long-term durability can be simultaneously realized in the synergistic and hybrid nano-structure. J Mater Chem A 5(33):17221–17229
11. Kötz R, Stucki S (1986) Stabilization of RuO_2 by IrO_2 for anodic oxygen evolution in acid media. Electrochim Acta 31(10):1311–1316

12. Audichon T, Mayousse E, Morisset S, Morais C, Comminges C, Napporn TW, Kokoh KB (2014) Electroactivity of RuO_2–IrO_2 mixed nanocatalysts toward the oxygen evolution reaction in a water electrolyzer supplied by a solar profile. Int J Hydrogen Energy 39(30):16785–16796
13. Zou X, Zhang Y (2015) Noble metal-free hydrogen evolution catalysts for water splitting. Chem Soc Rev 44(15):5148–5180
14. Anantharaj S, Ede SR, Sakthikumar K, Karthick K, Mishra S, Kundu S (2016) Recent trends and perspectives in electrochemical water splitting with an emphasis on sulfide, selenide, and phosphide catalysts of Fe Co, and Ni: a review. ACS Catal 6(12):8069–8097
15. McCrory CCL, Jung S, Peters JC, Jaramillo TF (2013) Benchmarking heterogeneous electrocatalysts for the oxygen evolution reaction. J Am Chem Soc 135(45):16977–16987
16. Merrill MD, Dougherty RC (2008) Metal oxide catalysts for the evolution of O_2 from H_2O. J Phys Chem C 112(10):3655–3666
17. Gorlin Y, Jaramillo TF (2010) A bifunctional nonprecious metal catalyst for oxygen reduction and water oxidation. J Am Chem Soc 132(39):13612–13614
18. Chen S, Duan J, Jaroniec M, Qiao S-Z (2014) Nitrogen and oxygen dual-doped carbon hydrogel film as a substrate-free electrode for highly efficient oxygen evolution reaction. Adv Mater 26(18):2925–2930
19. Zheng Y, Jiao Y, Li LH, Xing T, Chen Y, Jaroniec M, Qiao SZ (2014) Toward design of synergistically active carbon-based catalysts for electrocatalytic hydrogen evolution. ACS Nano 8(5):5290–5296
20. Cui W, Liu Q, Cheng N, Asiri AM, Sun X (2014) Activated carbon nanotubes: a highly-active metal-free electrocatalyst for hydrogen evolution reaction. Chem Commun 50(66):9340–9342
21. Zhao Y, Nakamura R, Kamiya K, Nakanishi S, Hashimoto K (2013) Nitrogen-doped carbon nanomaterials as non-metal electrocatalysts for water oxidation. Nat Commun 4:2390
22. Zhuo JQ, Wang TY, Zhang G, Liu L, Gan LB, Li MX (2013) Salts of C-60(OH)(8) electrodeposited onto a glassy carbon electrode: surprising catalytic performance in the hydrogen evolution reaction. Angew Chem-Int Ed 52(41):10867–10870
23. Tian GL, Zhao MQ, Yu DS, Kong XY, Huang JQ, Zhang Q, Wei F (2014) Nitrogen-doped graphene/carbon nanotube hybrids: in situ formation on bifunctional catalysts and their superior electrocatalytic activity for oxygen evolution/reduction reaction. Small 10(11):2251–2259
24. Fu Q, Saltsburg H, Flytzani-Stephanopoulos M (2003) Active nonmetallic Au and Pt species on ceria-based water-gas shift catalysts. Science 301(5635):935–938
25. Qiao B, Wang A, Yang X, Allard LF, Jiang Z, Cui Y, Liu J, Li J, Zhang T (2011) Single-atom catalysis of CO oxidation using Pt_1/FeO_x. Nat Chem 3:634
26. Guimaraes RR, Parussulo ALA, Toma HE, Araki K (2013) New tunable ruthenium complex dyes for TiO_2 solar cells. Inorg Chim Acta 404:23–28
27. Yang XF, Wang AQ, Qiao BT, Li J, Liu JY, Zhang T (2013) Single-atom catalysts: a new frontier in heterogeneous catalysis. Acc Chem Res 46(8):1740–1748
28. Ebadi M, Marchiori C, Mindemark J, Brandell D, Araujo CM (2019) Assessing structure and stability of polymer/lithium-metal interfaces from first-principles calculations. J Mater Chem A 7(14):8394–8404
29. Damas G, Marchiori CFN, Araujo CM (2018) On the design of donor acceptor conjugated polymers for photocatalytic hydrogen evolution reaction: first-principles theory-based assessment. J Phys Chem C 122(47):26876–26888
30. Ertem MZ, Konezny SJ, Araujo CM, Batista VS (2013) Functional role of pyridinium during aqueous electrochemical reduction of CO_2 on Pt(111). J Phys Chem Lett 4(5):745–748
31. Ebadi M, Nasser A, Carboni M, Younesi R, Marchiori CFN, Brandell D, Araujo CM (2019) Insights into the Li-metal/organic carbonate interfacial chemistry by combined first-principles theory and X-ray photoelectron spectroscopy. J Phys Chem C 123(1):347–355
32. Nørskov JK, Bligaard T, Rossmeisl J, Christensen CH (2009) Towards the computational design of solid catalysts. Nat Chem 1:37
33. Hohenberg P, Kohn W (1964) Inhomogeneous electron gas. Phys Rev B 136(3B):B864

34. Kohn W, Sham LJ (1965) Self-consistent equations including exchange and correlation effects. Phys Rev 140(4A):1133
35. Becke AD (1988) Density-functional exchange-energy approximation with correct asymptotic-behavior. Phys Rev A 38(6):3098–3100
36. Perdew JP, Wang Y (1992) Accurate and simple analytic representation of the electron-gas correlation-energy. Phys Rev B 45(23):13244–13249
37. Perdew JP, Burke K, Ernzerhof M (1996) Generalized gradient approximation made simple. Phys Rev Lett 77(18):3865–3868
38. Tao JM, Perdew JP, Staroverov VN, Scuseria GE (2003) Climbing the density functional ladder: nonempirical meta-generalized gradient approximation designed for molecules and solids. Phys Rev Lett 91(14)
39. Blochl PE (1994) Projector augmented-wave method. Phys Rev B 50(24):17953–17979
40. Kresse G, Hafner J (1993) Abinitio molecular-dynamics for liquid-metals. Phys Rev B 47(1):558–561
41. Vanderbilt D (1990) Soft self-consistent pseudopotentials in a generalized eigenvalue formalism. Phys Rev B 41(11):7892–7895
42. Cottenier S (2004) Density functional theory and the family of (L)APW-method a step-by-step introduction. Belgium
43. Martin RM (2004) Electronic structure: basic theory and practical methods. Cambridge University Press
44. Patel AM, Ringe S, Siahrostami S, Bajdich M, Norskov JK, Kulkarni AR (2018) Theoretical approaches to describing the oxygen reduction reaction activity of single-atom catalysts. J Phys Chem C 122(51):29307–29318
45. George SM (2010) Atomic layer deposition: an overview. Chem Rev 110(1):111–131
46. Cheng N, Stambula S, Wang D, Banis MN, Liu J, Riese A, Xiao B, Li R, Sham T-K, Liu L-M et al (2016) Platinum single-atom and cluster catalysis of the hydrogen evolution reaction. Nat Commun 7:13638
47. Sun S, Zhang G, Gauquelin N, Chen N, Zhou J, Yang S, Chen W, Meng X, Geng D, Banis MN et al (2013) Single-atom catalysis using Pt/graphene achieved through atomic layer deposition. Sci Rep 3:1775
48. Stambula S, Gauquelin N, Bugnet M, Gorantla S, Turner S, Sun S, Liu J, Zhang G, Sun X, Botton GA (2014) Chemical structure of nitrogen-doped graphene with single platinum atoms and atomic clusters as a platform for the PEMFC electrode. J Phys Chem C 118(8):3890–3900
49. Deng J, Li H, Xiao J, Tu Y, Deng D, Yang H, Tian H, Li J, Ren P, Bao X (2015) Triggering the electrocatalytic hydrogen evolution activity of the inert two-dimensional MoS_2 surface via single-atom metal doping. Energy Environ Sci 8(5):1594–1601
50. Tavakkoli M, Holmberg N, Kronberg R, Jiang H, Sainio J, Kauppinen EI, Kallio T, Laasonen K (2017) Electrochemical activation of single-walled carbon nanotubes with pseudo-atomic-scale platinum for the hydrogen evolution reaction. ACS Catal 7(5):3121–3130
51. Li J-C, Wei Z, Liu D, Du D, Lin Y, Shao M (2019) Dispersive single-atom metals anchored on functionalized nanocarbons for electrochemical reactions. Top Curr Chem 377(1):4
52. Chen W, Pei J, He C-T, Wan J, Ren H, Zhu Y, Wang Y, Dong J, Tian S, Cheong W-C et al (2017) Rational design of single molybdenum atoms anchored on N-doped carbon for effective hydrogen evolution reaction. Angew Chem Int Ed 56(50):16086–16090
53. Martensson N, Eriksson M (2018) The saga of MAX IV, the first multi-bend achromat synchrotron light source. Nucl Instrum Methods Phys Res, Sect A 907:97–104
54. Bogan MJ, Benner WH, Boutet S, Rohner U, Frank M, Barty A, Seibert MM, Maia F, Marchesini S, Bajt S et al (2008) Single particle X-ray diffractive imaging. Nano Lett 8(1):310–316
55. Hufner S (2003) Photoelectron spectroscopy—principles and applications. Springer, Tokyo
56. Masuda T (2018) Various spectroelectrochemical cells for in situ observation of electrochemical processes at solid–liquid interfaces. Top Catal 61(20):2103–2113
57. Salmeron M (2018) From surfaces to interfaces: ambient pressure XPS and beyond. Top Catal 61(20):2044–2051

58. Kolmakov A, Gregoratti L, Kiskinova M, Günther S (2016) Recent approaches for bridging the pressure gap in photoelectron microspectroscopy. Top Catal 59(5):448–468
59. Starr DE, Liu Z, Havecker M, Knop-Gericke A, Bluhm H (2013) Investigation of solid/vapor interfaces using ambient pressure X-ray photoelectron spectroscopy. Chem Soc Rev 42(13):5833–5857
60. Stoerzinger KA, Hong WT, Crumlin EJ, Bluhm H, Shao-Horn Y (2015) Insights into electrochemical reactions from ambient pressure photoelectron spectroscopy. Acc Chem Res 48(11):2976–2983
61. Axnanda S, Crumlin EJ, Mao BH, Rani S, Chang R, Karlsson PG, Edwards MOM, Lundqvist M, Moberg R, Ross P et al (2015) Using "tender" X-ray ambient pressure X-Ray photoelectron spectroscopy as a direct probe of solid-liquid interface. Sci Rep 5
62. Faubel M, Steiner B, Toennies JP (1997) Photoelectron spectroscopy of liquid water, some alcohols, and pure nonane in free micro jets. J Chem Phys 106(22):9013–9031
63. Winter B, Weber R, Widdra W, Dittmar M, Faubel M, Hertel IV (2004) Full valence band photoemission from liquid water using EUV synchrotron radiation. J Phys Chem A 108(14):2625–2632
64. Winter B, Faubel M (2006) Photoemission from liquid aqueous solutions. Chem Rev 106(4):1176–1211
65. Jungwirth P, Winter B (2008) Ions at aqueous interfaces: from water surface to hydrated proteins. Annu Rev Phys Chem 59(1):343–366
66. Ottosson N, Wernersson E, Söderström J, Pokapanich W, Kaufmann S, Svensson S, Persson I, Öhrwall G, Björneholm O (2011) The protonation state of small carboxylic acids at the water surface from photoelectron spectroscopy. Phys Chem Chem Phys 13(26):12261–12267
67. Ottosson N, Børve KJ, Spångberg D, Bergersen H, Sæthre LJ, Faubel M, Pokapanich W, Öhrwall G, Björneholm O, Winter B (2011) On the origins of core–electron chemical shifts of small biomolecules in aqueous solution: insights from photoemission and ab initio calculations of glycineaq. J Am Chem Soc 133(9):3120–3130
68. Ottosson N, Ohrwall G, Bjorneholm O (2012) Ultrafast charge delocalization dynamics in aqueous electrolytes: new insights from Auger electron spectroscopy. Chem Phys Lett 543:1–11
69. Artiglia L, Edebeli J, Orlando F, Chen S, Lee M-T, Corral Arroyo P, Gilgen A, Bartels-Rausch T, Kleibert A, Vazdar M et al (2017) A surface-stabilized ozonide triggers bromide oxidation at the aqueous solution-vapour interface. Nat Commun 8(1):700
70. Ekholm V, Caleman C, Bjärnhall Prytz N, Walz M-M, Werner J, Öhrwall G, Rubensson J-E, Björneholm O (2018) Strong enrichment of atmospherically relevant organic ions at the aqueous interface: the role of ion pairing and cooperative effects. Phys Chem Chem Phys 20(42):27185–27191
71. Xiong W, Hickstein DD, Schnitzenbaumer KJ, Ellis JL, Palm BB, Keister KE, Ding C, Miaja-Avila L, Dukovic G, Jimenez JL et al (2013) Photoelectron spectroscopy of CdSe nanocrystals in the gas phase: a direct measure of the evanescent electron wave function of quantum dots. Nano Lett 13(6):2924–2930
72. Milosavljevic AR, Bozanic DK, Sadhu S, Vukmirovic N, Dojcilovic R, Sapkota P, Huang WX, Bozek J, Nicolas C, Nahon L et al (2018) Electronic properties of free-standing surfactant-capped lead halide perovskite nanocrystals isolated in Vacuo. J Phys Chem Lett 9(13):3604
73. Bak S-M, Shadike Z, Lin R, Yu X, Yang X-Q (2018) In situ/operando synchrotron-based X-ray techniques for lithium-ion battery research. NPG Asia Mater 10(7):563–580
74. Liu X, Yang W, Liu Z (2014) Recent progress on synchrotron-based in-situ soft X-ray spectroscopy for energy materials. Adv Mater 26(46):7710–7729
75. Young NA (2014) The application of synchrotron radiation and in particular X-ray absorption spectroscopy to matrix isolated species. Coord Chem Rev 277–278:224–274
76. Dong C-L, Vayssieres L (2018) In situ/operando X-ray spectroscopies for advanced investigation of energy materials. Chem A Eur J 24(69):18356–18373
77. Li X, Wang H-Y, Yang H, Cai W, Liu S, Liu B (2018) In situ/operando characterization techniques to probe the electrochemical reactions for energy conversion. Small Methods 2(6):1700395

78. Lukashuk L, Foettinger K (2018) In situ and operando spectroscopy: a powerful approach towards understanding catalysts. Johns Matthey Technol Rev 62(3):316–331
79. González-Flores D, Klingan K, Chernev P, Loos S, Mohammadi MR, Pasquini C, Kubella P, Zaharieva I, Smith RDL, Dau H (2018) Nickel-iron catalysts for electrochemical water oxidation – redox synergism investigated by in situ X-ray spectroscopy with millisecond time resolution. Sustain Energy Fuels 2(9):1986–1994
80. Zhu C, Fu S, Shi Q, Du D, Lin Y (2017) Single-atom electrocatalysts. Angew Chem Int Ed 56(45):13944–13960
81. Fei H, Dong J, Arellano-Jiménez MJ, Ye G, Dong Kim N, Samuel ELG, Peng Z, Zhu Z, Qin F, Bao J et al (2015) Atomic cobalt on nitrogen-doped graphene for hydrogen generation. Nat Commun 6:8668
82. Zhang Q-H, Xiao D-D, Gu L (2016) Aberration-corrected scanning transmission electron microscopy for complex transition metal oxides. Chin Phys B 25(6):066803
83. Jaramillo TF, Jørgensen KP, Bonde J, Nielsen JH, Horch S, Chorkendorff I (2007) Identification of active edge sites for electrochemical H_2 evolution from MoS_2 nanocatalysts. Science 317(5834):100–102
84. Hinnemann B, Moses PG, Bonde J, Jørgensen KP, Nielsen JH, Horch S, Chorkendorff I, Nørskov JK (2005) Biomimetic hydrogen evolution: MoS_2 nanoparticles as catalyst for hydrogen evolution. J Am Chem Soc 127(15):5308–5309
85. Zeng X, Shui J, Liu X, Liu Q, Li Y, Shang J, Zheng L, Yu R (2018) Single-atom to single-atom grafting of Pt_1 onto Fe–N4 Center: Pt_1@Fe–N–C multifunctional electrocatalyst with significantly enhanced properties. Adv Energy Mater 8(1):1701345
86. Chao T, Luo X, Chen W, Jiang B, Ge J, Lin Y, Wu G, Wang X, Hu Y, Zhuang Z et al (2017) Atomically dispersed copper-platinum dual sites alloyed with palladium nanorings catalyze the hydrogen evolution reaction. Angew Chem Int Ed 56(50):16047–16051
87. Liang H-W, Brüller S, Dong R, Zhang J, Feng X, Müllen K (2015) Molecular metal–N_x centres in porous carbon for electrocatalytic hydrogen evolution. Nat Commun 6:7992
88. Qiu H-J, Ito Y, Cong W, Tan Y, Liu P, Hirata A, Fujita T, Tang Z, Chen M (2015) Nanoporous graphene with single-atom nickel dopants: an efficient and stable catalyst for electrochemical hydrogen production. Angew Chem Int Ed 54(47):14031–14035
89. Fan L, Liu PF, Yan X, Gu L, Yang ZZ, Yang HG, Qiu S, Yao X (2016) Atomically isolated nickel species anchored on graphitized carbon for efficient hydrogen evolution electrocatalysis. Nat Commun 7:10667
90. Zhang H, An P, Zhou W, Guan BY, Zhang P, Dong J, Lou XW (2018) Dynamic traction of lattice-confined platinum atoms into mesoporous carbon matrix for hydrogen evolution reaction. Sci Adv 4(1)
91. Rossmeisl J, Logadottir A, Nørskov JK (2005) Electrolysis of water on (oxidized) metal surfaces. Chem Phys 319(1):178–184
92. Fei H, Dong J, Feng Y, Allen CS, Wan C, Volosskiy B, Li M, Zhao Z, Wang Y, Sun H et al (2018) General synthesis and definitive structural identification of MN_4C_4 single-atom catalysts with tunable electrocatalytic activities. Nat Catal 1(1):63–72
93. Hong WT, Risch M, Stoerzinger KA, Grimaud A, Suntivich J, Shao-Horn Y (2015) Toward the rational design of non-precious transition metal oxides for oxygen electrocatalysis. Energy Environ Sci 8(5):1404–1427
94. Liu D, Ding S, Wu C, Gan W, Wang C, Cao D, Rehman Z, Sang Y, Chen S, Zheng X et al (2018) Synergistic effect of an atomically dual-metal doped catalyst for highly efficient oxygen evolution. J Mater Chem A 6(16):6840–6846
95. Zheng Y, Jiao Y, Zhu Y, Cai Q, Vasileff A, Li LH, Han Y, Chen Y, Qiao S-Z (2017) Molecule-level g-C_3N_4 coordinated transition metals as a new class of electrocatalysts for oxygen electrode reactions. J Am Chem Soc 139(9):3336–3339
96. Wang J, Ge X, Liu Z, Thia L, Yan Y, Xiao W, Wang X (2017) Heterogeneous electrocatalyst with molecular cobalt ions serving as the center of active sites. J Am Chem Soc 139(5):1878–1884

97. Yang L, Shi L, Wang D, Lv Y, Cao D (2018) Single-atom cobalt electrocatalysts for foldable solid-state Zn-air battery. Nano Energy 50:691–698
98. Meng F, Zhong H, Bao D, Yan J, Zhang X (2016) In situ coupling of strung Co_4N and intertwined N–C fibers toward free-standing bifunctional cathode for robust, efficient, and flexible Zn–air batteries. J Am Chem Soc 138(32):10226–10231
99. Tao L, Lin C-Y, Dou S, Feng S, Chen D, Liu D, Huo J, Xia Z, Wang S (2017) Creating coordinatively unsaturated metal sites in metal-organic-frameworks as efficient electrocatalysts for the oxygen evolution reaction: Insights into the active centers. Nano Energy 41:417–425
100. Ding Y, Klyushin A, Huang X, Jones T, Teschner D, Girgsdies F, Rodenas T, Schlögl R, Heumann S (2018) Cobalt-bridged ionic liquid polymer on a carbon nanotube for enhanced oxygen evolution reaction activity. Angew Chem Int Ed 57(13):3514–3518
101. Gonçalves JM, Matias TA, Toledo KCF, Araki K (2019) Electrocatalytic materials design for oxygen evolution reaction. In: Advances in inorganic chemistry. Academic Press
102. Zhang Y, Wu C, Jiang H, Lin Y, Liu H, He Q, Chen S, Duan T, Song L (2018) Atomic iridium incorporated in cobalt hydroxide for efficient oxygen evolution catalysis in neutral electrolyte. Adv Mater 30(18):1707522
103. Zhang J, Liu J, Xi L, Yu Y, Chen N, Sun S, Wang W, Lange KM, Zhang B (2018) Single-atom Au/NiFe layered double hydroxide electrocatalyst: probing the origin of activity for oxygen evolution reaction. J Am Chem Soc 140(11):3876–3879
104. Chen P, Zhou T, Xing L, Xu K, Tong Y, Xie H, Zhang L, Yan W, Chu W, Wu C et al (2017) Atomically dispersed iron-nitrogen species as electrocatalysts for bifunctional oxygen evolution and reduction reactions. Angew Chem Int Ed 56(2):610–614
105. Lin C, Zhao Y, Zhang H, Xie S, Li Y-F, Li X, Jiang Z, Liu Z-P (2018) Accelerated active phase transformation of NiO powered by Pt single atoms for enhanced oxygen evolution reaction. Chem Sci 9(33):6803–6812
106. Ohn S, Kim SY, Mun SK, Oh J, Sa YJ, Park S, Joo SH, Kwon SJ, Park S (2017) Molecularly dispersed nickel-containing species on the carbon nitride network as electrocatalysts for the oxygen evolution reaction. Carbon 124:180–187

Electrocatalysis: Application of Nanocomposite Materials

Manorama Singh, Ankita Rai and Vijai K. Rai

Abstract In the last few years, much attention has been given to the design and fabricate efficient electrocatalysts for different applications in energy storage devices, electroanlytical sensors and organic synthesis. Nanocomposite materials have arisen as some of the most proficient electrocatalysts because of their exceptional physicochemical and electronic properties. We focus our significant importance on different construction approaches for synthesis and applications of nanocomposites and their influence on inherent electronic and catalytic properties. Lastly, we discuss the applications and future prospects leading to develop advanced nanocomposites for efficient electrocatalysis.

Keywords Electrocatalysis · Nanocomposite · Fuel cell · Sensor · Electro-organo synthesis

1 Electrocatalysis

Electrocatalysis is one of the most important field in 'Electrochemistry', which has been grown after the late eighties because of the application of new hybrid techniques. Nowadays, the application of new nanocomposites based on carbon nanotubes and graphene, metal nanoparticles, metal oxide nanoparticles, polyaniline etc. for electrocatalysis has been in interest and the attraction of chemists as well as for engineers. Therefore, we here discuss significant advances in electrocatalysis based on different composition and functions of nanocomposite as an electrocatalyst using in different fields like energy conversion devices (*e.g.* solar cells, fuel cells and batteries) developing electrochemical sensors and in electro-organic synthesis [1].

M. Singh (✉) · V. K. Rai
Department of Chemistry, Guru Ghasidas Vishwavidyalaya, Bilaspur, Chhattisgarh 495009, India
e-mail: manoramabhu@gmail.com

A. Rai
School of Physical Sciences, Jawaharlal Nehru University, New Delhi 1100067, India

Inamuddin et al. (eds.), *Methods for Electrocatalysis*,
https://doi.org/10.1007/978-3-030-27161-9_4

1.1 Electrocatalysts and Its Features

Common necessities of high-performance electrocatalysts are in terms of high catalytic activity, reducing the energy barriers of electrocatalytic reactions, rate promotion of electron transfer etc. Generally, features of a good electrocatalyst are high surface area, high catalytic activity, better electrical conductivity and long-lasting stability [2], which not only affect strongly the electrocatalyst in terms of physical and chemical properties, but the interaction between electrode and electrolyte also. To achieve high performance of electrocatalyst, the development of a newfangled "*Nanocomposite based Electrocatalysts*" is nowadays getting much attention because they offer enhanced catalytic activity, good stability, high selectivity and better efficiency required for the application in energy conversion/storage research, sensor technology and electro-organic synthesis [3].

1.2 Nanocomposite Material as an Electrocatalyst

The performance of nanocomposite as an electrocatalyst towards a particular reaction or application depends upon the result of chemistry among a large number of factors, including the nature of the different components present in electrocatalytic nanocomposite material such as size, shape, surface structure, electron transfer properties and synergistic effect of different components [4]. Fabrication of nanocomposite materials offers the improved properties than their original properties, which is an important subject in nanoscience and nanotechnology. With the time, metal nanoparticles, polymer/metal nanoparticles, graphene, carbon nanotubes (CNT) based nanocomposites have arisen as the most significant contenders for electrocatalysis due to their exceptional electronic and physico-chemical properties. Electrocatalysts with nanoscale and high dispersibility results in remarkable enhancement in electrocatalytic activity [5, 6].

Number of examples are there to explore the performance of nanocomposite based electrocatalysis in electroanalytical sensors [7–10], energy storage devices such as fuel cells [11, 12], batteries, solar cells and electro-organic synthesis [13, 14]. The objective of this chapter is mainly focused on development strategies in using "*nanocomposite based electrocatalysis*". This chapter presents first, an introduction followed by advantages of using nanocomposite as an electrocatalyst in energy conversion devices, sensors, electro-organic synthesis and finally, accomplished with brief concluding remarks and outlook.

2 Different Applications of Nanocomposite as an Electrocatalyst

Here, we discuss the role of different nanocomposites as an electrocatalyst in different fields:

*2.1 Nanocomposite Based Electrocatalysis in Oxygen Reduction (*i.e. *Fuel Cell)*

The fuel cell (FC) is a well-known device, in which chemical energy is directly converted into electrical energy and is now well-thought-out to be one of the proficient ecofriendly methods to resolve the crisis of energy required in future because of its low emitted high energy conversion efficiency [15–18]. A suitable electrocatalyst is required to improve the efficiency of FCs. Usually, low amount Pt thin film has been investigated as an effective catalyst [19, 20]. The use of Pt offers the good catalytic efficiency here but, it is not economical to be commercialized and thus, it was a driving force to develop novel catalysts to minimize the need of Pt [21]. Among several electrochemical reactions investigated in FCs, the oxygen reduction reaction (ORR) is found to be as the core of FCs because it occurs on cathode.

Researchers are involved to develop cheaper alternatives to reach up to this aim and for this purpose, Carbon (carbon nanotube, graphene and other carbon-based entities) are common catalysts support which could help to advance the performance of the catalyst [22–26]. For example: economical cobalt-polypyrrole MWCNTs composite has explored the better power density as compared to Pt. The nanocomposite of MWCNTs and SnO_2 has been established as a very desirable anode material constituting microbial cells on electrode because of its greater power density [27]. Nanocomposite of PdCo (alloy of two metals) and MWCNTs has shown the better activity [11]. Conducting polymers such as 'polyaniline' coating on CNTs can enhance the electroconductive properties [28]. Therefore, CNTs may give the more stability to the fuel cell [29] and offers higher corrosion resistance [28–30]. The CNT gives a good support for Pt and high surface area [31–33]. Co_3O_4 has lower electrocatalytic activity because of its low dissolution and low electrical conductivity, small active site-density and its agglomeration during electrocatalytic methods [34, 35]. However, additional studies have revealed that the synergistic effect of Co_3O_4 with carbon nanomaterials (*i.e.* CNTs and graphene) offers a massive advancement of the electrocatalytic activity [36–38]. Uniformly dispersed Co_3O_4 nanostructures (*i.e.* core-shell, nanoparticles, and hollow sphere) was investigated by many research groups to advance the electrocatalytic activity of electrocatalyst [34, 39, 40]. Here, it was shown that the shape and size of the nanocatalysts are extremely associated to their electrocatalytic activities and development of hybrid catalysts is found to be one of the best approaches to improve stability and catalytic activity [41]. Pt-Ni-Fe/CNT/carbon paper nanocomposite electrode was reported and its electrochemical

impedance spectroscopy illustrated the increased power density and reduced charge transfer resistance if compares with commercial Pt/C loaded carbon paper. Triple catalyst such as alloy of Pt/Ni/Fe results the outstanding catalytic activity making them a suitable contender as a cathode employed in proton exchange membrane fuel cells [42].

Use of 'Graphene nanosheets (GN)' offers superior durability and high electrical activity of the catalyst and therefore, they are established as an ideal alternate with other traditional carbon support materials [43]. The combination of catalyst metals and graphene-based composites is now being used to ensure improved electronic and thermal conductivities, catalytic efficiency, stability and specific surface area of the catalyst support materials. Novel ternary nanocomposites such as Pt, $MnCo_2O_4$ and graphene nanosheets with compositional formula, 20 wt% Pt/mwt% $MnCo_2O_4$/GN (where m = 20, 15, 10, 8, 6 and 0) have been synthesized and investigated as electrocatalysts for the oxidation of methanol in H_2SO_4 (0.5 M) using cyclic voltammetry and chronoamperometry [44]. Here, low amounts of the oxide (6–20 wt%) was added into 20 wt%Pt/GNS is greatly helpful to enhance the accessible Pt sites, electrocatalytic activity, CO poisoning tolerance and stability of the composite. Furthermore, the increase of the oxide content from 6 to 10 wt% in the composite greatly enhances the rate of oxidation of methanol. Thus, ternary composite electrocatalyst containing 10 wt% oxide could be a possible Pt-based anode in direct methanol-based fuel cell [44].

The electrocatalytic behavior of NiO/graphene and CoO/graphene nanocomposites was investigated as candidate catalyst for the methanol oxidation in acidic environment. It has been shown that the electrocatalytic activity of the CoO/graphene catalyst is advanced than that of the NiO/graphene because of its controlled diffusion. An interesting behavior has been noticed for the electrocatalytic activity of the cobalt oxide/graphene catalyst towards the oxygen reduction reaction [45]. Polyaniline/Pd nanoparticles coupled vertical reduced graphene oxide (VrGO) nanosheet was reported, where, rGO exposes the surface for stabilizing Pd nanoparticles in Polyaniline@VrGO nanosheet. Further, exceptional durability and high catalytic activity of Pd/Polyaniline@VrGO electrocatalyst were found for alcohol oxidation reaction [43]. A three-dimensional $NiCo_2O_4$ nanospheres are prepared by entangled 2D-ultrathin mesoporous nanosheets. Large specific surface area and good long-lasting stability of nanosphere-like $NiCo_2O_4$ has been successfully employed to electrocatalyse the methanl oxidation [46]. The electrocatalytic activity of a new ternary complex system Pt/PdCu nanoboxes anchored on 3D graphene for the oxidation of ethanol are considerably better as compared to pure Pt and PdCu electrodes and 4-fold improved catalyst over established commercial catalysts in direct ethanol fuel cells [6].

Pt/polypyrrole/GN-based nanocomposites was fabricated by in situ polymerization coating of polypyrrole on graphene nanosheets as a new catalyst [47]. Under optimized conditions, novel AuNPs/PEDOT:PSS core-shell nanocomposite with enhanced catalytic activity was produced and reactive species diffusion and effective electron transfer was investigated on porous polymer network [3]. An efficient electrocatalyst gold nanoclusters (AuNCs)/polyvinyl pyrrolidone/reduced graphene

oxide nanocomposite has been prepared for ORR in which excellent reactivity and robust stability was provided by using metal nanoclusters supported with graphene for ORR [48]. A review was reported recently, in which, metal@carbon core@shell nanocomposites have developed as a exclusive class of functional nanocomposite materials with superficial electrocatalytic activity towards a range of reactions, such as oxygen or hydrogen evolution, oxygen or CO_2 reduction reactions, that are important in fuel cells, water splitting, metal-air batteries. Interfacial charge transfer between the metal core and carbon shell manipulate the electronic interactions of reaction intermediated with catalytic surface, and it varies with the structural and morphological characteristics of the carbon shell and metal core. A third structural component can further manipulate it [49, 50].

2.2 Nanocomposite Based Electrocatalysis in Sensors

Nowadays, using nanocomposite in electrochemical and electrocatalytic sensing represents one of the interesting topics in current science. Since, most of the analytes such as drugs, biomolecules (*i.e.* NADH *etc.*), different heavy metal ions [51–53] etc. are electroactive, electrochemical sensing of these analytes are growing rapidly, mainly because electrochemical techniques are fast, simple, possessing high accuracy and precision and cost effective. Cyclic voltammetry (CV) is the most common and earnest method to analyse the electrocatalytic behavior of a nanocomposite. With the purpose of developing electrochemical sensors with higher sensitivity and selectivity, fabrication of "*chemically modified electrode*" surfaces have been a major attention of research. Chemically modified electrodes improve mass transfer kinetics at low overpotential resulting decrease the interferences' effect and to avoid surface fouling. Different nanocomposites prepared by integration of either two or three from the list of carbon materials (carbon nanotubes, graphite, graphene *etc.*), metal or metal oxide nanoparticles, conducting polymers, organic dyes, ionic liquids etc. are being used for electrocatalytic sensing application and having new characteristics differed from original components [54, 55]. In electroanalytical sensor technology, amplification of a detection signal is required and electrocatalysis is one of the effective methods for it. The nanocomposite based electrocatalysts accelerate the kinetics of the reaction and allows the quantification of analytes at less extreme overpotentials, because nanocomposite based electrocatalyst catalyzed the reactions usually near the formal redox potential of the electrocatalyst and in this way, one can improve both detectability and selectivity of the sensor as compared to those obtained in the absence of the catalyst [56].

Literature reports a number of nanocomposite based electrocatalysis in electroanalytical sensors. Our group also reported several works representing the electrocatalysis with prepared nanocomposite modified electrode for the recognition of different analytes and further their quantification such as hydrogen peroxide (H_2O_2), ascorbic acid, *p*-phenylenediammine (a constituent of hair dye), organophosphate pesticide methyl parathion, metronidazole *etc*. [7–10, 51]. Due to the significance of H_2O_2 in

biological applications, the fabrication of sensitive electrochemical sensors attracts a special attention of researchers. Prussian blue (PB), hemeproteins, carbon nanotubes (CNTs) and metals nanoparticles have been utilized for the development of H_2O_2 sensors [57].

g-C_3N_4 nanosheets (also known as organic semiconductor), a polymeric graphitic carbon nitride, possess a mild band gap energy of 2.7 eV [58]. Nitrogen doped graphene increases electrochemically active part (*i.e.* edge plane-like sites) and g-C_3N_4 offers exciting catalytic activity [59], which has been attractive alternative for fabricating nonenzymatic electrochemical sensing of H_2O_2, NADH, nitrobenzene, [60] and glucose. However, g-C_3N_4 is very poor conductor for applying in electrochemical sensing, therefore, the combination of g-C_3N_4 with other materials (such as graphene [61], CPs [62]) provides it a greater conductivity and efficient electron transfer. [63, 64]. A nonenzymatic electrochemical approach for the detection of PSA was reported using NiCoBP-doped MWCNTs (NiCoBP–MWCNTs) nanocomposite. Here, an induced-electrodes plating technique was applied for the preparation of nanocomposite followed by conjugation with anti-PSA antibody. NiCoBP–MWCNT shows excellent oxidase-like ability to catalyze the glucose oxidation [65].

2.3 Nanocomposite Based Electrocatalysis in Synthetic Organic Electrochemistry

The electrochemistry has been known as the most efficient tool for providing spontaneous interaction between nuclei and electrons by applying direct electoral potential thereby adding or removing electrons. The most intuitive mean of interacting with molecules is electrostatic attraction between electrons and nuclei *i.e.* electrochemistry, which leads to addition or removal of electrons from such interactions through direct application of electrical potential. The electrochemical method generates different reactive species *viz.*, free radicals, anions, cations, radical anions and radical cations at ambient reaction conditions through electron-transfer reactions of organic molecule electrochemically. Moreover, reactive intermediates such as carbon-free radicals, carbanions and carbocations could be obtained by bond making and/or bond-breaking which open-up a new scope for their utilization in valuable organic transformations, particularly C–C bond forming reactions. This approach is nowadays better termed as *Synthetic Organic Electrochemistry* and receiving much attention of synthetic chemists from academics and industries as most powerful technique for developing "greener" synthetic routes for valuable organic transformations *via* reduction and oxidation at electrode. Furthermore, electron transfer leads to polarity reversal of functional groups known as umpolung, which provides a different way to access new reactions that would not possible by conventional synthesis. This is because, when an electron-rich nucleophilic character of a functional group is changed into electron-deficient electrophilic or vice versa, the serendipity occurs and unusual reaction sequence leads to new results [66].

In spite of these advantages, most of basic as well as advanced organic chemistry courses have not paid appropriate attention to discuss these electron-transfer reactions in synthetic organic electrochemistry. In this field, pioneer effort was made by Faraday in 1830s to run nonspontaneous organic reactions [67]. Then, Kolbe electrolysis was envisaged (1847) involving electrochemical anodic oxidation of CO_2H group to afford alkyl radicals [68]. A typical electrochemical setup consists of two electrodes; reacting (working) electrode and at another end (counter) electrode. Reacting electrode connected with a power source and is put in reaction mixture where reactant undergoes electron transfer for generating a reaction intermediate and to fringe the power circuit reaction electrode is connected to counter electrode at another end. Nature of reaction whether oxidation or reduction with substrate occurs either at anode or cathode and any one of these two could be working electrode and other be counter electrode. In the simple way, both the working as well as counter electrodes are placed in one pot as an undivided cell. However, the situation is different when high energy intermediates are generated and get reduced at cathode prematurely. This problem could be solved by separating both cathodic and anodic environments using permeable membranes or a salt-bridge [66].

In the end of 20th century considerable progress in synthetic electrochemistry has been witnessed by significant efforts made for developing new organic transformations. In 2008, Yoshida *et al*. demonstrated the application electro-auxiliaries for introducing Sulfur and Silicon-containing functional groups into substrates by lowering their electrochemical potentials and thus developed regio-/chemoselective reactions [69]. Later on, Little developed cathodic reduction as an efficient tool to perform cyclization reactions which would else demand metal catalyst as single electron reductants [70]. Schäfer, in 1981 [71] and Wright, in 2006 [72] studied the advancement in anodic and cathodic reactions both respectively. Schafer focused on cascade reactions based-on Kolbe classical approach by extending its scope. In 2000, Moeller surveyed anodic oxidations comprehensively for olefin coupling based-on radical cations polarity, which further opens-up a new direction to various in organic synthesis in next century [73]. Furthermore, Frontana-Uribe [74] and Yoshida [75] have addressed the environmental impact of electrochemistry as green and sustainable tool in chemical science. Furthermore, α-functionalization of alkyl amides was reported *via* Shono oxidation [76, 77] with an undivided cell. In addition to general organic transforming reactions, organic electrosynthesis extended its scope for constructing heterocyclic rings and thus it provides an alternative greener path as it eliminates the requirement of stoichiometric amount of catalyst/regents in conventional chemical synthesis [78].

Very recently, Phil S. Baran group has very effectively described the role of electrochemistry in modern organic synthesis. The synthetic organic electrochemistry covers almost all types organic transformations. However, mechanism involves (i) oxidation at anode (ii) reduction at cathode (iii) reduction-oxidation occurs in same pot, known as paired electrolysis [66]. At anode, different oxidation reactions have been performed and the best example is oxidation of carboxylates via Kolbe reaction. Moreover, oxidation of sulfinates into the corresponding sulfonyl radicals, Shono-oxidation of amides/amines or that of amides and amines *via* nitrenes

and nitrogen-radical is reported using electrochemical set-up. In addition, oxidation of alcohols, aldehydes, arene nucleus, phenols, olefins, enol ethers and ketene acetals, aliphatic C–H bonds and miscellaneous functional groups have been successfully reported so far. Furthermore, synthetic organic electrochemistry has also been exploited in electrochemical generation of oxocarbenium/thionium ions, α-oxidation of carbonyls, anodic benzylic functionalization, aromatic functionalization, oxidation of Meisenheimer complexes, fluorination, electrocatalytic cycloadditions of olefins, oxidation of electron-rich alkenes and that with anodically generated electrophiles, dehydrogenation, heteroarene synthesis and anodic oxidation in palladium catalysis [66].

Reduction at cathode is also well-cited in literature and a variety of cathodic reduction has been successfully achieved so far. For examples, reduction of aldehydes and ketones, esters and amides, C = C double bonds, alkyl, aryl, vinyl and alkenyl halides, and that of miscellaneous functional groups. Furthermore, formation of Ni and Co-catalysts in their low-valent state, reduction in palladium catalysis, carboxylation of olefins, alkynes, carbonyls and halogenated compounds at cathode are also demonstrated using electrochemical reaction. In an alternating way, both desirable half reactions may be performed simultaneously in paired electrolysis fashion by choreographed electrochemical process. Paired electrolysis could be effective in organic synthesis and ample number of works have been reported in the literature *viz* one-pot conversion of aryl aldoximes into aryl nitriles producing water as by-product [79].

Operation of electrocatalytic systems using nanocatalysts on electrode supports are recently drawn attention in electro-organic synthesis [80, 81]. Recently, electrooxidation of glycerol in basic medium is reported using porous nanocomposite, Pd_4Bi self-supported catalysts. Electrocatalytic activity using bimetallic Au–Ag nanocages and the role of Ag-oxidation was observed electrochemically [82]. Recently, reduced graphene oxide wrapped with Geobacter sulfur reductants has been synthesized and used as nano-electrocatalyst for mild evolution of oxygen in organic reaction [13]. In addition, Hofmann-type bimetallic organic based-nanoparticles are also used as nano-electrocatalyst mild evolution of oxygen [83]. Huang *et al*., in 2018, has recently disclosed H_2O_2-assisted municipal sludge-derived nanocatalyst-promoted degradation of phenol electrochemically [84]. Very recently, Li *et al*. [14] has investigated electrochemical nitrogen fixation reaction using γ-Fe_2O_3 nanomaterial as efficient electrochemical catalyst.

3 Future Prospects and Concluding Remarks

Though, literature has cited a good number of metal-based nanocomposites, development of state-of-the-art electrocatalysts using economical commercially available precursors is an essential step in the development of next-generation electrochemical energy storage devices/conversion systems/electroanalytical sensors/electro-organo synthesis. In this regard, nowadays, a number of nanocomposite is of particular

interest, which are based on CNTs, graphene, metal nanoparticles, due to their high electrical conductivity, large catalytic surface area, high speed electron mobility, and good mechanical strength etc.

Among differing types of composite materials, nanocomposite materials hold nice promise towards engineering economical electrocatalysts and have attracted increasing interest in each scientific communities and industrial associates around the world.

References

1. Liu L, Deng D, Sun W, Yang X, Yang S, He S (2018) Int J Electrochem Sci 13:10496
2. Begum H, Ahmed MS, Jeon S (2017) ACS Appl Mater Interfaces 9:39303
3. Ahmed MS, Choi B, Kim YB (2018) Sci Rep 8:2543
4. Shaijumon MM, Ramaprabhu S, Rajalakshmi N (2006) Appl Phys Lett 88:253105
5. Ahmadi TS, Wang ZL, Green TC, Henglein A, El-Sayed MA (1996) Science 272:1924
6. Hu C, Cheng H, Zhao Y, Hu Y, Liu Y, Dai L, Qu L (2012) Adv Mater 24:5493
7. Singh M, Bhardiya SR, Kashyap H, Verma F, Rai VK, Tiwari I (2016) RSc Adv 6:104868
8. Kashyap H, Singh PK, Verma F, Rai VK, Rai A, Singh M (2017) New J Chem 41:4937
9. Singh M, Sahu A, Mahata S, Shukla P, Rai A, Rai VK (2019) New J Chem. https://doi.org/10.1039/C9NJ00837C
10. Singh M, Kashyap H, Singh PK, Mahata S, Rai A, Rai VK (2019) Sens Actuat B: Chem (in press)
11. Wang Y, Li B, Cui D, Xiang X, Li W (2014) Biosens Bioelectron 51:349
12. Kausar A, Hussain A, Khan MY, Siddiuq M (2013) J Plastic Film Sheet 30:314
13. Kalathil S, Katuri KP, Alazmi AS, Pedireddy S, Kornienko N, Costa PMFJ, Saikaly PE (2019) Chem Mater. https://doi.org/10.1021/acs.chemmater.9b00394
14. Li Y, Kong Y, Hou Y, Yang B, Li Z, Lei L, Wen Z (2019) ACS Sustainable Chem Engg. https://doi.org/10.1021/acssuschemeng.9b00852
15. Luo C, Xie H, Wang Q, Luo G, Liu C (2015) Int J Nanomat 2015: 10. Article ID 560392
16. Aric'o AS, Srinivasan S, Antonucci V (2001) Fuel Cells 1: 133
17. Wagner FT, Lakshmanan B, Mathias MF, Phys J (2010) Chem Lett 1:2204
18. Deb MK (2012) Nature 486:43–51
19. Wee JH, Lee KY, Kim SH (2007) J Power Sources 165:667–677
20. Negro E, Latsuzbaia R, Dieci M, Boshuizen I, Koper GJ (2015) Appl Cat B: Environ 166:155
21. Debe MK, Schmoeckel AK, Vernstrom GD, Atanasoski R (2006) J Power Sources 161:1002
22. Matsumoto T, Komatsu T, Arai K et al (2004) Chem. Comm. 10(7):840–841
23. Sun X, Li R, Villers D, Dodelet JP, D´esilets S (2003) Chem Phy. Lett 379:99
24. Liu H, Song C, Zhang L, Zhang J, Wang H, Wilkinson DP (2006) J Power Sources 155:95
25. Tang JM, Jensen K, Waje M et al (2007) J Phys Chem C 111(48):17901
26. Luo C, Xie H, Wang Q, Luo G, Liu C (2015) J Nanomaterials 2015: 10. Article ID 560392
27. Mehdinia A, Ziaei E, Jabbari A (2014) Electrochim Acta 130:512
28. Deyab MA (2014) J Power Sources 268:50
29. Zhang W, Sherrell P, Minett AI, Razal JM, Chen J (2010) Energy Environ Sci 3:1286
30. Mink JE, Hussain MM (2013) ACS Nano 7:6921
31. Matsumoto T, Komatsu T, Nakano H et al (2004) Catal Today 90:277
32. Wang C, Waje M, Wang X, Tang JM, Haddon RC, Yan Y (2004) Nano Lett 4:345
33. Girishkumar G, Vinodgopal K, Kamat PV (2004) J Phys Chem B 108:19960
34. Aijaz A et al (2016) Angew Chem Int Ed 55:4087
35. Yeo BS, Bell AT (2011) J Am Chem Soc 133:5587
36. Huang Y, Zhang M, Liu P, Cheng F, Wang L (2016) Chinese. J Catal 37:1249

37. Nguyen TT et al (2016) Solid State Sci 53:71
38. Begum H, Ahmed MS, Jeon S (2017) RSC Adv 7:3554
39. Lu H, Huang Y, Yan J, Fan W, Liu T (2015) RSC Adv. 5:94615
40. Li X et al (2017) Green Energy & Environ 2:316
41. Begum H, Ahmed SM, Jeon S (2017) J Nanosci Nanotechnol 17:4961
42. Litkohi HR, Bahari A, Ojani R (2017) J Nanopart Res 19:278
43. Yang L, Tang Y, Yan D, Liu T, Liu C, Luo S, Appl ACS (2016) Mater Interfaces 8:169
44. Kumar A, Srirapu VKVP, Sharma CS, Singh RN (2015) Int J Innov Res Sci Eng Technol 4: 6289 (An ISO 3297: 2007 Certified Organization). https://doi.org/10.15680/ijirset.2015.0407137
45. Elzatahry AA, Abdullah AM, Salah El-Din TA, Al-Enizi AM, Maarouf AA, Galal A, Hassan HK, El-Ads EH, Theyab SS, Ghamdi AA (2012) Int J Electrochem Sci 7:3115
46. Gu L, Qian L, Lei Y, Wang Y, Li J, Yuan H, Xiao D (2014) J Power Sources 261:317
47. Saner B, Gürsel SA, Yürüm Y (2010) MRS Fall Meeting
48. Wang C, Li N, Wang Q, Tang Z, Wang et al (2016) Nanoscale Res Lett 11: 336
49. Peng Y, Chen S (2018) Green Energy Environ 3:335
50. Sambandam S, Valluri V, Chanmanee W, DE Tacconi NR, Wampler WA, Lin WY, Carlson TF, Ramani V, Rajeshwar K (2009) J Chem Sci 121:655
51. Sahu A, Shukla P, Mahata S, Rai VK, Rai A, Singh M (2019) Sensors and Actuat B: Chem 281:1045
52. Huang J, Wang D, Hou H, You T (2008) Adv Funct Mater 18:441
53. Kumar R, Bhuvana T, Sharma A (2017) RSC Adv 7:42146
54. Xiao F, Zhao F, Mei D, Mo Z, Zeng B (2009) Biosens Bioelectron 24:3481
55. Naveen MH, Gurudatt NG, Shim YB (2017) Appl Mater Today 9:419
56. Sherigara BS, Kutner W, DeSouza F (2003) Electroanalysis 15
57. Chen W, Cai S, Ren QQ, Wen W, Zhao YD (2012) Analyst 137:49
58. Mamba G, Mishra AK (2016) Appl Catal B 198:347
59. Tian J, Liu Q, Asiri AM, Qusti HA, Ai-Yuobi AO, Sun X (2013) Nanoscale 5:11604
60. Zhang Y, Bo X, Nasabimana A, Luhana C, Wang G, Wang H, Li M, Guo I (2014) Biosens Bioelectron 53:250
61. Gu H, Zhou T, Shi G (2015) Talanta 132:871
62. Xu Y, Lei W, Su J, Hu J, Yu X, Zhou T, Tang Y, Mandler D, Hao Q (2018) Electrochim Acta 259:994
63. Wongkaew N, Simsek M, Griesche C, Baeumner AJ (2019) Chem Rev 119: 120. acs.chemrev.8b00172
64. Ragupathy D, Gopalan AI, Lee KP (2010) Sens Actuators B 143:696
65. Tang J, Tang D (2015) Microchim Acta 182:2077
66. Yan M, Kawamata MY, Baran PS (2017) Chem Rev 117:13230
67. Faraday M (1834) Ann Phys Leipzig 47:438
68. Kolbe H (1847) J Prakt Chem 41:137
69. Matsubara Y, Matsuda T, Kato A, Yamaguchi Y, Yoshida Z (2000) Tetrahedron Lett 41:7901
70. Little RD, Fox DP, Van HL (1988) J Org Chem 53:2287
71. Schäfer HJ (1981) Angew Chem Int Ed Engl 20:911
72. Sperry JB, Wright DL (2006) Chem Soc Rev 35:605
73. Moeller KD (2000) Tetrahedron 56:9527
74. Frontana-Uribe BA, Zittle RD, Ibanez JG, Palma A, Vasquez-Medrano R (2010) Green Chem 12:2099
75. Yoshida JI, Kataoka K, Horcajada R, Nagaki A (2008) Chem Rev 108:2265
76. Shono T, Hamaguchi H, Matsumura Y (1975) J Am Chem Soc 97:4264
77. Shono T (1984) Tetrahedron 40:811
78. Jiang Y, Xu K, Zeng C (2018) Chem Rev 118:4485
79. Hartmer MF, Waldvogel SR (2015) Chem Comm 51:16346
80. Bentley CL, Kang M, Unwin PR (2019) J Am Chem Soc. https://doi.org/10.1021/jacs.8b09828
81. Zalineeva A, Serov A, Padilla M, Martinez U, Artyushkova K, Baranton S, Countanceau C, Atanassov PB (2014) J Am Chem Soc 140:9317

82. Nazemi M, El-Sayed MA (2019) J Phys Chem C. https://doi.org/10.1021/acs.jpcc.9b01107
83. Gao J, Cong J, Wu Y, Sun L, Yao J, Chen B (2018) ACS Appl Energy Mater 1:5144
84. Huang BC, Jiang J, Wang WK, Li WW, Zhang F, Jiang H, Yu HQ (2018) ACS Sustainable Chem Engg 6:5540

Polymer Electrocatalysis

M. Ramesh and M. Muthukrishnan

Abstract Electro-catalysis is a fast growing process from the basic research to real time industrial applications. This is possible because of the major improvements achieved in this during the recent decades. Polymers are finding applications in several fields of science and technology, such as metallization of dielectric process, manufacturing of batteries, polymeric coatings, electro-chromic polishing, electro-magnetic protection, etc. One of the most important characteristic of any polymeric material is their ability to catalyze some reactions. This property not only helped for a better understanding about the polymer but also proved predictive capabilities for good catalysts. In addition to the latest theoretical advancements that have helped to improvise electro-chemical catalysts, the progress in the usage of new experimental methods is closely associated to polymer electro-catalysis research. In this chapter a detailed discussion on electro-catalysis of polymers is presented.

Keywords Electro-catalysis · Polymers · Electro-catalysts · Photo-catalysis · Bio-catalysts

1 Introduction

Polymers comprise repeated structure of large molecules. In day-to-day life, plastics are generally used as insulators around electrical wires to protect it from short circuit. In the widely expanding field of electronics, organic electronics is one among the high demand study areas within the material science research that concerns with the design, synthesis, and characterization of organic molecules or polymers that demonstrates variable electrical conducting properties. Organic electronics when comparing to silicon based inorganic electronics offers flexible and low cost applications [1, 2]. Electro-active polymers (EAPs) or electrochemically active polymers are attractive properties of polymeric conductors which include electric conductivity, mechanical flexibility and thermal stability that depends on varying chemical and

M. Ramesh (✉) · M. Muthukrishnan
Department of Mechanical Engineering, KIT-Kalaignarkarunanidhi Institute of Technology, Coimbatore, Tamil Nadu 641402, India
e-mail: mramesh97@gmail.com

Inamuddin et al. (eds.), *Methods for Electrocatalysis*,
https://doi.org/10.1007/978-3-030-27161-9_5

physical properties in accordance with potential purpose in the field of energy storage, photo electro-chemistry, electro-catalysis, bio-electrochemistry, micro-system technologies electro-analysis, microwave screening sensors, electro-chromic displays, electronic devices, and corrosion protection [3]. Thus EAPs have the flexibility of changing its shape and size under the simulation of external electrical field.

Natta et al. [4] reported electrical conductivity of poly-acetylene on the order of 10^{-5} S/m of the poly-acetylene sample. But, the sample lost its conductivity on exposure to air. Similarly poly-sulphur nitride known as synthetic metal was developed with an improved conductivity of 0.24 K [5]. Copper colored poly-acetylene films was successfully developed with the room temperature conductivity of 1.7×10^{-9} S/m and silver colored poly-acetylene films with 4.4×10^{-9} S/m conductivity [6–8]. By exposing poly-acetylene pellets to the vapors of BF_3 and BCl_3 an increase in conductivity has been observed [9]. Similar attempts have been made to improve the conductivity of the polymers in twelve orders by exposing poly-acetylene film to different vapor medium of iodine, bromine, sodium, chlorine, etc. [10, 11]. Though these films give promising results in conductivity, they still remain unstable when exposed to air. Soon, attempts have been made to identify stable conductive polymers at ambient environments. Polymers as shown in Fig. 1 are categorized as conducting polymers (CPs) that have unique characteristics of improved opto-electronic and mechanical properties. CPs are widely used in applications involving electrochemical devices owing to its simple processing procedure and better redox activity [12, 13].

A catalyst is a material that increases the rate of a chemical reaction. Thus, a catalyst works as agent in increasing the speed of the desired action. Catalysts are generally classified into five types; (i) bio-catalysts, (ii) homogeneous catalysts,

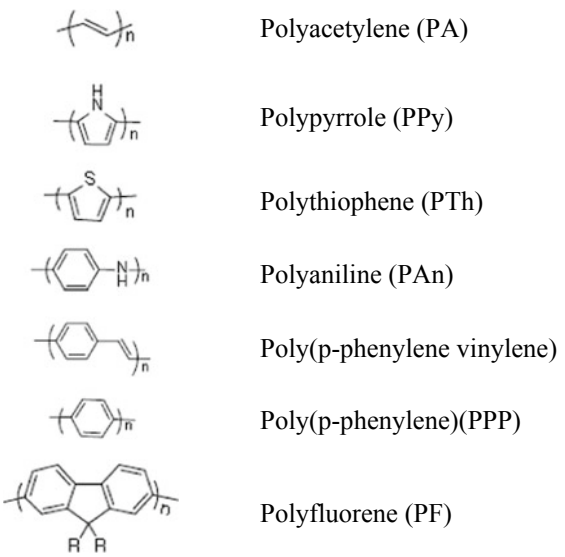

Fig. 1 Structures of conductive polymers [14]

(iii) electro-catalysts, (iv) heterogeneous catalysts, and (v) auto-catalysis. Bio-catalysts require ambient temperature and pressure in aqueous medium for ideal reaction. Examples are enzymes and H_2O oxidation in photosynthesis. Homogeneous catalysts are in the same phase as the reactants. Electro-catalysts are special catalysts that participate in the electrochemical reactions by acting as electrodes. An electro-catalyst can be of surface coating, nanoparticles, homogeneous. Hetero-catalysts comprises different phases of catalysts and the reactants. In autocatalysis, catalytic chemical reaction is initiated by one of the products of reactants.

2 Polymer Electro-Catalysis

Polymer electro-catalysis is defined as the ability of the polymeric substances as catalyst electrode surfaces to accelerate the given electrochemical process. Thus polymers will act as a catalyst in the electrochemical reactions. The electro-catalysts form a transitional chemical reaction and aides in transferring of electrons between electrode and reactants. A typical polymer electrochemical system comprises three layers such as first order conductor, second order conductor and catalyst. Generally metals are used as first order conductor and electrolyte solution as second order conductor. An electrochemical conducting polymer acts as a catalyst by attaching to the metal surface by adhesion. For example, polymers like polyaniline and polypyrrole are used as catalysts for the first order metal conductors like Pt, Pb, Au and bimetallics like Pt/Sn and Pt/Pd. Also recent research interests in nano-metal particles in technologically relevant applications demand enhanced conductive polymers for effective use of the metals as devices [15–17]. Electro-catalysis can be of different forms like photo-catalysis, solution phase electro-catalysis and surface electro-catalysis. Similarly, electro-catalysts are classified into three forms viz., metallic, metal complexes and metal free.

2.1 Photo-Catalysts

Photo-catalyst is defined as increasing the rate of photoreaction in the presence of catalyst. Thus, an increase in chemical reaction takes place by irradiation. A photo-catalyst breaks down the organic matter and creates electron holes pairs and strong oxidation agent which generate free radicals which further initiates secondary reactions. Thus, a photo-catalyst does not degrade or consumed during the process of photoreaction. Organic polymers owing to its light weight, easy process-ability is widely used for photo-catalytic applications [18] (Fig. 2).

For polymers as photo-catalyst, there are certain inherent properties that are to be considered. They are stability of the polymer materials, high absorption in the visible range, variable optical band gaps and longer excited states. The polymerization of the photo-catalysts can be enhanced by modifying the ratios of the polymer building

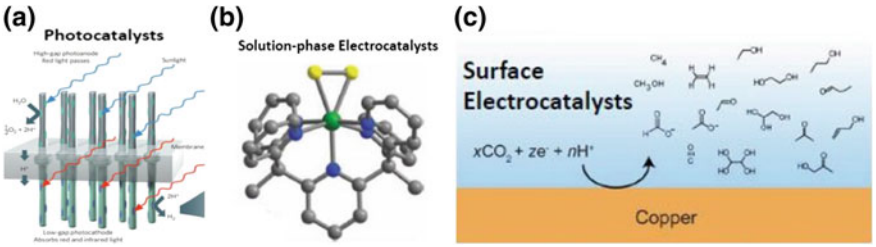

Fig. 2 **a** Photo-catalyst, **b** solution phase electro-catalyst and **c** surface electro-catalysts [19, 20]

blocks during polymerization. Redox polymers are electron conducting polymers that can be oxidized and reduced with electron transfer or electron hopping between localized redox groups takes place due to the presence of electrostatically and spatially local redox sites. Redox polymer will not work in dry state and instead water or any other solvent is required as plasticizer.

2.1.1 Mechanism of Photo-Catalytic Water Splitting

Water splitting involves two redox half reactions.

$$2H^+ + (aq)2e^- = H_2(g) \tag{1}$$

$$O_2(g) + 4\,H^+ + 4e^- = 2H_2O \tag{2}$$

The potential polymers for water splitting are identified in terms of potentials [21]. (a) Polymer's ionization potential (IP), (b) Polymer's electron affinity (EA), (c) Exciton can in analogy is represented as EA* and IP* where P is neutral polymer, P^* is the localized exciton polymer. For effective photo-catalyst water splitting, the net potential of the polymer as given by the driving force of oxidative part (IP/EA*) and reductive part (EA/IP*) should be maintained positive by straddling the IP/EA* and EA/IP* half reaction potentials as shown in Fig. 3.

The role of polymers in water splitting also depends on (i) rate of photon absorption affects exciton generation, (ii) exciton loss as a result of de-excitation, (iii) association and dissociation rate of exciton, (iv) electron and hole transfer rate towards adsorbed catalysts, (v) surface wettability, (vi) rate of water adsorption on photo-catalyst and (vii) kinetics of elementary reaction steps.

2.1.2 Application of TiO_2 as Potential Photo-Catalyst

The practical application of photo-catalysis is successfully provided by Akira et al. [23] by improvising water electrolysis using TiO_2 and platinum electrodes which

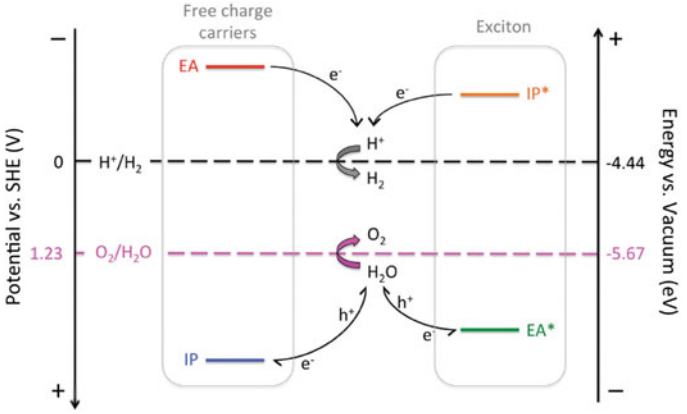

Fig. 3 Illustration of half reaction potentials of photo-catalyst in water splitting [22]

paves way for the clean and cost effective fuel source, hydrogen. TiO_2 among similar semiconductors like ZNO, Fe_2O_3, CdS and ZNS is widely used for photo-catalysis of water splitting owing to its low processing cost, chemical stability and better photoconductivity activity [24, 25]. In the above photo catalysis reaction, TiO_2 electrodes are used as cathode and platinum electrodes are used as anode. When TiO_2 absorbs ultra violet (UV) rays, electrons from anode transfer to cathode which results in the production of hydrogen at the cathode site. Further advancement of electro-chemical photo-catalysis activity takes place with the metal like gold and platinum without external potential [26]. Additional research activities enable the hydrogen to be produced from illumination of TiO_2 and PtO_2 in ethanol [27]. Polymers like polystyrene (PS), polyethylene (PE), polyamide (PA), poly (methyl methacrylate) (PMMA), poly (ethylene terephthalate) (PET) are coated with TiO_2 for high transmittance in the UV-A region which is a highly effective process for photo-catalytic treatment of water and air [28, 29]. Some polymers like polypropylene, PMMA and polycarbonate are used as insulators in transparent insulation materials (TIMs) which are a small honey combed structure used in the development of facades [30].

TIMs are widely used in structural applications for its opaque insulation and solar collection ability [31]. However, the issues in developing stable, UV transparent photo-catalytic active polymer materials are due to its imminent thermal and photo-degeneration. The major hurdle in the research of photo-catalytic process is the shorter lives of photo-generated electrons and redox hole sites which highly affects the quantum yields [32]. Also, to restrict the recombination of photo electron pair and redox holes sites, several methods are attempted by the researchers like (i) cation doping by Cr^{3+}, Fe^{3+}, Mn^{2+}, V^{5+}, etc., (ii) modifying the structure on photo-catalytic surface by metal particles (Pt, Ag, etc.), or (iii) metaloxides (NiO, ZnO, etc.), (iv) sacrificial agent addition (methanol, triethylamine (TEA), ethylene diamine tetraacetic acid, ethanol etc.) [33–36]. Sacrificial agents are compounds that sacrifice their molecules by donating their electron pairs and allow their hole sites to

scavenging by other molecules thus reducing the photo electron and hole recombination [37]. (v) Bias potential application where the electron hole pair is driven by an external electric field in the opposite direction [38].

(i) **Cation doping**

The studies on the effects of Cu^{2+}, Fe^{3+}, Zn^{2+}, Al^{3+} and Cd^{2+} on dyes resulted in improved redox potential and depressed photo-degradation [39]. In photo-catalytic studies of the titania, the doping of metals ions such as Cr^{3+} and Mo^{5+} affects the band gap shift and increased life time of electron-hole pair [40]. Similarly reaction rate of photo-catalytic bleaching of erythrosine-B, eosin Y and congo-red is found to be increased with doping of metal ions like Ni^{2+}, Fe^{2+}, Cu^{2+}, Ag^{+}, V^{2+}, Co^{2+} and Mn^{2+} ions [41]. Similarly enhanced photo-catalytic activity is reported by Vaya et al. when ZnS is dopped with transition metal ions [42].

(ii) **Modifying the structure of photo-catalyst by metal deposition (nanoparticles, nanorods)**

Titanium oxide is a formidable photo-catalytic material that demonstrates improved efficiency with formic acid and oxalic acid. On the other hand, it has lower active specific surface area owing to Titania's wider band gap energy. Thus, for higher photo-catalysis, combination of metallic and nonmetallic elements in the form of nanoparticle and nanorods are added. Noble metals like gold, platinum and silver are highly favorable photo-catalytic elements added to TiO_2 owing to its favorable catalytic characteristics [43–47]. Also, Ag nanoparticle is found to be highly effective in trapping electron and in preventing the recombination of electron hole pair. Platinum dopped with titania improves photo oxidation rate of ethanol, acetaldehyde and acetone in the vapourous phase [48]. Li et al. [49] has prepared a mesoporous photo-catalyst titania (Au/TiO_2) by embedding gold nanoparticles with $AuCl_3$ and ethanol.

(iii) **Modifying the structure of photo-catalyst by metal oxides**

Transitional metal oxides form stable compounds and are widely used in water splitting owing to its high electro-negativity of oxygen atoms. Transitional metals like Fe, Mn, Co and Ni encase involves d orbitals groups little band holes and solid d-d changes however need effective charge transporter because of little polar on conductivity related with high resistivity [50]. It is overcome by developing multicomponent metal oxides like metal sulphides and metals nitrides. Also, the band gap is further tuned for better catalytic performance by doping with cations such as Ag^{+}, V^{5+}, and W^{6+} and by other ternary metal oxides like $CuWO_4$, $ZnFe_2O_4$, $CaFe_2O_4$, $CuBi_2O_4$, and $CuNb_3O_8$, etc. [51–58]. Various metal oxides with different band structure with respect to their redox potentials are given in Fig. 4.

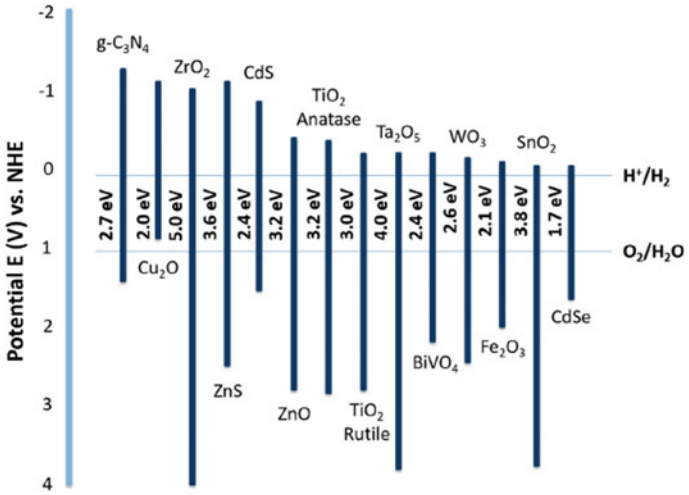

Fig. 4 Metal oxides band structure with respect to redox potentials [59]

2.2 Sacrificial Reagents

Sacrificial reagents (SRs) are electron donors that improve hydrogen production during water splitting. SRs prevent photo electrons and holes to recombine during photo-catalysis reaction of water splitting [59]. Some of the common SRs are Na_2S–Na_2SO_3, methanol, tri-ethanolamine, lactic acid, acetic acid, oxalic acid, methylamines, ethylene glycol, etc. The significant role of SRs in the hydrogen production was demonstrated by Hong et al. [60] in his investigations with photo-catalyst C_3N_4 and NiS co-catalyst in lactic, oxalic, tri-ethanolamine and ascorbic acid solutions. The results indicated that H_2 production was significant with tri-ethanolamine solution whereas other three SRs do not produce significant results in water splitting. Similarly, Wang et al. [61] attempts on the effects of different SRs in H_2 production over C_3N_4, $Zn_{0.5}Cd_{0.5}S$ and TiO_2 as photo-catalyst is given in Figs. 5, 6 and 7 respectively.

The capacity of the electron donors to supply electrons is established by the oxidation potential. Lower oxidation potential means SRs can be oxidized easily and the holes can be trapped. The results indicated that for sustained H_2 photocatalytic evolution rate, low oxidation potential and higher permittivity are identified as suitable parameters.

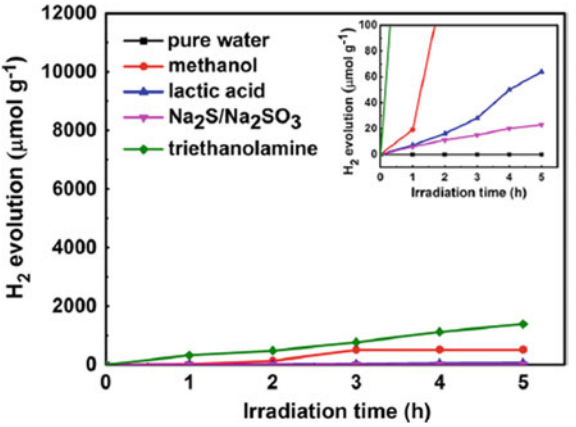

Fig. 5 Comparison of different SRs used in H_2 production over C_3N_4 photo-catalyst

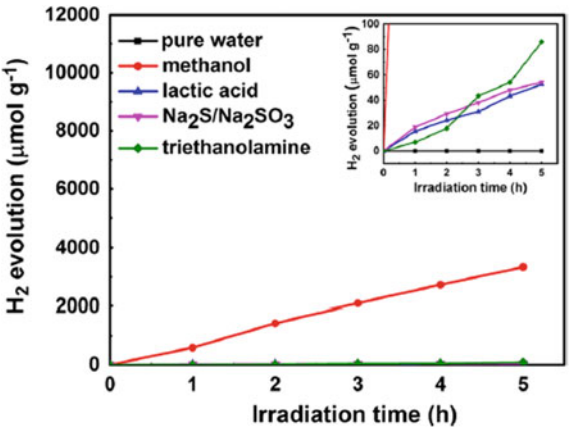

Fig. 6 Comparison of different SRs used in H_2 production over $Zn_{0.5}Cd_{0.5}$ S photo-catalyst

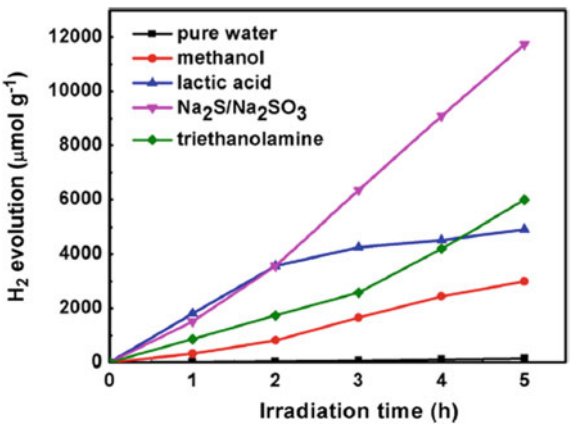

Fig. 7 Comparison of different SRs used in H_2 production over TiO_2 photo-catalyst

Fig. 8 PEC cell

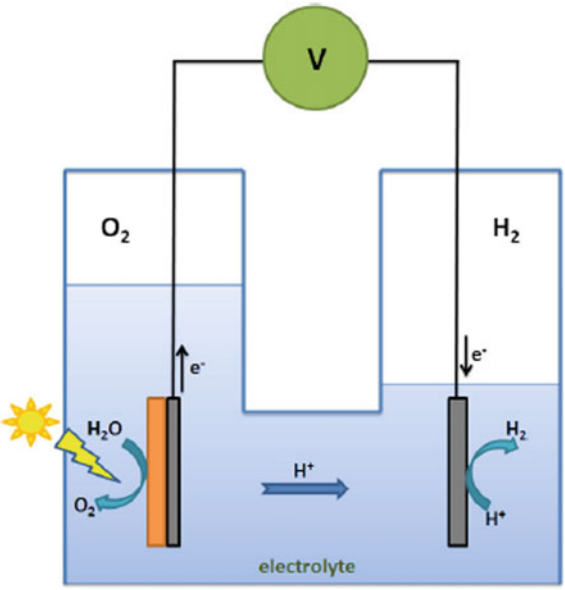

2.3 *Application of External Bias Voltage*

External bias voltage is used in photo electro-chemical cell to transfer photoelectrons to the cathode and to prevent photoelectron hole recombination. In a photo-electro-chemical (PEC) cell, water splitting is aided by the photo-catalyst that is deposited in the form of thin substrate acts as photo electrode. The PEC cell, as shown in the schematic diagram in Fig. 8 achieve its required internal bias potential by changing the photo anode combination of different materials of photo-catalyst [62]. The standard open circuit potential for water splitting is 1.23 V. Also, in case of any further reduction in the water splitting potential lesser than 1.23 V, external bias may be applied linking electrodes for additional increase of the reduction potential energy which improve the evolution rate of H_2. Wrighton et al. [63] demonstrated the increase in the yield of hydrogen by adding an external bias in a $SrTiO_3$ electrode in a PEC cell.

2.4 *Solution Phase Electro-Catalysis*

Electro-chemical method is widely used method in developing polymer films by oxidative coupling of polymers with functional groups. Based on the application of polymers in the electrochemical system, it is classified into two groups: (i) ion exchange polymers and (ii) electron conducting polymers. Ion exchanging polymers

do conduct electrons and have found its place prominently in electro-catalytic applications where polymer films with ionic conductions are applied onto the conductive supports that are functionalised by redox groups. Thus polymer films are attached to the cathode electrode by chemical bonding and adsorption interaction where the solubility of the polymer is the important factor. The conducting polymers are identified by conjugated bonds between electro-active groups in the polymer chains, acts as catalysts in accelerating the polymer films and cathode electrode process.

Electro-catalysts are also used as stabilizers for heterogeneous catalysts i.e., porous solid matrices [64]. The stabilizers that support the electro-catalysis are of the form monolayers, polymers, dentrimers, and functional organics polymers [65–70]. The solution phase electro-catalysis offers advantages over photo-catalytic process is that (i) more reactions are able to optimized in the solution phase with the availability of all reactive group of solid materials, (ii) reactions in heterogeneous solutions are often takes lesser steps and shorter time, and (iii) selective interaction between adsorbent and molecules is possible. Also, many chemical transformations are possible with solution phase electro-catalysis like hydrogenation, oxidation, and epoxidation reactions. Kaurunadasa et al. [20] demonstrated the use of low cost molybdenum disulfide (MoS_2), an industrial catalyst, in generating hydrogen from solution phase environment of petapyridyl ligand upon electro-chemical reaction.

Ito et al. [71] has successful in developing this film of acetylene that is called as Shirakawa's poly-acetylene by adding $Ti(OBu)_4/AlEt_3$ catalyst. Similarly, $NaBH_4/CO(NO_3)_{2.6}H_2O$ also known as Luttinger catalysts developed by Luttinger [72] for acetylene polymerization. Sener et al. [73] using co-polymerization method reported improvement in the sensing properties of conducting polymers in detecting glucose. In this method, 3,4-ethylenedioxythiophene is copolymerized with 4-amino-N-benzamide to supply an amperometric glucose sensor that is based on glucose oxidase. Metal nanoparticles conducting polymer matrix can be developed by the facile oxidation in the presence of metal salts with the monomers like aniline, pyrrole, and thiophene [74–77]. For illustration, 3,4-ethylenedioxythiophene (EDOT), a thiophene monomer is of recent interests owing to its role as heterogeneous catalysts for hydrogenation reactions in the metal-CP composites [78, 79]. Similarly, nanoparticles synthesized by solution phase achieves fine grain size and shape control by use of surfactant. Triblock polymers such as polyethylene oxide (PEO) and polypropylene oxide (PPO) are effectively used in the synthesis of nanoparticles owing to their availability and bio-compatibility [80–84]. Wang et al. [85] synthesized $Ir_xSn_1xO_2$ electro-catalysts by using TBP Pluronics F127 (PEO100-PPO65-PEO100) as stabilizer. TBP Pluronics F127 is soft-template and weak reductant and has significant control over $IrxSn1xO_2$ preparation. In methanol electro oxidation, the usage of different conjugated polymers and various metal combinations is widely reported [86–91]. Kost et al. [89] developed cathode electrode catalysts for effective hydrogen reduction and methanol electro oxidation wherein the Pt nanoparticles are dispersed in conducting polymers.

2.5 Surface Electro-Catalysis

In recent years, application and use of metal nanoparticles have gained importance owing to its role in the relevant technological applications like enhancing the properties of electro-catalysts [15, 16, 92]. These nanoparticles are brought into practical applications by embedding or depositing those nanoparticles on the polymers [93, 94]. For instance, liquid fuel cells make use of methanol through electro-catalytic oxidation of methanol on metal surface [95]. Poisoning effect due to the displacement of highly scattered single metals [96–102], bimetals [103, 104], multi-metals [105–107] and the synergistic effects of CPs and the metals is one of the main causes of the decrease in the catalytic activity in the cathode electrodes [108, 109].

Polymer metal composites are prepared either by addition of metal particles into polymer film during electro-polymerization or by electro-deposition of catalyst particles on the polymer films using metallic salt solution. The second method is advantageous over the first method in yielding more metal particles to access to species in solution by three types of modes like constant potential also known as controlled-potential electrolysis or potentiostatic coulometry, double potential step chronoamperometry (DPSCA) and cyclic potential or cyclic voltammetry mode. Kelaidopoulou et al. [105] by using constant potential method found the homogeneously dispersed Pt particles settle down above the polymer matrix. The cyclic potential method improves the metal particle dispersion by activating the deposited metal particle periodically [15, 17]. In double potential step method, improved penetration complex into the conducting polymer film facilitates better catalyst distribution. For example Pt deposited in an electrode by electrochemical method may have 2D or 3D crystallographic orientation of the metals deposited.

The catalytic related performances of metal polymer matrix are assessed by some of the metrics like surface-specific activity, mass activity, and electro-chemically active surface area that are frequently used among the researchers. Oxygen reduction reaction (ORR) is one of the fundamental reaction techniques used in the research of renewable energy. For example, proton electrolyte membrane fuel cells (PEMFCs) are widely used where the ORR is taking place at the cathode. Owing to the slow kinetics of ORR, the performance of fuel cells is affected [110–113]. Platinum, owing to its balanced ORR activity and high stability in the acidic medium, it is highly preferred metal in PEMFCs. Thus, to improve the ORR activity of the PEMFCs, efforts are taken to have more active catalytic surface centres. Surface modification is an important aspect of removing one type of site without changing the electric structure of the rest of the surface [114].

The electro-catalytic reactions between the metal electrode and the electrolyte play a key role in optimizing fuel cell performance. Thus, the interfacial electrochemistry involves the study of metal electrode and electrolyte that depends upon the certain characteristics like surface structure that involves species of the solution and the electrode surface, surface reactivity, kinetics and various other mechanisms involved in and around the electrochemical interface [115, 116]. Another significant

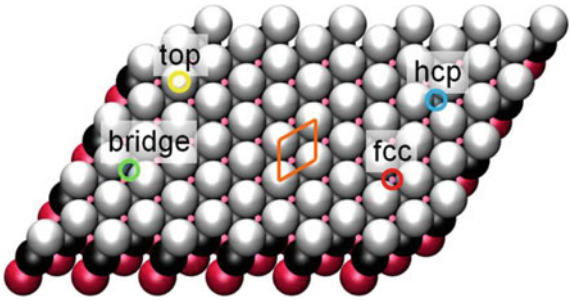

Fig. 9 Ball models of different adsorption on active sites [118]

factor in the electro-science is the investigation of adsorption between the reactants and intermediates and the particular adsorption destinations of the terminal are the unmistakable spot for adsorption to occur. Adsorption of inter-metallic and inter-mediates like catalysts at surface occurs at all electro-catalytic reactions [117]. Adsorption may occur in the following ways as shown in Fig. 9 (a) when the bonding takes place between the single electrode surface atom and molecule it is called as on top, (b) when the molecular adsorption takes place in between two adjacent metal atoms it is called as bridge and (c) threefold hollow represents molecular bonding of three surface atoms.

The three fold hollow is again diverged into FCC and HCP. At the point when the three overlap empty layer corresponds with the opening in the layer underneath it is called as FCC-hollow and instead of hole if its coincides with an atom underneath, it is called as HCP-hollow. Thus, the improvement of the electrochemical reactions can be achieved by chemical modification of the electrode's active surfaces by adsorption of reaction intermediates, breaking and forming of bonds. These active sites depend upon the geometric arrangement that induce chemisorption bonds and affects the properties of the catalyst in the form of (i) electronic effects and (ii) geometric atomic ensemble effects.

2.5.1 Electronic Effects

The electronic properties of the electrode ascertain the electronic structure constituents of the electrode like (i) surface potential of zero charge density (E_{pzc}) and (ii) local density of states (LDOS) [119]. E_{pzc} is a significant property in determining the electronic properties of the electrode. Electrode potential is linearly associated with the minimum energy required to transfer an electron outside electrode surface from the Fermi level within the electrode [120]. On the other hand, within an energy band, the distribution of the electronic levels is described by the LDOS. All potential electro-catalysts possess d-band centers near the Fermi level which determines the d-electrons at the surface's ability to readily interact with the polymer absorbate [121]. Figure 10 describes the local density states of the d-band and sp-band at platinum surface with regard to the Fermi level. Platinum exhibits good catalytic properties

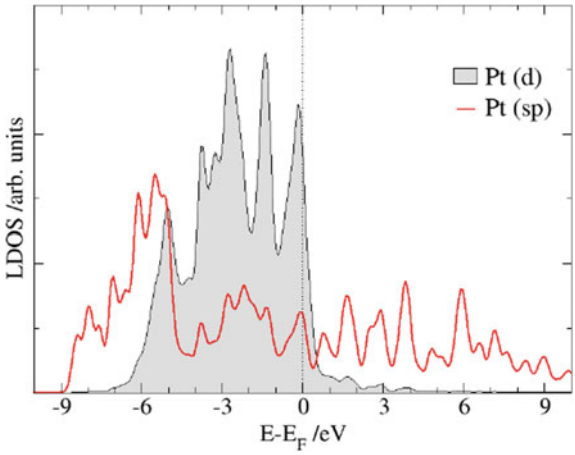

Fig. 10 LDOS of d-band and sp-band of platinum surface

by possessing its surface d-band centers in close proximity to Fermi level, where electron transfer takes place for the ORR.

2.5.2 Geometric Atomic Ensemble Effects

Atomic ensemble effects play an important role in electrocatalysis, where a small group of atoms in the geometric configuration act as an active site for reactant adsorption. For understanding, the electro-catalytic reaction mechanisms and for designing efficient electro-catalysts, the study of this smallest group of atoms is very important. Cuesta [115] studied the atomic ensemble effects in the oxidation of formic acid and methanol on modified single crystal platinum electrodes. Generally, increased catalytic action is attributed to the combined effects of electronic effects and atomic ensemble effects. Site knockout strategy is one-way of surface modification where a specific adsorption surface site in the geometric configuration is removed without modifying the electronic structure of the remaining configuration. The specific determination of the group of smallest atoms is necessary to identify the rate determining transition rate in an electro-chemical reaction [122].

3 Fuel Cells

Fuel cell is an electro-chemical device that generates current by converting chemical energy to electrical energy. An electro-chemical cell comprises three constituents such as fuel, oxidizing agent and electrolyte. Thus current is generated by a pair of redox reactions through the oxidation of fuel in the presence of catalysts [123]. Generally, fuels represent hydrogen, formic acid, alkali, methanol, ethanol, etc. Fuel cell consists of two electrodes, an anode where oxidation of fuel takes place and a cathode

where reduction of oxidant takes place. Both anode and cathode are connected by external circuit and are separated by electrolyte. The electrolyte is typically made of polymer, immobilized alkali or acid, ceramic, etc. In general, fuel cells have reported higher efficiency than that of the internal combustion engines that follows thermal cycle and the energy produced is virtually pollution free energy.

3.1 Classification of Fuel Cells

Fuel cells are classified based on operating temperature into two groups [124]: (i) low-temperature fuel cells, where the operation temperature is below 250 °C. Owing to its faster start-up times, low-temp fuel cells widely popular among portable applications in the area of propulsion systems. (ii) In high-temperature fuel cells, the operation temperatures are above 600 °C. Since the electro-catalysis do not have a significant role at high temperatures, several fuel types are used in high-temperature fuel cells. Based on the electrolyte utilized in the fuel cell (Fig. 11), it is classified into

(i) Polymer electrolyte membrane fuel cell (PEMFC)
(ii) Direct methanol fuel cell (DMFC)
(iii) Alkaline fuel cell (AFC)

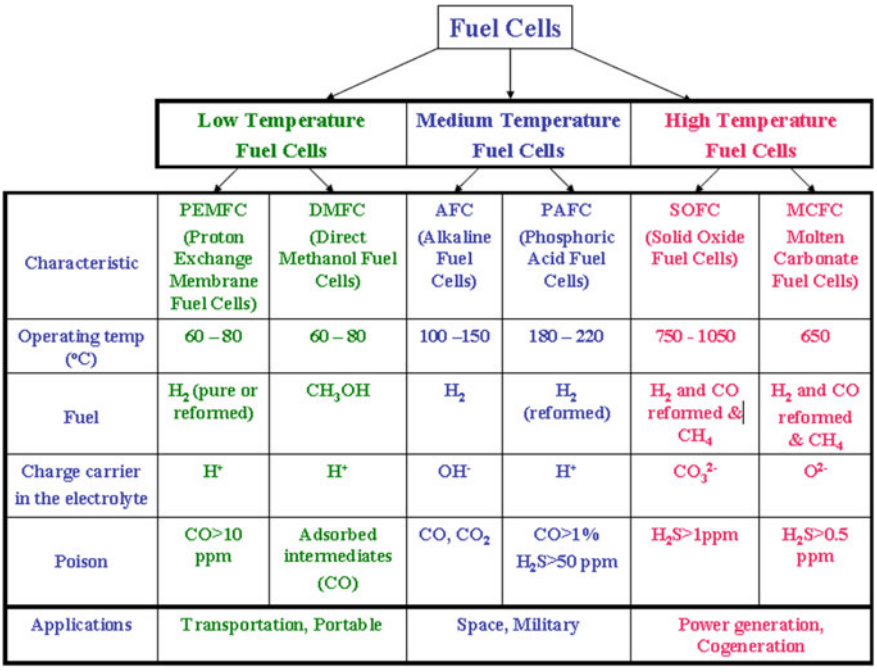

Fig. 11 Classification of fuel cells based on electrolyte utilized [125]

(iv) Phosphoric acid fuel cells (PAFCs)
(v) Solid oxide fuel cell (SOFC)
(vi) Molten carbonate fuel cells (MCFC).

3.1.1 Polymer Electrolyte Membrane Fuel Cell (PEMFC)

It is also commonly known as proton electrolyte fuel cells. Polymer electrolyte membrane (PEM) uses solid polymeric membrane as electrolyte and porous carbon electrodes containing platinum or platinum alloy as catalysts. The fuel cell typically feeds on pure hydrogen supply source like storage tanks, oxygen from air and ample supply of water to operate. Here, the protons from hydrogen source. Thus electrical energy is produced through chemical energy liberated in the form of protons and electrons during electrochemical reaction between hydrogen and oxygen.

PEM fuel cells (Fig. 12) encompass membrane electrode assemblies (MEA) system that comprises electrodes, catalysts, and electrolyte and gas diffuser. The electrolyte is a specially treated material that allows proton exchange and blocks electron. For optimum performance of the electro-chemical reaction, electro-catalysts play a vital role by positioning them on either side of the electrolyte. A catalyst is made of special materials like platinum nanoparticles coated with carbon paper or cloth. The catalyst has rough surface that facilitates maximum area to be exposed to the reaction between hydrogen and oxygen. Triple phase boundary (TPB) is the important part of the cell where the reactions between the constituents like electrolyte, catalyst and reactants mix at the operating temperature of around 100 °C. Hydrogen as a fuel is supplied to the anode side where in the presence of electro-catalyst; it divides into protons and electrons. This oxidation half-cell reaction is represented by:

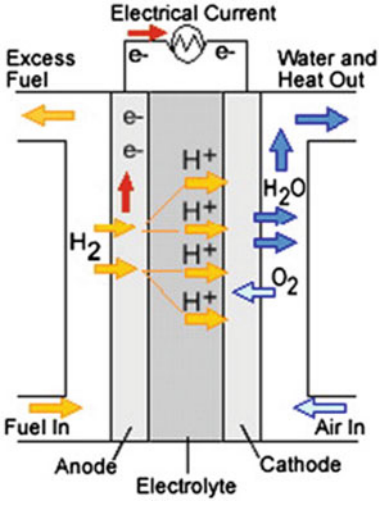

Fig. 12 Polymer electrolyte fuel cell [126]

$$H_2 \rightarrow 2H^+ + 2e^-$$

The protons that are formed through half reaction oxidation are permitted through the polymer membrane. Electrons are supplied though external circuit. A stream of oxygen supplied at the cathode side reacts with protons and electrons forming water molecules and current. The half reaction is given by:

$$\frac{1}{2}O_2 + 2H^+ + 2e^- \rightarrow H_2O$$

PEMFC are the perfect candidates for power source in cars, buildings and other smaller applications. They offer considerable density of power, light weight and quick start. The disadvantage is that it requires costly noble metal catalyst like platinum for the hydrogen electro-chemical reactions. The platinum catalyst is not resistant and is sensitive to CO poisoning. Thus, an additional reactor is necessary to be employed for reduction of CO poisoning.

3.1.2 Alkaline Fuel Cells (AFC)

AFC are medium temperature (100–150 °C) fuel cells that make use of aqueous potassium hydroxide as electrolyte, non-precious metals as catalyst and utilize an alkaline membrane. AFC's utilize hydrogen and oxygen and generate heat, water and electricity. Some of the fuels that are compatible to use as fuel in AFC are methanol, ethanol, propanol, ethylene glycol, and sodium borohydride. AFC's efficiency is around 70% and was used in the famous NASA's space shuttle Apollo in 1960. A Nafion-based alkaline polymer electrolyte fuel cell was developed where the catalyzed Ni-Cr serves as anode side and Ag as cathode side. The principle is similar to other AFC's where OH^- ions are produced by ORR. These ions produce H_2O transfer to the anode and reacts with H_2O which results in the production of electrical energy to the external circuit [127] (Figs. 13 and 14).

The challenges faced by the AFC's are CO_2 poisoning where the performance of hydrogen and oxygen are highly affected by the presence of CO_2. Thus constant purification of hydrogen and oxygen is necessary and it increases the cost. Also the electrolytes are facing issues with wettability, increased corrosion, etc. Alkaline membrane fuel cells (AMFCs) also known as alkaline anion exchange membrane fuel cell (AAEMFC) or anion-exchange membrane fuel cells (AEMFCs) are developed to address the issues faced in AFC, where the liquid electrolyte has lower susceptibility to CO_2 poisoning [130]. Instead of standard KOH used in AFC, a solid polymer electrolyte membrane is used to transport hydroxide OH^- ions. The major challenge of AMFC is the fabricate anion exchange polymer membrane with good OH^- ion conductivity. Qiao et al. [131] produce three types of polymer membranes using polyvinyl alcohol (PVA) base matrix and developed PVA-KOH (Potassium hydroxide), PVA_PAADDA_GA (poly(acrylamide-co-diallyl dimethyl ammonium chloride)) [132] and PVA/PDDA-OH (poly(diallyl dimethyl ammonium chloride))

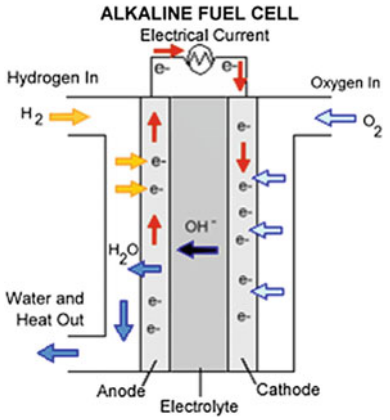

Fig. 13 Alkaline fuel cell [128]

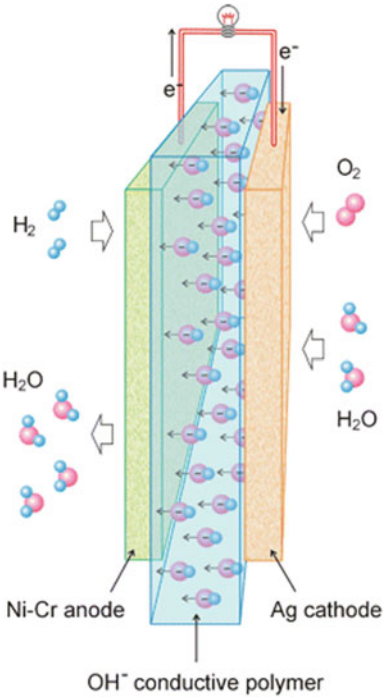

Fig. 14 Alkaline polymer electrolyte fuel cell [129]

[133]. These membranes are found to exhibit good thermal stability and ionic conductivity. Another polymer material, poly(arylene ether)s satisfies the requirements of AAEMs with their excellent properties of stability and water resistant [134]. Tanaka et al. [135] synthesized polymer membrane of arylene ether by block copolycondensation of fluorene containing hydrophilic oligomers and linear hydropho

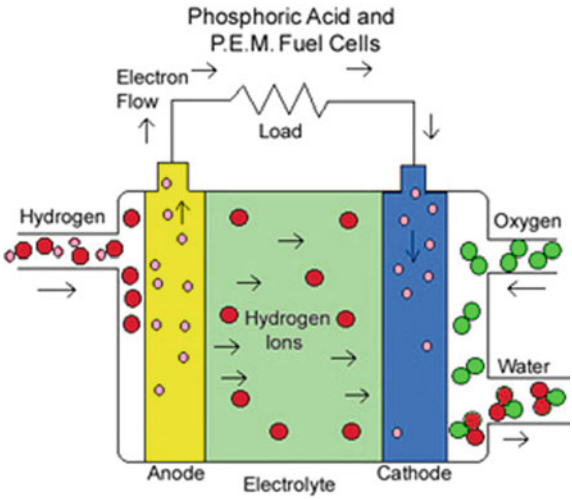

Fig. 15 Phosphoric acid fuel cells [139]

bicoligomers, chloromethylation, quaternization, and ion-exchange reactions. Similarly poly(2,6-dimethyl-1,4-phenyleneoxide) (PPO) [136], poly (tetrafluoroethylene) (PTFE) [137], poly(arylene ether sulfone) [138] are polymers used for their excellent mechanical properties, thermal stability, minimal water absorption, no toxicity, low flammability and electrical properties.

3.1.3 Phosphoric Acid Fuel Cells (PAFCs)

PAFCs (Fig. 15) operates between 170 and 200 °C uses phosphoric acid (H_3PO_4) as electrolyte in highly concentrated form where it is contained in Teflon bonded silicon carbon matrix to protect the other internal parts from corrosion. PAFC uses porous carbon electrodes coated with platinum catalyst. PAFCs are more CO_2 tolerant of 1% at 200 °C and as a result wide range of fuels like natural gas; petroleum products, coal liquids, etc. are used. PAFCs are suitable for distributed power generation with its efficiency of 85%.

3.1.4 Molten Carbonate Fuel Cells (MCFCs)

MCFSs are high temperature fuel cell that operates at 650 °C. Molten carbonate salt mixture (62% Li_2CO_3 and 38% K_2CO_3) contained in lithium aluminate ($LiAlO_2$) is used as electrolyte because of its corrosive nature [140]. Instead of costly platinum, non-precious metals like nickel is favoured as catalyst at anode and cathode. MCFCs are not susceptible to CO_2 poisoning. The schematic representation of MCFC unit is given in Fig. 16.

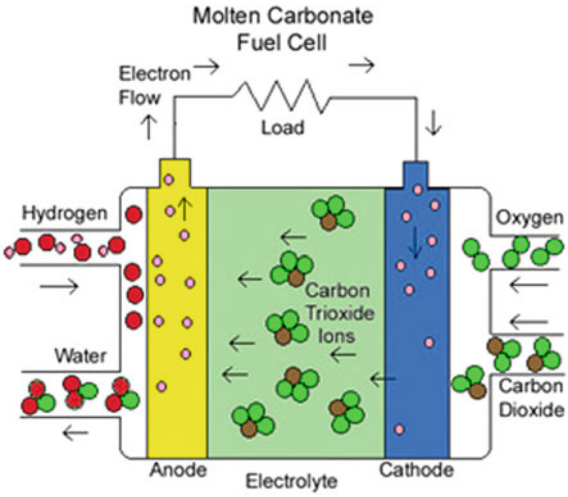

Fig. 16 Molten carbonates fuel cells [141]

3.1.5 Solid Oxide Fuel Cells (SOFCs)

SOFCs are high temperature fuel cells (650–1000 °C) that use Yttria-doped zirconia (YSZ) as electrolyte for adequate mechanical strength, chemical stability and better ionic conductivity. Due to its high temperature workability, hydrocarbon fuels like methane, butane, propane, gasoline, jet fuel, diesel and bio-diesel can be used as fuel. SOFCs are 60% efficient in converting fuel to electricity and 85% efficient after reusing the system waste heat. The anodes used in SOFCs are usually zirconia cermet and the cathodes are made of strontium-doped-lanthanum manganite. Non precious metals like nickel are used as catalyst. SOFCs are acid resistant fuel cells and are not poisoned by CO_2 gas.

4 Conclusion

Now-a-days, many new analyzes in polymer electro-catalysis process have been carried out. This chapter provides an overview of this materials and process, latest characterization techniques, and fundamental studies of degradation methods. Electro-catalysis studies show significant differences when compared with other conventional process of polymer catalysis. From this chapter the following conclusion have been arrived:

- The metal-melamine based polymers can be promising pre-cursors for the preparation of efficient metal-embedded nitrogen-doped carbon materials for electro-catalysis process.
- It is expected that the processing of polymeric materials, as catalyst and supports, will have major influence on the processing of catalysis in future.

- Despite the knowledge in the field of electro-catalyst and catalyst layer degradation mechanisms on the polymers, one of the major challenges in the near future is to develop new catalyst supports that improve the durability of the catalyst layer and also impact the properties of the active phase to improve the catalyst kinetics.
- The durability properties also have highly attracted the attention of researchers in coming years.
- Therefore focus will be given on expanding the family of polymers as well as investigation on the electro-chemical properties in future.

References

1. Klauk H (ed) (2006) Organic electronics: materials, manufacturing and applications. Wiley-VCH, Weinheim. ISBN 9783527312641
2. Klauk H (ed) (2010) Organic electronics. More materials and applications. Wiley-VCH, Weinheim. ISBN 9783527640218 (Electronic Bk)
3. Guarino V, Alvarez-Perez MA, Borriello A, Napolitano T, Ambrosio L (2013) Adv Healthc Mater 2:218–227
4. Natta G, Mazanti G, Corradini P (1959) Chem Abstr 53:13985
5. Walatka VV, Labes MM, Perstein JH (1973) Phys Rev Lett 31:1139
6. Shirakawa H, Ikeda S (1971) Poly J 2:231
7. Shirakawa H, Ito T, Ikeda S (1974) J Polym Sci Polym Chem Edn 12:11
8. Ito T, Shirakawa H, Ikeda S (1975) J Polym Sci Polym Chem Edn 12:1943
9. Berets DJ, Smith DS (1969) Trans Faraday Soc 64:823
10. Shirikawa H, Louise EJ, Macdiarmid AG, Chiag CK, Heeger AJ (1977) J Chem Soc Chem Commun 578
11. Chiang CK, Fincher CR, Park YW, Heeger AJ, Shirakawa H, Louse EJ, Gau SC, Macdiarmid AG (1977) Phy Rev Lett 39:1098
12. Shirakawa H, Louis EL, Mac Diarmid AG, Chiang CK, Heeger AJ (1977) J Chem Soc Chem Commun 16:578
13. Chiang CK, Fincher CR, Park YW, Heeger AJ, Shirakawa H, Louis EJ, Gau SC, Mac Diarmid AG (1978) Phys Rev Lett 40:1472
14. Li Y (ed) (2015) Organic optoelectronic materials. Lecture notes in chemistry, vol 91. Springer. https://doi.org/10.1007/978-3-319-16862-3-2
15. Reetz MT, Quaiser SA, Breinbauer R, Tesche B (1995) Angew Chem Int Ed Engl 34:2728
16. Qi Z, Pickup PG (1998) Chem Commun 28:15
17. Hepel MJ (1998) Electrochem Soc 145:124
18. Portela R, Sanchez B, Coronado JM, Candal R, Suarez S (2007) Catal Today 129:223–230
19. Hao Y (2012) Nat Mater 11:155–161
20. Karunadasa HI, Montalvo E, Sun Y, Majda M, Long JR, Chang CJ (2012) Science 335:698. https://doi.org/10.1126/science.1215868
21. Guiglion P, Butchosa C, Zwijnenburg MA (2014) J Mater Chem A 2:11996
22. Guiglion P, Butchosa C, Zwijnenburg MA (2016) Macromol Chem Phys 217:344–353
23. Fujishima A, Honda K (1972) Nature 238:37–38
24. Mofidi AA, Min JH, Palencia LS, Coffey BM, Liang S, Green JF (2002) California energy commission sacramento, California
25. Fujishima A, Honda K, Kikuchi S (1969) Kogyo. Kagaku Zasshi 72:108
26. Nozik AJ (1977) Appl Phys Lett 30(11):567–570
27. Sakata T, Kawai T (1981) Chem Phys Lett 80:341–344
28. Imoberdorf GE, Cassano AE, Irazoqui HA, Alfano OM (2007) Chem Eng Sci 62:1138–1154

29. Laoufi NA, Tassalit D, Bentahar F (2008) Global NEST J 10(3):404–418
30. Wong IL, Eames PC, Perera RS (2007) Sol Energy 81:1058–1071
31. Goetzberger A (1991) Transparent insulation technology for solar energy conversion, 2nd edn. Fraunhofer Institute for Solar Energy Systems, Freiburg
32. Chen HW, Ku Y (2007) Chemosphere 69:184–190
33. Nowotny MK, Sheppard LR, Bak T, Nowotny JJ (2008) Phys Chem C 112:5230–5275
34. Dholam R, Patel N, Adami M, Miotello A (2009) Int J Hydrogen Energy 34:5337–5346
35. Chen HW, Ku Y, Kuo YL (2007) Water Res 41:2069–2078
36. Ku Y, Lin CN, Hou WM (2011) J Mol Catal A: Chem 349:20–27
37. Galinska A, Walendziewski J (2005) Energy Fuels 19:1143–1147
38. Ku Y, Lee YC, Wang WY, Ku Y, Lee YC, Wang WY (2006) Voltage. J Hazard Mater 138:350–356
39. Chen C, Li X, Ma W, Zhao J, Hidika H, Serpone N (2002) J Phys Chem 106B:318
40. Wilke K, Breuer HD (1999) J Photochem Photobiol 121A:49
41. Bhandari S, Vardia J, Malkani RK, Ameta SC (2006) Toxicol Enviorn Chem 88:35
42. Primo A, Corma A, Garcia H (2011) Phys Chem Chem Phys 13:886–910
43. Sreethawong T, Yoshikawa S (2012) Chem Eng J 197:272–282
44. Alonso F, Riente P, Rodriguezreinoso F, Ruizmartinez J, Sepulvedaescribano A, Yus M (2008) J Catal 260:113–118
45. Yun HJ, Lee H, Kim ND, Yi J (2009) Electrochem Commun 11:363–366
46. Chou CS, Yang RY, Yeh CK, Lin YJ (2009) Power Technol 194:95–105
47. Kryukova GN, Zenkovets GA, Shutilov AA, Wilde M, Gunther K, Fassler D, Richter K (2007) Appl Catal B 71:169–176
48. Aramendia MA, Colmenares JC, Marinas A, Marinas JM, Moreno JM, Navio JA, Urbano FJ (2007) Catal Today 128:235–244
49. Li H, Bian Z, Zhu J, Huo Y, Li H, Lu Y (2007) Mesoporous Au/TiO_2 nanocomposites with enhanced photocatalytic activity. J Am Chem Soc 129:4538–4539
50. Sivula K, van de Krol R (2016) Nat Rev Mater 70: 15010:1–15010:7
51. Liang Y, Tsubota T, Mooij LPA, van de Krol R (2011) J Phys Chem C 115:17594–17598
52. Ye H, Lee J, Jang JS, Bard AJ (2010) J Phys Chem C 114:13322–13328
53. Zhong DK, Choi S, Gamelin DR (2011) J Am Chem Soc 133:18370–18377
54. Yourey JE, Bartlett BMJ (2011) Mater Chem 21:7651–7660
55. McDonald KJ, Choi K-S (2011) Chem Mater 23:4863–4869
56. Ida S, Yamada K, Matsunaga T, Hagiwara H, Matsumoto Y, Ishihara T (2010) J Am Chem Soc 132:17343–17345
57. Patil R, Kelkar S, Naphade R, Ogale SJ (2014) Mater Chem A 2:3661–3668
58. Joshi UA, Maggard PA (2012) J Phys Chem Lett 3:1577–1581
59. Ong WJ, Tan L, Ng YH, Yong ST, Chai SP (2016) Chem Rev 116:7159–7329
60. Chen X, Mao SS (2007) Chem Rev 107(7):2891–2959
61. Hong JD, Wang YS, Wang YB, Zhang W, Xu R (2013) Chem Sus Chem 6(12):2263–2268
62. Liao CH, Huang CW, Wu JCS (2012) Catalysts 2: 490–516. https://doi.org/10.3390/catal2040490
63. Wrighton MS, Ellis AB, Wolczanski PT, Morse DL, Abrahamson HB, Ginley DS (1976) J Am Chem Soc 98:2774–2779
64. Harish S, Mathiyarasu J, Phani KLN, Yegnaraman V (2009) Catal Lett 128:197–202
65. Ulman A (1996) Chem Rev 96:1533
66. Cole DH, Shull KR, Baldo P, Rehn L (1999) Macromolecules 32:771
67. Wang R, Yang J, Zheng Z, Carducci MD, Jiao J, Seraphin S (2001) Angew Chem Int Ed 40:549
68. Zheng J, Stevenson MS, Hikida RS, Van Patten PG (2002) J Phys Chem B 106:1252
69. Oh SK, Niu Y, Crooks RM (2005) Langmuir 21:10209
70. Kralik M, Biffis A (2001) J Mol Catal A: Chem 177:113
71. Ito T, Shirakawa H, Ikeda IJ (1974) Polym Sci. Polym Chem 12:11
72. Luttinger LB (1962) J Org Chem 27:1591

73. Tekbasoglu TY, Soganci T, Ak M, Koca A, Sener MK (2017) Biosens Bioelectron 87:81
74. Park JE, Atobe M, Fuchigami T (2005) Electrochim Acta 51:849
75. Tseng RJ, Huang J, Ouyang J, Kaner RB, Yang Y (2005) Nano Lett 5:1077
76. Li W, Jia QX, Wang HL (2006) Polymer 47:23
77. Kumar SS, Sivakumar C, Mathiyarasu J (2007) Phani KLN Langmuir 23:3401
78. Drelinkiewicza A, Waksmundzka A, Makowski W, Sobczak JW, Krol A, Zieba A (2004) Catal Lett 94:143
79. Gelder Elaine A, David Jackson S, Martin Lok C (2002) Catal Lett 84:205
80. Ortel E, Reier T, Strasser P, Kraehnert R (2011) Chem Mater 23:3201
81. Alexandridis P, Tsianou M (2011) Eur Polym J 47:569
82. Yang JC, Chen CH, Wu RJ (2012) Cryst Eng Comm 14:2871
83. Ataee-Esfahani H, Wang L, Yamauchi Y (2010) Chem Commun 46:3684
84. Wang L, Yamauchi Y (2009) J Am Chem Soc 131:9152
85. Li G, Yu H, Wang X, Sun S, Li Y, Shao Z, Yia B (2013) Phys Chem Chem Phys 15:2858–2866
86. Rajesh B, Ravindranathan TK, Bonard J-M, Xanthopoulos N, Mathieu HJ, Viswanathan B (2002) Electrochem Solid-State Lett 5:E71
87. Rajesh B, Ravindranathan TK, Bonard J-M, Mathieu HJ, Xanthopoulos N, Viswanathan B (2003) Chem Commun 9:2022
88. Hable CT, Wrighton MS (1991) Langmuir 7:1305
89. Kost KM, Bartak DE, Kazee B, Kuwana T (1988) Anal Chem 60:2379
90. Prasad KR, Munichandraiah N (2002) J Power Sources 103:300
91. Patra S, Munichandraiah N (2009) Langmuir 25:1732
92. Hepel M (1998) J Electrochem Soc 145:124
93. Deki S, Akamatsu K, Yano T, Mizuhata M, Kajinami A (1998) J Mater Chem 8:1865
94. Li Y, Lenigk R, Wu X, Gruending B, Dong S, Renneberg R (1998) Electroanalysis 10:671
95. Parsons R, VanderNoot T (1988) J Electroanal Chem 257:9
96. Bouzek K, Mangold KM, Jutter K (2000) Electrochim Acta 46:661
97. Laborde H, Leger JM, Lamy C (1994) J Appl Electrochem 24:219
98. Strike DJ, De Roou NF, Koudelka-Hep M (1992) J Appl Electrochem 22:922
99. Laborde H, Leger JM, Lamy C, Garnier FC, Yassar A (1990) J Appl Electrochem 20:524
100. Yang H, Lu TH, Xue K, Sun SG, Lu GQ (1997) Chen SP J Electrochem Soc 144:2302
101. Castro Luna AM (2000) J Appl Electrochem 30:1137
102. Niu L, Li QH, Wei FH, Chen X, Wang H (2003) J Electroanal Chem 544:121
103. Napporn WT, Laborade H, Leger JM, Lamy C (1996) J Electroanal Chem 404:153
104. Laborde H, Leger JM, Lamy C (1994) J Appl Electrochem 24:1019
105. Kelaidopoulou A, Abelidou E, Papoutsis A, Polychroniadis EK, Kokkinidis G (1998) J Appl Electrochem 28:1101
106. Kelaidopoulou A, Papoutsis A, Kokkinidis G (1999) J Appl Electrochem 29:101
107. Vigier F, Gloaguen F, Leger JM, Lamy C (2001) Electrochim Acta 46:4331
108. Lima A, Coutanceau C, Leger JM, Lamy C (2001) J Appl Electrochem 31:379
109. Lenoe A, Marino W, Scharifker BR (1992) J Electrochem Soc 139:438
110. Zhong QL, Li WH, Tian ZQ (1994) Acta Physchim Sin 10:813
111. Gasteiger HA, Markovic NM (2009) Science 324:48
112. Debe MK (2012) Nature 486:43
113. Shao MH, Shoemaker K, Peles A, Kaneko K, Protsailo L (2010) J Am Chem Soc 132:9253
114. Bandarenka AS, Hansen HA, Rossmeisl J, Stephens IEL (2014) Phys Chem Chem Phys 16:13625
115. Cuesta A (2011) Chem Phys Chem 12:2375
116. Schmickler W, Santos E (2010) Interfacial electrochemistry. Springer, Berlin, Heidelberg
117. Kolb DM (2002) Surf Sci 500:722
118. Markovic NM, Ross PN (2002) Surf Sci Rep 45:117
119. Bligaard T, Norskov JK (2007) Electrochim Acta 52:5512
120. Climent V, Garcia-Araez N, Feliu JM (2009) Fuel cell catalysis. A surface science approach. In: Koper MTM (ed) John Wiley & Sons, Inc., Hoboken

121. Hammer B, Norskov JK (1995) Surf Sci 343:211
122. Kozuch S, Martin JML (2011) Chem Phys Chem 12:1413
123. Schmidt-Rohr K (2015) J Chem Educ 92:2094–2099
124. Steele BCH, Heinzel A (2001) Materials for fuel-cell technologies. Nature 414:345–352
125. web.iitd.ac.in/…/2Prof.%20B.Viswanthan%20IITChennai.pdf
126. Wang Y, Chen KS, Mishler J, Cho SC, Adroher XC (2011) Appl Energy 88(4):981–1007
127. Vaghari H, Malmiri HJ, Berenjian A, Anarjan N (2013) Sustain Chem Process 1:16
128. Lu S, Pan J, Huang A, Zhuang L, Lu J (2008) PNAS 105(52): 20611–20614. https://doi.org/10.1073/pnas.0810041106
129. An L, Zhao TS, Li YS (2015) Carbon-Renew Sustain Energy Rev 50:1462–1468
130. Fu J, Qiao JL, Wang XZ, Ma JX, Okada T (2010) Synth Met 160:193–199
131. Qiao JL, Fu J, Liu LL, Zhang J, Xie J, Li G (2012) Solid State Ion 214:6–12
132. Qiao JL, Zhang J, Zhang J (2013) J Power Sources 237:1–4
133. Zhang J, Qiao JL, Jiang GP, Liu LL, Liu YY (2013) J Power Sources 240:359–367
134. Jasti A, Shahi VK (2014) J Power Sources 267:714–722
135. Tanaka M, Fukasawa K, Nishino E, Yamaguchi S, Yamada K, Tanaka H, Bae B, Miyatake K, Watanabe M (2011) J Am Chem Soc 133:10646–10654
136. Ong AL, Saad S, Lan R, Goodfellow RJ, Tao SW (2011) J Power Sources 196:8272–8279
137. Benipal N, Qi J, Gentile JC, Li WZ (2017) Renew Energy 105:647–655
138. Zhou JF, Unlu M, Vega JA, Kohl PA (2009) J Power Sources 190:285–292
139. Behling NH (2013) Fuel cells, pp 7–36
140. Baizeng F, Xinyu L, Xindong W, Shuzhen D (1998) J Electroanal Chem 441(1–2):65–68
141. Salameh Z (2014) Renewable energy system design, pp 201–298. https://doi.org/10.1016/b978-0-12-374991-8.00004-0

Oxygen Evolution Reaction

A. Brouzgou

Abstract Oxygen evolution reaction is evinced as one of the main rate-determining steps for clean energy production, energy security supply and therefore for the evolution of a sustainable society. The production of clean energy, the security of energy supply (autonomy) and lower cost of energy supply constitute the main key points for a sustainable future. It is known, that a sustainable future can be achieved only if the current power supply shifts to other sources than the conventional ones; with the renewable energy sources and hydrogen fuel to own a leading role. The oxygen evolution reaction mechanism in acidic and alkaline media remains a mystery even today, after so many years of research activities. Bockris in 1954 and then Bockris and Huq in 1956 were the initial founders of the oxygen evolution reaction mechanism study. Then, many mechanisms were suggested and up-to-date many materials have been studied, with the metal perovskite oxides to be the most promising candidates. When this 'mystery' is solved, then a big step towards a sustainable future will become.

Keywords Oxygen evolution reaction · Metal perovskite oxides · Water electrolysis · Metal-air batteries · Materials for oxygen evolution reaction

1 Introduction

The advances in oxygen evolution reaction (OER) materials are an instigator for the further development of the main energy storage and energy conversion electrochemical devices. Their development, can be a significant step towards the target of the socioeconomic and environmental intendment for 'clean' energy production, via the renewable energy sources, and the feasibility of great energy capacity storage [1].

Oxygen evolution reaction is evinced as one of the main rate-determining steps [2] for clean energy production, energy security supply and therefore for the evolution of a sustainable society (Fig. 1). The production of clean energy, the security of energy

A. Brouzgou (✉)
Laboratory of Alternative Energy Conversion Systems, Department of Mechanical Engineering, University of Thessaly, Volos, Greece
e-mail: amprouzgou@uth.gr; brouzgou@gmail.com

Inamuddin et al. (eds.), *Methods for Electrocatalysis*,
https://doi.org/10.1007/978-3-030-27161-9_6

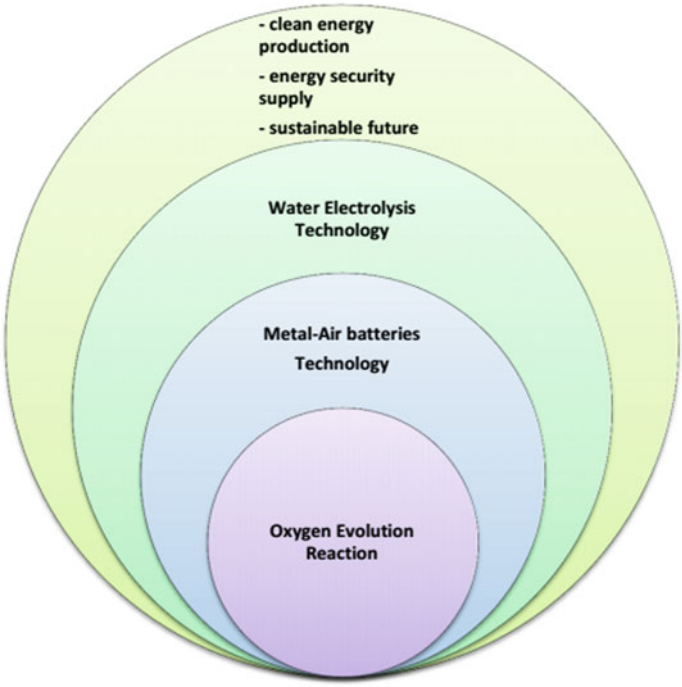

Fig. 1 The role of OER for a sustainable and energetically-secure future

supply (autonomy) and lower cost of energy supply constitute the main key points for a sustainable future. It is known, that a sustainable future can be achieved only if the current power supply shifts to other sources than the conventional ones; with the renewable energy sources and hydrogen fuel to own a leading role.

Up-to-date, fossil fuels constitute the main hydrogen source (96% production). In the market there are many available technologies for hydrogen's production, but all of them emit greenhouse gases contributing more to the environmental pollution [3].

Thereupon, hydrogen production from water electrolysis appears as the most environmentally friendly approach. Today, the power-to-gas system to which the required energy is derived from renewable energy sources it is supported as the most promising one; holding 4% of the current hydrogen production. By 2050, if the main challenges of the water splitting process (or water electrolysis), be overcome, it is envisaged an increment of its share at 22% [3].

In 2015, the Department of Hydrogen Energy of U.S.A set the target for 'green' H_2 production efficiency (%LVH based), from wind-based water electrolysis (onshore and offsite) at 30% with the respective cost to be 5–7 €/kg; 15% from solar-based water electrolysis (offsite) with a cost of 6.5–8.5 €/kg and 33% from nuclear energy with an estimated cost of 4.5–6.5 €/kg [4].

However, over and above the obstacle of clean energy production, energy storage establishes another one that must be overcome. The energy production from renewable energy sources renders instantly the power supply unreliable, while at the same time make the necessity for reliable energy storage devices indispensable. Among the current energy storage technologies, electrochemical devices offer the most encouraging operational characteristics.

Specifically, today metal-air batteries due to their high energy density (0.5–0.7 kWh/kg vs. 0.02–0.05 kWh/kg of lead-acid batteries) are one of the most promising electric energy-storage technologies [5]. During their charging and discharging processes two main electrochemical reactions take place, respectively: (i) the oxygen evolution reaction and (ii) oxygen reduction reaction (Eq. 1):

$$4OH^- \rightarrow O_2 + H_2O + 4e^- \tag{1}$$

The main challenge for the metal-air batteries is the increase in the rate of charging by improving the OER electrode performance. The increment of catalytic efficiency towards OER will also increase the reversibility of the two reactions and consequently will increase the cyclic life of the batteries. For this reason, two main pathways have been followed, the one that aims at the electrode reaction rate or electrode surface-area increment and the other that aims at the internal resistance electrode reduction. The increased resistance is attributed to the produced gas bubbles [6].

1.1 Challenges to Be Overcome

Up-to-date, oxygen evolution reaction, has been studied mainly as half-reaction of water electrolysis process. The water electrolysis is an endergonic reaction (thermodynamically non-spontaneous) meaning that energy must be consumed in order to be processed. The reaction can take place either in acidic media or in alkaline one:

Acidic media:

$$\text{anode:} \quad H_2O\,(l) \rightarrow 1/2\ O_2(g) + 2H^+ + 2e^- \tag{2a}$$

$$\text{cathode:} \quad 2H^+ + 2e^- \rightarrow H_2(g) \tag{2b}$$

$$\text{full reaction:} \quad H_2O\,(l) \rightarrow H_2(g) + 1/2\ O_2(g) \tag{2c}$$

Alkaline media:

$$\text{anode : :} \quad 2OH^- \rightarrow H_2O + 1/2\ O_2(g) + 2e^- \tag{3a}$$

$$\text{cathode:} \quad 2H_2O + 2e^- \rightarrow H_2(g) + 2OH^- \tag{3b}$$

$$\text{full reaction:} \quad H_2O(l)H_2(g) + 1/2\ O_2(g) \tag{3c}$$

Comparable to acidic media, in alkaline media, can be used materials of low costs, such as nickel or cobalt and their respective oxides which in acidic media are corroded. This one advantage of the alkaline water electrolysis systems was considered as the main motive for the ultra-domination of the market with alkaline water electrolysis technology. Nevertheless, independently of the kind of the media that the reaction takes place as well as the electrode material, OER (Eqs. 2a and 3a) constitutes the rate-determining step [7]. Oxygen evolution reaction kinetics are much more sluggish than hydrogen evolution reaction, creating high overvoltage at the anode electrode.

Dating back in 1789 and 1800, Holland Paets van Troostwijk with J. R. Demain and the British W. Nicholson with A. Carlislie, respectively were the pioneers of the water electrolysis process [8]. Even though the many years that passed since this great discovery, up-to-date the exact mechanism that oxygen evolution reaction follows remains a mystery, 'the great enigma' as has been named by some researchers [9]. When the exact mechanism of OER is realized, then may highest efficiency of water electrolysis reaction as well as a higher rate of batteries charging be succeeded. Thus, the realization of the OER mechanism is one of the main challenges that must be overcome.

2 The History of Oxygen Evolution Reaction Proposed Mechanisms

The initial OER mechanisms that were proposed suggested metal centers as the active sites of the reaction. It worths being mentioned that the first patent of water electrolysis device is recorded back in 1874 [10]. However, there was no relative information about OER. The first reference about OER mechanism is tracked down in 1954 in a published work of Bockris [11]. His electrode materials were limited to noble metals; the main problem that he faced was the failure to achieve the potential of reversible oxygen electrode and as a result the recorded data deviated from Tafel line linearity.

The above deviation was corrected from Bockris and Huq [12] who then studied the OER mechanism on platinum (Pt) electrode. Those years the main problem for the kinetic studies of the OER was the presence of impurities on the metals, whose reaction could cover the oxygen evolution reaction. Thus, Bockris and Huq solving that problem proposed the first OER mechanism:

$$OH^- \rightarrow MOH + e_0^- \tag{4a}$$

$$MOH^- + OH^- \rightarrow MO + H_2O + e_0^- \tag{4b}$$

$$MO + OH^- \rightarrow MHO_2 + e_0^- \quad (4c)$$

So, it becomes known that at 25 °C a Tafel slope of 0.1 is connected with a three-step reaction of hydroxyl ions discharge [12]. According to the authors [12] all the three chemical Eqs. (4a–4c) could be the rate-determining step of OER. Moreover, one of each chemical equations could lead to many different pathsways through which the oxygen would be produced. But even so, those years the researchers did not have access to the appropriate equipment in order to further into OER mechanism. It is remarkable, that even today that we have the necessary equipment the OER mechanism remains a mystery.

In 1957 Wade and Hackerman [13] proposed the following OER mechanism in acidic environment:

$$2M + 2H_2O \rightarrow MO + MH_2O + 2H^+ + 2e^- \quad (5a)$$

$$MO + 2MOH^- \rightarrow 2M + MH_2O + O_2 + 2e^- \quad (5b)$$

(M: active site = transition metal cation)

Oxygen evolution reaction mechanism had been studied over nickel and nickel oxides in 1959 by Conway and Bourgault [14]. Those years nickel and nickel oxides were the most interesting materials for nickel-cadmium and nickel-iron batteries. The authors suggested a third different reaction pathway, being consisted of four steps:

$$M + OH^- \rightarrow MOH + e^- \quad (6a)$$

$$MOH + OH^- \rightarrow MO + H_2O + e^- \quad (6b)$$

$$MO + MOH \rightarrow MHO_2 \quad (6c)$$

$$MHO_2 + MOH \rightarrow M + H_2O + O_2, \quad (6d)$$

where M is the electronically conducting bulk oxide phase.

Later in 1963 Krasil'shchkov proposed two different OER pathways in acidic and alkaline media, respectively [15]:

Acidic media:

$$M + H_2O \rightarrow M - OH + H^+e^- \quad (7a)$$

$$M - OH \rightarrow M - O + H^+ \quad (7b)$$

$$M - O^- \rightarrow M - O + e^- \quad (7c)$$

$$2M - O \rightarrow 2M + O_2 \tag{7d}$$

Alkaline media:

$$M + OH^- \rightarrow M - OH + e^- \tag{8a}$$

$$M - OH + OH^- \rightarrow M - O^- + H_2O \tag{8b}$$

$$M - O^- \rightarrow M - O + e^- \tag{8c}$$

$$2M - O \rightarrow 2M + O_2 \tag{8d}$$

(M: active site = transition metal cation)

They supported that at the onset potential of OER firstly an unstable oxide layer is formed which then decomposes with oxygenproduction. The same theory was also supported by Tsinman [16].

The dependence of OER kinetics on pH value over nickel electrodes, in sulfate electrolyte, was evaluated and confirmed in 1965 by Sato and Okamoto [17]. According to them in acidic media the rate-determining step was observed in a relative high current-density region:

$$H_2O \rightarrow OH_{(ads)} + H^+ + e^- \tag{9}$$

On the contrary, in alkaline media, the rate-determining step was noted in a low current region suggesting the following equations as a possible reaction pathway for O_2 evolution. The adsorbed hydroxide anions (Eq. 10b) were found to determine the rate of OER:

$$OH^- \rightarrow OH_{(ads)} + H^+ + e^- \tag{10a}$$

$$OH_{(ads)} + OH^- \rightarrow O_{(ads)} + H_2O + e^- \tag{10b}$$

$$2O_{(ads)} \rightarrow O_2 \tag{10c}$$

Then, in 1976 Damjavonic and Jovanovic [18] studied the OER kinetics and mechanism over Pt electrode in acidic media. They stated that after the first charge transfer, a chemical step takes place which constitutes the rate determining step to the OER. Specifically, the two formed H^+ ions are not involved in the rate determining step process with the following reactions to be a possible pathway of the reaction:

$$H_2O \leftrightarrow H^+ + OH + e^- \tag{11a}$$

$$OH + X \rightarrow [X \ldots OH] \text{ or } [X \ldots O - + H^+] \tag{11b}$$

$$\left[2X \ldots OH \leftrightarrow 2X + O_2 + 2H^+ + 2e^-\right], \tag{11c}$$

where X is a site on the surface of the formed oxide film.

Moreover for the first time is proposed the direct involvement of oxygen atom from the metal's oxide film. Thus, after (11a) reaction takes place, the formed OH bonds to the oxygen of metal oxide. In sequence the H^+ departs from OH and so O^- remains bonded to the oxygen of metal oxide; which both leaves the metal forming the O_2 (Fig. 2).

After the release of O_2 an oxygen vacancy appears on metals surface, which is supposed to be filled via the (11a) and (Fig. 3) reactions that take place in a parallel pathway with the first pair of reactions and in a sequence way being combined with oxidation.

The fact that the oxygen is part of the catalyst lattice structure makes it automatically a constant factor to the OER mechanism. The characteristic of this reaction

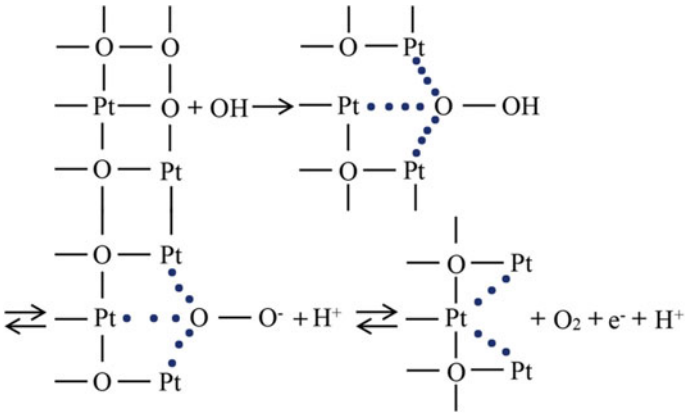

Fig. 2 OER suggested by Damjavonic and Jovanovic mechanism, in 1976

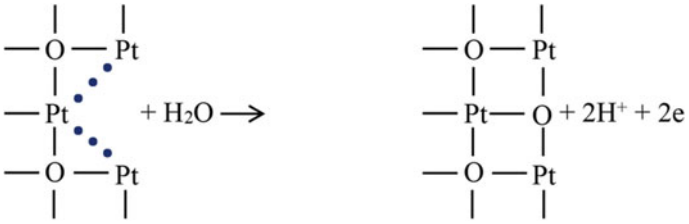

Fig. 3 A series of 4d reactions

pathway is that the reaction intermediates are not necessary in order to play the role of the metallic surface coverage layer.

Damjavonic and Jovanovic [18] reported that the first hint for the lattice oxygen implication in OER was given by Rosenthal and Veselovski. The latter observed that when ^{18}O was sent to the platinum's oxide surface then the initial gas that was produced was enriched with ^{18}O.

The assumption of a chemical step to be the rate-determined step was also supported by Hoare [19]. They stated that when transfer coefficient takes the value of 1.5, means that the second electron is transported very slow. Additionally, O' Grady et al. [20] and in [21] who experimented in alkaline media reported the inclusion of the formed oxide film and an oxidation-reduction cycle of an active surface site, as part of OER mechanism:

$$M + OH^- \rightarrow M - OH + e^- \tag{12a}$$

$$M^Z - OH \rightarrow M_{z+1}\text{-}OH + e^- \tag{12b}$$

$$2M_{z+1}\text{-}OH + 2\,OH^- \rightarrow 2M + 2H_2O + O_2 \tag{12c}$$

Indeed this film was not observed when other reactions conducted.

In 1978 Miles et al. [22] investigated the OER over Ru-Ir, Ru-Pt, and Ir–Pt (50:50 at.%) alloys in acidic media. Moreover, for comparison reasons they experimented over RuO_2/TiO_2 or Ir electrodes. They concluded that the presence of oxide (either formed during OER or from the beginning of OER) has a positive impact on oxygen production.

Bronoel and Reby [23] made an attempt to validate the hitherto theoretical assumptions about OER mechanism over nickel electrodes in an alkaline environment. From the five proposed hypothetical mechanisms, the one that includes OH_{ads} and OH^- chemical association with the OH^- and O^-_{ads} chemical discharge was validated experimentally:

$$OH^- \rightleftarrows OH_{ads} + e^- \tag{13a}$$

$$OH_{ads} + OH^- \rightleftarrows O^-_{ads} + H_2O \tag{13b}$$

$$O^-_{ads} \rightleftarrows O_{ads} + e^- \tag{13c}$$

$$2O_{ads} \rightleftarrows O_2 \tag{13d}$$

In 1983 Bockris and Otagawa [24] studied the OER on perovskite materials. They concluded that lattice oxygen was involved into OER, but none change of transition metal oxidation state was observed Bockris and Otagawa [24]. Thus, it was supported

that OER progression is provoked by the lattice oxygen ions oxidation and not by the move of cations to higher valence states.

In 1987 the OER over Ru and RuO_2 was investigated by Wohlfahrt-Mehrens and Heitbaum [25]. They pointed out that the produced oxygen gas comes from both: (i) the electrolyte and (ii) the lattice oxygen. Moreover, they assumed that in the case of RuO_2, not only the metal acts as active site, but also the total metal oxide. In the case of pure metal (Ru) an oxide layer is created over which the OER progresses in the same way with the metal oxide.

According to Matsumoto and Sato [26] review work about studied catalysts for OER the OER activity had the following order: $RuO_2 > IrO_2 >$ Co and Ni > Fe > Mn and Pb. Matsumoto stated that two main factors engrossed up to 1986 investigations: (i) the strength of the M-O bond and (ii) the transfer of the electron. More specifically, about the electron transfer, the Franck-Condon principle was supported, according to which the orbitals of the active sites and of the adsorbed species overlap each other. The degree of overlapping along with the density of states of the electron at the Fermi level are the key-elements for the electron transfer rate.

It is characteristic that all the works up to 1986 that investigated the OER over noble and non-noble metals reported that the oxide layer is always formed which certain is engaged into the reaction and that metal oxides have higher stability than their respective pure metals. An additional general feature is that the Langmuir or Temkin models were adopted for adsorption process, making at the same time also the assumptions that the potential drop takes place into the Helmholtz layer on the side of electrolyte. So, the area into which the activation drop occurs was also those years under investigation. In Fig. 4 the founders of the OER mechanism over the years, are summarized.

Over the years the OER mechanism has been studied more thoroughly, but still, the exact reaction pathway remains unknown and under investigation. Today a proton-coupled electron transfer that includes a 4-step reaction pathway is proposed (Fig. 5).

More precisely, the d-band position of the metal and the p-band position of the metal oxides constitute a key-element to the water electrolysis procedure. Figure 3 shows that the metal center has the role of the adsorption site and of the redox site, synchronously. At the same time the transport of four electrons occurs. This transport of electrons shall take place if an amount of energy will be provided which will be close to the thermodynamic energy. The formation of hydrogen peroxide intermediate during step 2 is considered as the rate-determining step.

Additionally, today it is suggested that in the OER process proton-coupled electron transfer occurs in a continuous way along with spin states changeover. Thus, for the last action, OER requires extra energy except for the overpotential energy.

Distinctively, when the metal state is $3^+/4^+$ the d-band and p-band are engaged and so the redox active site is not consisted only by metal. Thus, at a potential higher than 1.23 V versus RHE the OER is evolved through the lattice oxygen oxidation reaction, as had been reported by Damjavonic and Jovanovic in [18] and some more recent works [27, 28]. In 2015 Binnigner et al. [29] named it as lattice oxygen evolution reaction (LOER) mechanism.

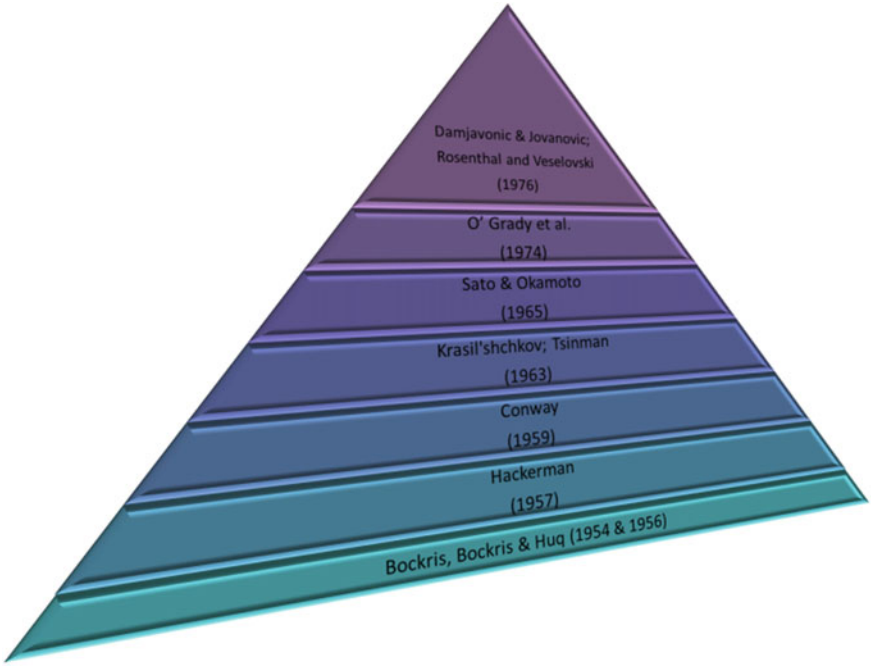

Fig. 4 The founders of the OER mechanism

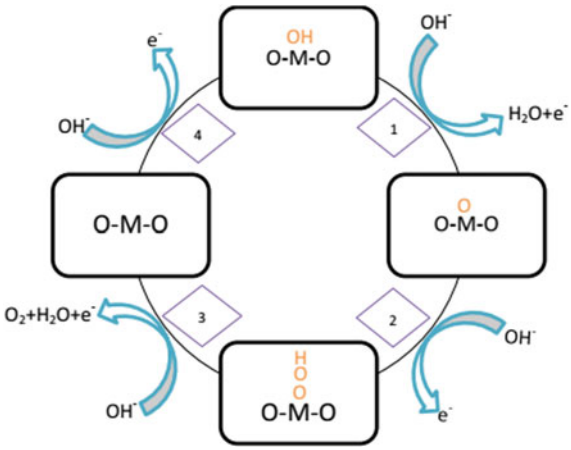

Fig. 5 Currently proposed OER mechanism in alkaline media

Considering all the above-mentioned historical evolvement of OER study all the following three chemical reactions it is possible to take place [9]:

$$\text{common OER}: \quad 2OH^-_{aq} \leftrightarrow 1/2\,O_2 + H_2O + 2e^- \tag{14}$$

$$\text{metal oxide chemical dissolution}: M^{2n+}O_n^{2-} + nH_2O \leftrightarrow M_{aq}^{2n+} + 2nOH_{aq}^{-} \quad (15)$$

$$\text{LOER}: \quad M^{2n+}O_n^{2-} \leftrightarrow M_{aq}^{2n+} + 1/2\ nO_2 + 2ne^{-} \quad (16)$$

Thermodynamically and kinetically, OER and LOER are very close and so fairly can be distinguishable, as except for the lattice oxygen also oxygen from the electrolyte contributes to the OER process. In this case, it is proposed [9] that at the onset potential of OER and LOER the cations of the metal that are produced from the latter 'render' into the electrolyte and then either are oxidized to higher valence states or are reconnected with electrolyte's hydroxide ions. When the first scenario happens electrodes mass is lost, while when the latter scenario is followed an oxyhydroxide layer is formed, which make the catalyst more stable [30]. In the following subsection, the most promising materials for OER that have been appeared in literature in the last years are reported and analyzed.

3 Trends of Materials for Oxygen Evolution Reaction

Among the studied materials for OER perovskites and their respective oxides are the most promising ones. Perovskites as materials own rich chemical structure due to which the electronic properties of oxides, are defined. In literature, many efficient OER has been reported when electropositive metals with high oxidation states have been reported. Some kind of perovskite materials that have shown increased OER activity has also presented increased M-O covalency; with a p-band close to Fermi level.

The OER process swap from a cationic redox to an anionic one. It is known that in the case of metal transition oxides, the bond between two oxygen composes the rate-determining factor. Thence, most of the works considered the Sabatier's principle which states that the most active electrocatalyst is the one which binds oxygen with a median strength (neither too strong nor too weak) have focused on the bond strength between the catalytic surface and the oxygen.

Based on the above-mentioned findings the research interest focuses to the alteration of materials structure in order to move the oxygen p-band closer to the Fermi level. Tuning the surface electronic structure of perovskite oxides has shown to reduce the p-band—Fermi level distance and therefore enhances the catalytic activity. It worths being mentioned that $IrO_2$is considered as the state-of–the-art material for efficient OER. Since in the last decade the main research interest focuses on metal perovskite oxide materials, are the main topic in the current Chapter.

3.1 Transition Metal Perovskite Oxide Materials

Transition metal-based perovskite oxide materials present the advantages of low cost, very good stability and favorable electrocatalytic activity [31]. In 2011g Suntivich et al. [32] suggested a diagram of volcano-shape which expressed OER efficiency in terms of surface transition metal cations e_g electrons. Thus it is confirmed that the OER activity depends on the occupancy of the 3d electron with an e_g symmetry of surface transition metal cations in an oxide. The spin state of the magnetic ions was intermediate which attributes to the e_g electrons a value of 1.2. This finding functioned as a guideline for the next materials investigations about OER.

3.2 Ferroelectricity Feature of Metal Perovskite Oxides

Since in composites the above-mentioned finding cannot be fully defined and the e_g electron number has limitations concerning its regulation a numerous of works appear about the e_g electrons regulation efficiency. Increasing the available surface area by changing its morphology is proved an effective approach [33].

Another possible approach is the exploitation of the internal polarization of ferroelectrics. Ferroelectricity is a property of a material that has a spontaneous electrical polarization reversible by the application of an external electric field. Transformed material systems that do not contain ferroelectric components are expected to show no organization associated with ferroelectricity. In heterostructures consisting of transition metal oxides, however, the disorder that introduces an interface can affect the balance of the antagonistic interactions between the electronic self-charges, charges, and orbits. This has led to the emergence of emerging properties that are absent in the original building blocks of a heterostructure, including metallicity, magnetism and superconductivity at interfaces of insulating materials.

Instead of only adjusting the electronic structure, as well in order to accelerate the OER Li et al. [34, 35] utilized ferroelectric polarization. They utilized layered perovskite materials which conserve similar characteristics with the perovskite source, such as couplings between orbitals, charge and others. Those materials also can be modulated easier since they have more degrees of freedom. So, the e_g electron number was tuned by growing an in situ ferroelectric matrix (secondary phase). Specifically, many $BiCoO_3$ layers were introduced into a three-layered perovskite $Bi_4Ti_3O_{12}$, but finally only one layer was acceptable, in terms of thermodynamics and structural stability, to the three-layered perovskite. The as-prepared electrocatalyst displayed 320 mV overpotential and 34 mV dec^{-1} Tafel slope (Table 1). The ferroelectricity also for photocatalytic OER assigns higher activity to the electrocatalysts. A $Bi_6Fe_2Ti_3O_{18}$−BiOBr (BFTO/BOB) heterostructure with intimate 2D/2D interfaces leads to seven times higher activity in comparison to the non-ferroelectric BFTO/BOB or pure BFTO [36].

Table 1 Sample of studied materials for OER in 2019 literature

Catalyst	Overpotential (mV vs. RHE @10 $mAcm^{-2}$)	Tafel slope (mV dec^{-1})	pH (or electrolyte)	Stability (hrs) (or %degradation)	Refs
$Ni_{0.5}Fe_{0.5}$	372	37	1 M KOH	–	[37]
CoP (phosphide)	370	96	0.1 M KOH	5	[38]
Amorphous Co–MoO_x	340	49	1 M KOH	3	[39]
$BiCoO_3$ layer into a three-layered-$Bi_5CoTi_3O_{15}$	320	34	1 M NaOH	–	[34]
Mn-Ni_2P-0.053	330	116.7	1 M KOH	24	[40]
2D Co-based bimetallic MOFs (Co-Fe/Ni@HPA-MOF nanosheets)	320	58	1 M KOH	–	[41]
N-doped CoO nanowire arrays (N–CoO)	319	74	1 M KOH	24	[42]
MoxC-FeCo@NC	318	80	1 M KOH	–	[43]
$Sr_2Fe_{0.8}Co_{0.2}Mo_{0.65}Ni_{0.35}O_{6-\delta}$	310	56	–	–	[44]
Oxygen-enriched nickel-iron layered double hydroxide (NiFe-LDH) nanosheets	310	74	1 M KOH	10	[45]
Anionic metal–organic framework nanowire arrays not only directly grown on Cu foam but also captured Ni (II) ions hybrid	310 (@20 $mAcm^{-2}$)	102	1 M KOH	–	[46]
$CoSe_2$@N-Doped-carbon-nanorods	310	95	1 M KOH	–	[47]
$LaFe_xNi_{1-x}O_3$ nanorods	302	50	1 M KOH	20	[48]
Boronized Ni plate	300	43	1 M KOH	>1500	[35]
Au/Ir nanochains	300	52.94	1 M KOH	32	[49]
NCO-Na	300	70.32	1 M KOH	13.1%	[50]
Co_3O_4@Ni_2P-CoP/NF	298 (@50 mA cm^{-2})	75	1 M KOH	40	[51]
Nanocoral-like $NiSe_2$/g-C_3N_4	290 (@40 mA cm^{-2})	143	1 M KOH	10	[52]
$MnCo_2S_4$ flakes	290	72	1 M KOH	100	[53]
Nanosheet-like $Co_3(OH)_2(HPO_4)_2$	290	82	1 M KOH	8%	[54]
$Co_xNi_{1x}S_2$, CNS)	290	46	1 M KOH	10	[55]
Mn_3O_4@$Co_xMn_{3-x}O_4$	284	73.1	1 M KOH	20	[56]
Cu_2S/TiO_2/Cu_2S core-branch arrays	284	72	1 M KOH	–	[57]
$CoSe_2$ ultrathin nanomeshes	284	46.3	1 M KOH	20	[58]

(continued)

Table 1 (continued)

Catalyst	Overpotential (mV vs. RHE @10 $mAcm^{-2}$)	Tafel slope (mV dec^{-1})	pH (or electrolyte)	Stability (hrs) (or %degradation)	Refs
CoNi oxyhydroxide nanosheet	279	32	1 M KOH	60	[59]
$3DMo_1Ni_1P$ hollow nanoflowers	275	56.3	1 M KOH	36	[60]
Co/Fe double hydroxide nanofilm	275	34	1 M KOH	10	[61]
$AgCoO_2$ (ACO)	271	–	1 M KOH	2.58%	[62]
e–Co based bimetallic Prussian blue analog	271	53.7	1 M KOH	24	[63]
P-NiFe-800 NPs	270.1	39	1 M KOH	12	[64]
Co_3O_4 2D nanosheets	270	46	13.6		[33]
Mn_2O_3 nanotube arrays	270	85	1 M KOH	10%	[65]
$Co_{0.15}Fe_{0.85}N_{0.5}$	266	30	1 M KOH	90	[66]
Excavated trimetallic Prussian blue analogue	261	38	1 M KOH	15	[67]
$Co_{1-x}S$ embedded in porous carbon	260	85	1 M KOH	80	[68]
Fe_1Co_3/VO-800	260	53	1 M KOH	15	[69]
NiOOH-decorated α-FeOOH nanosheet array	256	45	1 M KOH	53.8% (30 h)	[70]
IrO_2@Ir	255	45	1 M KOH	–	[71]
NieFeeSn film	253	61.5	1 M KOH	12	[72]
$Fe_xNi_{1-x}Se_2$ nanotubes	253	49	1 M	10	[73]
2D Nanolayers of Ni(II) doped	239	90.4	pH = 9	–	[74]
Ultrathin wrinkled $Ni_1Fe_{0.8}P$ nanosheets	237	39.7	1 M KOH	30	[75]
Plasma modified C-doped Co_3O_4 nanosheets	235	83	0.1 M KOH	10	[76]
Co_3O_4 nanosheets (Co_xO_{y-0}) were treated under NH3 plasma	234	68	0.1 M KOH	–	[76]
CoCo-LDH 2D nanomesh layered double hydroxide	220	42	1 M KOH	6	[77]
3D binder-free np-$Ir_{70}Ni_{15}Co_{15}$	220	44.1	0.1 M $HClO_4$	24	[78]
triple Hierarchy and Double Synergies of NiFe/Co_9S_8/Carbon Cloth	219	55	1 M KOH	20	[79]
Ni Foam Supported Fe-doped	219	53	1 M KOH	–	[80]
D Fe-containing cobalt phosphide/cobalt oxide (Fe-CoP/CoO)	219	52	1 M KOH	12	[81]
$Mn_{0.8}Ir_{0.2}$)O2:10F(fluorine)	200	38	1 N H_2SO_4	24	[82]

(continued)

Table 1 (continued)

Catalyst	Overpotential (mV vs. RHE @10 $mAcm^{-2}$)	Tafel slope (mV dec^{-1})	pH (or electrolyte)	Stability (hrs) (or %degradation)	Refs
NiFe alloy onto three-dimension nickel foam	191	44.1	1 M KOH	9	[83]
Mo_6Ni_6C precatalyst reconstructing in the bulk form small MoNi alloys clusters interconnected with atomically dispersed carbon	190	65.35	1 M KOH	100	[84]
$Cr_{0.6}Ru_{0.4}O_2$	178	58	0.5 M H_2SO_4	10	[85]
CoP_2@3D-NPC	167 (@20mAcm-2)	59	1 M	8	[86]
CoP_2@3D-NPC	126	–	0.5 M H_2SO_4	8	[86]
$PrBaCo_{2(1-x)}Fe_{2x}O_{6-\delta}$ (PBCF55)	–	50	0.1 M KOH	32%	[87]
$Cu_2WS_{3.4}P_{0.6}$	–	194	–	24	[88]

Ferroelectricity constitutes a novel feature (as it is indicated by the limited number of relative publications) of metal perovskite oxides which can be given to them via special techniques. Perovskite metal oxides structure is ABO_3, where A and B are cations. Their powerful structure omits to intervene to materials properties for tunable effects into the e_g filling for succeeding an ideal electron occupancy [89].

3.3 Double Perovskites

In double perovskites $AA'BB'O_6$ the A and B are replaced with a different cation delivering enhanced OER electrocatalytic properties. More precisely, when B is substituted by another transition metal, the d-band center shifts closer to the Fermi level. Moreover when p-band centre of O moves to an appropriate position to Fermi level double perovskites exhibit stable structure during OER [90]. Today, the high durability, intrinsic activity and mass activity still remain the main challenges of this groups of materials [91].

A double perovskite $LaFe_xNi_{1-x}O_3$ (LFNO) nanorods (NRs) was reported by Wang et al. [48, 52]. The authors attributed the good catalysts OER activity to the tailored electronic structure and the strong hybridization between O and Ni (Table 1). Sun et al. managed to interact active sites by designing a novel $Sr_2Fe_{0.8}Co_{0.2}Mo_{0.65}Ni_{0.35}O_{6-\delta}$ double perovskite electrocatalyst [44]. More specifically step by step they substituted Mo-sites with Ni and Fe-sites by Co establishing in this way a synergistic interplay among the transition metal elements. As it is reported

in Table the as-prepared material show a 310 mV overpotential value, with a 56 mV dec^{-1} Tafel slope.

Among the studied double perovskites the $PrBaCo_2O_{6-\delta}$ (PBC) layered one has been identified as the most promising, in alkaline media [92]. In general since the involvement of lattice oxygen in LOER mechanism does not require the cover of the catalysts surface with OH^- from the alkaline electrolyte, the layered double perovskite oxides are benefited. To be more specific, the A-site ordering restrains the oxygen vacancies that are present into the layers hence promoting the oxygen mobility.

After this finding several studies have been focused on investigating the role of Fe in Co-based perovskite oxides. It was found that the insertion of Fe to PBC ($PrBaCo_{2(1-x)}Fe_{2x}O_{6-\delta}$) reduces the Tafel slope from 72 to 50 $mVdec^{-1}$. Additionally, the insertion of Fe inhibits the Co corrosion whose layer serve as oxy(hydroxide) layer.

One key-element of enhanced OER activity is the as above-mentioned oxy(hydroxide) layer that the B cations form (Co/Fe) when we refer to $Ba_{0.5}Sr_{0.5}Co_{0.8}Fe_{0.2}O_{3-\delta}$ [87]. This is a self-assembled layer which is evolved due to the LOER mechanism. The high oxygen vacancy in combination with the structural flexibility facilitate the LOER mechanism.

3.4 Studied Materials in 2019 Literature

The main key-issues for the development of OER electrocatalysts are: (i) the high overpotential, (ii) the high Tafel slope and (iii) the stability. It is known that at pH = 0, at 25 °C an $E_{eq} = 1.23$ V versus NHE potential shall be applied in order water electrolysis reaction to occur. In literature for it has been established the overpotential value to be referred at 10 mA cm^{-2} current density. In Table 1 are reported the overpotential values η_{10} of a big sample of 2019 publications.

The value of Tafel slope indicates the electrocatalyst 'behavior' with the reactnats. A low value of Tafel slope implies good electrocatalytic activity. When a Tafel slope is lower means that with a small overpotential change (meaning faster reaction rate) the current density increases faster. Finally, stability is a parameter of the same importance with overpotential and Tafel slope. This is measured even in galvanostatic or in potentiostatic mode and usually must exceed the 24 h in order to say that the material is very stable.

Comparing the as-reported in Table 1 materials, it is characteristic that the majority of the materials show overpotential values into the range 200–300 mV versus RHE. The lowest η_{10} was reported 126 mV, but in acidic media [86] presenting so the disadvantage of short time stability, only for 8 h. In alkaline media (comparable to acidic media) the lowest reported overpotential (190 mV) at 10 mA cm^{-2} [84] show 100 h stability indicating the better performance that the electrocatalyst

present in alkaline media. The electrocatalyst with those characteristics was a three-dimensional one (CoP_2@3D-NPC). In general 3D materials offer the possibility of higher electrochemical active surface area [93].

It is not random that almost all the experimental investigations take place in alkaline electrolyte (Table 1). Up-to-date, there have not been fabricated any material that will fulfill the low overpotential and Tafel values along with the very high stability. This will be succeeded only of OER mechanism is fully realized.

Acknowledgements Dr. Angeliki Brouzgou thankfully acknowledges the post-doc program: "Strengthening Postdoctoral Researchers", co-funded by the Greek State Scholarships Foundation, the "Human Resource Development, Education and Lifelong Learning with Priority Axes 6,8,9, by the European Commission Social Fund-ECB and the Greek government".

References

1. Chapman A, Itaoka K, Hirose K, Davidson FT, Nagasawa K, Lloyd AC, Webber ME, Kurban Z, Managi S, Tamaki T (2019) A review of four case studies assessing the potential for hydrogen penetration of the future energy system. Int J Hydrogen Energy
2. Jing S, Zhang Y, Chen F, Liang H, Yin S, Tsiakaras P (2019) Novel and highly efficient cathodes for Li-O_2 batteries: 3D self-standing NiFe@NC-functionalized N-doped carbon nanonet derived from Prussian blue analogues/biomass composites. Appl Catal B 245:721–732
3. Maggio G, Nicita A, Squadrito G (2018) How the hydrogen production from RES could change energy and fuel markets. A review of recent literature. In: Transforming energy markets, 41st IAEE international conference, 10–13 June 2018. International Association for Energy Economics
4. Godula-Jopek A, Stolten D (2015) Hydrogen production: by electrolysis. Wiley, Germany
5. Zu C-X, Li H (2011) Thermodynamic analysis on energy densities of batteries. Energy Environ Sci 4:2614–2624
6. Lu C-T, Chiu Y-W, Li M-J, Hsueh K-L, Hung J-S (2017) Reduction of the electrode overpotential of the oxygen evolution reaction by electrode surface modification. Int J Electrochem
7. Wendt H, Kreysa G (2013) Electrochemical engineering: science and technology in chemical and other industries. Springer, Berlin Heidelberg, Germany
8. Pera MC, Hissel D, Gualous H, Turpin C (2013) Electrochemical components. Wiley, USA
9. Fabbri E, Schmidt TJ (2018) Oxygen evolution reaction—the enigma in water electrolysis. ACS Publications
10. Casselberry E, Edgerton NH (1874) Electrolytic apparatus. USA patent application
11. Bockris JM (1954) Modern aspects of electrode kinetics. Annu Rev Phys Chem 5:477–500
12. Bockris JOM, Shamshul Huq A (1956) The mechanism of the electrolytic evolution of oxygen on platinum. Proc R Soc London Ser A Math Phys Sci 237:277–296
13. Wade WH, Hackerman N (1957) Anodic phenomena at an iron electrode. Trans Faraday Soc 53:1636–1647
14. Conway B, Bourgault P (1959) The electrochemical behavior of the nickel–nickel oxide electrode: Part I. Kinetics of self-discharge. Can J Chem 37:292–307
15. Krasilshchikov AI (1963) Intermediate stages of anodic oxygen evolution. Russ J Phys Chem 37:273
16. Tsinman AI (1963) Zh. Fiz. Khim 37:273
17. Sato N, Okamoto G (1965) Reaction mechanism of anodic oxygen evolution on nickel in sulphate solutions. Electrochim Acta 10:495–502

18. Damjanovic A, Jovanovic B (1976) Anodic oxide films as barriers to charge transfer in O_2 evolution at Pt in acid solutions. J Electrochem Soc 123:374–381
19. Hoare JP (1975) J Phys Chem 79:2175
20. O' Grady W, Iwakura C, Hnang J, Yeager E (1976) In: Breiter MW (ed) Proceedings of the symposium on Efecrrocaralysis, Princeton. ECS, pp 286–301
21. O'Grady W, Iwakura C, Yeager E (1976) American Society of Mechanical Engineers 76-ENAS-37
22. Miles M, Klaus E, Gunn B, Locker J, Serafin W, Srinivasan S (1978) The oxygen evolution reaction on platinum, iridium, ruthenium and their alloys at 80 °C in acid solutions. Electrochim Acta 23:521–526
23. Bronoel G, Reby J (1980) Mechanism of oxygen evolution in basic medium at a nickel electrode. Electrochim Acta 25:973–976
24. Bockris JOM, Otagawa T (1983) Mechanism of oxygen evolution on perovskites. J Phys Chem 87:2960–2971
25. Wohlfahrt-Mehrens M, Heitbaum J (1987) Oxygen evolution on Ru and RuO_2 electrodes studied using isotope labelling and on-line mass spectrometry. J Electroanal Chem Interfacial Electrochem 237:251–260
26. Matsumoto Y, Sato E (1986) Electrocatalytic properties of transition metal oxides for oxygen evolution reaction. Mater Chem Phys 14:397–426
27. Surendranath Y, Kanan MW, Nocera DG (2010) Mechanistic studies of the oxygen evolution reaction by a cobalt-phosphate catalyst at neutral pH. J Am Chem Soc 132:16501–16509
28. Wang H, Lee H-W, Deng Y, Lu Z, Hsu P-C, Liu Y, Lin D, Cui Y (2015) Bifunctional non-noble metal oxide nanoparticle electrocatalysts through lithium-induced conversion for overall water splitting. Nat Commun 6:7261
29. Binninger T, Mohamed R, Waltar K, Fabbri E, Levecque P, Kötz R, Schmidt TJ (2015) Thermodynamic explanation of the universal correlation between oxygen evolution activity and corrosion of oxide catalysts. Sci Rep 5:12167
30. Fabbri E, Nachtegaal M, Binninger T, Cheng X, Kim B-J, Durst J, Bozza F, Graule T, Schäublin R, Wiles L (2017) Dynamic surface self-reconstruction is the key of highly active perovskite nano-electrocatalysts for water splitting. Nat Mater 16:925
31. Chen D, Chen C, Baiyee ZM, Shao Z, Ciucci F (2015) Nonstoichiometric oxides as low-cost and highly-efficient oxygen reduction/evolution catalysts for low-temperature electrochemical devices. Chem Rev 115:9869–9921
32. Suntivich J, May KJ, Gasteiger HA, Goodenough JB, Shao-Horn Y (2011) A perovskite oxide optimized for oxygen evolution catalysis from molecular orbital principles. Science 334(6061):1383–1385
33. Zhang W, Zhou K (2017) Ultrathin two-dimensional nanostructured materials for highly efficient water oxidation. Small 13:1700806
34. Li X, Liu H, Chen Z, Wu Q, Yu Z, Yang M, Wang X, Cheng Z, Fu Z, Lu Y (2019) Enhancing oxygen evolution efficiency of multiferroic oxides by spintronic and ferroelectric polarization regulation. Nat Commun 10:1409
35. Li J, Chen H, Liu Y, Gao R, Zou X (2019) In situ structural evolution of a nickel boride catalyst: synergistic geometric and electronic optimization for the oxygen evolution reaction. J Mater Chem A 7:5288–5294
36. Gu W, Li X, Zhang W, Wang J, Yin X, Zhu L, Chen Z, Zou W, Fu Z, Lu Y (2019) Self-limited ion-exchange grown $Bi_6Fe_2Ti_3O_{18}$-BiOBr ferroelectric heterostructure and the enhanced photocatalytic oxygen evolution. Appl Surf Sci 479:137–147
37. Geerts L, Cosentino S, Liao T-W, Yadav A, Lin P-C, Zharinov VS, Hu K-J, Longo A, Pereira LM, Grandjean D (2019) Highly active oxygen evolution reaction model electrode based on supported gas-phase NiFe clusters. Catal Today
38. Shanmugam S, Sivanantham A, Matsunaga M, Simon U, Osaka T (2019) Metal phosphide nanoparticles embedded in carbon as efficient electrocatalyst for oxygen evolution reaction. Electrochim Acta 297:749–754

39. Guo C, Sun X, Kuang X, Gao L, Zhao M, Qu L, Zhang Y, Wu D, Ren X, Wei Q (2019) Amorphous Co-doped MoOx nanospheres with a core–shell structure toward an effective oxygen evolution reaction. J Mater Chem A 7(3):1005–1012
40. Xu P, Qiu L, Wei L, Liu Y, Yuan D, Wang Y, Tsiakaras P (2019) Efficient overall water splitting over Mn doped Ni_2P microflowers grown on nickel foam. Catal Today
41. Lu M, Li Y, He P, Cong J, Chen D, Wang J, Wu Y, Xu H, Gao J, Yao J (2019) Bimetallic metal-organic framework nanosheets as efficient electrocatalysts for oxygen evolution reaction. J Solid State Chem 272:32–37
42. Zhang K, Xia X, Deng S, Xie D, Lu Y, Wang Y, Wu J, Wang X, Tu J (2019) N-doped CoO nanowire arrays as efficient electrocatalysts for oxygen evolution reaction. J Energy Chem 37:13–17
43. Liu Z, Yuan C, Teng F, Tang M, Abideen ZU, Teng Y (2019) First insight on Mo (II) as electrocatalytically active species for oxygen evolution reaction. Int J Hydrogen Energy 44:1345–1351
44. Sun H, Xu X, Hu Z, Tjeng LH, Zhao J, Zhang Q, Lin H-J, Chen C-T, Chan T-S, Zhou W, Shao Z (2019) Boosting the oxygen evolution reaction activity of a perovskite through introducing multi-element synergy and building an ordered structure. J Mater Chem A 7:9924–9932
45. Chen H, Zhao Q, Gao L, Ran J, Hou Y (2019) Water-plasma assisted synthesis of oxygen-enriched Ni-Fe layered double hydroxide nanosheets for efficient oxygen evolution reaction. ACS Sustain Chem Eng
46. Jiang Z-Q, Li Y-F, Zhu X-J, Lu J, Wen T, Zhang L (2019) Ni (ii)-doped anionic metal–organic framework nanowire arrays for enhancing the oxygen evolution reaction. Chem Commun
47. Lu J, Wang S, Ding C, Lv W, Zeng Y, Liu N, Wang H, Meng Q, Liu Q (2019) Metal organic frameworks derived $CoSe_2$@ N-Doped-carbon-nanorods as highly efficient electrocatalysts for oxygen evolution reaction. J Alloy Compd 778:134–140
48. Wang H, Wang J, Pi Y, Shao Q, Tan Y, Huang X (2019) Double Perovskite $LaFexNi_{1-x}O_3$ nanorods enable efficient oxygen evolution electrocatalysis. Angew Chem Int Ed 58:2316–2320
49. Ke Z, Li L, Jia Q, Yang Y, Cui H (2019) Facile synthesis of jagged Au/Ir nanochains with superior electrocatalytic activity for oxygen evolution reaction. Appl Surf Sci 463:58–65
50. Fu H, Liu Y, Chen L, Shi Y, Kong W, Hou J, Yu F, Wei T, Wang H, Guo X (2019) Designed formation of $NiCo_2O_4$ with different morphologies self-assembled from nanoparticles for asymmetric supercapacitors and electrocatalysts for oxygen evolution reaction. Electrochim Acta 296:719–729
51. Guo M, Li Y, Zhou L, Zheng Q, Jie W, Xie F, Xu C, Lin D (2019) Hierarchically structured bimetallic electrocatalyst synthesized via template-directed fabrication MOF arrays for high-efficiency oxygen evolution reaction. Electrochim Acta 298:525–532
52. Wang S, He P, Jia L, He M, Zhang T, Dong F, Liu M, Liu H, Zhang Y, Li C (2019) Nanocoral-like composite of nickel selenide nanoparticles anchored on two-dimensional multi-layered graphitic carbon nitride: a highly efficient electrocatalyst for oxygen evolution reaction. Appl Catal B 243:463–469
53. Jadhav HS, Roy A, Thorat GM, Chung W-J, Seo JG (2019) Hierarchical free-standing networks of $MnCo_2S_4$ as efficient Electrocatalyst for oxygen evolution reaction. J Ind Eng Chem 71:452–459
54. Lu W-X, Wang B, Chen W-J, Xie J-L, Huang Z-Q, Jin W, Song J-L (2019) Nanosheet-like $Co_3(OH)_2(HPO_4)_2$ as a highly efficient and stable electrocatalyst for oxygen evolution reaction. ACS Sustain Chem Eng 7:3083–3091
55. Hong Y-R, Mhin S, Kim K-M, Han W-S, Choi H, Ali G, Chung KY, Lee HJ, Moon S-I, Dutta S (2019) Electrochemically activated cobalt nickel sulfide for an efficient oxygen evolution reaction: partial amorphization and phase control. J Mater Chem A 7:3592–3602
56. Hu C, Zhang L, Huang Z, Zhu W, Zhao Z-J, Gong J (2019) Facet-evolution growth of Mn_3O_4@ $Co_xMn_{3-x}O_4$ electrocatalysts on Ni foam towards efficient oxygen evolution reaction. J Catal 369:105–110
57. Deng S, Shen Y, Xie D, Lu Y, Yu X, Yang L, Wang X, Xia X, Tu J (2019) Directional construction of Cu_2S branch arrays for advanced oxygen evolution reaction. J Energy Chem 39:61–67

58. Zhang Y, Zhang C, Guo Y, Liu D, Yu Y, Zhang B (2019) Selenium vacancy-rich $CoSe_2$ ultrathin nanomeshes with abundant active sites for electrocatalytic oxygen evolution. J Mater Chem A 7:2536–2540
59. Yu C, Lu J, Luo L, Xu F, Shen PK, Tsiakaras P, Yin S (2019) Bifunctional catalysts for overall water splitting: CoNi oxyhydroxide nanosheets electrodeposited on titanium sheets. Electrochim Acta 301:449–457
60. Chen S, Dai J, Ren F, Xu H, Du Y (2019) 3D hollow nanoflowers assembled by ultrathin molybdenum-nickel phosphide nanosheets as robust electrocatalysts for oxygen evolution reaction. J Colloid Interface Sci 536:71–79
61. Liu S, Liu B, Gong C, Li Z (2019) Finely prepared and optimized Co/Fe double hydroxide nanofilms at an ionic layer level on rough Cu substrates for efficient oxygen evolution reaction. Appl Surf Sci 478:615–622
62. Zhang R, Sun Z, Zong C, Lin Z, Huang H, Yang K, Chen J, Liu S, Huang M, Yang Y (2019) Increase of Co 3d projected electronic density of states in $AgCoO_2$ enabled an efficient electrocatalyst toward oxygen evolution reaction. Nano Energy 57:753–760
63. Zhang W, Song H, Cheng Y, Liu C, Wang C, Khan MAN, Zhang H, Liu J, Yu C, Wang L (2019) Core–shell prussian blue analogs with compositional heterogeneity and open cages for oxygen evolution reaction. Adv Sci 6(7):1801901
64. Gao W-K, Chi J-Q, Wang Z-B, Lin J-H, Liu D-P, Zeng J-B, Yu J-F, Wang L, Chai Y-M, Dong B (2019) Optimized bimetallic nickel-iron phosphides with rich defects as enhanced electrocatalysts for oxygen evolution reaction. J Colloid Interface Sci 537:11–19
65. Liu P-P, Zheng Y-Q, Zhu H-L, Li T-T (2019) Mn_2O_3 hollow nanotube arrays on Ni foam as efficient supercapacitors and electrocatalysts for oxygen evolution reaction. ACS Appl Nano Mater 2:744–749
66. An L, Feng J, Zhang Y, Zhao Y-Q, Si R, Wang G-C, Cheng F, Xi P, Sun S (2019) Controllable tuning of Fe-N nanosheets by Co substitution for enhanced oxygen evolution reaction. Nano Energy 57:644–652
67. Liu J, Wei S, Li N, Zhang L, Cui X (2019) Delicate excavated trimetallic Prussian blue analogues for efficient oxygen evolution reactions. Electrochim Acta 299:575–581
68. He D, Wu X, Liu W, Lei C, Yu C, Zheng G, Pan J, Lei L, Zhang X (2019) $Co_{1-x}S$ embedded in porous carbon derived from metal organic framework as a highly efficient electrocatalyst for oxygen evolution reaction. Chin Chem Lett 30:229–233
69. Chen W, Zhang Y, Chen G, Huang R, Zhou Y, Wu Y, Hu Y, Ostrikov KK (2019) Mesoporous cobalt–iron–organic frameworks: a plasma-enhanced oxygen evolution electrocatalyst. J Mater Chem A 7:3090–3100
70. Zhang D, Kong X, Jiang M, Lei D, Lei X (2019) NiOOH-decorated α-FeOOH nanosheet array on stainless steel for applications in oxygen evolution reaction and supercapacitor. ACS Sustain Chem Eng
71. Zhong W, Lin Z, Feng S, Wang D, Shen S, Zhang Q, Gu L, Wang Z, Fang B (2019) Improved oxygen evolution activity of IrO_2 by in situ engineering of an ultra-small Ir sphere shell utilizing a pulsed laser. Nanoscale 11:4407–4413
72. Wu Y, Gao Y, He H, Zhang P (2019) Electrodeposition of self-supported Ni–Fe–Sn film on Ni foam: An efficient electrocatalyst for oxygen evolution reaction. Electrochim Acta 301:39–46
73. Qiu B, Cai L, Wang Y, Ma S, Tsang YH, Chai Y (2019) Accelerated oxygen evolution kinetics on nickel–iron diselenide nanotubes by modulating electronic structure. Mater Today Energy 11:89–96
74. Tolstoy V, Kuklo L, Gulina L (2019) Ni (II) doped FeOOH 2D nanocrystals, synthesized by Successive Ionic Layer Deposition, and their electrocatalytic properties during oxygen evolution reaction upon water splitting in the alkaline medium. J Alloy Compd 786:198–204
75. Tian L, Wo H, Wang K, Wang X, Zhuang W, Li T, Du X (2019) Ultrathin wrinkled NiFeP nanosheets enable efficient oxygen evolution electrocatalysis. J Taiwan Inst Chem Eng 97:200–206
76. Xu A, Dong C, Wu A, Li R, Wang L, Macdonald DD, Li X (2019) Plasma-modified C-doped Co_3O_4 nanosheets for the oxygen evolution reaction designed by Butler-Volmer and first-principle calculations. J Mater Chem A 7:4581–4595

77. Qin M, Li S, Zhao Y, Lao CY, Zhang Z, Liu L, Fang F, Wu H, Jia B, Liu Z (2019) Unprecedented synthesis of Holey 2D layered double hydroxide nanomesh for enhanced oxygen evolution. Adv Energy Mater 9:1803060
78. Zhao Y, Luo M, Chu S, Peng M, Liu B, Wu Q, Liu P, de Groot FM, Tan Y (2019) 3D nanoporous iridium-based alloy microwires for efficient oxygen evolution in acidic media. Nano Energy 59:146–153
79. Zhan C, Liu Z, Zhou Y, Guo M, Zhang X, Tu J, Ding L, Cao Y (2019) Triple hierarchy and double synergies of NiFe/Co_9S_8/carbon cloth: a new and efficient electrocatalyst for the oxygen evolution reaction. Nanoscale 11:3378–3385
80. Kou T, Wang S, Hauser JL, Chen M, Oliver SRJ, Ye Y, Guo J, Li Y (2019) Ni foam-supported Fe-Doped β-$Ni(OH)_2$ nanosheets show ultralow overpotential for oxygen evolution reaction. ACS Energy Lett 4:622–628
81. Hu X, Zhang S, Sun J, Yu L, Qian X, Hu R, Wang Y, Zhao H, Zhu J (2019) 2D Fe-containing cobalt phosphide/cobalt oxide lateral heterostructure with enhanced activity for oxygen evolution reaction. Nano Energy 56:109–117
82. Ghadge SD, Velikokhatnyi OI, Datta MK, Shanthi PM, Tan S, Damodaran K, Kumta PN (2019) Experimental and theoretical validation of high efficiency and robust electrocatalytic response of one-dimensional (1D) (Mn, Ir)O_2:10F nanorods for the oxygen evolution reaction in PEM-based water electrolysis. ACS Catalysis 9:2134–2157
83. Jin J, Xia J, Qian X, Wu T, Ling H, Hu A, Li M, Hang T (2019) Exceptional electrocatalytic oxygen evolution efficiency and stability from electrodeposited NiFe alloy on Ni foam. Electrochim Acta 299:567–574
84. Zu MY, Wang C, Zhang L, Zheng LR, Yang HG (2019) Reconstructing bimetallic carbide Mo_6Ni_6C for carbon interconnected MoNi alloys to boost oxygen evolution electrocatalysis. Mater Horiz 6:115–121
85. Lin Y, Tian Z, Zhang L, Ma J, Jiang Z, Deibert BJ, Ge R, Chen L (2019) Chromium-ruthenium oxide solid solution electrocatalyst for highly efficient oxygen evolution reaction in acidic media. Nat Commun 10:162
86. Yang S, Xie M, Chen L, Wei W, Lv X, Xu Y, Ullah N, Judith OC, Adegbemiga YB, Xie J (2019) Cobalt phosphide nanoparticles embedded in 3D N-doped porous carbon for efficient hydrogen and oxygen evolution reactions. Int J Hydrogen Energy 44:4543–4552
87. Kim B-J, Fabbri E, Abbott DF, Cheng X, Clark AH, Nachtegaal M, Borlaf M, Castelli IE, Graule T, Schmidt TJ (2019) Functional role of Fe-doping in Co-based perovskite oxide catalysts for oxygen evolution reaction. J Am Chem Soc 141:5231–5240
88. Novak TG, Prakash O, Tiwari AP, Jeon S (2019) Solution-phase phosphorus substitution for enhanced oxygen evolution reaction in Cu_2WS_4. RSC Adv 9:234–239
89. Hwang J, Feng Z, Charles N, Wang XR, Lee D, Stoerzinger KA, Muy S, Rao RR, Lee D, Jacobs R, Morgan D, Shao-Horn Y (2019) Tuning perovskite oxides by strain: Electronic structure, properties, and functions in (electro)catalysis and ferroelectricity. Mater Today
90. Grimaud A, May KJ, Carlton CE, Lee Y-L, Risch M, Hong WT, Zhou J, Shao-Horn Y (2013) Double perovskites as a family of highly active catalysts for oxygen evolution in alkaline solution. Nat Commun 4:2439
91. Zhao B, Zhang L, Zhen D, Yoo S, Ding Y, Chen D, Chen Y, Zhang Q, Doyle B, Xiong X (2017) A tailored double perovskite nanofiber catalyst enables ultrafast oxygen evolution. Nat Commun 8:14586
92. Han B, Shao-Horn Y (2018) In-situ study of the activated lattice oxygen redox reactions in metal oxides during oxygen evolution catalysis. In: Meeting abstracts. The Electrochemical Society, pp 1935–1935
93. Cai S, Meng Z, Tang H, Wang Y, Tsiakaras P (2017) 3D Co-N-doped hollow carbon spheres as excellent bifunctional electrocatalysts for oxygen reduction reaction and oxygen evolution reaction. Appl Catal B 217:477–484
94. Xu L, Zou Y, Xiao Z, Wang S (2019) Transforming Co_3O_4 nanosheets into porous N-doped Co_xO_y nanosheets with oxygen vacancies for the oxygen evolution reaction. J Energy Chem 35:24–29

Electrocatalysts for Photochemical Water-Splitting

Shankara S. Kalanur and Hyungtak Seo

Abstract The photochemical water splitting to produce O_2 and H_2 is considered as the most promising, sustainable, renewable and cost-effective energy technology for the future. In photochemical water splitting process, the efficiency of H_2 and O_2 production rates depends on the properties of the selected semiconductor material. However, most of the semiconductors face various limitations which confines their water splitting efficiency. Different strategies could be implemented to improve the water splitting efficiency of semiconductors. Among them, loading of catalyst onto the water splitting material is known to be one of the effective strategy to enhance the H_2 and O_2 production rates. Given this, several catalytic materials have been explored and successfully utilized in efficient O_2 and H_2 production systems. In this chapter, we summarize some of the effective O_2 and H_2 production catalysts derived from noble metal, noble metal oxides, earth-abundant metals and oxides, metal phosphides and metal chalcogenides. The surface deposited catalysts were known to reduce the surface trap states, which decreases the charge recombination and acts as protective layer to minimize photo-corrosion of the light absorbing semiconductors. Conclusively, to explore the efficient catalysts for photochemical water splitting require more research contribution towards the understanding of the core reaction mechanism of catalytic process with the use of sustainable and stable materials.

Keywords Photochemical water splitting · Catalysts · Noble metals · Metal oxides · Gas production

S. S. Kalanur (✉) · H. Seo
Department of Materials Science and Engineering, Ajou University,
Suwon 443-739, Republic of Korea
e-mail: shankarask@ajou.ac.kr; skshankara@gmail.com

Inamuddin et al. (eds.), *Methods for Electrocatalysis*,
https://doi.org/10.1007/978-3-030-27161-9_7

1 Introduction

1.1 General

A viable alternative to the depleting fossil fuels is in high demand to cope with the future energy requirements that backbones the industrial and economic advancements [6, 72]. Moreover, the extensive usage of fossil fuels requires stricter restriction to protect the environment and the global climate [96]. Therefore, the production and the utilization of a viable alternative energy source to fossil fuels must be sustainable and renewable. Moreover, the production of energy sources must par the requirement and the global demand and should be primarily derived from the abundant resources such as solar, wind, geothermal etc., and at the same time environment-friendly with a minimal impact. Based on these critical requirements, the scientific community has been working intensively to explore and develop a sustainable and renewable source of energy for the future.

At present, a variety of renewable and sustainable energy technologies are being utilized in society. However, to meet the commercial necessity and to serve as energy on demand, the proposed energy source needs to fulfil the crucial requirements such as efficiently storable, transportable and accessible whenever required [102]. Currently, solar power is considered as one of the significant clean energy contributing source along with wind and other means of green energy production technology [55]. However, the solar energy or other means of energy production routes are limited due to the day and night rotations, weather factors, climate conditions and economic viability [92]. Moreover, the storage and transportation of such energy sources face various limitations. Therefore, a clean, sustainable and renewable source of energy is required, which could be easily storable, transportable and importantly must provide energy on demand.

Based on the above crucial requirements and the available energy sources, the hydrogen (H_2) gas emerge as a best clean energy candidate because it is storable, transportable and could be easily accessible whenever required [41]. Importantly, the hydrogen as a source of energy is considered to be the worthy alternatives to fossil fuels for future energy advancements and economy. By using a fuel cell system, the hydrogen gas could be utilized to produce electricity on demand and could be effectively employed in vehicles and industries as a clean energy production system [20, 94]. In the fuel cell system, a thermodynamically favourable reaction is utilized in which H_2 and oxygen were combined to undergo reaction yielding electricity as the primary energy product along with water as a waste product. Also, H_2 could also be employed in CO_2 conversion reaction into useful chemicals that help in protecting the environment by decreasing carbon footprint [76]. Conclusively, H_2 could play a vital role in mitigating climate change and ocean acidification [81]. Therefore, H_2 is currently considered as a future energy carrier and the best alternative to fossil fuels [40].

1.2 H_2 Production Routes

The efficient, clean, sustainable and economical production of H_2 becomes a vital task based on the significant role and impact it can contribute to the future energy system and economy. The H_2 can be produced by a variety of methods derived explicitly from the hydrogen-containing molecules. Currently, the most widely used hydrogen production methods (Fig. 1) include electrolysis (electricity is used across specific electrodes to split water), biological process (the interaction of microbes such as bacterias and microalgae using sunlight or organic matter), solar water splitting (the semiconductors exposed to light in an electrolyte to split water to hydrogen), thermally assisted water splitting (utilization of thermal energy in reactors to break water into H_2), cracking of petroleum and hydrocarbon reforming (the reaction of natural gas with steam), fermentation (H_2 production by the fermentation of sugar-rich feedstocks derived from biomass), renewable liquid reforming (producing H_2 from high-temperature reaction of ethanol) [3, 15, 30]. These methods are different from each other based on their, production efficiency, rate, cost-effectiveness and mainly the impact on the environment.

The total amount of H_2 produced by combining all the above methods is incapable of satisfying the production requirement and accounts for only 3% of energy demand

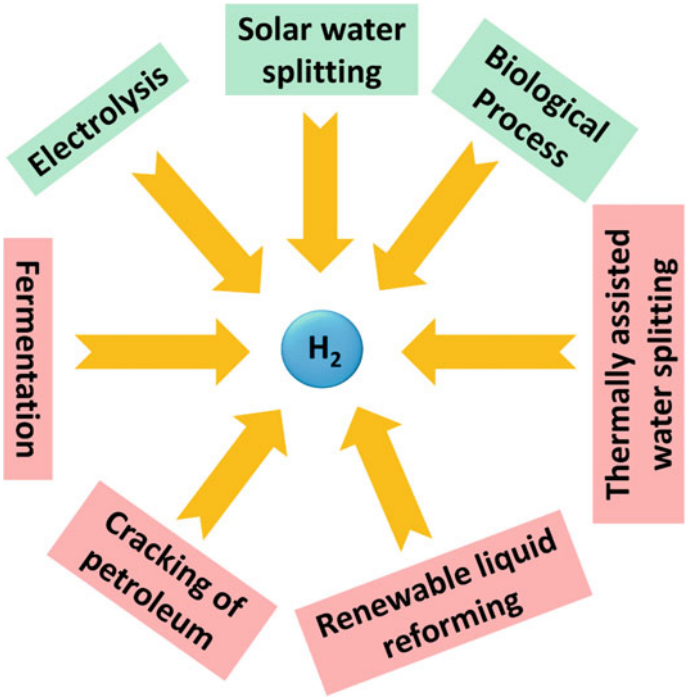

Fig. 1 Various routes of producing hydrogen gas

globally [4, 18]. At present, the major portion of the hydrogen is produced via steam reforming of fossil fuels or by the partial oxidation of methane and coal gasification [3]. Whereas, cleaner techniques such as water electrolysis and solar water splitting are rarely used. Moreover, the steam reforming process of fossil fuels is believed to be the most efficient and cost-effective method. Unfortunately, the steam reforming process of hydrogen production is not viable for future energy demand as the fossil fuels are depleting. Importantly, the steam reforming process produces enormous amounts of greenhouse gases, which are the primary concern of global warming. Therefore, a sustainable and renewable route of hydrogen synthesis needs to be explored and practically made viable to meet the energy demand without harming the environment. Given this, the hydrogen production routes such as electrolysis and solar assisted water splitting could play a significant role in the future energy systems. Despite being clean, sustainable and renewable nature of the electrolysis and solar water-splitting methods; these routes are known to be inefficient in producing H_2 and importantly less cost-effective. Therefore, the practical application of these techniques face a considerable challenge and require a great deal of scientific advancement. Thus the future of sustainable and renewable energy technology depends on the level of research contribution in these fields.

2 Water Splitting

2.1 Solar Water Splitting

Among the available and sustainable hydrogen production routes, the solar water splitting was found to be the most promising future energy technology as it utilizes the most renewable, abundant and exploitable resources such as solar energy and water [46]. The solar water splitting process captures and stores solar energy in the form of H_2 molecule without producing any undesirable pollutants [36, 50]. Consequently, thus produced hydrogen can be storable, transportable and accessible based on the requirements via fuel cell system. The first successful water splitting process under sunlight was demonstrated using TiO_2 semiconductor in 1972 [24], and that initiated tremendous research establishing significant milestones and outcomes. As seen from the Fig. 2, a rapid increase in the number of publication since last ten years indicates the dedication and research contribution towards the optimization and exploration of suitable of materials and system for the efficient solar water splitting reaction. Such an increase in the research contribution mainly indicates the significance of solar water splitting technology and its potential to meet the energy demand of the future.

The mechanism of solar water splitting involves the dissociation of a water molecule into H_2 and O_2 (present in the solution) at the material surface in the presence of light. The photoexcited electrons and holes produced in the material are known to drive the water oxidation and reduction reactions. Hence, the semiconductors capable of producing electron-hole pair under illumination are generally utilized

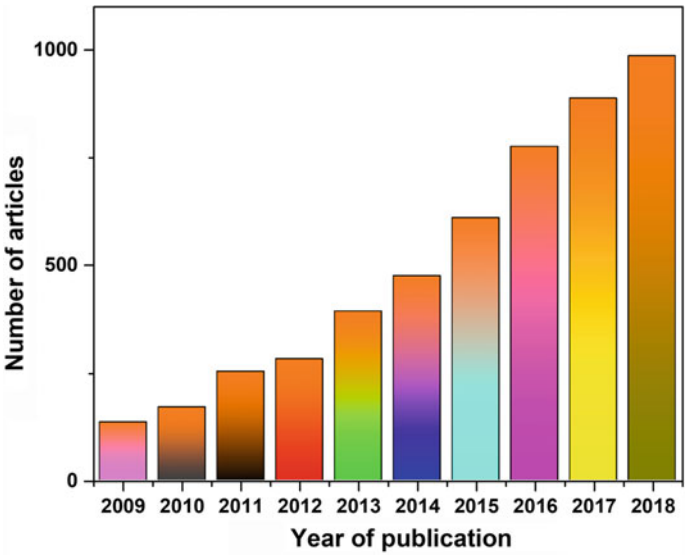

Fig. 2 Number of research articles published since last 10 years related to solar water splitting (obtained from scopus)

as suitable materials for solar water splitting. The reaction involved in the solar water splitting process is shown below:

$$H_2O \rightarrow H_2 + 1/2\,O_2$$

The solar water splitting process involves three crucial stages, as shown in Fig. 3. First, the absorption of photons by a semiconductor, secondly the generation and separation of electron-hole pair and lastly the diffusion of photogenerated charges towards the material surface to carry out water oxidation (holes) and reduction (electrons) reactions. Precisely, the materials require a suitable optical, electrical, and band edge properties and stability to perform efficient solar water splitting reaction. For example, the appropriate bandgap necessary for the absorption of a significant portion of incident light is ~1.5 eV. As per the band edge position requirements with respect to the reversible hydrogen electrode (RHE) scale, the valence band edge potential need to be located more positive than water oxidation to O_2 potential (1.23 V) whereas, the conduction band potential need to be more negative than the water reduction to H_2 potential (Fig. 3). Furthermore, the semiconductor needs to show efficient charge separation, mobility, and stability during water splitting conditions in an aqueous system in a wide pH range. Therefore, the semiconductors need to satisfy above all mentioned conditions to perform efficient solar water splitting reactions.

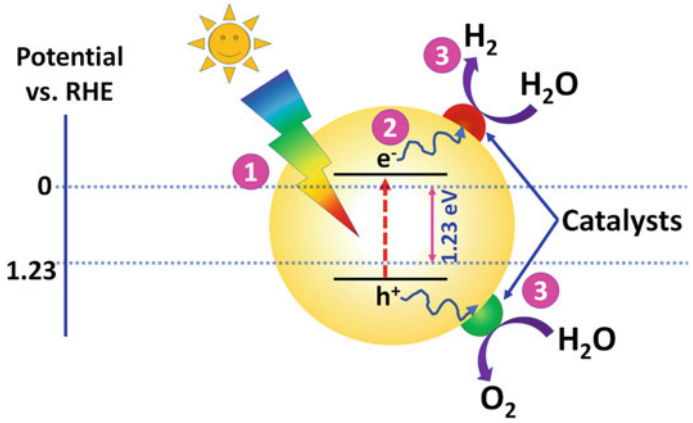

Fig. 3 Photochemical water splitting process showing the (1) absorption of photons by the material, (2) generation and separation of electron-hole pair, and (3) diffusion of photogenerated charges to carry out water oxidation and reduction reactions

Currently, an intense effort is being made to develop and optimize the suitable materials that fulfil all the above-required conditions to perform efficient water splitting reaction. However, the efficiency of water splitting has not been productive as it faces numerous limitations. Mainly, the solar water splitting reaction of producing H_2 and O_2 is considered as thermodynamically (change in Gibbs free energy $\Delta G^0 = +237.2$ kJ mol^{-1}) and kinetically uphill process [58]. Hence, the generation of H_2 and O_2 does not occur spontaneously due to the energy requirement and inefficient carrier dynamics. More precisely, the production of oxygen is considered highly challenging as it requires four electron transfer process and efficient hole dynamics. As shown in Fig. 3, a minimum of 1.23 eV of photon energy is needed to drive the water oxidation reaction as per the thermodynamic limitations. Theoretically, a maximum solar to hydrogen (STH) conversion efficiency of 31% is achievable in ideal solar water splitting conditions with the appropriate semiconductor material [7]. However, based on the several preliminary reports the highest STH efficiency achieved so far is only about 14% [68] using a tandem cell design and about 18.3% [60] with a multijunction device. Therefore, more significant research contribution is necessary to reach higher efficiency in solar water splitting.

2.2 Types of Solar Water Splitting

The solar water splitting process is further divided into two categories, namely photochemical (PC) water splitting and photoelectrochemical (PEC) water splitting. The underlying working mechanism of water splitting in both PC and PEC system remains the same. However, both the PC and PEC water splitting techniques have

some advantages and limitations over one other, indicating their utilization based on the requirements and conditions. In a PC system, the suitable semiconductor/catalyst material is suspended in the solution and illuminated with a light source. Here, the photogenerated electrons and holes drive water oxidation and reduction reaction in the aqueous medium on the material surface; as a result, the bubbles of both H_2 and O_2 are generated in the same reaction chamber. In contrast, the PEC water splitting reactions were carried out in an electrochemical cell containing photoanode/photocathode and a counter electrode with or without an applied bias potential. Mainly in PEC system, the electrodes are placed in different compartments separated using a membrane or salt bridge, and as a result, the production of H_2 and O_2 occurs in separate chambers [39]. Hence, in the PEC system, the produced gases do not need separation procedure whereas in PC system, the H_2 and O_2 have to be separated. However, the PC system has advantages such as it can be used with simple experimental setup without any instrumentation or additional potential energy. In contrast, the PEC system requires a specific experimental setup and a potentiostat for bias input. Overall, both PC and PEC water splitting methods have their advantages and limitations and highlighting the superior system among the two is still under debate. Hence, both techniques are believed to be productive and employable based on the requirement. In this chapter, the material and catalytic system utilized in the PC water splitting system is discussed (PEC water splitting system are presented in the different chapter and out of the scope of this chapter).

3 Photochemical Water Splitting

Since from the early years of research, a variety of materials have been introduced, explored and investigated their efficiency of water splitting reaction. However, the ability of a material to perform overall or partial water splitting were found to be different based on their optical and band edge properties. Hence, the photochemical water splitting was further categorized into photocatalytic water splitting and Z-scheme water splitting system. The essential requirement of the material and working principle of both of these systems remains similar. Mainly, the production of both H_2 and O_2 occurs in the same compartment in the solution. However, the employed materials are different based on their properties. Because the majority of the materials are incapable of performing overall water splitting and most of the materials could only show efficient and partial or simply water splitting. Here, the overall water splitting refers to the evolution of both H_2 and O_2 products during the illumination in the reactor. In contrast, the partial or just water splitting could simply mean the production of a single gas product that is either O_2 or H_2 only. The partial water splitting reactions occurs due to the unsuitable band edge positions of the materials, and in such cases, either sacrificial electron/hole donor or acceptor could be utilized to perform and balance gas evolution chemical reactions. Therefore, the materials were selected for the suitable technique of water splitting based on their properties.

3.1 Photocatalytic Water Splitting

The working mechanism of photocatalytic water splitting is the same, as shown in Fig. 3. Specifically, during the illumination of light on semiconductor, both the evolution of O_2 and H_2 takes place at the same material surface. Hence the material could be utilized in the powder form inside the reactor. Notably, both the generation and mass transfer of photogenerated electrons and holes occur within the same particle. In such systems, both the water oxidation and reduction catalysts can be deposited on the same particle that minimizes the overall synthesis complications. Overall, the photocatalytic water splitting scheme offers simple, rapid, and cost-effective system, with the only issue of separating the generated H_2 and O_2 gases [54, 65].

The choice of suitable materials for efficient photocatalytic water splitting reaction remains the main challenge due to the optical, electrical and band gap requirements of the semiconductor material. That is, the narrow bandgap semiconductors capable absorbing sufficient portion of sunlight and which are having suitable band edge positions between water redox potentials are recommended. Importantly, the material has to be highly stable during the water-splitting reaction under the illumination. However, none of the single element semiconductor materials satisfies the above-mentioned requirements alone. For example, the wide band gap of semiconductors such as TiO_2 [24, 71], $SrTiO_3$ [86], ZnO [49], $NaTaO_3$ [91], $ZnGa_2O_4$ [125], $K_4Nb_6O_7$ [88], ZrO_2 [85] etc. have well positioned band edge positions with respect to water redox potential (vs. RHE) to perform overall water splitting to generate both H_2 and O_2. Furthermore, these materials are easy to synthesize and are known to be stable and show efficient charge mobility. However, the wide bandgap these materials allow the absorption of very limited (4%) or insignificant amount of incident sunlight that too mainly in the UV spectrum that effects their water splitting efficiencies. Because the sunlight reaching the earth's surface mostly consists of the visible and IR region, which are unutilized by these materials. Therefore, these materials are considered unsuitable for performing overall water splitting even though they possess well-matched band edge positions.

Semiconductors such as Ta_3N_5 [113], Cu_2O [28, 77], CdS [43, 45], CdSe [112], GaAs [51] etc. have narrow band gaps to absorb significant portion of sunlight and suitably positioned band edges for overall water splitting. However, these materials show poor stability during solar water splitting activity due to the photo-corrosion when they come in direct contact with aqueous electrolytes [32]. Furthermore, most of the oxide materials derived from single element and multiple elements such as Fe_2O_3 [26], WO_3 [41, 42], $BiVO_4$ [107], $Cu_xV_xO_x$ [47], $CuWO_4$ [44] etc. exhibit excellent stability and significant light absorption ability. However, their band edge positions are not suitably aligned with the water reduction potentials. That is, the valence band edge positions are located at the positively higher potential to carry out water oxidation reaction whereas the conduction band edge is not positioned significantly near water reduction potential. Therefore, during the illumination spontaneous evolution O_2 will be achieved whereas H_2 could be produced. As a result, performing an efficient overall water splitting using the single absorber semiconductor material

face severe limitation. Hence, the single absorber semiconductors are generally utilized in PEC water splitting systems with an applied bias potential to perform overall water splitting reaction. However, to achieve overall PC water splitting using the single absorber material is done using Z scheme water splitting, which is discussed in the following section.

3.2 Z-Scheme Water Splitting

The selection of an appropriate material for performing efficient photochemical overall water splitting is challenging due to the stringent material property requirements. Based on the band gap and electrical properties, the oxide semiconductors are well suited for photochemical water splitting reactions. Moreover, the high stability of metal oxides makes them ideal materials for water splitting. However, achieving unassisted overall water splitting using oxide semiconductors is challenging due to their unmatched band edge positions with respect to water redox potentials; as a result, partial water splitting reaction (either H_2 or O_2 production) is accomplished. Therefore, a unique strategy needs to be adopted to achieve overall and unassisted water splitting using most of the stable materials.

Given this, Z-scheme water splitting schemes are proposed [5] in 1979, which utilizes the two-step photoexcitation pathways instead of a single step. The working principle of Z-scheme water splitting is similar to the natural photosynthesis process of plants and is depicted in Fig. 4 [1, 14, 101]. In this method, two semiconductors are used to carry out H_2 and O_2 evolution separately instead of single absorber material. This strategy adds up the band gaps of the two materials allowing the absorption of the broader range of incident wavelength. The two materials were carefully selected

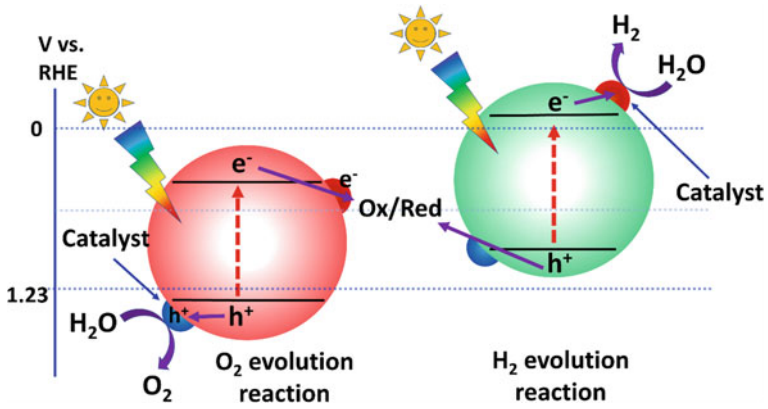

Fig. 4 Overview of a Z-scheme water splitting process showing the two-step photoexcitation pathways to produce both H_2 and O_2

based on their band edge positions. Importantly, the materials were chosen to overcome the limitation of band alignment faced by each of the material with respect to water oxidation and reduction potentials. Precisely, the conduction band edge position of one of the material should be situated in H_2 production potential, and simultaneously, the valence band edge of another material must be located at O_2 production potential. That is, one of the material allows the spontaneous water oxidation reaction (O_2 production) using the photogenerated holes whereas the photogenerated electrons will be utilized to drive water reduction (H_2 production) reaction by another material. To maintain the charge balance within the material and solution and to carry out unassisted overall water splitting, the photogenerated electrons from the water oxidizing material and the photogenerated holes on the water reduction material are short-circuited through a medium. Generally, the short circuit between these charges is achieved using the redox mediators in the solution or by the solid-state electron mediator.

As shown in Fig. 4, the unassisted overall water splitting proceeds via the two-step excitation route. Thermodynamically, such a two-step excitation pathway reaction are favourable, whereas kinetically challenging due to the increase in the number of excitation pathways compared to that in single material excitation. Specifically, a poor charge balance kinetics will lead to the significant energy loss via recombination reactions. Furthermore, the two-step pathways involved in the Z-scheme process allows the utilization of a wide range of materials having different absorbance in UV, visible and also in IR region. Conclusively, the Z-scheme water splitting reaction offers an promising strategy to perform unassisted overall water splitting.

4 Catalysts for Photochemical Water Splitting

A wide range of materials have been introduced and explored for the photochemical water splitting process till today. However, most of the materials face severe limitations in fulfilling the necessary condition for overall water splitting, as a result, the efficiencies are reported to be insignificant. Therefore, to improve the solar water splitting efficiency of the materials, various strategies have been implemented. These strategies include the tuning of size and morphology, engineering to design the electronic band structure to satisfy overall water splitting potential condition, doping, sensitization with narrow bandgap elements, heterojunction formation, and utilization of catalyst to carry out efficient water oxidation/reduction reaction [103, 122]. Among these, the use of catalysts or cocatalysts has been considered as one of the essential strategies that could effectively improves the water splitting efficiencies. Importantly, during the overall water splitting, the water oxidation reaction is known to be more challenging and rate determining process compared to water reduction reaction as it involves photogenerated holes and four electron transfer pathway. Hence, the use of catalyst becomes essential to catalyse of water oxidation reaction to avoid the recombination and to improve the overall water splitting efficiency. The catalysis are chosen based on their specificity and selectivity to carry out either

water oxidation or reduction reaction. That is, the catalyst are briefly categorized as water oxidation and water reduction catalysts. The water oxidation and reduction catalysts are selective towards extracting holes and electrons, respectively, to carry out the desired reaction and product. Therefore, based on the reaction selectivity, the catalyst are chosen. In this chapter, the most effective catalysts employed in the photochemical water splitting are discussed demonstrating their positive impacts on the reaction efficiencies.

4.1 Effect of Cocatalyst

Cocatalyst are the conductive materials deposited on the water-splitting materials assisting them indirectly during gas evolution reactions. Generally, cocatalysts does not harvest light and tends to tune the kinetics of the water redox reactions [48]. Hence, the cocatalysts deposited on the material were used to lower the overpotential and activation energy required to split water [57]. Precisely, the cocatalyst captures the photogenerated charges that are diffused at surface of the material and provide them an active reaction sites for the efficient water splitting reactions [116]. Most of the cocatalysts exhibit selectivity in carrying out reactions and hence the photogenerated electrons, and holes are selectively and rapidly captured by the cocatalysts to carry out either oxidation or reduction of water. Such an selectively ensures the efficient separation of electron-hole pairs and the distribution of charges [48, 116].

The interface between the material and the electrolyte is a critical region as it involves the charge transfer process to oxidize and reduce water during illumination. When the semiconductor material come in contact with the aqueous solution, the band bending occurs at the material/electrolyte interface due to the mutual charge transfer and energy level alignment between redox potential and Fermi energy [41]. The band bending will be either upwards or downwards depending on p-type or n-type material, respectively. However, in photochemical water splitting the band bending is not significant due to the absence of applied bias potential as in case of PEC water splitting system leading to the recombination of charges. Therefore, at the interface, an intimate junction could be formed by depositing an selective co-catalyst that could affect its band bending. Importantly, the presence of catalyst enhances the upward band bending at the interface that ensures efficient charge separation. Hence, efficient depletion of charges is believed to occur at the space charge region where catalyst provides active sites for water oxidation reaction. Thus the presence of catalyst decreases the hole concentration the at interface and shifts that in turn reduces the surface recombination [12, 83, 128]. The presence of catalyst on the material surface effectively reduces the recombination process by removing the surface trap states at the surface as shown in Fig. 5 [52, 22]. The surface trap states present on the material are known to act as a recombination centres for photogenerated charges.

The addition of a catalyst protects the material from photo-corrosion during the water oxidation and reduction reactions. The photogenerated holes during the illumination are known to be the major cause of photo-corrosion during water splitting

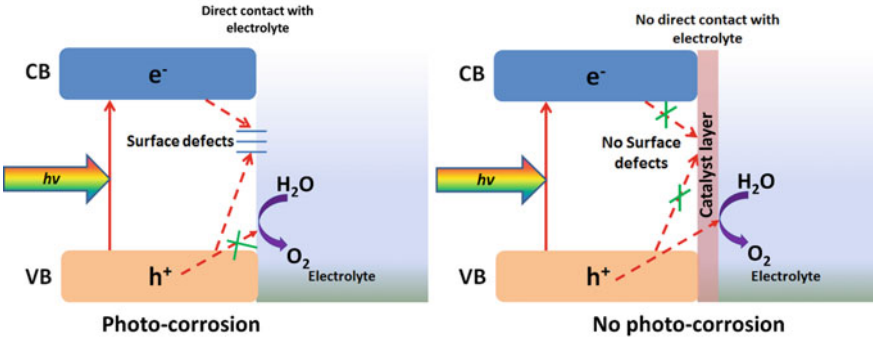

Fig. 5 The charge recombination pathways and photo-corrosion in the absence and presence of catalyst on the material surface

reaction. Therefore, the presence of catalyst on the material surface tends to consume the photo-generated holes and push them to undergo rapid water oxidation reaction (Fig. 5). For example, the photo-corrosion is generally observed in case of sulfide, nitrides, (oxy)nitrides and (oxy)sulfides materials during water splitting that decreases their efficiency significantly. Therefore, by the addition of a catalyst, the photo-corrosion in such materials could be avoided. Moreover, the presence of catalyst could also prevent the direct contact of materials with the surface, which also decreases the photo-corrosion process [83] (Fig. 5). Furthermore, the catalyst on the material surface give increased reaction sites compared to bare materials. The increase in reaction sites causes the decrease in the overpotential required to carry out water oxidation or reduction reactions [13, 83, 120].

The amount of catalysts deposited on the material surface and its thickness was found to affect its reaction efficiencies. For example, higher amounts of catalysts could block the light, reaching the material causing efficient light harvesting and carrier formation. Therefore, the optimization of catalyst amount is necessary. Furthermore, the selection of a suitable catalyst on a specific material is crucial for the efficient working of water splitting reactions. Figure 6 shows the effect of catalyst amount on the water splitting activity of the material. Conclusively, the presence of catalyst on the water splitting material surface is reported to be an effective strategy to enhance the water splitting reaction. Till now, a variety of catalysts have been proposed for improving the water splitting efficiency, and in the next section, few of the important catalysts have been highlighted and discussed.

4.2 Noble Metal and Their Oxide as Catalysts

Noble metals are widely used as catalysts on the semiconductor material for efficient solar water splitting reactions [56, 63, 118]. Mainly, the noble metals are known to act as very efficient hydrogen production catalysts rather than oxygen evolution reaction

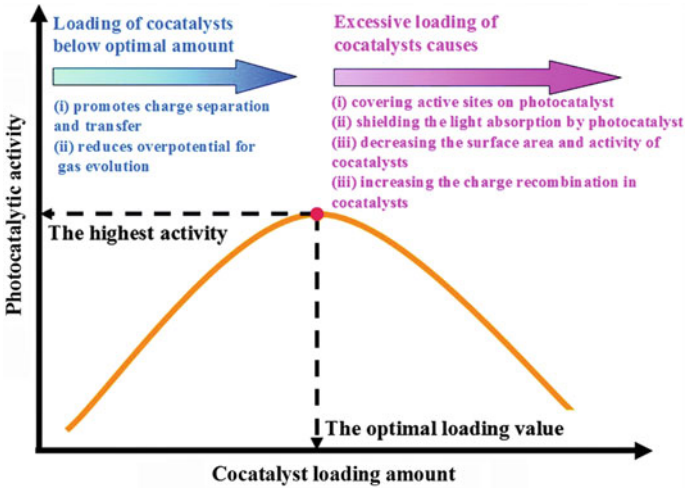

Fig. 6 The water splitting performance of the catalyst loaded on to the material and its relationship with the concentration of the cocatalyst. Adapted with permission from the Royal Society of Chemistry [83]

when loaded on to semiconductors. The noble metals such as Pt [56, 63, 118], Au [62, 73] Ru [29], Pd [89], Rh [87], and Ag [53, 75] have been broadly employed as the most efficient for water splitting to hydrogen generation. Particularly, Pt catalyst is believed to be most effective catalyst among the noble metals. Because, compared to other metal elements, Pt exhibit highest work function and provide low overpotential for water reduction reaction [120].

The formation of a favourable Schottky junction (SJ) between the noble metal and the semiconductor is believed to be the main cause of improved charge separation and higher H_2 production efficiency [120]. That is, when metal catalyst come in contact with semiconductors, a SJ is formed due to the transfer of charges across interface. The SJ creates a unique barrier that limits the flow of charges [82]. Mainly, the SJ allows the efficient diffusion of only electrons towards the metal atom facilitating the effective charge separation. For example, the Au nanoparticles deposited on the TiO_2 semiconductor experience shift in Fermi level to more negative potentials providing improved charge separation and enhances the efficiency of hydrogen generation during water splitting (Fig. 7a). In this system, Au selectively and rapidly captures photogenerated electrons, thus efficiently separating it form holes and decreases the recombination rate. Importantly, the loading of noble metal on semiconductor yield a favourable band alignment due to the position of conduction band edge of semiconductor being higher than the Fermi level of metal catalyst. Unlike noble metals, the oxides of noble metal elements act as water oxidation catalysts rather than water reduction catalyst. Some of the routinely used catalysts are RuO_2 [21, 38, 74] and IrO_2 [23, 59]. However, based on the necessity and price factor, the use of noble metal and their oxides as catalyst for water splitting is not practical. Moreover,

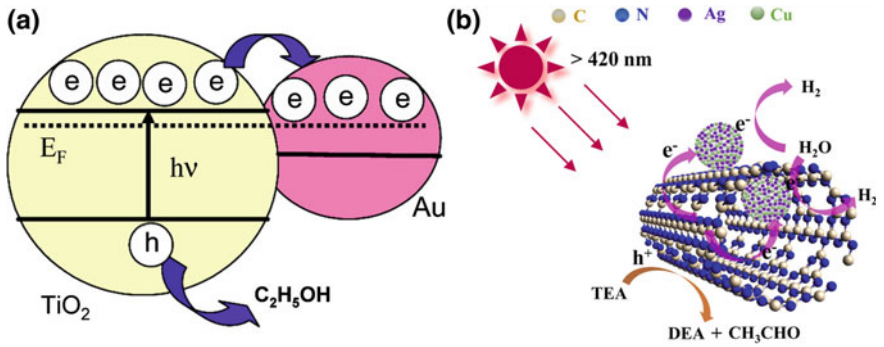

Fig. 7 **a** The Fermi-level alignment between the metal catalyst and the semiconductor due to the charge distribution. Adapted with permission from American Chemical Society [37]. **b** photocatalytic H_2 production on the Cu-Ag supported graphitic carbon nitride via the photodegradation of triethylamine (TEA) into diethylamine (DEA) and acetaldehyde. Adapted with permission from American Chemical Society [130]

some of the noble metals are less abundant. Hence, a viable alternative to the noble metals is required as catalyst for water splitting reaction. In view of this, variety of catalyst were introduced derived from abundant and cheap transition metal elements which are discussed in the following sections.

4.3 Earth-Abundant Metal Catalysts

The noble metal catalysts are highly expensive and are not economically viable for high quantity usage. Hence alternatively, earth-abundant metals were explored as catalysts for photochemical water splitting. The metal elements such as Cu, Ni, Cd, Fe, Co and Ti have been reported to perform as an effective catalyst during water-splitting reaction [121]. Like noble metals, Cu catalyst acts as a efficient hydrogen evolution catalyst due to its excellent electrical and optical properties [64, 105] and low price. Cu metal catalyst is found to extracts the electrons from semiconductors allowing effective charge separation. However, Cu catalyst are known to be less stable compared to noble metal catalysts and hence require stabilization during water-splitting reactions. The Cu metal is prone to under oxidation to form CuO or Cu_2O during the synthesis and water splitting process [67, 79]. A unique strategy proposed by Huang et al. indicate that Cu catalyst can be stabilized by loading it on the TiN surface [34]. Furthermore, the Cu metal can be alloyed with Ni, Ag, and Au, to enhance the catalytic effect of water splitting [61, 130]. For example, the hydrogen evolution from the graphitic carbon nitride nanotubes can be achieved by loading the bimetallic Cu-Ag alloy, as demonstrated by Yuxiang et al. [130]. Figure 7b illustrate the mechanism of photocatalytic H_2 production on the Cu-Ag supported graphitic

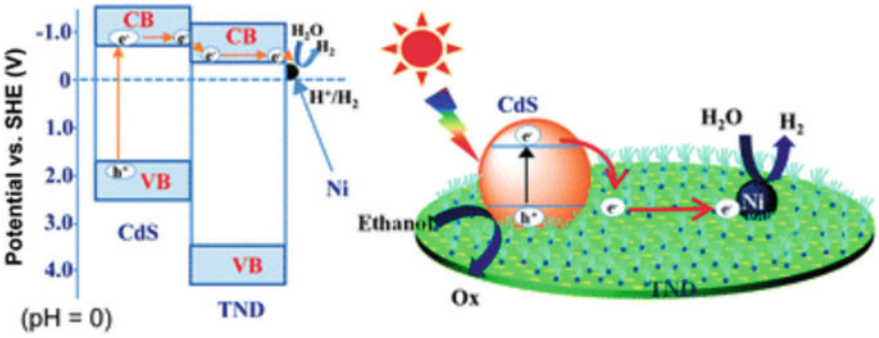

Fig. 8 The charge transfer process undergoing during the illumination on Ni catalyst loaded on CdS-titanate nanodisc composite. Here the photogenerated electrons are used to produce hydrogen in the presence of ethanol in the water as sacrificial electron donor to the composite, reproduced with permission of Royal Society of Chemistry [19]

carbon nitride via the photodegradation of triethylamine (TEA) into diethylamine (DEA) and acetaldehyde [130].

Metallic Ni can also be utilized as an cost-effective catalyst alternative to the noble metals for the production of hydrogen during water splitting [19]. Although its utilization has not been popular compared to the noble metals, but show some promising results as a catalyst. For example, metallic Ni nanoparticles deposited on the CdS–titanate composite has exhibited significant hydrogen production [19]. The Ni nanoparticles were deposited on CdS–titanate nanodiscs using the photo-deposition method. As shown in Fig. 8 during the irradiation the photo-generated electrons from CdS are ejected into the titanate conduction band which are extracted by Ni nanoparticle to carry out efficient water reduction to hydrogen production reaction whereas the holes from the CdS are removed into the water-ethanol electrolyte. Such a heterojunction with Ni catalyst offers efficient separation of charge carriers resulting in hydrogen evolution rate of 11.038 mmol $h^{-1}g^{-1}$. Similarly, Ni metal catalyst has explicitly been loaded on to CdS in several other reports for H_2 production and reached the highest quantum yield 53% and H_2 production rate of 63 mmol $g^{-1}h^{-1}$ [11, 93, 109]. Furthermore, the earth-abundant metals such as Co, Cd, Ti and Fe [33, 70, 90, 106, 111] have been rarely used as catalysts for hydrogen production either separately or in conjugation with various oxides and noble metals. Interestingly, more than two metals could be combined to form multimetal catalysts. However, the extensive usage of such catalysts has been utilized in electrochemical water splitting and electrolysis rather than photochemical water splitting.

4.4 Earth-Abundant Metal Oxide Catalysts

The limitation of using noble metals as a catalyst has opened the research focus on new and efficient water splitting catalysts derived from earth-abundant materials. Recently, the earth-abundant catalysts derived from the transition metal oxides are considered as the best alternative to the expensive noble metal catalysts. Moreover, most of the catalysts of earth-abundant metal oxides are stable in aqueous water splitting condition in the presence of light. Among the catalysts, the widely used metal oxides are namely Co_3O_4, CoO_x, MnO_x, FeO_x, and NiO_x (Note that the number of catalysts explored for photoelectrochemical water splitting and electrolysis are large compared to photochemical water splitting and are discussed in other chapters).

The cobalt-based catalysts are the widely studied earth-abundant metal oxide catalyst due to their unique properties. Interestingly, the oxides of Co could be used as both water oxidation and reduction catalyst. For example, Co_3O_4 catalyst has been utilized for hydrogen production, whereas the CoO_x catalyst is known for its water oxidation abilities makes. The Co_3O_4 water reduction catalyst shows significant light harvesting properties and efficient electron mediation. The Co_3O_4 catalyst loaded onto the semiconductor has been found to produce H_2 [25] at the highest rate of 8275 μmol h^{-1} g^{-1} [66]. In contrast, CoO_x has been employed as water oxidation catalyst on various semiconductors and Z scheme water splitting systems [35, 69, 108]. Importantly CoO_x is found to decrease the activation energy of water oxidation via the formation of built-in electric field and shows high selectivity. For example, Fig. 9a shows the Z-scheme water splitting system consisting of CoO_x catalyst loaded onto $BiVO_4$ semiconductor for water oxidation reactions [35]. Similarly, CoO_x could be used on various semiconductors as efficient water oxidation catalyst [35, 69, 108].

The oxides of Ni are also reported to be a very popular catalyst for PEC, PC water splitting and electrolysis. Interestingly, NiO_x has been utilized as both water reduction [2, 95] and water oxidation catalyst [129]. The low cost and stability of

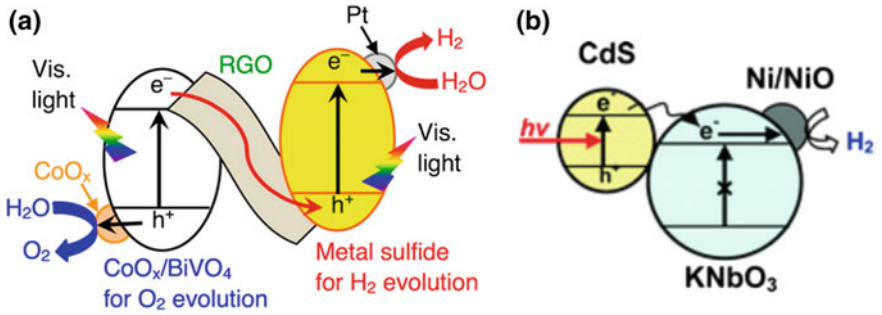

Fig. 9 **a** Z-scheme water splitting system containing CoO_x water oxidation catalyst and Pt water reduction catalyst on $BiVO_4$ and metal sulfide semiconductors for overall water splitting. Adapted with permission from American Chemical Society [35]. **b** photochemical water splitting to H_2 production under visible light irradiation at Ni/NiO catalyst supported on $KNbO_3$/CdS composite, Reproduced with permission of Royal Society of Chemistry [17]

the NiO catalyst make it very suitable for efficient water splitting reactions. Furthermore, NiO catalyst can be conjugated with metallic Ni to boost its hydrogen production efficiency [17, 123]. Figure 9b shows The Ni/NiO catalyst loaded on $KNbO_3$/CdS electrode for efficient H_2 evolution reaction. Here, the Ni/NiO catalyst produces hydrogen by combining the photoelectrons generated at both CdS and $KNbO_3$ composite [17]. In addition to the above catalysts, there are numerous oxide based catalysts reported. However their usage was mainly constrained to PEC water splitting and electrolysis techniques.

4.5 Metal Chalcogenides as Catalysts

Metal chalcogenides are considered as excellent catalysts for photochemical water splitting reactions. In particular, the metal sulfides have been reported as a superior catalyst for water reduction reactions for H_2 production. The most routinely used metal sulfide catalyst are NiS [31, 110, 127], NiS_2[124], CoS [110], MoS_3 [104], CuS [110, 126], MoS_2 [132], Mo_6S_4 [119] and WS_2 [131]. The metal sulfide catalysts are generally loaded on to the semiconductors to extract photogenerated electrons during illumination to carry out water reduction reactions. Figure 10a shows the carrier dynamics of photogenerated charges in metal sulfide supported semiconductor in presence of light irradiation [110]. That is, during the irradiation the photogenerated electron and holes are generated at the semiconductor. Here the photogenerated holes are generally extracted into the electrolyte of $S^{2-}/SO_3{}^{2-}$ whereas the electrons are diffused towards the metal sulfide catalyst to carry out H_2 production reaction. The metal sulfide catalyst is capable of extracting electrons efficiently from the conduction band of the supported semiconductor. Hence, the effective separation of photogenerated charges can be achieved. With the optimized catalyst system, the enhanced H_2 production efficiency can be achieved as sown in Fig. 10b [110]. Note that compared to Co and Cu, the 0.1 wt% NiS loaded catalyst show similar H_2 production rate as that of noble metal Pt catalyst. This indicates that metal sulfide catalyst has the potential to replace noble metals as efficient H_2 production catalyst.

In the absence of metal sulfide catalysts, the photogenerated charges are believed to be inefficient in utilizing electrons for H_2 production, as shown in Fig. 10c [131]. Even though the photogenerated holes are consumed by the lactic acid, the photogenerated electrons are incapable of reduction water to H_2 due to the lack of active reaction sites on the CdS semiconductor surface. Therefore, the metal sulfides (WS_2) provides enough active sites for hydrogen production under the irradiation. Among the metal sulfide catalyst, the Mo-based sulfides have shown promising results comparable to the noble metal catalysts. As demonstrated by Zong et al., a very small amount of MoS_2 loaded onto CdS with the optimization can achieve hydrogen evolution rate even higher than ideal CdS/Pt system as shown in Fig. 10d and also other noble metal catalysts [27, 132]. Furthermore, the utilization of graphene sheets between the semiconductor and MoS_2 catalyst was found to favour efficient H_2 production as shown in Fig. 11 [115]. As in Fig. 11 the superior catalyst and conductive property

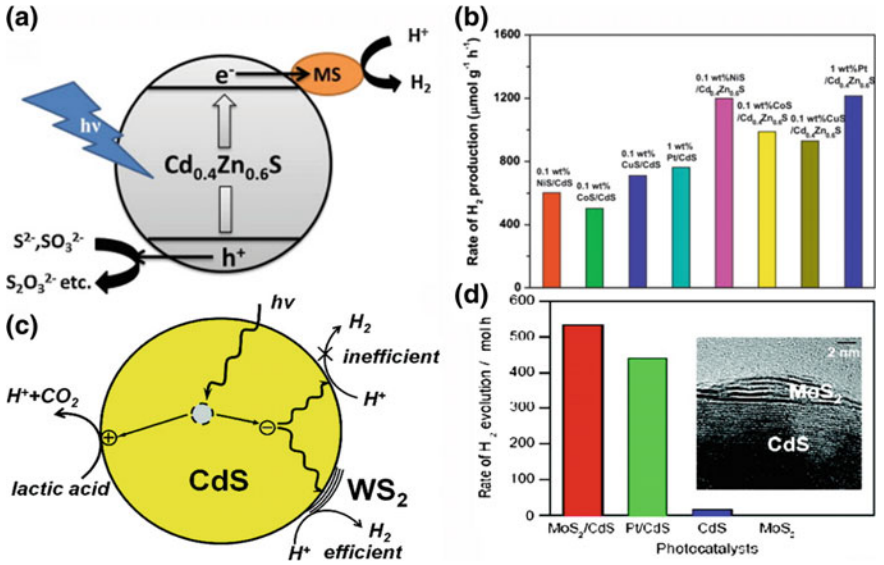

Fig. 10 **a** The carrier dynamics in metal sulfide catalyst supported CdZnS. **b** H_2 production rates at various metal sulfide catalyst loaded CdZnS material compared to the Pt catalyst under visible light irradiation Reprinted with permission from Elsevier [110]. **c** The pathways of photogenerated charges in WS_2 coated CdS showing the efficient and inefficient H_2 production routs. Adapted with permission from American Chemical Society [131]. **d** The superior H_2 production rate of CdS/MoS_2 composite compared to Pt catalyst. Adapted with permission from American Chemical Society [132]

of graphene allow the effective extraction of photogenerated electrons from TiO_2 and carrying out water reduction reaction on its own or by transporting it to MoS_2 catalyst. In both ways, the photogenerated electrons were utilized efficiently for H_2 production. Therefore, compositing metal sulfides with carbon materials is a valuable strategy for solar H_2 production.

4.6 Metal Phosphides as Catalysts

Recently, metal phosphides have been introduced as a very useful catalysts for photocatalytic water splitting reactions [10]. Importantly, the superior catalytic activity and stability of metal phosphides have the potential to replace some of the noble metal catalysts. In metal phosphides, the ratio of metal and phosphide can be tuned that affects its catalytic properties, and hence its features are quite similar to metals and ceramics. Also, the metal phosphides are found to be excellent electrical conductors and are thermally and chemically stable [10]. The first successful employment of metal phosphides for photocatalytic water splitting reaction was demonstrated in 2013 using Ni_2P and FeP [80, 117]. Since then, various metal phosphides have been

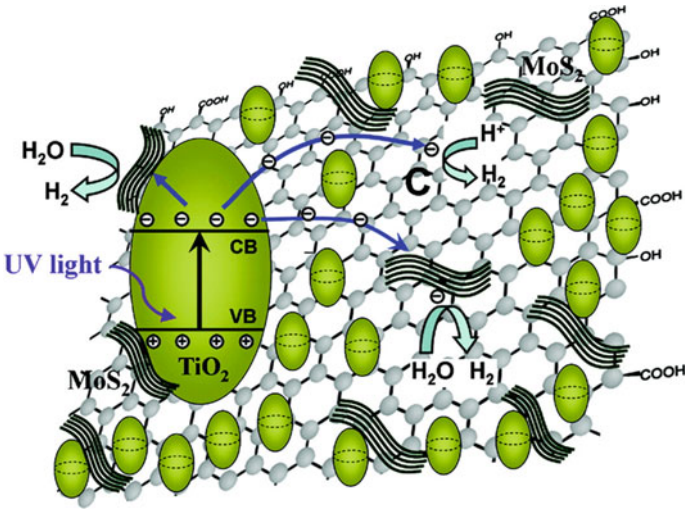

Fig. 11 The hydrogen production using TiO_2/MoS_2/graphene composite under illumination. The ejection of photogenerated electrons from TiO_2 to the MoS_2 and graphene sheets. The superior catalytic and charger transport property MoS_2 and graphene sheets synergically allow efficient reduction to H_2 production reaction. Adapted with permission from American Chemical Society [115]

introduced, explored and efficiently employed as a catalyst in photochemical water splitting reactions.

In photochemical water splitting, the metal phosphides perform as water reduction catalysts for hydrogen production. The literature survey shows that metal phosphides have been extensively used as catalysts for CdS and C_3N_4 and rarely with other materials. The metal phosphides catalysts reported so far include Ni_2P [8], CoP [9], Cu_3P [9], FeP [16], Fe_2P [97], and $Ni_{12}P_5$ [114]. Generally, the metal phosphides are loaded onto the semiconductor that absorbs light and produces photogenerated charges. During the illumination, the photogenerated electrons from semiconductors are transferred to metal phosphides which are used to reduce water to hydrogen. Therefore, the anchoring mode of metal phosphides to semiconductors is highly crucial. In the homogeneous reaction system, the metal phosphides and semiconductors were suspended in liquid media without mutual attachment/bonding. In such cases, the electron transfer is believed to take place only during the collision between semiconductor and metal phosphides; as a result, the efficiency is found to be limited. Therefore, it is beneficial to anchor metal phosphides onto the semiconductors for enhanced hydrogen production efficiency. The metal phosphides can be directly anchored to semiconductors or by using capping or stabilizing agents. In some synthesis schemes, the use of stabilizing and capping agents is necessary during the synthesis to regulate particle size and morphology. However, the use of capping and stabilizing agent is believed to decrease the active sites for hydrogen evolution catalysis, and hence the water splitting efficiency gets affected. Therefore, direct contact

of metal phosphides with semiconductors is necessary for efficient charge transfer and increased H_2 productivity.

A theoretical study on metal phosphide-semiconductor interface showed that an inherent electric field is introduced at the interface. Mainly, the stable bonding interface is formed between semiconductor (CdS) and the metal phosphide (FeP) without any defects at the heterojunction. Such bonding is expected to increase the charge diffusion capability between the interface without posing any significant resistance. The band edge alignment between semiconductor (CdS) and the metal phosphide (FeP) before and after coming in contact indicate that, during the equilibrium, the Fermi level alignment causes the band bending and hence the electrons and holes are selectively separated by diffusing towards metal phosphide and semiconductor systems, respectively. This ensures effective separation of electrons to carry out H_2 evolution and the holes participate in the solution oxidation reactions. Therefore, the metal phosphides could be utilized more efficiently than the noble metal catalysts for hydrogen production reactions. In fact, the optimized metal phosphides systems such as CdS-FeP show superior hydrogen production rate even compared to the productions performed by in situ photo-deposited noble metal catalysts such as Pt, Pd, Ru, and Au [16].

The metal phosphides anchored to semiconductors have already achieved remarkable hydrogen production efficiencies. Mainly, the CdS has been extensively used as a suitable semiconductor for metal phosphide catalytic H_2 production. Figure 12a shows the Ni_2P catalyst loaded onto CdS nanorods producing H_2 over 90 h under visible light illumination [100]. Here, the H_2 production rate is found to be dependent on the ratio of semiconductor and the catalyst, as shown in Fig. 12b. Furthermore, the use of graphene is known to facilitate the electron transfer between the metal phosphides and semiconductors as demonstrated by Reddy et al. [84]. In their work [84] the CoP catalyst was loaded with CdS were incorporated into the reduced graphene MoS_2 nanosheets (Fig. 12c). In such systems, the graphene layer act as a backbone to semiconductor and metal phosphide and support effective electron-transfer and suppresses the charge recombination [84]. Using the CdS/MoS_2-graphene@CoP composite, a remarkable hydrogen production rate of 83,907 $\mu mol\ h^{-1}\ g^{-1}$ was reported [84]. Similarly, Fe_2P catalyst incorporated on CdS nanorods (Fig. 12d) show the H_2 production rate of 186 $\mu mol\ h^{-1}\ mg^{-1}$ [97].

Conclusively, using various semiconductors systems the metal phosphides such as Fe_2P, Cu_3P, FeP, CoP and Ni_2P have reached a highest H_2 production rate of 186,000 $\mu mol\ h^{-1}\ g^{-1}$ [97], Cu_3P 200,000 $\mu mol\ h^{-1}\ g^{-1}$ [99], FeP, 202,000 $\mu mol\ h^{-1}1\ g^{-1}$ [16], CoP, 500 $\mu mol\ h^{-1}1\ mg^{-1}$ [98], 1200 $mmol\ h^{-1}\ mg^{-1}$, respectively. Among these, the Ni_2P catalyst has created a milestone by exhibiting the record H_2 production rate of 1200 $mmol\ h^{-1}\ mg^{-1}$ [100] that even surpasses the efficiency showed by noble metal catalysts. Even though almost all the metal phosphides show water reduction to H_2 production capability, the CoP catalyst has surprisingly shown the O_2 production ability as demonstrated by Pan et al. [78]. However, unlike H_2 production, the O_2 production rate was observed to be significantly low. Using a sacrificial electron acceptor (without H_2 production) a maximum O_2 production rate of 42 $mmol\ h^{-1}$ was recorded, whereas the overall water splitting has yielded H_2 and O_2 production

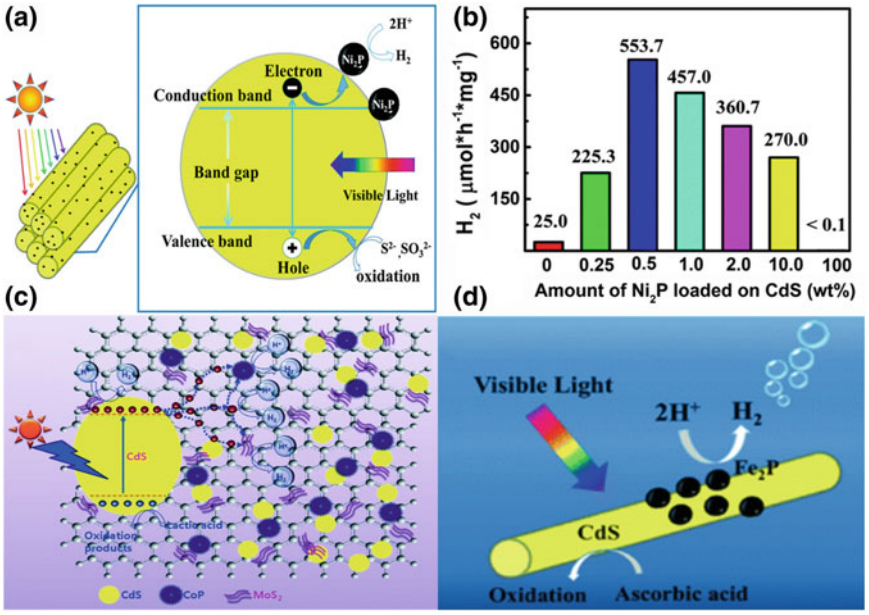

Fig. 12 **a** Morphology, band structure and carrier dynamics of Ni_2P integrated CdS nanorods for the efficient H_2 production under visible light irradiation. **b** The plot showing the dependence of rate of H_2 evolution on the Ni_2P loading amount. Reproduced with permission of Royal Society of Chemistry [99]. **c** The H_2 production by CoP catalyst loaded on to CdS and reduced graphene oxide (RGO)-MoS_2 nanosheets, Reproduced with permission of Royal Society of Chemistry [84]. **d** The photocatalytic H_2 production on the CdS nanorod supported with Fe_2P catalyst, Reproduced with permission of Royal Society of Chemistry [97]

rates of about 2.1 and 1.0 mmol h^{-1}, respectively. This result clearly indicate that the metal phosphides has a promising future as water oxidation (O_2 production) catalyst in addition to the efficient H_2 production catalyst. Overall, the superior efficiency, stability and low cost of metal phosphides has demonstrated their potential candidature for H_2 production catalyst and an ideal replacement for noble metal catalyst.

5 Summary and Outlook

Photochemical water splitting is one the most cost-effective technique of producing both O_2 and H_2 with a simple experimental design. In addition to the light absorbing material utilized in photochemical water splitting, the choice of a suitable and selective catalyst is very crucial in water splitting. The catalysts are generally loaded on to the semiconductor materials to utilize either electrons or holes to carry out water splitting reactions. Hence, the development of catalysts for photochemical water splitting

has seen tremendous progress and milestones till today. A variety of catalyst have been reported based on noble metal, noble metal oxides, earth-abundant metals and oxides, metal phosphides and metal chalcogenides. Among the wide range of available materials, the suitable catalysts were chosen based on either water oxidation or reduction capabilities. The selected catalyst need optimization to exhibit enhanced water splitting ability. For example, the amount of catalysts deposited on the semiconductor surface and its thickness determines its effective working. In addition to the water splitting, the surface deposited catalysts were known to reduce surface trap states, which are the leading cause of charge recombination. Importantly, the surface deposited catalysts can also act as protective layer that could reduce the photo-corrosion of the light absorbing semiconductors. It is imperative to note that, the catalysts proposed for photochemical water splitting are comparatively less in number than the catalyst reported for photoelectrochemical water spitting and electrolysis. Because the photochemical water splitting is carried out in solutions containing particle suspension. Hence thin films and the applied bias potential could not be implemented. Consequently, the loading/deposition of some catalysts is not possible, which uses thin film deposition techniques. Therefore, more research contribution on the synthesis and deposition of broad range of catalyst is needed. Furthermore, the future research on catalyst should be focused on understanding the core reaction mechanism of catalyst process, introduction of sustainable and stable materials, and designing multifunction catalysts.

References

1. Abe R (2011) Development of a new system for photocatalytic water splitting into H_2 and O_2 under visible light irradiation. BCSJ 84:1000–1030. https://doi.org/10.1246/bcsj.20110132
2. Agegnehu AK, Pan C-J, Rick J, Lee J-F, Su W-N, Hwang B-J (2012) Enhanced hydrogen generation by cocatalytic Ni and NiO nanoparticles loaded on graphene oxide sheets. J Mater Chem 22:13849–13854. https://doi.org/10.1039/C2JM30474K
3. Badwal SPS, Giddey S, Munnings C (2013) Hydrogen production via solid electrolytic routes. Wiley Interdisc Rev Energy Environ 2:473–487. https://doi.org/10.1002/wene.50
4. Balat M (2008) Potential importance of hydrogen as a future solution to environmental and transportation problems. Int J Hydrogen Energy 33:4013–4029. https://doi.org/10.1016/j.ijhydene.2008.05.047
5. Bard AJ (1979) Photoelectrochemistry and heterogeneous photo-catalysis at semiconductors. J Photochem 10:59–75. https://doi.org/10.1016/0047-2670(79)80037-4
6. Birol F (2006) World energy prospects and challenges. Aust Econ Rev 39:190–195. https://doi.org/10.1111/j.1467-8462.2006.00411.x
7. Bolton JR, Strickler SJ, Connolly JS (1985) Limiting and realizable efficiencies of solar photolysis of water. Nature 316:495. https://doi.org/10.1038/316495a0
8. Cao S, Chen Y, Wang C-J, He P, Fu W-F (2014) Highly efficient photocatalytic hydrogen evolution by nickel phosphide nanoparticles from aqueous solution. Chem Commun 50:10427–10429. https://doi.org/10.1039/C4CC05026F
9. Cao S, Chen Y, Wang C-J, Lv X-J, Fu W-F (2015) Spectacular photocatalytic hydrogen evolution using metal-phosphide/CdS hybrid catalysts under sunlight irradiation. Chem Commun 51:8708–8711. https://doi.org/10.1039/C5CC01799H

10. Cao S, Wang C-J, Fu W-F, Chen Y (2017) Metal phosphides as Co-catalysts for photocatalytic and photoelectrocatalytic water splitting. Chemsuschem 10:4306–4323. https://doi.org/10.1002/cssc.201701450
11. Cao S, Wang C-J, Lv X-J, Chen Y, Fu W-F (2015) A highly efficient photocatalytic H_2 evolution system using colloidal CdS nanorods and nickel nanoparticles in water under visible light irradiation. Appl Catal B 162:381–391. https://doi.org/10.1016/j.apcatb.2014.07.014
12. Carroll GM, Gamelin DR (2016) Kinetic analysis of photoelectrochemical water oxidation by mesostructured Co-Pi/α-Fe_2O_3 photoanodes. J Mater Chem A 4:2986–2994. https://doi.org/10.1039/C5TA06978E
13. Chemelewski WD, Lee H-C, Lin J-F, Bard AJ, Mullins CB (2014) Amorphous FeOOH oxygen evolution reaction catalyst for photoelectrochemical water splitting. J Am Chem Soc 136:2843–2850. https://doi.org/10.1021/ja411835a
14. Chen S, Takata T, Domen K (2017) Particulate photocatalysts for overall water splitting. Nat Rev Mater 2:17050. https://doi.org/10.1038/natrevmats.2017.50
15. Chen X, Zhang Z, Chi L, Nair AK, Shangguan W, Jiang Z (2016) Recent advances in visible-light-driven photoelectrochemical water splitting: catalyst nanostructures and reaction systems. Nano-Micro Lett 8:1–12. https://doi.org/10.1007/s40820-015-0063-3
16. Cheng H, Lv X-J, Cao S, Zhao Z-Y, Chen Y, Fu W-F (2016) Robustly photogenerating H_2 in water using FeP/CdS catalyst under solar irradiation. Sci Rep 6:19846. https://doi.org/10.1038/srep19846
17. Choi J, Ryu SY, Balcerski W, Lee TK, Hoffmann MR (2008) Photocatalytic production of hydrogen on Ni/NiO/$KNbO_3$/CdS nanocomposites using visible light. J Mater Chem 18:2371–2378. https://doi.org/10.1039/B718535A
18. Clarke RE, Giddey S, Badwal SPS (2010) Stand-alone PEM water electrolysis system for fail safe operation with a renewable energy source. Int J Hydrogen Energy 35:928–935. https://doi.org/10.1016/j.ijhydene.2009.11.100
19. Dinh C-T, Pham M-H, Kleitz F, Do T-O (2013) Design of water-soluble CdS–titanate–nickel nanocomposites for photocatalytic hydrogen production under sunlight. J Mater Chem A 1:13308–13313. https://doi.org/10.1039/C3TA12914D
20. Eftekhari A, Fang B (2017) Electrochemical hydrogen storage: opportunities for fuel storage, batteries, fuel cells, and supercapacitors. Int J Hydrogen Energy 42:25143–25165. https://doi.org/10.1016/j.ijhydene.2017.08.103
21. Fang Y-H, Liu Z-P (2010) Mechanism and tafel lines of electro-oxidation of water to oxygen on RuO_2(110). J Am Chem Soc 132:18214–18222. https://doi.org/10.1021/ja1069272
22. Le Formal F, Pendlebury SR, Cornuz M, Tilley SD, Grätzel M, Durrant JR (2014) Back electron-hole recombination in hematite photoanodes for water splitting. J Am Chem Soc 136:2564–2574. https://doi.org/10.1021/ja412058x
23. Frame FA, Townsend TK, Chamousis RL, Sabio EM, Dittrich Th, Browning ND, Osterloh FE (2011) Photocatalytic water oxidation with nonsensitized IrO_2 nanocrystals under visible and UV light. J Am Chem Soc 133:7264–7267. https://doi.org/10.1021/ja200144w
24. Fujishima A, Honda K (1972) Electrochemical photolysis of water at a semiconductor electrode. Nature 238:37–38. https://doi.org/10.1038/238037a0
25. Gupta B, Melvin AA, Matthews T, Dash S, Tyagi AK (2014) Facile gamma radiolytic synthesis of synergistic Co_3O_4-rGO nanocomposite: direct use in photocatalytic water splitting. Mater Res Express 1:045507. https://doi.org/10.1088/2053-1591/1/4/045507
26. Gurudayal Bassi PS, Sritharan T, Wong LH (2018) Recent progress in iron oxide based photoanodes for solar water splitting. J Phys D Appl Phys 51:473002. https://doi.org/10.1088/1361-6463/aae138
27. Han B, Hu YH (2016) MoS_2 as a co-catalyst for photocatalytic hydrogen production from water. Energy Sci Eng 4:285–304. https://doi.org/10.1002/ese3.128
28. Hara M, Kondo T, Komoda M, Ikeda S, Kondo JN, Domen K, Hara M, Shinohara K, Tanaka A (1998) Cu_2O as a photocatalyst for overall water splitting under visible light irradiation. Chem Commun 3:357–358. https://doi.org/10.1039/A707440I

29. Hara M, Nunoshige J, Takata T, Kondo JN, Domen K (2003) Unusual enhancement of H_2 evolution by Ru on TaON photocatalyst under visible light irradiation. Chem Commun 24:3000–3001. https://doi.org/10.1039/B309935K
30. Holladay JD, Hu J, King DL, Wang Y (2009) An overview of hydrogen production technologies. Catal Today 139:244–260. https://doi.org/10.1016/j.cattod.2008.08.039
31. Hong J, Wang Y, Wang Y, Zhang W, Xu R (2013) Noble-metal-free NiS/C_3N_4 for efficient photocatalytic hydrogen evolution from water. Chemsuschem 6:2263–2268. https://doi.org/10.1002/cssc.201300647
32. Hu S, Lewis NS, Ager JW, Yang J, McKone JR, Strandwitz NC (2015) Thin-film materials for the protection of semiconducting photoelectrodes in solar-fuel generators. J Phys Chem C 119:24201–24228. https://doi.org/10.1021/acs.jpcc.5b05976
33. Hu Z, Yu JC (2013) Pt_3Co-loaded CdS and TiO_2 for photocatalytic hydrogen evolution from water. J Mater Chem A 1:12221–12228. https://doi.org/10.1039/C3TA12407J
34. Huang Y, Liu Z, Gao G, Xiao G, Du A, Bottle S, Sarina S, Zhu H (2017) Stable copper nanoparticle photocatalysts for selective epoxidation of alkenes with visible light. ACS Catal 7:4975–4985. https://doi.org/10.1021/acscatal.7b01180
35. Iwase A, Yoshino S, Takayama T, Ng YH, Amal R, Kudo A (2016) Water splitting and CO_2 reduction under visible light irradiation using Z-scheme systems consisting of metal sulfides, CoO_x-Loaded $BiVO_4$, and a reduced graphene oxide electron mediator. J Am Chem Soc 138:10260–10264. https://doi.org/10.1021/jacs.6b05304
36. Jacobsson TJ, Fjällström V, Edoff M, Edvinsson T (2014) Sustainable solar hydrogen production: from photoelectrochemical cells to PV-electrolyzers and back again. Energy Environ Sci 7:2056–2070. https://doi.org/10.1039/C4EE00754A
37. Jakob M, Levanon H, Prashant VK (2003) Charge Distribution between UV-Irradiated TiO_2 and Gold Nanoparticles: Determination of Shift in the Fermi Level. Nano Letters 3:353–358. https://doi.org/10.1021/nl0340071
38. Janáky C, Chanmanee W, Rajeshwar K (2013) On the substantially improved photoelectrochemical properties of nanoporous WO_3 through surface decoration with RuO_2. Electrocatalysis 4:382–389. https://doi.org/10.1007/s12678-013-0177-7
39. Jian J, Jiang G, van de Krol R, Wei B, Wang H (2018) Recent advances in rational engineering of multinary semiconductors for photoelectrochemical hydrogen generation. Nano Energy 51:457–480. https://doi.org/10.1016/j.nanoen.2018.06.074
40. Kalanoor BS, Seo H, Kalanur SS (2018) Recent developments in photoelectrochemical water-splitting using WO_3/$BiVO_4$ heterojunction photoanode: a review. Mater Sci Energy Technol 1:49–62. https://doi.org/10.1016/j.mset.2018.03.004
41. Kalanur SS, Duy LT, Seo H (2018) Recent progress in photoelectrochemical water splitting activity of WO_3 photoanodes. Top Catal 61:1–34. https://doi.org/10.1007/s11244-018-0950-1
42. Kalanur SS, Hwang YJ, Chae SY, Joo OS (2013) Facile growth of aligned WO3 nanorods on FTO substrate for enhanced photoanodic water oxidation activity. J Mater Chem A 1:3479–3488. https://doi.org/10.1039/C3TA01175E
43. Kalanur SS, Hwang YJ, Joo O-S (2013) Construction of efficient CdS–TiO_2 heterojunction for enhanced photocurrent, photostability, and photoelectron lifetimes. J Colloid Interface Sci 402:94–99. https://doi.org/10.1016/j.jcis.2013.03.049
44. Kalanur SS, Hwang J-Y, Seo H (2017) Facile fabrication of bitter-gourd-shaped copper (II) tungstate thin films for improved photocatalytic water splitting. J Catal 350:197–202. https://doi.org/10.1016/j.jcat.2017.04.008
45. Kalanur SS, Lee SH, Hwang YJ, Joo O-S (2013) Enhanced photoanode properties of CdS nanoparticle sensitized TiO2 nanotube arrays by solvothermal synthesis. J Photochem Photobiol, A 259:1–9. https://doi.org/10.1016/j.jphotochem.2013.02.018
46. Kalanur SS, Seo H (2019) Intercalation of barium into monoclinic tungsten oxide nanoplates for enhanced photoelectrochemical water splitting. Chem Eng J 355:784–796. https://doi.org/10.1016/j.cej.2018.08.210
47. Kalanur SS, Seo H (2019) Facile growth of compositionally tuned copper vanadate nanostructured thin films for efficient photoelectrochemical water splitting. Appl Catal B 249:235–245. https://doi.org/10.1016/j.apcatb.2019.02.069

48. Kanan MW, Surendranath Y, Nocera DG (2008) Cobalt–phosphate oxygen-evolving compound. Chem Soc Rev 38:109–114. https://doi.org/10.1039/B802885K
49. Kegel J, Povey IM, Pemble ME (2018) Zinc oxide for solar water splitting: a brief review of the material's challenges and associated opportunities. Nano Energy 54:409–428. https://doi.org/10.1016/j.nanoen.2018.10.043
50. Kenney MJ, Gong M, Li Y, Wu JZ, Feng J, Lanza M, Dai H (2013) High-performance silicon photoanodes passivated with ultrathin nickel films for water oxidation. Science 342:836–840. https://doi.org/10.1126/science.1241327
51. Khaselev O, Turner JA (1998) A monolithic photovoltaic-photoelectrochemical device for hydrogen production via water splitting. Science 280:425–427. https://doi.org/10.1126/science.280.5362.425
52. Klahr B, Gimenez S, Fabregat-Santiago F, Bisquert J, Hamann TW (2012) Photoelectrochemical and impedance spectroscopic investigation of water oxidation with "Co–Pi"-coated hematite electrodes. J Am Chem Soc 134:16693–16700. https://doi.org/10.1021/ja306427f
53. Korzhak AV, Ermokhina NI, Stroyuk AL, Bukhtiyarov VK, Raevskaya AE, Litvin VI, Kuchmiy SY, Ilyin VG, Manorik PA (2008) Photocatalytic hydrogen evolution over mesoporous TiO_2/metal nanocomposites. J Photochem Photobiol, A 198:126–134. https://doi.org/10.1016/j.jphotochem.2008.02.026
54. Kudo A, Miseki Y (2008) Heterogeneous photocatalyst materials for water splitting. Chem Soc Rev 38:253–278. https://doi.org/10.1039/B800489G
55. Lewis NS, Nocera DG (2006) Powering the planet: chemical challenges in solar energy utilization. PNAS 103:15729–15735. https://doi.org/10.1073/pnas.0603395103
56. Li Q, Guo B, Yu J, Ran J, Zhang B, Yan H, Gong JR (2011) Highly efficient visible-light-driven photocatalytic hydrogen production of Cds-cluster-decorated graphene nanosheets. J Am Chem Soc 133:10878–10884. https://doi.org/10.1021/ja2025454
57. Li J, Wu N (2015) Semiconductor-based photocatalysts and photoelectrochemical cells for solar fuel generation: a review. Catal Sci Technol 5:1360–1384. https://doi.org/10.1039/C4CY00974F
58. Li X, Yu J, Low J, Fang Y, Xiao J, Chen X (2015) Engineering heterogeneous semiconductors for solar water splitting. J Mater Chem A 3:2485–2534. https://doi.org/10.1039/C4TA04461D
59. Li Y, Yu Z, Meng J, Li Y (2013) Enhancing the activity of a SiC–TiO_2 composite catalyst for photo-stimulated catalytic water splitting. Int J Hydrogen Energy 38:3898–3904. https://doi.org/10.1016/j.ijhydene.2013.01.077
60. Licht S, Wang B, Mukerji S, Soga T, Umeno M, Tributsch H (2000) Efficient solar water splitting, exemplified by RuO_2-Catalyzed AlGaAs/Si photoelectrolysis. J Phys Chem B 104:8920–8924. https://doi.org/10.1021/jp002083b
61. Lin Z, Li J, Li L, Yu L, Li W, Yang G (2017) Manipulating the hydrogen evolution pathway on composition-tunable CuNi nanoalloys. J Mater Chem A 5:773–781. https://doi.org/10.1039/C6TA09169E
62. Lin H-Y, Yang H-C, Wang W-L (2011) Synthesis of mesoporous Nb_2O_5 photocatalysts with Pt, Au, Cu and NiO cocatalyst for water splitting. Catal Today 174:106–113. https://doi.org/10.1016/j.cattod.2011.01.052
63. Lingampalli SR, Gautam UK, Rao CNR (2013) Highly efficient photocatalytic hydrogen generation by solution-processed ZnO/Pt/CdS, ZnO/Pt/$Cd_{1-x}Zn_xS$ and ZnO/Pt/$CdS_{1-x}Se_x$ hybrid nanostructures. Energy Environ Sci 6:3589–3594. https://doi.org/10.1039/C3EE42623H
64. Linic S, Christopher P, Ingram DB (2011) Plasmonic-metal nanostructures for efficient conversion of solar to chemical energy. Nat Mater 10:911–921. https://doi.org/10.1038/nmat3151
65. Maeda K, Domen K (2007) New non-oxide photocatalysts designed for overall water splitting under visible light. J Phys Chem C 111:7851–7861. https://doi.org/10.1021/jp070911w
66. Mangrulkar PA, Joshi MM, Tijare SN, Polshettiwar V, Labhsetwar NK, Rayalu SS (2012) Nano cobalt oxides for photocatalytic hydrogen production. Int J Hydrogen Energy 37:10462–10466. https://doi.org/10.1016/j.ijhydene.2012.01.112

67. Marimuthu A, Zhang J, Linic S (2013) Tuning selectivity in propylene epoxidation by plasmon mediated photo-switching of Cu oxidation state. Science 339:1590–1593. https://doi.org/10.1126/science.1231631
68. May MM, Lewerenz H-J, Lackner D, Dimroth F, Hannappel T (2015) Efficient direct solar-to-hydrogen conversion by *in situ* interface transformation of a tandem structure. Nat Commun 6:8286. https://doi.org/10.1038/ncomms9286
69. Mei Z, Li Y, Yang X, Ren W, Tong S, Zhang N, Zhao W, Lin Y, Pan F (2018) Tuning nanosheet Fe_2O_3 photoanodes with C3N4 and p-type CoO_x decoration for efficient and stable water splitting. Catal Sci Technol 8:3144–3150. https://doi.org/10.1039/C8CY00729B
70. Melchionna M, Beltram A, Stopin A, Montini T, Lodge RW, Khlobystov AN, Bonifazi D, Prato M, Fornasiero P (2018) Magnetic shepherding of nanocatalysts through hierarchically-assembled Fe-filled CNTs hybrids. Appl Catal B 227:356–365. https://doi.org/10.1016/j.apcatb.2018.01.049
71. Miyoshi A, Nishioka S, Maeda K (2018) Water splitting on rutile TiO_2-based photocatalysts. Chem Eur J 24:18204–18219. https://doi.org/10.1002/chem.201800799
72. Moore GF, Brudvig GW (2011) Energy conversion in photosynthesis: a paradigm for solar fuel production. Annu Rev Condens Matter Phys 2:303–327. https://doi.org/10.1146/annurev-conmatphys-062910-140503
73. Murdoch M, Waterhouse GIN, Nadeem MA, Metson JB, Keane MA, Howe RF, Llorca J, Idriss H (2011) The effect of gold loading and particle size on photocatalytic hydrogen production from ethanol over Au/TiO_2 nanoparticles. Nat Chem 3:489–492. https://doi.org/10.1038/nchem.1048
74. Nishiyama H, Kobayashi H, Inoue Y (2011) Effects of distortion of metal-oxygen octahedra on photocatalytic water-splitting performance of RuO_2-loaded niobium and tantalum phosphate bronzes. Chemsuschem 4:208–215. https://doi.org/10.1002/cssc.201000294
75. Onsuratoom S, Puangpetch T, Chavadej S (2011) Comparative investigation of hydrogen production over Ag-, Ni-, and Cu-loaded mesoporous-assembled TiO_2–ZrO_2 mixed oxide nanocrystal photocatalysts. Chem Eng J 173:667–675. https://doi.org/10.1016/j.cej.2011.08.016
76. Osterloh FE (2013) Inorganic nanostructures for photoelectrochemical and photocatalytic water splitting. Chem Soc Rev 42:2294–2320. https://doi.org/10.1039/C2CS35266D
77. Pan L, Kim JH, Mayer MT, Son M-K, Ummadisingu A, Lee JS, Hagfeldt A, Luo J, Grätzel M (2018) Boosting the performance of Cu_2O photocathodes for unassisted solar water splitting devices. Nat Catal 1:412. https://doi.org/10.1038/s41929-018-0077-6
78. Pan Z, Zheng Y, Guo F, Niu P, Wang X (2017) Decorating CoP and Pt nanoparticles on graphitic carbon nitride nanosheets to promote overall water splitting by conjugated polymers. Chemsuschem 10:87–90. https://doi.org/10.1002/cssc.201600850
79. Pastoriza-Santos I, Sánchez-Iglesias A, Rodríguez-González B, Liz-Marzán LM (2009) Aerobic synthesis of Cu nanoplates with intense plasmon resonances. Small 5:440–443. https://doi.org/10.1002/smll.200801088
80. Popczun EJ, McKone JR, Read CG, Biacchi AJ, Wiltrout AM, Lewis NS, Schaak RE (2013) Nanostructured nickel phosphide as an electrocatalyst for the hydrogen evolution reaction. J Am Chem Soc 135:9267–9270. https://doi.org/10.1021/ja403440e
81. Porosoff MD, Yan B, Chen JG (2016) Catalytic reduction of CO_2 by H_2 for synthesis of CO, methanol and hydrocarbons: challenges and opportunities. Energy Environ Sci 9:62–73. https://doi.org/10.1039/C5EE02657A
82. Potje-Kamloth K (2008) Semiconductor junction gas sensors. Chem Rev 108:367–399. https://doi.org/10.1021/cr0681086
83. Ran J, Zhang J, Yu J, Jaroniec M, Qiao SZ (2014) Earth-abundant cocatalysts for semiconductor-based photocatalytic water splitting. Chem Soc Rev 43:7787–7812. https://doi.org/10.1039/C3CS60425J
84. Reddy DA, Choi J, Lee S, Kim Y, Hong S, Kumar DP, Kim TK (2016) Hierarchical dandelion-flower-like cobalt-phosphide modified CdS/reduced graphene oxide-MoS_2 nanocomposites as a noble-metal-free catalyst for efficient hydrogen evolution from water. Catal Sci Technol 6:6197–6206. https://doi.org/10.1039/C6CY00768F

85. Reddy VR, Hwang DW, Lee JS (2003) Photocatalytic water splitting over ZrO_2 prepared by precipitation method. Korean J Chem Eng 20:1026–1029. https://doi.org/10.1007/BF02706932
86. Saadetnejad D, Yıldırım R (2018) Photocatalytic hydrogen production by water splitting over Au/Al-$SrTiO_3$. Int J Hydrogen Energy 43:1116–1122. https://doi.org/10.1016/j.ijhydene.2017.10.154
87. Sasaki Y, Iwase A, Kato H, Kudo A (2008) The effect of co-catalyst for Z-scheme photocatalysis systems with an Fe^{3+}/Fe^{2+} electron mediator on overall water splitting under visible light irradiation. J Catal 259:133–137. https://doi.org/10.1016/j.jcat.2008.07.017
88. Sayama K, Yase K, Arakawa H, Asakura K, Tanaka A, Domen K, Onishi T (1998) Photocatalytic activity and reaction mechanism of Pt-intercalated K4Nb6O17 catalyst on the water splitting in carbonate salt aqueous solution. J Photochem Photobiol, A 114:125–135. https://doi.org/10.1016/S1010-6030(98)00202-0
89. Sayed FN, Jayakumar OD, Sasikala R, Kadam RM, Bharadwaj SR, Kienle L, Schürmann U, Kaps S, Adelung R, Mittal JP, Tyagi AK (2012) Photochemical hydrogen generation using nitrogen-doped TiO_2–Pd nanoparticles: facile synthesis and effect of Ti^{3+} incorporation. J Phys Chem C 116:12462–12467. https://doi.org/10.1021/jp3029962
90. Seger B, Laursen AB, Vesborg PCK, Pedersen T, Hansen O, Dahl S, Chorkendorff I (2012) Hydrogen production using a molybdenum sulfide catalyst on a titanium-protected n^+p-silicon photocathode. Angew Chem Int Ed 51:9128–9131. https://doi.org/10.1002/anie.201203585
91. Seo SW, Park S, Jeong H-Y, Kim SH, Sim U, Lee CW, Nam KT, Hong KS (2012) Enhanced performance of $NaTaO_3$ using molecular co-catalyst $[Mo_3S_4]^{4+}$ for water splitting into H_2 and O_2. Chem Commun 48:10452–10454. https://doi.org/10.1039/C2CC36216C
92. Shi J, Guo L (2012) ABO_3-based photocatalysts for water splitting. Progr Nat Sci Mater Int 22:592–615. https://doi.org/10.1016/j.pnsc.2012.12.002
93. Simon T, Bouchonville N, Berr MJ, Vaneski A, Adrović A, Volbers D, Wyrwich R, Döblinger M, Susha AS, Rogach AL, Jäckel F, Stolarczyk JK, Feldmann J (2014) Redox shuttle mechanism enhances photocatalytic H_2 generation on Ni-decorated CdS nanorods. Nat Mater 13:1013–1018. https://doi.org/10.1038/nmat4049
94. Sinigaglia T, Lewiski F, Santos Martins ME, Mairesse Siluk JC (2017) Production, storage, fuel stations of hydrogen and its utilization in automotive applications-a review. Int J Hydrogen Energy 42:24597–24611. https://doi.org/10.1016/j.ijhydene.2017.08.063
95. Sreethawong T, Suzuki Y, Yoshikawa S (2005) Photocatalytic evolution of hydrogen over mesoporous TiO_2 supported NiO photocatalyst prepared by single-step sol–gel process with surfactant template. Int J Hydrogen Energy 30:1053–1062. https://doi.org/10.1016/j.ijhydene.2004.09.007
96. Stern PC, Sovacool BK, Dietz T (2016) Towards a science of climate and energy choices. Nature Climate Change 6:547–555. https://doi.org/10.1038/nclimate3027
97. Sun Z, Chen H, Huang Q, Du P (2015) Enhanced photocatalytic hydrogen production in water under visible light using noble metal-free ferrous phosphide as an active cocatalyst. Catal Sci Technol 5:4964–4967. https://doi.org/10.1039/C5CY01293G
98. Sun Z, Lv B, Li J, Xiao M, Wang X, Du P (2016) Core–shell amorphous cobalt phosphide/cadmium sulfide semiconductor nanorods for exceptional photocatalytic hydrogen production under visible light. J Mater Chem A 4:1598–1602. https://doi.org/10.1039/C5TA07561K
99. Sun Z, Yue Q, Li J, Xu J, Zheng H, Du P (2015) Copper phosphide modified cadmium sulfide nanorods as a novel p–n heterojunction for highly efficient visible-light-driven hydrogen production in water. J Mater Chem A 3:10243–10247. https://doi.org/10.1039/C5TA02105G
100. Sun Z, Zheng H, Li J, Du P (2015) Extraordinarily efficient photocatalytic hydrogen evolution in water using semiconductor nanorods integrated with crystalline Ni2P cocatalysts. Energy Environ Sci 8:2668–2676. https://doi.org/10.1039/C5EE01310K
101. Tachibana Y, Vayssieres L, Durrant JR (2012) Artificial photosynthesis for solar water-splitting. Nat Photonics 6:511–518. https://doi.org/10.1038/nphoton.2012.175

102. Takata T, Domen K (2019) Particulate photocatalysts for water splitting: recent advances and future prospects. ACS Energy Lett 4:542–549. https://doi.org/10.1021/acsenergylett.8b02209
103. Takata T, Pan C, Nakabayashi M, Shibata N, Domen K (2015) Fabrication of a core–shell-type photocatalyst via photodeposition of group IV and V transition metal oxyhydroxides: an effective surface modification method for overall water splitting. J Am Chem Soc 137:9627–9634. https://doi.org/10.1021/jacs.5b04107
104. Tang ML, Grauer DC, Lassalle-Kaiser B, Yachandra VK, Amirav L, Long JR, Yano J, Alivisatos AP (2011) Structural and electronic study of an amorphous MoS_3 hydrogen-generation catalyst on a quantum-controlled photosensitizer. Angew Chem Int Ed 50:10203–10207. https://doi.org/10.1002/anie.201104412
105. Tian H, Zhang XL, Scott J, Ng C, Amal R (2014) TiO_2-supported copper nanoparticles prepared via ion exchange for photocatalytic hydrogen production. J Mater Chem A 2:6432–6438. https://doi.org/10.1039/C3TA15254E
106. Tran PD, Xi L, Batabyal SK, Wong LH, Barber J, Loo JSC (2012) Enhancing the photocatalytic efficiency of TiO_2 nanopowders for H_2 production by using non-noble transition metal co-catalysts. Phys Chem Chem Phys 14:11596–11599. https://doi.org/10.1039/C2CP41450C
107. Trześniewski BJ, Smith WA (2016) Photocharged $BiVO_4$ photoanodes for improved solar water splitting. J Mater Chem A 4:2919–2926. https://doi.org/10.1039/C5TA04716A
108. Wan S, Ou M, Zhong Q, Zhang S, Song F (2017) Construction of Z-scheme photocatalytic systems using $ZnIn_2S_4$, CoO_x-loaded Bi_2MoO_6 and reduced graphene oxide electron mediator and its efficient nonsacrificial water splitting under visible light. Chem Eng J 325:690–699. https://doi.org/10.1016/j.cej.2017.05.047
109. Wang C, Cao S, Fu W-F (2013) A stable dual-functional system of visible-light-driven Ni(II) reduction to a nickel nanoparticle catalyst and robust in situ hydrogen production. Chem Commun 49:11251–11253. https://doi.org/10.1039/C3CC46623J
110. Wang J, Li B, Chen J, Li N, Zheng J, Zhao J, Zhu Z (2012) Enhanced photocatalytic H_2-production activity of $CdxZn_{1-x}S$ nanocrystals by surface loading MS (M = Ni Co, Cu) species. Appl Surf Sci 259:118–123. https://doi.org/10.1016/j.apsusc.2012.07.003
111. Wang X, Liu G, Wang L, Chen Z-G, Lu GQ, Cheng H-M (2012) ZnO–CdS@Cd heterostructure for effective photocatalytic hydrogen generation. Adv Energy Mater 2:42–46. https://doi.org/10.1002/aenm.201100528
112. Wang Z, Wang J, Li L, Zheng J, Jia S, Chen J, Liu B, Zhu Z (2017) Fabricating efficient CdSe–CdS photocatalyst systems by spatially resetting water splitting sites. J Mater Chem A 5:20131–20135. https://doi.org/10.1039/C7TA06085H
113. Wang Y, Zhu D, Xu X (2016) Zr-doped mesoporous Ta_3N_5 microspheres for efficient photocatalytic water oxidation. ACS Appl Mater Interfaces 8:35407–35418. https://doi.org/10.1021/acsami.6b14230
114. Wu W, Yue X, Wu X-Y, Lu C-Z (2016) Efficient visible-light-induced hydrogen evolution from water splitting using a nanocrystalline nickel phosphide catalyst. RSC Adv 6:24361–24365. https://doi.org/10.1039/C5RA25286E
115. Xiang Q, Yu J, Jaroniec M (2012) Synergetic effect of MoS_2 and graphene as cocatalysts for enhanced photocatalytic H_2 production activity of TiO_2 Nanoparticles. J Am Chem Soc 134:6575–6578. https://doi.org/10.1021/ja302846n
116. Xu X-T, Pan L, Zhang X, Wang L, Zou J-J (2019) Rational Design and construction of cocatalysts for semiconductor-based photo-electrochemical oxygen evolution: a comprehensive review. Adv Sci 6:1801505. https://doi.org/10.1002/advs.201801505
117. Xu Y, Wu R, Zhang J, Shi Y, Zhang B (2013) Anion-exchange synthesis of nanoporous FeP nanosheets as electrocatalysts for hydrogen evolution reaction. Chem Commun 49:6656–6658. https://doi.org/10.1039/C3CC43107J
118. Yan H, Yang J, Ma G, Wu G, Zong X, Lei Z, Shi J, Li C (2009) Visible-light-driven hydrogen production with extremely high quantum efficiency on Pt–PdS/CdS photocatalyst. J Catal 266:165–168. https://doi.org/10.1016/j.jcat.2009.06.024
119. Yang T, Bao Y, Xiao W, Zhou J, Ding J, Feng YP, Loh KP, Yang M, Wang SJ (2018) Hydrogen evolution catalyzed by a molybdenum sulfide two-dimensional structure with active

basal planes. ACS Appl Mater Interfaces 10:22042–22049. https://doi.org/10.1021/acsami.8b03977
120. Yang J, Wang D, Han H, Li C (2013) Roles of cocatalysts in photocatalysis and photoelectrocatalysis. Acc Chem Res 46:1900–1909. https://doi.org/10.1021/ar300227e
121. Yi S-S, Zhang X-B, Wulan B-R, Yan J-M, Jiang Q (2018) Non-noble metals applied to solar water splitting. Energy Environ Sci 11:3128–3156. https://doi.org/10.1039/C8EE02096E
122. Yoshida M, Takanabe K, Maeda K, Ishikawa A, Kubota J, Sakata Y, Ikezawa Y, Domen K (2009) Role and function of noble-metal/Cr-layer core/shell structure cocatalysts for photocatalytic overall water splitting studied by model electrodes. J Phys Chem C 113:10151–10157. https://doi.org/10.1021/jp901418u
123. Yu S-H, Chiu C-W, Wu Y-T, Liao C-H, Nguyen V-H, Wu JCS (2016) Photocatalytic water splitting and hydrogenation of CO_2 in a novel twin photoreactor with IO_3^-/I^- shuttle redox mediator. Appl Catal A 518:158–166. https://doi.org/10.1016/j.apcata.2015.08.027
124. Yuan Y-P, Cao S-W, Yin L-S, Xu L, Xue C (2013) NiS_2 Co-catalyst decoration on $CdLa_2S_4$ nanocrystals for efficient photocatalytic hydrogen generation under visible light irradiation. Int J Hydrogen Energy 38:7218–7223. https://doi.org/10.1016/j.ijhydene.2013.03.169
125. Zeng C, Hu T, Hou N, Liu S, Gao W, Cong R, Yang T (2015) Photocatalytic pure water splitting activities for $ZnGa_2O_4$ synthesized by various methods. Mater Res Bull 61:481–485. https://doi.org/10.1016/j.materresbull.2014.10.041
126. Zhang L, Jiang T, Li S, Lu Y, Wang L, Zhang X, Wang D, Xie T (2013) Enhancement of photocatalytic H_2 evolution on Zn0.8Cd0.2S loaded with CuS as cocatalyst and its photogenerated charge transfer properties. Dalton Trans 42:12998–13003. https://doi.org/10.1039/C3DT51256H
127. Zhang L, Tian B, Chen F, Zhang J (2012) Nickel sulfide as co-catalyst on nanostructured TiO_2 for photocatalytic hydrogen evolution. Int J Hydrogen Energy 37:17060–17067. https://doi.org/10.1016/j.ijhydene.2012.08.120
128. Zhang Z, Yates JT (2012) Band bending in semiconductors: chemical and physical consequences at surfaces and interfaces. Chem Rev 112:5520–5551. https://doi.org/10.1021/cr3000626
129. Zhou X, Liu R, Sun K, Friedrich D, McDowell MT, Yang F, Omelchenko ST, Saadi FH, Nielander AC, Yalamanchili S, Papadantonakis KM, Brunschwig BS, Lewis NS (2015) Interface engineering of the photoelectrochemical performance of Ni-oxide-coated n-Si photoanodes by atomic-layer deposition of ultrathin films of cobalt oxide. Energy Environ Sci 8:2644–2649. https://doi.org/10.1039/C5EE01687H
130. Zhu Y, Marianov A, Xu H, Lang C, Jiang Y (2018) Bimetallic Ag–Cu supported on graphitic carbon nitride nanotubes for improved visible-light photocatalytic hydrogen production. ACS Appl Mater Interfaces 10:9468–9477. https://doi.org/10.1021/acsami.8b00393
131. Zong X, Han J, Ma G, Yan H, Wu G, Li C (2011) Photocatalytic H_2 evolution on CdS loaded with WS_2 as cocatalyst under visible light irradiation. J Phys Chem C 115:12202–12208. https://doi.org/10.1021/jp2006777
132. Zong X, Yan H, Wu G, Ma G, Wen F, Wang L, Li C (2008) Enhancement of photocatalytic H_2 evolution on CdS by loading MoS_2 as cocatalyst under visible light irradiation. J Am Chem Soc 130:7176–7177. https://doi.org/10.1021/ja8007825

Role of Earth-Abundant/Carbonaceous Electrocatalysts as Cocatalyst for Solar Water Splitting

Mohit Prasad, Vidhika Sharma and Sandesh Jadkar

Abstract Solar energy can be tapped and stored efficiently using photoelectrochemical (PEC) cells. PEC cell utilizes influx of photons to drive uphill chemical reactions and thereby transforming their inherent energy into chemicals bonds. PEC reaction is one of the most important reactions for generating hydrogen and oxygen. Moreover, as the reaction is reversed and hydrogen is combusted in presence of oxygen; water is obtained as by-product. A lot of research efforts are underway for realizing efficient photoactive material that can absorb sunlight in visible region and has proper straddling band edges that can oxidize and reduce water. The water oxidation half cell reaction also restrains the technology as water oxidation is slow at the surface of photoanodes compared to other loss processes. Semiconductor (SC) photoanodes modified with earth abundant electrocatalyst (EC) can be a important proposition for realizing electrodes with high photocatalytic activity and stability for proficient PEC splitting of water. This approach allows optimization of different processes such as photon absorption, charge separation and surface catalysis independently. The PEC reactions are catalyzed by electrocatalyst by lowering the activation energy. For PEC H_2 generation reaction, the main earth abundant electrocatalyst comprises of transition metal chalcogenides, carbides, phosphides, whereas for O_2 generation mixed transition metal oxides can be utilized. Bifunctional (HER/OER) electrocatalyst such as NiFeOOH and Co-Mn oxide nanoparticle can be used for PEC splitting of water. Hybridization of composite photoanodes, provide flexibility for adjustment of different components with different properties but raises new issues at the interfacial forefront.

Keywords Photoelectrochemical cell · Electrocatalyst · Carbon · HER · OER · Bifunctional

M. Prasad · S. Jadkar (✉)
Department of Physics, Savitribai Phule Pune University, Pune 411007, India
e-mail: sandesh@physics.unipune.ac.in

V. Sharma (✉) · S. Jadkar
School of Energy Studies, Savitribai Phule Pune University, Pune 411007, India
e-mail: vidhika15@gmail.com

Inamuddin et al. (eds.), *Methods for Electrocatalysis*,
https://doi.org/10.1007/978-3-030-27161-9_8

1 Introduction

Global energy demand and environment sustainability issues can be ameliorated by the emerging efficient technologies which can transform and efficiently store solar energy. PEC cleavage of water is the most important technology which utilizes the influx of solar photons to drive the PEC process in water to release H_2 and O_2 at respective electrodes. The influx photon energy is stockpiled in the form of chemicals bonds of H_2. Hydrogen with atomic mass 1.00007825 g mol^{-1}, ionic radius 0.208 nm, first ionization energy of 1311 kJ mol^{-1}, and high energy density of 0.0899 gm^{-3} at 20 °C makes it an attractive energy carrier for green combustion.

PEC cell has been inspired from the photosynthetic process, which uses chlorophyll (Mg at the centre and phytol chain) to harvest sunlight and drive the uphill chemical reaction. In photosystem I and II, incident radiations are stored as proton gradient across trans-membrane, rather than molecular hydrogen [1–3]. Fujishima and Honda mimicked the natural photosynthesis process by using semiconductor titanium dioxide for absorbing sunlight, segregating charge carriers and catalyzing water to evolve hydrogen and oxygen [4]. In the basic PEC cell electrons were transferred to platinum counter electrode via external circuit, where protons are reduced to generate hydrogen, whereas holes move towards the photoelectrode/electrolyte interface to release oxygen. One of the foremost advantage of the PEC cell is the use of metal oxide semiconductors for absorbing influx solar radiation, and charge segregation, as these metal oxides are stable in aqueous media [5]. Highly oxidizing valence band holes of metal oxides are delivered to the surface electrode for water oxidation reaction. The performance of metal oxides based PEC cells is often limited by the recombination rate of valence band holes and conduction band electrons at the semiconductor electrolyte interface, which in turn leaves fewer holes to oxidize water. To circumvent the problem of recombination the coupling of electrocatalyst on the semiconductor surface can be a very good proposition.

2 Electrocatalyst in Solar Water Splitting: An Adaptive Junction

There are three important steps in overall PEC water splitting reaction, (i) generation of photogenerated electron/hole pairs in a semiconductor (ii) segregation and migration of these charge carriers towards the surface of the semiconductor and (iii) utilization of these charge carriers for reduction and oxidation. The PEC water splitting reaction can be split into two half cell reactions (i) hydrogen evolution reaction (HER), and (ii) Oxygen evolution reaction (OER). The HER reaction takes place at cathode where H^+ ions are reduced to hydrogen, whereas OER takes place at photoanode, where water molecules are oxidized. In PEC devices, electrocatalyst can help in accelerating the overall water splitting process by providing reaction sites and catalyzing HER and OER reactions. Electrocatalysts help photogenerated

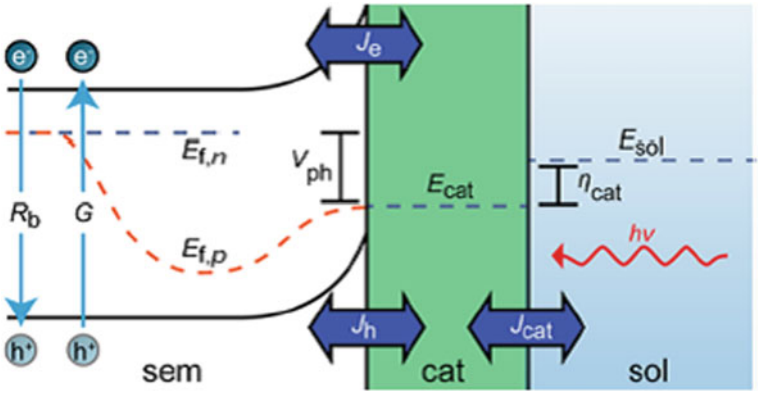

Fig. 1 Iluminated electrocatalyst modified n-type semiconductor with Fermi levels and steady state currents in solution. Here, E_{fn}, E_{cat} and E_{sol} denote electrochemical potentials which equilibrate in dark. E_{fp} is hole quasi Fermi level, which drops down to electron level E_{fn}. V_{ph} denotes photovolatge at semiconductor/catalyst interface. J_h, J_e are the hole and electron current density and η_{cat} indicates catalytic efficiency. Adapted from Ref. Nellist et al. [8]; copyright 2016 American Chemical Society

charge carriers to separate and migrate efficiently due to formation of effective interfaces between them and the light harvesting semiconductor as shown in Fig. 1 [6–9]. Moreover, electrocatalyst helps in photocorrosion suppression and in enhancing the chemical stability of semiconductor photoelectrodes. It is very important to develop electrocatalyst which are highly stable, efficient and can easily facilitate the PEC, HER and OER reactions which in turn can help in improving the overall solar energy conversion process. Volcano plot can be used to select and screen the electrocatalyst for efficient HER activity [10]. The electrocatalyst which are present at the top of the volcano plot generally possess high activity towards a specific reaction. Owing to long term operation, chemical diffusion may occur at the semiconductor/electrocatalyst interface. The mass loading of electrocatalyst on semiconductor surface plays a major role in enhancing the PEC performance. A high amount of mass loading can block the incident influx of radiations because electrocatalysts are normally opaque in nature [11]. A more appropriate solution will be to have a photoactive electrocatalyst which absorb influx of radiation in a region complementary to that of underlying semiconductor. MoS_2 for example not only catalyzes the HER but is also photoactive when coupled with a charge carrier shuttle [12–14]. Currently, for PEC water splitting the most efficient electrocatalysts comprises of precious metals. The highest HER activity is exhibited by Pt based compounds and for OER activity Ir (Ru) group metal are the best candidates [15, 16]. Large scale commercial applications of these HER and OER electrocatalysts is hindered by their high cost and rare natural availability. To replace precious metals with earth abundant cost effective electrocatalysts for the synthesis of HER/OER electrocatalysts a lot of research efforts are being devoted. HER electrocatalyst comprises of transition metal phosphides, chalcogenides, carbides and nitrides, whereas OER consist of oxides, hydroxides, phosphides etc. The high stability, low cost of these earth

abundant electrocatalysts makes them an ideal candidate for PEC splitting of water. To evaluate PEC activity and stability electrochemical measurements can be carried out which consist of linear sweep voltammetry (LSV), cyclic voltammetry (CV), chronoamperometry (CA), and electrochemical impedance spectroscopy (EIS). PEC and electrochemical reactions are driven by different driving forces. In case of PEC, it is light which carries forward the reaction, where as in electrochemical reactions bias plays a key role. So, to describe and ascertain the photo-catalytic and electrocatalytic properties different parameters are required. One common parameter in both the reactions is faradic efficiency. Faradic efficiency is the effectual utilization of charges for generating target productions of hydrogen and oxygen [17]. Overpotential at a certain current density ascertains the activity of synthesized electrocatalysts for HER and OER activity. High electrocatalytic activity can be directly correlated to small overpotential value of electrocatalysts. From Eq. 1, one can easily calculate the tafel slope and exchange current densities which can help in evaluating the activity of different types of electrocatalysts.

$$|\eta| = \frac{2.3RT}{\alpha nF} \log \frac{J}{J_0} \tag{1}$$

Equation 1, establish a relationship between tafel slope and exchange current density and can help in establishing the limiting step in HER and OER reactions. Here in Eq. 1 η denotes no. of electrons involved in rate limiting step. R and T denotes gas constant and absolute temperature. Whereas α and F represents charge transfer coefficient and Faraday constant. The tafel plot explains the reaction mechanism whereas (J_o) describes under equilibrium, the electrocatalytic activity of materials. To have efficient HER and OER activity it is desirable that tafel slope is low and value of J_o is high. The durability of the electrocatalyst is studied by recording continuous/intermittent polarization under a fixed operating current and variation of potential is recorded with time. The photogenerated voltage compensates the overpotential required for proton reduction/water oxidation. In PEC systems, HER/OER occur at potential higher than 0 V versus RHE or lower than 1.23 V versus RHE. The catalytic performance can be evaluated using basic parameters such as onset potential and photocurrent densities at 0 V versus RHE for HER and 1.23 V versus RHE for OER. For the photocathode and photoanode, the benchmark points are served by J_0 and $J_{1.23}$ (photocurrent densities) V versus RHE during electrochemical durability tests. Under zero bias conditions, to compare overall efficiency of different PEC devices, a benchmark value known as solar-to-hydrogen (STH) conversion efficiency is used. A two electrode system is procured to measure STH efficiency by short circuiting working electrode (WE) and counter electrode (CE). The influx of solar radiations is sufficient to drive the reaction. STH efficiency is defined as chemical energy evolved to that of solar influx of incident radiations. Rather than using cumbersome process of gas chromatography for estimating hydrogen production, Eq. 2, can be used to evaluate STH efficiency for HER reaction.

$$STH\ (\%) = \frac{|J_{sc}|\left(\text{mA cm}^{-2}\right) \times 1.23(\text{V}) \times \eta_F}{P_{total}\left(\text{mW cm}^{-2}\right)} \times 100 \tag{2}$$

Here P_{total} is incident sunlight having intensity of 100 mW/cm^2. Considering ηF as 100% for HER, Eq. (2) at AM1.5G can be reduced to Eq. 3.

$$STH\ (\%) = |J_{sc}|\left(\text{mA cm}^{-2}\right) \times 1.23(\text{V}) \tag{3}$$

A two electrode PEC device can also be used to determine STH efficiency [17]. An external bias is generally required between WE and CE in order to have water splitting reaction in a PEC cell. Thus applied bias photon-to-current efficiency (ABPE) as given by Eq. 4 is used to calculate and decipher the conversion efficiency in PEC devices. The ABPE for PEC water splitting is estimated as follows assuming ηF is 100%.

$$ABPE\ (\%) = |J_{bias}|\left(\text{mA cm}^{-2}\right) \times (1.23 - |V_{bias}|)(\text{V}) \tag{4}$$

When J_{bias} is the photocurrent achieved under external bias (V_{bias}) [17]. In this chapter we will cover the recent advancements of earth abundant heterogeneous electrocatalyst for PEC cleavage of water. The whole text is split in two parts (i) earth abundant HER and OER electrocatalysts which also include bifunctional electrocatalyst, and (ii) carbonaceous electrocatalyst which are metal free such as graphitic carbon nitride, graphene and carbon nanofiber. In order to improve the catalytic properties, different strategies that can be formed and implemented are discussed. The composition/structure catalytic modification of catalysts which forms the primary strategy is also discussed in detail. Finally, major challenges and the future prospects of efficient PEC cells using earth abundant electrocatalyst is discussed in detail in the conclusion section.

3 Catalysts for Photoelectrochemical HER

Platinum is the most sorted and well known element for HER electrocatalysts. Since Pt is scarce and expensive. Hence considerable interest of research community is in developing low cost HER electrocatalysts. A comparison of different types of earth abundant HER electrocatalysts for PEC applications has been enlisted in Table 1. Thus, earth abundant element materials integrated with silicon (Si) photoelectrode has also been reported as a model platform for HER electrocatalysts. The photoelectrode with earth abundant catalysts and Si ranged between 1.2 and 7.6% [18]. The alloys of Ni and Co with Mo, at low overpotentials exhibit high photocurrent densities leading to H_2 production.

In order to describe HER/OER activity of electrocatalyst there is a need of metrics. Tafel slopes helps in comparing the activity of different electrocatalysts

Table 1 Earth-abundant PEC-HER systems

S. No.	Electro-catalyst	Photoactive substrate	Current density (mA cm^{-2})	pH	References
1.	Mo_3S_4	p-Si	−10.0	0	Hou et al. [19]
2.	W_2C	p-Si	−4.0	0	Berglund et al. [20]
3.	1T-MoS_2	n^+p-Si	−17.6	0	Ding et al. [21]
4.	CoPS	n^+pp^+-Si	−35.0	0	Cabán-Acevedo et al. [22]
5.	NiMo	p-Si	−15.0	4.5	McKone et al. [23]
6.	Mo_2C	p-Si	−11.2	14.0	Morales-Guio et al. [24]
7.	2H-MoS_2	p-Si	24.6	0	Kwon et al. [25]
8.	2H-MoS_2	p-Si	21.7	0	Oh et al. [26]
9.	$CoMoS_x$	p-Si	17.5	4.2	Chen et al. [27]
10.	$CoMoS_x$	p-Si	17.2	0	Chen et al. [28]
11.	MoO_xS_y	p-Si	9.8	1	Bao et al. [29]
12.	S:MoP	p-Si	33.1	0	Kwon et al. [30]
13.	$CoSe_2$	p-Si	9.0	1	Basu et al. [31]
14.	NiCoSe	p-Si	37.5	0	Zhang et al. [32]
15.	$Ni_{12}P_5$	p-Si	21.0	0	Huang et al. [33]
16.	NiFe LDH	p-Si	7.0	13.6	Zhao et al. [34]
17.	MoS_xCl_y	n^+pp^+-Si	43.0	0	Ding et al. [35]
18.	$MoSe_xCl_y$	n^+pp^+-Si	38.8	0	Ding et al. [35]
19.	MoS_x	n^+p-Si/Ti/TiO_2	>16	0	Seger et al. [36]
20.	MoS_2	n^+p-Si/Al_2O_3	35.6	0	Fan et al. [37]
21.	CoP	n^+p-Si/Co	15.6	1	Bao et al. [38]
22.	NiMo	n^+p-Si/TiO_2	14.3	0	Shaner et al. [11]
23.	NiP_2	n^+p-Si/Ni	12.0	0	Chen et al. [39]
24.	NiMo	ZnO/p-i-n a-Si/TiO_2	11.0	4.5	Lin et al. [40]

whereas, overpotential helps in quantifying the current density required for HER (~10 mA cm^{-2}) and OER (~1 mA cm^{-2}) activity [9]. Volcano plots help in correlating HER exchange current densities of different materials and chemisorption energy of H_2 on them. Volcano plots and mapping of electrocatalysts was first reported by Trasatti in 1970 [10]. Volcano plots reveal that maximum catalytic activity is obtained when hydrogen binding energy of an electrocatalyst is optimum. Pt is the ideal metal for electrocatalytic activity as it lies at the apex of the volcano. Hinnemann et al. in [41] utilized the above mentioned relationship and using DFT calculations, identified materials which have nearly zero free energy change which is linked with atomic H_2

binding to the electrocatalyst surface. For HER activity, despite bulk MoS_2 being a poor catalyst, they predicted in layered form MoS_2 can serve as a suitable material [41]. MoS_2 is a promising HER electrocatalyst in acidic solution, so lot of focus has been on coupling it with crystalline silicon. p-Si nanowire arrays decorated with MoS_2 using photoassisted electrodeposition technique exhibited properties of an efficient HER electrocatalyst [42]. MoS_2 loaded on Si NWs sets the onset potential at 0.25 V versus RHE with considerable anodic shift of 0.2 V [26, 43]. Although, photocurrent density observed in bare Si substrate is very low (0.080 mA cm^{-2} at −0.2 V vs. RHE), due to inherent poor charge segregation. Seger et al. introduced a metallic thin layer of Ti before the photo-electrodeposition of MOS_x catalyst to protect silicon from oxidation [36]. The synthesis of MoS_x/Ti/n^+p-Si photocathode exhibited a photocurrent density of ~16 mA cm^{-2} at 0 V versus RHE with onset potential of 0.33 V versus RHE [36]. Even bulk phase of MoS_2 has been utilized for HER activity by incorporating foreign heteroatoms such as Co, Fe or Ni [7]. These heteroatoms (Co, Fe, Ni) improved the HER activity due to increased surface area. Heterometal doping leads to defects exposure and S-terminated edges as active HER sites. Si@MM_oS_x (M = Fe, Co, Ni) photocathode exhibited optimum activity when doped with Co heteroatoms. The photoanodes had a turn on voltage and photocurrent density of +0.192 V and −17.2 mA cm^{-2} respectively. Nonmetal dopants such as O_2, P or Cl^- ions can be used to dope bulk MoS_2 in order to enhance its HER activity. Bao et al. loaded amorphous molybdenum oxysulfide (MoO_xS_y) electrocatalyst on p-Si microwires by photo-assisted electro-deposition. The loading amount of electrocatalyst can be controlled by varying number of deposition cycles. Si-MWs@MoO_xS_y exhibited analogous properties to that of Si-MWs@PtNPs and was also considerably stable in acidic medium [29, 38]. Ding et al. loaded MoQ_xCl_y (Q=S, Se) electrocatalyst on Si micropyramids and recorded a onset potential of 0.41 V with photocurrent density of ~43 mA cm^{-2} at 0 V versus RHE, and a fill factor of 0.35 [35]. The outstanding PEC response exhibited by MoS_xCl_y/npp-Si was due to favorable band bending in the n^+pp^+ design, efficient light trapping by pyramidal morphology and high-transparency of the catalyst. The authors extended chemical vapor deposition to realize $MoSe_xCl_y$/n^+pp^+-Si photocathode which has photocurrent density of 38.8 mA cm^{-2} at 0 V versus RHE and an onset potential of 0.35 V [35]. A deep impact on the electrochemical HER activity can be exhibited by the phase structure of MoS_2 [12, 21]. Lukowski et al. reported that metallic 1T-MoS_2 obtained via exfoliation from 2H-MoS_2 displayed superior properties as HER catalyst. It opens active catalytic active sites and has simple electrode kinetics [12]. Ding et al. loaded p-Si surface with the 1T-MoS_2 and 2H-MoS_2 using chemical vapor deposition method. p-Si loaded with 1T MoS_2 exhibted a much higher photocurrent density ~17.6 mA cm^{-2} compared to photocurrent density of 4.2 mA cm^{-2} in 2H-MoS_2 (p-Si) [21]. The small charge transfer resistance across the semiconductor/catalyst/electrolyte interface is responsible for the enhancement in PEC activity, slow carrier recombination dynamics and consequently efficient charge carrier separation. This enhancement is confirmed and supported by electrochemical impedance and surface photoresponse measurements [21]. Oh et al. coated p-Si with MoS_2 using atomic layer deposition. The synthesized MoS_2/p-Si with an onset potential of 0.23 V

and photocurrent density of ~21.7 mA cm^{-2} at 0 V versus RHE without degradation for 24 h in 0.5 M H_2SO_4 under 1 sun illumination [26, 43]. Molybdenum boride, carbide and phosphide have been recognized as proficient electrocatalysts for electrochemical splitting of water to produce H_2. MoS_2 electrocatalysts are chemically stable in acidic solution, whereas Mo_2C is stable in basic medium. The activity in alkaline solutions is surprisingly high and is comparable to that in acidic solutions [44, 45].

Popczun et al. have confirmed experimentally the high electrocatalytic activity of Ni_2P for HER [46]. Ti modified n^+p Si surface was loaded with NiP_2 as shown in Fig. 2. The photocathode has onset potential of 0.41 V versus RHE in 0.5 M H_2SO_4 and exhibited photocurrent density of 12 mA cm^{-2} at 0 V [39]. $Ni_{12}P_5$ nanoparticle derived from solvothermal technique is an excellent electrocatalyst which can be integrated with p-type silicon nanowire photocathode and photoconversion efficiency of 2.97% was achieved together with photocurrent density of 21 mA cm^{-2} at 0 V versus RHE [33]. Ni-Fe was coupled with Ti/p-Si to realize stable photocathode systems. The Ni-Fe acts as a HER catalyst and play multiple roles (i) it

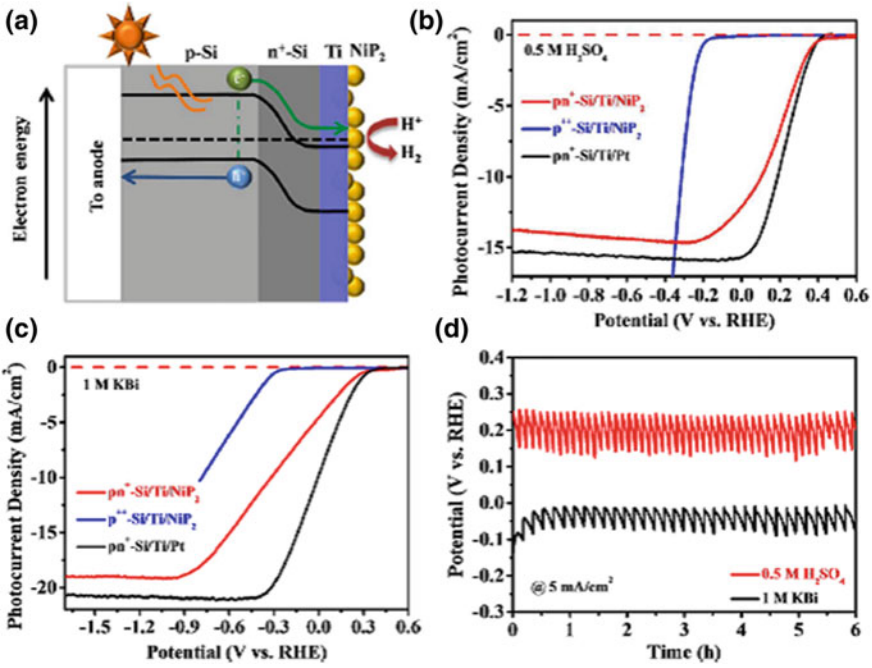

Fig. 2 PEC performance of pn^+-Si/Ti/NiP_2 photoelectrode. **a** Diagram showing light absorption, charge segregation and HER on photoelectrode surface. **b**, **c** Photocurrent density curves of pn^+-Si/Ti/NiP_2 photoelectrode as a function of potential under 100 mW cm^{-2} simulated solar light with different electrolyzers. **d** Chronopotentiometric curves as a function of time for pn^+-Si/Ti/NiP_2 photoelectrode (at a photocurrent density of 5 mA cm^{-2}). Adapted from Ref. Chen et al. [39]; copyright 2016 American Chemical Society

promotes surface reaction kinetics (ii) promote stability by protecting the layer and (iii) form junction to alleviate segregation. NiFe catalyzed p-type Si demonstrated generation of 10 mA cm^{-2} photocurrent in 1 M KOH electrolyte for 24 h [34]. Shaner et al. employed TiO_2 as antireflection coating over the surface of Si microwire array deposited with NiMo alloy [11]. The photocathode exhibited an onset potential of 0.42 V with photocurrent density of ~14.3 mA cm^{-2} at 0 V versus RHE. Caban-Acevedo et al. first predicted the HER activity of ternary pyrite-type cobalt phosphosulphide (CoPS) using DFT calculations. CoPS intregated with Si micropyramids exhibited a photocurrent of 35 mA cm^{-2} at 0 V versus RHE [22]. This integrated p-type silicon photocathode has superior and stable catalytic performance among the non precious electrocatalyst used for HER activity. Recently, p-Si nanowires arrays were deposited with $NiCoSe_x$ electrocatalyst to form a core-shell structure using photo-assisted electrodeposition technique [32]. With this configuration a record high photocurrent of 37.5 mA cm^{-2} at 0 V versus RHE was achieved. Mo based electrocatalyst are more efficient compared to Ni and Co based electrocatalysts. They work as co-catalyst in synchronization with the silicon-based photocathode electrocatalyst present on the photoelectrode surface. It reduces the overpotential required for HER activity by facilitating charge transfer across solid/liquid interface and also alters the bands for improved charge segregation. For proficient PEC activity the electrocatalyst with higher activity can serve as an excellent co-catalyst for reaction. Although Ni based electrocatalyst are very good for HER activity but Si photocathodes loaded with these exhibited very low PEC activity. The main reason attributed to this low activity of Ni based co-catalysts is their poor optical transparency. However, Ni co-catalysts exhibit outstanding stability and their independency from pH. It is clear from the research reports that electrocatalyst based on MoS_2 can serve as efficient co-catalyst for HER activity. Doping by heteroatoms had a significant impact on the catalytic as well as optical properties of the MoS_x based heterostructure. Thus utilizing doped MoS_x based co-catalysts can be an efficient strategy for enhancing HER activity in PEC cells.

4 Catalysts for the Photoelectrochemical OER

Cobalt based electrocatalyst has emerged as a viable alternative of noble metal based electrocatalyst for OER activity. Co-based catalyst comprises of oxides, phosphate and borates, which can be synthesized using different synthesis routes such as hydrothermal, electrodeposition and photo-assisted electrodeposition. Moreover, synthesis procedure of these Co-based electrocatalyst is very simple. Yang et al. deposited CoO_x catalyst on n-type silicon surface using plasma enhanced atomic layer deposition method. A high photocurrent density of 17 mA cm^{-2} at 1.23 V was achieved [47]. Compared to planar Si, high photocurrent is attributed to reduced silicon oxide thickness that provides more intimate interfacial contact between light absorber and catalyst [47]. Zhou et al. deposited a 50 nm thin layer of CoO_x on

planar Si substrate via atomic layer deposition to realize $CoO_x/SiO_x/Si$ photoanode [48]. The synthesized photoelectrode exhibited photocurrent-onset potentials of -205 ± 20 mV and solar-to-O_2 (g) conversion efficiencies of $1.42 \pm 0.20\%$, for a duration of 100 days. The reported photoelectrode is one of the robust photocurrent reported till date [48]. Plasma enhanced atomic layer deposition at low temperature was used by Sharp et al. to load p^+n-Si substrate with $Co(OH)_2/Co_3O_4$ electrocatalyst [49]. The synthesized photoanode resulted in a photocurrent density of 30.8 mA cm^{-2} at 1.23 V versus RHE. These characteristics were observed under simulated solar radiation, for duration of 72 h (continuous operation) surmounting the performance of previously reported Si based photoelectrodes. On the other hand Hill et al. employed electrodeposition method and reported growth of nanoscale CoOOH/Co core shell electrocatalyst on n-Si [50]. These cells comprise of individual units of $Co(OH)_2/Co_3O_4/p^+n$-Si, in which CoOOH/Co islands served as water oxidation reaction centres whereas holes are collected from n-Si/SiO_x solar cell as shown in Fig. 3. The synthesized photoanode has non uniform barrier height together with low over potential which is governed by the Co coverage. The barrier height elevates from 0.7 to 0.91 eV as thickness profile of Co increase [50]. Nocera et al. in 2008 discovered CoPi as an excellent co-catalyst for OER activity. CoPi has remarkable catalytic activity in neutral media and can be easily prepared. Thin layer of CoPi was introduced in different types of semiconductor materials to enhance the OER activity of synthesized photoelectrodes [51–53]. Similarly, cobalt borate (CoBi) can be used as an overlayer over thin film or nanoparticles co-catalysts [54]. Li et al. found that integration of CoBi with electrodeposited $BiVO_4$ anode, shifts the water oxidation onset potential by ~0.3 V. The cobalt borate co-catalyst accelerates the water oxidation process and also reduces recombination by promoting charge transfer process at semiconductor electrolyte interface [55]. A comparison of different types of earth abundant OER electrocatalysts for PEC applications has been enlisted in Table 2.

Metallic nickel in alkaline solution can withstand corrosion, so inspired by it Kenney et al. deposited an ultrathin film of (5 nm) nickel as a protective layer over substrates of Si [56]. The NiO_x/Ni/n-Si operates for long duration (80 h) exhibiting photocurrent of 10 mA cm^{-2} in 1 M KOH. The sputtered NiO_x has proved to be an excellent OER catalyst which can be easily integrated with n-type silicon [56]. Sun

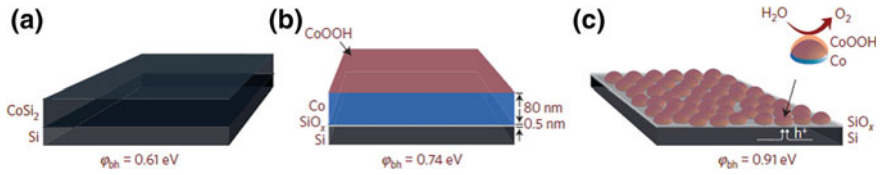

Fig. 3 Diagram of solid state Schottky barrier and electrodeposited n-Si/SiO_x/C_o/C_oOOH junction. **a** Solid state, epitaxial n-Si/$CoSi_2$ schottky barrier produced in vacuum with barrier height 0.61 eV. **b** Electrodeposited n-Si/SiOx/Co/CoOOH junction with barrier height 0.74 eV. **c** Inhomogeneous growth of Co layer with barrier height of 0.91 eV. Adapted from Ref. Hill et al. [50]; copyright 2015 Springer Nature

Table 2 Earth-abundant PEC-OER systems

S. No.	Electro-catalyst	Photoactive substrate	Current density (mA cm^{-2})	pH	References
1.	Co	npp^+ Si	1.2	7.0	Pijpers et al. [52]
2.	Ni	n-Si	1.6	9.5	Kenney et al. [56]
3.	$Co/Co(OH)_2$	n-Si	~16.0	13.6	Hill et al. [50]
4.	CoO_x	n-Si	23.2	13.6	Zhou et al. [48]
5.	Ni/NiO_x	n-Si	~10.0	9.5	Kenney et al. [56]
6.	CoO_x/NiO_x	n-Si	28.0	13.6	Zhou et al. [57]
7.	CoO_x	p^+n-Si	17.0	13.6	Yang et al. [47]
8.	$Co_3O_4/Co(OH)_2$	p^+n-Si	30.8	13.6	Yang et al. [49]
9.	Ni/NiO_x	p^+n-Si	29.0	13.6	Sun et al. [58]
10.	NiFe alloy	p^+n-Si	31.2	13.6	Oh et al. [43]
11.	$NiSe_2$	a-Si	5.80	13.6	Kwak et al. [59]
12.	NiO_x	a-Si/c-Si	21.8	13.6	Wang et al. [60]
13.	NiOOH	$n\text{-Si}/TiO_2$	18	14.0	Yao et al. [61]

et al. reported stabilization and continuous operation of np^+-Si(100) and n-Si(111) photoanodes for 1200 h [58]. Under simulated solar illumination, NiO_x-coated np^+-Si(100) photoanodes can give photocurrent up to 29 ± 1.8 mA cm^{-2} with onset potentials of −180 ± 20 mV and a solar-to-O_2(g) conversion efficiency of 2.1%. The NiO_x has a band gap of ~3.7 eV. Zhou et al. introduced an ultra thin layer of CoS_x between NiO_x layer and n-Si enhancing electrochemical performance [57]. The $NiO_x/CoO_x/SiO_x$/n-Si photoanode exhibited photocurrent of ~28 mA cm^{-2} at 1.23 V. Doping of Fe atom into nickel oxides is an efficient way to improve the electrochemical OER activity. Optimized Fe/Ni ratio in electrocatalysts helps in achieving high OER activity for water oxidation process compared to NiO_x, NiOOH or $Ni(OH)_2$ catalysts [62].

$NiSe_2$ has recently been discovered as active OER electrocatalyst. n-Si nanowire array loaded with $NiSe_2$ nanocrystal OER catalyst a photocurrent density of 5.8 mA cm^{-2} at 1.23 V versus RHE is achieved with an onset potential of 0.7 V [59]. Oh et al. recently synthesized 3D porous Ni inverse opal and combined it with Si substitution in a micro pattern. The patterned nanostructures yielded photocurrent of 31.2 mA cm^{-2} and onset potential of 0.94 V versus RHE [26, 43]. At moderate onset potential oxygen can easily evolve when Fe based OER catalyst such as FeOOH is used. Although FeOOH has low light absorption characteristic but low cost and easy preparation method makes it an ideal candidate for catalytic activity [63, 64]. Another electrocatalyst based on Fe, Co-Fe-OOH was synthesized using electrodeposition method. The Co-Fe-hydroxide catalyst with amorphous nanosheet structure exhibited enhanced OER activity than individual Co-H and Co-Fe based

catalyst [65]. In plants manganese is found as oxygen evolving complex of photosystem II and it is a favourable choice for OER catalyst. However, manganese oxide has not been proved an active OER electrocatalyst. Active manganese oxide as OER catalyst exhibits structural disorder and it also co-exist in more than one oxidation states. The role of multiple oxidation state in catalysis is still not well understood, some group claim that MnO_2, Mn_2O_3 or other mixtures of all these phases is essential for efficient catalysis and OER. The activity of OER gets diminished when Mn^{3+} disproportionately changes into Mn^{2+} and Mn^{4+} ions in the acidic medium.

Sustainable water splitting reaction requires optimum HER and OER reactions should occur in the same electrolyte with minimum overpotential. For this to take place bifunctional electrocatalysts are required which can ease the water splitting reaction and at the same time reduce the production cost. A lot of progress has been made in realizing bifunctional electrocatalyst such as phosphides, sulfides, selenides, metal oxides and alloys etc. Transition metal oxides based electrocatalysts have evolved as excellent bifunctional electrocatalysts. An impressive water photolysis efficiency ~12.3% was obtained using NiFe layered double hydroxides (LDH) as electrocatalyst and pervoskite photovoltaics as power supply. For overall water splitting in a basic medium NiFe-LDH based water system delivered a photocurrent of 10 mA cm^{-2} at an overpotential of 1.7 V [66]. CoSe and NiSe nanowalls can be used as efficient and robust bifunctional electrocatalysts with low onset potentials in alkaline media. It exhibited photocurrent density of 10 mA cm^{-2} at −0.078 V versus RHE for HER and 150 mA cm^{-2} at 1.74 V versus RHE for OER evolution reaction [67]. Liu et al. [68] realized bi-functional H_2CuCat catalyst film using water soluble copper complexes as catalyst precursor. By integrating the developed material with a GaAs solar cell, a photoassisted water splitting scenario was successfully demonstrated with STH efficiency of 18.01%, based on $NiCo_2S_4$ bifunctional catalysts as shown in Fig. 4. CoMn@CN bi-functional electrocatalyst was developed for photovoltaics driven water splitting reaction. Current density of 1 mA cm^{-2} at 1.5 V was achieved using CoMn@CN based electrocatalysts. CoMN@CN bifunctional electrocatalyst in amalgamation with a photovoltaic cell yielded photocurrent density of 6.43 mA cm^{-2} which corresponds to STH conversion efficiency of ~8.0% [69]. When a photovoltaic solar cell is coupled with an electrolyte based PEC cell, the system forms a photovoltaic driven electrolysis and it can generate sufficient voltage required to split water which is comparable to that of electrocatalysts. In photovoltaic-electrolysis system, the efficiency of water splitting strongly depends on the conversion efficiency of solar cells and reactivity of bifunctional electrocatalyst. In spite of many advances, research in the area of integrated studies is still in its nascent stage. Thus more work is needed to understand the underlying concepts of efficient overall HER/OER reactions.

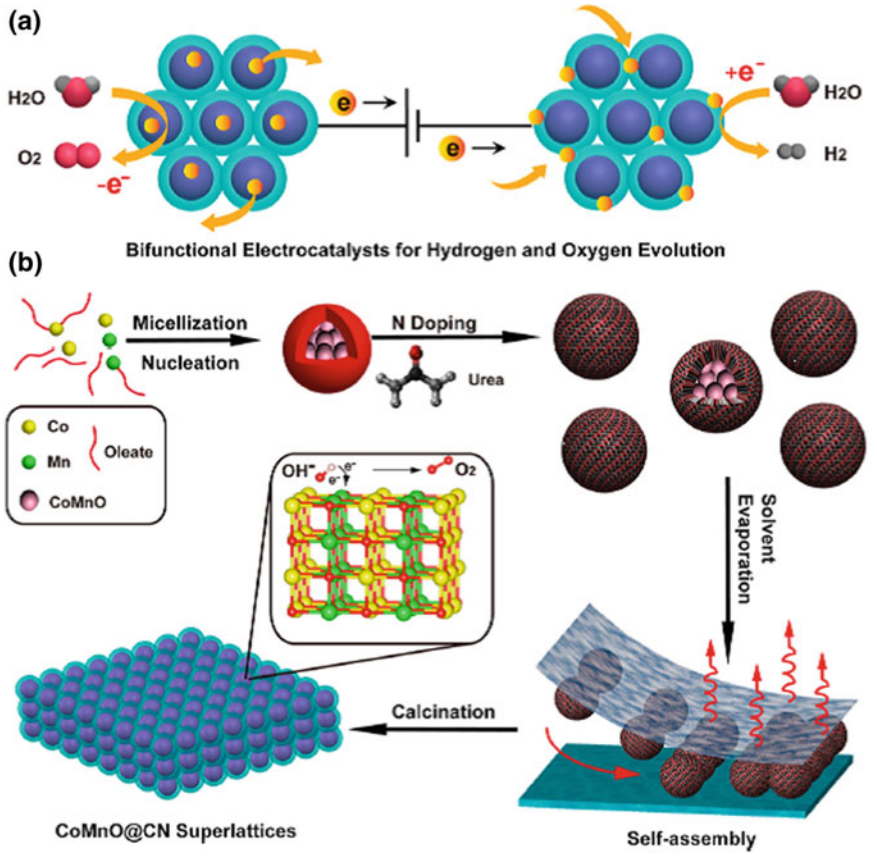

Fig. 4 **a** Schematic of CoMnO@CN superlattice acting as a bi-functional catalyst. **b** Synthesis procedure of CoMnO@CN superlattice. Adapted from Ref. Li et al. [69]; copyright 2015 American Chemical Society

5 Carbonaceous

A lot of advances in the synthesis and characterization of different types of nanostructures based on carbon in the area of energy have been made. Carbonaceous materials which comprises of g-C_3N_4, graphene, CNTs and other different forms of carbon have been utilized for water splitting reaction [70]. These materials, without any alteration do not show any activity in HER/OER reactions [71, 72]. In order to modify these catalysts for HER/OER activity, doping with heteroatoms, creation of defects, are some of the strategies that could be adapted. Together with these modifications, a lot of research has been focused to modify the morphological properties optimum performance.

g-C_3N_4 is a polymeric semiconductor material which can have implications as an efficient catalyst in the area of water splitting [73]. Although g-C_3N_4 is a facile

photocatalyst which can reduce water to H_2, activity of the photocatalyst is high when it is amalgamated with noble metal on other transition based co-catalysts [74]. A lot of efforts have been carried out by different research groups to enhance the photocatalytic activity of g-C_3N_4. The amalgamation of g-C_3N_4 with other carbon-based materials is also an effectual way to enhance the photocatalyst performance [75]. Another effective strategy to improve the photocatalytic activity of g-C_3N_4 is using carbon-based materials in conjunction with g-C_3N_4. Liu et al. reported that loading of C-dots in the matrix of g-C_3N_4 can lead to very stable water splitting catalysts that can last up to 200 days. A quantum efficiency of ~16%, with overall STH efficiency of 2% is obtained under AM1.5 G solar simulation [68]. g-C_3N_4 consist of high nitrogen content (presence of graphite and pyridine nitrogen moieties). These moieties can serve as active reaction sites and thus g-C_3N_4 can potentially act as metal free electrocatalyst. These moieties help in enhancing the conductivity of g-C_3N_4 [71, 72]. Ma et al. have applied conductive medium to g-C_3N_4 in the form of multiwalled carbon nanotubes to construct an OER catalyst [76].

Graphene with high surface area, excellent ionic and electric conductivity and good mechanical strength is an important material for electrochemical applications in the same context [77]. Although, graphene is inherently chemically inert, and thereby exhibits poor electrocatalytic activity. In heterogenous catalysis, active sites play key role and different approaches can be employed to create them. A symmetric band structure is exhibited by the pristine graphene and it can be considered a zero band gap semiconductor. Thereby, pristine graphene demonstrate weak or absolutely nil catalytic activity. The structural properties of pristine graphene are unique and modification strategies can open its band gap thereby enhancing the catalytic activity. Pristine graphene can be compositionally modified by incorporating heteroatoms into the graphene network. This incorporation could attain the sp^2 network and create sp^3 defects in the graphene lattice thereby, changing the electron density within the graphene sheet [78]. Graphene oxide compared to graphene has a much wide band gap and may serve as semiconductor [79]. The introduction of functional group containing oxygen on the surface of graphene distorts the conjugated structure as sp^3 hybridization of graphene occurs and this lead to change in the structural and electronic properties thereby making graphene oxide (GO) a prospective candidate of the metal free photocatalyst family [80, 81]. In 2010, Yeh et al. pioneered the use of GO as photocatalyst for hydrogen production using methanol solution [81]. For water splitting reactions, heteroatom doped graphene is a different type of carbonaceous photocatalyst which is free from metal. On the other hand, phosphorus doped graphene exhibited high catalytic activity of H_2 generation under UV light irradiation from a mixture of water and methanol. Moreover, dual elemental doping in graphene structure can lead to an efficient OER electrocatalyst since both the dopants act in synergism [82]. CNTs have hollow structure and long range conjugated p-electron structure due to which it can exhibit outstanding properties compared to other carbon based materials. Bare CNTS have very poor HER activity. To change their surface chemistry, a suitable post treatment is normally required. CNTS have reported to be efficient OER when their surface functionalization is carried out [83, 84]. The remarkable properties of CNTS, have fascinated and motivated researchers

to look into other analogous materials such as boron nitride (BN) nanosheets for PEC applications. These materials have been employed as active OER electrocatalysts. CVD method has been used to embed N atoms into CNTS surface [85]. The high content of nitrogen on the CNTS leads to more active sites which are exposed for the reaction. Thus N doped CNTs exhibit high OER activity. The results can be useful in designing catalyst material which has active sites with controllable locations. Recently, several type of organic photocatalyst have been synthesized and realized for utilizing solar radiations [86, 87]. Sprick et al. synthesized a series of amorphous, microporous organic polymers with exquisite synthetic control over the optical gap in the range 1.94–2.95 eV signifying their application as hydrogen evolving photocatalysts [86]. Another class of carbonaceous materials comprises of boron carbide and its derivative. Liu et al. have studied the photocatalytic activity of two different types of boron carbides for H_2 production [88]. Wang et al. synthesized carbon doped born nitride nanosheet (B-C-N alloy), as active photocatalyst under visible light irradiation. The band gap of the B-C-N alloys nanosheet can be controlled and reduced by the incorporation of aromatic carbon [89].

6 Conclusion

The quest for affordable, reliable photosynthesis for solar-driven water splitting is still underway as there are challenges that need to be undertaken. Normally, the dimensions of the testing device are of the order of few centimeters in order to produce hydrogen which can cater even the smallest need, arrays having dimension of the order of several meters is required. Therefore, scaling of device and the processes is necessary. In order to scale up there should be nanostructures with better charge transport properties together with realization of cheaper components such as electrocatalysts, membranes and light absorber/nanostructures etc. Moreover, the design of the devices should be free of maintenance. The above requirements put constraints on material properties and device conditions for mass production of hydrogen.

One of the primary and an important question which still remains unanswered is regarding safe storage of hydrogen. Assuming current densities reaching up to 10 mA cm^{-2} on irradiation, the generation of hydrogen and oxygen across the nafion membrane could lead to intermixing of both the gases. There are methods that can be deployed in the electrolyzer which prevents intermixing of gases and building up dangerous gas mixtures, but this reduces the overall solar to hydrogen efficiencies. The most difficult task is to safely and efficiently produce hydrogen from all large arrays. Electron coupled proton buffer (ECPB) addresses some of the issues listed above. It decouples the HER and OER so that hydrogen and oxygen are not generated at the same instant and thus intermixing of gases could be circumvented. In a conventional n-type PEC cell generation of hydrogen take place at counter electrode, whereas, when we use ECPB reduction and protonation of its take place. The ECPB is re-oxidized electrochemically thereby, co-generating hydrogen.

Acknowledgements Mohit Prasad is thankful to University Grants Commission, Government of India for Dr. D. S. Kothari PostDoc Fellowship. Vidhika Sharma is thankful to Indo-French Centre for the Promotion of Advanced Research-CEFIPRA, Department of Science and Technology, New Delhi for the Research Associateship. Sandesh Jadkar is also thankful to Indo-French Centre for the Promotion of Advanced Research-CEFIPRA, Department of Science and Technology, New Delhi for financial support.

References

1. Cox N, Pantazis DA, Neese F, LubitzW (2015) Artificial photosynthesis: understanding water splitting in nature. Interface Focus 5(3):20150009
2. Gratze lM (1981)Artificial photosynthesis:water cleavage into hydrogen and oxygen by visible light. Acc Chem Res 14(12):376–384
3. Tachibana Y, Vayssieres L, Durrant JR (2012) Artificial photosynthesis for solar water-splitting. Nat Photonics 6(8):511
4. Fujishima A, Honda K (1972) Electrochemical photolysis of water at a semiconductor electrode. Nat 238(5358):37
5. Prasad M, Sharma V, Rokade A, Jadkar S (2018) Photoelectrochemical cell: a versatile device for sustainable hydrogen production. Photoelectrochemical Sol Cells 30:59–119
6. Lin F, Bachman BF, Boettcher SW (2015) Impact of electrocatalyst activity and ion permeability on water-splitting photoanodes. J Phys Chem Lett 6(13):2427–2433
7. Lin F, Boettcher SW (2014) Adaptive semiconductor/electrocatalyst junctions in water-splitting photoanodes. Nat Mater 13(1):81
8. Nellist MR, Laskowski FA, Lin F, Mills TJ, Boettcher SW (2016) Semiconductor–electrocatalyst interfaces: theory, experiment, and applications in photoelectrochemical water splitting. Acc Chem Res 49(4):733–740
9. Roger I, Shipman MA, Symes MD (2017) Earth-abundant catalysts for electrochemical and photoelectrochemical water splitting. Nat Rev Chem 1(1):0003
10. Trasatti S (1972) Work function, electronegativity, and electrochemical behaviour ofmetals: III. electrolytic hydrogen evolution in acid solutions. J Electroanal Chem Interfacial Electrochem 39(1):163–184
11. Shaner MR, McKone JR, Gray HB, Lewis NS (2015) Functional integration of Ni–Mo electrocatalysts with Si microwire array photocathodes to simultaneously achieve high fill factors and light-limited photocurrent densities for solar-driven hydrogen evolution. Energy Environ Sci 8(10):2977–2984
12. Lukowski MA, Daniel AS, Meng F, Forticaux A, Li L, Jin S (2013) Enhanced hydrogen evolution catalysis from chemically exfoliated metallic MoS_2 nanosheets. J Am Chem Soc 135(28):10274–10277
13. Parzinger E, Miller B, Blaschke B, Garrido JA, Ager JW, Holleitner A, Wurstbauer U (2015) Photocatalytic stability of single-and few-layer MoS_2. ACS Nano 9(11):11302–11309
14. Voiry D, Salehi M, Silva R, Fujita T, Chen M, Asefa T, Shenoy VB, Eda G, Chhowalla M (2013) Conducting MoS_2 nanosheets as catalysts for hydrogen evolution reaction. Nano Lett 13(12):6222–6227
15. Kemppainen E, Bodin A, Sebok B, Pedersen T, Seger B, Mei B, Bae D, Vesborg PC, Halme J, Hansen O, Lund PD (2015) Scalability and feasibility of photoelectrochemical H_2 evolution: the ultimate limit of Pt nanoparticle as an HER catalyst. Energy Environ Sci 8(10):2991–2999
16. Reier T, Oezaslan M, Strasser P (2012) Electrocatalytic oxygen evolution reaction (OER) on Ru, Ir, and Pt catalysts: a comparative study of nanoparticles and bulk materials. Acs Catal 2(8):1765–1772

17. Chen Z, Jaramillo TF, Deutsch TG, Kleiman-Shwarsctein A, Forman AJ, Gaillard N, Garland R, Takanabe K, Heske C, Sunkara M, McFarland EW (2010) Accelerating materials development for photoelectrochemical hydrogen production: standards for methods, definitions, and reporting protocols. J Mater Res 25(1):3–16
18. Yang X, Liu R, He Y, Thorne J, Zheng Z, Wang D (2015) Enabling practical electrocatalyst assisted photoelectron-chemical water splitting with earth abundant materials. Nano Res 8(1):56–81
19. Hou Y, Abrams BL, Vesborg PC, Björketun ME, Herbst K, Bech L, Setti AM, Damsgaard CD, Pedersen T, Hansen O, Rossmeisl J (2011) Bioinspired molecular co-catalysts bonded to a silicon photocathode for solar hydrogen evolution. Nat Mater 10(6):434
20. Berglund SP, He H, Chemelewski WD, Celio H, Dolocan A, Mullins CB (2014) p-Si/W_2C and p-Si/W_2C/Pt photocathodes for the hydrogen evolution reaction. J Am Chem Soc 136(4):1535–1544
21. Ding Q, Meng F, English CR, Cabán-Acevedo M, Shearer MJ, Liang D, Daniel AS, Hamers RJ, Jin S (2014) Efficient photoelectrochemical hydrogen generation using heterostructures of Si and chemically exfoliated metallic MoS_2. J Am Chem Soc 136(24):8504–8507
22. Cabán-Acevedo M, Stone ML, Schmidt JR, Thomas JG, Ding Q, Chang HC, Tsai ML, He JH, Jin S (2015) Efficient hydrogen evolution catalysis using ternary pyrite-type cobalt phosphosulphide. Nat Mater 14(12):1245
23. McKone JR, Warren EL, Bierman MJ, Boettcher SW, Brunschwig BS, Lewis NS, Gray HB (2011) Evaluation of Pt, Ni, and Ni–Mo electrocatalysts for hydrogen evolution on crystalline Si electrodes. Energy Environ Sci 4(9):3573–3583
24. Morales-Guio CG, Thorwarth K, Niesen B, Liardet L, Patscheider J, Ballif C, Hu X (2015) Solar hydrogen production by amorphous silicon photocathodes coated with a magnetron sputter deposited Mo_2C catalyst. J Am Chem Soc 137(22):7035–7038
25. Kwon KC, Choi S, Hong K, Moon CW, Shim YS, Kim DH, Kim T, Sohn W, Jeon JM, Lee CH, Nam KT (2016) Wafer-scale transferable molybdenum disulfide thin-film catalysts for photoelectrochemical hydrogen production. Energy Environ Sci 9(7):2240–2248
26. Oh S ,Kim JB, Song JT, Oh J, Kim SH (2017) Atomic layer deposited molybdenum disulfide on Si photocathodes for highly efficient photoelectrochemical water reduction reaction. J Mater Chem A 5(7):3304–3310
27. Chen Y, Tran PD, Boix P, Ren Y, Chiam SY, Li Z, Fu K, Wong LH, Barber J (2015) Silicon decorated with amorphous cobalt molybdenum sulfide catalyst as an efficient photocathode for solar hydrogen generation. ACS Nano 9(4):3829–3836
28. Chen CJ, Yang KC, Liu CW, Lu YR, Dong CL, Wei DH, Hu SF, Liu RS (2017) Silicon microwire arrays decorated with amorphous heterometal-doped molybdenum sulfide for water photoelectrolysis. Nano Energy 1(32):422–432
29. Bao XQ, Petrovykh DY, Alpuim P, Stroppa DG, Guldris N, Fonseca H, Costa M, Gaspar J, Jin C, Liu L (2015) Amorphous oxygen-rich molybdenum oxysulfide decorated p-type silicon microwire arrays for efficient photoelectrochemical water reduction. Nano Energy 1(16):130–142
30. Kwon KC, Choi S, Lee J, Hong K, Sohn W, Andoshe DM, Choi KS, Kim Y, Han S, Kim SY, Jang HW (2017) Drastically enhanced hydrogen evolution activity by 2D to 3D structural transition in anion-engineered molybdenum disulfide thin films for efficient Si-based water splitting photocathodes. J Mater Chem A 5(30):15534–15542
31. Basu M, Zhang ZW, Chen CJ, Chen PT, Yang KC, Ma CG, Lin CC, Hu SF, Liu RS (2015) Heterostructure of Si and$CoSe_2$: a promising photocathode based on a non-noble metal catalyst for photoelectrochemical hydrogen evolution. Angew Chem Int Ed 54(21):6211–6216
32. Zhang H, Ding Q, He D, Liu H, Liu W, Li Z, Yang B, Zhang X, Lei L, Jin S (2016) A p-Si/$NiCoSe_x$ core/shell nanopillar array photocathode for enhanced photoelectrochemical hydrogen production. Energy Environ Sci 9(10):3113–3119
33. Huang Z, Chen Z, Chen Z, Lv C, Meng H, Zhang C (2014) $Ni_{12}P_5$ nanoparticles as an efficient catalyst for hydrogen generation via electrolysis and photoelectrolysis. ACS Nano 8(8):8121–8129

34. Zhao J, Cai L, Li H, Shi X, Zheng X (2017) Stabilizing silicon photocathodes by solution deposited Ni–Fe layered double hydroxide for efficient hydrogen evolution in alkaline media. ACS Energy Lett 2(9):1939–1946
35. Ding Q, Zhai J, Cabán-Acevedo M, Shearer MJ, Li L, Chang HC, Tsai ML, Ma D, Zhang X, Hamers RJ, He JH (2015) Designing efficient solar-driven hydrogen evolution photocathodes using semitransparent MoQ_xCl_y (Q = S, Se) catalysts on Si micropyramids. Adv Mater 27(41):6511–6518
36. Seger B, Laursen AB, Vesborg PC, Pedersen T, Hansen O, Dahl S, Chorkendorff IB (2012) Hydrogen production using a molybdenum sulfide catalyst on a titanium-protected n+p-silicon photocathode. Angew Chem Int Ed 51(36):9128–9131
37. Fan R, Mao J, Yin Z, Jie J, Dong W, Fang L, Zheng F, Shen M (2017) Efficient and stable silicon photocathodes coated with vertically standing nano-MoS_2 films for solar hydrogen production. ACS Appl Mater Interfaces 9(7):6123–6129
38. Bao XQ, Cerqueira MF, Alpuim P, Liu L (2015) Silicon nanowire arrays coupled with cobalt phosphide spheres as low-cost photocathodes for efficient solar hydrogen evolution. Chem Commun 51(53):10742–10745
39. Chen F, Zhu Q, Wang Y, Cui W, Su X, Li Y (2016) Efficient photoelectrochemical hydrogen evolution on silicon photocathodes interfaced with nanostructured NiP_2 cocatalyst films. ACS Appl Mater Interfaces 8(45):31025–31031
40. Lin Y, Battaglia C, Boccard M, Hettick M, Yu Z, Ballif C,Ager JW, JaveyA(2013)Amorphous Si thin film based photocathodes with high photovoltage for efficient hydrogen production. Nano Lett 13(11):5615–5618
41. Hinnemann B, Moses PG, Bonde J, Jørgensen KP, Nielsen JH, Horch S, Chorkendorff I, Nørskov JK (2005) Biomimetic hydrogen evolution: MoS_2 nanoparticles as catalyst for hydrogen evolution. J Am Chem Soc 127(15):5308–5309
42. Tran PD, Pramana SS, Kale VS, Nguyen M, Chiam SY, Batabyal SK, Wong LH, Barber J, Loo J (2012) Novel assembly of an MoS_2 electrocatalyst onto a silicon nanowire array electrode to construct a photocathode composed of elements abundant on the earth for hydrogen generation. Chem Eur J 18(44):13994–13999
43. Oh S, Song H, Oh J (2017) An optically and electrochemically decoupled monolithic photoelec trochemical cell for high-performance solar-drivenwater splitting. Nano Lett 17(9):5416–5422
44. McEnaney JM, Crompton JC, Callejas JF, Popczun EJ, Biacchi AJ, Lewis NS, Schaak RE (2014) Amorphous molybdenum phosphide nanoparticles for electrocatalytic hydrogen evolution. Chem Mater 26(16):4826–4831
45. Vrubel H, Hu X (2012) Molybdenum boride and carbide catalyze hydrogen evolution in both acidic and basic solutions. Angew Chem Int Ed 51(51):12703–12706
46. Popczun EJ, McKone JR, Read CG, Biacchi AJ, Wiltrout AM, Lewis NS, Schaak RE (2013) Nanostructured nickel phosphide as an electrocatalyst for the hydrogen evolution reaction. J Am Chem Soc 135(25):9267–9270
47. Yang J, Walczak K, Anzenberg E, Toma FM, Yuan G, Beeman J, Schwartzberg A, Lin Y, Hettick M, Javey A, Ager JW (2014) Efficient and sustained photoelectrochemical water oxidation by cobalt oxide/silicon photoanodes with nanotextured interfaces. J Am Chem Soc 136(17):6191–6194
48. Zhou X, Liu R, Sun K, Papadantonakis KM, Brunschwig BS, Lewis NS (2016) 570 mV photovoltage, stabilized n-Si/CoO_x heterojunction photoanodes fabricated using atomic layer deposition. Energy Environ Sci 9(3):892–897
49. Yang J, Cooper JK, Toma FM, Walczak KA, Favaro M, Beeman JW, Hess LH, Wang C, Zhu C, Gul S, Yano J (2017) A multifunctional biphasic water splitting catalyst tailored for integration with high-performance semiconductor photoanodes. Nat Mater 16(3):335
50. Hill JC, Landers AT, Switzer JA (2015) An electrodeposited inhomogeneous metal–insulator–semiconductor junction for efficient photoelectrochemical water oxidation. Nat Mater 14(11):1150
51. Abdi FF, Han L, Smets AH, Zeman M, Dam B, Van De Krol R (2013) Efficient solar water splitting by enhanced charge separation in a bismuth vanadate-silicon tandem photoelectrode. Nat Commun 29(4):2195

52. Pijpers JJ, Winkler MT, Surendranath Y, Buonassisi T, Nocera DG (2011) Light-induced water oxidation at silicon electrodes functionalized with a cobalt oxygen-evolving catalyst. Proc Natl Acad Sci 108(25):10056–10061
53. Young ER, Costi R, Paydavosi S, Nocera DG, Bulovic´ V (2011) Photo-assisted water oxidation with cobalt-based catalyst formed from thin-film cobalt metal on silicon photoanodes. Energy Environ Sci 4(6):2058–2061
54. Esswein AJ, Surendranath Y, Reece SY, Nocera DG (2011) Highly active cobalt phosphate and borate based oxygen evolving catalysts operating in neutral and natural waters. Energy Environ Sci 4(2):499–504
55. Ding C, Shi J, Wang D, Wang Z, Wang N, Liu G, Xiong F, Li C (2013) Visible light driven overall water splitting using cocatalyst/$BiVO_4$ photoanode with minimized bias. Phys Chem Chem Phys 15(13):4589–4595
56. Kenney MJ, Gong M, Li Y, Wu JZ, Feng J, Lanza M, Dai H (2013) High-performance silicon photoanodes passivated with ultrathin nickel films for water oxidation. Science 342(6160):836–840
57. Zhou X, Liu R, Sun K, Friedrich D, McDowell MT, Yang F, Omelchenko ST, Saadi FH, Nielander AC, Yalamanchili S, Papadantonakis KM (2015) Interface engineering of the photoelectrochemical performance of Ni-oxide-coated n-Si photoanodes by atomic-layer deposition of ultrathin films of cobalt oxide. Energy Environ Sci 8(9):2644–2649
58. Sun K, McDowell MT, Nielander AC, Hu S, Shaner MR, Yang F, Brunschwig BS, Lewis NS (2015) Stable solar-driven water oxidation to O_2 (g) by Ni-oxide-coated silicon photoanodes. J Phys Chem Lett 6(4):592–598
59. Kwak IH, Im HS, Jang DM, Kim YW, Park K, Lim YR, Cha EH, Park J (2016) $CoSe_2$ and $NiSe_2$ nanocrystals as superior bifunctional catalysts for electrochemical and photoelectrochemical water splitting. ACS Appl Mater Interfaces 8(8):5327–5334
60. Wang HP, Sun K, Noh SY, Kargar A, Tsai ML, Huang MY, Wang D, He JH (2015) High performance *a*-Si/c-Si heterojunction photoelectrodes for photoelectrochemical oxygen and hydrogen evolution. Nano Lett 15(5):2817–2824
61. Yao T, Chen R, Li J, Han J, Qin W, Wang H, Shi J, Fan F, Li C (2016) Manipulating the interfacial energetics of n-type silicon photoanode for efficient water oxidation. J Am Chem Soc 138(41):13664–13672
62. Trotochaud L, Young SL, Ranney JK, Boettcher SW (2014) Nickel–iron oxyhydroxide oxygen evolution electrocatalysts: the role of intentional and incidental iron incorporation. J Am Chem Soc 136(18):6744–6753
63. Seabold JA, Choi KS (2012) Efficient and stable photo-oxidation ofwater by a bismuth vanadate photoanode coupled with an iron oxyhydroxide oxygen evolution catalyst. J Am Chem Soc 134(4):2186–2192
64. Yuan Y, Gu J, Ye KH, Chai Z, Yu X, Chen X, Zhao C, Zhang Y, Mai W (2016) Combining bulk/surface engineering of hematite to synergistically improve its photoelectrochemical water splitting performance. ACS Appl Mater Interfaces 8(25):16071–16077
65. Liu W, Liu H, Dang L, Zhang H, Wu X, Yang B, Li Z, Zhang X, Lei L, Jin S (2017) Amorphous cobalt–iron hydroxide nanosheet electrocatalyst for efficient electrochemical and photo-electrochemical oxygen evolution. Adv Func Mater 27(14):1603904
66. Luo J, Im JH, Mayer MT, Schreier M, Nazeeruddin MK, Park NG, Tilley SD, Fan HJ, Grätzel M (2014) Water photolysis at 12.3% efficiency via perovskite photovoltaics and Earth-abundant catalysts. Science 345(6204):1593–1596
67. Li X, Zhang L, Huang M, Wang S, Li X, Zhu H (2016) Cobalt and nickel selenide nanowalls anchored on graphene as bifunctional electrocatalysts for overall water splitting. J Mater Chem A 4(38):14789–14795
68. Liu J, Liu Y, Liu N, Han Y, Zhang X, Huang H, Lifshitz Y, Lee ST, Zhong J, Kang Z (2015) Metal-free efficient photocatalyst for stable visible water splitting via a two-electron pathway. Science 347(6225):970–974
69. Li J, Wang Y, Zhou T, Zhang H, Sun X, Tang J, Zhang L, Al-Enizi AM, Yang Z, Zheng G (2015) Nanoparticle superlattices as efficient bifunctional electrocatalysts for water splitting. J Am Chem Soc 137(45):14305–14312

70. Xu Y, Kraft M, Xu R (2016) Metal-free carbonaceous electrocatalysts and photocatalysts for water splitting. Chem Soc Rev 45(11):3039–3052
71. Kumar P, Boukherroub R, Shankar K (2018) Sunlight-driven water-splitting using two dimensional carbon based semiconductors. J Mater Chem A 6(27):12876–12931
72. Kumar S, Karthikeyan S, Lee A (2018) g-C3N4-based nanomaterials for visible light-driven photocatalysis. Catalysts 8(2):74
73. 61)Ye S,Wang R,WuMZ, Yuan YP (2015) A review on g-C_3N_4 for photocatalytic water splitting and CO_2 reduction. Appl Surf Sci 15(358):15–27
74. Liu M, Xia P, Zhang L, Cheng B, Yu J (2018) Enhanced photocatalytic H_2-production activity of g-C_3N_4 nanosheets via optimal photodeposition of Pt as cocatalyst. ACS Sustain Chem Eng 6(8):10472–10480
75. Patnaik S, Martha S, Acharya S, Parida KM (2016) An overview of the modification of gC_3N_4 with high carbon containing materials for photocatalytic applications. Inorg Chem Front 3(3):336–347
76. Ma TY, Dai S, Jaroniec M, Qiao SZ (2014) Graphitic carbon nitride nanosheet–carbon nanotube three-dimensional porous composites as high-performance oxygen evolution electrocatalysts. Angew Chem Int Ed 53(28):7281–7285
77. Li J, Zhao Z, Ma Y, Qu Y (2017) Graphene and their hybrid electrocatalysts for water splitting. ChemCatChem 9(9):1554–1568
78. Hu C, Liu D, Xiao Y, Dai L (2018) Functionalization of graphene materials by heteroatom doping for energy conversion and storage. Prog Nat Sci Mater Int 28(2):121–132
79. Velasco-Soto MA, Pérez-García SA, Alvarez-Quintana J, Cao Y, Nyborg L, Licea-Jiménez L (2015) Selective band gap manipulation of graphene oxide by its reduction with mild reagents. Carbon 1(93):967–973
80. Yeh TF, Cihlář J, Chang CY, Cheng C, Teng H (2013) Roles of graphene oxide in photocatalytic water splitting. Mater Today 16(3):78–84
81. Yeh TF, Syu JM, Cheng C, Chang TH, Teng H (2010) Graphite oxide as a photocatalyst for hydrogen production from water. Adv Func Mater 20(14):2255–2262
82. Latorre-Sánchez M, Primo A, García H (2013) P-doped graphene obtained by pyrolysis of modified alginate as a photocatalyst for hydrogen generation from water–methanol mixtures. Angew Chem Int Ed 52(45):11813–11816
83. Chen X, Yu Z, Wei L, Zhou Z, Zhai S, Chen J, Wang Y, Huang Q, Karahan HE, Liao X, Chen Y (2019) Ultrathin nickel boride nanosheets anchored on functionalized carbon nanotubes as bifunctional electrocatalysts for overall water splitting. J Mater Chem A 7(2):764–774
84. Cheng Y, Memar A, Saunders M, Pan J, Liu C, Gale JD, Demichelis R, Shen PK, Jiang SP (2016) Dye functionalized carbon nanotubes for photoelectrochemical water splitting–role of inner tubes. J Mater Chem A 4(7):2473–2483
85. Tian GL, Zhang Q, Zhang B, Jin YG, Huang JQ, Su DS, Wei F (2014) Toward full exposure of "active sites": nanocarbon electrocatalyst with surface enriched nitrogen for superior oxygen reduction and evolution reactivity. Adv Func Mater 24(38):5956–5961
86. Sprick RS, Jiang JX, Bonillo B, Ren S, Ratvijitvech T, Guiglion P, Zwijnenburg MA, Adams DJ, Cooper AI (2015) Tunable organic photocatalysts for visible-light-driven hydrogen evolution. J Am Chem Soc 137(9):3265–3270
87. Vyas VS, Haase F, Stegbauer L, Savasci G, Podjaski F, Ochsenfeld C, Lotsch BV (2015) A tunable azine covalent organic framework platform for visible light-induced hydrogen generation. Nat Commun 30(6):8508
88. Liu J, Wen S, Hou Y, Zuo F, Beran GJ, Feng P (2013) Boron carbides as efficient, metal-free, visible-light-responsive photocatalysts. Angew Chem Int Ed 52(11):3241–3245
89. Wang X, Maeda K, Thomas A, Takanabe K, Xin G, Carlsson JM, Domen K, Antonietti M (2009) A metal-free polymeric photocatalyst for hydrogen production from water under visible light. Nat Mater 8(1):76

Cationic Electrocatalysis in Effecting the Electrosynthesis of Tungsten Carbide Nanopowders in Molten Salts

I. A. Novoselova, I. N. Skryptun, A. A. Omelchuk and V. V. Soloviev

Abstract The chapter presents the theoretical and experimental concepts of the phenomenon of cationic electrocatalysis during the discharge of complicated anionic complexes in molten salts. These ideas are based on the acid-base mechanism of formation of electrochemically active species (EASs). The essence of cationic electrocatalysis is the transformation of anionic complexes into a new active state under the action of cations with a strong polarizing effect. This leads to a change in the energy, electronic, and structural state of the anion, the formation of new EASs, a change in their composition, in the rate of EAS formation and charge transfer. The performed quantum chemical calculations allow one to conclude that the cationic composition of the melt catalyzes the formation of new EASs both in the bulk phase of the melt and at the electrode-melt interface. Using voltammetry, it was shown that the addition of Mg^{2+} cations to tungstate-containing melts leads to a change of the nature of the electrode process and to an increase of an order of magnitude in heterogeneous rate constant for charge transfer. The tungsten deposition potential shifts to the positive potential values up to the potentials of carbon deposition from CO_2. The proposed approach allowed us to realize in practice the synthesis of nanoscale powders of tungsten carbides and composite mixtures based on them by electrolysis of molten salt electrolytes. The obtained materials have a high potential for application for solving various tasks of electrocatalysis.

Keywords Electrochemical synthesis · Tungsten carbides · Cationic electrocatalysis · Ab initio calculations · Molten salts

I. A. Novoselova (✉) · I. N. Skryptun · A. A. Omelchuk
V.I. Vernadskii Institute of General and Inorganic Chemistry, National Academy of Sciences of Ukraine, 32/34 Pr. Palladina, 03680 Kiev, Ukraine
e-mail: iness@ionc.kiev.ua

V. V. Soloviev
Technical National University of Poltava, Pershotravnevyi Prospekt 24, 36011 Poltava, Ukraine

Inamuddin et al. (eds.), *Methods for Electrocatalysis*,
https://doi.org/10.1007/978-3-030-27161-9_9

1 Introduction

The wide use of refractory metal carbides in industry as structural and tool materials that are able to operate at high temperatures and loads in aggressive media causes great interest for the development of novel highly efficient and environmentally safe methods for their production. Tungsten carbides WC and W_2C, which are distinguished by a high hardness and the thermal stability of mechanical properties, have found the greatest use in the production of wear-resistant hard alloys, which make up the bulk of all tool materials. The further improvement of the operating characteristics of WC-based hard alloys, which are fabricated in industry by traditional thermochemical methods, is no more possible. Therefore, a topical way of improving the characteristics of these materials is reducing the carbide grain in the alloy to nanosize. Tungsten carbides are known to show catalytic activity in many chemical and electrochemical reactions. They possess a high electronic conductivity and corrosion resistance, which makes it possible to use them as independent catalysts instead of platinum and ruthenium, and as platinum carriers in catalysts for fuel cells. The nanoscale and high specific surface of catalytic powders are key factors, which determine their successful use in catalysis. Today, there are many modern methods for producing tungsten carbide nanopowders. These are, above all, gaseous-phase synthesis, plasmochemical synthesis, self-propagating high-temperature synthesis in melts, mechanosynthesis, detonation synthesis, exploding wire method, high-temperature electrosynthesis (HTES) in salt melts. HTES has a great promise due to significant disadvantages of other methods: they are mainly multistage and energy-consuming methods, which require expensive precursors and the use of complex equipment, long and complex stages of removing the synthesis medium from the end product. Using the HTES method, one can obtain both single-phase tungsten carbides and composite mixtures of carbides with carbon and other metals in the form of coatings and ultrafine powders in one stage at relatively low temperatures (700–750 °C) using cheap starting reagents.

2 Background. Cationic Electrocatalysis of the Electroreduction of Complicated Oxyanions in Salt Melts

The possibility of producing carbides by the electrolysis of the molten salt system $LiF–Na_2BO_3–WO_3–Na_2CO_3$ was first shown by Andriux and Weiss as early as the late 1940s [1]. Because of the complexity of processes and the absence of clear ideas about electrode reactions involving refractory metal oxycompounds and carbon, electrosynthesis has not been realized in practice. Only in the 1970s, thanks to the studies by the Kyiv School of electrochemists working in the field of molten salt electrolytes [2–5], certain successes in the understanding of complex mechanisms of electrochemical processes began to show up, which were than takes as a basic of the

HTES of carbides. In the above studies, based on concepts of acid-base interactions in salt melts [6], the acid-base mechanism of the formation of electrochemically active species (EASs) has been theoretically substantiated and experimentally proved, and the concepts of the limiting role of these interactions in the discharge of complicated oxyanions have been developed. The proposed approach made it possible to control the composition of the electrode product (the path of reaction), the potential and rate of the electrode process and to realize conditions for the occurrence of many-electron reactions in a narrow potential range (practically in one stage).

The theory of the HTES method, which was presented in Refs. [7–10], has been developed and this method practically implemented for the production of tungsten carbides under the guidance of professor V. I. Shapoval, Corresponding Member of the Ukrainian National Academy of Sciences, in the 1980–1990s at the V. I. Vernadskii Institute of General and Inorganic Chemistry of the Ukrainian Academy of Sciences (IGIC of UNAS). The essence of the HTES of refractory compounds (carbides, borides, silicides) is the joint or sequential occurrence of many-electron reactions of refractory metal and nonmetal electrodeposition, as a result of which the desires product is formed and deposited on the cathode. It should be noted that the electronic conductivity of the compound to be deposited is the necessary condition for stable synthesis.

The HTES of carbides can be effected in two ways. In the first case, the molten electrolyte contains one synthesis component in the molecular or ionic form, which is discharged at the second synthesis component. The formation of carbide takes place as a result of the reaction diffusion of discharge products deep into the electrode material. Either—alkali (alkaline-earth) metal carbonates, which can be reduced to elemental carbon on the cathode made of a refractory metal (electrochemical carbidization) [11–13], or refractory metal ions, which are reduced to metal on the graphite cathode [14, 15], are used as discharging component. The above processes occur at a low rate at relatively high temperatures and produce compounds of variable composition in the form of coatings.

In the second case, the electrolyte contains both synthesis components, which can discharge together (thermodynamic or quasi-equilibrium synthesis conditions) or sequentially (kinetic synthesis conditions) at the neutral electrode [10]. After that, a chemical interaction of discharge products takes place at the cathode to from a new carbide phase. The thermodynamic synthesis conditions are undoubtedly more interesting theoretically and promising in practical use. By varying the electrolysis conditions and modes (electrolytic bath composition, current density, temperature), one can obtain single-phase carbides of a given composition in the form of coatings or ultrafine powders, as well as composite mixtures with other metals and carbon.

To effect electrosynthesis under thermodynamic conditions in a wide current density range, two conditions must be fulfilled:

1. The synthesis must take place at close values of refractory metal and carbon deposition potential. The theoretical analysis of the electrowinning of alloys, presented in [16], showed that if the deposition potential difference of alloy components (ΔE) is not over 0.2 V, the alloy composition will not depend on the

current density used, viz the process will take place under quasi-equilibrium conditions. In the case of formation of tungsten carbides WC and W_2C, compounds with high formation energy, the potential difference at which the synthesis process will occur under quasi-equilibrium conditions can increase by an additional value of depolarization potential (ΔE_{depol}) owing to the formation of a chemical compound. ΔE_{depol} can be estimated based on thermo-chemical data:

$$\Delta E_{depol} = -\Delta G_T / nF, \tag{1}$$

where ΔG_T is the Gibbs free energy of the carbide formation reaction from elements at the temperature T, n is the number of electrons involved in the discharge processes of synthesis components (n = 10 for WC and n = 16 for W_2C), F is the Faraday constant. We have calculated the values of possible depolarization of electrodes owing to the formation of WC and W_2C and they are equal, respectively 0.03 and 0.04 V.

2. Electrosynthesis is a many-electron process. Therefore, the second necessary condition for synthesis is effecting partial many-electron reduction reactions of synthesis precursors over a narrow potential range practically in one stage. The sources of metal and carbon are their oxycompounds M_xWO_4, M_xCO_3 (M = Li, Na, Ca, Ba, Mg) and CO_2. The discharge products react chemically with each other to form carbides.

Electrochemical processes in ionic melts at high temperature differ greatly from low-temperature processes in aqueous electrolytes. At high temperature, the effect of catalytic properties of the electrode material on the electrode kinetics becomes weaker. At the same time, the catalyzing role of the medium (electrolyte composition) becomes more pronounced. The effect of the medium on the kinetics of electrode reactions is clearly manifested in the reduction processes of tungstate anions (complex coordination compounds of *d* metals in the higher valent state) and carbonate anions. The specific mechanism of formation of EASs and many-electron charge-transfer reaction are characteristic peculiarities of the electroreduction of the above compounds. The mechanism of cation catalysis was proposed by V. I. Shapoval and coworker [17, 18] to explain the peculiarities of partial processes of electroreduction of carbonate and tungstate anions in chloride melts.

The essence of cation catalysis is the transformation of complicated complex anionic species into a new active state by the action of cations with strong polarizing effect (Li^+, Ba^{2+}, Ca^{2+}, Mg^{2+}) [19, 20]. This leads to a change in the electronic and energy state of anion, the formation of new EASs, and a change in their composition, the rate of EASs formation and charge transfer reactions.

This chapter is devoted to the application of the cation catalysis phenomenon for effecting the HTES of nanoscale tungsten carbide powders in salt melts.

As was already noted earlier, a necessary condition for stable synthesis in a wide current density range is the closeness of the deposition potentials of the components

forming carbide. Therefore, that main objective of research was the correct choice of suitable synthesis precursors, viz carbon and tungsten compounds which would be discharged at the cathode at close potentials. An analysis of literature data showed that tungsten and carbon deposit well from their oxide components. Calculations of the deposition potentials of different discharge products and a comparison of the obtained values have been made [7, 21]. Based on this analysis, pair of components has been chosen for synthesis (Table 1).

From Table 1 if follows that synthesis is possible under thermodynamic electrolysis conditions for the presented pairs of precursors. To effect the synthesis, we have chosen the pair CO_2–$MgWO_4$. However, in the thermodynamic consideration of electrode processes, the kinetic peculiarities of electroreduction of complicated complex anions, the stability of the chosen precursors at the synthesis temperature, their solubility in supporting electrolytes, the possibility of side reactions are not taken into account. The electrode kinetics plays a key role in effecting stable electrosynthesis.

As was already noted above, the necessary condition for the stable synthesis of carbides in the form of powders is the closeness of carbon and tungsten deposition potentials. It is known from publications [8, 22, 23] that in NaCl–KCl melt, the Na_2WO_4 discharge potential is 0.4 V more negative than the potential of carbon deposition from carbon dioxide in the same melt, and that the cathodic product is tungsten bronze powder (Na_xWO_3 (x = 0.1–0.9)).

Table 1 Conditions and components for the electrosynthesis of tungsten carbide

Temperature *T* (K)	Potential of tungsten deposition from a tungsten precursor (V)	Potential of carbon deposition from a carbon precursor (V)	Components for synthesis	Potential difference (V)
900	WO_3 (1.05)	CO_2 (1.03)	CO_2–WO_3	0.02
900	WO_2Cl_2 (1.30)	CO_2 (1.03)	CO_2–WO_2Cl_2	0.14
900	$MgWO_4$ (1.17)	CO_2 (1.03)	CO_2–$MgWO_4$	0.14
900	Na_2WO_4 (1.56)	Na_2CO_3 (1.51)	Na_2CO_3–Na_2WO_4	0.05
900	$CaWO_4$ (1.36)	$BaCO_3$ (1.36)	$BaCO_3$–$CaWO_4$	0.02
900	$MgWO_4$ (1.17)	Li_2CO_3 (1.34)	Li_2CO_3–$MgWO_4$	0.14
900	$CaWO_4$ (1.36)	Li_2CO_3 (1.34)	Li_2CO_3–$CaWO_4$	0.02
900	WO_2Cl_2 (1.30)	Li_2CO_3 (1.34)	Li_2CO_3–WO_2Cl_2	0.04
900	WOF_4 (1.36)	Li_2CO_3 (1.34)	Li_2CO_3–WOF_4	0.02
900	WO_3 (1.05)	$MgCO_3$ (0.93)	$MgCO_3$–WO_3	0.12
900	$MgWO_4$ (1.17)	$CaCO_3$ (1.12)	$CaCO_3$–$MgWO_4$	0.05

To change the reaction path (to obtain metallic tungsten) and to shift its deposition potential to more positive values, an approach has been proposed to forming a new, more electrophilic EAS (which is reduced at more positive potentials) by cation catalysis. The present paper proposes a quantum-chemical model of the formation of a tungstate complex cationized by Mg^{2+} cations. To experimentally confirm this theoretical approach, it is necessary to study the electrochemical behavior of each carbide component (to determine the deposition potential range, partial currents, the mechanism of electrode processes) and to develop methods for bringing their discharge potentials into coincidence.

Research objectives: (a) to create a quantum-chemical model of cation catalysis for the reduction of tungstate anions; (b) to determine the conditions for the partial and join electrodeposition of tungsten and carbon in a chloride melts with additions of $MgCl_2$; (c) to effect the HTES of tungsten carbide powders and to characterize them.

3 Cation Catalysis of the Electroreduction of Tungstate Anion in the Na,K|Cl Melt

3.1 Quantum-Chemical Estimation of Influence of Outer-Sphere Cations (Mg^{2+}) on Charge Transfer During $[WO_4]^{2-}$ Reduction

Methodology of quantum chemical calculations. The analysis of the changes in structural peculiarities of charge and energy distribution of EAS, as well as in its forms during successive or simultaneous electron transfer was performed using the GAMESS software package in the SBK-31G basic set [24], taking into account the exchange of electron correlation by the second-order Möller-Plesset procedure (MP2) [25]. The priority of simultaneous electron transfer in a cationized tungsten complex $\{M_n^{m+}[WO_4]^{2-}\}^{(mn-2)+}$ during its discharge was justified by the SCF MO LCAO method based on the analysis the values of the activation energy of electron transfer at different stages [26].

The traditional electrochemical methods for the analysis of the electroreduction of multicharged anions with complex structure in molten salts are inapplicable since elementary stages of charge transfer proceed very rapidly and practically at the same potential. The methods of quantum chemistry, which are effective means of the study of species and activated complexes with short lifetime, allow interpreting the experimental data at the electronic level and are of great importance. Quantum chemical calculations and their analysis give us possibility to show the probability of formation of stable cationized species of $\{M_n^{m+}\ [WO_4]^{2-}\}^{(mn-2)+}$ type ($M = Li^+$, Ca^{2+} and Mg^{2+}) in the bulk phase of chloride melt. This type of EASs was proposed on the basis of experimental data [18, 22].

The assessment of the possibility of cationized species formation in the bulk of electrolyte based only on the analysis of energy characteristics does not give the full information about the character of the tungstate anion interaction with cations in the melt. Therefore, the effect of the Mg^{2+}cation on the changes in the geometrical and electronic structure of WO_4^{2-} anions has been studied.

The potential energy surface (PES) of $nMg^{2+}\cdots WO_4^{2-}$ interaction is shown in Fig. 1. The presence of three recesses indicates the influence of the cations contained in the melt both on the restoration of the outer coordination sphere and on the probable "electron attack" sites in the subsequent reactions of the electroreduction of EASs. So, it was found for n = 1 that the bidentate interaction of single- and double-charged cations with the anion (Fig. 1a) is the most energetically favorable in comparison with mono-and tri-dentate variants of cation-anion interaction (Fig. 1b, c). With increasing n all minima of the PES are realized for other positions of cations relative to anion.

A comparison of the charge characteristics of atoms in the "isolated" WO_4^{2-} anion according to Lowdin [27–29] and cationized species showed that the cationization of the outer sphere of the tungstate complex is accompanied by charge redistribution from anion to cations (Fig. 2).

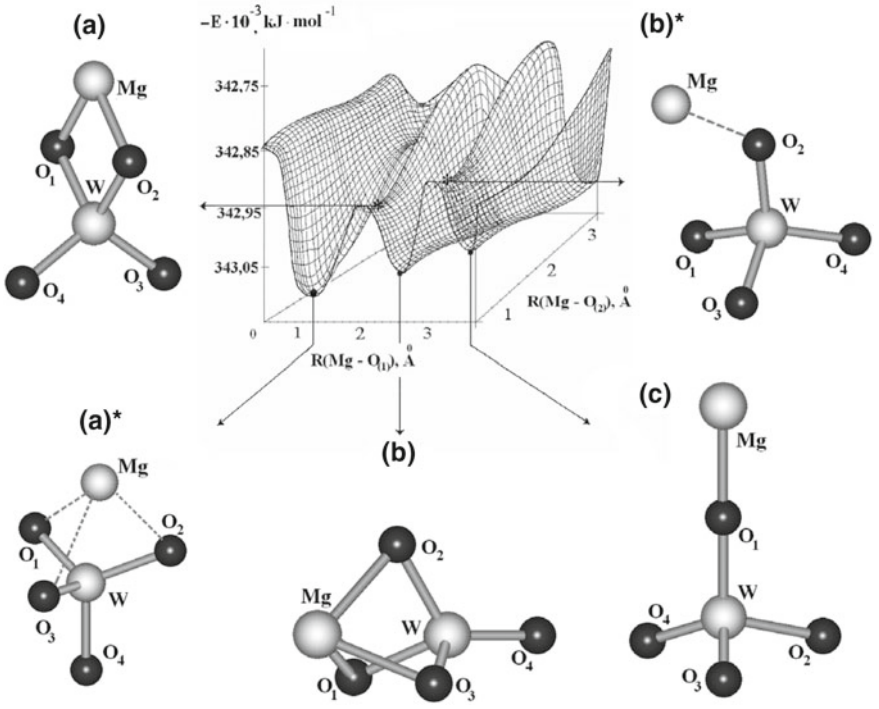

Fig. 1 Fragment of PES of the interaction $nMg^{2+}\cdots WO_4^{2-}$ configurations (**a**) is the absolute minimum, (**b**) and (**c**)—are local minima; (**a**)* and (**b**)*—are transitional states of the system

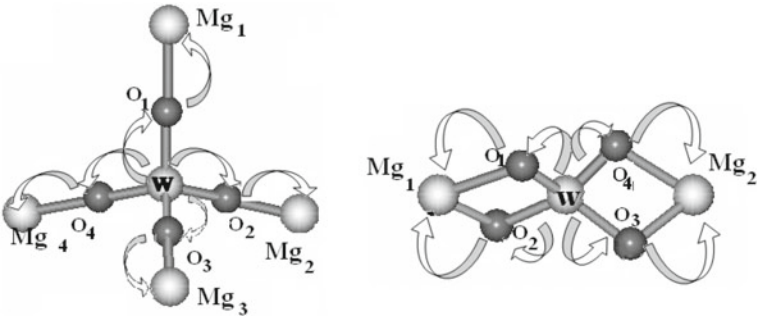

Fig. 2 Conceptual models of the charge redistribution in WO_4^{2-} anion under the influence of 4 and 2 Mg^{2+} cations

Table 2 Charge (Q, a. u.) characteristic of atoms in tungstate anions of different type (sampled data)

Q, a. u./Species	n	W	$O_{(1)}$	$O_{(4)}$	$Mg_{(1)}$
"isolated" $[WO_4]^{2-}$	0	0.378	−0.595	−0.595	–
$\{Mg_n^{2+}[WO_4]^{2-}\}^{(2n-2)+}$	1	0.698	−0.717	−0.370	1.472
	2	0.875	−0.535	−0.535	1.633
	3	1.066	−0.695	−0.185	1.730
	4	1.186	−0.600	−0.600	1.800
	5	1.342	−0.589	−0.314	1.725

The degree of charge transfer increases with increasing cation concentration (Table 2).

In the case of interaction of one Mg^{2+} cation (n = 1) with the $[WO_4]^{2-}$ anion the charge changes by 0.320 a. u. on W atom, by 0.122 a. u. on atoms O(1) and O(2), by 0.225 a. u. on atoms O(3) and O(4) in the tungstate anion. In other words, the presence of cations in the coordination sphere of the anion stimulates the manifestation of donor properties of the central atom (W) of the anion (much more in comparison with such properties of oxygen atom). So, W atom becomes a possible center of "electron attack" together with cations in the subsequent reactions of the electroreduction of EASs at the cathode. The more cations in the coordination sphere of the anion (for example, n = 2; 4; Fig. 2, Table 2) the higher the probability of the effect of charge transfer. A comparative analysis of the occupation of atomic orbitals (AOs) according to Lowdin showed that the distribution of electron density in the "isolated" anion changed under the influence of cations; and that the main "load" in the direction of this process is taken by the d-orbits of tungsten atom.

The concepts of the Marcus theory of homogeneous reactions, which found experimental confirmation [30], make it possible to explain the nature of many phenomena associated with electron transfer in various fields of science and technology (electrical conductivity of polymers, corrosion, chemiluminescence, membrane gas separation,

charge transfer in electrode reaction, etc.). Based on the concepts of the Marcus theory, a quantum-mechanical theory of electrode reactions for ionic melts was created [30]. This made it possible to create methodological principles for performing a more adequate evaluation of the results of various experimental methods for obtaining new substances with tailor-made properties.

When studying experimentally [7, 8, 31] the electroreduction of various ionic forms of tungsten, a reversible transfer of six electrons in one stage was observed. This statement was based on the fact that electron transfer takes place practically at the same potentials within a very short period of time.

According to the results of calculation by the Lowdin procedure, the only electron accepter can be W atom in the "isolated" tungsten anion (Table 3). On the contrary, when a cationized tungstate complex is discharged, the electron is transferred to different cations and to a tungsten atom (Table 3), which indicates the presence of several electron accepters. It should be noted that additional allowance for electron correlation using the MP2 method at a qualitative level allows one to obtain the same result as in the calculation of the basis, without taking into account the electron correlation. The effect is enhanced with an increase in the specific charge of the cation and with an increase in coordination number in the cationic complex, passing through a maximum at $n = 4$ in the case of Li^+ and $n = 2$ for Mg^{2+} ions (Table 3) both with simultaneous and consecutive charge transfer.

Despite the insignificant difference in the values of charges on EASs, complete disregard for simultaneous or consecutive charge transfer is inadmissible, since a change in charge value leads to a change in the structure of complex. The obtained results indicate that at the stage of simultaneous transfer of two electrons, a change

Table 3 Sampled data on charge values on atoms of EASs (**a**) and their reduced forms with simultaneous (**b**) and sequential (**c**) charge transfer

EAS	The mechanism of electron transfer	WO_4^{2-}		$\left\{Mg_2^{2+}[WO_4]^{2-}\right\}^{2+}$	
		SBK-31G	MP2*	SBK-31G	MP2*
W	a	0.378	0.401	0.875	0.870
	b	−5.410	−5.409	0.531	0.530
	c	−5.410	−5.409	0.517	0.570
$O_{(1)}$	a	−0.595	−0.590	−0.536	−0,.535
	b	−0.612	−0.612	−0.517	−0.513
	c	−0.630	−0.623	−0.508	−0.494
$M_{(1)}$	a	–	–	1.633	1.632
	b	–	–	−1.077	−0.899
	c	–	–	−1.079	−1.065

* The calculations were performed on the same basis, taking into account electron correlation within the Peller-Plesset procedure of the 2nd order

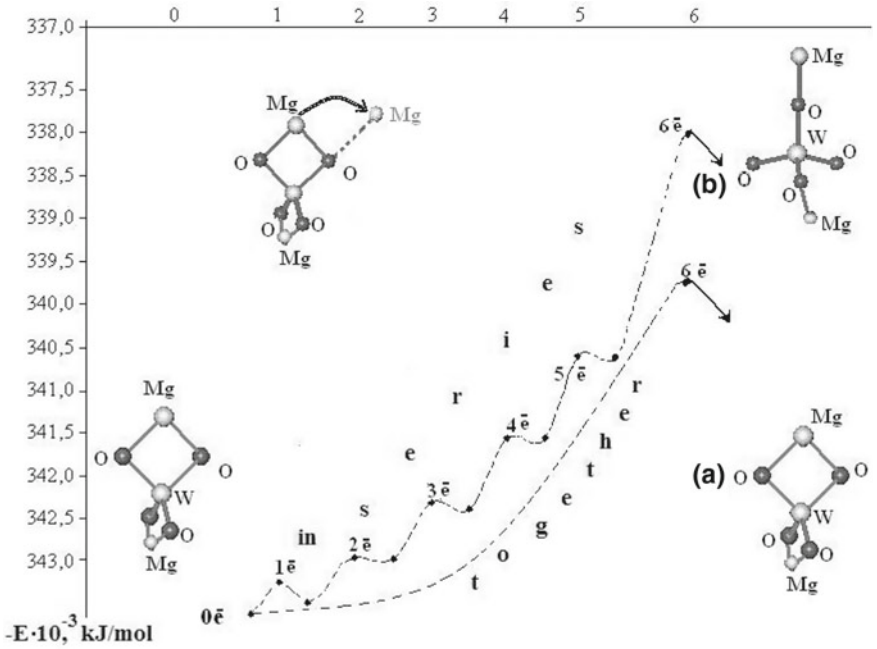

Fig. 3 PES energy profile along the generalized reaction coordinate while simultaneous (**a**) and sequential (**b**) attachment of 6 electrons to electrochemically active particles $\{Mg_2^{2+}[WO_4]^{2-}\}^{2+}$

in the geometric structure of the EAS is observed, which ultimately leads to a change in the position of the cations in the complex.

The change in complex geometry occurs in several stages (Fig. 3). Point 0 corresponds to the geometry of the complex which it had up to the moment of electron transfer. This corresponds to the bidentate arrangement of Mg^{2+} cations. The same complex geometry will persist at Point 1, corresponding to the attachment of one electron. Point 2 corresponds to the geometric structure, where one Mg^{2+} cation is in the bidentate position, and the second one has passed to the monodentate position due to the successive transfer of the 2nd electron. This geometry of the metal complex is also preserved for points 3–5 (Fig. 3), which corresponds to the 6th electron. At point 6, the geometry of the metal complex is characterized by a monodentate arrangement of both cations as a result of the successive transfer of the 6th electron.

When the anionic tangstate complex is reduced by the transfer of six electrons, the magnesium cations remain in the bidentatate position. If anionic complex are reduced with successive electron transfer, the outer-sphere cations (magnesium cations in this particular case) occupy a monodentate position [32].

3.2 *Voltammetric Study of the Effect of Mg^{2+} Cations on the Discharge of Tungstate Anion in a Chloride Melt*

3.2.1 Experimental

A binary mixture of potassium and sodium chlorides (extra pure) in a molar ratio of 1:1 with a melting point of 660 °C was used as background electrolyte. Salt mixture firstly was dried during 10 h at 150 °C in air and then was melted in platinum crucible. Sodium tungstate of "chemical pure" reagent grate was dried for 5 h under vacuum at 500 °C. Magnesium chloride (fused anhydrous) was prepared by the procedure described in [33]. Gaseous CO_2 was used from the gas cylinder of the reagent grate "chemical pure" after drying with silica gel.

A platinum wire (diameter 0.5 mm; electrode area 0.2 cm^2) was used as the working electrode (cathode) during voltammetry study. The counter-electrode (anode) and at the same time the container for the melt were crucibles made of glassy carbon (GC) or platinum. Because of the unstable work of the reference electrodes, which are commonly used in chloride melts, in conditions of excess gas pressure a quasi-reference electrode (a platinum wire, dipped into the molten electrolyte) was used. The electrolysis of the molten system was carried out on GC or platinum plate electrodes.

Electrochemical measurements were performed on PI-50-1 potentiostat with potential sweep rates 0.1–10 V s^{-1}. A detailed description of the used electrochemical cell and the methodology of voltammetric measurements are given in [34].

After electrolysis the powdery product was collected from the cathode and from the volume of frozen salt electrolyte. The product was purified from the salts of the synthesis medium by the method of decantation with hot water and dried at 100 °C. The obtained products were analyzed by chemical, XRD- analyses methods, scanning electronic microscopy.

3.2.2 Influence of Mg^{2+} Cations on the Kinetics of $[WO_4]^{2-}$ Electroreduction

Figure 4a shows current-voltage curves in sodium tungstate-containing chloride melt. The tungstate anion is electrochemically inactive in NaCl–KCl melts when Mg^{2+} cations are not present (Fig. 4a, curve 2) in the electrolyte. When Mg^{2+} cations are added to the melt, reduction waves of $WO_4{}^{2-}$ appear on current-voltages curves at potentials of −1.3 to –1.5 V against a platinum reference electrode. The wave shifts to more positive values with increasing Mg^{2+} ion concentration, and the limiting (or peak) currents increase. A metallic tungsten powder is the electrolysis product obtained under potentiostatic condition (E = −1.4 V) in the system NaCl–KCl–Na_2WO_4 (3 mol%)–$MgCl_2$ (6 mol%).

Figure 4b shows a plot of wave current against Mg^{2+} ion concentration. The current is directly proportional to Mg^{2+} ion concentration up to a 3 to 3.5-fold excess

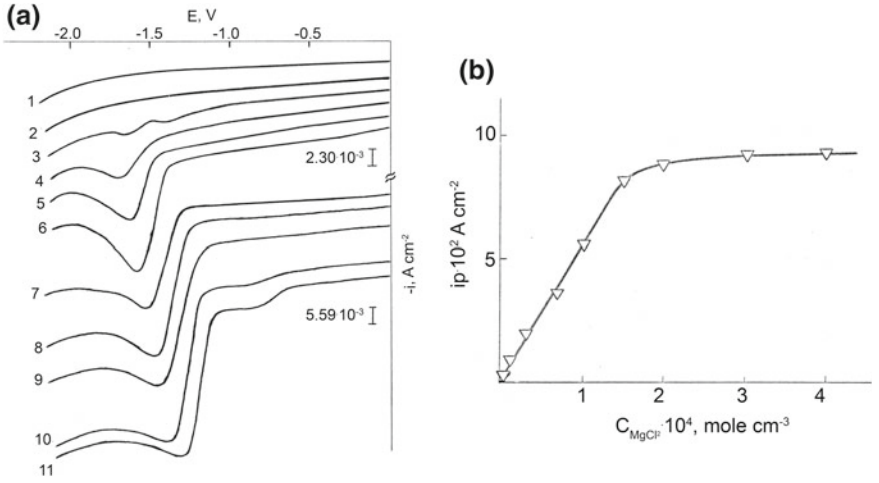

Fig. 4 **a** Voltammograms of the melt Na,K|Cl (1), containing 5×10^{-5} mol/cm^3 Na_2WO_4 (2) with the sequential addition of $MgCl_2$ ($\times 10^{-5}$ mol/cm^3): 0.5 (3); 1.3 (4); 3.2 (5); 6.6 (6); 10 (7); 15 (8); 20 (9); 30 (10); 40 (11), polarization rate—0.1 Vs^{-1}. **b** The graph of current peak of the reduction waves $[WO_4]^{2-}$ (concentration of $NaWO_4$ is 5×10^{-5} mol/cm^3) in the Na,K|Cl melt versus $MgCl_2$, the polarization rate is 0.1 Vs^{-1}

of Mg^{2+}. The highest limiting current is attained when $[Mg^{2+}] \approx 4\,[WO_4]^{2-}$. Under this conditions the ratio $i_d/nFc = 2.0 \times 10^{-3}$ cm s^{-1} is commensurate with diffusion constant. The peak currents that are proportional to the Mg^{2+} concentration and values of i_d/nFc indicate the diffusion character of steady-state waves.

In accordance with the mechanism of cation catalysis of anion electroreduction, which was described above, the following mechanism of the formation of EASs in tungstate-anion containing melts acidified with Mg^{2+} cations can be suggested:

$$\begin{aligned} &\text{Path I} && n\,Mg^{2+} + [WO_4]^{2-} \rightarrow \left\{Mg_n[WO_4]\right\}^{(2n-2)+} \\ &\text{Path II} && n\,Mg^{2+} + [WO_4]^{2-} \rightarrow n\,MgO + WO_{4-n}^{2(n-1)} \end{aligned} \qquad (3)$$

The cathodic reaction under experiment conditions (path I) can be formulated as

$$\left\{Mg_n[WO_4]\right\}^{(2n-2)+} + 6\,e = W + n\,MgO + (4-n)O^{2-} \qquad (4)$$

Reaction (3) can be shifted according to the path II when the Mg^{2+} ion is present in more than 10-fold excess. In this case the coefficient *n* assumed values larger than unity, i.e. the $[WO_4]^{2-}$ anions will be subject to strong polarizing influence of the Mg^{2+} ions, which leads to the destruction of the anionic complex and formation of tungsten oxides. The calculated heterogeneous charge-transfer rate constant (k_s) of the process under study increases from 8.34×10^{-4} to 24.62×10^{-3} cm s^{-1} with increasing of Mg^{2+} ion concentration from 4.6×10^{-5} to 62×10^{-5} mol/cm^3.

The experimental results show that the multielectron process of electroreduction of tungstate anions to metallic tungsten can be effected within a narrow range of potentials which are close to the potential for carbon deposition from CO_2, and that the potential and mechanism of the process can be controlled using the acid-base properties (Mg^{2+} concentration) of the melt.

4 Using the Phenomenon of Cationic Electrocatalysis for the Joint Reduction of Carbon Dioxide and Tungstate Anion in Chloride Melts

4.1 Peculiarities of the Discharge of CO_2 Dissolved in Chloride Melts

It was found that at sweep rates of over 0.1 V s^{-1}, the electroreduction of CO_2 dissolved in molten Na,K|Cl electrolyte at 750 °C under high pressure took place in one stage at potentials $-\{0.9 \div 1.2\}$ V against the platinum reference electrode (Fig. 5a). A linear dependence of the wave's limiting current against the gas pressure in the system was revealed (Fig. 5b). The product obtained by electrolysis at constant potential ($E = -1.0$ V) at a CO_2 pressure of 1.0 MPa is a dispersed powder of carbon. The kinetic features of this process and the characteristics of obtained carbon are described in detail in [23]. In this process, CO_2 acts as a precursor of carbon and as an acceptor of oxide ions, which are released at the near-cathode space as a result of the CO_2 discharge. In general, the reaction of CO_2 electroreduction up to carbon can be represented in the way

$$CO_2 + 4e^- \rightarrow C + 2O^{2-} \tag{5}$$

$$2CO_2 + 2O^{2-} = 2CO_3^{2-} \tag{5a}$$

$$3CO_2 + 4e^- \rightarrow C + 2CO_3^{2-} \tag{5b}$$

4.2 Joint Electroreduction of $[WO_4]^{2-}$ and CO_2 in Chloride Melts Having Different Acidities

The joint electroreduction of CO_2 and $[WO_4]^{2-}$ in chloride melts acidified with Mg^{2+} ions was studied as follows. Firstly, we established a certain acidity of the melt by adding Mg^{2+} cations to the melt and recorded a current-voltage curve corresponding

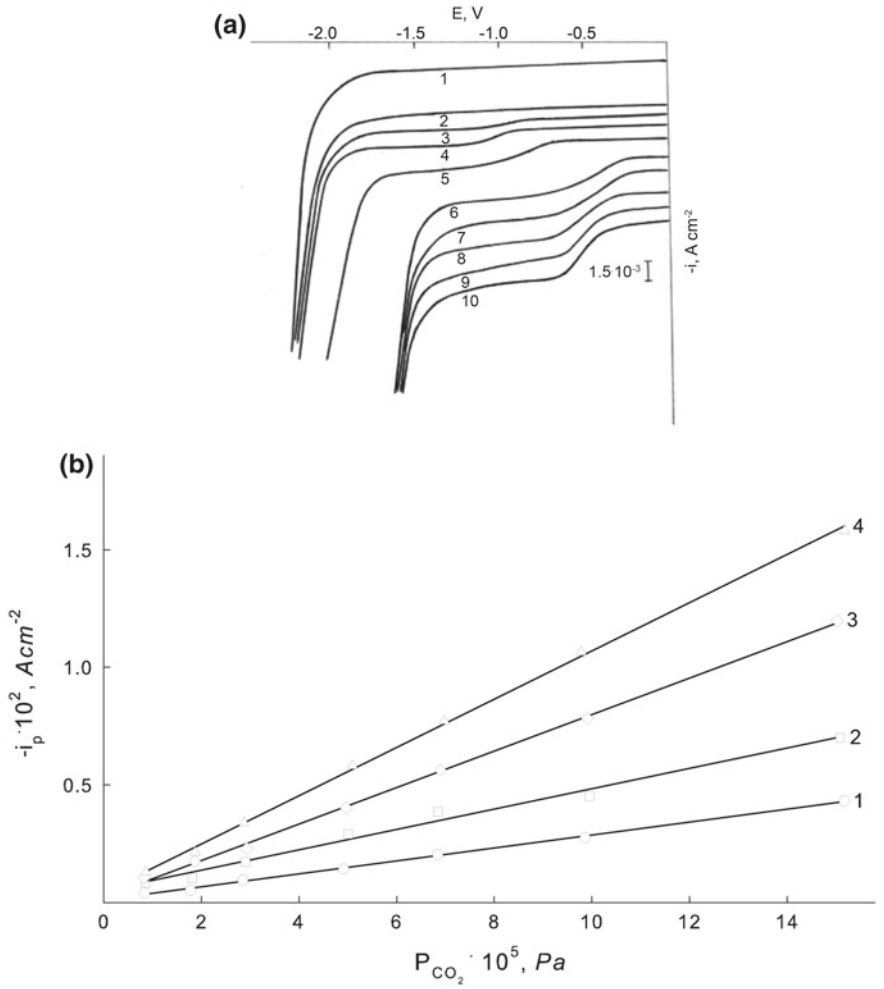

Fig. 5 **a** Voltammograms of the melt Na,K|Cl (1) under an excessive pressure of CO_2, Pa × 10^5: 1 (3); 2.5 (4); 5 (5); 7.5 (6); 10 (7); 12.5 (8); 17 (9); 17.7 (10), the polarization rate is 0.1 Vs^{-1}. **b** Graph of current peak of the reduction wave of CO_2 in the Na,K|Cl melt at different polarization rates, Vs^{-1}: 0.1 (1); 0.2 (2); 0.5 (3); 1 (4)

to $Mg_x[WO4]^{2-}$ discharge at this acidity. Then carbon dioxide was fed into the system under different pressures (Fig. 6).

The cationized tungstate complex is reduced at potentials of −1.3 to −1.6 V (curve 2 in Fig. 6), which is 0.4 V more negative than the discharge of CO_2. As gas is fed into the system, voltammograms exhibit a reduction wave of CO_2 ($E_{1/2}$ = −1.05 V). An increase in CO_2 pressure leads to an increase in the height of CO_2 discharge wave and a shift of the reduction wave potentials of the $Mg_x[WO_4]$ to

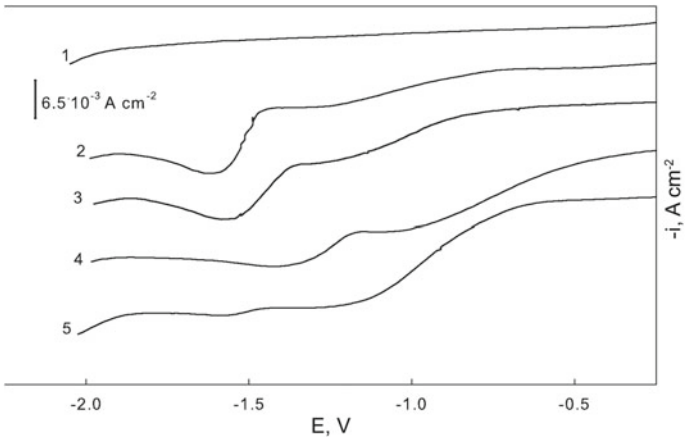

Fig. 6 Voltammograms of the melt Na,KlCl (1), containing 5×10^{-5} mol/cm^3 Na_2WO_4 and 3.1×10^{-5} mol/cm^3 $MgCl_2$ (2) at an excess pressure of CO_2, Pa 10^5: 5 (3); 10 (4); 15 (5); polarization rate is 0.1 Vs^{-1}

more positive values. At $PCO_2 = 15 \times 10^5$ Pa, one co-reduction wave of CO_2 and $Mg_x[WO_4]^{2x-2}$ is observed (Fig. 6, curve 5).

Thus the overall process of the electrochemical synthesis of tungsten carbide can be described by the reaction

$$Mg[WO_4] + 3CO_2 + 10e^- = WC + MgO + 3O^{2-} + 2CO_3^{2-} \quad (6)$$

4.3 Practical Implementation of the Electrochemical Synthesis of Tungsten Carbide Nanopowders in Chloride-Oxide Melts

An electrolysis in the system NaCl–KCl–Na_2WO_4(3 mol%)–$MgCl_2$(6 mol%)–CO_2 with different cathode current densities (i_k) and at different gas pressures has been carried to produce the cathodic product. By changing the concentration ratio of the synthesis components, the current density, the duration of the electrolysis single-phase tungsten carbides WC and W_2C, as well as composite mixtures based on them with metallic tungsten and carbon were obtained (Fig. 7). The lattice parameters of hexagonal α-WC are {a = 2.9081 ± 0.005, c = 2.8211 ± 0.01}, the average size of powder grains is (10 ± 20 nm).

The single-phase WC powder was produced in the system under investigation at an electrodeposition rate of 0.4 g A^{-1} h^{-1} at a current density of 0.05–0.2 A cm^{-2}. The specific surface of the product is 10 (25) m^2/g at i_k = 0.05 (0.2) A cm^{-2} correspondingly.

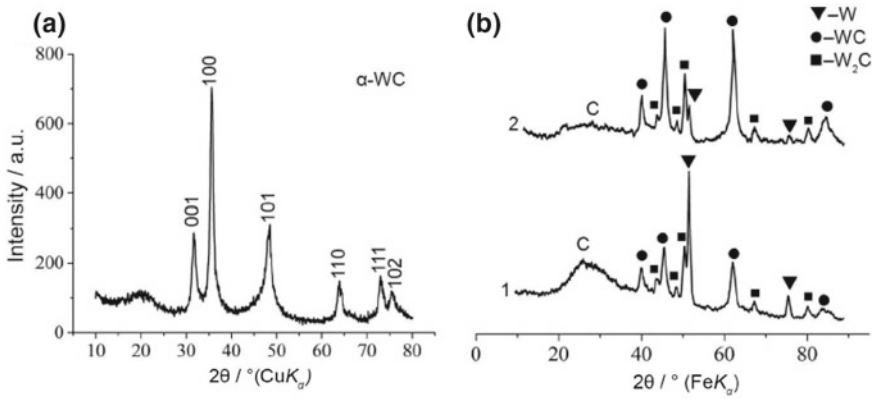

Fig. 7 Diffractograms of the cathode product obtained by electrolysis of the system NaCl–KCl–Na_2WO_4–$MgCl_2$ at different CO_2 pressures: **a** 15 atm, **b** 7 atm, (1)—faction from the cathode, (2)—faction from the electrolyte

SEM images show that nanoparticles of WC are combined into conglomerates 150–400 nm in size (Fig. 8a), which are shrouded in a layer consisting, apparently, of amorphous carbon. The contour of conglomerates is bounded by complex-shaped lines, and the image resembles a curdled mass consisting of individual nano-sized α-WC crystals. Among the large conglomerates, individual nanofibres, nanorods and "strands of fibers" (Fig. 8c) were found. Four types of electrolytic WC particles have been established: (1) curdled; poorly bonded conglomerates (300–500 nm); (2) layered particles (100–300 nm) (Fig. 8d); (3) individual nanofibers and (4) nanorods (diameter 25–200 nm, length 5.5 μm). The as-prepared (without annealing) electrolytic products are enveloped in a "fur coat" of slightly ordered carbon.

In [35, 36] the catalytic activity of the electrode material based on electrolytic tungsten carbide and its mixtures with nanocarbon and platinum was evaluated. Studies have shown the feasibility of using tungsten carbide as an electrode material for producing hydrogen from acidic electrolytic solutions. Doping the electrode with platinum increases its electrocatalytic activity, namely, it increases the exchange current and reduces the process overvoltage.

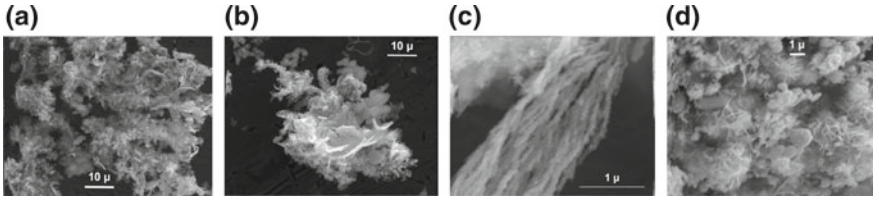

Fig. 8 SEM images of electrolytic tungsten carbide WC

5 Conclusions

For the practical realization of the HTES of nano-scale powders of tungsten carbides in a wide range of current densities, it is necessary to bring into coincidence the deposition potentials of the components of the synthesis—tungsten and carbon.

This can be achieved by applying the phenomenon of cationic electrocatalysis for the discharge of complicated species—tungsten oxyanions. It is possible to change the path of the discharge reaction, forming new electrochemically active species with more electrophilic properties, by creating the desired acidity of the melt by introducing into it cations with high specific charge (Ca^{2+}; Li^{+}; Mg^{2+}). The quantum-chemical calculations of changes in energy, charge, and shape of the geometric structures of the $[WO_4]^{2-}$ anionic complex under the action of its interaction with Mg^{2+} cations made it possible to determine the features of the deformation polarization of the formed cationized complex $Mg_x[WO_4]^{2x-2}$. The essence of these specific features lies in the cationization of the outer sphere of the $[WO_4]^{2-}$ anion, which stimulates the manifestation of the donor properties of the central atom (W) of the anion to a greater extent than that of oxygen atoms. The main "load" in this process is taken by the d-orbitals of the W atom, which makes it and Mg^{2+} cations possible centers of "electron attack" in electroreduction reactions of EASs. The quantum chemical calculations performed in the framework of the proposed model allow us to conclude that the cationic composition of the melt catalyzes the formation of new EASs both in the homogeneous bulk phase of the melt and at the electrode-melt interface.

It was shown using the method of cyclic voltammetry that the addition of Mg^{2+} cations to tungstate-containing chloride melts leads to the formation of new EASs (cationized complexes) in the bulk melt and to a changes in the nature of the electrode process. Metallic tungsten becomes a cathodic product instead of tungsten bronze. It has been experimentally shown that an increase in the Mg^{2+} concentration in the electrolyte leads to a change in the composition of cationized complexes and to an increase by an order of magnitude in the rate constant for heterogeneous charge transfer. At the same time, the tungsten deposition potential shifts to the positive values up to the potentials of carbon deposition from CO_2. The proposed approach allowed us to effect in practice the electrochemical synthesis of nanoscale tungsten monocarbide powders and composite mixtures based on it. The materials obtained have a high potential for use as new electrocatalysts in the reactions of electroreduction and oxidation of hydrogen, oxygen, and oxidation of methanol.

References

1. Andrieux JI, Weiss G (1948) Reparation des composes du molybdene et du tungstene par electrolyss ignee. Bull Soc Chem France 15(5):598–601
2. Shapoval VI, Delimarskii YK (1973) Polarographic regularities of kinetic waves taking into account the acid-base properties of electrolytes. Theor Exp Chem 9(6):748–754 (in Russian)

3. Shapoval VI, Delimarskii YK, Grishenko VF (1974) Electrochemical processes with fast and slow acid-base reactions in molten electrolytes. In: Ionic melts, iss. 1. Naukova Dumka, Kiev, pp 222–241 (in Russian)
4. Delimarskii YK, Gorodyskii AV, Zarubitskii OG, Panov EV, Shapoval VI (eds) (1975) Electrode processes in ionic melts. Naukova Dumka, Kiev (in Russian)
5. Shapoval VI (1975) Kinetics of electroreduction of oxygen-containing anions in molten salts. Dissertation, Institute of General and Inorganic Chemistry, Kiev (in Russian)
6. Flood H, Forland T (1947) The acid-base reaction in molten salts. Acta Chem Scand 1:591–604
7. Shapoval VI, Kushkhov KB, Novoselova IA (1982) Thermodynamic foundation of electrochemical synthesis of tungsten, molybdenum and boron carbides. Ukr Khim Zh 46(7):738–742 (in Russian)
8. Shapoval VI, Kushkov KB, Novoselova IA (1985) High-temperature electrochemical synthesis of tungsten carbide. Rus J Appl Chem 58(5):1027–1030 (in Russian)
9. Shapoval VI, Malyshev VV, Novoselova IA et al (1995) Modern problems of high-temperature electrochemical synthesis of IV-VI A groups transaction metals compounds. Usp Khim 64(2):133–141 (in Russian)
10. Novoselova IA, Malyshev VV, Shapoval VI et al (1997) Theory of high-temperature electrochemical synthesis in ionic melts. Theor Found Chem Eng 31(3):286–295 (in Russian)
11. Arai T, Yo Sugimoto, Komatasu N (1981) Carbide coating and bonding onto chromium-plated steel by immersion process in fused borax bath. J Met Finish Soc Jpn 32(5):240–245
12. Stulov YuV, Dolmatov VS, Dubrovskii AR et al (2017) Coatings by refractory metal carbides: deposition from molten salts, properties, application. Russ J Appl Chem 90(5):676–683 (in Russian)
13. Zhang Zh, Song Q, Jiang B et al (2019) Electrochemically assisted carbonization of Nb in molten salt. Surf Coat Technol 25:865–872
14. Narayan R, Narayana BH (1981) Electrodeposited chromium-graphite composite coatings. J Electrochem Soc 128(8):1704–1708
15. Xie H, Zhao H, Liao J et al (2018) Electrochemically controllable coating of a functional silicon film on carbon materials. Electrochim Acta 269:610–616
16. Baraboshkin AN (1978) Electrocrystalization of metals in molten salts. Nauka, Moscow (in Russian)
17. Shapoval VI (1981) Cationic catalysis during electroreduction of complex anions in molten salts. In: Proceedings of the XII Mendeleev congress, vol 3. Nauka, Moscow, pp 336–337 (in Russian)
18. Shapoval VI, Kushkov KhB (1986) Cation catalysis in complex processes of electroreduction in molten salts. In: Kublanovskii VS, Litovchenko KI (eds) Electrocatalysis and electrocatalytical processes. Naukova Dumka, Kiev, pp 17–29 (in Russian)
19. Zhang Y (1982) Electronegativities of elements in valence states and their applications. 1. Electronegativities of elements in valence states. Inorg Chem 21(11):3886–3889
20. Zhang Y (1982) Electronegativities of elements in valence states and their applications. 2. A scale for strengths of Lewis acids. Inorg. Chem. 21(11):3889–3893
21. Kushkhov KB, Shapoval VI, Novoselova IA (1986) Thermodynamic foundation of electrochemical synthesis of refractory metal compounds. Available from VINITI, Moscow. pp 7147–V86 (in Russian)
22. Shapoval VI, Kushkhov KB, Vasilenko VA (1979) The effect of Mg^{2+} cations on kinetics of electroreduction of WO_4^{2-} in the melt KCl-NaCl. Ukr Khim Zh 45(6):509–515 (in Russian)
23. Novoselova IA, Kuleshov SV, Volkov SV et al (2016) Electrochemical synthesis, morphological and structural characteristics of carbon nanomaterials produced in molten salts. Electrochim Acta 211:343–355
24. http://www.msg.ameslab.gov/GAMESS/GAMESS.html. Last visit 20.09.2018
25. Nemukhin AV, Grigorenko BL, Granovsky AA (2004) Molecular modeling by using the PC GAMESS program: from diatomic molecules to enzymes. Vestn Mosk Univ Khim 45(2):75–102 (in Russian)

26. Soloviev VV, Chernenko LO (2005) Modeling of the joint influence of the electrode surface and cationic and electric fields on the processes of tungstate anion electroreduction. Vestn Kharkov National Univ 648:210–213 (in Russian)
27. Lowdin P (1964) Molecular orbitals in the exact SCF theory. In: Molecular orbitals in chemistry, physics, and biology. Mulliken dedicatory volume, Academic Press, Inc., New York, pp 37–55
28. Lowdin P (1966) The calculation of upper and lower bounds of energy Eigen values in perturbation theory by means of partitioning techniques. In: Wilcox CH (ed) Perturbation theory and its application in quantum mechanics. Proceedings of Madison Symposium, John Wiley and Sons, Inc, pp 255–294
29. Lowdin P (1967) Quantumn theory of time-dependent phenomena treated by the evolution operator technique. Adv Quant Chem 3:323–381
30. Krishtalik LI (1979) Electrode reactions. The mechanism of the elementary act. Nauka, Moscow, pp 34–44 (in Russian)
31. Kushkhov KB, Shapoval VI (1982) The effect of cations of acids on thermodynamics and kinetics of electroreduction of WO_4^{2-} in KCl-NaCl melt. In: Ionic melts, Naukova Dumka Kiev, pp. 55–64 (in Russian)
32. Soloviev VV, Chernenko LO (2009) Modeling of the effect of the cationic composition of the melt on the structural features of electrochemical active species. Ukr Khim Zh 75(1):47–52 (in Russian)
33. Brauer G (1981) Handbuch der praparativen anorganischen chemie. Handbook of preparative inorganic chemistry, 3rd edn. vol 3. F. Enke, Stuttgart. Russian translation: Mir Moscow (1985) p 974 (in Russian)
34. Novoselova IA, Volkov SV, Oliinyk NF et al (2003) High-temperature electrochemical synthesis of carbon-containing inorganic compounds under excessive carbon dioxide pressure. J Min Metallurgy B: Metallurgy 39(1–2):281–293
35. Novoselova IA, Kuleshov SV, Fedoryshena OM et al (2016) Electrochemical synthesis of Tungsten carbides in molten salts for electrocatalysis. Ukr Khim Zh 82(11):67–76 (in Ukraine)
36. Novoselova IA, Kuleshov SV, Fedoryshena EN et al (2018) Electrochemical synthesis of tungsten carbide in molten salts, its properties and applications. ECS Trans 86(14):81–94

I. A. Novoselova candidate of chemical sciences (Ph.D., electrochemistry).
Scopus ID: 7004650001.
Research interests: thermodynamics and electrochemistry of molten salts, high temperature electrochemical synthesis of refractory compounds (carbides, borides, silicides).

I. N. Skryptun candidate of chemical sciences (Ph.D., physical chemistry).
Scopus ID: 6507844695.
Research interests: chemistry of molten salts, thermodynamics, electrolysis of melts.

A. A. Omelchuk corresponding member of National Academy of Sciences of Ukraine (Technical Chemistry), professor, doctor of chemical sciences (Dr., electrochemistry).
Scopus ID: 7004008408.
Research interests: electrochemistry of molten salts, solid-state electrolytes, thin-layer electrolysis of melts.

V. V. Soloviev professor, doctor of chemical sciences (Dr., electrochemistry).
Scopus ID: 7202070919.
Research interests: electrochemistry of molten salts, quantum-chemical calculations and modeling of electrochemically active species.

Microalgae-Based Systems Applied to Bioelectrocatalysis

Rosangela R. Dias, Rafaela B. Sartori, Ihana A. Severo, Mariany C. Deprá, Leila Q. Zepka and Eduardo Jacob-Lopes

Abstract The increasing demand by energy and the current need of the replace fossil resources it is leading the research and development (R&D) sector to search by renewable feedstock and renewable processes. Thus, major emphasis is being put into sustainable technologies and environmentally benign. In this context, microalgae have been extensively exploited for their versatility and capacity of the produce a broad spectrum of bioproducts. In particular, the viability of these microorganisms to generate electrical energy from organic and inorganic residues is an attractive technological route. The use of microalgae in electrochemical systems has the potential to produce bioelectricity associated with bioremediation and wastewater treatment. This integration could be advantageously exploited to the development of a self-sustaining biobased system. In this sense, this chapter is intended to provide a overview of various aspects associated with the bioelectricity production from microalgae.

Keywords Microalgae · Photosynthesis · Microbial fuel cells · Bioelectricity

1 Introduction

In the last years, significant advances have been made towards robust technologies, cost-effective and eco-friendly, aiming to overcome the excessive dependence of fossil resources [14]. Among recently developed technologies, the microbial fuel cell (MFC) gained great scientific and technological importance [48]. These bioelectrochemical systems are an attractive technology because of their sustainability at harvest of energy from readily available substrates [41, 83]. Biological entities as catalysts of electrochemical processes offer a means of produce clean energy associated with bioremediation of wastes [15, 47, 56].

In MFCs, microorganisms convert a diversity of substrates into electricity from a series of oxireduction reactions [67]. The system consists of a set of electrodes

R. R. Dias · R. B. Sartori · I. A. Severo · M. C. Deprá · L. Q. Zepka · E. Jacob-Lopes (✉)
Bioprocess Intensification Group, Federal University of Santa Maria (UFSM),
97105-900 Santa Maria, RS, Brazil
e-mail: ejacoblopes@gmail.com

Inamuddin et al. (eds.), *Methods for Electrocatalysis*,
https://doi.org/10.1007/978-3-030-27161-9_10

linked by an outer electric circuit, physically divided by a membrane or not [77]. The distinguishing feature, central these biotechnological devices, is the application of living microorganisms. Besides that, in contrast to traditional fuel cells, the MFC has the advantage of using wastewater treating it and producing bioelectricity simultaneously [76].

Since the turn of the century, MFCs research has advanced, and new projects have been launched towards in direction the synchronization of technologies and bioenergy sources sustainable. In this context, considerable researches are being realized to investigate the potential biotechnological of microalgae at the distinct bioelectrochemical processes. The microalgae present high photosynthetic efficiency and can be applied in MFCs to produce an electron acceptor in the cathodic compartment (photosynthetic microalgae), electron donor in the anode and/or remove organic matter also in the anode (heterotrophic microalgae) [23].

Microalgae as efficient solar energy converters have been utilized in the cathode of MFCs to O_2 generate and capture CO_2, with parallel biomass production and biocompounds of high value-added [17]. The application of bio-cathodes based in these microorganisms allows noble catalysts, used for oxygen reduction, to be substituted by natural materials, improving sustainability and cost-effectiveness [3]. On the other hand, microalgae also can be applied in the anode as fuel/substrate for exoelectrogenic bacteria, owing to the adequately elevated content of carbohydrate, protein and lipid [71]. Besides, recently discovered, some species of microalgae can be utilized as the sole electron-donating source. The utilization of electrogenic microalgae in the anode compartment is an extraordinary opportunity [75].

The use of microalgae in electrochemical processes as the MFCs has been recognized as a versatile technology and potentially promising. Thereby, this chapter intends to furnish a comprehensive review of the fundamental elements of microalgae-based microbial fuel cells (mMFCs), their configurations, limitations, and applications.

2 Biological Fuel Cells

A fuel cell is an electrochemical device that involves the transfer of electrons and conversion of chemical energy of a fuel into electricity. In these systems, anodic (electron addition) reactions are fed continuously by a fuel, while cathodic reactions (electron consumption) are fed continuously by an oxidizer. Natural gas and hydrogen are the more commonly used fuels in these systems, while the oxygen of the air is utilized as the oxidant [72]. All these reactions occur through a medium (electrolyte) containing dissolved ions capable of withstanding the current flow and allowing electric charge transfer [24].

The concept of electricity generation from biological sources arose even in the eighteenth century. However, it was only in 1911 that the disaggregation of substrates by organisms accompanied by the clearance of electricity was demonstrated [59,

73]. Despite extensive research in the last century on routes and bioelectrochemical generation, few prototypes were reported [43].

The traditional generation of energy for methods such as chemical fuel cells is not able to supply the need for sustainable energy of high demand and recent advances in microbiological research have led to the bioelectricity production through fuel cells by microorganisms. These current systems have become a promising, innovative, economical and environmentally favourable technology for sustainable electricity production [75].

The microorganisms growth in MFCs can be termed as a self-sustaining cycle. They may develop in suspension to shape a biofilm at the electrode and superficies of the anode chamber. This biofilm can directly exchange electrons through physical contact with the cell. Also, in this compartment is carried out the reaction of oxidation of the organic matter, producing protons and finally an electric current of biomass [58, 69].

In the so-called direct electron transfer, the microorganisms present have active and efficient electrochemical redox enzymes in their membranes that cross the MFC circuit without the need for exogenous chemicals to accompany the transfer of electrons to the electrode [34, 62]. However, when they are unable to perform this process, intermediary mediators are used to capturing the electrons in the cell, to reduce and promote the extracellular transfer [31].

In general, the oxidation of substrate in the anode chamber generates CO_2, protons, and electrons. The electrons are transported to the electrode, then flowing to the cathode, and the protons are directed to the cathode by means of a permeable membrane. These, when consumed in the cathodic chamber, reduce O_2 to H_2O and produce electrical energy [72, 89].

The consideration of MFCs as a issue negligence has been following another notions of bioconversion in last times. Substantial research is being conducted, new projects have evolved, and the operation has advanced towards microalgae-based fuel cells for bioelectricity production through the reaction of photosynthesis [77].

In comparison with conventional MFCs, microalgae-based fuel cells (mMFCs) represent a more developed technology since are able of capture carbon dioxide with parallel wastewater treatment and energy production [67]. This integration has the potential to generate fuel and oxygen for cells, providing the development of a system that satisfies with sustainable and economic metrics [71].

3 Factors Influencing the Bioelectricity Production from Microalgae

Several factors such as pH, temperature, light intensity, substrate, carbon dioxide, electrode material, and membrane can severely affect the power output and overall performance of the mMFCs. These parameters are discussed below.

The pH as an environmental parameter affects the microbial activity and, consequently, the anodic and cathodic performance. In the anode and cathode chambers, the pH should be maintained between 6 and 8, which is considered ideal for metabolic activity of the microorganisms [75]. Undesirable pH variations reduce the bioelectricity production and perturb the physiological reactions that occur inside the cell. In traditional mMFCs, can maintain distinct pH conditions in each compartment to optimize their reactions, which is impossible for single-chamber configurations, because merely one electrolyte is present [25].

In the cathodic chamber, the O_2 reduction reaction and the accumulation of cation species (for example, Na^+ and Ca_2^+) that permeate the membrane result in alkaline pH (8–10), decreasing the cathodic potential. For mMFCs of air cathode or single chamber, this is favourable the cathodic reactions and for the general performance, but can inhibit the activity of the microorganisms. Addition of tampons such as carbonate, phosphate and carbon dioxide helps the maintain the pH [61]. In single-chambered mMFCs, the CO_2 generated by bacteria from the oxidation of the fuel can assist in the growth of microalgae and reducing the pH of the electrolyte and, in two-chamber mMFCs, the carbon dioxide of the anodic compartment can be diverted for the cathodic compartment for the same purpose [77].

In the anodic chamber, the electrochemical oxidation of fuels elevates the generation of protons [98]. This production is superior to its transport through the membrane. The accumulation of protons in the anodic compartment causes changes in pH, reducing the microbial activity, the electron transfer, and the cathodic reactions due to the limited supply of protons. Therefore, it is suggested, that the anodic pH be controlled keeping next to neutrality for optimizing the energy output.

The temperature can significantly affect mMFCs performance through the metabolism microbial. Control the temperature fluctuations in mMFCs allows the formation of anodic biofilms more quickly, resulting in shorter startup times. In general, the mMFCs can be classified into thermophiles and mesophiles depending on the microorganism employed. In the thermophilic mMFCs, the microorganisms require high temperatures for their development; therefore, the mMFC operate at elevated temperature. On the other hand, in mesophilic mMFCs, the microorganisms perform better under moderate temperature conditions [78]. Most of the mMFCs operate in the mesophilic range, and the optimal temperatures vary according to the microorganism employed. It is evident, from studies [90, 99], what taller potency densities can be obtained by maintaining a suitable temperature range for the microorganisms. Thus, similar to other biological processes, environmental parameters as temperature and pH must be adjusted to reach a high-performance system.

The photosynthesis exercises a critic function in mMFCs, and its performance can be optimized to potentiate the generation of bioelectricity. Both the intensity of light such as its duration can affect the photosynthetic efficiency of the microalgae and, consequently, the oxygen supply in the cathode [13]. Therefore, several investigations have been realized to evaluate the different conditions of intensity and regime of light in the efficiency of mMFCs [93].

It is reported that the augmentation in light energy increases proportionally the dissolved O_2 and the potency density of the system [92]. However, exist a range

of light intensity considered optimal which needs to be applied. Variations in light intensity affect both the performance of the mMFC, such as biomass production and its composition. The feasibility of parallel generation of value-added biomass enables the development of economically viable systems. Therefore, its influence on the productivity and composition of biomass is also evaluated in mMFCs [22].

Studies show that as light intensity increases, a higher concentration of biomass is obtained, but at the same time, occurs the shortening the life useful of microalgae. This is attributed to the damage caused to the photosynthetic apparatus by photoinhibition [45]. Regarding the effect of light/dark cycles, higher power densities are obtained under continuous illumination. Besides that, in this condition, it favours the supply of dissolved oxygen positively on the cathode, with a reduction during the dark period. However, it is pointed out that continuous lighting also reduces the life useful of microalgae. In this sense, intermittent lighting is indicated to prolong the life cycle of microalgae cultures [4]. Concomitant, the light source is also reported by influencing the photosynthetic rate of microalgae and, therefore, the system performance [38].

In this context, it is observed that higher bioelectric generation can be obtained from the optimizing the photosynthetic rate, applying a light intensity, duration (light/dark cycle) and adequate light source.

The mMFCs utilize a variety of substrates, including, for example, wastewater. Still, detention time and organic loading rates (OLRs) can also influence the performance of these systems, which is notably reliant on the substrate utilized [16, 54].

According to the system configuration and the kind of wastewater to be treated, it is necessary to use an adequate load of OLR for utmost chemical oxygen demand removal. Typically, in between 0.05 and 2.0 kg COD/m^3 d of OLR is used to obtain an increase in the power density of the mMFC [57, 72]. The potency density is proportional to the degradation of the substrate rate, but it is still necessary to use pretreatment systems on more complex substrates to achieve better results [21, 32, 46].

Domestic and industrial wastewater and substrates highly digestible as acetate and proteins, have been quite studied and utilized in mMFCs for effluent treatment as well as for energy generation [35, 50, 74, 97].

The supply of carbon dioxide in mMFCs is essential to promote healthy growth of microalgae. The photosynthetic microalgae use carbon dioxide to perform the photosynthesis and produce oxygen and biomass [86]. The ideal growth of microalgae in the cathode of mMFCs can be obtained by the continuous bubbling of CO_2 or by the supply of carbon dioxide diverted of the anodic chamber. The carbon dioxide diverted of the anodic chamber is suggested by optimum produce growth and, therefore, the bubbling of carbon dioxide in the cathodic chamber is not necessary [10, 40].

The existence of carbon dioxide dissolved in the cathodic chamber decline the pH of the electrolyte, requiring the control of the same for that the inoculum of the microalga is not affected and ensures the operation of the processes. The microalgae growth kinetics increase as the carbon dioxide concentration increases, however, can

reduce significantly in high or very low concentrations of the same. Furthermore, the carbon dioxide concentration also influences the chemical composition of microalgae biomass [80].

The success of an mMFC is associated with the selection of the electrode material. Both electrodes follow different selection criteria, but specific properties must be presented equally. Are necessary electrodes with a great superficial area, high electrical conductivity, durability and stability, biocompatible and low cost [70]. By decreasing the resistance, using electrode materials of high electrical conductivity, it is possible to augmentation the superficial area and, consequently, the efficiency of the system. In terms of durability, stability, the materials should be able to withstand both acid and basic medium. The durability can be augmented with increased surface roughness, however, this can result in contamination and, in the long run, the performance of the mMFC would be reduced.

The metallic materials have higher conductivity than carbon materials, but the corrosion propensity limited the choice of these. The low costs, support of microbial adherence to form steady biofilms and electrical conductivity, make the carbon the material more used and versatile, available as graphite plates, rods, and granules. The biofilm helps in the capture of the electron, therefore, have been used coatings like platinum and Teflon to potentiate the formation of these structured communities. In the cathode, ferricyanide, and oxygen are the electron acceptors most popular. Due to the oxidation potential, free cost and water as the final product, oxygen is the best option for mMFCs and, Based on the application, the cathodic material is selected. In general, most anodic materials can be used as cathodes. Graphite and carbon screen are the more commonly used cathodic materials [79].

The functions of a membrane are to segregate the reactions occurring in the cathodic and anodic compartment; reduce the passage of O_2 of the cathodic compartment to the anodic, and ensure the sustainable operation and lasting [52]. Before being used in any system, the choice of a membrane requires considering divers relevant aspects. The ideal characteristics of selection be an excellent ionic conductor, electronic insulating, ion selective, durable, chemically steady, biocompatible, insensible to biofouling and mainly of viable economic cost [72].

Currently, the main membranes utilized in mMFCs are cation exchange membrane (CEM) and anion exchange membrane (AEM) [63, 68]. A CEM allows only the passage of cations, per carrying negatively charged groups fixed to membrane skeleton. The most widely used materials are perfluorosulfonic acid polymers (PFSA). Within the family of PFSA membranes, the Nafion (DuPont) is the most applied. However, commercialization of Nafion-based membranes has been complicated by the high cost and environmental incompatibility of perfluorinated material processing [95].

In contrast, AEM has the potential to reduce costs, since a more comprehensive selection of cheap materials can be realized. In addition, the utilization of low-cost porous membranes has also been evaluated, for example, nylon and glass fibers. These membranes are not selective of ions, allowing the transfer of anions and cations in opposite directions. Despite being cheap, these separators present limitations such as high internal resistance [77].

4 Interactions Between Microalgae and Electrodes

4.1 Microalgae at the Cathode

The limitations that are put forward with the utilize traditional catalysts (chemical and metal) for the cathode have boosted researchers cogitate other alternatives. The microalgae biocathodes can supply oxygen jointly with the bioconversion of nutrients and CO_2, through the process of photosynthesis. As consequence of photosynthesis, biomass is produced and can be utilized to generate value-added compounds or serve as anodic fuel of the mMFC [93].

The photosynthetic microalgae use sunlight and the CO_2 diverted from the anodic compartment for their development and oxygen production. The in situ production oxygen plays as an electron acceptor and help in replacing the traditional mechanical agitation techniques. Studies of Gajda et al. [19] and Wu et al. [91] evidenced the use of microalgae as efficient in situ oxygenators. In comparative studies, it was possible to demonstrate that the aeration of microalgae at the cathode significantly favours acquisition a higher potency density, when compared to mechanical agitation [33, 88].

The utilize of microalgae as cathodic reaction catalysts have the capacity to improve electricity production. In addition, expenditures can be substantially reduced by using them, because they can replace the use of expensive catalysts. Another advantage of biocathodes, in contrast to abiotic cathodes, is biomass production and the possibility of removing nutrients using microalgae metabolism [63].

Beyond the already existent basic systems, other projects are developed for the application of microalgae biocathodes such as the mMFCs connected to photobioreactors [20]. These systems are operated to provide sustainably dissolved oxygen by recirculating of the catholyte connected to the photobioreactors. It is worth mentioning that the application of the different species of microalgae requires distinct inoculation media. Consequently, they exhibit different growth parameters. Therefore, the application of each configuration, substrate, as well as the utilized of the different species microalgae, either in the anodic or cathodic compartment, take to variations in power density. Table 1 summarizes some microalgae-based MFCs systems and their power density.

4.2 Microalgae at the Anode

Different sources of the substrate are evaluated for their utilization in the anode of mMFCs. The more common are formate, glucose, and acetate. Other sources include microalgae biomass (either living cells or dry biomass/powder) and wastewater [15]. The substrate a nutrient source for bacteria is a determining factor in mMFCs According to Parkash et al. [55], the anolyte type used and its internal resistance affect the power production, which also depends on following factors: membrane resistance,

Table 1 Microalgae-based MFCs systems and their respective potency densities

Cathodic content	Anodic content	Power output (mW/m^2)	References
C. vulgaris	Activated sludge	13.50	del Campo et al. [12]
C. vulgaris	*S. cerevisiae* and glucose	0.95	Powell et al. [60]
C. pyrenoidosa	Synthetic wastewater and sodium acetate	60.60	Jadhav et al. [28]
C. pyrenoidosa	Potassium ferricyanide	6030.00	Xu et al. [94]
Bacterial community	*C. vulgaris*	327.67	Huarachi-Olivera et al. [27]
Desmodesmus sp.	Synthetic wastewater	99.09	Wu et al. [92]
C. vulgaris	bacteria	24.40	Wu et al. [91]
C. vulgaris	Enriched bacterial consortium	62.70	Gouveia et al. [22]
S. quadricauda	Domestic wastewater	62.93	Yang et al. [96]
C. reinhardtii	*G. sulferreducens*	41.00	Nishio et al. [51]
C. reinhardtii	*G. sulferreducens* and Formate	140.00	Nishio et al. [51]
C. reinhardtii	*G. sulferreducens* and Acetate	630.00	Nishio et al. [51]
S. obliquus	GM media	153.00	Kakarla and Min [33]
Ferricyanide	*S. obliquus* and wastewater	102.00	Kondaveeti et al. [36]
Potassium hexacynoferrate (III) and KH_2PO_4 buffer	*C. reinhardtii transformation*	12.94	Lan et al. [38]
Ferricyanide	*C. vulgaris* and anaerobic consortium	15.00	Lakaniemi et al. [37]
Ferricyanide	*D. tertiolecta* and anaerobic consortium	5.30	Lakaniemi et al. [37]
C. vulgaris	Sediment	38.00	Wang et al. [88]
C. vulgaris	*Scenedesmus* and microbes	1926.00	Cui et al. [10]
Mixed microalgae	Photosynthetic bacteria	103.00	Chandra et al. [8]

high generation of ions in the anode compartment, and crossing of oxygen through the membrane. The substrates oxidation by bacteria is directly related to electron transfer and sequentially to the electric current production. Therefore, the substrate influences the microbial community and the performance general of mMFCs.

The microalgae as anodic substrate are passable to be oxidized by bacteria to produce electrons. The degradation of microalgae biomass in an mMFC can produce

by-products such as acetate and lactate, which are used to generate bioelectricity. However, the conversion efficiency of the biomass is identified as being low, which, consequently, not generate a tall potency density [36]. Therefore, a pre-treatment of biomass is proposed as a method to rupture the cell wall and do it more digestible for bacteria. Another critical factor is the biomass concentration employed, as shown by [65], which can considerably intervene in the efficiency of the mMFC.

Researches have also been done with microalgae used at the anode of mMFCs as the only electron donor source. de Caprariis et al. [11] and Xu et al. [94] highlighted in their studies the interesting potential of such an application. By regulating the O_2 concentration, light intensity and the density of microalgae cells in the anode, microalgae generate bioelectricity without the need for substrates and mediators.

It is essential that in mMFCs with exoelectrogenic microalgae the unfavourable effect of the microalgae on the anode be minimized, this is, there should be control of the oxygen content since the presence of O_2 in the anodic compartment plays like a competitive electron acceptor. In this case, oxygen inhibitors, like activated carbon and iron powder, can be utilized. In contrast, suitable dosages should be administered to avoid disturbances in redox reactions.

5 Microalgae-Based Microbial Fuel Cells Configurations

Normally, the microalgae are cultivated in closed photobioreactors or raceway ponds, where they can utilize sunlight, CO_2 and nutrients for their growth [14, 44]. Thus, projects have been developed to allow microalgae to would generate electricity in an MFC. The overall process involving microalgae and the configurations of the anode chamber and the cathodic chamber is shown in Fig. 1. To create cost-effective processes, several configurations are proposed. Among the main stand out the mMFCs of single-chambered, two-chambered, sediment and coupled types [66]. New configurations with biotechnological development are still emerging with the goal of will improve the power output, the coulombic efficiency, the stability, the longevity and the cost-effective of the mMFCs [55].

In single-chambered mMFCs, bacteria and microalgae coexist parallel in the same chamber and may not contain membrane. They are generally configured with an air cathode. Microalgae absorb the CO_2 produced by the microbes, and both cultures are grown synergistically without the presence of a membrane (Fig. 2). The main advantage of these systems is the relatively simple architecture and the low cost of construction. However, have limitations, such as the high diffusion of oxygen, which may lead to a diminution in coulombic efficiency [6].

In a single-chambered mMFC configured with an air cathode, the oxygen supply to the cathode is given by microalgae and atmospheric air [26]. Similar projects include the integration of a biofilm from microalgae at the mMFC [96]. In these, the presence of a microalgae biofilm fixed about support, that establishes an interface among the anode and the cathode, permit minimizing the adverse effects of the microalgae on the

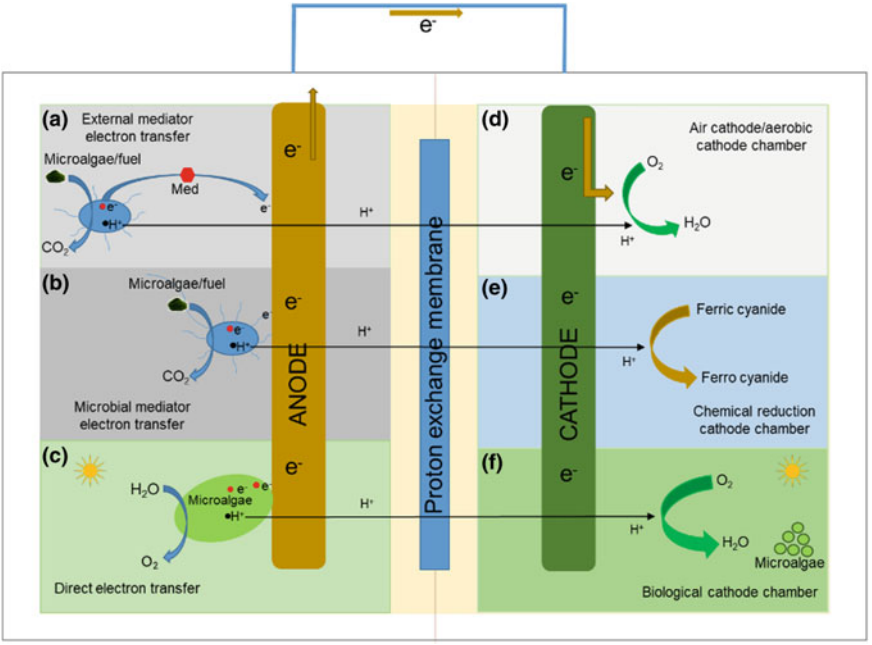

Fig. 1 Representation of various configurations of the anode chamber and the cathodic chamber of mMFCs. **a**, **b**, **c** Anodic chamber dependent on the mediator and dependent on bacterial mediator fed with microalgae substrate, and, of direct electron transfer. d, **e**, **f** cathodic chamber of air, of chemical acceptance of electrons and biological acceptance of electrons, respectively. Adapted from [78]

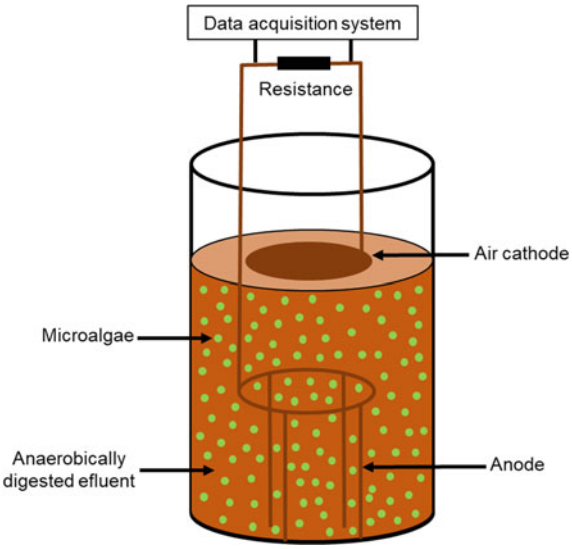

Fig. 2 Schematic of one single-chambered mMFC. *Source* Adapted from [26]

anode (this is, O_2 as a concurrent electron acceptor). This approach aims to achieve a better performance, as well as facilitating the removal of nutrients of the system.

On the same configuration, projects are developed using microalgae exoelectrogenic [11]. Microalgae are employed in the anodic compartment without the need for mediators. To date, there are few reports of microalgae being used to produce electrons in the anode compartment [71]. The use of such microalgae represents a potential possibility and, therefore, new studies are being realized out in this new field [17].

In two-chambered mMFCs, the anode and cathode chamber is physically divided by a membrane. The employ of the membrane helps to reduce the dissemination of oxygen into the anode, which easily occurs in the single-chamber mMFCs. The use of microalgae to generate O_2 in the cathodic compartment is the more promising project of this configuration [79]. Generally, a light source is positioned in the cathodic compartment to supply photons for photosynthetic reactions of microalgae and the anode compartment is covered. The compartments usually present forms cylindrical, rectangular, miniature and can be operated in batch and fed-batch mode [15].

A typical two-chamber mMFC, as mentioned above, is shown in Fig. 3 and exemplified by Gouveia et al. [22] and del Campo et al. [12]. About these mMFCs different projects have been proposed as, for example, the two-chamber mMFC in H-shaped [27]. However, it has been observed that these configurations have, as a disadvantage, a very small membrane area between the catholyte and the anolyte. Therefore, ionic exchange among the two compartments is much low, and membrane encrustation and internal resistance are some of the limitations presented by the H-shaped mMFCs [69].

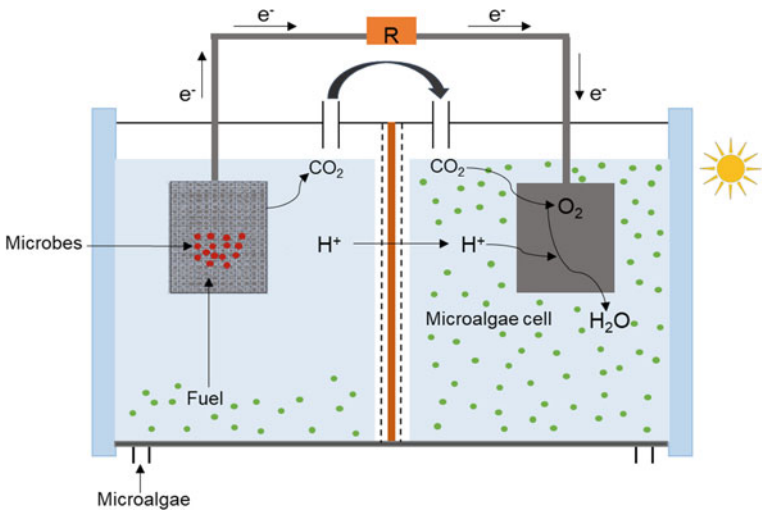

Fig. 3 Schematic of one two-chambered mMFC. *Source* Adapted from [10]

Similarly, some projects two-chamber mMFC are enriched with microalgae in the anodic and cathodic compartment [10]. The anode compartment, which contains bacteria, is fed with microalgae biomass a substrate. The CO_2 generated in the degradation of biomass is carried through a tube, arrested on the compartments, and can be utilized by microalgae cells at the cathodic compartment to stimulate their development and generate oxygen. These projects prove that microalgae-based fuel cells can be economically viable with the self-sustaining generation of bioelectricity and biomass of microalgae.

In the three-chamber mMFC configurations, the third compartment is among the anode and the cathode. The partial desalination is detected in the intermediate compartment, where the cations displace to the cathode and anion to the anode. However, the power density of that configuration has been observed to be minor than two-chamber mMFCs [77].

In sediment mMFCs, energy can be generated by the application of an anode disposed into sediment and a cathode filled with microalgae which are above the same [78]. Typically, the sedimentary mMFC is composed of an anode and a cathode positioned in contrary sides of a chamber. Electrodes are connected externally, and the anode is deposited in the centre of the sediment. Posteriorly, the sediment is sheeted with sterile sand [9, 29]. Figure 4 presents a model of sedimentary mMFC, membrane-less, composed of a microalgae biocathode.

Lastly, the coupled mMFCs are systems developed for the concomitant generation of electricity and distinct bioprocesses. The application of coupled systems provides a means of treat wastewater, produce bioelectricity and biomass simultaneously [20, 30]. Figure 5 features a coupled mMFC model.

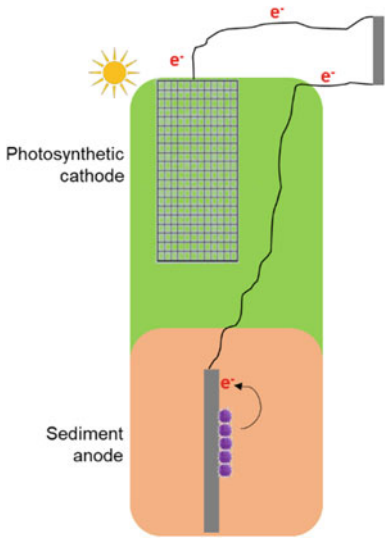

Fig. 4 Schematic of one sediment-type mMFC. *Source* Adapted from [9]

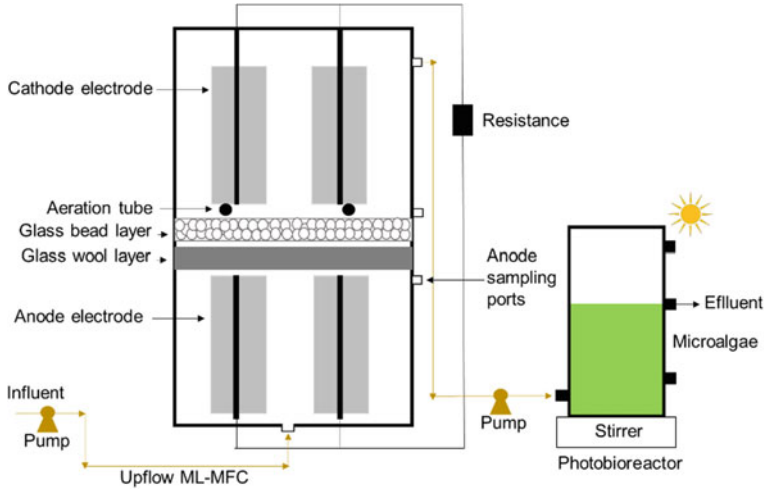

Fig. 5 Schematic of one coupled type mMFC. *Source* Adapted from [30]

6 Applicability of the Process

The use of microalgae has attracted considerable interest and has been gaining much prominence in the field of bioeconomics mainly to its practical value in the development of alternative biofuels and the implementation of mMFCs in several other applications.

The incorporation of microalgae as bioenergy sources into an mMFC serves as a promising alternative due to its inherent advantages in its rapid and versatile growth, energy conversion efficiency, carbon dioxide fixation, wastewater recovery and the parallel biomass production of high added value [67].

Several authors have presented the efficiency of these processes and researches have been intensively conducted through the light energy conversion into bioelectricity by the metabolic and electrochemical reactions of photosynthetic organisms [5, 7, 39, 64, 71, 75].

The integration of mMFCs technology based on microalgae has the advantage of reusing the nutrients in the same system, do not require special catalysts and still have intermediate organic material which helps them in the conversion of bioelectricity in the dark. This makes these systems achieve high performance with a low maintenance cost [17, 77].

Another term in evidence in microalgae mMFCs is the CO_2 sequestration with simultaneous treatment of wastewater and bioenergy generation. The mMFCs use the anode and the cathode to accomplish the process of photosynthesis and by-products production through the O_2 generated in situ. This has led many to evaluate aspects of biocathodes as a practical solution to the oxygen-limiting processes of conventional processes while enabling low-cost aeration with the parallel biomass production [17, 49, 67]. Still, one of the most promising applications of mMFCs is

to recuperate energy from low-quality substrates, which make a process sustainable and economically viable [39].

Although the concept of mMFCs shows a promising option, there are still some problems to be solved mainly due to their limited energy production. The challenge to be overcome today is to convert the technologies developed into laboratory scales into a much larger projection field. High costs with membranes, electrode materials and other problems that are sometimes not observed on small scales could affect the industrial practice of this system [2].

Different from already consolidated traditional projects, the progress in diverse renewable energy technologies yet need considerable investment. Based on statistics and analysis from U.S. Energy Information Administration the bioenergy generation costs for alternative sources as hydro, solar, wind and biomass can reach average values of $0.062, $0.063, $0.059 and $0.095 per kW/h, respectively. While theoretically, the operating cost of an mMFC equals $0.120 per kW/h [1, 42, 82].

Economically, recent advancement in the overall efficiency of mMFCs and the integration of new technologies are presented as a promising aspect shortly [81]. A clear benefit of this technology is the opportunity to unite and rearrangement of sundry processes in one place. Separation techniques, CO_2 conversion, waste treatment, and power generation is probably the best option and certainly has a profound socio-environmental impact [54, 84].

The cooperation of regulatory policies, interdisciplinary aids and life cycle assessments (LCAs) are essential to enhance production and economics for microalgae-based bioelectricity generation [85]. Life cycle assessment is a crucial tool for analyzing all the environmental and economic impingement of a process or product, particularly before being applied on a large commercial scale [55].

Few economic analyzes have been detailed so far for mMFCs. To date, the R&D has focused on laboratory-scale projections, however it is expected that commercialization of larger scale configurations will be possible in the coming years [53, 87]. Also, the cost comparison of these processes with conventional chemical systems is not feasible because of the substantial costs of substrates used in these systems.

Future advancements should take into account the elevated efficiency and low cost for scheduling mMFCs configurations, as well as new advances should contain energy management systems to improve performance and system capacity for practical use and real [18].

Finally, the configuration and integration of microalgae-based fuel cell systems play a significant role, and today many advances are being made toward the applicability of production processes. Ongoing projects of new modularities and programming, material longevity, inclusion of bioenergy collection and storage processes and the understanding built on pilot researches are driving innovation and consolidation into broader market acceptance of mMFCs.

7 Conclusions and Future Prospects

The strategy of integrating microalgae into microbial fuel cells is a technology that benefits sustainable energy production. Nonetheless, some limitations are persisting scale-up. A steady voltage is necessary to operate, however, the voltage generated in the mMFCs is small, and the robustness of generation is also inconstant. The solution would be to make adjustments to the operating parameters regularly, including microbial load and oxidant concentration. Among other limitations, the high internal resistance found in mMFCs can be surpassed by decrease the space among the electrodes; the low electron transfer can be solved by recognizing good mediators without toxicity and; the low potency density of the systems can be improved by using microbial consortia or by identifying microalgae with effective electrogenic potential. Another bottleneck of the mMFC system is the reduction of proton transfer efficiency due to biological encrustation occurred at the membrane. Therefore, a regular exchange of the membrane is required to operate continuously.

Most mMFCs configurations feature advantages and disadvantages, but all have the potential for bioelectricity production. What needs to be done is to select the most sensitive parameters and perfect them. It is expected that the utilization of a single configuration or the integration of mMFCs projects will be simplified towards field scale application. Integrated systems must be developed to simultaneously solve different problems, such as waste treatment and CO_2 sequestration. Moreover, life-cycle analysis and technical-economic of the mMFCs is necessary to propose the feasibility of this technology on an industrial scale.

Despite the existing bottlenecks, currently, the mMFCs have proven to be a potential technology for the generation of electricity associated with bioremediation of wastes, CO_2 fixation, and production of value-added biomass. The application of microalgae in these systems has the possibility of making the fuel cells a doable technology. In comparison to conventional fuel cells, mMFCs exhibit attractive resources, which will influence future applications and the development of this technology. Recent research results suggest that of the mMFCs will become, in the next future, of practical use and the best choice among the sustainable bioenergy processes.

References

1. Abourached C, English MJ, Liu H (2016) Wastewater treatment by Microbial Fuel Cell (MFC) prior irrigation water reuse. J Clean Prod 137:144–149. https://doi.org/10.1016/j.jclepro.2016.07.048 (Access. in: 30/04/19)
2. Amulya K, Dahiya S, Venkata Mohan S (2016) Building a bio-based economy through waste remediation: innovation towards sustainable future. In: Bioremediation and bioeconomy. Elsevier, 497–521. https://doi.org/10.1016/b978-0-12-802830-8.00019-8 (Access. in: 13/04/19)
3. Baicha Z, Salar-García MJ, Ortiz-Martínez VM, Hernández-Fernández FJ, De los Ríos AP, Labjar N, … Elmahi M (2016) A critical review on microalgae as an alternative source for

bioenergy production: a promising low cost substrate for microbial fuel cells. Fuel Process Technol 154:104–116. https://doi.org/10.1016/j.fuproc.2016.08.017 (Access. in: 13/03/19)
4. Bazdar E, Roshandel R, Yaghmaei S, Mardanpour MM (2018) The effect of different light intensities and light/dark regimes on the performance of photosynthetic microalgae microbial fuel cell. Biores Technol 261:350–360. https://doi.org/10.1016/j.biortech.2018.04.026 (Access. in: 25/03/19)
5. Bombelli P, Bradley RW, Scott AM, Philips AJ, McCormick AJ, Cruz SM, Anderson A, Yunus K, Bendall DS, Cameron PJ, Davies JM, Smith AG, Howe CJ, Fisher AC (2011) Quantitative analysis of the factors limiting solar power transduction by *Synechocystis* sp. PCC 6803 in biological photovoltaic devices. Energy Environ Sci 4:4690–4698. https://doi.org/10.1039/c1ee02531g (Access. in: 29/03/19)
6. Bruno LB, Jothinathan B, Rajkumar M (2018). Microbial fuel cells: fundamentals, types, significance and limitations. In: Microbial fuel cell technology for bioelectricity. Springer, Berlin, 23–48. https://doi.org/10.1007/978-3-319-92904-0 (Access. in: 25/03/19)
7. Cao XX, Huang X, Lig P, Boon N, Fan MZ, Zhang L, Zhang XY (2009) A completely anoxic microbial fuel cell using a photo-biocathode for cathodic carbon dioxide reduction. Energy Environ Sci 2:498–501. https://doi.org/10.1039/b901069f (Access. in: 29/03/19)
8. Chandra R, Sravan JS, Hemalatha M, Kishore Butti S, Venkata Mohan S (2017) Photosynthetic synergism for sustained power production with microalgae and photobacteria in a biophotovoltaic cell. Energy Fuels 31(7):7635–7644. https://doi.org/10.1021/acs.energyfuels.7b00486 (Access. in: 13/04/19)
9. Commault AS, Lear G, Novis P, Weld RJ (2014) Photosynthetic biocathode enhances the power output of a sediment-type microbial fuel cell. NZ J Bot 52(1):48–59. https://doi.org/10.1080/0028825X.2013.870217 (Access. in: 15/04/19)
10. Cui Y, Rashid N, Hu N, Rehman MSU, Han JI (2014) Electricity generation and microalgae cultivation in microbial fuel cell using microalgae-enriched anode and bio-cathode. Energy Convers Manag 79:674–680. https://doi.org/10.1016/j.enconman.2013.12.032 (Access. in: 13/04/19)
11. de Caprariis B, De Filippis P, Di Battista A, Di Palma L, Scarsella M (2014) Exoelectrogenic activity of a green microalgae, *Chlorella vulgaris*, in a bio-photovoltaic cells (BPVs). Chem Eng Trans 38:523–528. https://doi.org/10.3303/CET1438088 (Access. in: 15/03/19)
12. del Campo AG, Cañizares P, Rodrigo MA, Fernández FJ, Lobato J (2013) Microbial fuel cell with an algae-assisted cathode: a preliminary assessment. J Power Sources 242:638–645. https://doi.org/10.1016/j.jpowsour.2013.05.110 (Access. in: 13/04/19)
13. del Campo AG, Perez JF, Cañizares P, Rodrigo MA, Fernandez FJ, Lobato J (2015) Characterization of light/dark cycle and long-term performance test in a photosynthetic microbial fuel cell. Fuel 140:209–216. https://doi.org/10.1016/j.fuel.2014.09.087 (Access. in: 25/03/19)
14. Deprá MC, dos Santos AM, Severo IA, Santos AB, Zepka LQ, Jacob-Lopes E (2018) Microalgal biorefineries for bioenergy production: can we move from concept to industrial reality? BioEnergy Res 11(4):727–747 (Access. in: 30/04/19)
15. Do MH, Ngo HH, Guo WS, Liu Y, Chang SW, Nguyen DD, … Ni BJ (2018) Challenges in the application of microbial fuel cells to wastewater treatment and energy production: a mini review. Sci Total Environ 639:910–920. https://doi.org/10.1016/j.scitotenv.2018.05.136 (Access. in: 13/04/19)
16. dos Santos AM, dos Santos AM, Sartori RB, Queiroz LZ, Jacob-Lopes E (2018) Influence of poultry and swine blood shocks on the performance of microalgal heterotrophic bioreactor. Desalin Water Treat 114:128–134. https://doi.org/10.5004/dwt.2018.22359 (Access. in: 30/04/19)
17. Fischer F (2018) Photoelectrode, photovoltaic and photosynthetic microbial fuel cells. Renew Sustain Energy Rev 90:16–27. https://doi.org/10.1016/j.rser.2018.03.053 (Access. in: 13/03/19)
18. Gajda I, Greenman J, Ieropoulos LA (2018) Recent advancements in real-world microbial fuel cell applications. Current Opin Electrochem 11:78–83. https://doi.org/10.1016/j.coelec.2018.09.006 (Access. in: 15/04/19)

19. Gajda I, Greenman J, Melhuish C, Ieropoulos I (2013) Photosynthetic cathodes for microbial fuel cells. Int J Hydrogen Energy 38(26):11559–11564. https://doi.org/10.1016/j.ijhydene.2013.02.111 (Access. in: 16/04/19)
20. Gajda I, Stinchcombe A, Greenman J, Melhuish C, Ieropoulos I (2014) Algal 'lagoon' effect for oxygenating MFC cathodes. Int J Hydrogen Energy 39(36):21857–21863. https://doi.org/10.1016/j.ijhydene.2014.05.173 (Access. in: 19/03/19)
21. Ghosh RS, Ghangrekar MM (2015) Enhancing organic matter removal, biopolymer recovery and electricity generation from distillery wastewater by combining fungal fermentation and microbial fuel cell. Biores Technol 176:8–14. https://doi.org/10.1016/j.biortech.2014.10.158 (Access. in: 25/04/19)
22. Gouveia L, Neves C, Sebastião D, Nobre BP, Matos CT (2014) Effect of light on the production of bioelectricity and added-value microalgae biomass in a photosynthetic alga microbial fuel cell. Biores Technol 154:171–177. https://doi.org/10.1016/j.biortech.2013.12.049 (Access. in: 13/04/19)
23. Gude, V. G. (2016). Microbial fuel cells for wastewater treatment and energy generation. In Microbial Electrochemical and Fuel Cells (pp. 247–285). Woodhead Publishing. https://doi.org/10.1016/b978-1-78242-375-1.00008-3 (Access. in: 13/03/19)
24. Hayes P (2014) Chemical Reaction Kinetics. Treatise on Process Metallurgy 1:831–852. https://doi.org/10.1016/B978-0-08-096986-2.00015-1 (Access. in: 28/03/19)
25. He Z, Huang Y, Manohar AK, Mansfeld F (2008) Effect of electrolyte pH on the rate of the anodic and cathodic reactions in an air-cathode microbial fuel cell. Bioelectrochemistry 74(1):78–82. https://doi.org/10.1016/j.bioelechem.2008.07.007 (Access. in: 23/03/19)
26. Hou Q, Nie C, Pei H, Hu W, Jiang L, Yang Z (2016) The effect of algae species on the bioelectricity and biodiesel generation through open-air cathode microbial fuel cell with kitchen waste anaerobically digested effluent as substrate. Biores Technol 218:902–908. https://doi.org/10.1016/j.biortech.2016.07.035 (Access. in: 15/03/19)
27. Huarachi-Olivera R, Dueñas-Gonza A, Yapo-Pari U, Vega P, Romero-Ugarte M, Tapia J, … Esparza M (2018) Bioelectrogenesis with microbial fuel cells (MFCs) using the microalga *Chlorella vulgaris* and bacterial communities. Electron J Biotechnol 31:34–43. https://doi.org/10.1016/j.ejbt.2017.10.013 (Access. in: 18/03/19)
28. Jadhav DA, Jain SC, Ghangrekar MM (2017). Simultaneous wastewater treatment, algal biomass production and electricity generation in clayware microbial carbon capture cells. Appl Biochem Biotechnol 183(3):1076–1092 (Access. in: 16/04/19)
29. Jeon HJ, Seo KW, Lee SH, Yang YH, Kumaran RS, Kim S, … Kim HJ (2012) Production of algal biomass (*Chlorella vulgaris*) using sediment microbial fuel cells. Bioresour Technol 109:308–311. https://doi.org/10.1016/j.biortech.2011.06.039 (Access. in: 16/03/19)
30. Jiang HM, Luo SJ, Shi XS, Dai M, Guo RB (2013) A system combining microbial fuel cell with photobioreactor for continuous domestic wastewater treatment and bioelectricity generation. J Central South Univ 20(2):488–494 (Access. in: 18/03/19)
31. Jothinathan D, Mylsamy P, Bruno BL (2018) Electricigens: role and prominence in microbial fuel cell performance. In: Microbial fuel cell technology for bioelectricity. Springer, Berlin, 169–186. https://doi.org/10.1007/978-3-319-92904-0 (Access. in: 11/04/19)
32. Juang D, Yang P, Chou H, Chiu L (2011) Effects of microbial species, organic loading and substrate degradation rate on the power generation capability of microbial fuel cells. Biotech Lett 33:2147. https://doi.org/10.1007/s10529-011-0690-9 (Access. in: 25/04/19)
33. Kakarla R, Min B (2014) Photoautotrophic microalgae *Scenedesmus obliquus* attached on a cathode as oxygen producers for microbial fuel cell (MFC) operation. Int J Hydrogen Energy 39(19):10275–10283. https://doi.org/10.1016/j.ijhydene.2014.04.158 (Access. in: 13/04/19)
34. Kim BH, Kim HJ, Hyun MS, Park DH (1999) A microbial fuel cell type lactate biosensor using a metal-reducing bacterium, *Shewanella putrefaciens*. J Microbiol Biotechnol 9:365–367 (Access. in: 14/04/19)
35. Kim H, Kim B, Kim J, Yu J (2015) Effect of organic loading rates and influent sources on energy production in multi-baffled single chamber microbial fuel cell. Desalin Water Treat 56:1217–1222. https://doi.org/10.1080/19443994.2014.950986 (Access. in: 25/04/19)

36. Kondaveeti S, Choi KS, Kakarla R, Min B (2014) Microalgae *Scenedesmus obliquus* as renewable biomass feedstock for electricity generation in microbial fuel cells (MFCs). Front Environ Sci Eng 8(5):784–791 (Access. in: 13/04/19)
37. Lakaniemi AM, Tuovinen OH, Puhakka JA (2012) Production of electricity and butanol from microalgal biomass in microbial fuel cells. BioEnergy Res 5(2):481–491 (Access. in: 13/04/19)
38. Lan JCW, Raman K, Huang CM, Chang CM (2013) The impact of monochromatic blue and red LED light upon performance of photo microbial fuel cells (PMFCs) using *Chlamydomonas reinhardtii transformation* F5 as biocatalyst. Biochem Eng J 78:39–43. https://doi.org/10.1016/j.bej.2013.02.007 (Access. in: 13/04/19)
39. Lee DJ, Chang JS, Lai JY (2015) Microalgae-microbial fuel cell: a mini review. Bioresour Technol 198:891–895. https://doi.org/10.1016/j.biortech.2015.09.061 (Access. in: 27/03/19)
40. Li M, Zhou M, Luo J, Tan C, Tian X, Su P, Gu T (2019) Carbon dioxide sequestration accompanied by bioenergy generation using a bubbling-type photosynthetic algae microbial fuel cell. Biores Technol 280:95–103. https://doi.org/10.1016/j.biortech.2019.02.038 (Access. in: 25/04/19)
41. Li M, Zhou M, Tian X, Tan C, McDaniel CT, Hassett DJ, Gu T (2018) Microbial fuel cell (MFC) power performance improvement through enhanced microbial electrogenicity. Biotechnol Adv. https://doi.org/10.1016/j.biotechadv.2018.04.010 (Access. in: 13/04/19)
42. Li WW, Yu HQ, He Z (2014) Towards sustainable wastewater treatment by using microbial fuel cells-centered technologies. Energy Environ Sci 7:911–924. https://doi.org/10.1039/c3ee43106a (Access. in: 30/04/19)
43. Majumdar P, Pant D, Patra S (2017) Integrated photobioelectrochemical systems: a paradigm shift in artificial photosynthesis. Trends Biotechnol 35(4):285–287. https://doi.org/10.1016/j.tibtech.2017.01.004 (Access. in: 14/04/19)
44. Maroneze MM, Queiroz MI (2018) Microalgal production systems with highlights of bioenergy production. In: Energy from microalgae. Springer, Cham, pp 5–34 (Access. in: 30/04/19)
45. Maroneze MM, Siqueira SF, Vendruscolo RG, Wagner R, de Menezes CR, Zepka LQ, Jacob-Lopes E (2016) The role of photoperiods on photobioreactors—a potential strategy to reduce costs. Biores Technol 219:493–499. https://doi.org/10.1016/j.biortech.2016.08.003 (Access. in: 03/05/19)
46. Modestra AJ, Navaneeth B, Venkata Mohan S (2015) Bio-electrocatalytic reduction of CO_2: enrichment of homoacetogens and pH optimization towards enhancement of carboxylic acids biosynthesis. J CO_2 Util 10:78–87. https://doi.org/10.1016/j.jouou.2015.04.001 (Access. in: 25/04/19)
47. Nancharaiah YV, Mohan SV, Lens PNL (2016) Recent advances in nutrient removal and recovery in biological and bioelectrochemical systems. Biores Technol 215:173–185. https://doi.org/10.1016/j.biortech.2016.03.129 (Access. in: 12/04/19)
48. Neto SA, Reginatto V, De Andrade AR (2018) Microbial fuel cells and wastewater treatment. In: Electrochemical water and wastewater treatment, pp 305–331. https://doi.org/10.1016/b978-0-12-813160-2.00012-2 (Access. in: 13/04/19)
49. Nguyen HTN, Kakarla R, Min B (2017) Algae cathode microbial fuel cells for electricity generation and nutrient removal from landfill leachate wastewater. Int J Hydrogen Energy 42:29433–29442. https://doi.org/10.1016/j.ijhydene.2017.10.011 (Access. in: 29/03/2019)
50. Niessen J, Schroder U, Scholz F (2004) Exploiting complex carbohydrates for microbial electricity generation—a bacterial fuel cell operating on starch. Electrochem Commun, 955–958. https://doi.org/10.1016/j.jouou.2015.04.001 (Access. in: 25/04/19)
51. Nishio K, Hashimoto K, Watanabe K (2013) Light/electricity conversion by defined cocultures of *Chlamydomonas* and *Geobacter*. J Biosci Bioeng 115(4):412–417. https://doi.org/10.1016/j.jbiosc.2012.10.015 (Access. in: 13/04/19)
52. Paidar M, Fateev V, Bouzek K (2016) Membrane electrolysis—history, current status and perspective. Electrochim Acta 209:737–756. https://doi.org/10.1016/j.electacta.2016.05.209 (Access. in: 25/04/19)
53. Pant D, Singh A, Bogaert GV, Gallego YA, Diels L, Vanbroekhoven K (2011) An introduction to the life cycle assessment (LCA) of bioelectrochemical systems (BES) for sustainable energy

and product generation: relevance and key aspects. Renew Sustain Energy Rev 15:1305–1313. https://doi.org/10.1016/j.rser.2010.10.005 (Access. in: 12/04/19)
54. Pant P, Van Bogaert G, Diels L, Vanbroekhoven K (2010) A review of the substrates used in microbial fuel cells (MFCs) for sustainable energy production. Biores Technol 101(6):1533–1543. https://doi.org/10.1016/j.biortech.2009.10.017 (Access. in: 14/04/19)
55. Parkash A (2016) Microbial fuel cells: a source of bioenergy. J Microb Biochem Technol 8(3):247–255. https://doi.org/10.4172/1948-5948.1000293 (Access. in: 16/04/19)
56. Peng X, Pan X, Wang X, Li D, Huang P, Qiu G, … Chu X (2018) Accelerated removal of high concentration p-chloronitrobenzene using bioelectrocatalysis process and its microbial communities analysis. Bioresour Technol 249:844–850. https://doi.org/10.1016/j.biortech.2017.10.068 (Access. in: 12/04/19)
57. Penteado ED, Fernandez-Marchante CM, Zaiat M, Gonzalez ER, Rodrigo MA (2018) Optimization of the performance of a microbial fuel cell using the ratio electrode-surface area/anode-compartment volume. Braz J Chem Eng 35(1):141–146. https://doi.org/10.1590/0104-6632.20180351s20160411(Access. in: 25/04/19)
58. Philips J, Verbeeck K, Rabaey K, Arends JBA (2016) Electron transfer mechanisms in biofilms. In: Microbial electrochemical and fuel cells: fundamentals and applications. Woodhead Publishing, 67–114. https://doi.org/10.1016/b978-1-78242-375-1.00001-0 (Access. in: 14/04/19)
59. Potter MC (1911) Electrical effects accompanying the decomposition of organic compounds. Proc R Soc London. Ser B Contain Pap Biol Character 84(571):260–276. https://doi.org/10.1098/rspb.1911.0073 (Access. in: 14/03/19)
60. Powell EE, Evitts RW, Hill GA, Bolster JC (2011) A microbial fuel cell with a photosynthetic microalgae cathodic half cell coupled to a yeast anodic half cell. Energy Sour Part A Recover Util Environ Effects 33(5):440–448. https://doi.org/10.1080/15567030903096931 (Access. in: 16/04/19)
61. Puig S, Serra M, Coma M, Cabré M, Balaguer MD, Colprim J (2010) Effect of pH on nutrient dynamics and electricity production using microbial fuel cells. Biores Technol 101(24):9594–9599. https://doi.org/10.1016/j.biortech.2010.07.082 (Access. in: 23/03/19)
62. Rachinski S, Carubelli A, Mangoni AP, Mangrich AS (2010) Microbial fuel cells used in the production of electricity from organic waste: a perspective of future. Química Nova 33(8). https://doi.org/10.1590/s0100-40422010000800026 (Access. in: 13/04/19)
63. Rahimnejad M, Adhami A, Darvari S, Zirepour A, Oh SE (2015) Microbial fuel cell as new technology for bioelectricity generation: a review. Alex Eng J 54(3):745–756. https://doi.org/10.1016/j.aej.2015.03.031 (Access. in: 16/04/19)
64. Raschitor A, Soreanu G, Fernandez Marchante CM, Lobato J, Canizares P, Cretescu I, Rodrigo MA (2015) Bioelectro-Claus processes using MFC technology: influence of co-substrate. Biores Technol 189:94–98. https://doi.org/10.1016/j.biortech.2015.03.115 (Access. in: 29/03/19)
65. Rashid N, Cui YF, Rehman MSU, Han JI (2013) Enhanced electricity generation by using algae biomass and activated sludge in microbial fuel cell. Sci Total Environ 456:91–94. https://doi.org/10.1016/j.scitotenv.2013.03.067 (Access. in: 20/03/19)
66. Rathinavel L, Jothinathan D, Sivasankar V, Agastian P, Mylsamy P (2018) Algal microbial fuel cells—nature's perpetual energy resource. In: Microbial fuel cell technology for bioelectricity. Springer, Berlin, pp. 81–116. https://doi.org/10.1007/978-3-319-92904-0_5 (Access. in: 16/03/19)
67. Reddy CN, Kakarla R, Min B (2019) Algal biocathodes. In: Microbial electrochemical technology. Elsevier, pp 525–547. https://doi.org/10.1016/b978-0-444-64052-9.00021-2 (Access. in: 13/03/19)
68. Ren H, Lee HS, Chae J (2012) Miniaturizing microbial fuel cells for potential portable power sources: promises and challenges. Microfluid Nanofluid 13(3):353–381 (Access. in: 22/03/19)
69. Saba B, Christy AD, Yu Z, Co AC (2017) Sustainable power generation from bacterio-algal microbial fuel cells (MFCs): an overview. Renew Sustain Energy Rev 73:75–84. https://doi.org/10.1016/j.rser.2017.01.115 (Access. in: 13/03/19)

70. Santoro C, Arbizzani C, Erable B, Ieropoulos I (2017) Microbial fuel cells: from fundamentals to applications. A review. J Power Sour 356:225–244. https://doi.org/10.1016/j.jpowsour.2017.03.109 (Access. in: 18/04/19)
71. Saratale RG, Kuppam C, Mudhoo A, Saratale GD, Periyasamy S, Zhen G, … Kumar G (2017) Bioelectrochemical systems using microalgae—a concise research update. Chemosphere 177:35–43. https://doi.org/10.1016/j.chemosphere.2017.02.132 (Access. in: 13/03/19)
72. Scott K (2016) An introduction to microbial fuel cells. In: Microbial electrochemical and fuel cells: fundamentals and applications, 3–28. Woodhead Publishing. https://doi.org/10.1016/b978-1-78242-375-1.00001-0 (Access. in: 13/03/19)
73. Scott K, Yu EH (eds) (2015) Microbial electrochemical and fuel cells: fundamentals and applications. Woodhead Publishing (Access. in: 13/03/19)
74. Sharma Y, Li BK (2010) The variation of power generation with organic substrates in single-chamber microbial fuel cells (SCMFCs). Bioresour Technol, 101–1844. https://doi.org/10.1021/es0491026 (Access. in: 25/04/19)
75. Shukla M, Kumar S (2018) Algal growth in photosynthetic algal microbial fuel cell and its subsequent utilization for biofuels. Renew Sustain Energy Rev 82:402–414. https://doi.org/10.1016/j.rser.2017.09.067 (Access. in: 13/03/19)
76. Sillanpää M, Shestakova M (2017) Electrochemical water treatment methods: fundamentals, methods and full scale applications. Butterworth-Heinemann. https://doi.org/10.1016/b978-0-12-811462-9.00003-7 (Access. in: 13/04/19)
77. Sivakumar P, Ilango K, Praveena N, Sircar A, Balasubramanian R, Sakthisaravanan A, Kannan R (2018) Algal fuel cell. In: Microalgal biotechnology. IntechOpen. https://doi.org/10.5772/intechopen.74285 (Access. in: 13/03/19)
78. Sivasankar V, Mylsamy P, Omine K (eds) (2018) Microbial fuel cell technology for bioelectricity. Springer, Berlin. https://doi.org/10.1007/978-3-319-92904-0 (Access. in: 21/03/19)
79. Slate AJ, Whitehead KA, Brownson DA, Banks CE (2019) Microbial fuel cells: an overview of current technology. Renew Sustain Energy Rev 101:60–81. https://doi.org/10.1016/j.rser.2018.09.044 (Access. in: 18/04/19)
80. Tang D, Han W, Li P, Miao X, Zhong J (2011) CO_2 biofixation and fatty acid composition of *Scenedesmus obliquus* and *Chlorella pyrenoidosa* in response to different CO_2 levels. Biores Technol 102(3):3071–3076. https://doi.org/10.1016/j.biortech.2010.10.047 (Access. in: 25/04/19)
81. Trapero JR, Horcajada L, Linares JJ, Lobato J (2017) Is microbial fuel cell technology ready? An economic answer towards industrial commercialization. Appl Energy 185(1):698–707. https://doi.org/10.1016/j.apenergy.2016.10.109 (Access. in: 16/04/19)
82. U.S. Energy Information Administration (2019) Levelized cost and levelized avoided cost of new generation resources in the annual energy outlook 2019. Annual Energy Outlook. Available in: https://www.eia.gov/outlooks/aeo/pdf/electricity_generation.pdf (Access. in: 29/04/19)
83. Ummalyma SB, Sahoo D, Pandey A, Prajeesh KV (2019) Microalgae-microbial fuel cell. Microb Fuel Cells Mater Appl 46:1–20. https://doi.org/10.21741/9781644900116-1 (Access. in: 17/04/19)
84. Venkata Mohan S (2014) Sustainable waste remediation: a paradigm shift towards environmental biorefinery. Chem Eng World 49(12):29–35. https://doi.org/10.1007/978-81-322-2598-0 (Access. in: 15/04/19)
85. Venkata Mohan S, Butti SK, Amulya K Dahiya S, Modestra JA (2016) Waste biorefinery: a new paradigm for a sustainable bioelectro economy. Trends Biotechnol 34(11):852–855)
86. Verma R, Srivastava A (2018) Carbon dioxide sequestration and its enhanced utilization by photoautotroph microalgae. Environ Dev. https://doi.org/10.1016/j.envdev.2018.07.004 (Access. in: 25/04/19)
87. Vidyashankar S, Ravishankar GA (2016) Algae-based bioremediation: bioproducts and biofuels for biobusiness. In: Bioremediation and bioeconomy. Elsevier, 2457–493. https://doi.org/10.1016/b978-0-12-802830-8.00019-8 (Access. in: 14/04/19)
88. Wang DB, Song TS, Guo T, Zeng Q, Xie J (2014) Electricity generation from sediment microbial fuel cells with algae-assisted cathodes. Int J Hydrogen Energy 39(25):13224–13230. https://doi.org/10.1016/j.ijhydene.2014.06.141 (Access. in: 13/04/19)

89. Wang ZJ, Deng H, Chen LH, Xiao Y, Zhao F (2013) In situ measurements of dissolved oxygen, pH and redox potential of biocathode microenvironments using microelectrodes. Biores Technol 90:132–387. https://doi.org/10.1016/j.biortech.2012.11.026)
90. Wei L, Han H, Shen J (2013) Effects of temperature and ferrous sulfate concentrations on the performance of microbial fuel cell. Int J Hydrogen Energy 38(25):11110–11116. https://doi.org/10.1016/j.ijhydene.2013.01.019 (Access. in: 25/03/19)
91. Wu XY, Song TS, Zhu XJ, Wei P, Zhou CC (2013) Construction and operation of microbial fuel cell with *Chlorella vulgaris* biocathode for electricity generation. Appl Biochem Biotechnol 171(8):2082–2092 (Access. in: 19/03/19)
92. Wu YC, Wang ZJ, Zheng Y, Xiao Y, Yang ZH, Zhao F (2014) Light intensity affects the performance of photo microbial fuel cells with *Desmodesmus* sp. A8 as cathodic microorganism. Appl Energy 116:86–90. https://doi.org/10.1016/j.apenergy.2013.11.066 (Access. in: 13/04/19)
93. Xiao L, He Z (2014) Applications and perspectives of phototrophic microorganisms for electricity generation from organic compounds in microbial fuel cells. Renew Sustain Energy Rev 37:550–559. https://doi.org/10.1016/j.rser.2014.05.066 (Access. in: 16/04/19)
94. Xu C, Poon K, Choi MM, Wang R (2015) Using live algae at the anode of a microbial fuel cell to generate electricity. Environ Sci Pollut Res 22(20):15621–15635 (Access. in: 20/03/19)
95. Yan J, Zhu L, Chaloux BL, Hickner MA (2017) Anion exchange membranes by bromination of tetramethylbiphenol-based poly (sulfone) s. Polymer Chemistry 8(16):2442–2449. https://doi.org/10.1039/C7PY00026J (Access. in: 22/03/19)
96. Yang Z, Pei H, Hou Q, Jiang L, Zhang L, Nie C (2018) Algal biofilm-assisted microbial fuel cell to enhance domestic wastewater treatment: nutrient, organics removal and bioenergy production. Chem Eng J 332:277–285. https://doi.org/10.1016/j.cej.2017.09.096 (Access. in: 15/03/19)
97. Yu J, Seon J, Park Y, Cho S, Lee T (2012) Electricity generation and microbial community in a submerged exchangeable microbial fuel cell system for low-strength domestic wastewater treatment. Biores Technol 117:172–179. https://doi.org/10.1016/j.biortech.2012.04.078 (Access. in: 24/04/19)
98. Zhang ER, Liu L, Cui YY (2013) Effect of pH on the performance of the anode in microbial fuel cells. In: Advanced materials research, vol. 608. Trans Tech Publications, pp. 884–888. doi:10.4028/www.scientific.net/AMR.608-609.884 (Access. in: 23/03/19)
99. Zhang Y, Sun J, Hu Y, Wang Z, Li S (2014) Effects of periodically alternating temperatures on performance of single-chamber microbial fuel cells. Int J Hydrogen Energy 39(15):8048–8054. https://doi.org/10.1016/j.ijhydene.2014.03.110 (Access. in: 25/03/19)

Current Trends in Electrodeposition of Electrocatalytic Coatings

V. S. Protsenko and F. I. Danilov

Abstract Among different methods of fabrication of electrocatalytic coatings, the electrodeposition seems to be the most convenient and widely used. The electrodeposition is an available, inexpensive, versatile, simple and fast technique which allows synthesizing materials with controlled composition, structure, surface morphology and electrocatalytic activity. This review reports recent trends, promising directions and novel approaches concerning cathodic electrodeposition and characterization of electrocatalytic coatings. A special attention is paid to the electrocatalysts based on electrodeposited nickel, iron, cobalt, copper, chromium, noble metals, their alloys and composites. The application of non-stationary current regimes (pulse current and linear potential sweep) as well as new type of plating baths (room-temperature ionic liquids and deep eutectic solvents) is highlighted. The influence of alloying and after-treatment (dealloying, selective anodic dissolution, etc.) on the electrocatalytic properties of electrodeposits is considered. Favorable influence of the formation of nanostructures upon the electrocatalytic performance of electrodeposited materials is shown. Potential ways for improving the electrocatalytic characteristics of electrodeposited coatings are described.

Keywords Electrocatalysis · Electrodeposition · Coatings · Nickel · Iron · Copper · Chromium · Noble metals · Alloy · Composite · Nanostructured materials

1 Introduction

Electrocatalytic coatings as electrode materials for various electrochemical processes can be fabricated by means of different physicochemical methods, electrodeposition being one of the most convenient and widely used in practice [1–3]. The electrodeposition is an available, inexpensive, versatile, simple and fast technique which allows producing materials with controlled composition, structure, surface morphology and

V. S. Protsenko (✉) · F. I. Danilov
Ukrainian State University of Chemical Technology, Gagarin Ave., 8,
Dnipro 49005, Ukraine
e-mail: Vprotsenko7@gmail.com

Inamuddin et al. (eds.), *Methods for Electrocatalysis*,
https://doi.org/10.1007/978-3-030-27161-9_11

electrocatalytic activity and ensuring a high adhesion to the substrate. All these characteristics can be flexibly adjusted by fitting of plating electrolyte chemistry and electrolysis conditions [1, 2]. Electrodeposition also provides easily restoring worn layers.

Different physicochemical processes can occur in the course of the electrodeposition of a catalytic film. They include both electroreduction of metal ions generating metal or alloy coatings and electrooxidation yielding oxides (hydroxides, salts) layers. In addition, micro- and nano-sized dispersed particles can be incorporated into a growing matrix from suspension or colloidal electrolyte forming a composite coating. Also, electrodeposition technique can be used to prepare polymer films, various semiconductors, etc.

Thus a wide spectrum of electrocatalytic coatings can be obtained by electrodeposition method, including metal and alloys, oxides, composites, nanoparticles, nanorods, nanowires, nanoclusters, etc. Such materials can be electrodeposited both on the cathode and on the anode using aqueous solutions, non-aqueous solvents, ionic melts and ionic liquids. It should be noted that electrocatalytic oxide/hydroxide layers formed via cathodic and anodic deposition were earlier characterized in a number of review and original papers [3–9]; these coatings will not be considered in the present work. Also, polymer and semiconductor films are not described here.

The goal of this chapter is to survey the most important works on the problem of the electrodeposition of electrocatalytic coatings, the synthesis of which involves cathode electroreduction with the formation of metal-containing layers. Therefore, we confine our mini-review to the processes of cathodic electrochemical synthesis of electrocatalytic coatings consisting of metals, alloys and metal-based composites. A special attention is paid to some new trends described in papers published in the past few years.

2 Nickel and Nickel-Based Alloys

Electrodeposited nickel and nickel-based alloys can be considered as the most significant and widespread electrocatalysts [10–13]. A great attention to Ni and Ni-based alloys is due to their high chemical stability and corrosion resistance, especially in an alkaline medium, and a high electrocatalytic activity towards both cathodic and anodic electrochemical reactions [14]. The introduction of various alloying components into the Ni matrix allows flexible controlling the electrocatalytic properties of electrodeposits.

Binary alloys of Ni with some transition metals were electrodeposited on mild steel and tested as cathodes for the hydrogen production in a water alkaline electrolyte [11, 12]. It was concluded that their electrocatalytic activity changes in the following sequence: Ni–Mo > Ni–Zn > Ni–Co > Ni–W > Ni–Fe > Ni–Cr > Ni electroplated steel. The activation energy of the hydrogen evolution reaction on alloy deposits was stated to be very low as compared with that of pure nickel. The authors concluded that the nickel–molybdenum alloy, deposited from an alkaline citrate bath on a steel

substrate, is an effective and promising cathodic material to perform alkaline water electrolysis [11]. It should be observed that pure molybdenum cannot be deposited from water solutions, thus co-deposition with Ni expands the spectrum of promising electrocatalytic materials.

Not only binary but also ternary Ni-based alloys, such as Ni–Mo–Zn, Ni–Mo–Fe, Ni–Mo–Cu, Ni–Mo–W, Ni–Mo–Co and Ni–Mo–Cr, can be electroplated to further use them as electrocatalysts [13]. It was reported that the electrocatalyst activity in the hydrogen evolution reaction diminishes in the following range: Ni–Mo–Fe > Ni–Mo–Cu > Ni–Mo–Zn > Ni–Mo–Co ~ Ni–Mo–W > Ni–Mo–Cr > Ni-plated steel. It was concluded that Ni–Mo–Fe alloyed coating exhibited the highest activity and good stability towards hydrogen evolution, it demonstrated the value of an overpotential of ca. 0.187 V in 6 M KOH solution during a long-term electrolysis (>1500 h) when the temperature was 353 K and the current density was 300 mA cm^{-2}.

The electrodeposition of Ni–Co alloy under the condition of cyclic voltammetry yielded coating electrodes showing an increased catalytic activity with respect to the oxygen evolution reaction in 1 M solution of potassium hydroxide at the temperature of 20 °C [15]. Electrodeposited nickel–cobalt cathodes exhibited improved electrocatalytic ability in the oxygen evolution reaction as compared with the "pure" nickel catalysts. An increase in the content of cobalt ions in the electrolyte led to an increase in the electrocatalytic performance of the binary alloy. This may be presumably associated with the growth of the cobalt content in electrodeposited alloy, since an anomalous co-deposition is typical of Ni–Co alloy plating process (that is to say, the ratio between Ni and Co in electrodeposits does not correspond to the corresponding ratio between the concentration of these metal ions in the plating bath). It was shown that the thermal treatment of the deposited alloys electrodes at the temperature of 500 °C in vacuum results in an enhancement of electrocatalytic activity, because the heat treatment of electrodeposits eliminates the internal defects in metal structure and produces grains with higher crystallinity [15].

The electrodeposition and characterization of macroporous Ni, Co and Ni–Co films as electrocatalysts for the hydrogen evolution reaction was reported [10]. The developed coatings manifested a very high hydrogen evolution activity in 30 wt% KOH solution, this was principally associated with their relatively high surface area. The electrocatalysts with Co contents ca. 40–60 at.% yielded the highest intrinsic catalytic activities caused by the synergetic combination of Ni and Co.

Electrodeposition of nanocrystalline Ni–Co alloy on a 301 stainless steel substrate was used to prepare an electrocatalytic electrode for alcoholic fuel cell [16]. The coatings with a cobalt content of 15–35% showed high current density in anodic electrochemical oxidation of methanol solution. The longer the deposition time, the higher is the efficiency of the electrodeposited nanocrystalline Ni–Co electrodes for more methanol electrooxidation and very good oxidation of the strongly adsorbed molecules of CO on the electrode surface.

Ni–Fe alloy coatings can be easily deposited and applied as a catalyst in reactions of hydrogen and oxygen evolution [14, 17, 18]. The electrocatalytic behavior in the hydrogen production on electrodeposited Ni–Fe films was estimated in 6 M KOH solution [17]. It was observed that at a constant value of electrode potential, the

peak cathodic current of the hydrogen evolution reaction increases with increasing current density of alloy deposition. Thus, the Ni–Fe coatings obtained at 6.0 A dm^{-2} exhibited the highest activity. This phenomenon was connected with an increased surface area resulted from the change in the alloy composition: the content of Ni component in deposits was 64.9, 50.4 and 35.7 when the current density value was 2.0, 4.0 and 6.0 A dm^{-2}, respectively [17].

Similarly the hydrogen evolution reaction, the electrocatalytic activity of deposited nickel–iron alloy for the oxygen evolution reaction in 40 wt% KOH at 80 °C increases with increasing the iron content [18]. The lowest oxygen overvoltages were observed with 55 at.% Fe in the coating. These electrodes exhibited the oxygen overpotential that was 50 and 30 mV lower at anode current densities of 0.01 and 1 A cm^{-2}, respectively, as compared with "pure" nickel.

The review [19] highlighted recent achievements in the fabrication of Ni–Fe-based materials as effective electrocatalysis for the oxygen evolution reaction. It was stressed that nickel–iron alloys are well-known as high-performance catalysts for oxygen evolution since the 20th century, and there is a renewed deep interest in developing and using advanced nickel–iron-based materials with improved catalytic activity and stability. It is important that electrodeposited Ni–Fe alloy coatings ensure a satisfactory electrical contact with the substrate on which the alloy has been deposited. However, nickel-iron layers show only moderate catalytic activity and relatively low mechanical strength due to the phase transformations and changes occurring in the course of the oxygen evolution reaction catalysis.

Ni, Fe, Ni–Fe coatings with different chemical compositions were electrodeposited on a Cu substrate and evaluated as electrocatalysts towards the hydrogen production by water electrolysis using an alkaline solution [20]. The presence of nickel with iron was stated to increase the electrocatalyst activity of the coating in the reaction of hydrogen evolution if being compared with individual nickel and iron electrodeposited films. According to the results of corrosion tests, the corrosion stability of the coated electrodes was appreciably decreased after the electrolysis.

As already mentioned above, Ni–Mo electrodeposited alloy shows especially high electrocatalytic performance in the hydrogen evolution reaction as compared with Ni electrode. In a number of works, the electrodeposition and properties of such electrocatalysts were studied more particularly [21–26].

Figure 1 demonstrates the polarization curves for the hydrogen evolution reaction which were obtained using 1 M NaOH aqueous medium at the temperature of 30 °C with different values of Ni/Mo ratio in the electrolyte, pH and substrate nature [21]. Table 1 also gives the corresponding experimental conditions. As follows from Fig. 1 and Table 1, all nickel–molybdenum deposited films manifest improved electrochemical activity in the reaction of hydrogen evolution as compared with "pure" Ni. With increasing the content of Mo component in the deposited alloy, the onset electrode potential associated with the hydrogen evolution reaction shifts to more positive values indicating that the H_2 evaluation will occur at lower cathodic overpotentials. The Ni–Mo coating containing about 41 wt% of Mo exhibits the

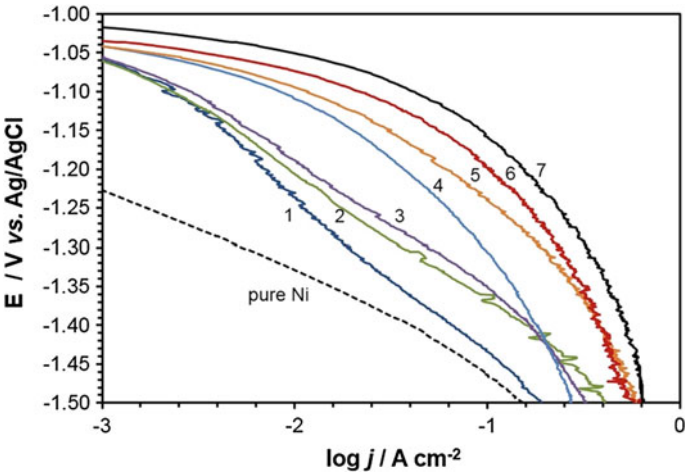

Fig. 1 The polarization curves of different Ni–Mo alloys and a pure Ni film recorded in 1 M NaOH at 30 °C. Numbering of curves is explained in Table 1. Reprinted from [21] by permission of Springer Nature

Table 1 Electrolyte compositions of Ni and Ni–Mo alloy samples and corresponding potetials for hydrogen evolution at −100 mA cm^{-2}

Substrate/sample no	Ni/Mo ratio	pH±0.05	Exposure time HER (min)	wt% Mo in alloy	−E (V)	$-E_{eq}$ (V)
Cu/1	3/2	10.5	10	9.7 ± 1.5	1.434	1.018
Cu/2	1/1	10.5	10	11.9 ± 1.9	1.367	1.011
Cu/3	2/3	10.5	10	13.8 ± 1.9	1.352	1.016
Cu/4	1/12	10.5	10	28.3 ± 2.1	1.307	1.017
Cu/5	1/12	9.5	10	40.1 ± 3.2	1.240	1.023
Cu/6	1/12	9.5	60	40.1 ± 3.2	1.200	1.021
Cu/Ni/7	1/12	9.5	60	40.1 ± 3.2	1.154	1.007
Cu/Ni		5.2	10	–	1.465	0.999

Reprinted from [21] by permission of Springer Nature

highest electrocatalytic activity in the electrochemical reaction of hydrogen evolution ($\eta_{100} = -48$ mV for the current density of 100 mA cm^{-2} and the temperature of 80 °C) [21].

It is noteworthy that Ni–Mo alloys exhibit an enhanced catalytic activity not only in the process of hydrogen evolution on the cathode but also in the oxygen evolution reaction on the anode showing a good corrosion resistance [23]. Improved electrocatalytic behavior of nickel-molybdenum coatings is attributed to the expansion of the real surface area of the electrode [22, 23, 26] and the achievement of higher exchange current density [24].

An enhancement of the electrocatalytic activity of nickel–molybdenum alloy electrodeposits relative to hydrogen evolution reaction by means of an induced magnetic field was reported [25]. The increased electrocatalytic activity of H_2 production on Ni–Mo alloy coatings, fabricated at higher limits of the applied magnetic field, was associated with the combined effect of both increased porosity and content of Ni and increased limiting current density of Ni electrodeposition.

Commonly, Ni–Mo alloy deposits are fabricated using aqueous solutions containing dissolved Ni(II) salt (mainly, $NiSO_4$ or $NiCl_2$) and sodium or ammonium molybdate (Na_2MoO_4 and $(NH_4)_2MoO_4$). An attempt was made to use new type of plating electrolytes containing urea–choline chloride–citric acid ternary mixtures to electrochemically synthesize Ni–Mo coatings with good electrocatalytic properties [26]. It should be observed that the so-called deep eutectic solvents (DES) are composed of some inorganic and (or) organic constituents which are taken in a eutectic ratio. Due to intermolecular interaction, the melting point of the obtained mixture is substantially lower than those of either individual constituent and electrolytic dissociation occurs in the liquid system [27]. DESs are thought to be a novel and highly promising kind of room-temperature ionic liquids, they can be successfully applied in various fields of science and technology. DESs are characterized by a number of impressive features, such as high solubility of salts of various metals, relatively high electroconductivity, very wide electrochemical potential window and minute vapor pressure. In addition, DESs are easy and cheap to synthesize and they are not harmful to the environment [27].

Because of these advantageous properties, deep eutectic solvents call great attention in different fields of practical applications, including electrochemistry and electroplating. Electrodeposition of metallic coatings from this novel kind of ionic liquids has been reported in quite a number of papers [28–30].

The results described in [26] showed that Ni–Mo alloyed electrodeposits prepared using the electrolytes containing choline chloride may be a challenging approach to synthesize efficient materials showing an excellent electrocatalytic activity towards the electrochemical reactions of water electrolysis.

In this connection, it should be mentioned that recent study [31] reported the electrodeposition of nanocrystalline Ni films from the electrolytes containing $NiCl_2 \cdot 6H_2O$ dissolved in deep eutectic solvents that are based on the mixtures of choline chloride with ethylene glycol or urea. The fabricated nanocrystalline nickel layers were estimated as an electrocatalyst in the hydrogen evolution reaction occurring in a basic water solution. An increased electrocatalytic properties was stated which was explained by both the enhanced surface area available to an electrochemical process and the production of needles surface morphology. The obtained data revealed that the electrochemical deposition from DES-based systems provides a successful method to synthesize nanostructured electrodeposited Ni electrocatalysts for the hydrogen evolution reaction, although the authors noted that the catalytic durability and stability of the obtained Ni layers remain to be further improved [31].

An interest in the study of ternary electrodeposited Ni-based alloys with improved electrocatalytic properties is motivated by the anticipation of benefits from synergistic interaction between different components of an alloy, although it is necessary to take

into account the significant complication of the electroplating process. Thus, Xia et al. [32] described ternary Ni–Mo–Cu alloy electrodeposits. The coatings were characterized as possible electrocatalysts towards the hydrogen evolution reaction in the process of water electrolysis. An appreciable increase in the hydrogen evolution activity an alkaline solution was observed when copper was introduced into nickel–molybdenum coating. The electrodeposited Ni–Mo–Cu coatings showed higher rate of electrochemical process, lower energy of activation and higher stability than those typical of Ni–Mo films. The improved electrocatalytic performance of the Ni–Mo–Cu coating electrode in the course of hydrogen evolution was associated with synergistic effects of the developed surface area and the interaction between the individual components of the alloy.

Allam et al. [33] investigated the effect of the alloy formation with the transition metals having hypo-hyper-d-electronic structure on the electrocatalytic behavior. It was emphasized that the alloying of metals that have empty or half-filled vacant d-orbitals (i.e. the elements (transition metals) located in the left half of the Periodic Table) with those metals that have paired d electrons (i.e. the elements situated in the right half of the series) causes a remarkable increase in the electronic density of states. As a result, a clear synergetic effect is observed in their electrocatalytic behavior towards the hydrogen evolution reaction. It was stated that alloying of nickel ([Ar] 3d8 4s2) with molybdenum ([Kr] 4d5 5s1) or/and tungsten ([Xe] 4f145d4 6s2) ensures fulfilling these requirements. This consideration allows explaining a high electrocatalytic activity typical of Ni–Mo alloys. Hopefully, the electrochemical deposition of ternary Ni–Mo–W coating may additionally improve the electrocatalytic properties. Indeed, electrochemically synthesized ternary Ni–Mo–W alloy films showed appreciably greater exchange current densities towards hydrogen evolution when tested as electrocatalysts in a medium of 30 wt% KOH than individual binary alloys Ni–Mo and Ni–W [33].

The electrodeposition process of ternary Ni–Co–Zn alloy yielding a high-performance cathode material for the hydrogen evolution process was developed [34, 35]. The main idea of the co-deposition of zinc with Ni-based alloys is to leach Zn component in an alkaline solution after electrodeposition. As a result of leaching Zn, the porous structure is formed providing a very high surface area (resembling Raney electrodes type). The long-term test indicated that the electrocatalytic activity of Ni–Co–Zn electrode in the reaction of H_2 evolution was somewhat increased with electrolysis duration, which was associated with the fact that any existing corrosion products were removed and some cracks appeared in the course of hydrogen gas evolution [34].

Electrochemical dealloying of Ni–Cu electrodeposited alloy was performed to fabricate an efficient elecrtocatalyst for the electrochemical reaction of hydrogen evolution [36]. The dealloying was conducted by means of linear sweep voltammetry method using a 1 M sodium sulfate solution to selectively remove Cu component. The activity of deposited Ni–Cu samples towards hydrogen evolution was determined before and after selective removal of the copper constituent. The treated films were more electroactive when low overpotentials were applied, but less active in the range of high overpotentials. A decrease in the activity at higher overpotentials

was connected with the trapping of H_2 gas bubbles which evidently diminishes the real surface area available to the electrochemical process. Generally, the dealloying procedure (chemical and electrochemical) seems to be an efficient way to produce high-performance electrocatalysts.

The electrocatalytic efficiency of nickel can be improved by co-deposition not only with metals but also with some nonmetals. For instance, the electrodeposition of amorphous Ni–P alloy was reported to produce cathodes for hydrogen production in water electrolysis [37]. The electrodeposited nickel–phosphorus layers contained about 6–7 wt% of phosphorous. They demonstrated an enhanced electrocatalytic activity relative to the hydrogen evolution in 1 M sodium hydroxide solution, the electrochemical performance being correlated with the double layer capacitance of the electrode and therefore with the effective active sites. The fabricated electrodes with the highest catalytic activities also showed the smallest charge transfer resistance.

3 Iron, Cobalt and Their Alloys

Metallic iron and ferrous salts are relatively inexpensive, easily accessible and environmentally acceptable. Iron films can be easily obtained from common aqueous plating baths with a high deposition rate [38]. Iron and iron-based electrodeposits can be used both as anodes and cathodes in water electrolysis [39]. Nevertheless, pure iron coatings show low electrocatalytic activity compared with Ni, Co and noble metals; in addition, the corrosion stability of iron in not sufficiently enough. Therefore, the co-deposition of iron with other metals and non-metals is usually used to fabricate electrocatalytic coatings with an enhanced corrosion resistance. For instance, the introduction of Co into Fe deposits provides an enhanced activity relative to the reaction of hydrogen evolution in a 28% aqueous KOH solution [39].

Fe–Mo alloy electrodes containing 34–59 at.% Mo were synthesized by electroplating technique at constant values of current density using a pyrophosphate bath [40]. It was stated that an increase in the molybdenum content in the coatings led to the formation of more active electrodes, an increase in the actual surface area of the electrode was simultaneously observed. The key factor affecting the electrochemical performance was stated to be the real surface area of the electrocatalytic coatings.

Sequeira et al. [41] reported electroplating baths which allow depositing Fe–P, Fe–P–Ce and Fe–P–Pt films. These Fe-based coatings were tested as catalysts in the hydrogen production during alkaline water electrolysis. An improved electrocatalytic behavior in the reaction of hydrogen evolution was attributed to an increased effective surface area, the proper contribution of the platinum component, and the catalytic synergism with iron induced by the cerium co-deposition (in the case of Fe–P–Ce alloy). Medium-term tests confirmed a high corrosion stability of the investigated electrodeposited materials which reliably maintained their high electrocatalytic activity.

Nanocrystalline Fe–W alloys were electrochemically synthesized from a citrate-ammonia electrolyte, the content of wolfram in them being 20–30 at.% [42]. The prepared coatings exhibited good electrocatalytic properties relative to the process of ethanol oxidation when using an alkaline water solution and therefore they can be potentially acceptable as electrodes to directly oxidize ethanol in low-temperature fuel cells.

Cobalt deposits are considered as an appropriate catalytic material for the oxygen evolution reaction [43]. It is noteworthy that the presence of iron in cobalt electrodeposits (i.e. Co–Fe alloys) results in lower electrocatalytic activity in the reaction of O_2 evolution as compared with "pure" Co [44].

A very interesting approach toward producing electrodeposited electrocatalytic coatings was developed in works [45, 46]. Two activators, cobalt and chromium, were used to improve the efficiency of alkaline electrolytic production of hydrogen by the addition of ionic activators into the electrolyte. A thin Co and Cr-containing layer is formed in situ on the surface of nickel substrate directly during the hydrogen evolution. The obtained deposits have a rather uniform distribution of the pores and highly developed surface area. Possible mechanism through which ionic activators increases electrolytic efficiency was associated with a synergetic effect of two metals (Co and Cr) on the electrode surface, providing simultaneously a very large surface area and active centers [45]. A further study [46] showed that high electrocatalytic activity of Co–Cr catalyst obtained by in situ electrodeposition was ensured not only by the growth of the actual surface area of the electrodes, but also by the implementation of a "true" catalytic action. Thus, such electrodeposits exhibit promising characteristics as feasible cathode materials for the reaction of hydrogen production.

The properties of Co, Co–Zn and Co–Zn–Pt electrodeposits have been considered in the light of their eventual applications as cathode materials in the electrochemical hydrogen production [47]. The deposition was performed on a graphite electrode using a sulfate–chloride acid plating bath. Then the Co–Zn electrode was treated with a concentrated alkaline solution to achieve the partial leaching of the Zn and produce a highly porous electrode. This treatment promotes formation of a porous electrode with a high surface area. In some cases, the porous surface of electrode was modified via the electrodeposition of a small amount of platinum (using electroplating bath containing K_2PtCl_6 and KCl). It was determined that graphite electrodes, on which cobalt was coated, exhibited an increased catalytic activity relative to the hydrogen evolution reaction in an alkaline solution as compared with the uncoated surface of graphite electrode. The leaching in an alkaline solution appreciably increased the activity towards the hydrogen evolution. The modification of Co–Zn electrode surface with electrodeposited platinum ensured the highest electrocatalytic activity, the surface chemical composition of the leached and modified alloy being as follows: 95.8% Co, 2.3% Zn and 1.88% Pt.

Citrate-containing aqueous electrolytes were used to electrodeposit binary Co–W alloys [48]. The alloy films were prepared with various content of tungsten and microstructure ranged from nanocrystalline (3 and 18 at.% of tungsten) to amorphous (30 at.% of tungsten). These coatings were characterized as promising anodes in the electrooxidation methanol using the electrolyte containing 1 M CH_3OH and 0.1 M

H_2SO_4. The Co–W coatings (30 at.% of W) exhibited a high electrocatalytic activity towards methanol oxidation, whereas as-deposited Co–W (3 and 18 at.% of W) coatings proved to be entirely inactive towards the oxidation of methanol and only the electrodissolution of alloys occurred in the applied media. Moreover, this alloy was even more effective in the reaction of methanol electrooxidation than pure Pt. The Co–W deposit annealed at 600 °C showed a relatively low activity in the methanol electroxidation as compared with the untreated films.

Co–Mo alloys with nanocrystalline/amorphous structures were prepared via electrodeposition method using a tartrate bath [49]. It was shown that the alloying of cobalt with molybdenum allows increasing the catalytic performance of the obtained electrodeposits in the reaction of hydrazine electrooxidation when compared to "pure" cobalt coatings. It is important that Co–Mo electrode exhibited very good resistance against electrode poisoning by hydrazine oxidation intermediates/products.

4 Copper and Copper-Based Alloys

A number of papers reported the electrodeposition of Cu–Ni alloys as catalysts for alkaline water electrolysis [51–53]. The prepared cathodes showed remarkably high catalytic activity for the reaction of hydrogen production both in an alkaline solution [50, 51] and in an acid one [52]. The activity of electrodeposited Cu–Ni alloy strongly depends on the content of copper, thus the Cu–Ni films with ~50–86% Cu content give great current densities at lower overpotential [52]. As can be seen from Fig. 2, the lowest hydrogen overpotential is detected for the Cu–Ni layers with a ~50% Cu content. Such a behavior was attributed to the effects of the synergetic interaction of nickel and copper [52]. Similar conclusions were drawn in [51], according to those the enhancement of electrocatalytic activity of the alloys with an appropriate quantity of copper (ca. 50%) can be associated with a number of factors including the changes in hydrogen binding energy as well as valence state of the electrode surface connected with the appearance and removal of H_2 bubbles.

Cu–Ni–Zn ternary alloys were electrodeposited on a Cu substrate and treated in a concentrated alkaline medium (30% NaOH) in order to obtain a highly porous and active surface which would be appropriate for the application in the hydrogen production by water electrolysis [53]. The alloy surface before leaching contained 3.8% Ni, 66.9% Cu and 29.3% Zn, whereas the surface composition was changed to 4.7% Ni, 83.0 Cu and 12.2% Zn after the treatment in an alkaline solution. Thus the zinc content was considerably diminished after selective dissolution, which ensured the appearance of cracks pores and produced a highly porous electrocatalytic surface. The electrocatalytic behavior of the Cu–Ni– and Zn layers towards the reaction of hydrogen evolution in a 1 M KOH solution was increased as a result of the treatment in an alkaline medium. The long-term test performed at the cathode current density of 0.1 A cm^{-2} showed good electrochemical stability over 120 h [53].

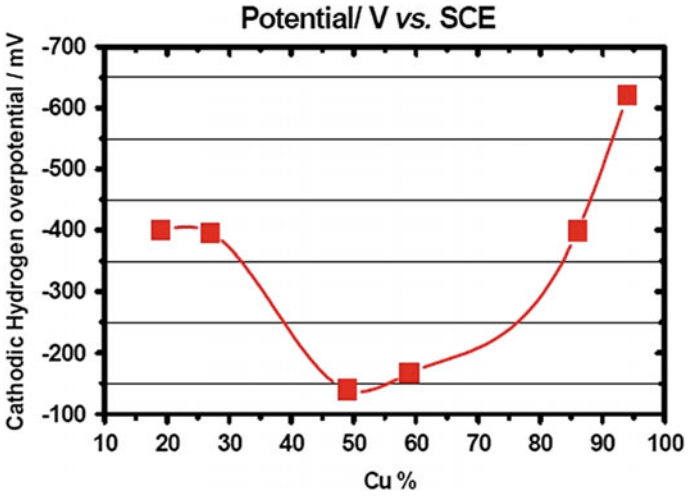

Fig. 2 Variation of the cathodic hydrogen overpotential with the atomic percent of Cu in the electrodeposited alloys in stagnant naturally aerated 0.5 M H_2SO_4 solutions at 25 °C and the current density of 30.0 mA cm^{-2}. Reprinted from [52] by permission of RSC Publishing

Milhano and Pletcher reported the electrodeposition of Cu–Pd alloys with a wide range of compositions using a simple acidic electrolyte [54]. It was determined that copper in the alloy is stabilized to anodic dissolution by the presence of palladium while the presence of copper in the alloy reduces the ability of palladium to absorb hydrogen. The Cu–Pd electrodeposited alloys in an alkaline medium are appreciably better catalysts for nitrate reduction than either palladium or copper. Nitrate reduction cannot be observed on smooth palladium and the reduction on copper occurs at a potential 250 mV more negative. It was stated that a relatively small addition of Pd to Co is sufficient to obtain the potential shift.

The electrodeposited Cu–Bi cathode was suggested as a new type of electrode in the field of electrocatalytic denitrification [55]. The alloys with the copper content of 5–15 wt% were deposited from an aqueous pyrophosphate bath and then tested in the reaction of the reduction of nitrate ions.

Pulse electrodeposition method was used to fabricate Cu electrode with an improved activity and selectivity for CH_4 in the electrochemical reduction of CO_2 [56]. The Cu electrodes demonstrated a very high faradaic efficiency: 79% and 85% at −2.5 V and −2.8 V, respectively. It is interesting that the value of current density of ca. 38 mA cm^{-2} for the reaction of methane electroreduction was observed in this work, which is the highest quantity ever achieved in this reaction at ambient pressure and room temperature. An increased electrocatalytic activity in the reaction of CO_2 electroreduction was explained by the more roughened surface morphology ensuring a large number of active sites. Clearly expressed electrocatalytic selectivity towards the electroreduction of carbon dioxide to methane was associated with the increased surface roughness of the electrodeposited copper surface showing a great amount of

stepped facets. Thus, pulse electrodeposition technique allows significantly influencing the surface morphology and hence the electrocatalytic performance and product Cu electrocatalytic coatings which would be highly selective relative to the CO_2 electrochemical reduction [56].

5 Noble Metals and Their Alloys

Electrodeposited noble metals and their alloys are extremely widely used as electrocatalysts for different electrochemical processes. It is well-known that the electrocatalytic activity of metals toward the H_2 evolution during water electrolysis is simultaneously determined by the kinetics of hydrogen adsorption/desorption processes, which can be characterized by the hydrogen binding energy on the electrode that is different for each electrocatalyst. So, the interrelation between exchange current density and hydrogen binding energy demonstrates a volcano behavior [57]. This concept implies that noble metals (Pt, Pd, Ir, etc.) show the highest activity which explains a steady interest to these electrocatalysts. A major and obvious disadvantage of noble metals is their high cost. Therefore, efforts are being made to reduce the loading of noble metals, increase surface area and provide high electrocatalytic activity.

One of the current challenges consists in fabrication and characterization of nanostructured electrocatalysts based on noble metals. Thus the papers dealing with electrochemical synthesis and properties of Au nanomaterials have been reviewed in [58]. The analysis of literature data on design of these nanomaterials allowed establishing three main directions. The first concerns the design of monodisperse Au nanoparticles showing rich high-index facets. The second is connected with the synthesis of multimetallic nanoparticles having different compositions and morphologies. And the third is associated with the determination of the effects of the features of the supports (their geometry, nature, physicochemical characteristics) on the controlled micro(nano)-structure of Au-containing nanomaterials and, consequently, their catalytic ability [58].

A fabrication of Au nanoplate structures via an electroplating process using an electrolyte based on Au(I) cyanide complex in the absence of any additives and without any pretreatment of the substrate has been reported [59]. The well-defined Au nanoplate structures were electrodeposited in $Au(CN)_2^-$-containing solutions. It was shown that the synthesized nanoplates have a thickness of about 50 nm, while the width of the spans is within the range of 500–800 nm (Fig. 3). Such gold nanostructures seem to be unique in their form as compared with previously reported gold structures fabricated by means of electrodeposition from $AuCl_4^-$-containing plating baths. This observation was explained by the peculiar mechanism of electrochemical deposition reaction from $Au(CN)_2^-$ complexes under the condition of reduced overpotentials. The reported nanostructures revealed excellent electrocatalytic properties with respect to the electrochemical reduction of oxygen and oxidation of glucose (Fig. 4).

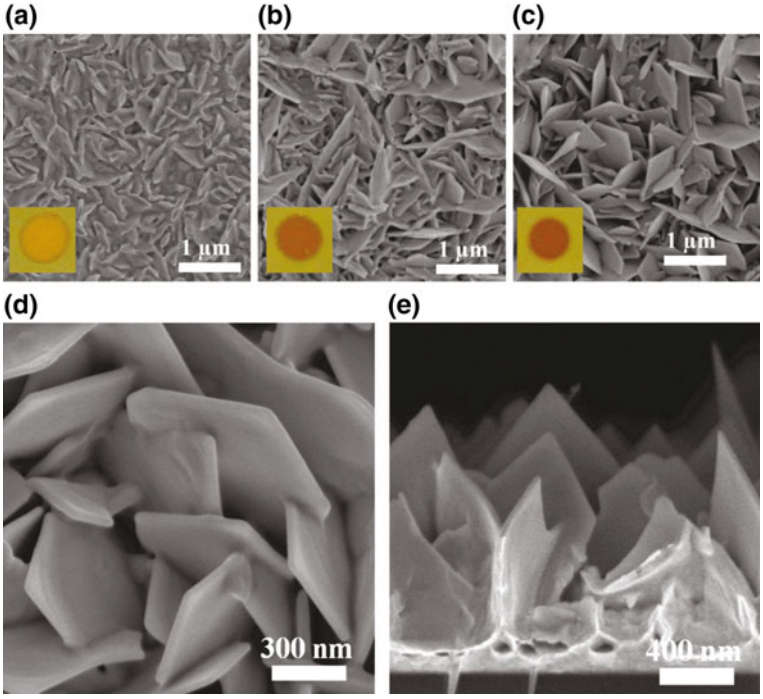

Fig. 3 SEM images of Au deposits electrodeposited from a solution containing 15 mM $KAu(CN)_2$ and 0.25 M Na_2CO_3 at **a** 0.9, **b** 1.0, and **c** 1.1 V. Total deposition charges are 0.04 C. **d** and **e** high-resolution and cross-sectional SEM images of (**c**). Reprinted with permission from [59]. Copyright (2011) American Chemical Society

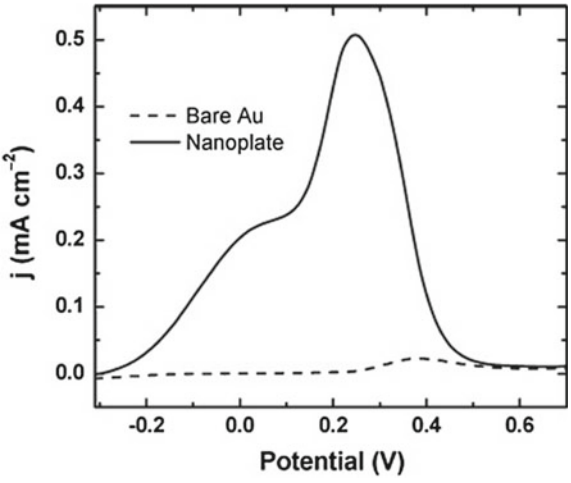

Fig. 4 Anodic scans obtained on bare and nanoplate Au surfaces in 10 mM glucose + 0.1 M phosphate buffer (pH 7.0). Scan rate was 10 mV s^{-1}. Reprinted with permission from [59]. Copyright (2011) American Chemical Society

Ye et al. [60] reported the electrodeposition of hierarchical dendritic Au microstructures showing secondary and tertiary branches. The electrodeposition was performed on an indium tin oxide electrode and neither special templates nor electrolyte additives were used. The applied potential is shown to significantly affect the morphologies of hierarchical dendritic gold microstructures; thus, uncommon flowerlike and stem-type tectorum-like structures are formed if the electrode potential is relatively high. The as-synthesized Au microstructures exhibit increased electrocatalytic behavior with respect to the electrooxidation of ethanol as compared with a commercially available Au electrode.

The co-deposition of gold with other metals (Au-based electrodeposited alloys) can be successfully used to improve the electrocatalytic performance [61–63]. The electrodeposition of Au–Pt alloy particles with cauliflower-like microstructures at a constant value of applied cathode potential has been reported [61]. The ratio between Pt and Au was varied as follows: 0:1; 1:6.05; 1:1.32; 1:0.39 and 1:0. The content of individual components in the formed gold–platinum particles was controllably adjusted by changing the molar ratios between metal Au and Pt-containing ions in the plating bath. The formation of Au–Pt cauliflower-like microstructures was associated with the result of two competitive processes: rapid appearance of Au seeds as a core and following simultaneous deposition of gold and platinum layers around the cores. The electrocatalytic behavior of Au–Pt alloyed coatings was tested in the reaction of methanol oxidation in H_2SO_4 solution. It was determined that the electrocatalytic activity diminishes in the following sequence: Pt_4Au_1 > Pt > Pt_1Au_1. The gold atoms in Au–Pt alloys were stated to stimulate the reaction of methanol electrooxidation chiefly due to electronic effects. Low energy of activation and consequently improved kinetics of CH_3OH electrooxidation was detected for the Pt_4Au_1 electrode in comparison with individual "pure" platinum electrode [61].

Electrodeposition of gold–platinum hybrid nanoparticles has been reported using $AuCl_4^-$ and $PtCl_6^{2-}$ mixed electrolyte and an indium tin oxide surface as a substrate [62]. It was shown that adjusting the number of electrodeposition cycles allows controlling the size of Au–Pt nanoparticles. For instance, Au–Pt hybrid nanoparticles obtained by 20 electrodeposition cycles had an average diameter of ca. 60 nm. Gold–platinum nanoparticles electrode displayed good electrocatalytic activity relative to the reactions of nitrite electrooxidation and oxygen electroreduction due to a synergistic effect from the Au–Pt alloy nanoparticles. Thus, the results demonstrated that the electrodeposited cauliflower-shaped structure of Au–Pt nanoparticles can find potential applications in electrocatalytic reactions and sensors [62] as well as in the production of new micro- and nano-structures and direct methanol fuel cells [61].

Non-stationary pulse electrolysis in dimethyl sulfoxide solutions yielded discrete Au–Pd nanoparticles within the range of 20–120 nm transformed into complete nanostructured films during a longer time of pulse electrodeposition [63]. Such nanostructured binary gold–palladium systems are promising due to their pronounced catalytic activity and stability, they can be used in a huge variety of electrochemical processes.

The platinized platinum electrode is the most widely used type of electrode in electrochemical science and technology [64]. It commonly serves in conductance cells, forms the basis of the hydrogen reference electrode, and is a typical electrocatalyst in fuel cells. The paper [64] gives an excellent review on historical origins, electrode kinetics and mechanism, main features of electrodeposition and practical guidelines concerning platinizing procedures.

There are several comprehensive review papers reporting synthesis, properties and applications of platinum-based nanostructured materials (including electrodeposited materials) [65], electrochemical and chemical deposition of Pt-group metals [66], methods for the production of Pt group metals as electrocatalysts used in fuel cells and for hydrogen production [67], current developments of Pt-based catalytic electrodes for direct methanol fuel cells [68], and nanostructure, activity, mechanism and application in proton exchange membrane fuel cells of Pt electrocatalysts for O_2 reduction reaction [69]. The reader is referred to those papers where a large number of publications are mentioned to get more detailed information of the topic. The present chapter does not claim to be exhaustive and we will further consider only some important and interesting case studies on electrodeposited Pt-based electrocatalysts.

Much attention is being paid to the electrodeposition and characterization of highly porous Pt nanostructures and nanoparticles [70–81]. Adjusting current mode (direct current, pulse current, etc.), the value of applied current density, the plating baths composition, the pretreatment and after-treatment of Pt coatings as well as a correct choice of a substrate allows ensuring developed surface area and achieving improved electrocatalytic performance.

The influence of the value of deposition potential on the surface morphology and electrocatalytic ability of Pt electrodeposits on a carbon paper was demonstrated in work [70]. The form of the electroplated platinum was changed from globular to dendritic and to rosette-like shape with an increase in the applied cathodic potential (Fig. 5). The observed transformation in shape was attributed to the changes in the kinetics of simultaneously occurring reaction of hydrogen evolution. It was noted that dendritic Pt/C structures (prepared through the electrodeposition at the potential of 0 V) exhibited higher electrocatalytic activity towards oxidation of formic acid (Fig. 6). The deposition of the catalyst in a sequential regime (i.e. layer-by-layer electrodeposition) appreciably improved the characteristics of a fuel cell, which was ascribed to the formation of respective triple phase boundary. Thus, the sequential regime of electrochemical deposition of platinum-based catalyst gives better efficiency than the single-time electroplating [70].

Zhong et al. [71] studied the electrocatalytic activity of the electrodeposited Pt for the ammonia oxidation. The applied cathode current density and time on were chosen as influencing factors. It was determined that the electroplated platinum layer shows better electrocatalytic characteristics than a simple “pure” platinum layer because of a more developed surface area of coatings available to the electrochemical process. An increase in the Pt loading leads to the improvement in the catalytic performance of the platinum electrocatalyst. Increasing current density also results in the growth of the catalytic activity of platinum films due to an increase in the amount of platinum loading. Higher current densities yield either small platinum

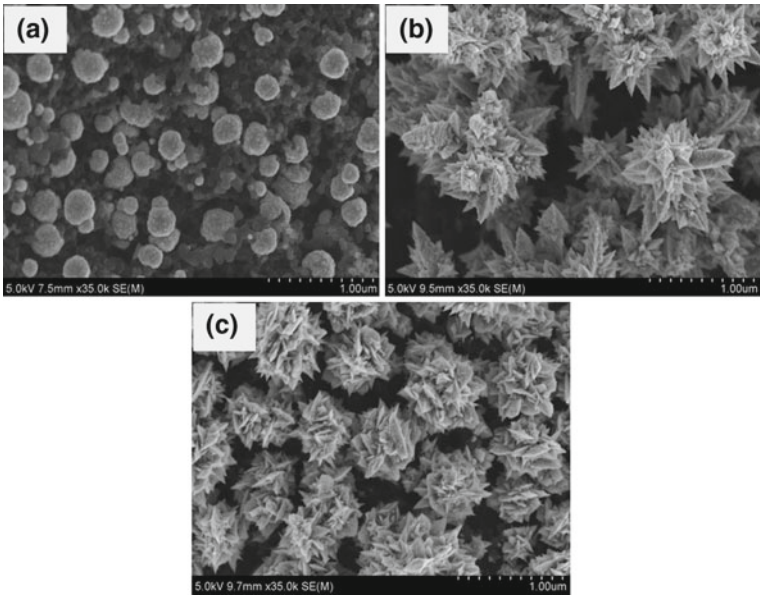

Fig. 5 Scanning electron microscope images of Pt electrodeposited on carbon black-coated carbon paper displaying different morphologies: **a** globular (0.2 V), **b** dendritic (0 V), and **c** rosette (–0.2 V). Reprinted from [70] by permission of Springer Nature

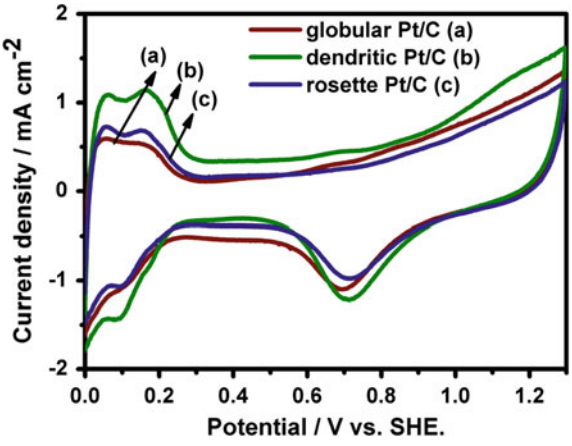

Fig. 6 Cyclic voltammogram of different Pt/C structures in 0.5 M H_2SO_4 at a scan rate of 50 mV s^{-1}. Reprinted from [70] by permission of Springer Nature

nanoparticles at a low electrodepositing duration or sheet-like dendritic particles at a long duration of electrodeposition. A decrease in the cathodic current densities gives larger platinum particulates with the size of several hundreds of nanometer showing a uniform surface morphology. The platinum electrocatalyst with the former morphological feature shows a better electrocatalytic performance in the reaction of

ammonia oxidation than the later which was explained by the expansion of the surface area of electrodes.

Change in the current conditions allows flexible controlling the deposition of Pt thin films with a preferential crystallographic orientation. For instance, highly {100}-oriented Pt thin films can be prepared via a potentiostatic method by varying the deposition charge without the use of any surfactants [72]. It was shown that the films prepared with a larger deposition charge have a much higher fraction of (100) surface sites. The abundance of Pt (100) surface sites results in an improvement in electrocatalytic activity with respect to the oxidation of NH_3 and HCOOH as compared with a "common" polycrystalline platinum electrode.

The electrosynthesis of nanoporous platinum structures with an average diameter of 89 and 2 nm pore sizes on a glassy carbon substrate was reported by means of double pulse deposition technique [73]. The development of the electrochemical surface area and an increase in the electrocatalytic activity towards the reaction of oxygen electroreduction at the highly porous structures were achieved as a consequence of the availability of the active sites within the nanopores.

Pt dendritic nanoparticles with a great surface area and increased electrocatalytic activity with respect to the O_2 reduction reaction were synthesized by a potentiostatic double-pulse process under the condition of forced convection [74]. The applied procedure ensured successive cycling of electrode potential within the region of hydrogen adsorption/desorption and platinum reduction/oxidation. As a result, a pronounced decrease in the active surface area is observed due to incomplete collapse of the open nano-sized pores and the formation of smoother and more compact surface structures.

Liquid crystal templates were used to produce mesoporous platinum films in which the amount of platinum was 0.60, 1.0 or 1.5 mg cm^{-2} [75]. The electrochemical deposition was carried out directly on a carbon cloth under the condition of a constant value of electrode potential. The mesoporous platinum electrocatalytic coatings were tested in the anodic process for a direct ethanol fuel cell. Although the content of Pt was relatively low, mesoporous films displayed equal or even higher catalytic efficiency in the direct C_2H_5OH fuel cell as compared to the commercially available platinum samples in which the Pt loading was 4.0 mg cm^{-2}.

Liu et al. [76] suggested a pulse electrodeposition method to synthesize shape-controllable ultrafine nanodendritic Pt particles in the electrolyte that does not contain any organic additive. The morphology of the nanoparticles could be easily controlled by adjusting electrode potential. Dendrites with the size of the nano-branches of about 10–20 nm were prepared. The electrocatalytic behavior of the synthesized dendritic Pt with respect to the methanol electrocatalytic combustion was superior to that of the hemispherical and flower-like Pt particles.

Pulse electrodeposition method was also used to produce highly active $PtSnO_2/C$ catalysts introducing SnO_2 into supports as an assisting agent [77]. While direct current deposition yields spherical Pt particles with particle sizes ranging between 400 and 500 nm (Fig. 7), pulse electrodeposition can produce uniform metal nanoclusters (about 200–300 nm). This increases the surface area of the catalyst and ensures higher electrocatalytic ability for methanol oxidation and oxygen reduction.

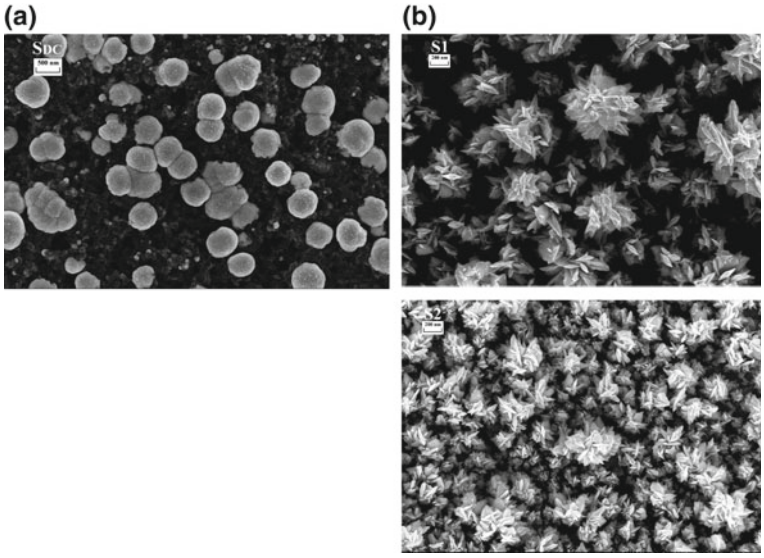

Fig. 7 Scanning electron micrographs of **a** Pt/C prepared by direct current electrodeposition and **b** Pt/C and $PtSnO_2$/C prepared by pulse electrodeposition. Reprinted with permission from [77]. Copyright (2008) American Chemical Society

In addition, using SnO_2 reagent can notably increase the active surface areas, and hence enhance electrocatalytic activity of Pt catalysts [77].

The electrodeposition of three-dimensional (3D) platinum nano-flowers was reported by using potentiostatic pulse plating technique on a silicon substrate [78]. The platinum nano-structured material was composed of bamboo-leaf-like nano-petals and had an overall rose-like morphology. The 3D platinum nano-flowers exhibited a highly developed surface area as compared with the "common" platinum thin film and was characterized by a preferable surface orientation of the (100) and (110) crystallographic planes. These features provided the synthesized 3D platinum nano-flower-like electrocatalyst with a perfect catalytic activity in the reaction of CH_3OH oxidation and a very satisfactory CO tolerance as compared to the thin platinum film.

An advanced technique for the electrochemical deposition of an isolated single Pt atom or small cluster, up to 9 atoms, on a Bi ultramicroelectrode has been described [79]. The limiting currents of hydrogen evolution reaction recorded by means of linear voltammetry technique allow determining the size and number of atoms in the clusters. The obtained results indicated that electrocatalytic nanostructures can be fabricated on an atom-by-atom basis.

An interesting approach to the preparation of electrodeposited platinum nanostructures involves utilizing solution dispersed platinum nanoparticles during Pt electrodeposition [80]. The presence of Pt nanoparticles significantly affects the morphology of Pt electrodeposited onto the electrode surface, although the surface area

of the deposits is similar (with and without Pt nanoparticles in the electrolyte). The Pt nanoparticles in the plating bath provide the formation of a compact film which is composed of platinum clusters manifesting the exposed Pt (100) and (110) crystallographic planes. The electrocatalytic activity of platinum electrodeposits obtained with the addition of nanoparticles was appreciably increased with respect to the reactions of ethylene glycol and methanol electrooxidation. Thus a controllable growth of platinum coatings in the presence of Pt nanoparticles in the plating bath is a convenient and efficient way to produce nanostructured electrocatalysts with improved service characteristics [80].

Electrodeposition of platinum was used to modify the surface morphology, microstructure, phase composition and electrochemical properties of Ebonex® electrodes (commercial trade name of titanium "sub-oxides" with having the general formula Ti_nO_{2n-1}, n = 4–10) [81, 82]. The thickness of deposits was ca. 1 μm (about 2 mg platinum per square centimeter in terms of Pt loading). The heat treatment of the coatings at the temperatures of 230–310 °C resulted in the changes of the microstructure and chemical composition of both the platinum upper layer and the porous Ebonex®. The acceleration of the diffusion of platinum into the Ebonex® was also observed. The formation of some newly found phases in Ti–Pt–O system was detected in the case of the heat-treated Ebonex®, this phenomenon was stated to influence the electrocatalytic properties of the coatings. The thermally treated platinized Ebonex® electrodes showed reduced activity relative to the reaction of Cr(III) ions electrooxidation and enhanced selectivity with respect to the electrochemical reaction of oxygen evolution. Thus they can be successfully used as efficient dimension-stable anodes in the process of chromium deposition from Cr(III) electrolytes [81].

Although aqueous plating baths are commonly used for electrodepositing of Pt, the electrolytes based on room-temperature ionic liquids seems to be very promising. For example, He et al. [83] considered the electrodeposition of platinum in two room-temperature ionic liquids, 1-n-butyl-3-methylimidazolium hexafluorophosphate and 1-n-butyl-3-methylimidazolium tetrafluoroborate, on a glassy carbon substrate. The electrocatalytic behavior of nanostructured Pt layers manufactured from these electrolytes was estimated with respect to the electrochemical oxidation of methanol. The platinum films prepared in both ionic liquids showed increased catalytic current densities, which are similar to that obtained in aqueous solution of perchloric acid. The size of Pt nanoclusters was determined by means of the atomic-force microscopy. The authors drew a conclusion that the Pt coatings synthesized from ionic liquids under consideration are distinguished by improved electrocatalytic activity than those fabricated using $HClO_4$-based aqueous electrolyte.

The electrocatalytic behavior of Pt-based catalysts can be improved by the alloying with some other metals, including co-deposition with Ni [84], Co [85], Au [86, 87], Ru [88], Ir [89], Pd [90], deposition of ternary Pt–Fe–Co [91] and Pt–Ru–Ni [92], electrodeposition of Pt–Cu alloy with subsequent dealloying by selective anodic dissolution of Cu [93], and electrodeposition of epitaxially grown Ag overlayers onto Pt [94]. Synergistic effects are often observed for bimetallic Pt-based catalysts. For instance, the nitrate reduction occurs at a higher rate on electrodeposited 70:30 Pt–Ir electrodes than on pure Pt electrodeposits [89]. It was stressed that the role played

by Ir in Pt–Ir electrodes is that of a bifunctional heterogeneous electrocatalyst, i.e. a synergetic effect in which the surface has a higher activity than the sum of those of the components. The electrocatalytic activity of electrodeposited ternary Pt–Fe–Co alloys toward the reaction of oxygen electroreduction was investigated with regard to geometric (Pt–Pt distance) and electronic (d-band center, core-level binding energy) approaches [91]. The current density of oxygen reduction reaction showed a double volcano plot depending on the alloy composition (Fig. 8). This unique double-volcano behavior was mainly attributed to different electronic aspects of iron and cobalt.

Highly nanoporous palladium (npPd) and platinum (npPt) catalysts, in which nanoporous microstructures were directed by reverse micelles of Triton X-100, were prepared by electrodeposition and their electrocatalytic performance was characterized for the reaction of O_2 reduction under alkaline conditions and H_2O_2 electrochemical reactions [95]. The electrocatalytic activity was observed in the following sequence: npPd > npPt $\geq$ Pt-20/C $\gg$ bulk Pt. A higher activity of npPd was connected with the difference in microstructures (npPd with nano- and microporosity vs. npPt with nano-porosity only).

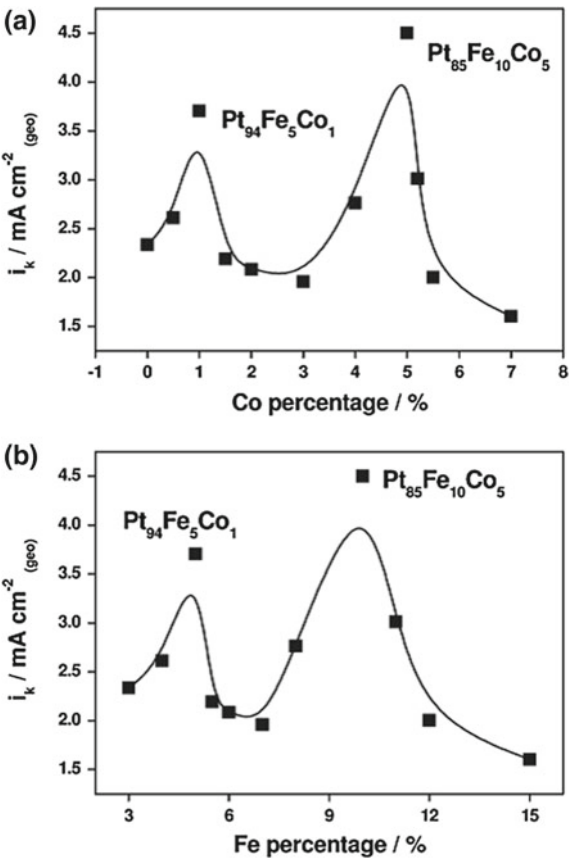

Fig. 8 Kinetic current densities for the oxygen reduction reaction at 0.65 V occurring on electrodeposited ternary Pt–Fe–Co alloys against the concentrations of **a** Co and **b** Fe atoms. Reprinted with permission from [91]. Copyright (2011) American Chemical Society

The electrodeposition of Pd layer on an activated carbon black substrate was investigated by means of potentiostatic method from an electrolyte containing an additive of polyethylene glycol (PEG-6000) [96]. Increasing additive concentration resulted in the variation of surface morphology of palladium films from spherical to flower like pattern. It was shown that palladium nanoflower consist of many nanopetals, which can ensure a high specific surface area. An increase in electrocatalytic activity of Pd nanoflowers relative to Pd spherical aggregates was observed toward the oxidation of HCOOH and reduction of O_2.

The fabrication of PtRu nanoparticles having a diameter of ca. 10–20 nm by the electrodepostion technique was demonstrated using multiwalled carbon nanotube-Nafion nanocomposite as a substrate [97]. The resulting PtRu-multiwalled carbon nanotube-Nafion nanocomposite exhibited the electrocatalysis activity in the reaction of the electrooxidation of methanol. A bimetallic PtRu electrocatalyst (with 1:1 atomic ratio) in a nanocomposite revelaed a higher catalytic activity than that containing only "pure" Pt, which was associated with the bifunctional mechanism of ruthenium and platinum action. This work indicated that the search for a suitable support is one of the modern trends in investigations dealing with electrodeposition of high-active electrocatalysts.

An approach to the manufacture of Pt/Ir/Pt multilayered structures was described using an inexpensive Ti substrate [98]. The current density of the reaction of CH_3OH oxidation was increased by 2.76 times as compared to the reference electrocatalyst (Ti/Pt anode), although both samples having equal electroactive surface area.

Zhang et al. [99] developed an interesting technique for electrodeposition of the Pd catalyst films on a graphite rod for direct HCOOH electrooxidation. This approach includes a repeated treatment by the electrochemical deposition of palladium layer, followed by the deposition of Nafion film. The electrode fabricated by the so-called repeated electrodeposition with Nafion coating exhibited a good catalytic activity and durability for the electrooxidation of HCOOH. The obtained data were ascribed to the increased usage of catalyst due to the multi-layer microstructure and the prevalence of the highly active Pd (111) crystallographic planes on the surface.

Two different techniques to prepare Ru-containing deposits on commercial-grade carbon-supported platinum nanoparticles as methanol oxidation electrocatalysts have been compared [100]. The first one involved the so-called Ru spontaneous chemical deposition by immersion of the Pt–C electrodes in "aged" $RuCl_3$ solution. The second one consisted in Ru electrodeposition at rotating Pt–C electrode by electrolysis of N_2-purged 0.1 M $HClO_4$ with 10^{-5} M $Ru(NO)(NO_3)_3$ (this complex does not yield any Ru spontaneous deposition). The maximum in electrocatalytic activity towards methanol oxidation was detected at ruthenium surface coverage of 10 and 20% for spontaneous chemical deposition and electrodeposition, respectively. However, increased rates of the electrochemical reaction of methanol oxidation were registered in the case of electrochemically deposited ruthenium layers.

Recently, the electrodeposition of palladium nanoparticles onto glassy carbon was reported from a plating bath prepared using a deep eutectic solvent [101]. The specific features of the Pd nucleation and growth from the deep eutectic solvents containing ethylene glycol and choline chloride were characterized. It was shown

that the Pd nanoparticles, containing mainly metallic palladium with small amounts of palladium oxides, exhibited a pronounced electrochemical activity with respect to the electrooxidation of HCOOH, which is even greater than that of other catalysts based on palladium nanoparticles reported previously.

6 Chromium and Chromium-Based Alloys

The electrocatalytic behavior of polycrystalline chromium electrodes during its cathodic polarization in sulfuric acid solutions of oxalic and formic acids was investigated in [102]. It was shown that the organic substances can chemisorb on the cathode surface and inhibit the hydrogen evolution on the metal, they also can take part in the electrocatalytic processes resulting in the formation of polymolecular compounds: linear hydrocarbons and carboxylic acids containing 12–27 carbon atoms.

These observations are in good agreement with the results of the study on the composition of Cr coatings obtained from Cr(III) sulfate electrolytes containing HCOOH or $(COOH)_2$ [103]. The authors stated that nano-dimensional chromium crystallites produced in electrodeposition process exhibited a very high electrocatalytic activity. This means that the electroreduction of trivalent chromium ions is accompanied by a deep reduction of the adsorbed organic ligands from the inner coordination sphere of a Cr(III) complex. As a result of such electrocatalytic behavior, the obtained coatings contain considerable amounts of chromium carbides [103].

The mechanism of electrocatalytic formation of Cr–C alloys from an aqueous trivalent plating bath containing trivalent chromium sulfate together with carbamide and formic acid as organic components was considered in detail in [104, 105]. It was concluded that the destruction of organic compounds, leading to carbon inclusion in the Cr–C alloy, is not an electrochemical stage. The formation of carbide carbon in the course of the electroplating of the chromium–carbon deposits can result from the fact that some of the active Cr ad-atoms electrogenerated during the discharge of Cr (II) ions are involved in a further chemical interaction with carbon of organic components of the plating bath, these carbon-containing particles being adsorbed on the growing cathode. The process proceeds according to the following reaction scheme [104]:

$$2Cr^{0}_{ad} + C(IV) \rightarrow 2Cr(II) + C(0)$$

The resulting carbon is included in the structure of the deposit and Cr^{2+} ions can again take part in the electrodeposition of chromium. Carbon enters into the coating and hinders both the surface diffusion of Cr ad-atoms and the growth of the crystal phase nucleus which provides nanocrystalline structure formation.

Although “pure” chromium is hardly considered as a feasible electrocatalyst in the reaction of hydrogen evolution, chromium-based alloys look as very promising materials to this effect. With reference to this, chromium-carbon alloys (i.e. chromium carbide) attract special attention. For example, Schmuecker et al. [106]

discovered that chromium carbide Cr_7C_3 exhibits a relatively high electrocatalytic activity towards the cathodic reaction of hydrogen production in a water solution of H_2SO_4. Chromium carbide demonstrated high hydrogen evolution activity in 100% phosphoric acid [107]. The changes in the hydrogen overvoltage values in the range of chromium carbides ($Cr_7C_3 < Cr_3C_2 \approx Cr_{23}C_6$) were also demonstrated in [108].

A number of papers reported the electrodeposition of Cr–C coatings with enhanced corrosion resistance and improved electrocatalytic activity using aqueous chromium plating baths [109–112]. However, it is known that aqueous chromium electroplating baths suffer from a number of shortcomings [113, 114]. In this context, non-aqueous chromium electrolytes based on deep eutectic solvents seem to be very promising [115–121]. It is important that DESs-based chromium plating electrolytes allow depositing coatings with a relatively high thickness [120]. These coatings include some carbon and show reduced overvoltage of the hydrogen evolution reaction [120]. A detailed study on the electrocatalytic characteristics of Cr–C films deposited from DESs-based trivalent chromium electrolyte has been performed in [122].

Chromium-carbon coatings (ca. 5 wt% of carbon) were deposited from a plating bath containing Cr (III) chloride, choline chloride and water in 2.5:1:15 molar ratios, respectively [122]. In order to estimate the electrocatalytic behavior with that typical of "pure" chromium, coatings were electrodeposited from conventional hexavalent chromium plating bath (Table 2).

Table 2 shows that the electrocatalytic properties of Cr–C coatings are substantially better than those of "usual" chromium deposits (the current exchange densities differ more than ten times). The results of electrochemical impedance spectroscopy revealed that the changes in the catalytic behavior can be attributed to the proper changes in the electronic structure rather than to the expansion of an actual surface area of the cathode [122]. Thus, the electrodeposited chromium-carbon coatings fabricated from a deep eutectic solvent can be used to develop new electrocatalysts towards the electrochemical process of hydrogen production for water-splitting devices.

In the context of discussion of the electrocatalytic properties of chromium-based coatings, the paper [123] should be mentioned in which the reaction of hydrogen

Table 2 Kinetic parameters[a] of the hydrogen evolution reaction obtained from Tafel dependences recorded in 1 M NaOH at 25 °C

Kinetic parameter	Electrode	
	Cr (deposited from Cr(VI)-based electrolyte)	Cr–C (deposited from Cr(III) DES-based electrolyte)
a, V	1.057	0.857
b, V dec^{-1}	0.146	0.139
α	0.40	0.43
i_0, A cm^{-2}	0.60×10^{-7}	6.58×10^{-7}

[a] a and b are the Tafel constants; α is the transfer coefficient, and i_0 is the exchange current density
Reprinted from [122]

formation on electrodeposited Zn–Cr alloy coatings was investigated. Although the studied alloys contained only a small quantity of Cr (3, 5 and 10 wt%), the observed electrocatalytic effect towards the hydrogen evolution was associated with the presence of chromium. It was suggested that at high polarizing currents the surface of alloys is enriched in Cr which is a good catalyst for adsorbing hydrogen as compared with zinc; therefore, the hydrogen overvoltage diminishes.

7 Composite Coatings

Electrodeposition of composite coatings is a promising branch of modern electroplating industry and surface engineering. It provides fabrication of finishing layers with enhanced microhardness, high wear and corrosion resistance and allows imparting a number of useful physicochemical and service properties to the surfaces, including improved electrocatalytic behavior [124, 125]. Electrodeposited composite coatings are composed of a metallic matrix and a dispersed phase of nano- or micro-sized particles entrapped into the matrix during electrodeposition process. Both metallic matrix and particles of a dispersed phase can manifest electrocatalytic activity towards different electrochemical reactions.

Among the various electrodeposited composites, TiO_2-containing coatings occupy a special place because they exhibit high activity toward electrocatalysis [126–136]. This is due to peculiar and valuable structural, chemical and electronic properties of titania [137].

Thus, Ni–TiO_2 electrodeposited films were prepared using a common Watts' nickel bath with the addition of TiO_2 powder and the electrochemical characteristics of the obtained composites with respect to the reaction of hydrogen evolution were evaluated [126]. The composite coatings revealed an increased electrocatalytic activity relative to the H_2 evolution in an alkaline medium. These composites showed a higher rate of hydrogen evolution and lower overpotential than the "pure" Ni coatings. An improved electrocatalytic activity of Ni–TiO_2 films was associated with the developed electrode surface and with the effect of TiO_2 particles entrapped within the nickel matrix.

Electrodeposited nickel–titania nanocomposite coatings were tested as potential electrocatalysts in the electrooxidation of methanol [127]. The nanocomposite Ni–TiO_2 coatings exhibited a higher catalytic activity with respect to the electrooxidation of CH_3OH than the "pure" Ni. The catalytic activity was stated to increase with increasing the titania content up to 9 wt%. It was concluded that the electroplated Ni–TiO_2 nanocomposite coatings can be recommended for fuel cell application.

Ni–P–TiO_2 electrocatalysts were fabricated by the co-deposition of nickel and TiO_2 on a copper electrode using an electrolyte in which TiO_2 particles were suspended by intensive agitation [128]. The introduction of TiO_2 into the amorphous Ni–P metallic matrix resulted in an acceleration of the H_2 evolution as compared with the blank nickel–phosphorus alloy and this phenomenon was observed both in acid

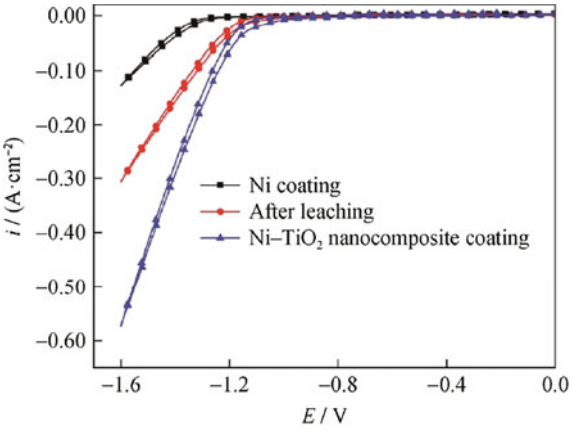

Fig. 9 Cyclic voltammograms recorded in 1 M KOH for modified Ni coatings in comparison to conventional Ni coating. Reprinted from [129] by permission of Springer Nature

and alkaline environments. An increase in the rate of the cathode reaction of hydrogen production on the synthesized Ni–P–TiO_2 composite coatings was explained by the fact that TiO_2 and its protonated state and(or) redox couple $Ti_2O_3 \Leftrightarrow$ TiOOH are present on the surface. These particles are responsible for an electrocatalytic action with respect to the hydrogen evolution process.

Recent study [129] reported the catalytic behavior of electrodeposited Ni and Ni–TiO_2 coatings towards the process of alkaline hydrogen production. The electrocatalytic efficiency of deposits was improved by both selective etching of as-deposited nickel films and incorporation of TiO_2 nanoparticles. It was shown that the introduction of titania into the metal matrix (ca. 4.2 wt%) ensures the acceleration of the hydrogen evolution reaction in a greater degree when compared with the effect of partial dissolution treatment that yields an increased surface area (Fig. 9).

Shibli and Dilimon suggested improving the electrocatalytic behavior of Ni-based deposits by electroless deposition of Ni–P–TiO_2 [130] and Ni–P–TiO_2-supported RuO_2 mixed oxides [131] composites. The reinforcement of the coatings with titanium (IV) oxide particles enhances the roughness factor and increases the number of electroactive sites and hydrogen adsorption ability which results in high electrocatalytic activity during hydrogen evolution reaction [130]. In addition, the mixed oxides containing RuO_2 having particle size at nano-level exhibit appreciably higher catalytic activity [131]. The catalytic behavior depends upon the size of the embedded RuO_2 particles. The reduction of the size at nano-level promotes the electrocatalytic properties. So the co-deposition of mixed oxides incorporated into an appropriate metallic matrix allows preparing high-performance electrocatalytic coatings.

An improvement in the deposition characteristics and electrocatalytic behavior may be achieved by using novel kind of plating electrolyte. A series of papers [132–136] reported the electrochemical sunthesis of Fe–TiO_2 composites using electrolytes based on methanesulfonate salts. It should be noted that metanesulfonate electrolytes are prepared with the use of methanesulfonic acid (CH_3SO_2OH) and its salts. They offer a versatile approach to produce new kinds of electrocatalytic coatings, since

such electrolytes are distinguished from common analogues by a considerable solubility of metal salts, enhanced electrical conductivity, weak toxicity, easy waste-water treatment and rapid biodegradability [138, 139].

Increased electrocatalytic ability with respect to the reactions of hydrogen and oxygen evolution in 1 M NaOH solution was detected for the electroplated Fe–TiO_2 composites (Fig. 10) [132]. It was concluded that an increment in the concentration of the surface active sites and the appearance of redox couples including titanium compounds in different valency states are responsible for a greater catalytic activity of Fe–TiO_2 composites relative to the electrochemical reactions of H_2 and O_2 evolution. A relatively low corrosion stability of iron matrix can be improved via the electrodeposition of a thin CeO_2 ceria layer on the surface which protects against corrosion damage. At the same time, the formation of ceria film does not deteriorate good electrocatalytic performance [134]. Titania nano-particles can be introduced into colloidal plating bath in the forms of both hydrosol fabricated using precipitation technique and commercially available Degussa P25 titania nano-powder [133]. A satisfactory catalytic stability of the iron–titania electrocatalysts was confirmed by the results obtained by chronoamperometry method, thus involving availability of these coatings to be efficiently used in alkaline electrolyzers for the manufacture of oxygen and hydrogen [132].

Ni–SiC nano-composite coatings with a nanocrystalline nickel matrix and dispersed inert SiC nanoparticles have been fabricated from a modified Watts bath containing SiC nanoparticles by using ultrasonic electroplating method [140]. The obtained composite coatings show not only lower corrosion current density but also possess much higher electrocatalytic hydrogen evolution activity in 30 wt% KOH solutions as compared with pure Ni deposits. The authors suggested that the improved hydrogen evolution activity is caused by an increase in the real surface area of Ni–SiC nanocomposite.

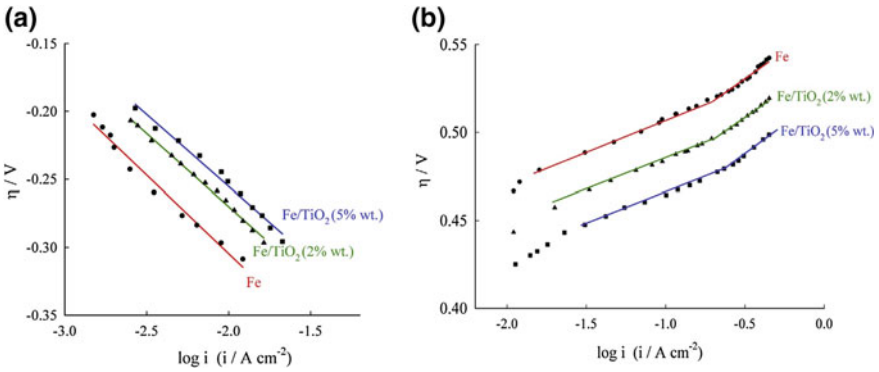

Fig. 10 Tafel lines for the hydrogen (**a**) and oxygen (**b**) evolution reactions recorded on Fe and Fe–TiO_2 electrodes in 1 M NaOH at 298 K. Reprinted from [132], Copyright 2016, with permission from Elsevier

Mirkova et al. [141] electrodeposited and characterized composite Ni–Co_3O_4 films. The coatings exhibited enhanced electrochemical activity towards hydrogen evolution reaction which was explained by the presence of Co and by more developed surface of electrode resulted from the incorporation of Co_3O_4 particles into the metallic matrix. It was stressed that the catalytic activity of composite Ni–Co_3O_4 electrodes towards hydrogen evolution may even approach that typical of Pd. High electrocatalytic ability with respect to O_2 evolution reaction was also detected in the case of Ni–Co_3O_4 coatings. Therefore, these composite coatings are very promising from the point of view of their application both in water electrolysis for hydrogen/oxygen production and in fuel cells.

Composite coatings Ni–C_3N_4 [142], Ni–OCNT (oxidized carbon nanotube), Ni–ONC (oxidized N-enriched carbon), Ni–rGO (reduced graphene oxide) [143], Ni–W–CNT (carbon nanotube), Ni–W–GO (graphene oxide) [144], Ni–Fe–Co–graphene [145], Ni–W–MWCNT (multi-walled carbon nanotube) [146], Ni–Co–$LaNi_5$ [147], Ni–CeO_2 [148], Ni–S/CeO_2 [149] and Co–W/CeO_2 [150] have been electrodeposited and successfully tested as electrocatalysts in the reaction of H_2 evolution. It was observed that the composites, where Ni matrix was coupled with graphitic carbon nitride, were better than those of the state-of-the-art hydrogen evolution-active materials based on nickel as well as the majority of other metal-free electrocatalysts, they even can compete with the catalytic activity of commercially available Pt/C materials [142].

Au/MnO_2 composites were electrodeposited on the substrate of glassy carbon [151]. They can effectively catalyze electrochemical reactions of the oxidation of glucose and hydrogen peroxide.

An interesting approach to the electrodeposition of composites was developed [152, 153] according to that metallic particles of a dispersed phase are incorporated in a metallic matrix. The Ni–Ni, Ni–Co and Ni–Fe composites were deposited from the plating bath containing dissolved NiCl2·6H2O and suspended metallic powders of nickel, cobalt and iron [152]. As a result, the electrodes with highly rough surface areas were synthesized. The observed improved catalytic activity with respect to the hydrogen evolution was attributed to an increase in the real surface areas. The idea on electrodepositing metal–metal composites was used in a recent study [153], in which the silver nanoparticles were introduced into Ni–P deposited matrix in the course of electrolysis process. A considerable improvement in the electrocatalytic property towards the hydrogen production was observed for the fabricated Ni–P–Ag composites. The electrocatalytic behavior was discussed in terms of the enhanced electroactive sites of Ag particles.

Electrocatalytic effects may manifest themselves not only post hoc, after the electrochemical synthesis of a composite coating, but also in situ, in the course of electrodeposition process. For instance, Refs. [154, 155] reported the electrocatalytic effects of SiO_2 and Al_2O_3 nanoparticles on nickel electrodeposition. It was shown that the overpotential of Ni deposition reaction was reduced if SiO_2 or Al_2O_3 nanoparticles were added to the plating bath and introduced into the coatings. This fact showed that oxides nanoparticles took part in the electrode reaction and could

catalyze electrodeposition of nickel, although SiO_2 and Al_2O_3 had no electrochemical activity itself and no electron exchange would happen between nanoparticle and electrode. Possible reasons for the observed electrocatalytic effect have been considered [154, 155].

8 Conclusions

Literature data show that much effort has been made to develop high-performance electrodeposited catalyst based on various metals, alloys and metal-containing composites. The electrodeposition technique permits flexible adjustment of composition, microstructure, surface morphology and electrocatalytic properties of electrodeposits. Although electrocatalysts based on noble metals (Pt, Pd, Ru, Au, etc.) remain the focus of attention due to their high activity, a huge number of papers deal with the synthesis and characterization of catalysts, in which base metals and earth abundant elements (Ni, Fe, Co, Cr, Cu) are used. Some works reported the fabrication of such electrocatalysts that can rival the electrocatalytic property of catalysts containing noble metals. Thus, much more research is needed to develop commercially valid non-noble electrocatalysts (alloys and composites). An optimal choice of components in alloys and a dispersed phase and a metallic matrix in composite coatings may provide the realization of synergistic interaction between different constituents and sufficiently improve the electrocatalytic performance of deposited layers.

An important direction in the electrodeposition of electrocatalytic coatings is associated with the application of non-stationary current regimes. The use of pulse current and linear potential sweep together with the right choice of applied current density, appropriate substrate, plating baths composition, pretreatment and after-treatment of coatings can ensure the formation of highly porous nanostructures and nanoparticles and achieve exclusively high electrocatalytic performance and utilization efficiency. Even isolated single atoms or small cluster, up to several atoms, can be produced by electrodeposition method on an atom-by-atom basis which may provide size effects at the nanoscale yielding an unique improvement in the electrocatalytic behavior.

A special success in electrodeposition of electrocatalysts can be also achieved by using novel kinds of plating baths, including those based on room-temperature ionic liquids and especially deep eutectic solvents. Only few studies considered the preparation of electrocatalysts with the use of deep eutectic solvents and this direction could have a bright future.

References

1. Mohanty US (2011) Electrodeposition: a versatile and inexpensive tool for the synthesis of nanoparticles, nanorods, nanowires, and nanoclusters of metals. J Appl Electrochem 41(3):257–270. https://doi.org/10.1007/s10800-010-0234-3
2. Safizadeh F, Ghali E, Houlachi G (2015) Electrocatalysis developments for hydrogen evolution reaction in alkaline solutions—a review. Int J Hydrogen Energy 40:256–274. https://doi.org/

10.1016/j.ijhydene.2014.10.109
3. Amadelli R, Ferro S, Barison S, Kötz R, Schnyder B, Velichenko AB (2013) A comparative study of cathodic electrodeposited nickel hydroxide films electrocatalysts. Electrocatalysis 4(4):329–337. https://doi.org/10.1007/s12678-013-0154-1
4. Lyons MEG, Cakara A, O'Brien P, Godwin I, Doyle RL (2012) Redox, pH sensing and electrolytic water splitting properties of electrochemically generated nickel hydroxide thin films in aqueous alkaline solution. Int J Electrochem Sci 7(12):11768–11795. http://www.electrochemsci.org/papers/vol7/71211768.pdf
5. Chialvo AC, Gennero de Chialvo MR (1991) Electrocatalytic activity of nickel black electrodes for the hydrogen evolution reaction in alkaline solutions. J Appl Electrochem 21(5):440–445. https://doi.org/10.1007/BF01024582
6. Jamesh MI (2016) Recent progress on earth abundant hydrogen evolution reaction and oxygen evolution reaction bifunctional electrocatalyst for overall water splitting in alkaline media. J Power Sources 333:213–236. https://doi.org/10.1016/j.jpowsour.2016.09.161
7. Chen R, Trieu V, Schley B, Natter H, Kintrup J, Bulan A, Weber R, Hempelmann R (2013) Anodic electrocatalytic coatings for electrolytic chlorine production: a review. Z Phys Chem 227(5):651–666. https://doi.org/10.1524/zpch.2013.0338
8. Shmychkova OB, Knysh VA, Luk'yanenko TV, Amadelli R, Velichenko AB (2018) Electrocatalytic processes on PbO_2 electrodes at high anodic potentials. Surf Eng Appl Electrochem 54(1):38–46. https://doi.org/10.3103/S1068375518010143
9. Li X, Pletcher D, Walsh FC (2011) Electrodeposited lead dioxide coatings. Chem Soc Rev 40:3879–3894. https://doi.org/10.1039/C0CS00213E
10. González-Buch C, Herraiz-Cardona I, Ortega E, García-Antón J, Pérez-Herranz V (2013) Synthesis and characterization of macroporous Ni, Co and Ni-Co electrocatalytic deposits for hydrogen evolution reaction in alkaline media. Int J Hydrogen Energy 38(25):10157–10169. https://doi.org/10.1016/j.ijhydene.2013.06.016
11. Raj IA, Vasu KI (1990) Transition metal-based hydrogen electrodes in alkaline solution—electrocatalysis on nickel based binary alloy coatings. J Appl Electrochem 20(1):32–38. https://doi.org/10.1007/BF01012468
12. Raj IA (1993) Nickel-based, binary-composite electrocatalysts for the cathodes in the energy-efficient industrial production of hydrogen from alkaline-water electrolytic cells. J Mater Sci 28(16):4375–4382. https://doi.org/10.1007/BF01154945
13. Raj IA, Vasu KI (1992) Transition metal-based cathodes for hydrogen evolution in alkaline solution: electrocatalysis on nickel-based ternary electrolytic codeposits. J Appl Electrochem 22(5):471–477. https://doi.org/10.1007/BF01077551
14. Torabinejad V, Aliofkhazraei M, Assareh S, Allahyarzadeh MH, Rouhaghdam AS (2017) Electrodeposition of Ni-Fe alloys, composites, and nano coatings – a review. J Alloys Compd 691:841–859. https://doi.org/10.1016/j.jallcom.2016.08.329
15. Chi B, Li J, Yang X, Gong Y, Wang N (2005) Deposition of Ni-Co by cyclic voltammetry method and its electrocatalytic properties for oxygen evolution reaction. Int J Hydrogen Energy 30(1):29–34. https://doi.org/10.1016/j.ijhydene.2004.03.032
16. Abdel-Karim R, Ramadan M, El-Raghy SM (2018) Morphology and electrochemical characterization of electrodeposited nanocrystalline Ni-Co electrodes for methanol fuel cells. J Nanomater. https://doi.org/10.1155/2018/9870732
17. Ullal Y, Hegde AC (2014) Electrodeposition and electro-catalytic study of nanocrystalline Ni–Fe alloy. Int J Hydrogen Energy 39:10485–10492. https://doi.org/10.1016/j.ijhydene.2014.05.016
18. Potvin E, Brossard L (1992) Electrocatalytic activity of Ni-Fe anodes for alkaline water electrolysis. Mater Chem Phys 31(4):311–318. https://doi.org/10.1016/0254-0584(92)90192-B
19. Gong M, Dai H (2015) A mini review of NiFe-based materials as highly active oxygen evolution reaction electrocatalysts. Nano Res 8(1):23–39. https://doi.org/10.1007/s12274-014-0591-z
20. Solmaz R, Kardaş G (2009) Electrochemical deposition and characterization of NiFe coatings as electrocatalytic materials for alkaline water electrolysis. Electrochim Acta 54:3726–3734. https://doi.org/10.1016/j.electacta.2009.01.064

21. Manazoğlu M, Hapçi G, Orhan G (2016) Effect of electrolysis parameters of Ni–Mo alloy on the electrocatalytic activity for hydrogen evaluation and their stability in alkali medium. J Appl Electrochem 46(2):191–204. https://doi.org/10.1007/s10800-015-0908-y
22. Abdel-Karim R, Halim J, El-Raghy S, Nabil M, Waheed A (2012) Surface morphology and electrochemical characterization of electrodeposited Ni-Mo nanocomposites as cathodes for hydrogen evolution. J Alloys Compd 530:85–90. https://doi.org/10.1016/j.jallcom.2012.03.063
23. Shetty S, Mohamed Jaffer Sadiq M, Bhat DK, Hegde AC (2017) Electrodeposition and characterization of Ni-Mo alloy as an electrocatalyst for alkaline water electrolysis. J Electroanal Chem 796:57–65. https://doi.org/10.1016/j.jelechem.2017.05.002
24. Xu C, Zhou JB, Zeng M, Fu XL, Liu XJ, Li JM (2016) Electrodeposition mechanism and characterization of Ni–Mo alloy and its electrocatalytic performance for hydrogen evolution. Int J Hydrogen Energy 41(31):13341–13349. https://doi.org/10.1016/j.ijhydene.2016.06.205
25. Shetty S, Hegde AC (2017) Magnetically induced electrodeposition of Ni-Mo alloy for hydrogen evolution reaction. Electrocatalysis 8(3):179–188. https://doi.org/10.1007/s12678-017-0350-5
26. Golgovici F, Pumnea A, Petica A, Manea AC, Brincoveanu O, Enachescu M, Anicai L (2018) Ni–Mo alloy nanostructures as cathodic materials for hydrogen evolution reaction during seawater electrolysis. Chem Pap 72(8):1889–1903. https://doi.org/10.1007/s11696-018-0486-7
27. Smith EL, Abbott AP, Ryder KS (2014) Deep eutectic solvents (DESs) and their applications. Chem Rev 114:11060–11082. https://doi.org/10.1021/cr300162p
28. Abbott AP, McKenzie KJ (2006) Application of ionic liquids to the electrodeposition of metals. Phys Chem Chem Phys 8:4265–4279. https://doi.org/10.1039/B607329H
29. Abbott AP, Ryder KS, König U (2008) Electrofinishing of metals using eutectic based ionic liquids. Trans Inst Met Finish 86:196–204. https://doi.org/10.1179/174591908X327590
30. Abbott AP, Frisch G, Ryder KS (2013) Electroplating using ionic liquids. Annu Rev Mater Res 43:335–358. https://doi.org/10.1146/annurev-matsci-071312-121640
31. Wang S, Zou X, Lu Y, Rao S, Xie X, Pang Z, Lu X, Xu Q, Zhou Z (2018) Electrodeposition of nano-nickel in deep eutectic solvents for hydrogen evolution reaction in alkaline solution. Int J Hydrogen Energy 43:15673–15686. https://doi.org/10.1016/j.ijhydene.2018.06.188
32. Xia M, Lei T, Lv N, Li N (2014) Synthesis and electrocatalytic hydrogen evolution performance of Ni-Mo-Cu alloy coating electrode. Int J Hydrogen Energy 39(10):4794–4802. https://doi.org/10.1016/j.ijhydene.2014.01.091
33. Allam M, Benaicha M, Dakhouche A (2018) Electrodeposition and characterization of NiMoW alloy as electrode material for hydrogen evolution in alkaline water electrolysis. Int J Hydrogen Energy 43(6):3394–3405. https://doi.org/10.1016/j.ijhydene.2017.08.012
34. Solmaz R, Döner A, Şahin I, Yüce AO, Kardaş G, Yazici B, Erbil M (2009) The stability of NiCoZn electrocatalyst for hydrogen evolution activity in alkaline solution during long-term electrolysis. Int J Hydrogen Energy 34(19):7910–7918. https://doi.org/10.1016/j.ijhydene.2009.07.086
35. Herraiz-Cardona I, Ortega E, Vázquez-Gómez L, Pérez-Herranz V (2011) Electrochemical characterization of a NiCo/Zn cathode for hydrogen generation. Int J Hydrogen Energy 36(18):11578–11587. https://doi.org/10.1016/j.ijhydene.2011.06.067
36. Koboski KR, Nelsen EF, Hampton JR (2013) Hydrogen evolution reaction measurements of dealloyed porous NiCu. Nanoscale Res Lett 8:528. https://doi.org/10.1186/1556-276X-8-528
37. Cheng C, Shah SSA, Najam T, Zhang L, Qi X, Wei Z (2017) Highly active electrocatalysis of hydrogen evolution reaction in alkaline medium by Ni–P alloy: a capacitance-activity relationship. J Energy Chem 26(6):1245–1251. https://doi.org/10.1016/j.jechem.2017.09.028
38. Protsenko VS, Vasil'eva EA, Smenova IV, Baskevich AS, Danilenko IA, Konstantinova TE, Danilov FI (2015) Electrodeposition of Fe and composite Fe/ZrO_2 coatings from a methanesulfonate bath. Surf Eng Appl Electrochem 51(1):65–75. https://doi.org/10.3103/S1068375515010123

39. De Carvalho J, Tremiliosi Filho G, Avaca LA, Gonzalez ER (1989) Electrodeposits of iron and nickel-iron for hydrogen evolution in alkaline solutions. Int J Hydrogen Energy 14(3):161–165. https://doi.org/10.1016/0360-3199(89)90049-9
40. Elezović NR, Jović VD, Krstajić NV (2005) Kinetics of the hydrogen evolution reaction on Fe–Mo film deposited on mild steel support in alkaline solution. Electrochim Acta 50:5594–5601. https://doi.org/10.1016/j.electacta.2005.03.037
41. Sequeira CAC, Santos DMF, Brito PSD (2011) Electrocatalytic activity of simple and modified Fe–P electrodeposits for hydrogen evolution from alkaline media. Energy 36:847–853. https://doi.org/10.1016/j.energy.2010.12.030
42. Bersirova OL, Bilyk SV, Kublanovs'kyi VS (2018) Electrochemical synthesis of Fe–W nanostructural electrocatalytic coatings. Mater Sci 53(5):732–738. https://doi.org/10.1007/s11003-018-0130-2
43. Brossard L (1992) Cobalt black electrodes for the oxygen evolution reaction from electrolysis of 40 wt% KOH. Int J Hydrogen Energy 17(9):671–676. https://doi.org/10.1016/0360-3199(92)90085-B
44. Brossard L, Lessard M (1993) Preparation of Co–Fe electrodeposits and their performance in relation to oxygen evolution in 40 wt% KOH at 70 °C. Int J Hydrogen Energy 18(10):807–816. https://doi.org/10.1016/0360-3199(93)90135-W
45. Miulovic SM, Maslovara SL, Seovic MM, Radak BB, Kaninski MPM (2012) Energy saving in electrolytic hydrogen production using Co–Cr activation—Part I. Int J Hydrogen Energy 37:16770–16775. https://doi.org/10.1016/j.ijhydene.2012.08.075
46. Kaninski MPM, Seović MM, Miulović SM, Žugić DL, Tasić GS, Šaponjić ĐP (2013) Cobalt-chrome activation of the nickel electrodes for the HER in alkaline water electrolysis—Part II. Int J Hydrogen Energy 38:1758–1764. https://doi.org/10.1016/j.ijhydene.2012.11.117
47. Döner A, Solmaz R, Kardaş G (2011) Enhancement of hydrogen evolution at cobalt–zinc deposited graphite electrode in alkaline solution. Int J Hydrogen Energy 36:7391–7397. https://doi.org/10.1016/j.ijhydene.2011.03.083
48. Vernickaite E, Tsyntsarua N, Cesiulis H (2016) Electrodeposited Co-W alloys and their prospects as effective anode for methanol oxidation in acidic media. Surf Coat Technol 307:1322–1328. https://doi.org/10.1016/j.surfcoat.2016.07.049
49. Abdolmaleki M, Bodaghi A, Hosseini J, Jamehbozorgi S (2018) Preparation of nanostructured Co–Mo alloy electrodes and investigation of their electrocatalytic activity for hydrazine oxidation in alkaline medium. J Chin Chem Soc, 1–7. https://doi.org/10.1002/jccs.201700344
50. Solmaz R, Döner A, Kardaş G (2008) Electrochemical deposition and characterization of NiCu coatings as cathode materials for hydrogen evolution reaction. Electrochem Commun 10(12):1909–1911. https://doi.org/10.1016/j.elecom.2008.10.011
51. Ahn SH, Park H-Y, Choi I, Yoo SJ, Hwang SJ, Kim H-J, Cho EA, Yoon CW, Park H, Son H, Hernandez JM, Nam SW, Lim T-H, Kim S-K, Jang JH (2013) Electrochemically fabricated NiCu alloy catalysts for hydrogen production in alkaline water electrolysis. Int J Hydrogen Energy 38(31):13493–13501. https://doi.org/10.1016/j.ijhydene.2013.07.103
52. Nady H, Negem M (2016) Ni-Cu nano-crystalline alloys for efficient electrochemical hydrogen production in acid water. RSC Adv 6:51111–51119. https://doi.org/10.1039/C6RA08348J
53. Solmaz R, Döner A, Kardaş G (2010) Preparation, characterization and application of alkaline leached CuNiZn ternary coatings for long-term electrolysis in alkaline solution. Int J Hydrogen Energy 35(19):10045–10049. https://doi.org/10.1016/j.ijhydene.2010.07.145
54. Milhano C, Pletcher D (2008) The electrodeposition and electrocatalytic properties of copper-palladium alloys. J Electroanal Chem 614(1–2):24–30. https://doi.org/10.1016/j.jelechem.2007.11.001
55. Gao W, Gao L, Li D, Huang K, Cui L, Meng J, Liang J (2018) Removal of nitrate from water by the electrocatalytic denitrification on the Cu-Bi electrode. J Electroanal Chem 817:202–209. https://doi.org/10.1016/j.jelechem.2018.04.006
56. Qiu Y-L, Zhong H-X, Zhang T-T, Xu W-B, Li X-F, Zhang H-M (2017) Copper electrode fabricated via Pulse electrodeposition: toward high methane selectivity and activity for CO_2 electroreduction. ACS Catal 7(9):6302–6310. https://doi.org/10.1021/acscatal.7b00571

57. Trasatti S (1972) Work function, electronegativity, and electrochemical behaviour of metals: III. Electrolytic hydrogen evolution in acid solutions. J Electroanal Chem Interfacial Electrochem 39(1):163–184. https://doi.org/10.1016/S0022-0728(72)80485-6
58. Saldan I, Dobrovetska O, Sus L, Makota O, Pereviznyk O, Kuntyi O, Reshetnyak O (2018) Electrochemical synthesis and properties of gold nanomaterials. J Solid State Electrochem 22:637–656. https://doi.org/10.1007/s10008-017-3835-5
59. Seo B, Choi S, Kim J (2011) Simple electrochemical deposition of Au nanoplates from Au(I) cyanide complexes and their electrocatalytic activities. ACS Appl Mater Interfaces 3(2):441–446. https://doi.org/10.1021/am101018g
60. Ye W, Yan J, Ye Q, Zhou F (2010) Template-free and direct electrochemical deposition of hierarchical dendritic gold microstructures: growth and their multiple applications. J Phys Chem C 114(37):15617–15624. https://doi.org/10.1021/jp105929b
61. Ye W, Kou H, Liu Q, Yan J, Zhou F, Wang C (2012) Electrochemical deposition of Au-Pt alloy particles with cauliflower-like microstructures for electrocatalytic methanol oxidation. Int J Hydrogen Energy 37(5):4088–4097. https://doi.org/10.1016/j.ijhydene.2011.11.132
62. Song Y, Ma Y, Wang Y, Di J, Tu Y (2010) Electrochemical deposition of gold-platinum alloy nanoparticles on an indium tin oxide electrode and their electrocatalytic applications. Electrochim Acta 55(17):4909–4914. https://doi.org/10.1016/j.electacta.2010.03.089
63. Dobrovetska O, Kuntyi O, Saldan I, Korniy S, Okhremchuk Y, Reshetnyak O (2015) Nanostructured gold–palladium electrodeposited in dimethylsulfoxide solutions. Mater Lett 158:317–321. https://doi.org/10.1016/j.matlet.2015.06.041
64. Feltham AM, Spiro M (1971) Platinized platinum electrodes. Chem Rev 71(2):177–193. https://doi.org/10.1021/cr60270a002
65. Chen A, Holt-Hindle P (2010) Platinum-based nanostructured materials: synthesis, properties, and applications. Chem Rev 110:3767–3804. https://doi.org/10.1021/cr9003902
66. Rao CRK, Trivedi DC (2005) Chemical and electrochemical depositions of platinum group metals and their applications. Coord Chem Rev 249:613–631. https://doi.org/10.1016/j.ccr.2004.08.015
67. Mathe MK, Mkwizu T, Modibedi M (2012) Electrocatalysis research for fuel cells and hydrogen production. Energy Procedia 29:401–408. https://doi.org/10.1016/j.egypro.2012.09.047
68. Singh RN, Awasthi R, Sharma CS (2014) Review: an overview of recent development of platinum-based cathode materials for direct methanol fuel cells. Int J Electrochem Sci 9:5607–5639. http://www.electrochemsci.org/papers/vol9/91005607.pdf
69. Sui S, Wang X, Zhou X, Su Y, Riffat S, Liu C (2017) A comprehensive review of Pt electrocatalysts for the oxygen reduction reaction: nanostructure, activity, mechanism and carbon support in PEM fuel cells. J Mater Chem A 5(5):1808–1825. https://doi.org/10.1039/c6ta08580f
70. Muthukumar V, Chetty R (2017) Morphological transformation of electrodeposited Pt and its electrocatalytic activity towards direct formic acid fuel cells. J Appl Electrochem 47(6):735–745. https://doi.org/10.1007/s10800-017-1076-z
71. Zhong C, Hu WB, Cheng YF (2011) On the essential role of current density in electrocatalytic activity of the electrodeposited platinum for oxidation of ammonia. J Power Sources 196:8064–8072. https://doi.org/10.1016/j.jpowsour.2011.05.058
72. Bertin E, Garbarino S, Guay D, Solla-Gullón J, Vidal-Iglesias FJ, Feliu JM (2013) Electrodeposited platinum thin films with preferential (100) orientation: characterization and electrocatalytic properties for ammonia and formic acid oxidation. J Power Sources 225:323–329. https://doi.org/10.1016/j.jpowsour.2012.09.090
73. Geboes B, Ustarroz J, Sentosun K, Vanrompay H, Hubin A, Bals S, Breugelmans T (2016) Electrochemical behavior of electrodeposited nanoporous Pt catalysts for the oxygen reduction reaction. ACS Catal 6:5856–5864. https://doi.org/10.1021/acscatal.6b00668
74. Ustarroz J, Geboes B, Vanrompay H, Sentosun K, Bals S, Breugelmans T, Hubin A (2017) Electrodeposition of highly porous Pt nanoparticles studied by quantitative 3D electron tomography: influence of growth mechanisms and potential cycling on the active surface area. ACS Appl Mater Interfaces 9:16168–16177. https://doi.org/10.1021/acsami.7b01619

75. Doan N, Figueiredo MC, Johans C, Kallio T (2016) Electrodeposited mesoporous Pt for direct ethanol fuel cells anodes. Int J Electrochem Sci 11:7631–7643. http://dx.doi.org/10.20964/2016.09.06
76. Liu J, Wang X, Lin Z, Cao Y, Zheng ZZ, Zeng Z, Hu Z (2014) Shape-controllable pulse electrodeposition of ultrafine platinum nanodendrites for methanol catalytic combustion and the investigation of their local electric field intensification by electrostatic force microscope and finite element method. Electrochim Acta 136:66–74. https://doi.org/10.1016/j.electacta.2014.05.082
77. Ye F, Li J, Wang T, Liu Y, Wei H, Li J, Wang X (2008) Electrocatalytic properties of platinum catalysts prepared by pulse electrodeposition method using SnO_2 as an assisting reagent. J Phys Chem C 112:12894–12898. https://doi.org/10.1021/jp803188s
78. Tiwari JN, Pan FM, Lin KL (2009) Facile approach to the synthesis of 3D platinum nanoflowers and their electrochemical characteristics. New J Chem 33:1482–1485. https://doi.org/10.1039/b901534p
79. Zhou M, Dick JE, Bard AJ (2017) Electrodeposition of isolated platinum atoms and clusters on bismuth—characterization and electrocatalysis. J Am Chem Soc 139(48):17677–17682. https://doi.org/10.1021/jacs.7b10646
80. Lertanantawong B, Surareungchai W, O'Mullane AP (2016) Utilising solution dispersed platinum nanoparticles to direct the growth of electrodeposited platinum nanostructures and its influence on the electrocatalytic oxidation of small organic molecules. J Electroanal Chem 779:99–105. https://doi.org/10.1016/j.jelechem.2016.04.030
81. Kasian OI, Luk'yanenko TV, Demchenko P, Gladyshevskii RE, Amadelli R, Velichenko AB (2013) Electrochemical properties of thermally treated platinized Ebonex® with low content of Pt. Electrochim Acta 109:630–637. https://doi.org/10.1016/j.electacta.2013.07.162
82. Kasian O, Luk'yanenko T, Velichenko A, Amadelli R (2012) Electrochemical behavior of platinized Ebonex® electrodes. Int J Electrochem Sci 7:7915–7926. http://www.electrochemsci.org/papers/vol7/7097915.pdf
83. He P, Liu H, Li Z, Li J (2005) Electrodeposition of platinum in room-temperature ionic liquids and electrocatalytic effect on electro-oxidation of methanol. J Electrochem Soc 152(4):E146–E153. https://doi.org/10.1149/1.1870754
84. Yao K, Cheng YF (2007) Electrodeposited Ni–Pt binary alloys as electrocatalysts for oxidation of ammonia. J Power Sources 173:96–101. https://doi.org/10.1016/j.jpowsour.2007.04.081
85. Woo S, Kim I, Lee JK, Bong S, Lee J, Kim H (2011) Preparation of cost-effective Pt–Co electrodes by pulse electrodeposition for PEMFC electrocatalysts. Electrochim Acta 56:3036–3041. https://doi.org/10.1016/j.electacta.2011.01.002
86. Hu Y, Zhang H, Wu P, Zhang H, Zhou B, Cai C (2011) Bimetallic Pt–Au nanocatalysts electrochemically deposited on grapheme and their electrocatalytic characteristics towards oxygen reduction and methanol oxidation. Phys Chem Chem Phys 13:4083–4094. https://doi.org/10.1039/c0cp01998d
87. Mkwizu TS, Mathe MK, Cukrowski I (2013) Multilayered nanoclusters of platinum and gold: insights on electrodeposition pathways, electrocatalysis, surface and bulk compositional properties. J Electrochem Soc 160(9):H529–H546. https://doi.org/10.1149/2.018309jes
88. Jow JJ, Yang SW, Chen HR, Wu MS, Ling TR, Wei TY (2009) Co-electrodeposition of Pt–Ru electrocatalysts in electrolytes with varying compositions by a double-potential pulse method for the oxidation of MeOH and CO. Int J Hydrogen Energy 34:665–671. https://doi.org/10.1016/j.ijhydene.2008.11.032
89. Ureta-Zañartu MS, Yáñez C, Reyes G, Gancedo JR, Marco JF (1998) Electrodeposited Pt–Ir electrodes: characterization and electrocatalytic activity for the reduction of the nitrate ion. J Solid State Electrochem 2:191–197. https://doi.org/10.1007/s100080050086
90. Venarusso LB, Sato RH, Fiorito PA, Maia G (2013) Platinum systems electrodeposited in the presence of iron or palladium on a sold surface effectively catalyze oxygen reduction reaction. J Phys Chem C 117(15):7540–7551. https://doi.org/10.1021/jp311343w
91. Hwang SJ, Yoo SJ, Jang S, Lim TH, Hong SA, Kim SK (2011) Ternary Pt–Fe–Co alloy electrocatalysts prepared by electrodeposition: elucidating the roles of Fe and Co in the oxygen reduction reaction. J Phys Chem C 115:2483–2488. https://doi.org/10.1021/jp106947q

92. Papaderakis A, Pliatsikas N, Prochaska C, Papazisi KM, Balomenou SP, Tsiplakides D, Patsalas P, Sotiropoulos S (2014) Ternary Pt–Ru–Ni catalytic layers for methanol electrooxidation prepared by electrodeposition and galvanic replacement. Front Chem 2:29. https://doi.org/10.3389/fchem.2014.00029
93. Liu H, He P, Li Z, Li J (2006) High surface area nanoporous platinum: facile fabrication and electrocatalytic activity. Nanotechnology 17:2167–2173. https://doi.org/10.1088/0957-4484/17/9/015
94. Kibler LA, Soliman KA, Plumer A, Wildi CS, Bringley E, Mueller JE, Jacob T (2017) Electrodeposition of Ag overlayers onto Pt(111): structural, electrochemical and electrocatalytic properties. Electrocatalysis 8(6):605–615. https://doi.org/10.1007/s12678-017-0386-6
95. Shim JH, Kim YS, Kang M, Lee C, Lee Y (2012) Electrocatalytic activity of nanoporous Pd and Pt: effect of structural features. Phys Chem Chem Phys 14:3974–3979. https://doi.org/10.1039/c2cp23429g
96. Maniam KK, Chetty R (2013) Electrodeposited palladium nanoflowers for electrocatalytic applications. Fuel Cells 13(6):1196–1204. https://doi.org/10.1002/fuce.201200162
97. Hong YH, Tsai YC (2009) Electrodeposition of platinum and ruthenium nanoparticles in multiwalled carbon nanotube-Nafion nanocomposite for methanol electrooxidation. J Nanomater 2009:892178. https://doi.org/10.1155/2009/892178
98. Zulke AA, Matos R, Pereira EC (2013) Metallic multilayered films electrodeposited over titanium as catalysts for methanol electro-oxidation. Electrochim Acta 105:578–583. https://doi.org/10.1016/j.electacta.2013.05.027
99. Zhang B, Ye D, Li J, Zhu X, Liao Q (2012) Electrodeposition of Pd catalyst layer on graphite rod electrodes for direct formic acid oxidation. J Power Sour 214:277–284. https://doi.org/10.1016/j.jpowsour.2012.04.007
100. Maillard F, Gloaguen F, Leger JM (2003) Preparation of methanol oxidation electrocatalysts: ruthenium deposition on carbon-supported platinum nanoparticles. J Appl Electrochem 33(1):1–8. https://doi.org/10.1023/a:1022906615060
101. Espino-López IE, Romero-Romo M, Montes de Oca-Yemha MG, Morales-Gil P, Ramírez-Silva MT, Mostany J, Palomar-Pardavé M (2019) Palladium nanoparticles electrodeposition onto glassy carbon from a deep eutectic solvent at 298 K and their catalytic performance toward formic acid oxidation. J Electrochem Soc 166(1):D3205–D3211. https://doi.org/10.1149/2.0251901jes
102. Vykhodtseva LN, Kulakova II, Safonov VA (2008) Electrocatalytic formation of polymolecular products at the cathodic polarization of polycrystalline chromium in sulfuric acid solutions of formic and oxalic acids. Russ J Electrochem 44(8):877–883. https://doi.org/10.1134/S1023193508080016
103. Safonov VA, Vykhodtseva LN, Polukarov YM, Safonova OV, Smolentsev G, Sikora M, Eeckhout SG, Glatzel P (2006) Valence-to-core X-ray emission spectroscopy identification of carbide compounds in nanocrystalline Cr coatings deposited from Cr(III) electrolytes containing organic substances. J Phys Chem B 110(46):23192–23196. https://doi.org/10.1021/jp064569j
104. Protsenko VS, Gordiienko VO, Danilov FI (2012) Unusual "chemical" mechanism of carbon co-deposition in Cr-C alloy electrodeposition process from trivalent chromium bath. Electrochem Commun 17:85–87. https://doi.org/10.1016/j.elecom.2012.02.013
105. Danilov FI, Protsenko VS, Gordiienko VO (2013) Electrode processes occurring during the electrodeposition of chromium–carbon coatings from solutions of Cr(III) salts with carbamide and formic acid additions. Russ J Electrochem 49(5):475–482. https://doi.org/10.1134/S1023193513050054
106. Schmuecker SM, Clouser D, Kraus TJ, Leonard BM (2017) Synthesis of metastable chromium carbide nanomaterials and their electrocatalytic activity for the hydrogen evolution reaction. Dalton Trans 46:13524–13530. https://doi.org/10.1039/c7dt01404j
107. Tomás-García AL, Jensen JO, Bjerrum NJ, Li Q (2014) Hydrogen evolution activity and electrochemical stability of selected transition metal carbides in concentrated phosphoric acid. Electrochim Acta 137:639–646. https://doi.org/10.1016/j.electacta.2014.06.087

108. Tsirlina GA, Petrii OA (1987) Hydrogen evolution on smooth stoichiometric tungsten and chromium carbides. Electrochim Acta 32:649–657. https://doi.org/10.1016/0013-4686(87)87056-1
109. Safonova OV, Vykhodtseva LN, Polyakov NA, Swarbrick JC, Sikora M, Glatzel P, Safonov VA (2010) Chemical composition and structural transformations of amorphous chromium coatings electrodeposited from Cr(III) electrolytes. Electrochim Acta 56:145–153. https://doi.org/10.1016/j.electacta.2010.08.108
110. Protsenko VS, Danilov FI, Gordiienko VO, Baskevich AS, Artemchuk VV (2012) Improving hardness and tribological characteristics of nanocrystalline Cr-C films obtained from Cr(III) plating bath using pulsed electrodeposition. Int J Refract Met Hard Mater 31:281–283. https://doi.org/10.1016/j.ijrmhm.2011.10.006
111. Danilov FI, Protsenko VS, Gordiienko VO, Baskevich AS, Artemchuk VV (2012) Electrodeposition of nanocrystalline chromium-carbon alloys from electrolyte based on trivalent chromium sulfate using pulsed current. Prot Met Phys Chem Surf 48:328–333. https://doi.org/10.1134/S2070205112030057
112. Protsenko VS, Gordiienko VO, Danilov FI, Kwon SC, Kim M, Lee JY (2011) Unusually high current efficiency of nanocrystalline Cr electrodeposition process from trivalent chromium bath. Surf Eng 27(9):690–692. https://doi.org/10.1179/1743294410Y.0000000019
113. Survilienė S, Nivinskienė O, Češunienė A, Selskis A (2006) Effect of Cr(III) solution chemistry on electrodeposition of chromium. J Appl Electrochem 36:649–654. https://doi.org/10.1007/s10800-005-9105-8
114. Protsenko VS, Danilov FI (2014) Chromium electroplating from trivalent chromium baths as an environmentally friendly alternative to hazardous hexavalent chromium baths: comparative study on advantages and disadvantages. Clean Techn Environ Policy 16(6):1201–1206. https://doi.org/10.1007/s10098-014-0711-1
115. Abbott AP, Al-Barzinjy AA, Abbott PD, Frish G, Harris RC, Hartley J, Ryder KS (2014) Speciation, physical and electrolytic properties of eutectic mixtures based on $CrCl_3{\cdot}6H_2O$ and urea. Phys Chem Chem Phys 16:9047–9055. https://doi.org/10.1039/C4CP00057A
116. Ferreira ESC, Pereira CM, Silva AF (2013) Electrochemical studies of metallic chromium electrodeposition from a Cr(III) bath. J Electroanal Chem 707:52–58. https://doi.org/10.1016/j.jelechem.2013.08.005
117. McCalman DC, Sun L, Zhang Y, Brennecke JF, Maginn EJ, Schneider WF (2015) Speciation, conductivities, diffusivities, and electrochemical reduction as a function of water content in mixtures of hydrated chromium chloride/choline chloride. J Phys Chem B 119:6018–6023. https://doi.org/10.1021/acs.jpcb.5b01986
118. Bobrova LS, Danilov FI, Protsenko VS (2016) Effects of temperature and water content on physicochemical properties of ionic liquids containing $CrCl_3{\cdot}xH_2O$ and choline chloride. J Mol Liq 223:48–53. https://doi.org/10.1016/j.molliq.2016.08.027
119. Protsenko VS, Bobrova LS, Danilov FI (2017) Physicochemical properties of ionic liquid mixtures containing choline chloride, chromium (III) chloride and water: effects of temperature and water content. Ionics 23:637–643. https://doi.org/10.1007/s11581-016-1826-7
120. Protsenko V, Bobrova L, Danilov F (2018) Trivalent chromium electrodeposition using a deep eutectic solvent. Anti-Corros Methods Mater 65:499–505. https://doi.org/10.1108/ACMM-05-2018-1946
121. Protsenko VS, Bobrova LS, Korniy SA, Kityk AA, Danilov FI (2018) Corrosion resistance and protective properties of chromium coatings electrodeposited from an electrolyte based on deep eutectic solvent. Funct Mater 25(3):539–545. https://doi.org/10.15407/fm25.03.539
122. Protsenko VS, Bobrova LS, Butyrina TE, Danilov FI (2019) Hydrogen evolution reaction on Cr–C electrocatalysts electrodeposited from a choline chloride based trivalent chromium plating bath. Voprosy Khimii i Khimicheskoi Tekhnologii (1):61–66. https://doi.org/10.32434/0321-4095-2019-122-1-61-66
123. Boiadjieva-Scherzer T, Kronberger H, Fafilek G, Monev M (2016) Hydrogen evolution reaction on electrodeposited Zn–Cr alloy coatings. J Electroanal Chem 783:68–75. https://doi.org/10.1016/j.jelechem.2016.10.059

124. Low CTJ, Wills RGA, Walsh FC (2006) Electrodeposition of composite coatings containing nanoparticles in a metal deposit. Surf Coat Technol 201:371–383. https://doi.org/10.1016/j.surfcoat.2005.11.123
125. Walsh FC, Ponce de Leon C (2014) A review of the electrodeposition of metal matrix composite coatings by inclusion of particles in a metal layer: an established and diversifying technology. Trans Inst Met Finish 92:83–98. https://doi.org/10.1179/0020296713Z.000000000161
126. Mirkova L, Monev M, Petkova N (2009) Hydrogen evolution, diffusion and solution in Ni/based composite electrodeposits. ECS Trans 19(10):105–112. https://doi.org/10.1149/1.3237112
127. Abdel Aal A, Hassan HB (2009) Electrodeposited nanocomposite coatings for fuel cell application. J Alloys Compd 477:652–656. https://doi.org/10.1016/j.jallcom.2008.10.116
128. Gierlotka D, Rówiński E, Budniok A, Łagiewka E (1997) Production and properties of electrolytic Ni–P–TiO_2 composite layers. J Appl Electrochem 27:1349–1354. https://doi.org/10.1023/A:1018416927715
129. Kullaiah R, Elias L, Hegde AC (2018) Effect of TiO_2 nanoparticles on hydrogen evolution reaction activity of Ni coatings. Int J Miner Metall Mater 25(4):472–479. https://doi.org/10.1007/s12613-018-1593-8
130. Shibli SMA, Dilimon VS (2007) Effect of phosphorous content and TiO_2-reinforcement on Ni–P electroless plates for hydrogen evolution reaction. Int J Hydrogen Energy 32:1694–1700. https://doi.org/10.1016/j.ijhydene.2006.11.037
131. Shibli SMA, Dilimon VS (2008) Development of TiO_2-supported nano-RuO_2-incorporated catalytic nickel coating for hydrogen evolution reaction. Int J Hydrogen Energy 33:1104–1111. https://doi.org/10.1016/j.ijhydene.2007.12.038
132. Danilov FI, Tsurkan AV, Vasil'eva EA, Protsenko VS (2016) Electrocatalytic activity of composite Fe/TiO_2 electrodeposits for hydrogen evolution reaction in alkaline solutions. Int J Hydrogen Energy 41:7363–7372. https://doi.org/10.1016/j.ijhydene.2016.02.112
133. Protsenko VS, Tsurkan AV, Vasil'eva EA, Baskevich AS, Korniy SA, Cheipesh TO, Danilov FI (2018) Fabrication and characterization of multifunctional Fe/TiO_2 composite coatings. Mater Res Bull 100:32–41. https://doi.org/10.1016/j.materresbull.2017.11.051
134. Protsenko VS, Vasil'eva EA, Tsurkan AV, Kityk AA, Korniy SA, Danilov FI (2017) Fe/TiO_2 composite coatings modified by ceria layer: Electrochemical synthesis using environmentally friendly methanesulfonate electrolytes and application as photocatalysts for organic dyes degradation. J Environ Chem Eng 5:136–146. https://doi.org/10.1016/j.jece.2016.11.034
135. Vasil'eva EA, Tsurkan AV, Protsenko VS, Danilov FI (2016) Electrodeposition of composite Fe–TiO_2 coatings from methanesulfonate electrolyte. Prot Met Phys Chem Surf 52:532–537. https://doi.org/10.1134/S2070205116030278
136. Protsenko VS, Vasil'eva EA, Smenova IV, Danilov FI (2014) Electrodeposition of iron/titania composite coatings from methanesulfonate electrolyte. Russ J Appl Chem 87:283–288. https://doi.org/10.1134/S1070427214030069
137. Chen X, Mao SS (2007) Titanium dioxide nanomaterials: synthesis, properties, modifications, and applications. Chem Rev 107:2891–2959. https://doi.org/10.1021/cr0500535
138. Gernon MD, Wu M, Buszta T, Janney P (1999) Environmental benefits of methanesulfonic acid: Comparative properties and advantages. Green Chem 1:127–140. https://doi.org/10.1039/a900157c
139. Walsh FC, Ponce de León C (2014) Versatile electrochemical coatings and surface layers from aqueous methanesulfonic acid. Surf Coat Technol 259:676–697. https://doi.org/10.1016/j.surfcoat.2014.10.010
140. Cai C, Zhu XB, Zheng GQ, Yuan YN, Huang XQ, Cao FH, Yang JF, Zhang Z (2011) Electrodeposition and characterization of nano-structured Ni–SiC composite films. Surf Coat Technol 205:3448–3454. https://doi.org/10.1016/j.surfcoat.2010.12.002
141. Mirkova L, Pashova V, Monev M (2011) Study of hydrogen evolution reaction on Ni/Co_3O_4 composite electrode in alkaline solution. ECS Trans 35(21):77–84. https://doi.org/10.1149/1.3641467

142. Wang L, Li Y, Yin X, Wang Y, Song A, Ma Z, Qin X, Shao G (2017) Coral-like-structured Ni/C_3N_4 composite coating: an active electrocatalyst for hydrogen evolution reaction in alkaline solution. ACS Sustain Chem Eng 5:7993–8003. https://doi.org/10.1021/acssuschemeng.7b01576
143. Wang L, Li Y, Yin X, Wang Y, Lu L, Song A, Xia M, Li Z, Qin X, Shao G (2017) Comparison of three nickel-based carbon composite catalysts for hydrogen evolution reaction in alkaline solution. Int J Hydrogen Energy 42:22655–22662. https://doi.org/10.1016/j.ijhydene.2017.06.215
144. Elias L, Hegde AC (2017) Effect of including the carbon nanotube and graphene oxide on the electrocatalytic behavior of the Ni–W alloy for the hydrogen evolution reaction. New J Chem 41:13912–13917. https://doi.org/10.1039/C7NJ02722B
145. Wang S, Li W, Qin H, Liu L, Chen Y, Xiang D (2019) Electrodeposition of Ni-Fe-Co-graphene composite coatings and their electrocatalytic activity for hydrogen evolution reaction. Int J Electrochem Sci 14:957–969. http://dx.doi.org/10.20964/2019.01.73
146. Elias L, Hegde AC (2018) Electrolytic synthesis of Ni-W-MWCNT composite coating for alkaline hydrogen evolution reaction. J Mater Eng Perform 27(3):1033–1039. https://doi.org/10.1007/s11665-018-3134-z
147. Wu G, Li N, Dai CS, Zhou DR (2004) Electrochemical preparation and characteristics of Ni–Co–$LaNi_5$ composite coatings as electrode materials for hydrogen evolution. Mater Chem Phys 83:307–314. https://doi.org/10.1016/j.matchemphys.2003.10.005
148. Chen Z, Shao G, Ma Z, Song J, Wang G, Huang W (2015) Preparation of Ni–CeO_2 composite coatings with high catalytic activity for hydrogen evolution reaction. Mater Lett 160:34–37. https://doi.org/10.1016/j.matlet.2015.07.081
149. Zhang K, Li J, Liu W, Liu J, Yan C (2016) Electrocatalytic activity and electrochemical stability of Ni–S/CeO_2 composite electrode for hydrogen evolution in alkaline water electrolysis. Int J Hydrogen Energy 41:22643–22651. https://doi.org/10.1016/j.ijhydene.2016.08.229
150. Sheng M, Weng W, Wang Y, Wu Q, Hou S (2018) Co–W/CeO_2 composite coatings for highly active electrocatalysis of hydrogen evolution reaction. J Alloys Compd 743:682–690. https://doi.org/10.1016/j.jallcom.2018.01.356
151. Yang YJ, Hu S (2010) Electrodeposited MnO_2/Au composite film with improved electrocatalytic activity for oxidation of glucose and hydrogen peroxide. Electrochim Acta 55:3471–3476. https://doi.org/10.1016/j.electacta.2010.01.095
152. Miao HJ, Piron DL (1993) Composite-coating electrodes for hydrogen evolution reaction. Electrochim Acta 38(8):1079–1085. https://doi.org/10.1016/0013-4686(93)80216-M
153. Elias L, Hegde AC (2016) Synthesis and characterization of Ni–P–Ag composite coating as efficient electrocatalyst for alkaline hydrogen evolution reaction. Electrochim Acta 219:377–385. https://doi.org/10.1016/j.electacta.2016.10.024
154. Tu WY, Xu BS, Dong SY, Wang HD (2006) Electrocatalytic action of nano-SiO2 with electrodeposited nickel matrix. Mater Lett 60:1247–1250. https://doi.org/10.1016/j.matlet.2005.11.008
155. Tu WY, Xu BS, Dong SY, Wang HD, Bin J (2008) Chemical and electrocatalytical interaction: influence of non-electroactive ceramic nanoparticles on nickel electrodeposition and composite coating. J Mater Sci 43:1102–1108. https://doi.org/10.1007/s10853-007-2259-5

Carbon Based Electrocatalysts

Sonal Singh, Rishabh Sharma and Manika Khanuja

Abstract Electrochemical energy conversion technologies, such as polymer electrolyte fuel cells, Direct Methanol fuel cells and metal-air batteries are of supreme significance to attain sustainable energy for future use. Nanocomposite materials have fast emerged as promising candidates as a replacement to commercial and state-of-the-art electrocatalysts. They show remarkably increasing progress in electrocatalysis including oxygen evolution, oxygen reduction, CO_2 reduction, hydrogen evolution etc. Carbon support with high surface area provides better utilization of the electrocatalysts to escalate its activity. Electrocatalysis has been the subject of growing interest for many concerned people as it caters to the escalating needs of fuel production. Researchers and manufacturers are keen to cash in the burgeoning demand of nanocomposite based electrocatalyst materials and devices as they exhibit distinctive surface/size-dependent and simplistic tunable structures which are pivotal for the performance of electrocatalysis process. Regulation and modulation of electronic properties is realizable through adaption of various surface chemistry techniques. This chapter gives an insight to the application of nanocomposite materials in electrocatalysis and their properties which gives perspective to probe further in this rising field of research to expand scientific understanding and build upon the current body of work.

Sonal Singh and Rishabh Sharma—Both the authors have contributed equal to this work.

S. Singh
Shaheed Rajguru College of Applied Sciences for Women, University of Delhi,
New Delhi 110096, India
e-mail: sonal.singh0811@gmail.com

R. Sharma
Thin Film Laboratory, Department of Physics, Indian Institute of Technology,
New Delhi 110016, India
e-mail: rishabh.rammstien@gmail.com

M. Khanuja (✉)
Centre for Nanoscience and Nanotechnology, Jamia Millia Islamia (A Central University),
New Delhi 110025, India
e-mail: manikakhanuja@gmail.com

Inamuddin et al. (eds.), *Methods for Electrocatalysis*,
https://doi.org/10.1007/978-3-030-27161-9_12

Keywords Nanocomposite materials · Electrocatalysis · Water splitting · Hydrogen evolution · Fuel cells

1 Introduction

Mounting concern towards future energy scenario demands the replacement of fossil fuels with renewable and sustainable energies. Green and clean splitting of water achieved through several renewable ways such solar-thermal and nuclear thermal energy can effectively cater to the need. Out of many forms of catalysis, electrocatalysis is one specific form that holds special interest in the field of Electrochemistry for the purpose of water splitting for hydrogen evolution. Until late eighties, most of the work was limited only for academic purposes, however with the emergence of new concepts in electrocatalysis later, it became a peremptory need for the industrialists and engineers as well [1]. The process of electrocatalysis basically involves the presence of electrocatalyst material (or electrodes) that enables a usually faster chemical rate of the reaction by either changing the reaction kinetics or mechanism sometimes. Electrocatalyst facilitates the electron charge transfer between the reactants and the electrode, and/or assists an intermediate chemical transformation described by an overall half-reaction [2]. The progression and advancements in electrocatalysis has become possible due to the significant improvement in the field of surface science as the preparation and design of an electrocatalyst are based upon new concepts such as atomic topographic profiles and atomic rearrangements, controlled surface roughness, defined catalytic center sites and phase transitions in the course of the electrochemical reactions. It has been well demonstrated that due to various fascinating properties, nanomaterials have become center of focus aiming at cost-effective and high-efficient electrocatalysis system by stepping into the role of precious metal catalysts, which have now been able to displace state-of-the-art and commercial precious metal-based catalysts such as Pt, RuO_2, IrO_2, Ir etc. [3]. Till date, numerous nano/nano-carbon/nanocomposite materials with unique structure and properties have been routinely used to enhance the metal utilization, fuel-selectivity and stability to reduce the metal loading [4]. Nanocarbons, when coupled with certain organic and inorganic nanomaterials, can perform multiple functions such as to accelerate inter-component charge transfer, modify composite growth or bring about confinement resulting in significantly enhanced performances [5, 6].

This field holds a great scope to welcome new scientific inventions and concepts with the help of nanocomposite materials that can stimulate breakthroughs and prove critical to the development of novel electrochemical technologies. In this chapter, we will focus on the applications of various nanocomposite materials based on carbon and its derivatives, metal and bimetals and use of doping and dual doping concepts in order to augment the cell performance.

2 Nanocomposite Applications in Electrocatalysis

Fuel cells, for long, have garnered major attention as promising power generator, especially DMFC's (Direct Methanol Fuel Cells), due to their low operating temperature, high energy conversion efficiency, ease of handling and low pollutant release [7]. Use of suitable electrocatalysts in fuel cells is one of the crucial factors to achieve high-energy densities. Due to high methanol oxidation activity, Platinum is one of the most sought-after, well-known and widely used catalyst. However, being a precious metal, platinum has a high cost and thus the amount of platinum used must be curtailed with a view to keep the prices of DMFC's low [8]. Also, platinum is readily oxidized by byproduct of methanol oxidation i.e. CO. Therefore, it is needed to invent more Pt-based alloy catalysts with higher methanol oxidation activity and substantial poison tolerance. Particle size, shape and dispersion of platinum-based electrocatalysts are prime parameters that govern their ORR (Oxygen Reduction Reaction) rate and performance of DMFCs. Scientists and researchers have come up with the variety of techniques such as use of hybrid electrode materials to cut down the cost of catalysis set-up. A variety of commonly used carbon support materials include graphite nanofibers (GNF), carbon black (CB), carbon aerogels and carbon nanotubes (CNTs) consisting of incorporated Platinum nanoparticles to form a nanocomposite type structures have been well explored. Researchers have been successful in preparing highly mesoporous, low-defect and functionalized nanocomposites as a high performance electrocatalysts for DMFC's [7, 9].

Here, we discuss in-depth about some prominent carbon-materials and their properties that are nowadays highly used to form nanocomposite electrodes for electrocatalysis.

2.1 Graphene

Over a decade has been passed in understanding the physiochemical properties of graphene with view of utilizing them as an essential carbon substrate in electrocatalysis. Graphene has already played an outstanding role in this regard and has been continuing to do so. It has been utilized in a wide number of ways such as- doped and undoped graphene supported platinum, graphene with non-precious metals, graphene-inorganic particle nanocomposites, heteroatom doped graphene catalysts, dual-doped graphene and graphene/nanostructured carbon composites. Graphene with its variant derivatives like graphene oxide (GO), graphite oxide and reduced graphene oxide (rGO) are also used. Graphene are essentially two-dimensional sheet like structures with hexagonal arrangements of carbon atoms bonded in sp2 configuration. It offers fascinating surface, electronic and mechanical properties which can be further fine-tuned or manipulated for application in electrocatalysis [10, 11]. Oxidation of graphite leads to the preparation of a solid material "Graphite oxide" which expands the interlayer spacing and functionalizes the basal planes. Graphite oxide in

the exfoliated form is known as “Graphene oxide”, a highly soluble material, which is generally synthesized by dispersing it in an aqueous solvent while rGO results from the reduction of Graphene oxide.

Scientists have strengthened the deposition of platinum nanoparticles on to the graphene nanoplatelets [12] or GO [13] by functionalizing them using poly(diallyldimethylammonium chloride), termed PDDA. It is however well known that platinum can be affected by surfactants, polymers and small adsorbing molecules that can potentially cause contamination over the surface and obstructs the viability of this approach [14]. Zeng et al. demonstrated this approach to functionalize GO with a polymer namely quaternary ammonia poly (2, 6-dimethyl-1, 4-phenylene oxide) which allowed better anchoring of even smaller platinum nanoparticles [15]. Similarly, He et al. used perfluorosulfonic acid functionalized rGO to uniformly disperse Pt nanoparticles of size approx 1–4 nm [16].

Functionalization has become a well-studied technique but yet has not achieved complete satisfactory results. Well-known are the effects of dopant introduction into the graphitic carbon support structures, which may exhibit up to three-fold beneficial influence on the stability and activity of nanoparticle catalysts, if conducted appropriately [17]. Heteroatom species favorably work by serving as nucleation sites which aids in deposition of well dispersed and uniformly sized Pt nanoparticles. The modulation of electronic structure and surface properties of Pt leads to enhanced ORR activity [18, 19]. Nitrogen [20–22] and Sulphur [23–25] are two extensively investigated dopants for this purpose in graphene based materials along with phosphorus [26], boron [27, 28] and iodine [29]. Many research groups have recently pursued the concept of dual doping i.e. incorporation of dopant species in combination with another dopant in graphene-based materials. It was found that dual doping in carbon structure tailored the properties of the surface in a manner that is favorable for oxygen reduction reaction kinetics [30–32]. Studies by Wang et al. [33] and Xue et al. [34] successfully synthesized boron- and nitrogen-doped graphene based structures desirable for electrocatalysis applications. Graphene doped with dual dopants like nitrogen and sulphur [30, 35] and phosphorus and nitrogen [36] has also been investigated.

To minimize the dependency of platinum, Graphene-based non-precious metal catalysts (NPMC) are also actively under investigation. Till date, complexes of transition metal-nitrogen-carbon have been reckoned as the most propitious NPMC of this class. Unfortunately, they sometimes lack adequate stability as compared to platinum-based materials. Nanostructured metal chalcogenides have emerged as one major class of NPMC [37]. Among all other NPMC chalcogenides, structures of Cobalt sulfide have arisen as ORR electrocatalysts showing tremendous activity in acidic electrolyte, ascribed to their exceptional phase-dependent electronic, catalytic and magnetic properties [38, 39]. A new cobalt sulfide-graphene-based catalyst synthesized via two-step process of solution-phase reaction at low-temperature followed by pyrolysis at high temperature was obtained by Wang et al. [39].

2.2 Carbon Nanotubes (CNTS)

Many groups show the successful synthesis of CNT's coupled with platinum metal to form low-defect MWNT_Pt, PtRu/Carbon Nanotube, Platinum/Carbon Nanotube nanocomposite etc. and exhibited enhanced electrocatalytic activity [7, 40, 41]. Due to unique structural and optical properties, such as good electronic conductivity, high external surfaces, high stability and large surface to volume ratio, CNTs are of particular interest [42, 43]. CNTs alone generally lack high loading efficiency of nanocrystals as they possess weak binding sites on their surface which becomes difficult to anchor metal nanoparticles or metal ions with high dispersion. In this regard, many strategies have been developed to decorate CNTs with platinum nanoparticles. Surface functionalization of carbon nanotubes is one such effective approach which can be achieved via two major routes. First is to covalently attach chemical groups such as carbonyl, carboxyl and hydroxyl groups through reactions onto the π-conjugated skeleton of the CNTs via acid treatment. However, this brings structural deformity of CNTs altering their mechanical, optical, and electrical properties, consequently leading to deterioration of electrochemical performance. Due to transformation of carbon atoms from a planar sp2-hybridized geometry to a distorted sp3-hybridized geometry results in subtle reduction of conductivity with increase in oxidation which is the major pitfall of this approach [44, 45]. Second route is absorption through noncovalent π_π stacking [45, 46] which involves coupling of modified organic compounds like aniline to support platinum nanoparticles onto the external walls of nanotubes [47–49]. However, excessive use of aromatic organic compounds should be avoided as they are highly toxic.

Lin et al. investigated the role of CNTs as carbon substrate to form nanocomposite with metal and bi-metal i.e. Platinum/CNT (Pt/CNT) and Platinum/ruthenium/CNT (PtRu/CNT) nanocomposites, respectively [40, 41]. They demonstrated supercritical fluid technique to successfully deposit Pt nanoparticles on surface of CNT which served as an effective electrocatalysts for low-temperature fuel cells. Decrease in methanol oxidation overpotential and large surface area of CNT were main factors attributed for its high catalytic activity. However, bi-metallic PtRu/CNT indicated even better performance than Pt/CNT nanocomposite. The presence of Ru with Pt proves beneficial since it lowers the onset potential and accelerates the rate of methanol oxidation by increasing the ratio of forward anodic peak current to reverse anodic peak.

2.3 Other Carbon Based and Metallic Nanocomposite Materials

Other types such as ordered porous carbon [50], carbon tubule membranes [51], films of C60 clusters [52], graphite nanofibers [53], and hard carbon spherules [54], have been used as carbon supports for DMFCs. Of late, carbon aerogels and carbon black

have been used in fuel cell applications as catalysts support. Fundamental properties of carbon aerogels such as high mesoporosity, high conductivity, and large surface area likely makes them worthy electrocatalyst anchors than carbon blacks. Mass transportation of fuel is affected by the pore structure in fuel cell electrodes. The mesoporous structure of carbon aerogel is attributed as one of the vital factors that can facilitate the mass transportation in the electrode [55]. Anderson et al. demonstrated the use of carbon-silica composite aerogels to develop highly active electro-catalytic nanostructured architectures which claimed to have improved the methanol oxidation by 4 times per gram of Pt over Pt-modified carbon powder [56]. Sometimes, in case of carbon black, catalytic nanoparticles have tendency to weakly get adsorbed on the carbon which agglomerates over time limiting the device operating lifetime. Ding et al. carried out an interesting study on Metallic Mesoporous Nanocomposites for electrocatalysis in which they used atomically thin layer of Pt over nanoporous gold core [9].

3 Conclusion

New ways related to methodical research in material design & synthesis, mechanism understanding, and device optimization and integration have to be found out to eliminate or minimize common problems associated with DMFCs such as low catalytic activity of electrodes both for methanol oxidation reaction and ORR. Platinum, alone, due to high cost and toxicity demands a replacement or some coupling materials that can minimize its use in electrocatalysis that can lead to a high-efficiency and targeted development of electrocatalysis system. Carbon based nanocomposite structures, due to their unique features, are a great hope which provides ample opportunity in this direction that can highly dilute the obstacles inhibiting the applications of fuel cells and turn suggestive approaches into practical accomplishments. The on-going research is mainly based on trial-and-error approaches that paves the way for optimization of relationship between nanocarbon-based electrocatalysts structure and its activity. Discoveries like use of metallic and bimetallic catalysts in supercritical carbon dioxide, doing using single and dual dopants demonstrated the practicality of processing for fuel cell applications but still needs to bridge the gap by various progresses. For example, the various impacts of nitrogen and its behavior on graphene are not fully studied. Systematic studies to gain understanding on how a dopant species in graphene can influence the rate of corrosion and how might show different ORR activities are still lacking. In order to take graphene technology related to a higher level it is critical to consider the relation of nanostructures with NPMC catalyst and effects on graphene by changing dopant concentrations.

Acknowledgements Authors are highly grateful to the institution for providing facilities for carrying out this piece of work.

References

1. Zinola CF, Martins ME, Tejera EP, Pimenta N Jr (2012) Electrocatalysis: fundamentals and applications. Int J Electrochem 2012:2012–2014. https://doi.org/10.1155/2012/874687
2. Elbaz L (2014) INREP Electrochemistry Summer School
3. Tang C, Titirici M, Zhang Q (2017) A review of nanocarbons in energy electrocatalysis: multifunctional substrates and highly active sites. J Energy Chem. https://doi.org/10.1016/j.jechem.2017.08.008
4. Su DS, Centi G (2013) A perspective on carbon materials for future energy application. J Energy Chem 22:151–173
5. Wang H, Dai H (2013) Strongly coupled inorganic–nano-carbon hybrid materials for energy storage. Chem Soc Rev 42:3088–3113
6. Tang C, Wang H, Zhu X, Li B, Zhang Q (2016) Advances in hybrid electrocatalysts for oxygen evolution reactions: rational integration of NiFe layered double hydroxides and nanocarbon. Part Part Syst Charact 33:473–486
7. Huang H, Sun D, Wang X (2011) Low-defect MWNT–Pt nanocomposite as a high performance electrocatalyst for direct methanol fuel cells, 19405–19412
8. Wang JJ, Yin G-P, Zhang J, Wang ZB, Gao YZ (2007) High utilization platinum deposition on single-walled carbon nanotubes as catalysts for direct methanol fuel cell. Electrochim Acta 52:7042–7050
9. Ding Y, Chen M, Erlebacher J (2004) Metallic mesoporous nanocomposites for electrocatalysis, 6876–6877
10. Geim AK, Novoselov KS (2010) The rise of graphene, nanoscience and technology: a collection of reviews from nature journals. World Sci, 11–19
11. Allen MJ, Tung VC, Kaner RB (2009) Honeycomb carbon: a review of graphene. Chem Rev 110:132–145
12. Shao Y, Zhang S, Wang C, Nie Z, Liu J, Wang Y, Lin Y (2010) Highly durable graphene nanoplatelets supported Pt nanocatalysts for oxygen reduction. J Power Sour 195:4600–4605
13. He W, Jiang H, Zhou Y, Yang S, Xue X, Zou Z, Zhang X, Akins DL, Yang H (2012) An efficient reduction route for the production of Pd–Pt nanoparticles anchored on graphene nanosheets for use as durable oxygen reduction electrocatalysts. Carbon 50:265–274
14. Borup R, Meyers J, Pivovar B, Kim YS, Mukundan R, Garland N, Myers D, Wilson M, Garzon F, Wood D (2007) Scientific aspects of polymer electrolyte fuel cell durability and degradation. Chem Rev 107:3904–3951
15. Zeng L, Zhao TS, An L, Zhao G, Yan XH, Jung CY (2015) Graphene-supported platinum catalyst prepared with ionomer as surfactant for anion exchange membrane fuel cells. J Power Sources 275:506–515
16. He D, Cheng K, Li H, Peng T, Xu F, Mu S, Pan M (2012) Highly active platinum nanoparticles on graphene nanosheets with a significant improvement in stability and CO tolerance. Langmuir 28:3979–3986
17. Zhou Y, Neyerlin K, Olson TS, Pylypenko S, Bult J, Dinh HN, Gennett T, Shao Z, O'Hayre R (2010) Enhancement of Pt and Pt-alloy fuel cell catalyst activity and durability via nitrogen-modified carbon supports. Energy Environ Sci 3:1437–1446
18. Zhu J, Xiao M, Zhao X, Liu C, Ge J, Xing W (2015) Strongly coupled Pt nanotubes/N-doped graphene as highly active and durable electrocatalysts for oxygen reduction reaction. Nano Energy. 13:318–326
19. Higgins D, Hoque MA, Seo MH, Wang R, Hassan F, Choi J, Pritzker M, Yu A, Zhang J, Chen Z (2014) Development and simulation of sulfur-doped graphene supported platinum with exemplary stability and activity towards oxygen reduction. Adv Funct Mater 24:4325–4336
20. Geng D, Chen Y, Chen Y, Li Y, Li R, Sun X, Ye S, Knights S (2011) High oxygen-reduction activity and durability of nitrogen-doped graphene. Energy Environ Sci 4:760–764
21. Lai L, Potts JR, Zhan D, Wang L, Poh CK, Tang C, Gong H, Shen Z, Lin J, Ruoff RS (2012) Exploration of the active center structure of nitrogen-doped graphene-based catalysts for oxygen reduction reaction. Energy Environ Sci 5:7936–7942

22. Vikkisk M, Kruusenberg I, Joost U, Shulga E, Kink I, Tammeveski K (2014) Electrocatalytic oxygen reduction on nitrogen-doped graphene in alkaline media. Appl Catal B Environ 147:369–376
23. Yang S, Zhi L, Tang K, Feng X, Maier J, Müllen K (2012) Efficient synthesis of heteroatom (N or S)-doped graphene based on ultrathin graphene oxide-porous silica sheets for oxygen reduction reactions. Adv Funct Mater 22:3634–3640
24. Zhang Y, Chu M, Yang L, Deng W, Tan Y, Ma M, Xie Q (2014) Synthesis and oxygen reduction properties of three-dimensional sulfur-doped graphene networks. Chem Commun 50:6382–6385
25. Chen Y, Li J, Mei T, Hu X, Liu D, Wang J, Hao M, Li J, Wang J, Wang X (2014) Low-temperature and one-pot synthesis of sulfurized graphene nanosheets via in situ doping and their superior electrocatalytic activity for oxygen reduction reaction. J Mater Chem A 2:20714–20722
26. Zhang C, Mahmood N, Yin H, Liu F, Hou Y (2013) Synthesis of phosphorus-doped graphene and its multifunctional applications for oxygen reduction reaction and lithium ion batteries. Adv Mater 25:4932–4937
27. Jiao Y, Zheng Y, Jaroniec M, Qiao SZ (2014) Origin of the electrocatalytic oxygen reduction activity of graphene-based catalysts: a roadmap to achieve the best performance. J Am Chem Soc 136:4394–4403
28. Sheng Z-H, Gao H-L, Bao W-J, Wang F-B, Xia X-H (2012) Synthesis of boron doped graphene for oxygen reduction reaction in fuel cells. J Mater Chem 22:390–395
29. Yao Z, Nie H, Yang Z, Zhou X, Liu Z, Huang S (2012) Catalyst-free synthesis of iodine-doped graphene via a facile thermal annealing process and its use for electrocatalytic oxygen reduction in an alkaline medium. Chem Commun 48:1027–1029
30. Bag S, Mondal B, Das AK, Raj CR (2015) Nitrogen and sulfur dual-doped reduced graphene oxide: synergistic effect of dopants towards oxygen reduction reaction. Electrochim Acta 163:16–23
31. Choi CH, Chung MW, Kwon HC, Park SH, Woo SI (2013) B, N-and P, N-doped graphene as highly active catalysts for oxygen reduction reactions in acidic media. J Mater Chem A 1:3694–3699
32. Chang Y, Hong F, He C, Zhang Q, Liu J (2013) Nitrogen and sulfur dual-doped non-noble catalyst using fluidic acrylonitrile telomer as precursor for efficient oxygen reduction. Adv Mater 25:4794–4799
33. Wang S, Zhang L, Xia Z, Roy A, Chang DW, Baek J, Dai L (2012) BCN graphene as efficient metal-free electrocatalyst for the oxygen reduction reaction. Angew Chemie Int Ed 51:4209–4212
34. Xue Y, Yu D, Dai L, Wang R, Li D, Roy A, Lu F, Chen H, Liu Y, Qu J (2013) Three-dimensional B, N-doped graphene foam as a metal-free catalyst for oxygen reduction reaction. Phys Chem Chem Phys 15:12220–12226
35. You J-M, Ahmed MS, Han HS, eun Choe J, Üstündağ Z, Jeon S (2015) New approach of nitrogen and sulfur-doped graphene synthesis using dipyrrolemethane and their electrocatalytic activity for oxygen reduction in alkaline media. J Power Sour 275:73–79
36. Choi CH, Park SH, Woo SI (2012) Binary and ternary doping of nitrogen, boron, and phosphorus into carbon for enhancing electrochemical oxygen reduction activity. ACS Nano 6:7084–7091
37. Gao M-R, Xu Y-F, Jiang J, Yu S-H (2013) Nanostructured metal chalcogenides: synthesis, modification, and applications in energy conversion and storage devices. Chem Soc Rev 42:2986–3017
38. Higgins DC, Hassan FM, Seo MH, Choi JY, Hoque MA, Lee DU, Chen Z (2015) Shape-controlled octahedral cobalt disulfide nanoparticles supported on nitrogen and sulfur-doped graphene/carbon nanotube composites for oxygen reduction in acidic electrolyte. J Mater Chem A 3:6340–6350
39. Wang H, Liang Y, Li Y, Dai H (2011) $Co_{1-x}S$–graphene hybrid: a high-performance metal chalcogenide electrocatalyst for oxygen reduction. Angew Chemie Int Ed 50:10969–10972
40. Lin Y, Cui X, Yen C, Wai CM (2005) Platinum/carbon nanotube nanocomposite synthesized in supercritical fluid as electrocatalysts for low-temperature fuel cells, 14410–14415

41. Lin Y, Cui X, Yen CH, Wai CM (2005) PtRu/carbon nanotube nanocomposite synthesized in supercritical fluid : a novel electrocatalyst for direct methanol fuel cells, 11474–11479
42. Baughman RH, Zakhidov AA, De Heer WA (2002) Carbon nanotubes—the route toward applications. Science (80-.) 297:787–792
43. Prabhuram J, Zhao TS, Tang ZK, Chen R, Liang ZX (2006) Multiwalled carbon nanotube supported PtRu for the anode of direct methanol fuel cells. J Phys Chem B 110:5245–5252
44. Chu H, Wei L, Cui R, Wang J, Li Y (2010) Carbon nanotubes combined with inorganic nanomaterials: preparations and applications. Coord Chem Rev 254:1117–1134
45. Wu B, Kuang Y, Zhang X, Chen J (2011) Noble metal nanoparticles/carbon nanotubes nanohybrids: synthesis and applications. Nano Today 6:75–90
46. Tasis D, Tagmatarchis N, Bianco A, Prato M (2006) Chemistry of carbon nanotubes. Chem Rev 106:1105–1136
47. Wang D, Lu S, Jiang SP (2010) Tetrahydrofuran-functionalized multi-walled carbon nanotubes as effective support for Pt and PtSn electrocatalysts of fuel cells. Electrochim Acta 55:2964–2971
48. Hsu C-H, Liao H-Y, Kuo P-L (2010) Aniline as a dispersant and stabilizer for the preparation of Pt nanoparticles deposited on carbon nanotubes. J Phys Chem C 114:7933–7939
49. Mu Y, Liang H, Hu J, Jiang L, Wan L (2005) Controllable Pt nanoparticle deposition on carbon nanotubes as an anode catalyst for direct methanol fuel cells. J Phys Chem B 109:22212–22216
50. Chai GS, Yoon SB, Yu J-S, Choi J-H, Sung Y-E (2004) Ordered porous carbons with tunable pore sizes as catalyst supports in direct methanol fuel cell. J Phys Chem B 108:7074–7079
51. Che G, Lakshmi BB, Fisher CJ, Martin CR (1998) Nature 393:346
52. Vinodgopal K, Haria M, Meisel D, Kamat P (2004) Fullerene-based carbon nanostructures for methanol oxidation. Nano Lett 4:415–418
53. Bessel CA, Laubernds K, Rodriguez NM, Baker RTK (2001) Graphite nanofibers as an electrode for fuel cell applications. J Phys Chem B 105:1115–1118
54. Yang R, Qiu X, Zhang H, Li J, Zhu W, Wang Z, Huang X, Chen L (2005) Monodispersed hard carbon spherules as a catalyst support for the electrooxidation of methanol. Carbon 43:11–16
55. Yaldagard M, Jahanshahi M, Seghatoleslami N et al (2013) Carbonaceous nanostructured support materials for low temperature fuel cell electrocatalysts—a review, 121–153
56. Anderson ML, Stroud RM, Rolison DR (2002) Enhancing the activity of fuel-cell reactions by designing three-dimensional nanostructured architectures: catalyst-modified carbon–silica composite aerogels. Nano Lett 2:235–240

State-of-the-Art Advances and Perspectives for Electrocatalysis

Kabelo E. Ramohlola, Mpitloane J. Hato, Gobeng R. Monama, Edwin Makhado, Emmanuel I. Iwuoha and Kwena D. Modibane

Abstract Electrocatalysis stands as a heart for realization of hydrogen gas (H_2) as a source of energy to replace conventional and traditional fossil fuel based energy. In this chapter, we present a comprehensive overview of the state-of-the-art molybdenum disulphide (MoS_2) nanostructures for application in electrolytic hydrogen evolution reaction (HER). MoS_2 is a crystalline compound consisting of Mo sandwiched between two sulfur atoms and can be identified in four poly-type structures, namely 1T, 1H, 2H and 3R. Firstly, the reaction accompanied with water splitting electrolysis, HER mechanisms as well as parameters to monitor HER reactions are discussed. Furthermore, the chapter describes different types of MoS_2 poly-types, chemical synthetic routes and key approaches to activate inert S-containing basal plane of MoS_2. This led to superior performance of new materials by combining the advantages of MoS_2 components and others. Finally, future integration approaches which can be used to attain MoS_2 with exposed edges and excellent electron transport channel are also outlined in this chapter.

Keywords Hydrogen gas · Electrocatalysis · Hydrogen evolution reaction · Molybdenum disulphide nanostructures

K. E. Ramohlola · M. J. Hato · G. R. Monama · E. Makhado · K. D. Modibane (✉)
Nanotechnology Research Lab, Department of Chemistry, School of Physical and Mineral Sciences, University of Limpopo, Polokwane, Sovenga 0727, South Africa
e-mail: kwena.modibane@ul.ac.za

M. J. Hato
e-mail: mpitloane.hato@ul.ac.za

E. I. Iwuoha
SensorLab, Chemical Science Department, University of the Western Cape, Bellville, Cape Town 7535, South Africa

M. J. Hato
Department of Environmental Sciences, College of Agriculture and Environmental Sciences, University of South Africa, Florida Science Campus, Johannesburg 1710, South Africa

Inamuddin et al. (eds.), *Methods for Electrocatalysis*,
https://doi.org/10.1007/978-3-030-27161-9_13

1 Introduction

Hydrogen (H_2) gas has been considered as a favourable candidate to substitute the non-sustainable conventional fossil fuels based energy sources, to alleviate the energy problem and environmental pollution [17, 77, 153]. Among several hydrogen production methods, electrochemical water splitting is regarded as an efficient and clean technology as it offers H_2 with high purity and free greenhouse gas emissions [85]. The water splitting electrolysis is an energy driven reaction and consists of two major reactions, namely; the reduction of hydrogen proton on the cathode known as hydrogen evolution reaction (HER) and oxidation process on the anode called oxygen evolution reaction (OER) [1, 51, 127]. In principle, electrocatalysts stand as a major component to minimize the energy barrier by lowering the overpotential and increasing the rate of an electrochemical reaction occurring on an electrode surface. In this case, realization and commercialization of HER requires development of an abundant, stable and active electrocatalyst. Therefore, there is an increase in the number of studies conducted in electrocatalysis with the great hope of finding a best suitable electrocatalyst for HER. The advanced and ideal electrocatalyst should have the following requirements on the fundamental level [80, 90, 135]:

- Low overpotential to achieve current density of 10 mA/cm^2,
- High active surface which facilitates adsorption and desorption of hydrogen proton (H^+) and molecular hydrogen (H_2) efficiently,
- High electrical and intrinsi conductivity (allows diffusion of electrons),
- Superior chemical stability (able to work properly in different media (acidic, neutral and alkaline),
- Good electrochemical stability (resist corrosion at long ranges overpotentials),
- Excellent mechanical stability (compatible to work on harsh conditions i.e. high temperature),
- Long term durability and stability (maintain its catalytic performance for a long time and cycles).

Furthermore, commercialization also requires cheap electrocatalyst in order to compete with traditional fossil fuel based energy systems [32]. In this direction, Platinum group metal (PGM) based electrocatalysts meet various requirements for HER electrocatalyst as they exhibit low overpotential, high catalytic activity, fast kinetics and are most stable [50, 73, 92]. However, their costness and scarcity are the key hindrances for trade applications [70, 146]. For that reason, realization of large-scale electrochemical generation of hydrogen for large-scale production needs the development of cheap, containing-earth-abundant elements electrocatalysts with catalytic performance matching the ones of Pt electrocatalysts [37, 91, 108]. Electrocatalysts based on metal-free materials such as conducting polymers (CPs) and carbonaceous (graphene, carbon nanotubes and activated carbons) have also been rarely investigated for HER. CPs such as polypyrrole (Ppy) and polyaniline (PANI) have shown great environmental stability on ranges of potential windows and they are inexpensive [74]. Based on this properties, CPs can be used to replace the PGM-based electrocatalysts as well as corrosion prone earth-abundant such as Fe, Ni, Mo

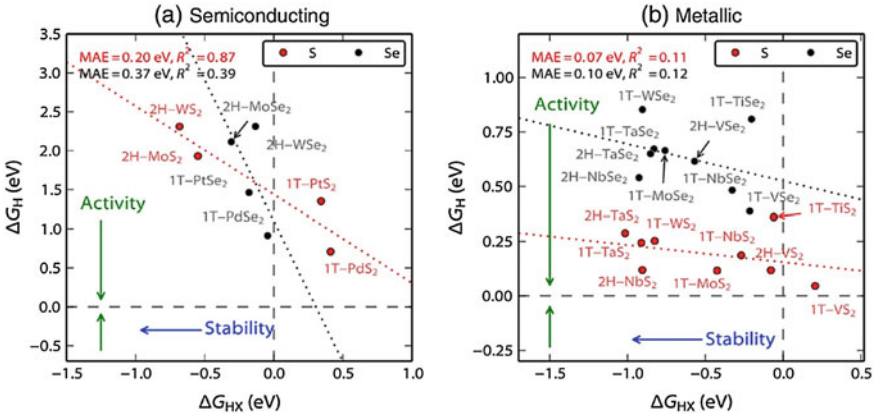

Fig. 1 Graph of Gibbs free energy of hydrogen adsorption, ΔG_H, versus the Gibbs free energy of adsorbed hydrogen on chalcogen, ΔG_{HX} (X = S or Se) of **a** Semiconducting single-layered and **b** Metallic monolayer transition metal chalcogenide basal planes [114]

and Co. PANI and Ppy have been greatly studied as a catalytic support on abundant metals for HER electrocatalysis [22, 43]. The key purpose for integrating the metal units into polymer matrices is to scatter the metal nanoparticles as to increase active site density of these materials resulting in enhanced HER performance [22]. The pristine carbon materials such as graphene oxide, activated carbon and carbon nanotubes (CNTs) are inert (electrochemically) and they possess low catalytic efficiency for HER [145]. In order to utilize carbon materials, chemical modification or functionalization on their surface with metal oxides is required to increase anchoring sites which consequently will increase their electrocatalytic activity [108, 145].

Recently, organometallic complexes have been proposed to be potential substitutes of Pt-group metals [64]. In order to utilize organometallic complexes as HER electrocatalysts, more efforts and attention need to be place in order to address their low activity in aqueous solution and instability due to their inherent vulnerability to disintegration [64, 77]. Porous coordination materials, particularly metal organic frameworks (MOFs) which are built from covalent bond coordination between cationic metal ions and anionic polydentate organic ligands have been used recently for electrochemical applications such as supercapacitor and gas sensing [13, 25, 76]. Based on this, MOFs bode well to be used as OER and HER electrocatalyst. Due to MOFs poor electrical conductivity which is attributed from insulation behaviour of organic precursor and poor overlap between organic linker π-orbital and metal ion d-orbital, little consideration has been paid to MOF as HER electrocatalyst [78]. Talin et al. [105] and Ramohlola et al. [86, 87] reported methods which can be used to address poor conductivity of MOF and this include: (1) introduction of channel-accessible functionalities on framework linkers, and (2) physical incorporation of donor (proton) or carriers into the tunable pores of MOF.

Transition-metal chalcogenides (Fig. 1) such as sulphides, carbides and nitrides electrocatalysts for HER have been recently focused on due to their outstanding

electrical conductivity and excellent durability [27, 133, 146, 119]. Molybdenum disulphide (MoS_2) has attracted widespread consideration as an alternative material to be used as a noble-free electrocatalysts in the HER due to its ease of synthesis, low cost, high catalytic activity as well as earth-abundance [45, 55, 130, 144]. MoS_2 has a hexagonally or vertically layered packed structure (graphite-like structure) consisting of a single layer of Mo sandwiched between two sulfur atoms in a trigonal prismatic arrangement held together by weak van der Waals force [5, 140]. From Fig. 1, it can be seen that both metallic and semiconductor MoS_2 (1T and 2H) possess great HER activity and the Gibbs free energy of adsorbed hydrogen (ΔG_{Had}) denoted by ΔG_{HX}, which is the broadly recognized pointer for the catalytic performance and its optimum value is 0 eV, for 1T-MoS_2 is close to that one of Pt. Till today, countless efforts have been made to improve the performance of MoS_2 as HER electrocatalysts as HER activity of MoS_2 correlates with the number of catalytically active edge sites [32, 100]. There are two approaches to improve the performance of MoS_2 which includes revealing active sites and increasing the electrical conduction for enhancing the electron transfer [89, 144]. Introducing defects has demonstrated to be an active method to create active sites [136].

In this chapter, the recent developments and advances of MoS_2 heterostructures for HER applications are summarized. This is achieved by doing comprehensive review on the insights reaction and their related mechanisms of water electrolysis as well as overview on parameters to monitor the activity of electrocatalyst. Then, we introduce the state-of-the-art MoS_2 heterostructures with great emphasis on the structure and synthetic routes. Furthermore, we describe the challenges and approaches faced by MoS_2 are described and highlights on the recent studies which are on addressing the limitation encountered by MoS_2 are outlined. Finally, we summarize and give a future perspective for realization of MoS_2 as electrocatalyst.

2 Hydrogen Evolution Reactions

2.1 Insight of Reactions During Water Electrolysis

In a typical water electrolysis system, H_2 and O_2 gases are produced at the cathode and anode through the hydrogen evolution reaction (HER) and oxygen evolution reaction (OER), respectively, and an external energy is applied to overcome the energy barrier of the reaction (2.46 eV) [1, 51, 124, 127]. The overall water splitting electrolysis can be represented by the following Equation (Eq. 1) [14, 111, 132]:

$$2H_2O \rightarrow 2H_2 + O_2 \quad E_p = 1.23\,V \tag{1}$$

As explained above, the overall process consists of hydrogen, H_2 and oxygen, O_2 generation on the cathode and anode, respectively. In different media, the water splitting processes have different equilibrium half-cell potentials. In acidic medium

(pH 0–6), the corresponding half-cell reactions are given by Eqs. 2 and 3:

$$4H^+ + 4e^- \rightarrow 2H_2 \quad E_c^\circ = 0.0\,V \tag{2}$$

$$2H_2O \rightarrow O_2 + 4H^+ + 4e^- \quad E_a^\circ = 1.23\,V \tag{3}$$

where, E_c° and E_a° are the cathodic and anodic equilibrium half-cell potentials at standard conditions (1 atm, 25 °C), respectively. In neutral solution (pH 7), the corresponding reactions (Eqs. 4 and 5) are:

$$4H_2O + 4e^- \rightarrow 2H_2 + 4OH^- \quad E_c^\circ = 0.413\,V \tag{4}$$

$$2H_2O \rightarrow O_2 + 4H^+ + 4e^- \quad E_a^\circ = 0.817\,V \tag{5}$$

In alkaline medium (pH 8–14), the reactions proceed following Eqs. 6 and 7:

$$4H_2O + 4e^- \rightarrow 2H_2 + 4OH^- \quad E_c^\circ = -0.826\,V \tag{6}$$

$$2H_2O \rightarrow O_2 + 4H^+ + 4e^- \quad E_a^\circ = -0.404\,V \tag{7}$$

Due to the presence of deprotonated water molecules in both acidic and alkaline solutions, water splitting is favoured in both solutions as compared to neutral solutions, hence the production of hydrogen in neutral solution is kinetically difficult to achieve [14].

2.2 *Mechanism of Electrochemical HER*

Electrochemical HER is an essential redox process that occur at the electrolyte/electrode interface. Most importantly, the nature of the electrolyte (acidic or alkaline) plays a vital part in the mechanistic progression of the reaction. The series of elementary steps involved can generate H_2 through proton (H^+) (acidic) or H_2O (alkaline) reduction.

2.2.1 HER in Acidic Media

In an acidic solution, initial step is the electrochemical discharge (Volmer reaction) in which hydrogen proton (H^+) adsorb onto the electrocatalyst surface as illustrated in Eq. 8 [94, 132, 152].

$$H^+ + e^- \rightarrow H_{ad} \quad b = \frac{2.3RT}{\alpha F} \approx 120\,mV\ dec^{-1} \tag{8}$$

where b, T, $\alpha \approx 0.5$, R and F are the Tafel slope (mV/dec), thermodynamic temperature (K), symmetry coefficient, gas constant (8.31451 J mol^{-1} K^{-1}) and Faraday's number (96,485 C mol^{-1}), respectively.

Progression of the reaction can be preceded by electrochemical desorption (Heyrovsky) or catalytic desorption (Tafel). During Volmer-Heyrovsky mechanism, there is a reaction between H_{ad} and a proton from the electrolyte giving off molecular hydrogen (H_2) (Eq. 9).

$$H_{ad} + H^+ + e^- \rightarrow H_2 \quad b = \frac{2.3RT}{(1+\alpha)F} \approx 40\,\text{mV dec}^{-1} \tag{9}$$

In the Volmer-Tafel mechanism, two adsorbed neighbouring protons on the electrocatalyst surface react together to form molecular H_2 (Eq. 10).

$$H_{ad} + H_{ad} \rightarrow H_2 \quad b = \frac{2.3RT}{2F} \approx 30\,\text{mV dec}^{-1} \tag{10}$$

The overall reaction in acidic HER is described in the Eq. 11 below:

$$2H^+ + 2e^- \rightarrow H_2 \tag{11}$$

The two elementary processes, adsorption (Volmer) and desorption (Heyrovsky or Tafel) on electrocatalyst surface are competitive, thus an electrocatalyst for HER must have a proper balance between the two successive processes. An catalyst with weak hydrogen bonding cannot absorb the hydrogen proton efficiently which needed to start HER process and an electrocatalyst with strong hydrogen bonding strength would have a difficulty in desorbing molecular hydrogen upon completion of HER [77].

2.2.2 HER in Basic Media

Unlike in acidic media, the HER proceeds in a different way in alkaline medium and the three elementary steps can be described by Eqs. 12–14 as follows [109, 120]. Due to the insufficient of H^+ in the electrolyte, in alkaline media, HER starts from H_2O molecules dissociation in order to deliver hydrogen proton, which will adsorb in the electocatalyst surface (Eq. 12) and combine with adsorbed hydrogen proton to give molecular hydrogen (Eq. 13) [97, 132].

$$H_2O + e^- \rightarrow OH^- + H_{ad} \text{ Volmer reaction} \tag{12}$$

$$H_{ad} + H_2O + e^- \rightarrow OH^- + H_2 \text{ Heyrovsky reaction} \tag{13}$$

$$H_{ad} + H_{ad} \rightarrow H_2 \text{ Tafel reaction} \tag{14}$$

The overall reaction process is represented in Eq. 15 below, and the E° is -0.826 V versus standard hydrogen electrode (SHE).

$$2H_2O + 2e^- \rightarrow 2OH^- + H_2 \tag{15}$$

The catalytic efficiency of most electrocatalyst for HER in an alkaline media is much weaker than that in an acidic electrolyte [137]. This is mainly attributed to the low efficiency of water dissociation on the surface, resulting in sluggish kinetics and high overpotential of HER [120, 138]. This implies that generation of hydrogen molecule in basic media requires high energy consumptions.

2.3 Key Parameters to Evaluate HER Performances

Catalyst material or electrocatalyst for HER is the supreme significant element for the upright performance of the reaction. Several factors particularly electrolyte nature, can influence the activity of the electrocatalyst during HER. In order to study HER performance of an electrocatalysts, parameters which include overpotential, onset potential, Tafel analysis, impedance, stability and durability need to be evaluated in different media.

2.3.1 Overpotential and Onset Potential

Considering the overall reversible HER reaction in acidic medium given by Eq. 16,

$$2H^+ + 2e^- \leftrightarrow H_2 \tag{16}$$

the interconversion of H^+ to molecular hydrogen is difficult to attain as the forward reduction reaction is associated with the SHE. The amount of electron supplied by SHE are insufficient for the reaction to proceed, thus external potential is required to accelerate the reaction [69]. The potentials needed to activate the intrinsic barrier of the reactions are known as onset potential and overpotential (η). Onset potential is the potential in which the current start to rise, thus the reaction start to take place and Overpotential is defined as the potential required to drive the HER reaction [3, 6].

2.3.2 Tafel Analysis

Tafel analysis is generally used to elucidate the mechanisms of electrocatalysis, intrinsic properties of the electrocatalyst as well as the electrocatalytic efficiency of the HER reaction [63, 58]. Most specifically, Tafel analysis gives the above information by deducing the two most important parameters, thus Tafel slope (b) and exchange current density (i_o) [79]. In order to determine these Tafel parameters, the

linear sweep voltammograms (LSV) is transformed into a plot of η versus log *j* from the Tafel relation (Eq. 17) [104]:

$$\eta = a + b \log j \tag{17}$$

where, η is the overpotential, *a* denotes the Tafel constant, b defines the Tafel slope and *j* denotes the current density.

Tafel slope (b) is a significant property of the electocatalyst gives information about the rate-determining step (slowest step during electrochemical reaction) of the HER. In principle, the kinetic model for HER suggest that Volmer, Heyrovsky or Tafel step must have values near 120, 40 or 30 mV dec^{-1}, respectively in order to be regards as the rate-determining step [5, 61, 78]. Additionally, to further assess the inherent activity of the electrocatalysts, the exchange current density (j_o) is determined by extrapolation of the Tafel plots to j/log(j) axis when η is zero [79, 152]. The large exchange current density obtained during HER studies specifies the large surface area, and faster electron transfer process [152].

2.3.3 Turnover Frequency

Turnover frequency (TOF) of an electrocatalyst for HER is defined as the mass of hydrogen produced per active site at a given time and it is measured in H_2/s. TOF can be calculated from the current density, *j* by using the relation given in Eq. 18 [36, 74]:

$$TOF = \frac{jM}{zFm} \tag{18}$$

where *M* represents mass percentage, m defines the mass per square centimeter, *F* is the Faradays constant and *z* is the stoichiometric number of electron which is 2 in HER. The higher the TOF value shows that the electrocatalyst has increased number of active sites and produce more hydrogen gas at a given time and this tells that an electrocatalyst possess high intrinsic properties [126].

2.3.4 Impedance

Electrochemical impedance spectroscopy (EIS) can be used to study the interfacial reactions occurring and to reveal the kinetics during HER. It does this by giving information about the size of the electric resistance which can tell on how energy is consumed during the process [24]. In order to deduce the two, the charge transfer resistance, R_{ct} is determined and related to the electrochemical processes on the electrode/electrocatalyst surface. The R_{ct} value obtained corresponds with how fast the HER process is and ideally it must be as low as possible as it shows that the electron transport ability is enhanced and this lead to excellent HER activity [126].

2.3.5 Stability and Durability

Stability and durability are the most significant measurements to probe the electrocatalyst performance for commercialization process. By evaluating the two parameters, the ability of the electrocatalyst to maintain its original activity over a long range of time (stability) or cycling (durability) can be determined [40]. The nature of the electrolyte (acidic or basic) can severely affect the electrochemical stability and durability of an electrocatalyst as most are very stable in basic medium but their performance suffers in acidic medium [103]. In addition, the component of working electrode (glass carbon, carbon cloth, ITO and Au) plays a serious role on the stability, and electrochemical synthesis of electrocatalyst on working electrode surface are more stable compared to the electrodeposited and pasted one [103]. To evaluate the durability of an electrocatalyst in different media, long-term potential cycling and current-time responses at fixed potentials over lengthy periods were performed. It is distinguished that after continuous cyclic voltammograms at an accelerated scanning rate for numerous cycles, the polarization curves practically overlays with the initial one, with insignificant cathodic current loss. Long-term stability can be measured by chronopotentiometry (CP) or chronoamperometry (CA), keeping for a period of time with a particular current density and applied potential.

3 Molybdenum Disulphide (MoS_2)

Transition-metal chalcogenides (TMDCs) are compounds which are produced by sandwiching a d-block metal between a two chalcogen atoms [55, 95]. They have a common structure of MX_2, where M is the d-block metal such as Zr, Ti, W, and Mo and X is the chalcogen (S, Se and Te) [55]. Bulk TMDCs have a multilayers which are held together by weak van der Waals interactions, thus they can be broken easily to monolayers or heterostructures [106]. Owing to their tremendous properties and features, TMDCs have attracted great attention in applications such as semiconductors, photocatalysis, transistors and lubricants [26]. Among TMDCs, molybdenum disulphide (MoS_2) have been a theme of significant research for applications such as catalytic hydrodesulfurization, lithium batteries, and wear resistance [28].

3.1 Structure of MoS_2

The basic crystal structural unit of MoS_2 consists of a layer of the Mo metal surrounded by a layer of S chalcogen (Fig. 2). The interlayer spacing in bulk MoS_2 allows intercalation process in which guest molecules can be introduced [107]. Since Mo is a Group 6 transition metal, it can form six coordination with S atoms to either form trigonal prismatic or octahedral environment around Mo [2, 46]. As explained, MoS_2 form a layered structure (vertically or hexagonally) of S-Mo-S covalently bonded

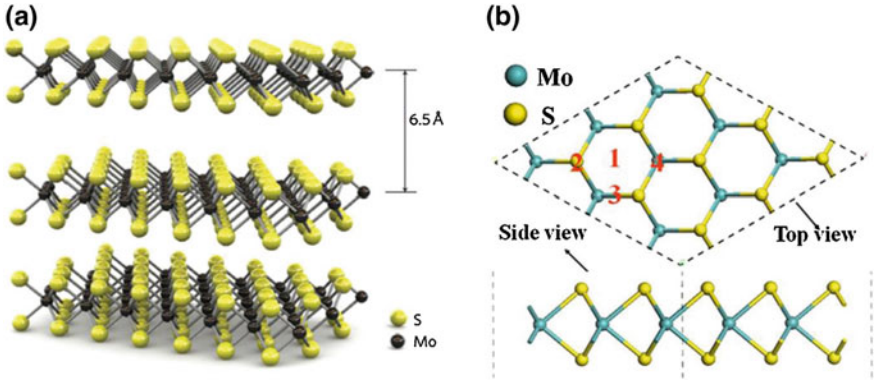

Fig. 2 **a** 3D structures of MoS_2 showing Mo sandwiched between two sulfur atoms (S-Mo-S) and the thickness of MoS_2 layers (6.5 Å). **b** Top and side view of MoS2 describing the four adsorption sites, i.e. (1) Hollow site, (2) S atom, (3) Mo-S bridge and (4) Mo atom [35]

(Mo sandwiched between S atoms), and the layers are joined together via weak van der Waals forces. The length of metal-chalcogen (Mo-S) bond is 2.42 Å and a monolayer with width of 3.18 Å [30, 140, 145]. MoS_2 monolayer has a band gap of around 1.8 eV (direct) as compared to 1.23 eV (indirect) for bulk MoS_2 [46, 140, 148]. MoS_2 has four most common structures namely, 1H, 1T, 2H and 3R (Fig. 3) and this different structure lead to MoS_2 with different properties [35].

1H- and 1T-MoS_2 are the two existing MoS_2 monolayer. In 1H-MoS_2, the Mo metal is coordinated by six S atoms in trigonal prismatic arrangement and has the space group of *P6/mmc* [35]. 1T-MoS_2 is a non-naturally occurring metastable metallic form of MoS_2. It can be obtained by exfoliating bulk 2H-MoS_2 at high temperatures. The first structure of 1T-MoS_2 was reported by Wyphch and Schöllhorn in 1992 [129]. They found that the single crystal of 1T-MoS_2 has a distorted layer

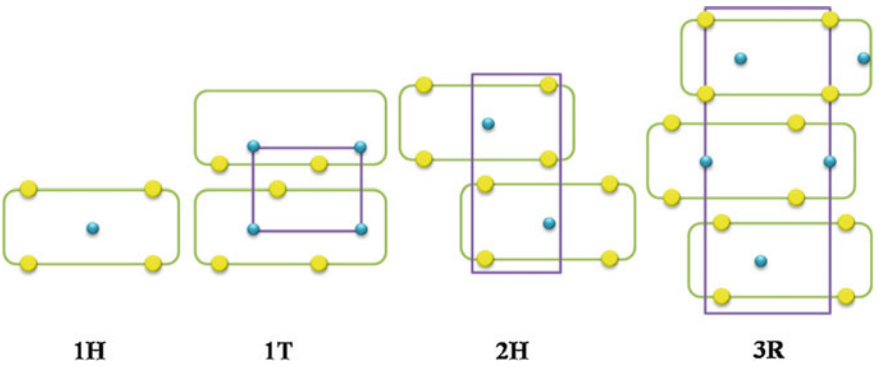

Fig. 3 Schematic illustration of different structures of MoS_2 poly-types. 1H and 1H are the existing monolayers and 2H and 3R are the polymorphs [35]

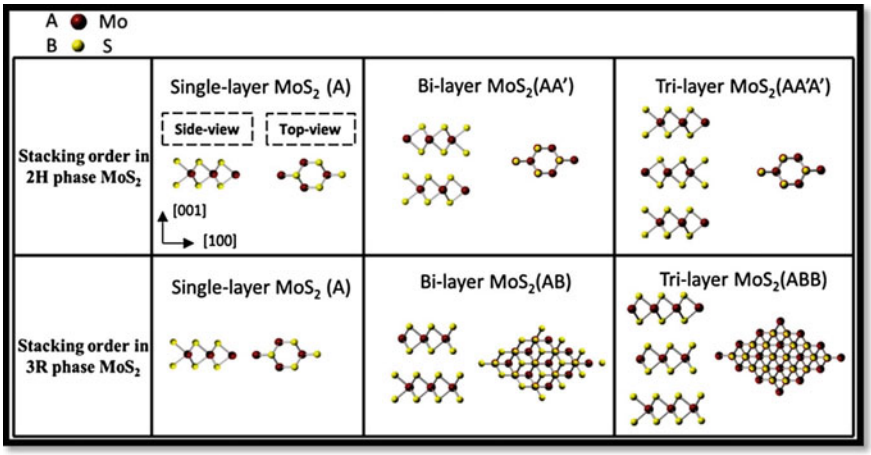

Fig. 4 Schematic showing the top and side view of MoS_2 polymorphs in different layers with their respective stacking orders [46]

with octahedral type structure. In Addition, the intercalated phases are monoclinic with one MoS_2 layer per unit cell with high crystallinity. The octahedral arranged 1T-MoS_2 has a space group of *p3m1* and the two S layers has *AB* packing mode [83, 107].

Bulk MoS_2 has two polymorphs, 2H-MoS_2 and 3R-MoS_2 with trigonal prismatic structure [83]. Hexagonally structured 2H-MoS_2 has two S-Mo-S units with space group *P63/mmc* and *ABABAB* stacking order, while 3R- MoS_2 has a rhombohedra structure (three S-Mo-S units) in space group *R3m* and *ABCABC* stacking order [46, 83, 107]. Stacking orders of both polymorphs are shown in Fig. 4. The 3R-MoS_2 structure is metastable, and will transform to 2H-MoS_2 upon annealing at 873 K for around 3 weeks.

3.2 Chemical Synthesis of MoS_2

Several approaches have been investigated to synthesis different kind of MoS_2 heterostructures. Synthetic route for MoS_2 can be categorized in two: physical method and chemical method. Physical methods involve high-energy techniques such as laser ablation, arc discharge and sputtering technique and gives MoS_2 structures which tend to aggregate. Chemical routes they involve methods which are cost effective and simple to operate such as hydro-/solvothermal, chemical vapour deposition (CVD) and sonochemical methods. In this section, we closely look at the chemical methods which were recently used for synthesis of MoS_2 structures.

3.2.1 Chemical Vapour Deposition

CVD is one of the most synthetic approach which is widely used to synthesis MoS_2 due to its advantages such as its simplicity, uniformity, low cost, and scalability, in comparison with the other chemical synthetic methods for MoS_2 [8, 31]. It involves gaseous constituents reacting in the vapour stage or on the substrate surface, forming solid products deposited directly on the substrates (Fig. 5) [39, 96]. The structural

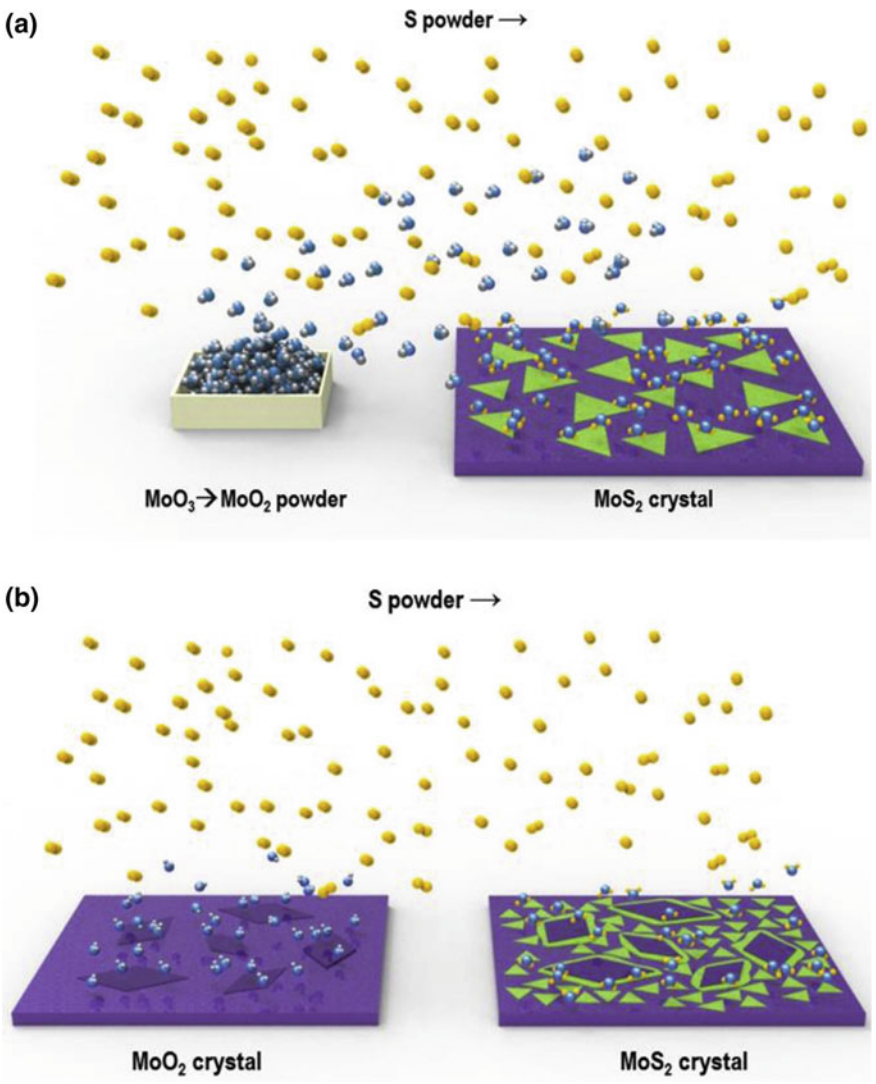

Fig. 5 Synthetic mechanism of MoS_2 synthesis using MoO_3 and molybdenum source and metallic sulfur as sulfur-precursor obtained via CVD [39]

morphology, number of MoS_2 layers, their size, and orientation, and dopants or defects introduction can be controlled efficiently by playing with the synthetic conditions/parameters such as temperature, pressure, flow rate, source–substrate distance and relative amounts of source materials. The CVD process its understood to follow three major steps, which are: (a) the MoO_3 reactant and gas-phase sulfur precursors such as H_2S and S_8 are vaporized and interacts in the CVD chambers, leading to formation of molybdenum oxysulfide (Mo-oxysulfide) intermediates; (b) this is followed by converting the Mo-oxysulfide intermediates into MoS_2 entities; and (c) the produced MoS_2 entities are deposited onto substrates and merged into MoS_2 layers [38]. Typical reactions for CVD synthesis are shown in Eqs. 19–21 below.

$$MoO_3 + 2H_2S + H_2 \rightarrow MoS_2 + 3H_2O \tag{19}$$

$$MoO_3 + 24H_2S \rightarrow 8\,MoS_2 + 24H_2O + S_8 \tag{20}$$

$$16MoO_3 + 7S_8 \rightarrow 16\,MoS_2 + 24SO_2 \tag{21}$$

From Eqs. 22 and 23 above, it can be deduced that during MoS_2 formation, by-products such SO_2 and S_8 are given off which can lead to environmental challenges such as global warming. In effort to reduce SO_2 and S_8 emission, Zhao et al. [151] reported the vapour transport behaviour of MoS_2 monolayer using MoS_2 powder as the precursor and H_2O as the transport agent. They suggested that the reaction occur via this pathways (Eqs. 22–24) and it can be deduced that the reaction gives H_2O (Eq. 24) as a by-product unlike S_8 and SO_2 (Eqs. 20 and 21):

$$MoS_2 + 4H_2O \rightarrow MoO_2 + H_2S + SO_2 + 3H_2 \tag{22}$$

$$2H_2S + SO_2 \rightarrow 3S + 2H_2O \tag{23}$$

$$MoO_2 + 2S + 2H_2 \rightarrow MoS_2 + 2H_2O \tag{24}$$

3.2.2 Solvothermal/Hydrothermal Synthesis

Solvothermal or hydrothermal route is one of the mostly used synthetic methods for preparation of nanomaterials with different morphologies and sizes. Hydrothermal method is defined as a chemical reaction in an aqueous medium above water boiling point and solvothermal as a reaction in a nonaqueous medium at relatively high temperatures. As compared to other synthetic routes, this method is very cheap, simple and fewer precursors are required [67, 118]. In addition, growth control, size of the particle as well as morphology can be controlled simultaneously in this process. During hydro-/solvothermal synthesis of MoS_2, molybdenum source such

as ammonium molybdate is used to react with sulfur precursors such as thiourea, potassium thiosulphate and thioacetimide in a Teflon autoclave at higher temperature and pressure for several hours (depending on the morphology and particle size of MoS_2 required). And because of high pressure and temperature, MoS_2 obtained is of high crystallinity and purity. For example, Choi et al. [16] and Wang et al. [119] studied the pressure and temperature effects during hydrothermal synthesis of MoS_2, respectively. From the X-ray diffraction (XRD) studies (Fig. 6a, b), it was deduced that an increase in pressure and temperature enhances the peaks and thus, the two parameters, pressure and temperature play a vital part in determining both crystallinity and purity of MoS_2.

In another study, Chaudhary et al. [12] reported the MoS_2 nanosheets with hexagonal rhombohedra structures prepared via hydrothermal route. Figure 7 presented the XRD, Ultraviolet-visible (UV-vis), Fourier transform infrared (FTIR) and Raman specta of their synthesized nanosheets. XRD showed that the MoS_2 nanosheets were crystalline with lattice constants a = b = 3.16 Å and c = 12.29 Å which correspond to ones reported theoretically. The UV-vis showed the optical band gap of 2.01 and 1.87 eV corresponding to two absorption peaks at 614 and 663 nm which were due to direct excitonic transition at the K-points of brillouin zone. FTIR and Raman confirmed the Mo-S (478 and 594 cm^{-1}), S-S (927 cm^{-1}) and Mo-O (1181 and 1695 cm^{-1}) on the synthesized MoS_2.

Recently, a facile hydrothermal synthesis assisted with surfactant was used to enhance the morphologies of MoS_2 [72, 123, 146]. Zhang et al. [148] prepared hierarchical 3D-MoS_2 nanospheres using hexadecyltrimethylammonium bromide (CTAB) as a surfactant. From scanning electron microscopy (SEM) images (Fig. 8), it can be seen that the increase in CTAB concentration results in MoS_2 nanospheres with different morphologies.

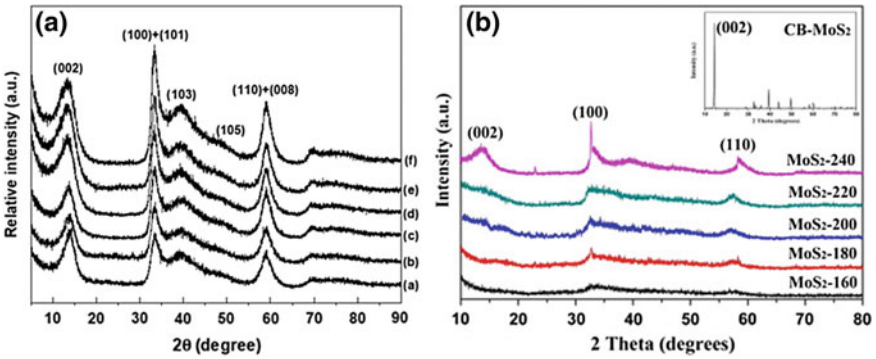

Fig. 6 XRD patterns of the MoS_2 prepared at different initial pressures: **a** 5–40 bar (**a**–**d**) and 300–400 °C (**d**–**f**) and various temperatures ranging between 160 and 240 °C [16, 119]

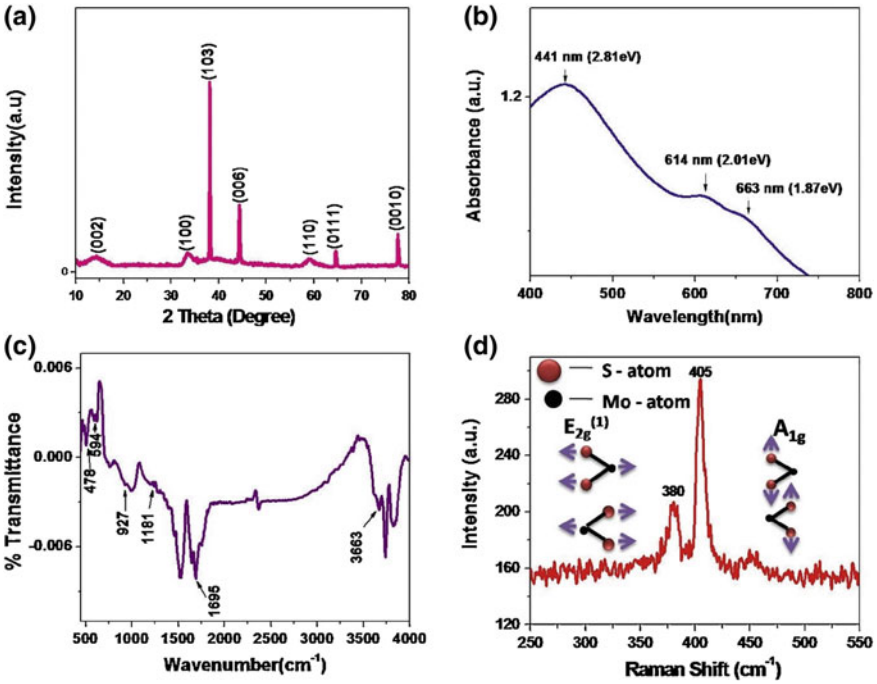

Fig. 7 **a** XRD pattern, **b** UV–vis, **c** FTIR, and **d** Raman Spectra of MoS_2 nanosheets [12]

3.2.3 Sonochemical Method

Sonochemical synthesis is a type of synthetic method in which molecules undergo chemical reaction due to ultrasound radiation (20 kHz–10 MHz). Sonochemical method have advantages such as faster reaction time, enhanced product yields and simplified experimental conditions as compared to conventional routes [155]. Discovery of sonochemical synthesis of MoS_2 was first reported by Mdleleni and co-workers in 1998 [75]. They prepared it by using molybdenum hexacarbonyl ($Mo(CO)_6$) and sulfur in isodurene (1,2,3,5-tetramethylbenzene) under 20 kHz ultrasound radiation in an Ar environment. The synthesized MoS_2 was found to have high surface area (50 m^2/g) as compared to conventional MoS_2 (32 m^2/g). Observed increase in surface area is attributed from the dispersion of metal particles on MoS_2 surface. Zuo et al. [156] reported MoS_2/Pd composite synthesized from facile sonochemical method (Fig. 9). The ultrasonic exfoliation of bulk MoS_2 yields MoS_2 nanosheets with high surface area which is essential for dispersion of Pd nanoparticles.

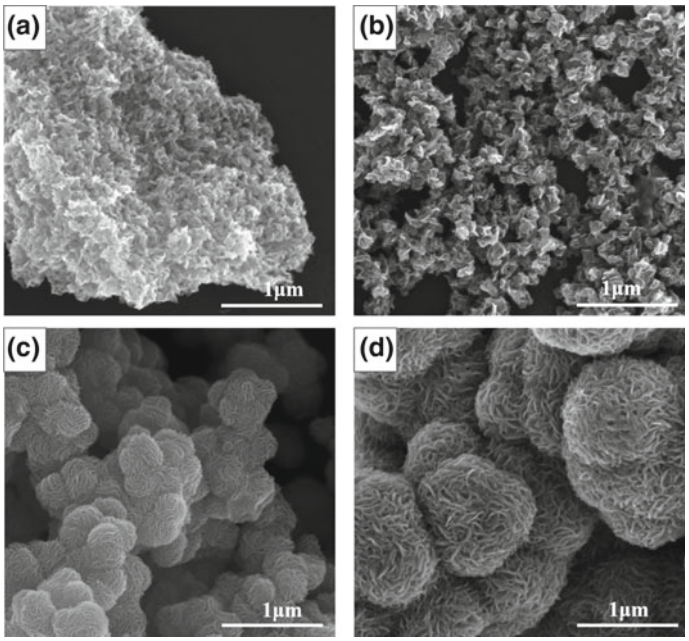

Fig. 8 Morphologies (**a**–**d**) of the prepared obtained from the facile hydrothermal route in the present of different amounts (0–0.5 g) of CTAB [148]

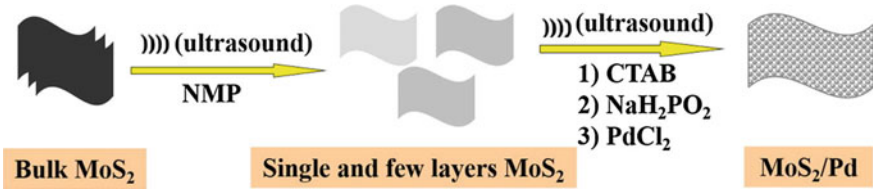

Fig. 9 Schematic design of the progress of fabrication process of sonochemical doping of Pd on MoS_2 to form MoS_2/Pd composite [157]

4 MoS_2 as HER Electrocatalyst

The first report for application of bulk MoS_2 as HER electrocatalyst was reported by Tributsch and Bennett in 1977 [112]. However, the bulk MoS_2 have a large band gap which results in sluggish HER kinetics [19]. In addition, one of the major limitation of MoS_2 is the number of active site present [41, 93, 99]. The S edges on MoS_2 are chemically and electrochemically inert, thus only Mo edges are the ones responsible to drive HER process [113, 134]. In this regards, usage of MoS_2 as electrocatalyst is hampered by the above mentioned problems. To overcome the above mentioned limitations, great determinations have MoS_2 with enhanced catalytic efficiency. Three

main approaches of improving the efficiency of MoS_2 includes: (1) optimizing the MoS_2 structure or preparing MoS_2 with different morphologies, (2) increasing the active sites density, and (3) improving the conductive properties of MoS_2 [19, 119, 139, 142]. This approaches can be achieved by activating the basal plane of MoS_2 to activate the inert S-edges, doping with other elements and forming MoS_2 hybrid structures with other compounds.

4.1 Activating Basal Plane of MoS_2

Bulk MoS_2 is crystalline in nature and have been the major revelation of HER application. Nanostructured MoS_2 can lead to different HER activities. This has been shown by several studies on fine tuning the MoS_2 structures into different nanostructures such as nanorods, nanodots, nanosheets and quantum dots). In addition, it was reported by Cao et al. [9] that MoS_x with amorphous structure offers extra active sites and enhance the conduction activities which plays a significant role towards HER activities. Benck et al. [4] presented a wet chemical synthesis for preparing amorphous MoS_2 and investigated change in morphology, composition and activity during HER performance. The amorphous wet-synthesized MoS_2 showed improved HER activity as compared to several reported molybdenum based catalysts (Fig. 10). The enhanced activity can be qualified to the rough nanostructured morphology of MoS_2 resulted from partial reduction of sulfur during catalysis. Additionally, the composition of Mo which is 22 and 78% of S played an important role since the wet synthesized MoS_2 resembled the structure of highly active molybdenum trisulfide (MoS_3).

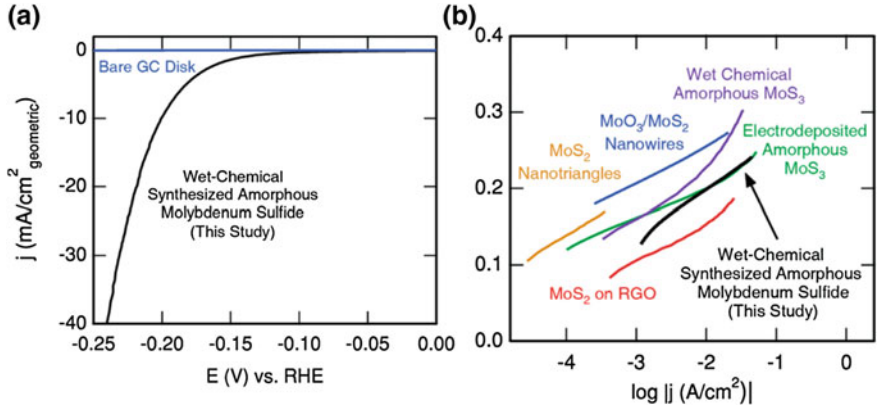

Fig. 10 **a** Linear sweep voltammogram (LSV) curves showing electrocatalytic performance of we-synthesized MoS_2 and **b** Tafel plot displaying wet-chemical-synthesized MoS_2 catalyst with other reported molybdenum based catalysts [4]

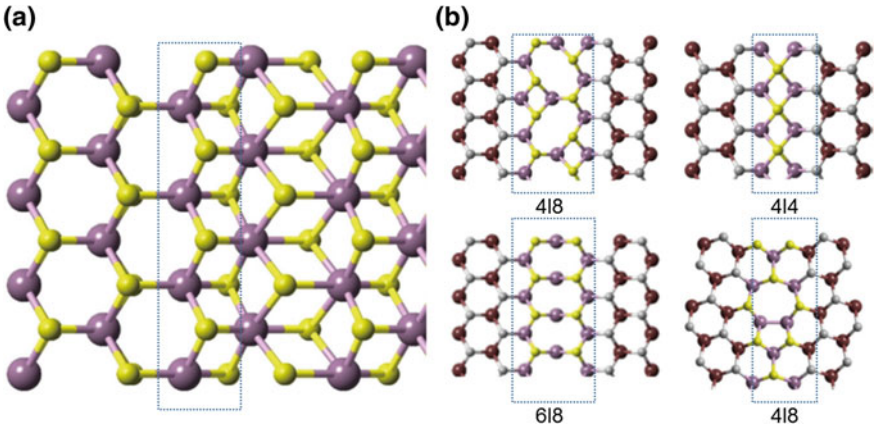

Fig. 11 DFT atomic models of **a** 2H-1T phase and **b** four different kinds of 2H-2H domain boundaries [154]

The other strategy of enhancing HER activity of MoS_2 was reported by Zhu et al. [154]. This can be achieved by generating domain boundaries in the MoS_2 inactive/inert basal plane. There are two types of boundaries that can be formed on the basal plane of MoS_2, 2H-1T phase and 2H-2H domain boundaries (Fig. 11). From the theoretical study, Density Functional Studies (DFT), ΔG_{Hads} of the 2H-2H domain boundary was found to be much small to the one of pristine MoS_2. And for the 2H-1T phase boundary, the ΔG_{Hads} was found to be near to the one of highly active Pt (111) surface and 2H-MoS_2. From this observation, it was deduced that phase boundaries can help in enhancing the HER activity of MoS_2. This is because the boundaries bring ultrahigh-density active sites, while maintaining the stability of MoS_2. The experimental HER results achieved enhanced HER performance with j_0 of 5.7×10^{-2} mA/cm^2, a b of 73 mV/dec, and a extraordinary enduring operation stability for 200 h.

Another route of improving the HER activity of MoS_2 is via desulfurization process which create the S-vacancies on the basal plane. It was reported by Li et al. [54] that creating and increasing S-vacancies number on the inactive MoS_2 basal plane stabilizes hydrogen atom adsorption and this lead to ΔGH_{ads} to be closer to zero. Tsai et al. [115] demonstrated that desulfurization process lead to morphological change as compared to pristine MoS_2 (Fig. 12a). In addition, they demonstrated that desulfurization decreases the Tafel slope and increases the current density 12 times, hence faster HER kinetics (Fig. 12b, c). This is attributed to more active sites generated after activating the basal plane of MoS_2. And duration and voltage of desulfurization (Fig. 12d, e) greatly affects the HER activity as the temper with the stability of the MoS_2. However, from the results, it was obtained that that S-vacancies stabilizes the MoS_2 structure further and improves the long term stability of the catalyst.

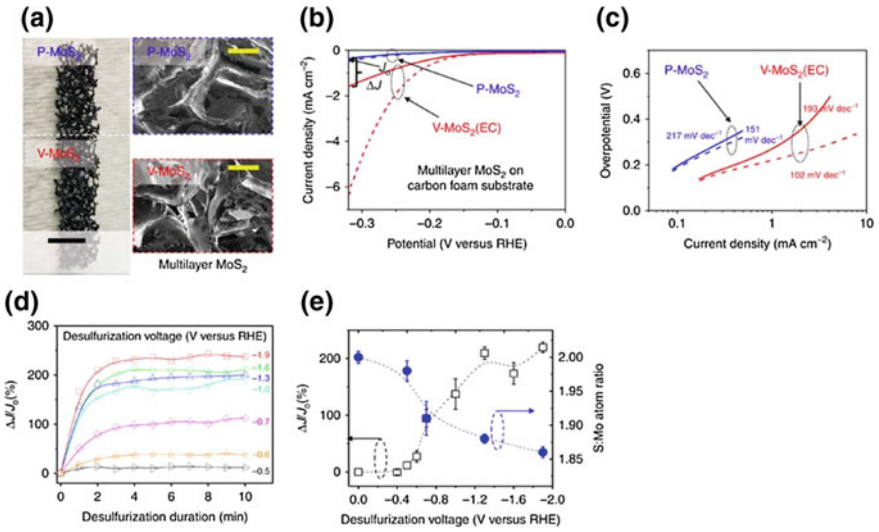

Fig. 12 **a** SEM micrographs, **b** LSV in 0.5 M H_2SO_4 and **c** Tafel plot of P-MoS_2 and V-MoS_2. **d** and **e** Shows effects of desulfurization duration and voltage on electrocatalytic performance of V-MoS_2 [115]

Lukowski and co-workers [66] examined intercalating effect on metallic MoS_2 nanosheets. They observed that the simple chemical exfoliation process enhances the HER performances. Intercalation with lithium for 48 h at 60 °C showed much enhanced electrocatalytic activity with exchange current density of 200 mA/cm^2 at overpotential of −400 mV as compared to Pt (Fig. 13a, b). Tafel analyses (Fig. 13c) showed that lithium intercalation decrease the Tafel slopes. The as-grown MoS_2 showed a slope of 117 mV/dec which suggest that Volmer step was the rate determining step while intercalated MoS_2 showed that the Heyrovsky step was the rate limiting step [43 mV/dec (iR corrected)]. The EIS results (Fig. 13d) revealed the faster kinetics after the charge resistance decreased from 232 Ω for as-grown MoS_2 to 4 Ω for exfoliated MoS_2. Cycle/scan dependent studies (Fig. 13e, f) showed a slight loss of HER activity, however the activity was still great as compared to the as-grown MoS_2. In another study, Voiry et al. [116] intercalated the MoS_2 nanosheets with lithium borohydride. This electrochemical oxidizing activates the S-edge basal plane and this increase the charge transfer process rate. Metallic 1T-, 2H-MoS_2 and Pt were used to compare with the edge oxidized MoS_2. From Fig. 14a, b, it can be deduced that the edge oxidized 1T- and 2H-MoS_2 showed enhanced activities as compared to their counterparts.

Another approach to activate the inert MoS_2 basal plane is to create defects (cracks or hole) on the monolayer of MoS_2 [15, 82, 128]. The two mostly common approaches to achieve MoS_2 monolayer with defects are oxygen plasma exposure and H_2 treatment at high temperatures [15]. Ye et al. [136] clearly showed formation after oxygen

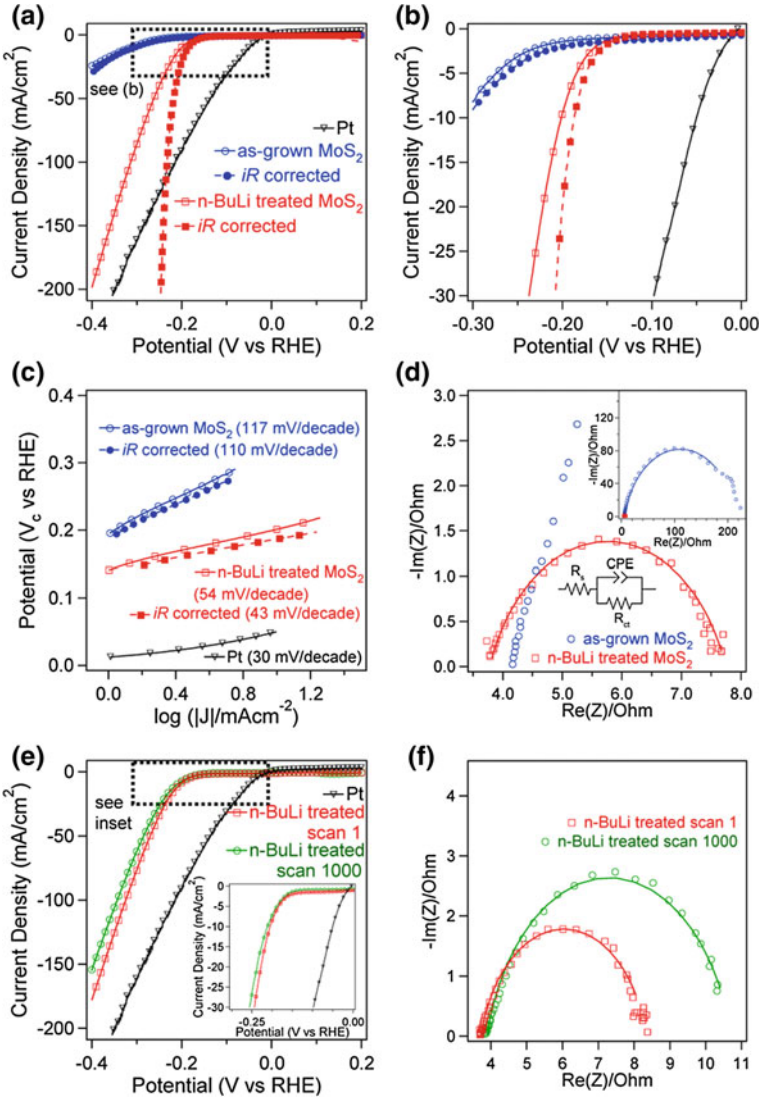

Fig. 13 **a**, **b** LSV polarization curves, **c** Tafel plot and **d** EIS results of lithium intercatalated MoS_2. LSV (**e**) and EIS **f** obtained after intercalating at 1000 scans [66]

plasma exposure and H_2 treatment. The SEM images are presented in Fig. 15a–d showed that after exposing MoS_2 monolayer with oxygen plasma, cracks started developing on the MoS_2 surface and cracks increased with oxygen exposure duration. Interestingly, after 20 s exposure, interconnected networks of cracks were observed which can enhance the HER activities. The Linear Sweep Voltammogram (LSV) in Fig. 15g showed that the 20 s plasma exposure resulted in small onset potential. In

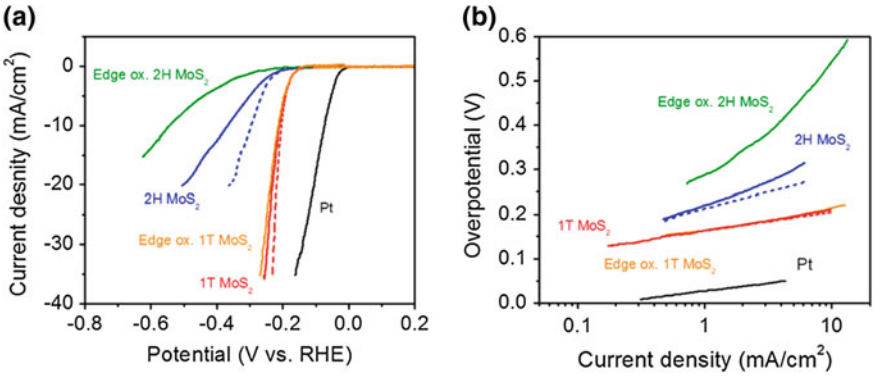

Fig. 14 HER activities of edge oxidized MoS_2 (Edge ox-2H and 1T-MoS_2) comparing them with un-oxidized counter metallic (1T) and semiconductor (2H) MoS_2 and commercial Pt. **a** LSV shows that activity of Edge ex. 1T MoS_2 has similar activity to its counterpart and low Tafel slope **b** which is close to that one of Pt [116]

addition, the Tafel slopes (Fig. 15h) decreased significantly from 342 mV/dec for MoS_2 monolayer to 162 and 171 mV/dec for 10 s- and 20 s-MoS_2 plasma exposed, respectively. H_2 treatment of MoS_2 resulted in formation of triangular holes on the basal plane of MoS_2 and this can be clearly observed in SEM images shown in Fig. 16a–c after H_2 treatment from 400 to 600 °C. The holes increased with increase in temperature until total decomposition was observed at 700 °C (Fig. 16d). From the LSV studies presented in Fig. 16f, it was deduced that 500 °C is the optimum H_2 annealing temperature since it gave onset potential of 300 mV which is smaller

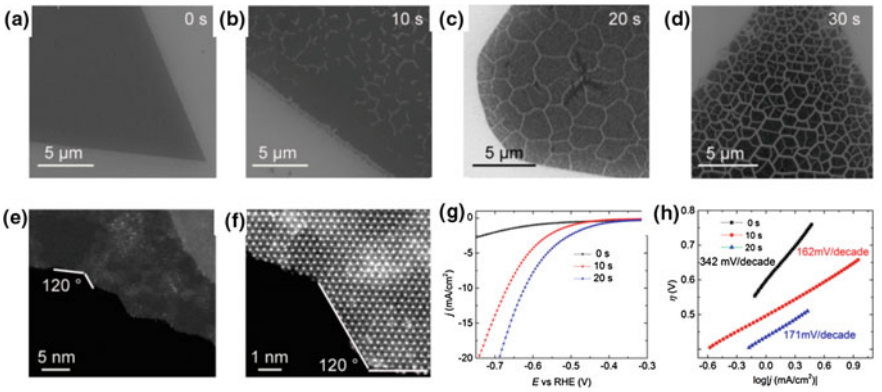

Fig. 15 **a–d** Illustrations and morphologies of MoS_2 after 0–30 s oxygen plasma exposure showing interconnected cracks. **e** and **f** are the STEM micrographs at 120° showing that oxygen plasma exposure is the correct approach to create cracks on the inert MoS_2 basal plane. **g** and **h** are the LSV and Tafel plots of MoS_2 exposed with oxygen plasma, respectively [136]

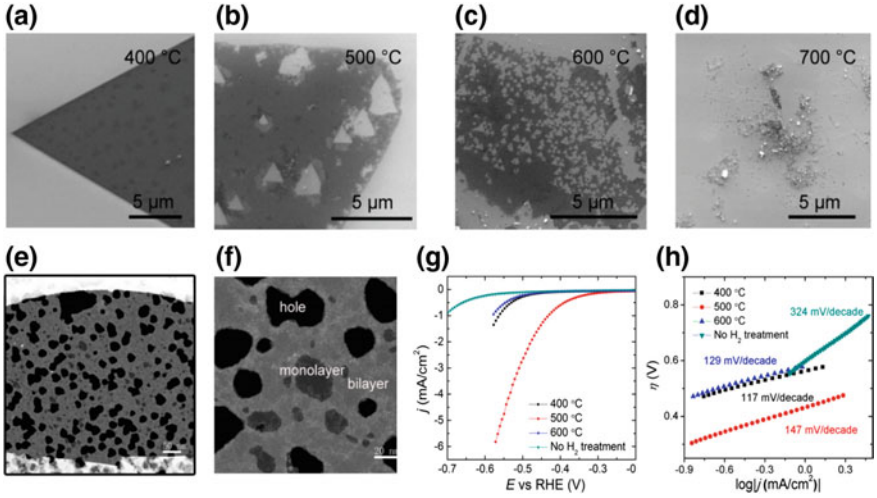

Fig. 16 SEM images (**a**–**c**) showing formation of triangular holes on MoS_2 basal plane and **d** decomposition of MoS_2 after H_2 treatment. STEM micrographs (**e** and **f**) shows MoS_2 monolayer and bilayer. **g** LSV, and **h** Tafel plots before and after H_2 treatment are shown. It can be deduced in the HER activities that the performance of MoS_2 was significantly improved after H_2 treatments [136]

as compared to annealing at 400 °C (470 mV) and 600 °C (450 mV). The corresponding Tafel slopes were 324, 129, 117 and 147 mV/dec for no H_2 treated MoS_2, 400 °C- 600 °C- and 500 °C-treated MoS_2 as depicted in Fig. 16g. The Tafel slopes of H_2 treated MoS_2 are much lower than that of pristine MoS_2, which is an evident that formation of triangular holes on MoS_2 plays an important part in understanding HER mechanism as well as rate-determing step during HER studies. STEM images (Figs. 15 and 16e, f) showed that both Oxygen plasma exposure and H_2 treatment are the best approaches to generate defects on the basal plane of MoS_2.

4.2 Heteroatom Doping on MoS_2 Structure

Although activating the basal plane of MoS_2 has been identified as a suitable way of increasing HER performance of MoS_2, the process of activating the basal plane still suffers from different setbacks. For example, formation of S-vacancies cause electron deficiency at the reaction interface resulting in limiting the charge transfer which is essential for HER catalyzation [68]. In addition, the basal S-edges activated still suffer from less favourable ΔG_{Hads} despite increasing the active site density. Furthermore, cycle or scan dependent studies by Lukowski et al. [66] showed activity loss resulted from loss of stability during desulfurization process. Moreover, plasma exposure and H_2 annealing are effective for flat surfaced MoS_2, thus it limits their practical application or large scale synthesis [115]. In this regard, more efforts must be place

in find other route to increase the performance of MoS_2 such as heteroatom doping which can be utilized to tailor the conductive properties of MoS_2. This can lead into more active site and increase the electron transport properties of MoS_2 monolayer [33, 63]. Metal (Co, Ni, Fe, and Cu) and non-metal (N, P, O, Se, and Cl) have been reported to modify electronic properties and improve intrinsic conductivities by replacing either Mo or S [53, 92]. Table 1 summarizes recent developments in doping metals and non-metal on MoS_2 in comparison with MoS_2 of different nanostructures.

Li et al. [53] reported the nitrogen doped MoS_2 (N-doped MoS_2) synthesized from hydrothermal method. SEM images (Fig. 17a) revealed that the N-doped MoS_2 comprises of graphene-sheet-like nanostructures which are more dispersed and homogeneous as compared to pristine MoS_2. The graphene sheet like morphologies can be clearly seen on the TEM images (Fig. 17b, c) and the HRTEM showed that N-doped MoS_2 have the lattice fringes with an inter-planar distance of 0.61 nm (002) and 0.27 nm (100). Elemental mapping revealed the presence of N atoms as well as other elements (Fig. 17d) present in the N-doped MoS_2. The HER activity in Fig. 17e of N-doped MoS_2 showed improved HER activity (20-fold) as compared to pure MoS_2. The cathodic current of 10 mA/cm^2 was achieved at 168 mV as compared to 395 mV of pure MoS_2. This is due to balance of dispersity and N amount in the MoS_2 structure as shown in SEM, TEM and EDS results in Fig. 17a–d. In addition, the N-doped MoS_2 gave lower Tafel slope of 40.5 mV/dec lesser than 101.7 mV/dec of pure MoS_2 (Fig. 17f). The EIS was used to provide information about the kinetics of HER. N-doped MoS_2 showed faster HER kinetics as the obtained charge transfer resistance was 58.4–295.5 Ω of pristine MoS_2 as depicted in Fig. 17g. The improvement in HER performance can be further explained by the electrochemical surface area (ECSA). The ECSA results showed in Fig. 17h of N-doped MoS_2 increased to 14.3 mF/cm^2 in relation to the one of pure MoS_2 (2.92 mF/cm^2) which shows that more active sites were generated. Furthermore, N-doped MoS_2 showed superior stability and good durability in acidic mead at 200 mV for 50 h and 5000 cycles, respectively.

Zhang et al. [146] assumed that since N-doped MoS_2 shows excellent HER activities, more active sites can be generated by doping N on the surface of much smaller MoS_2 quantum dots (QDs). The N-doped MoS_2 QDs were synthesized using sintering/etching/exfoliation method (Fig. 18a) which generate high concentration of N in QDs as compared to the one on MoS_2 nanosheets. The N-doped MoS_2 QDs showed excellent HER activities with onset potential, overpotential and Tafel slope of 82 mV, 165 mV at 10 mA/cm^2 and 51.2 mV/dec, respectively (Fig. 18b, c). This is supported by a high double-layer capacitance (C_{dl}) of 71.5 mF/cm^2 (N-doped MoS_2 QDs) to 42.6 mF/cm^2 (N-doped MoS_2) (Fig. 18d).The EIS in Fig. 18e of N-doped MoS_2 QDs revealed much smaller charge transfer resistance which reflect on the high conductivity and fast electron transfer process. Furthermore, it was shown that the N-doped MoS_2 QDs possessed great stability and durability.

Table 1 MoS_2 doped with metal and non-metals for HER

Catalyst	Dopant	Electrolyte	η* mV	b mV/dec	Cdl mF/cm^2	Rct Ω	References
MoS_2 nanosheets	–	0.5 M H_2SO_4	395	101.7	2.92	296	Li et al. [53]
MoS_2 nanosheets	N	0.5 M H_2SO_4	168	40.5	14.3	58.8	Li et al. [53]
MoS_2 QDs	N	0.5 M H_2SO_4	165	51.2	71.5	34.2	Zhang et al. [146]
1T-MoS_2	Pd	0.5 M H_2SO_4	78	80.0	–	1.50	Luo et al. [68]
MoS_2 nanorods	N	1.0 M KOH	148	70.0	20.1	–	Sun et al. [102]
MoS_2 nanorods	Mn	1.0 M KOH	107	62.0	25.0	–	Sun et al. [102]
MoS_2 nanorods	N, Mn	1.0 M KOH	66	50.0	30.2	–	Sun et al. [102]
MoS_2 nanoflowers	Fe	0.5 M H_2SO_4	136	82.0	–	–	Zhao et al. [150]
MoS_2/rGO	Co	0.5 M H_2SO_4	187	50.0	10.4	14.3	Dai et al. [21]
MoS_2/rGO	Mn	0.5 M H_2SO_4	–	76.0	17.4	1.50	Wu et al. [126]
MoS_2/CC	Se	0.5 M H_2SO_4	127	63.0	–	143	Pu et al. [84]
MoS_2	P	0.5 M H_2SO_4	39	39.0	5.58	–	Wang et al. [122]
MoS_2/NG	Co	0.5 M H_2SO_4	59	59.0	–	575	Ma et al. [71]
MoS_2@graphene	Al	0.5 M H_2SO_4	212	41.0	–	13.0	Su et al. [98]
MoS_2 nanosheets	Co	0.5 M H_2SO_4	40	64.7	–	0.990	Xiong et al. [131]
MoS_2 nanosheets	Co	1.0 M KOH	60	50.3	–	1.02	Xiong et al. [131]
MoS_2 nanosheets	Zn	0.5 M H_2SO_4	194	73.0	2.07	27.0	Wu et al. [128]
MoS_2/CNFs	Au	0.5 M H_2SO_4	92	126	14.4	10.0	Wen et al. [125]
MoS_2/rGO	Cu	0.5 M H_2SO_4	250	90	15.0	–	Li et al. [56]

η* overpotential needed to achieve 10 mA/cm^2

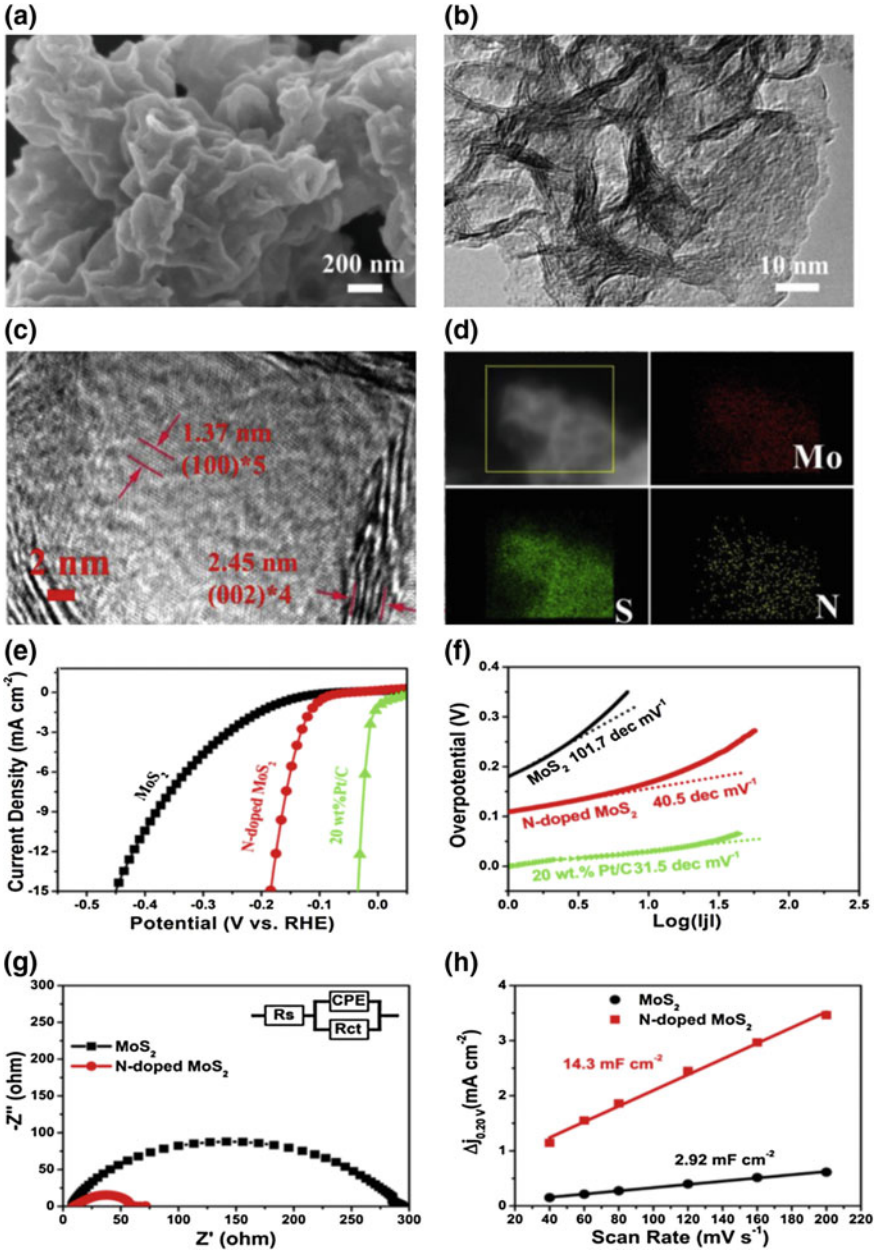

Fig. 17 **a** SEM, **b** TEM, **c** HRTEM and **d** elemental mapping of N-doped MoS_2. **e** LSV curves of various catalyst as indicated and corresponding Tafel plots (**f**); **g** EIS and **h** linear capacitive currents MoS_2 and N-doped MoS_2 [53]

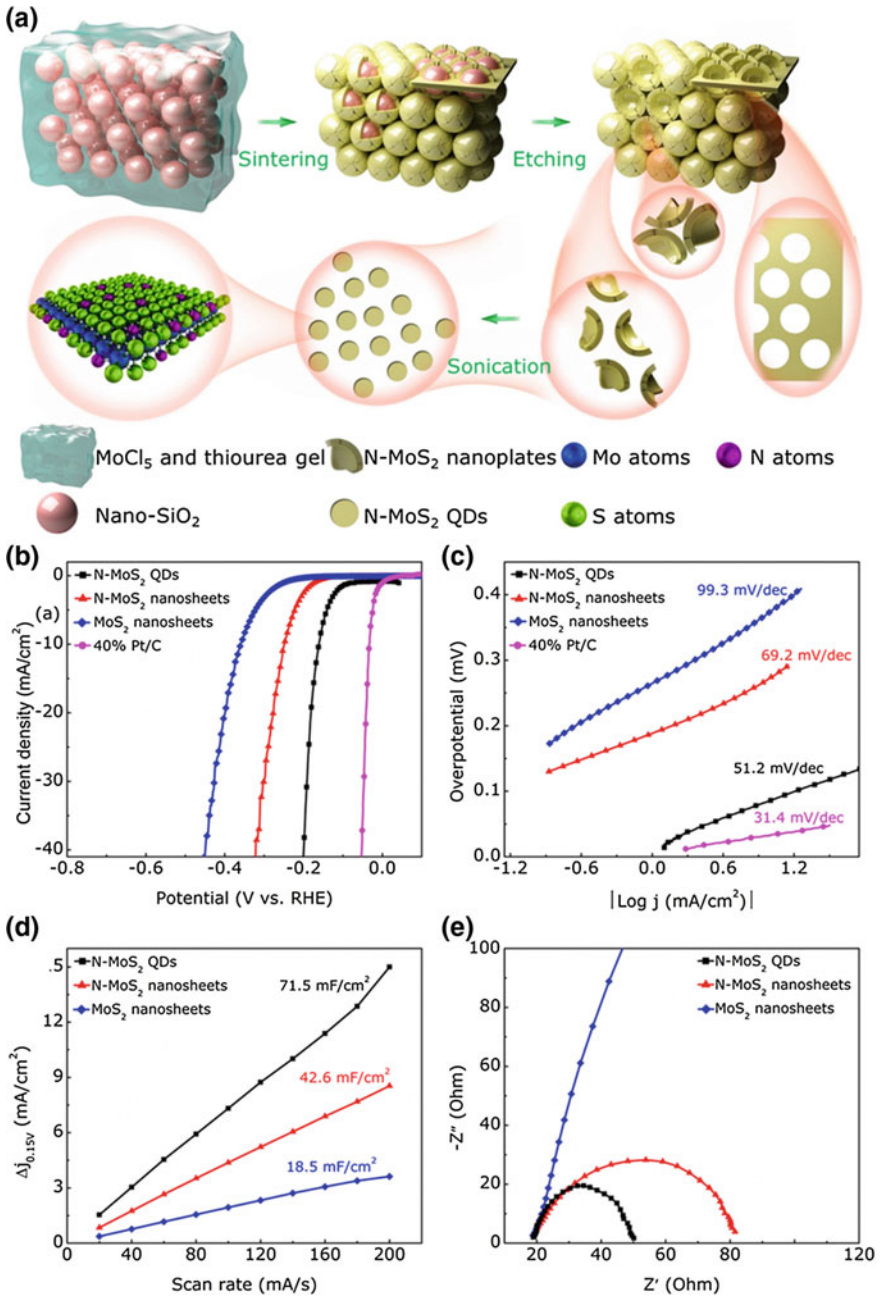

Fig. 18 **a** Schematic illustration of sintering/etching/exfoliation method for preparation of MoS_2 QDs. **b** LSV polarization curves of MoS_2 catalysts compared with 40% Pt/C in acidic medium. **c** Tafel plot, **d** Linear fitting capacitance currents vs scan rate, and **e** charge resistance derivation plot showed decrease in Tafel slope, increase in number of active sites and fast HER kinetics N-doped MoS_2 QDs in relation with N-doped MoS_2 and pure MoS_2 [146]

4.3 MoS_2 Hybrid Nanostructures for HER

Combining MoS_2 with secondary compounds, hybrid nanostructures, can address both drawbacks, limited active sites and poor conductivity MoS_2 suffers. The secondary compounds exposes the edges of MoS_2 and create an electron transport channel [30]. Materials such as TiO_2, CoS_2, CuS, carbon based (graphene, activated carbon, carbon nanofibers, and carbon nanotubes (CNTs)), porous based (zeolites, MOFs and conducting polymers have been studied for enhancement of HER activities of MoS_2 [54, 81, 104, 121, 143, 149] and are summarized in Table 2. In this review, we will briefly look at MoS_2 with carbon based, MOFs and conducting polymers.

4.3.1 Carbon Based Materials

Li et al. [48] recently developed MoS_2 confined graphene particles (MoS_2@G) using hydrothermal synthesis and the synthesis procedure is shown in Fig. 19a. Interestingly, it can be seen that there is a chelating interaction between $[Mo_7O_{24}]^{6-}$ and GO. The electrolytic studies revealed that MoS_2@G exhibited excellent HER activities with onset potential, overpotential, and Tafel slope of 32 mV, 132 to achieve 10 mA/cm^2 and 45 mV/dec, respectively. In order to understand the role played by GO during enhancement of HER performances, they proposed a scheme which shows the channel created by GO to facilitate electron transport process. It can be deduced that MoS_2 is fully dispersed on the surface of GO without any form of agglomeration which exposes the edges of MoS_2 in order to attain more active sites and this is deduced on the C_{dl} which increased from 26.33 mF/cm^2 (MoS_2/G) to 32.73 mF/cm^2 for MoS_2@G.. The electron diffusion model is presented in Fig. 20a. The electrons diffuse on the layer of GO and then channelled to the edges of MoS_2. The Nyquist plot (Fig. 20b) supported the electron transport process and this process occurs very fast as the Rct was lowered to 3.8 Ω (MoS_2@G) from 10.1 Ω (MoS_2/G). Moreover, Wu et al. [126] demonstrated the enhancement of HER activities by forming a hybrid between MoS_2 and reduced GO (rGO) and further dope with Mn. The electrochemical performance of MoS_2/rGO showed a Tafel slope of 105 mV/dec smaller compared to pure MoS_2 (135 mV/dec). This smaller Tafel slope resembles faster HER rate with increase potential. The slope was further reduced upon doping with Mn. To better understand the effect of both Mn and rGO, the TOF was determined and fount to be 0.029, 0.042 and 0.05 s^{-1} for MoS_2, MoS_2/rGO and Mn-MoS_2/rGO, respectively.

4.3.2 Metal Organic Frameworks

Metal organic frameworks are crystalline structure built from coordinating metal ion and organic linker/ligand covalently [42]. These MOFs exhibit tremendous characteristics which include ultra-high surface area, ordered and tunable structure, highly

Table 2 MoS_2 composites for HER in different electrolytes

Catalyst	Electrolyte	Onset Potential mV	η* mV	b mV/dec	C_{dl} mF/cm^2	R_{ct} Ω	References
MoS_2 nanosheets	0.5 M H_2SO_4	100	395	102	2.92	295	Li et al. [53]
MoS_2/VGNS	0.5 M H_2SO_4	160	212	41.3	7.96	39.2	Wang et al. [117]
MoS_2@G	0.5 M H_2SO_4	32.0	132	45.0	32.7	3.80	Li et al. [48]
MoS_2/rGO (MG3)	0.5 M H_2SO_4	110	30	41.0	–	–	Li et al. [56]
MoS_2 NSs/rGO	0.5 M H_2SO_4	210	130	57.0	–	180	Cao et al. [9]
MoS_2/N-rGO-H	0.5 M H_2SO_4	100	62.0	45.0	–	21.0	Dai et al. [20]
MoS_2 NF/rGO	0.5 M H_2SO_4	200	190	95.0	–	–	Ma et al. [71]
MoS_2/RGO	0.5 M H_2SO_4	150	100	41.0	–	250	Li et al. [52]
MoS_2/rGO	0.5 M H_2SO_4	–	222	59.8	–	32.0	Sun et al. [101]
Al-MoS_2@graphene	0.5 M H_2SO_4	225	212	41.0	–	13.0	Su et al. [98]
MoS_2/GO-CNT	0.1 M $HClO_4$	35	50.0	38.0	–	–	Khan et al. [44]
MoS_2/SWCNT	0.5 M H_2SO_4	140	205	40.8	–	9.10	Cai et al. [7]
MoS_2 NS/MWCNT	0.5 M H_2SO_4	50	155	43.0	–	100	Cao et al. [10]
MoS_2/N-MWCNTS	0.5 M H_2SO_4	90	59	40.0	3.84	20.6	Dai et al. [18]
MoS_2/O-MWCNT	0.5 M H_2SO_4	90	40	64.7	1.79	41.9	Dai et al. [18]
CoS_2-MoS_2/CNT	0.5 M H_2SO_4	70	31.3	64.0	–	150	Liu et al. [59]
MoS_2/CoS_2-10	0.5 M H_2SO_4	20	69	62.0	325	5	Ouyang et al. [81]
MoS_2@HKUST	0.5 M H_2SO_4	99	300	69.0	12.5	367	Wang et al. [121]
MoS_2-PANI	0.5 M H_2SO_4	160	300	82.0	–	229	Zhang et al. [143]
MoS_2/PANI	0.5 M H_2SO_4	100	250	45.0	–	70.9	Zhang et al. [143]

(continued)

Table 2 (continued)

MoS_2/Ppy	0.5 M H_2SO_4	150	215	80.5	–	–	Lu et al. [65]
DBC-MoS_2 QDs-PANI	0.5 M H_2SO_4	180	196	58.0	–	–	Das et al. [23]
Co_9S_8/NC@MoS_2	1.0 M KOH	4	67	60.3	22.9	40.2	Li et al. [49]
MoS_2/N-ZIF	0.5 M H_2SO_4	110	185	57.0	16.4	110	Tong et al. [110]
MoS_2/HG	0.5 M H_2SO_4	100	124	41.0	12.3	3.65	Han et al. [34]
MoS_2/RGO	0.5 M H_2SO_4	220	283	62.0	3.7	99.0	Liu et al. [60]
CoS_2/MoS_2/RGO	0.5 M H_2SO_4	80	160	56.0	11.9	35.0	Liu et al. [60]
MoS_2/CNFs	0.5 M H_2SO_4	145	207	60.0	15.7	19.6	Zhang et al. [147]
MoS_2/CuS	0.5 M H_2SO_4	150	290	63.0	14.4	45.0	Zhang et al. [149]
MoS_2/Ni_2P	1.0 M KOH	86	250	58.0	62.5	830	Yang et al. [133]
Co_3S_4@MoS_2	0.5 M H_2SO_4	–	210	88.0	8.10	–	Guo et al. [29]
TiO_2/MoS_2	0.5 M H_2SO_4	150	250	48.0	10.9	8.2	Tahira et al. [104]
TiO_2/MoS_2	1.0 M KOH	400	600	60.0	10.9	8.2	Tahira et al. [104]

η* overpotential needed to achieve 10 mA/cm^2

porous and robust (kinetically and thermodynamically stable) [58, 70]. Due to their insulating properties of MOF structures, there are limited reports for utilizing MOFs for electrochemical HER [78]. Previously, we reported on the synthesis of MOF with polyaniline and phthalocyanine as an electron transport channel to facilitate HER process [74, 77, 78, 86–88]. We deduced that, MOF can also be used as a great support for HER electrocatalyst owing to its excellent properties which can help in increasing the active sites density. Furthermore, it was reported that porous materials can enhance electrocatalyst performance by improving the electronic conductivity and smoothing proton delivery [37]. There are only few report on forming a MoS_2/MOF hybrid as electrocatalyst for HER.

Wang et al. [121] demonstrated the preparation of flower-like MoS_2@HKUST-1 nanohybrid following hydrothermal method. The fabricated catalyst possessed a remarkable HER electrochemical performance with onset potential of –99 mV and a Tafel slope of 69 mV/dec. The excellent HER activity was additionally supported by the impedance data which showed a faster kinetics (R_{ct} = 367 Ω) and increase

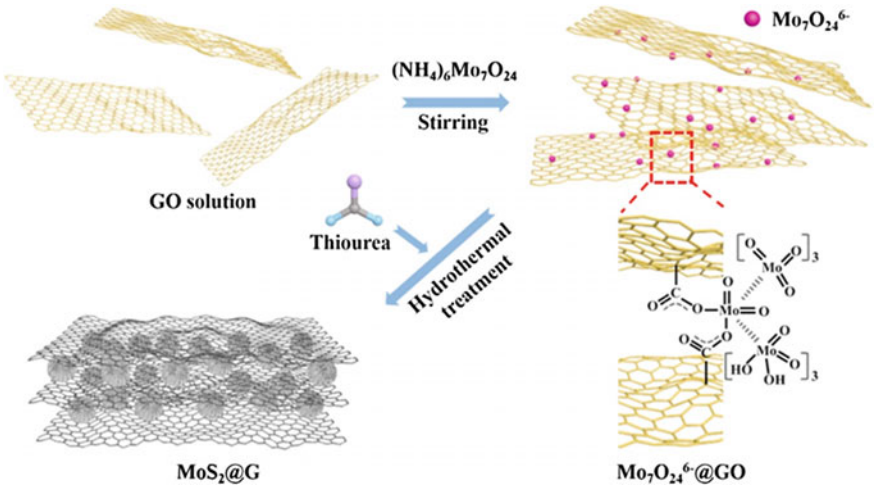

Fig. 19 Schematic diagram showing hydrothermal preparation of MoS2@G. The magnification described the chelating nature of $Mo_7O_{24}^{6-}$ with GO [48]

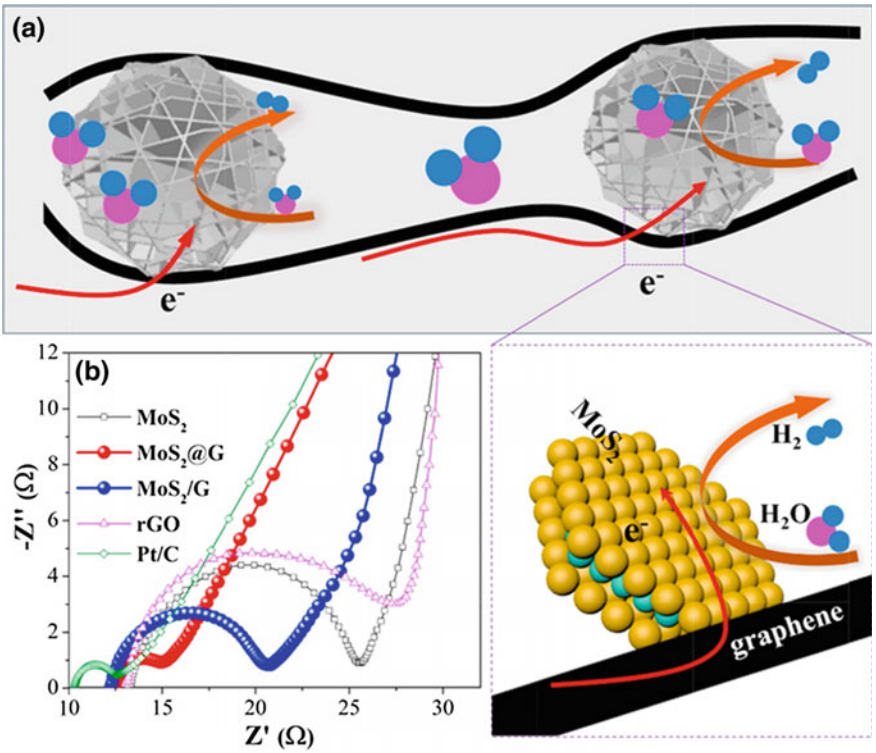

Fig. 20 Schematic images showing electron transport mechanism between GO and MoS_2. Nyquist plot of MoS_2@G compared to other catalysts as indicated [48]

in number of active sites deduced from ECSA results (C_{dl} = 12.5 mF/cm^2) as compared to pristine MoS_2 (R_{ct} = 542 Ω and C_{dl} = 1.1 mF/cm^2). The stability and durability study of the prepared MoS_2@HKUST-1 showed no decline which tells that the prepared catalyst can withstand harsh conditions and used for a long time without a loss of HER activity. In another study, Tong et al. [110] fabricated nitrogen doped MoS_2 with zeolitic imidazolate framework-8 (a subclass of MOFs) using hydrothermal route. The electrocatalytic findings (Fig. 21) showed that the prepared catalyst exhibited lowest overpotential (185 mV) to obtain 10 mA/cm^2 (a), Tafel slope (57 mV/dec) (b), C_{dl} (16.38 mF/cm^2), and R_{ct} = 110 Ω (c). From Figure d, it can be seen that the synthesized was stable, losing only 18 mV of potential during 1000 cycles. The electrochemical studies in both studies shows that MOFs can be used as a support to MoS_2 to enhance their HER activity.

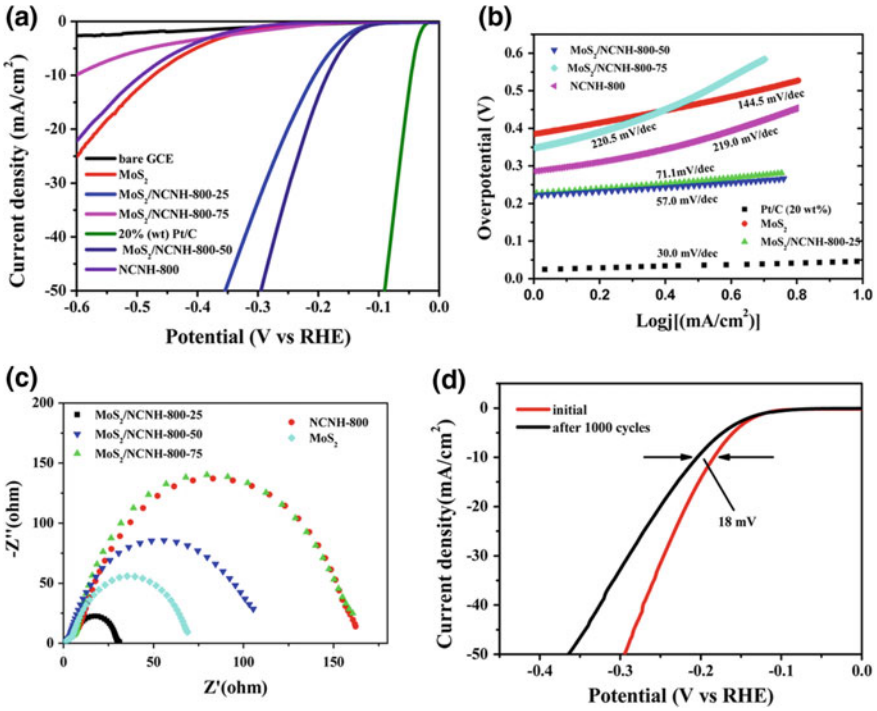

Fig. 21 **a** LSV polarization curves and **b** Tafel analysis of catalytic active MoS_2/NCNH-800-50 compared with various catalysts. **c** EIS plots and **d** Durability test for MoS_2/NCNH-800-50 [110]

4.3.3 Conducting Polymers

MoS_2-conducting polymer composites have been widely studied in supercapacitor applications and this is due to conducting polymer's low cost, environmental stability, simple synthetic process and high ECSA [47, 57, 62]. Conducting polymers such as polyaniline (PANI) and polypyrrole (Ppy) can be easily dispersed on the MoS_2 via several methods and interact with each other using electrostatic interaction using the metal on MoS_2 and nitrogen on PANI and Ppy [141]. The interaction of MoS_2 with PANI in particular results in a hybrid material with improved physical and mechanical properties (surface area and stability) as well as enhanced electronic/intrinsic properties. Moreover, Chao et al. [11] investigated integration of MoS_2 and PANI results in forming heterostructure interfaces with great mechanical stability (MoS_2) and high conductivity (PANI). In this regard, MoS_2/conducting polymer nanostructures are expected to possess great electrochemical HER activities and improved stabilities. Zhang and co-workers [143] researched on MoS_2 nanosheets rooted on PANI nanofibers for HER. They used two approaches, hydrothermal (MoS_2/PANI) and direct mixing (MoS_2-PANI) to attain integration between MoS_2 and PANI. From the two approaches, they found that hydrothermal synthesis gave MoS_2/PANI with exposed edges which is essential for HER, with uniform dispersed elements and the 2D MoS_2 nanosheets assembled into PANI nanowires to give 3D integrative hybrid. The hydrothermal synthesized MoS_2/PANI showed superior HER activity as compared to direct mixed (MoS_2-PANI) and pure MoS_2 and are presented in Fig. 22a. The magnified polarization (Fig. 22b) showed the small onset potential of 100 mV for MoS_2/PANI as compared to 160 mV and 190 mV for MoS_2-PANI and pristine MoS_2, respectively. In addition, the Tafel slope of the MoS_2/PANI was the smallest among the prepared catalysts (Fig. 22c). The effect on MoS_2 in the MoS_2/PANI was studied and the results are shown in Fig. 22d. It can be seen that the optimum MoS_2 was found to be 79.6% which suggest that at the mentioned percentage, more edges are exposed. The R_{ct} was found to increase from 70.92 Ω > 228.71 Ω > 421.65 Ω for MoS_2/PANI, MoS_2-PANI and MoS_2. The smaller R_{ct} for MoS_2/PANI shows faster HER kinetics and favourable activity.

Owing to its high surface area and superior conductivity than MoS_2 monolayer, Das et al. [23] synthesized conductive MoS_2 QDs-polyaniline aerogel as an electrocatalyst with enhanced HER activity. DBC-MoS_2-PANI aerogel showed better HER activity with overpotential of 196 mV at 10 mA/cm^2 and Tafel slope of 58 mV/dec with respect to other reference material. They suggested that the small slope arised from coupling between MoS_2 QDs and PANI allowing a good communication between the two. This good communication resulted in decreasing the R_{ct} signifying an increase HER performance and faster kinetics. Reasons for better HER activities in their study were summarized as: (i) PANI aerogels gives ultra-high surface area which allows fast electrolyte diffusion because of the porous network resulted from the structure, and (ii) the synergistic coupling between the MoS_2 QDs and PANI aerogels resulting in lowering the adsorption energy of adsorbed hydrogen.

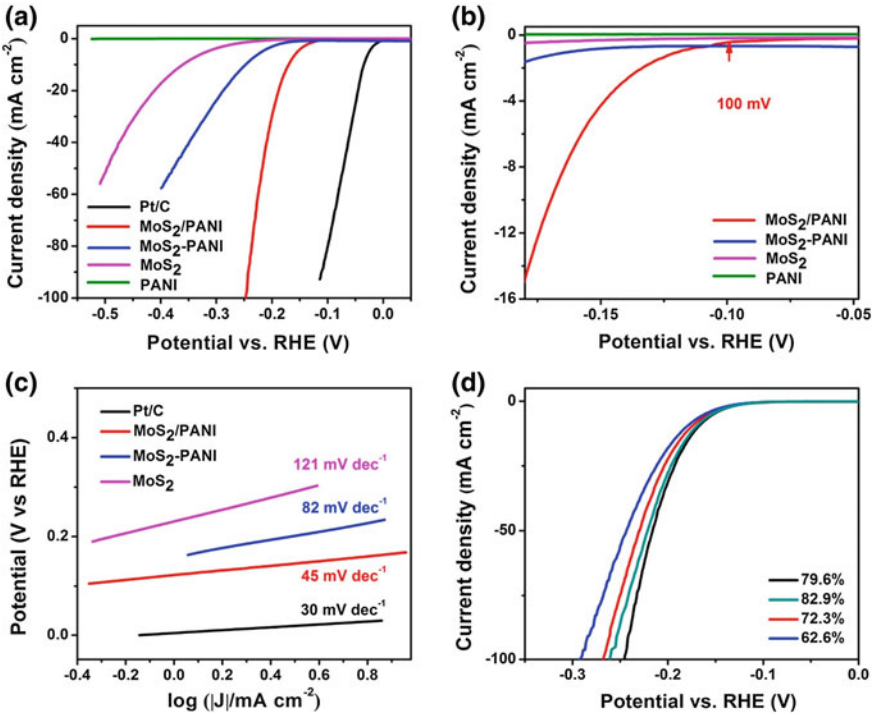

Fig. 22 HER catalytic activity of MoS_2 with its PANI composites. **a** and **b** shows that LSV curves and **c** the Tafel plots. It can be seen that the activity was enhanced upon composite formation and they are much closer to Pt/C commercial electrocatalyst. The LSV (**d**) of different Mo in MoS_2 percentage shows that 79.6% is the optimum amount of Mo to give catalyst with enhanced HER activity [143]

5 Summary and Future Perspectives

Electrochemical generation of hydrogen plays a significant role in driving the hydrogen economy towards commercialization. Developing a cost-effective, stable, durable and highly catalytic active catalyst is a crucial step in realizing the fruit of hydrogen energy. In this review, we clearly looked at the insight reaction during electrolysis in order to understand better the crucial steps which need to be taken into consideration during selection of catalyst. HER process need a catalyst with balanced energies in order for it to proceed and thus understanding the mechanism during catalysis is of great importance. We closely looked at the HER mechanisms in both alkaline and acidic media and found that HER can proceed via Volmer-Heyrovsky or Volmer-Tafel mechanisms. This depends mostly on the binding energies of the adsorbed hydrogens and corresponding slopes were found to be 30, 40, and 120 mV/dec for Tafel, Heyrovsky, and Volmer, respectively. Catalytic performance of the heterostructures can be monitored by studying electrochemical parameters

such as onset potential, overpotential, Tafel analysis, double-layer capacitance and charge resistance transfer. Theoretical background of the above mentioned parameters were illustrated. The stability and durability were other parameters which were explained in this review in relation to the suitable electrocalyst for HER.

The state-of-the-art approach was based on fine tuning the nanosheets of MoS_2 and its heterostructures for electrocatalysis. There have been great advances in using the above mentioned material for electrochemical application and this is mainly due to its enormous structural and electrical properties. Much focus was placed on the material design, synthesis strategies and electrochemical performance of MoS_2 heterostructures. It was noted that MoS_2 consists mostly of an inert basal plane which limits its application for HER performances as only few Mo-metal edges shows activity towards HER. Therefore approaches of increasing the intrinsic properties and exposing the edges to attain MoS_2 with more active sites we investigated. This included generating S-vacancies, creating defects and domain boundaries on the basal plane of MoS_2. Theoretical studies revealed that the Gibbs free energy of adsorbed hydrogen reaches near zero upon activating the basal plane using those three approaches. However, the stability of the nanostructure is compromised. Another route involved doping with metal or non-metal on the monolayer of MoS_2. These dopants are dispersed on the monolayer and fully expose the edges of MoS_2. Finally, hybrid of MoS_2 and other electron transport channeling compounds is a great way to address the poor intrinsic and limited active sites of MoS_2. The hybrid with graphene, metal organic frameworks and conducting polymers have been explored. Synergistic effect was used to explain the enhancement of HER activity of MoS_2. In addition, hydrothermal synthesis was deemed as a best synthetic route to prepare the hybrid composites rather than direct-mixing.

In future, more efforts are needed in order to attain MoS_2 nanostructures with superior HER activity. The first strategy can be creating S-vacancies, triangular holes, cracks and domains on the hybrid composites which formed without disrupting the heterostructures formed. Theoretical studies need to be conducted in order to illustrate the underlying processes and steps needed to achieve great activity. Ternary composite formation can be the second strategy to improve the HER activity of the MoS_2.

References

1. Abdolmaleki A, Mohamadi Z, Ensafi AA, Atashbar NZ, Rezaei B (2018) Efficient and stable HER electrocatalyst using Pt nanoparticles@ poly(3,4eethylene dioxythiophene) modified sulfonated graphene nanocomposite. Int J Hydrogen Energy 43:8323–8332
2. Akbari E, Jahanbin K, Afroozeh A, Yupapin P, Buntat Z (2018) Brief review of monolayer molybdenum disulfide application in gas sensor. Phys B 545:510–518
3. Appel AM, Helm ML (2014) Determining the overpotential for a molecular electrocatalyst. ACS Catal 4:630–633
4. Benck JD, Chen Z, Kuritzky LY, Forman AJ, Jaramillo TF (2012) Amorphous molybdenum sulfide catalysts for electrochemical hydrogen production: insights into the origin of their

catalytic activity. ACS Catal 2:1916–1923
5. Benson J, Li M, Wang S, Wang P, Papakonstantinou P (2015) Electrocatalytic hydrogen evolution reaction on edges of a few layer molybdenum disulfide nanodots. ACS Appl Mater Interfaces 7:14113–14122
6. Boiadjieva-Scherzer T, Kronberger H, Fafilek G, Monev M (2016) Hydrogen evolution reaction on electrodeposited Zn-Cr alloy coatings. J Electroanal Chem 783:68–75
7. Cai Y, Yang X, Liang T, Dai L, Ma L, Huang G, Chen W, Chen H, Su H, Xu M (2014) Easy incorporation of single-walled carbon nanotubes into two-dimensional MoS_2 for high performance hydrogen evolution. Nanotechnology 25:465401 (1–6)
8. Cai Z, Liu B, Zou X, Cheng HM (2017) Chemical vapor deposition growth and applications of two-dimensional materials and their heterostructures. Chem Rev (2017) https://doi.org/10.1021/acs.chemrev.7b00536
9. Cao J, Zhou J, Zhang Y, Zou Y, Liu X (2017) MoS_2 nanosheets direct support on reduced graphene oxide: an advanced electrocatalyst for hydrogen evolution reaction. PLoS ONE 12:e0177258
10. Cao J, Zhou J, Zhang Y, Liu X (2017) A clean and facile synthesis of MoS_2 nanosheets grown on multi-wall CNTs for enhanced hydrogen evolution reaction performance. Sci Rep 7 (2017b) https://doi.org/10.1038/s41598-017-09047-x
11. Chao J, Deng J, Zhou W, Liu J, Hu R, Yang L, Zhu M, Schmidt OG (2017) Hierarchical nanoflowers assembled from MoS_2/polyaniline sandwiched nanosheets for high performance supercapacitor. Electrochim Acta 243:98–104
12. Chaudhary N, Khanuja M, Islam ASS (2018) Hydrothermal synthesis of MoS_2 nanosheets for multiple wavelength optical sensing applications. Sens Actuators A 277:190–198
13. Chedid G, Yassin A (2018) Recent trends in covalent and metal organic frameworks for biomedical applications. Nanomaterials 8. https://doi.org/10.3390/nano8110916
14. Cheng Y, Jiang SP (2015) Advances in electrocatalysts for oxygen evolution reaction of water electrolysis-from metal oxides to carbon nanotubes. Prog Nat Sci Mater Int 25:545–553
15. Cheng CC, Lu AY, Tseng CC, Yang X, Hedhili MN, Cheng MC, Wei KH, Li LJ (2016) Activating basal-plane catalytic activity of two dimensional MoS_2 monolayer with remote hydrogen plasma. Nano Energy 30:846–852
16. Choi JM, Kim SH, Lee SJ, Kim SS (2018) Effects of pressure and temperature in hydrothermal preparation of mos_2 catalyst for methanation reaction. Catal Lett 148:1803–1814
17. Conte M, Di Mario F, Iacobazzi A, Mattucci A, Moreno A, Ronchetti M (2009) Hydrogen as future energy carrier: the ENEA point of view on technology and application prospects. Energies 2:150–179
18. Dai X, Du K, Li Z, Liu M, Ma Y, Sun H, Zhang X, Yang Y (2015) Co-doped MoS_2 nanosheets with dominant CoMoS phase coated on carbon as an excellent electrocatalyst for hydrogen evolution. ACS Appl Mater Interfaces 7:27242–27253
19. Dai X, Du K, Li Z, Sun H, Yang Y, Zhang X, Li X, Wang H (2015) Highly efficient hydrogen evolution catalyst by MoS_2-MoN/carbonitride composites derived from tetrathiomolybdate/polymer hybrids. Chem Eng Sci 134:572–580
20. Dai X, Du K, Li Z, Sun H, Yang Y, Zhang W, Zhang X (2015) Enhanced hydrogen evolution reaction of few-layer MoS_2 nanosheets-coated functionalized carbon nanotubes. Int J Hydrogen Energy 40:8877–8888
21. Dai X, Li Z, Du K, Sun H, Yang Y, Zhang X, Ma X, Wang J (2015) Facile synthesis of in-situ nitrogenated graphene decorated by few-layer MoS_2 for hydrogen evolution reaction. Electrochim Acta 171:72–80
22. Dalla Corte DA, Torres C, Correa PS, Rieder ES, Malfatti CF (2012) The hydrogen evolution reaction on nickel-polyaniline composite electrodes. Int J Hydrogen Energy 37:3025–3032
23. Das S, Ghosh R, Routh P, Shit A, Mondal S, Panja A, Nandi AK (2018) Conductive MoS_2 quatum dot/polyaniline aerogel for enhanced electrocatalytic hydrogen evolution and photoresponse properties. ACS Appl Nano Mater 1:2306–2316
24. Delgado D, Minakshi M, Kim DJ (2015) Electrochemical impedance spectroscopy studies on hydrogen evolution from porous Raney cobalt in alkaline solution. Int J Electrochem Sci 10:9379–9394

25. Dhaka S, Kumar R, Deep A, Kurade MB, Ji SW, Jeon BH (2019) Metal–organic frameworks (MOFs) for the removal of emerging contaminants from aquatic environments. Coord Chem Rev 380:330–352
26. Domask AC, Gurunathan RL, Mohney SE (2015) Transition metal–MoS_2 reactions: review and thermodynamic predictions. J Electron Mater 44:4065–4079. https://doi.org/10.1007/s11664-015-3956-5
27. Eftekhari A (2017) Electrocatalysts for hydrogen evolution reaction. Int J Hydrogen Energy 42:11053–11077
28. Gao MR, Chan MKY, Sun Y (2015) Edge-terminated molybdenum disulphide with a 9.4-Å interlayer spacing for electrochemical hydrogen production. Nat Commun 6:7493. https://doi.org/10.1038/ncomms8493
29. Guo X, Hou Y, Ren R, Chen J (2017) Temperature-dependent crystallization of MoS_2 nanoflakes on graphene nanosheets for electrocatalysis. Nanoscale Res Lett 12:479–488
30. Guo Y, Tang J, Qian H, Wang Z, Yamauchi Y (2017) One-pot synthesis of zeolitic imidazolate framework 67-derived hollow Co_3S_4@MoS_2 heterostructures as efficient bifunctional catalysts. Chem Mater 29:5566–5573
31. Guo Y, Fu X, Peng Z (2017a) Growth and mechanism of MoS_2 nanoflowers with ultrathin nanosheets. J Nanomater. https://doi.org/10.1155/2017/6865282
32. Gupta U, Rao CNR (2017) Hydrogen generation by water splitting using MoS_2 and other transition metal dichalcogenides. Nano Energy 41:49–65
33. Hakala M, Kronsberg R, Laasonen K (2017) Hydrogen adsorption on doped MoS_2 nanostructures. Sci Rep 7. https://doi.org/10.1038/s41598-017-15622-z
34. Han X, Tong X, Liu X, Chen A, Wen X, Yang N, Guo XY (2018) Hydrogen evolution reaction on hybrid catalysts of vertical MoS_2 nanosheets and hydrogenated graphene. ACS Catal 8:1828–1836
35. He Z, Que W (2016) Molybdenum disulfide nanomaterials: structures, properties, synthesis and recent progress on hydrogen evolution reaction. Appl Mater Today 3:23–56
36. Hellstern TR, Kibsgaard J, Tsai C, Palm DW, King LA, Abild-Pedersen F, Jaramillo TF (2017) Investigating catalyst–support interactions to improve the hydrogen evolution reaction activity of thiomolybdate $[Mo_3S_{13}]^{2-}$ nanoclusters. ACS Catal 7:7126–7130
37. Hod I, Deria P, Bury W, Mondloch JE, Kung CW, So M, Sampson MD, Peters AW, Kubiak CP, Farha OK, Hupp JT (2015) A porous proton-relaying metal-organic framework material that accelerates electrochemical hydrogen evolution. Nat Commun 6:8304. https://doi.org/10.1038/ncomms9304
38. Hong S, Sheng C, Krishnamoorthy A, Rajak P, Tiwari S, Nomura K, Misawa M, Shimojo F, Kalia RK, Nakano A, Vashishta P (2018) Chemical vapor deposition synthesis of MoS_2 layers from the direct sulfidation of MoO_3 surfaces using reactive molecular dynamics simulations. J Phys Chem C 122:7494–7503
39. Hyun CM, Choi JH, Lee SW, Park JH, Lee KT, Ahn JH (2018) Synthesis mechanism of MoS_2 layered crystals by chemical vapour deposition using MoO_3 and sulfur powders. J Alloy Compd 765:380–384
40. Jamesh MI, Sun X (2018) Recent progress on earth abundant electrocatalysts for oxygen evolution reaction (OER) in alkaline medium to achieve efficient water splitting—a review. J Power Sources 400:31–68
41. Karikalan N, Sundaresan P, Chen SM, Karthik R, Karuppiah C (2019) Cobalt molybdenum sulfide decorated with highly conductive sulfur-doped carbon as an electrocatalyst for the enhanced activity of hydrogen evolution reaction. Int J Hydrogen Energy 44:9164–9173
42. Kaur R, Kaur A, Umar A, Anderson WA, Kansal SK (2019) Metal organic framework (MOF) porous octahedral nanocrystals of Cu-BTC: Synthesis, properties and enhanced adsorption properties. Mater Res Bull 109:124–133
43. Kayan DB, Koçak D (2017) Enhanced catalytic activity of ppy-coated pencil electrode in the presence of chitosan and Au nanoparticles for hydrogen evolution reaction. J Solid State Electrochem. 21:2791–2798. https://doi.org/10.1007/s10008-017-3605-4

44. Khan M, Yousaf AB, Chen M, Wei C, Wu X, Huang N, Qi Z, Li L (2016) Molybdenum sulphide/graphene-carbon nanotube nanocomposite material for electrocatalytic applications in hydrogen evolution reactions. Nano Res 9:837–848
45. Kong Q, Wang X, Tang A, Duan W, Liu B (2016) Three-dimensional hierarchical MoS_2 nanosheet arrays/carbon cloth as flexible electrodes for high-performance hydrogen evolution reaction. Mater Lett 177:139–142
46. Krishnan U, Kaur M, Singh K, Kumar M, Kumar A (2019) A synoptic review of MoS_2: synthesis to applications. Superlattices Microstruct 128:274–297
47. Lei J, Jiang Z, Lu X, Nie G, Wang C (2015) Synthesis of few-layer MoS_2 nanosheets-wrapped polyaniline hierarchical nanostructures for enhanced electrochemical capacitance performance. Electrochim Acta 176:149–155
48. Li Y, He B, Liu X, Hu X, Huang J, Ye S, Shu Z, Wang Y, Li Z (2019) Graphene confined MoS_2 particles for accelerated electrocatalytic hydrogen evolution. Int J Hydrogen Energy 44:8070–8078
49. Li H, Qian X, Xu C, Huang S, Zhu C, Jiang X, Shao L, Hou L (2017) Hierarchical porous Co_9S_8/nitrogen-doped carbon@MoS_2 polyhedrons as pH universal electrocatalysts for highly efficient hydrogen evolution reaction. ACS Appl Mater Interfaces 9:28394–28405
50. Li H, Tsai C, Koh AL, Contryman AW, Fragapane AH, Zhao J, Han HS, Manoharan HC, Abild-Pedersen F, Nørskov JK, Zheng X (2016) Activating and optimizing MoS_2 basal planes for hydrogen evolution through formation of strained sulphur vacancies. Nat Mater 15:48–53
51. Li Y, Wang H, Wang R, He B, Gong Y (2018) 3D self-supported Fe-O-P film on nickel foam as a highly active bifunctional electrocatalyst for urea-assisted overall water splitting. Mater Res Bull 100:72–75
52. Li Y, Wang H, Xie L, Liang Y, Hong G, Dai H (2011) MoS_2 nanoparticles grown on graphene: an advanced catalyst for the hydrogen evolution reaction. J Am Chem Soc 133:7296–7299
53. Li R, Yang L, Xiong T, Wu Y, Cao L, Yuan D, Zhou W (2017) Nitrogen doped MoS_2 nanosheets via low-temperature process as electrocatalysts with enhanced activity for hydrogen evolution reaction. J Power Sources 356:133–139
54. Li F, Zhang L, Li J, Lin X, Li X, Fang Y, Huang J, Li W, Tian M, Jin J, Li R (2015) Synthesis of Cu-MoS_2/rGO hybrid as non-noble metal electrocatalysts for the hydrogen evolution reaction. J Power Sources 292:15–22
55. Li X, Zhu H (2015) Two-dimensional MoS_2: properties, preparation, and applications. J Materiomics 1:33–44
56. Li H, Yu K, Li C, Tang Z, Guo B, Lei X, Fu H, Zhu Z (2015a) Charge-transfer induced high efficient hydrogen evolution of MoS_2/graphene cocatalyst. Sci Rep 5:18730. https://doi.org/10.1038/srep18730
57. Lian M, Wu X, Wang Q, Zhang W, Wang Y (2017) Hydrothermal synthesis of polypyrrole/MoS_2 intercalation composite for supercapacitor electrodes. Ceram Int 43:9877–9883
58. Liu Y, Ghimire P, Jaroniec M (2019) Copper benzene-1,3,5-tricarboxylate (Cu-BTC) metal-organic framework (MOF) and porous carbon composites as efficient carbon dioxide adsorbents. J Colloid Interface Sci 535:122–132
59. Liu YR, Hu WH, Li X, Dong B, Shang X, Han GQ, Chai YM, Liu YQ, Liu CG (2016) Facile one-pot synthesis of CoS_2-MoS_2/CNTs as efficient electrocatalyst for hydrogen evolution reaction. Appl Surf Sci 384:51–57
60. Liu YR, Shang X, Gao WK, Dong B, Chi JQ, Li X, Yan KL, Chai YM, Liu YQ, Liu CG (2017) Ternary CoS_2/MoS_2/RGO electrocatalyst with CoMoS phase for efficient hydrogen evolution. Appl Surf Sci 412:138–145
61. Liu N, Yang L, Wang S, Zhong Z, He S, Yang X, Gao Q, Tang Y (2015) Ultrathin MoS_2 nanosheets growing within an in-situ-formed template as efficient electrocatalysts for hydrogen evolution. J Power Sources 275:588–594
62. Liu H, Zhang F, Li W, Zhang X, Lee CS, Wang W, Tang Y (2015) Porous tremella-like MoS_2/polyaniline hybrid composite with enhanced performance for lithium-ion battery anodes. Electrochim Acta 167:132–138

63. Liu Q, Wu Z, Ma Z, Dou S, Wu J, Tao L, Wang X, Ouyang C, Shen A, Wang S (2015b) One-pot synthesis of nitrogen and sulphur co-doped graphene supported MoS_2 as high performance anode materials for lithium-ion batteries. Electrochim Acta 177:298–303
64. Liu Y, Yu H, Quan X, Chen S, Zhao H, Zhang Y (2014) Efficient and durable hydrogen evolution electrocatalyst based on non-metallic nitrogen doped hexagonal carbon. Sci Rep 4:6843. https://doi.org/10.1038/srep06843
65. Lu X, Liu Y, Dong H, Dai W, Chen X, Qu X, Zhang X (2017) One-step hydrothermal fabrication of three-dimensional MoS_2 nanoflower using polypyrrole as template for efficient hydrogen evolution reaction. Sci Rep 7:42309. https://doi.org/10.1038/srep42309
66. Lukowski MA, Daniel AS, Meng F, Forticaux A, Li L, Jin S (2013) Enhanced hydrogen evolution catalysis from chemically exfoliated metallic MoS_2 nanosheets. J Am Chem Soc 135:10274–10277
67. Luo L, Shi M, Zhao Z, Tan W, Lin X, Wang H, Jiang F (2019) Hydrothermal synthesis of MoS_2 with controllable morphologies and its adsorption properties for bisphenol A. J Saudi Chem Soc. https://doi.org/10.1016/j.jscs.2019.01.005
68. Luo Z, Ouyang Y, Zhang H, Xiao M, Ge J, Jiang Z, Wang J, Tang D, Cao X, Liu C, Xing W (2018) Chemically activation MoS_2 via spontaneous atomic palladium interfacial doping towards efficient hydrogen evolution. Nat Commun 9:2120. https://doi.org/10.1038/s41467-018-04501-4
69. Lyon YA, Roberts AA, McMillin DR (2015) Exploring hydrogen evolution and the overpotential. J Chem Educ 92:2130–2133
70. Ma B, Chen TT, Li QY, Qin HY, Dong XY, Zang SQ (2019) Bimetallic-organic-framework derived nanohybrid $Cu_{0.9}Co_{2.1}.S_4@MoS_2$ for highly performance visible-light-catalytic hydrogen evolution. Materials 2:1134–1148
71. Ma CB, Qi X, Chen B, Bao S, Yin Z, Wu XJ, Luo Z, Wei J, Zhang HL, Zhang J (2014) MoS_2 nanoflower-decorated reduced graphene paper for high performance hydrogen evolution reaction. Nanoscale 6:5624–5629
72. Ma L, Ye J, Chen W, Chen D, Lee JM (2014) Gemini surfactant assisted hydrothermal synthesis of nanotile-like MoS_2/graphene hybrid with enhanced lithium storage performance. Nano Energy 10:144–152
73. Mahale NK, Ingle S (2017) Electrocatalytic hydrogen evolution reaction on nano-nickel decorated graphene electrode. Energy 119:872–878
74. Mashao G, Ramohlola KE, Mdluli SB, Monama GR, Hato MJ, Makgopa K, Molapo KM, Ramoroka ME, Iwuoha EI, Modibane KD (2019) Zinc-based zeolitic benzimidazolate framework/polyaniline nanocomposite for electrochemical sensing of hydrogen gas. Mater Chem Phys 230:287–298
75. Mdleleni MM, Hyeon T, Suslick KS (1998) Sonochemical synthesis of nanostructured molybdenum sulphide. J Am Chem Soc 120:6189–6190
76. Mir SH, Nagahara LA, Thundat T, Mokarian-Tabari P, Furukawa H, Khosla A (2018) Review—organic-inorganic hybrid functional materials: an integrated platform for applied technologies. J Electrochem Soc 165:B3137–B3156
77. Monama GR, Mdluli SB, Mashao G, Makhafola MD, Ramohlola KE, Molapo KM, Hato MJ, Makgopa K, Iwuoha EI, Modibane KD (2018) Palladium deposition on copper(II) phthalocyanine/metal organic framework composite and electrocatalytic activity of the modified electrode towards the hydrogen evolution reaction. Renew Energy 119:62–72
78. Monama GR, Modibane KD, Ramohlola KE, Molapo KM, Hato MJ, Makhafola MD, Mashao G, Mdluli SB, Iwuoha EI (2019) Copper(II) phthalocyanine/metal organic framework electrocatalyst for hydrogen evolution reaction application. Int J Hydrogen Energy. https://doi.org/10.1016/j.ijhydene.2019.02.052
79. Murthy AP, Theerthagiri J, Madhavan J (2018) Insights on Tafel constant in the analysis of hydrogen evolution reaction. J Phys Chem C 122:23943–23949
80. Noto V, Negro E, Vezzù K, Bertasi F, Nawn G (2015) Origins, developments, and perspectives of carbon nitride-based electrocatalysts for application in low-temperature FCs. Electrochem Soc Interface 24:59–62

81. Ouyang C, Feng S, Huo J, Wang S (2017) Three-dimensional hierarchical MoS_2/CoS_2 heterostructure arrays for highly efficient electrocatalytic hydrogen evolution. Green Energy Environ 2:134–141
82. Ouyang Y, Ling C, Chen Q, Wang Z, Shi L, Wang J (2016) Activating inert basal planes of MoS_2 for hydrogen evolution reaction through the formation of different intrinsic defects. Chem Mater 28:4390–4396
83. Presolski S, Pumera M (2016) Covalent functionalization of MoS_2. Mater Today 19:140–145
84. Pu Z, Wei S, Chen Z, Mu S (2016) 3D flexible hydrogen evolution electrodes with Se promoted molybdenum sulfide nanosheet arrays. RSC Adv 6:11077–11080
85. Pukazhselvan D, Kumar V, Singh SK (2012) High capacity hydrogen storage: basic aspects, new developments and milestones. Nano Energy 1:566–589
86. Ramohlola KE, Masikini M, Mdluli SB, Monama GR, Hato MJ, Molapo KM, Iwuoha EI, Modibane KD (2017) Electrocatalytic hydrogen evolution reaction of metal organic frameworks decorated with poly (3-aminobenzoic acid). Electrochim Acta 246:1174–1182
87. Ramohlola KE, Masikini M, Mdluli SB, Monama GR, Hato MJ, Molapo KM, Iwuoha EI, Modibane KD (2017) Electrocatalytic hydrogen production properties of poly(3-aminobenzoic acid) doped with metal organic frameworks. Int J Electrochem Sci 12:4392–4405
88. Ramohlola KE, Monana GR, Hato MJ, Modibane KD, Molapo KM, Masikini M, Mduli SB, Iwuoha EI (2018) Polyaniline-metal organic framework nanocomposite as an efficient electrocatalyst for hydrogen evolution reaction. Compos B 137:129–139
89. Ruiz KH, Liu J, Tu R, Li M, Zhang S, Garcia JRV, Mu S, Li H, Goto T, Zhang L (2018) Effect of microstructure on HER catalytic properties of MoS_2 vertically standing nanosheets. J Alloy Compd 747:100–108
90. Sapountzi FM, Gracia JM, Weststrate CJ, Fredriksson HOA, Niemantsverdriet JW (2017) Electrocatalysts for the generation of hydrogen, oxygen and synthesis gas. Prog Energy Combust Sci 58:1–35
91. Sarker S, Chaturvedi P, Yan L, Nakotte T, Chen X, Richins SK, Das S, Peters J, Zhou M, Smirnov SN, Luo H (2018) Synergistic effect of iron diselenide decorated multi-walled carbon nanotubes for enhanced heterogeneous electron transfer and electrochemical hydrogen evolution. Electrochim Acta 270:138–146
92. Shen X, Xia X, Ye W, Du Y, Wang C (2017) Hexagram-like CoS-MoS2 composites with enhanced activity for hydrogen evolution reaction. J Solid State Electrochem 21:409–417
93. Shi Y, Zhou Y, Yang DR, Xu WX, Wang C, Wang FB, Xu JJ, Xia XH, Chen HY (2017) Energy level engineering of MoS_2 by transition-metal doping for accelerating hydrogen evolution reaction. J Am Chem Soc 139:15479–15485
94. Shinagawa T, Garcia-Esparza AT, Takanabe K (2015) Insight on Tafel slopes from a microkinetic analysis of aqueous electrocatalysis for energy conversion. Sci Rep 5:13801. https://doi.org/10.1038/srep13801
95. Singh AK, Kumar P, Late DJ, Kumar A, Patel S, Singh J (2018) 2D layered transition metal dichalcogenides (MoS_2): synthesis, applications and theoretical aspects. Appl Mater Today 13:242–270
96. Singh A, Moun M, Singh R (2019) Effect of different precursors on CVD growth of molybdenum disulfide. J Alloy Compd 782:772–779
97. Strmcnik D, Lopes PP, Genorio B, Stamenkovic VR, Markovic NM (2016) Design principles for hydrogen evolution reaction catalyst materials. Nano Energy 29:29–36
98. Su W, Wang P, Cai Z, Yang J, Wang X (2019) One-pot hydrothermal synthesis of Al-doped MoS_2@graphene aerogel nanocomposite electrocatalysts for enhanced hydrogen evolution reaction. Results Phys 12:250–258
99. Su C, Xiang J, Wen F, Song L, Mu C, Xu D, Hao C, Liu Z (2016) Microwave synthesized three-dimensional hierarchical nanostructure CoS_2/MoS_2 growth on carbon fiber cloth: a bifunctional electrode for hydrogen evolution and supercapacitor. Electrochim Acta 212:941–949

100. Sultana UK, O'Mullane AP (2018) Electrochemical formation of amorphous molybdenum phosphosulfide for enabling the hydrogen evolution reaction in alkaline and acidic media. ACS Appl Energy Mater 1:2849–2858
101. Sun W, Li X, Shi J, Sun H, Tao Z, Li F, Chen J (2017) Size-controlled MoS_2 nanodots supported on reduced graphene oxide for hydrogen evolution reaction and sodium-ion batteries. Nano Res 10:2210–2222
102. Sun T, Wang J, Chi X, Lin X, Chen Z, Ling X, Qiu L, Xu Y, Song L, Chen W, Su C (2018) Engineering the electronic structure of MoS_2 nanorods by N and Mn dopants for ultra-efficient hydrogen production. ACS Catal 8:7585–7592
103. Tahir M, Pan L, Idrees F, Zhang X, Wang L, Zou JJ, Wang ZL (2017) Electrocatalytic oxygen evolution reaction for energy conversion and storage: a comprehensive review. Nano Energy 37:136–157
104. Tahira A, Ibupoto ZH, Mazzaro R, You S, Morandi V, Natile MM, Vagin M, Vomiero A (2019) Advanced electrocatalysts for hydrogen evolution reaction based on core−shell MoS_2/TiO_2 nanostructures in acidic and alkaline media. ACS Appl Energy Mater 2:2053–2062
105. Talin AA, Centrone A, Ford AC, Foster ME, Stavila V, Haney P, Kinney RA (2014) Tunable electrical conductivity in metal-organic framework thin-film devices. Science 343:66–69. https://doi.org/10.1126/science.1246738
106. Tan C, Cao X, Wu XJ, He H, Yang J, Zhang X, Chen J, Zhao W, Han S, Nam GH, Sindoro M, Zhang H (2017) Recent advances in ultrathin two-dimensional nanomaterials. Chem Rev 117:6225–6331
107. Tang Q, Jiang D (2015) Stabilization and band-gap tuning of the 1T-MoS_2 monolayer by covalent functionalization. Chem Mater 27:3743–3748
108. Theerthagiri J, Sudha R, Premnath K, Arunachalam P, Madhavan J, Al-Mayouf AM (2017) Growth of iron diselenide nanorods on graphene oxide nanosheets as advanced electrocatalyst for hydrogen evolution reaction. Int J Hydrogen Energy 42:13020–13030
109. Tian J, Wu W, Tang Z, Wu Y, Burns R, Tichnell B, Liu Z, Chen S (2018) Oxygen reduction reaction and hydrogen evolution reaction catalyzed by pd–ru nanoparticles encapsulated in porous carbon nanosheets. Catalysts 8:329. https://doi.org/10.3390/catal8080329
110. Tong T, Li Q, Li W, Ma W, Su B, Bo L (2017) MoS_2 thin sheet growing on nitrogen self-doped mesoporous graphic carbon derived from ZIF-8 with highly electrocatalytic performance on hydrogen evolution reaction. ACS Sustain Chem Eng 5:10240–10247
111. Tong SS, Wang XJ, Li QC, Han XJ (2016) Progress on electrocatalysts of hydrogen evolution reaction based on carbon fiber materials. Chin J Anal Chem 44:1447–1457
112. Tributsch H, Bennett JC (1977) Electrochemistry and photochemistry of MoS_2 layer crystals. I. J Electroanal Chem Interfacial Electrochem 81:97–111
113. Tsai C, Abild-Pedersen F, Nørskov JK (2014) Tuning the MoS_2 edge-site activity for hydrogen evolution via support interactions. Nano Lett 14:1381–1387
114. Tsai C, Chan K, Nørskov JK, Abild-Pedersen F (2015) Theoretical insights into the hydrogen evolution activity of layered transition metal dichalcogenides. Surf Sci 640:133–140
115. Tsai C, Li H, Park S, Park J, Han HS, Nørskov JK, Zheng X, Abild-Pedersen F (2017) Electrochemical generation of sulphur vacancies in the basal plane of MoS_2 for hydrogen evolution. Nat Commun 8 (2017) https://doi.org/10.1038/ncomm15113
116. Voiry D, Salehi M, Silva R, Fujita T, Chen M, Asefa T, Shenoy VB, Eda G, Chhowalla M (2013) Conducting MoS_2 nanosheets as catalysts for hydrogen evolution reaction. Nano Lett 13:6222–6227
117. Wang Y, Chen B, Seo DH, Han ZJ, Wong JI, Ostrikov KK, Zhang H, Yang HY (2016) MoS_2-coated vertical nanosheet for high performance rechargeable lithium-ion batteries and hydrogen production. NPG Asia Mater 8:e268. https://doi.org/10.1038/am.2016.44
118. Wang Y, Lia X, Wang C (2017) Synthesis and characterization of MoS_2 nanocomposites by a high pressure hydrothermal method. J Non-Oxide Glasses 9:47–54
119. Wang D, Pan Z, Wu Z, Wang Z, Liu Z (2014) Hydrothermal synthesis of MoS_2 nanoflowers as highly efficient hydrogen evolution reaction catalysts. J Power Sources 264:229–234

120. Wang G, Parrondo J, He C, Li Y, Ramani V (2017) Pt/C/Ni(OH)$_2$ bi-functional electrocatalyst for enhanced hydrogen evolution reaction activity under alkaline conditions. J Electrochem Soc 164:F1307–F1315
121. Wang C, Su Y, Zhao X, Tong S, Han X (2018) MoS_2@HKUST-1 flower-like nanohybrids for efficient hydrogen evolution reactions. Chem A Eur J 24:1080–1087
122. Wang D, Xie Y, Wu Z (2019) Amorphous phosphorus-doped MoS_2 catalyst for efficient hydrogen evolution reaction. Nanotechnology 30:205401–205407
123. Wang W, Zhang K, Qiao Z, Li L, Liu P, Yang Y (2014) Influence of surfactants on the synthesis of MoS_2 catalysts and their activities in the hydrodeoxygenation of 4-methylphenol. Ind Eng Chem Res 53:10301–10309
124. Wen L, Sun Y, Zhang T, Bai Y, Li X, Lyu X, Cai W, Li Y (2018) $MnMoO_4$ nanosheet array: an efficient electrocatalyst for hydrogen evolution reaction with enhanced activity over a wide pH range. Nanotechnology 29:335403. https://doi.org/10.1088/1361-6528/aac851
125. Wen Y, Zhu H, Zhang L, Zhang S, Zhang M, Du M (2019) Activating MoS_2 by interface engineering for efficient hydrogen evolution catalysis. Mater Res Bull 112:46–52
126. Wu L, Xu X, Zhao Y, Zhang K, Sun Y, Wang T, Wang Y, Zhong W, Du Y (2017) Mn doped MoS_2/reduced graphene oxide hybrid for enhanced hydrogen evolution. Appl Surf Sci 425:470–477
127. Wu Z, Zou Z, Huang J, Gao F (2018) Fe-doped NiO mesoporous nanosheets array for highly efficient overall water splitting. J Catal 358:243–252
128. Wu W, Niu C, Wei C, Jia Y, Li C, Xu Q (2019) Activating of MoS_2 basal planes for hydrogen evolution through zinc. Angew Chem. https://doi.org/10.1002/ange.201812475
129. Wypych F, Schollhorn R (1992) 1T-MoS_2, a new metallic modification of molybdenum disulfide. J Chem Soc Chem Commun 19:1386–1387
130. Xiang ZC, Zhang Z, Xu XJ, Zhang Q, Yuan C (2016) MoS_2 nanosheets array on carbon cloth as a 3D electrode for highly efficient electrochemical hydrogen evolution. Carbon 98:84–89
131. Xiong Q, Zhang X, Wang H, Liu G, Wang G, Zhang H, Zhao H (2018) One-step synthesis of cobalt-doped MoS_2 nanosheets as bifunctional electrocatalysts for overall water splitting under both acidic and alkaline conditions. Chem Commun 54:3859–3862
132. Xu W, Wang H (2017) Earth-abundant amorphous catalysts for electrolysis of water. Chin J Catal 38:991–1005
133. Yang F, Kang N, Yan J, Wang X, He J, Huo S, Song L (2018) Hydrogen evolution reaction property of molybdenum disulphide/nickel phosphide hybrids in alkaline solution. Metals 8:359–376
134. Yang L, Liu P, Li J, Xiang B (2017) Two-dimensional material molybdenum disulfides as electrocatalysts for hydrogen evolution. Catalysts 7:285. https://doi.org/10.3390/catal7100285
135. Yang Y, Yang H, Liang C, Zhu X (2018) Synthesis and characterization of Ni-Co electrocatalyst for hydrogen evolution reaction in acidic media. Int J Electrochem Sci 13:7193–7205
136. Ye G, Gong Y, Lin J, Li B, He Y, Pantelides ST, Zhou W, Vajtai R, Ajayan PM (2016) Defects engineered monolayer MoS_2 for improved hydrogen evolution reaction. Nano Lett 16:1097–1103
137. Yu X, Zhao J, Zheng LR, Tong Y, Zhang M, Xu G, Li C, Ma J, Shi G (2018) Hydrogen evolution reaction in alkaline media: Alpha- or beta-nickel hydroxide on the surface of platinum? ACS Energy Lett 3:237–244
138. Zang Y, Niu S, Wu Y, Zheng X, Cai J, Ye J, Xie Y, Liu Y, Zhou J, Zhu J, Liu X, Wang G, Qian Y (2019) Tuning orbital orientation endows molybdenum disulfide with exceptional alkaline hydrogen evolution capability. Nat Commun 10:1217. https://doi.org/10.1038/s41467-019-09210-0
139. Zeng X, Niu L, Song L, Wang X, Shi X, Yan J (2015) Effect of polymer addition on the structure and hydrogen evolution reaction property of nanoflower-like molybdenum disulfide. Metals 5:1829–1844
140. Zhang L, Guo Y, Igbal A, Li B, Gong D, Liu W, Igbal K, Liu W, Qin W (2018) One step synthesis of the 3D flower-like heterostructures MoS_2/CuS nanohybrid for electrocatalytic hydrogen energy. Int J Hydrogen Energy 43:1251–1260

141. Zhang WL, Jiang D, Wang X, Hao BN, Liu YD, Liu J (2017) Growth of polyaniline nanoneedles on MoS_2 nanosheets, tunable electroresponse, and electromagnetic wave attenuation analysis. J Phys Chem C 121:4989–4998
142. Zhang LF, Ke X, Ou G, Wei H, Wang LN, Wu H (2017) Defective MoS_2 electrocatalyst for highly efficient hydrogen evolution through ball-milling method. Sci China Mater 60:849–856
143. Zhang N, Ma W, Wu T, Wang H, Han D, Niu L (2015) Edge-rich MoS_2 nanosheets rooting into polyaniline nanofibers as effective catalyst for electrochemical hydrogen evolution. Electrochim Acta 180:155–163
144. Zhang C, Wang Z, Bhoyate S, Morey T, Neria BL, Vasirajn V, Gupta G, Palchoudhury S, Kahol PK, Mishra SR, Perez F, Gupta RK (2017) MoS_2 decorated carbon nanofibers as efficient and durable electrocatalyst for hydrogen evolution reaction. J Carbon Res 3:33–44
145. Zhang L, Xiao J, Wang H, Shao M (2017) Carbon-based electrocatalysts for hydrogen and oxygen evolution reactions. ACS Catal 7:7855–7865
146. Zhang P, Xu B, Chen G, Gao C, Gao M (2018) Large-scale synthesis of nitrogen doped MoS_2 quantum dots for efficient hydrogen evolution reaction. Electrochim Acta 270:256–263
147. Zhang X, Yang Y, Ding S, Que W, Zheng Z, Du Y (2017) Construction of high-quality SnO_2@MoS_2 nanohybrids for promising photoelectrocatalytic applications. Inorg Chem 56:3386–3393
148. Zhang Y, Zeng W, Li Y (2018) Hydrothermal synthesis and controlled growth of hierarchical 3D flowerlike MoS_2 nanospheres assisted with CTAB and their NO_2 gas sensing properties. Appl Surf Sci 455:276–282
149. Zhang Y, Zeng W, Li Y (2018) The hydrothermal synthesis of 3D hierarchical porous MoS_2 microspheres assembled by nanosheets with excellent gas sensing properties. J Alloy Compd 749:355–362
150. Zhao X, Ma X, Lu Q, Li Q, Han C, Xing Z, Yang X (2017) FeS_2-doped MoS_2 nanoflower with the dominant 1T-MoS_2 as an excellent electrocatalyst for high-performance hydrogen evolution. Electrochim Acta 249:72–78
151. Zhao S, Weng J, Jin S, Lv Y, Ji Z (2018) Chemical vapor transport deposition of molybdenum disulfide layers using H_2O vapor as the transport agent. Coatings 8:78–86
152. Zhou W, Jia J, Lu J, Yang L, Hou D, Li G (2016) Recent developments of carbon based electrocatalysts for hydrogen evolution reaction. Nano Energy 28:29–43
153. Zhou W, Zhou K, Hou D, Liu X, Li G, Sang Y, Liu H, Li L, Chen S (2014) Three-dimensional hierarchical frameworks based on MoS_2 nanosheets self-assembled on graphene oxide for efficient electrocatalytic hydrogen evolution. ACS Appl Mater Interfaces 6:21534–21540
154. Zhu J, Wang ZC, Dai H, Wang Q, Yang R, Yu H, Liao M, Zhang J, Chen W, Wei Z, Li N, Du L, Shi D, Wang W, Zhang L, Jiang Y, Zhang G (2019) Boundary activated hydrogen evolution reaction on monolayer MoS_2. Nat Commun 10. https://doi.org/10.1038/s41467-019-09269-9
155. Zuo LX, Jiang LP, Abdel-Halim ES, Zhu JJ (2017) Sonochemical preparation of stable porous MnO_2 and its application as an efficient electrocatalyst for oxygen reduction reaction. Ultrason Sonochem 35:219–225
156. Zuo LX, Jiang LP, Zhu JJ (2017) A facile sonochemical route for the synthesis of MoS_2/Pd composites for highly efficient oxygen reduction reaction. Ultrason Sonochem 35:681–688

Electrocatalysts for Photoelectrochemical Water Splitting

Yasser A. Shaban

Abstract The fast depletion of fossil fuels, the main energy sources, in addition to the emission of carbon dioxide (CO_2) from burning of these fuels intensifying the research for the development of alternative clean, sustainable and secure energy source. Hydrogen (H_2) is considered as one of the most promising alternatives that can play a significant role as a zero-carbon energy carrier with reduced fossil fuel dependence. Utilization of two of our most abundant resources, sunlight and water, for the production of hydrogen via mimicking the natural photosynthesis process by the photocatalytic water splitting by using a semiconductor photocatalyst is a fascinating way for the establishment of clean, sustainable and secure energy source. This chapter highlights the efforts that have been devoted for the development of photocatalysts that can efficiently harvest the maximum solar light for the photoelectrochemical water splitting into hydrogen and oxygen. The difficulties in achieving water splitting under visible light will be addressed. Furthermore, the strategies for overcoming these difficulties and approaches for improving the visible light response of the photocatalysts towards water splitting will be discussed.

Keywords Water splitting · Photocatalysis · Hydrogen · Bandgap · Photoelectrochemical · Non-metal doping · Metal doping · Semiconductor · Renewable energy · Dye sensitization

1 Introduction

Global economic growth and increasing world population further increase energy demand. Based on current projections, almost 1.3 billion new energy consumers will be added by 2030 [36]. Fossil fuels, the main energy sources, are depleting fast and cannot afford the predicted energy needs. Furthermore, the global warming caused by the emission of carbon dioxide (CO_2) from burning of these fuels is considered as one of the most serious environmental issues. Therefore, the establishment of

Y. A. Shaban (✉)
Marine Chemistry Department, Faculty of Marine Sciences, King Abdulaziz University, P.O. Box 80207 Jeddah 21589, Saudi Arabia
e-mail: ydomah@kau.edu.sa

Inamuddin et al. (eds.), *Methods for Electrocatalysis*,
https://doi.org/10.1007/978-3-030-27161-9_14

clean, sustainable and secure energy source is questionably one of the most critical challenges facing humankind in the 21st century.

Hydrogen (H_2) is considered as one of the most promising alternatives to provide non-polluting, viable, and secure energy [65]. Hydrogen can play a significant role as a zero-carbon energy carrier with reduced fossil fuel dependence with the versatility to be operated across different sectors such as electricity, industry, and transportation. Moreover, it has much larger calorific value per mass unit (142 MJ) which is quadruple that of natural gas and triple that of gasoline. However, the present industrial technology for H_2 production, steam methane reforming, is a non-sustainable process as it consumes huge quantities of fossil fuels (e.g., natural gas), and releases a huge amount of carbon dioxide to the environment. Therefore, production of hydrogen gas using renewable energy sources rather than fossil fuels has attracted much interest as a clean energy carrier.

Among renewables, solar energy is by far the cheapest and largest exploitable source; it could be considered as the ultimate renewable energy resource. Approximately 1000 W/m^2 of solar energy continuously reaches the Earth, by far exceeds all human energy needs [54], with 5% of this radiation at wavelengths less than 400 nm, in the ultraviolet (UV) range, and 49% within the visible spectrum, in the 400–750 nm wavelength [66]. Solar energy can be converted efficiently into electricity by photovoltaic devices, or into heat by solar thermal collectors. However, the capturing, conversion, storage and distribution of solar energy are the main factors that determine its exploitation as an energy source. Collecting and storing the solar energy into chemical bonds (solar fuel) are the major difficulties for its utilization.

A fascinating way to overcome all of these obstacles is the utilization of two of our most abundant resources, sunlight and water, for the production of hydrogen via mimicking the natural photosynthesis process by the photocatalytic water splitting. In this way, renewable solar energy is converted into an inherently more storable and transportable form of energy.

2 Photoelectrochemical Water Splitting

The pioneering study in the photocatalytic water splitting using a photo electrochemical cell (PEC) with a titanium dioxide (TiO_2) as the photo-catalyst was reported by Fujishima and Honda [22]. Generally, the photoelectrochemical reaction has been defined as a particular case of photochemical reactions, which is associated with the flow of an electric current through an external circuit [73]. For carrying out the water splitting reaction, the photocatalyst is utilized as a photo-anode or photo-electrode in a photoelectrochemical cell [57]. However, to direct the photo-generated electrons from the photo anode to the cathode, an external circuit is required. Production of hydrogen molecule is carried out by the reaction between the generated electron and the proton at the cathode side (Fig. 1).

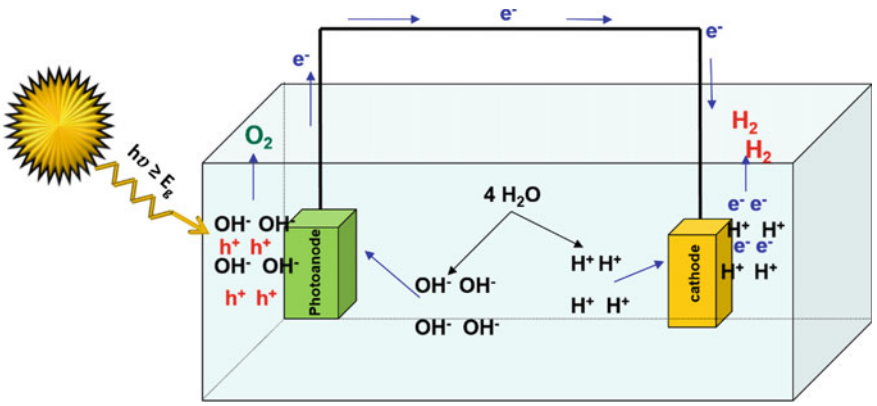

Fig. 1 Schematic diagram of a typical photo-electrochemical cell for water splitting

In a typical photoelectrochemical cell (PEC), the photoelectrochemical water splitting using semiconductor involves several processes at the photoelectrode/electrolyte interface, including the following [91]:

i. **Dissociation of water molecules**

Water molecules spontaneously dissociate into H^+ and OH^- in an electrolyte solution,

$$4H_2O \rightarrow 4H^+ + 4OH^- \tag{1}$$

ii. **Light-induced excitation**

Upon illumination of a semiconductor electrode by a light with photonic energy ($h\nu$) matches or exceeds its band gap energy (E_g), charge carrier electron/hole pairs are generated in the bulk of the semiconductor. Electrons are excited from the valence band (VB) to the conduction band (CB), leaving an equal number of vacant sites (holes), then the photogenerated electrons (e^-) and holes (h^+) diffuse to the semiconductor surface.

$$\text{photoanode} + \text{sunlight} \rightarrow 4h^+ + 4e^- \tag{2}$$

iii. ***Hydrogen evolution reaction***

The photo-generated electrons from the photoanode (Eq. 2) are then transferred to the cathode over the external circuit, resulting in the reduction of hydrogen ions (H^+) to gaseous hydrogen (H_2):

$$4H^+ + 4e^- \rightarrow 2H_2(\text{gas}) \quad \text{at cathode} \tag{3}$$

iv. ***Oxygen evolution reaction***

At the photoanode/electrolyte interface, the hydroxyl (OH^-) ions are oxidized by the light-induced holes from Eq. (2) to produce gaseous oxygen (O_2)

$$4OH^- + 4h^+ \rightarrow O_2(gas) + 2H_2O \quad \text{at photoanode} \tag{4}$$

The overall reaction will be

$$\text{photoanode} + \text{sunlight} + H_2O \rightarrow {}^1/_2O_2(gas) + H_2(gas) \tag{5}$$

3 Properties of Semiconductor Photocatalysts for Water Splitting

3.1 Bandgap

Thermodynamically, splitting of water into hydrogen and oxygen is associated by a large positive change in the standard Gibbs free energy (the Gibbs free energy change $\Delta G^\circ = +237$ kJ/mol, corresponding to $\Delta E^\circ = 1.23$ V). Therefore, for water splitting, a minimum energy of 1.229 eV/electron should be supplied.

As solar radiation cannot be absorbed by pure water and the electrochemical decomposition of water to hydrogen and oxygen is suggested to be achieved via a two-electron stepwise process, therefore, it is possible to utilize a photo-semiconductor that is capable of efficiently absorbing solar energy. The semiconductor electronic structure plays a major role in its photoactivity. The energy difference between its conduction band (CB) and valence band (VB) is called the bandgap (E_g), which should be less than 3.0 eV, but larger than 1.23 eV to split the water molecule in an indirect way through the generation of electrons and holes that can be, respectively, involved in the reduction and oxidation the water molecules adsorbed on photocatalysts [23, 45, 58, 67, 115].

3.2 Band Edges Positions

The electronic structure is doubtless the key parameter that decides the water splitting ability of the photocatalyst. Figure 2 depicts the band positions of various semiconductors for water oxidation/reduction processes at pH 0 [104]. The levels of conduction band (CB) and valence band (VB) of the semiconductor should satisfy the energy requirements set by the redox potentials for H_2O (Fig. 3). For efficient hydro-

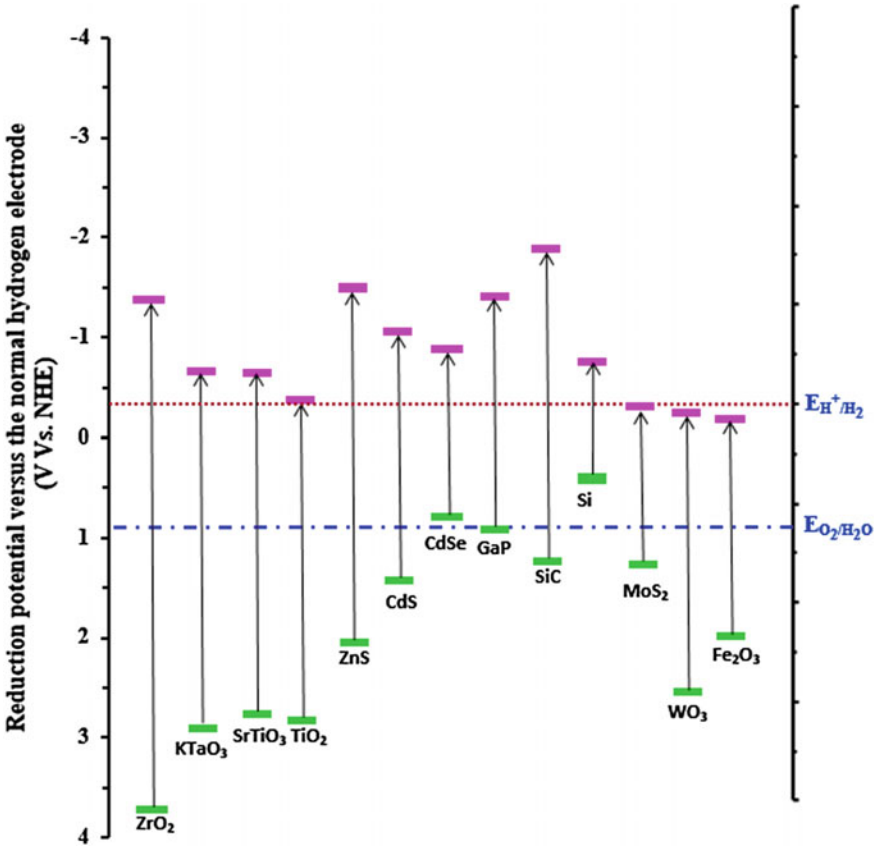

Fig. 2 Band gap positions of various potential semiconductors with respect to the redox potentials of H_2O [104]

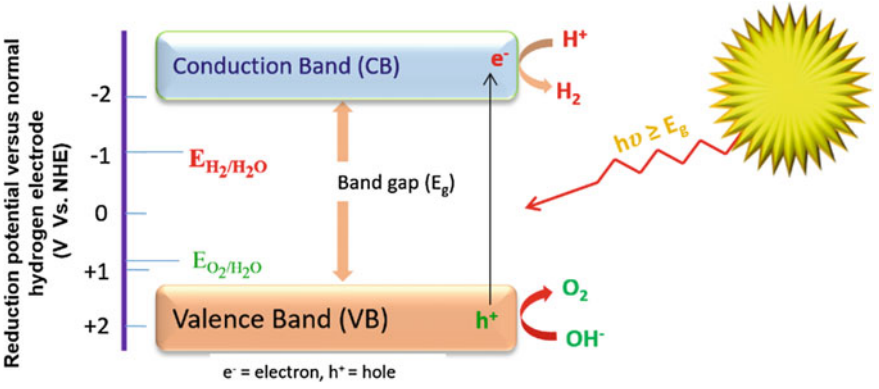

Fig. 3 Basic principle of photoelectrochemical water splitting on a photocatalyst

gen generation, the lowest level of its CB should be more negative than the reduction potentials of H_2O (E_{H_2O/H_2}) while the highest level of its VB should be located more positively than the oxidation potential of H_2O (E_{H_2O/O_2}) for oxygen production.

3.3 Charge Carriers Separation and Migration

The photocatalyst used for water splitting reaction should be capable to separate the photo-generated charge carriers. It is also essential for the separated charge carriers to be migrated to the solid-liquid interface during their life time and to find appropriate reaction partners, water molecules for holes and protons for electrons. Furthermore, the generation/separation of photo-excited electrons and holes should be associated with a minimal recombination rate. The migration of electrons and holes towards the photocatalyst surface strongly depends on the surface area of the photocatalyst which determined by its particle size. Efficient charge migration involves essentially longer diffusion lengths than the size of the photocatalyst particles. Therefore, upon decreasing the particle size of photocatalysts, the opportunity for the charge carrier to reach its surface increases [6].

The fast recombination of the separated electrons and holes to become trapped in surface sites is one of major factors that can minimize the efficiency of the photocatalyst towards water splitting [2]. Therefore, a suitable modification of the photocatalyst should be performed to promote the efficient charge carrier separation and migration of photogenerated electron-hole pairs (e^-/h^+) to the surface and suppress their recombination in the bulk.

3.4 Stability in Aqueous Media

Stability against photocorrosion and dissolution processes in aqueous environments is one of the necessary requirements that should be satisfied by the photocatalyst. Therefore, photo-electrodes utilized for water splitting must exhibit excellent oxidative/reductive stability in contact with aqueous electrolyte solution. The photocorrosion occurs when the photogenerated charge carriers (electrons/holes) decompose the photocatalyst itself instead of performing the water oxidation/reduction processes. The relative positions of the semiconductor band edges and the respective decomposition potentials are the main factors determining the photocorrosion reactions. When the cathodic decomposition potential is below the conduction band of the semiconductor, cathodic photocorrosion can occur. Conversely, in case of the anodic decomposition potential is above the valence band potential of the semiconductor, the anodic photocorrosion can happen.

4 Photocatalysts for Water Splitting

Typically, photocatalysts that can exhibit a significant photocatalytic activity towards water splitting are synthesized from metal oxides, metal sulfides, oxynitrides, oxysulfides and composites. In most cases, metal cations with the highest oxidative states in photocatalysts have d^0 or d^{10} electronic configuration, while O, S and N show their most negative states. Unfortunately, most of the photo-semiconductor materials are only active under UV light and those active under visible light are quite limited.

4.1 UV-Active Photocatalysts

Various types of semiconductors have been reported as efficient photocatalysts to split water into H_2 and O_2 under illumination of UV light. These photocatalysts can be classified into four groups.

4.1.1 Titanium Oxide (TiO_2) and Titanates

Overall water splitting using titanium oxide (TiO_2) [82] and $SrTiO_3$ [18] under illumination of UV light was reported for the first time in 1980. Shibata et al. [92] reported the photocatalytic H_2 evolution from aqueous methanol solutions by using layered titanates, such as $Na_2Ti_3O_7$, $K_2Ti_2O_5$ and $K_2Ti_4O_9$. Perovskite titanates, La_2TiO_5, La_2TiO_3 and $La_2Ti_2O_7$, with layered structures have been also described as materials with high photocatalytic activities under UV irradiation [43]. Titanates with cubic-pyrochlore structure $R_2Ti_2O_7$ (R = Y, Eu, Ga, La) showed a fairly high activity for overall water-splitting reaction [1].

4.1.2 Tantalates and Niobates

Oxides with tunneling and layered structures are considered as promising candidatess for efficient water splitting. According to this fact, tantalates and niobates oxides with corner-sharing of MO_6 (M = Ta, Nb) octahedra structure have been investigated as photocatalysts for water splitting. Due to of their wide bandgap energy (4.0–4.7 eV), tantalates and niobates oxides are highly active for water splitting only under UV light, even without co-catalysts [94]. This high activity of this layered compounds under UV light can be attributed to the easy separation and migration of the photogenerated charge carriers (electrons/holes) through the corner-shared framework of MO_6 units [49].

4.1.3 d^{10} Metal Oxides

It has been reported that metal oxides with d^{10} configuration including gallates (Ga^{3+}), indates (In^{3+}), stannates (Sn^{4+}), germinates (Ge^{4+}), and antimonates (Sb^{5+}) are efficient photocatalysts for water splitting under UV light. The potential of d^{10} metal oxides such as $NaInO_2$ and $CaSb_2O_6$, $Ca_2Sb_2O_7$ and $Sr_2Sb_2O_7$ and Zn_2GeO_4 for water splitting has been highlighted by Inoue [32]. B-Ga_2O_3 with a band gap of 4.5 eV has been reported as promising photocatalysts for water splitting under [106]. Significantly high water splitting rate was observed for $CaIn_2O_4$, $SrIn_2O_4$ and $BaIn_2O_4$ under UV irradiation [80]. Distorted octahedral and/or tetrahedral structures of some metal oxides with d^{10} configurations such as, $CaSb_2O_6$ [81], Zn_2GeO_4 [79], and $ZnGa_2O_4$ [29] were also reported to exhibit a photocatalytic H_2O splitting activity under UV irradiation.

4.1.4 Nonoxide

Sulfides, nitrides and phosphide photocatalysts that have wide band gap and VB at relatively negative potentials compared to oxides have also been reported as semiconductors for UV-driven photocatalysis. ZnS has been reported as high-active photocatalyst for hydrogen production from SO_3^{2-} solutions under UV irradiation [76]. InP was the sole reported phosphide that is able to produce hydrogen from aqueous sulfite solutions [69]. Nitrides photocatalysts with d^{10} electronic configuration (Ga^{3+}, Ge^{4+}) are another type of photocatalysts that can split water efficiently under UV light [3, 63].

4.2 Visible Light Active Photocatalysts

The number of visible light active photocatalysts for water splitting is quite limited. They can be divided into three groups.

4.2.1 Oxides

Despite some oxides, such as $BiVO_4$ and Ag_3VO_4 exhibit visible light response towards evolution of oxygen from aqueous silver nitrate solution, but they are unable to generate hydrogen from water due to too low conduction bands for water reduction [47]. These oxides possess steep absorption edges in the visible light region, revealing that the band-band transition is the reason for the visible light absorption of these oxides. In contrast with other oxides, the mixing of Bi and Ag orbitals with O2p states in the valence band of $BiVO_4$ and Ag_3VO_4, respectively, decreases their band gap energies and increases of the potentials of valence bands. Therefore, $BiVO_4$ and Ag_3VO_4 have the ability to absorb visible light [47].

4.2.2 Sulfides

Metal sulfide are considered as good candidates for visible light-driven photocatalysts due to their narrow band gap and the relatively negative potentials of valence band, compared to other oxides. However, the higher susceptibility of S^{2-} anions to oxidation than water causing the photo-degradation of the photocatalyst in the water oxidation reaction under visible light [20]. Therefore, appropriate strategies are designed to minimize the photo-degradation of sulfide photocatalysts to be suitable for water splitting. Among the available, CdS is one of the promising sulfide semiconductors due to its narrow band gap (2.4 eV) and a suitable CB potential to effectively reduce the H^+ [16, 77].

4.2.3 Other Materials

Some phosphate semiconductors has been reported as promising photocatalysts for water splitting under visible light. $Li_9FE_3(P_2O_7)_3(PO_4)_2$ has been confirmed to be an active photocatalyst for hydrogen production under irradiation of visible light using I^- ions as electron donor [33].

The development of graphitic carbon nitride (g-C_3N_4) having a bandgap of 2.7 eV has triggered considerable interests as an efficient photocatalyst for water splitting under the illumination of visible-light with the aid of sacrificial reagents [99]. Graphene oxide semiconductor photocatalyst with a band gap of 2.4–4.3 eV can also steadily produce H_2 from an aqueous methanol solution or pure water under visible light irradiation as reported recently by Yeh et al. [109].

5 Difficulties in Achieving Water Splitting Under Visible Light

Basically, it is difficult to develop an oxide semiconductor photocatalyst that has both an adequately narrow band gap (i.e., $E_g < 3.0$ eV) for visible light activity and a satisfactorily negative conduction band for H_2 production because of the highly positive valence band [84]. Indeed, most visible-light-responsive oxide photocatalysts, such as WO_3 [15, 21, 47, 83, 97], are not capable to produce H_2 from water splitting due to their conduction bands being too low for water reduction as can be seen for class B in Fig. 4. On the other hand, narrow bandgap of semiconductors, such as Fe_2O_3, are capable for visible light absorption, but the configuration of their band edges is not suitable for driving both water reduction and oxidation reactions. Accordingly, the only solution for these materials to be able to drive either oxidation or reduction of water, is to be used only in tandem cells.

Although some non-oxide such as sulfides [46, 53, 64, 113] and nitrides [26, 52] semiconductors possess suitable band levels for water splitting under visible

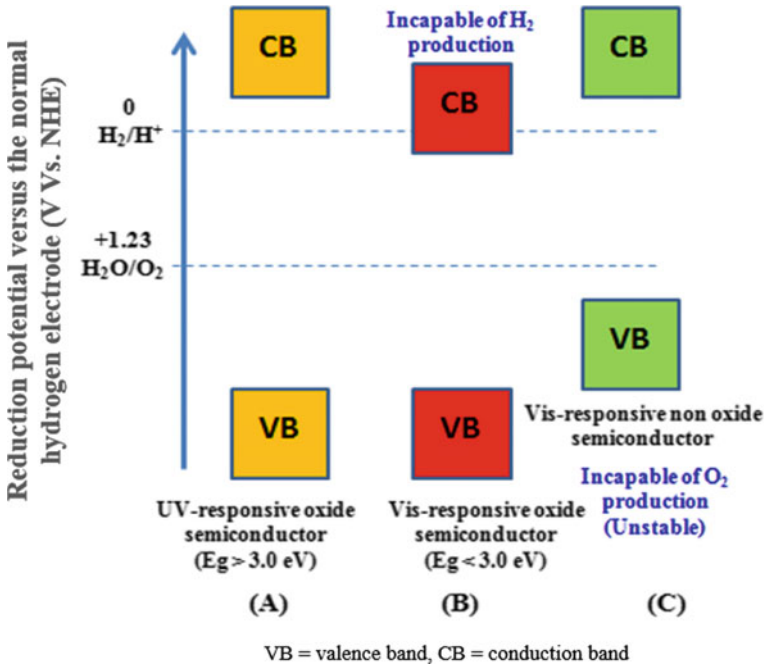

Fig. 4 Band energy levels of different classes of semiconductors

light (class C in Fig. 4), they are generally unstable against photocorrosion or self-oxidation, rather than O_2 evolution. For example, CdS, GaP, TaON exhibit suitable photocatalytic properties for solar energy conversion, but they are unstable in the water oxidation reaction due to the formation of an oxide layer at the surface as a result of the easily oxidation of the anions of these salts or oxy-salts more than water [20].

Despite, some semiconductors, such as TiO_2, fulfill the requirement to drive the overall water splitting as their band edges straddle the potentials of water redox reactions, their wide bandgap ($E_g > 3.0$ eV), so they can harvest only a small portion of the solar spectrum (class A in Fig. 4).

6 Strategies for Improving the Visible Response of UV-Active Photocatalysts

Most of UV-active photocatalysts are incapable for water splitting under visible light, due to their high bandgap energy. The following strategies have been reported to improve the solar light harvesting efficiency of a particular photocatalyst.

6.1 Doping with Metals

Metal ion doping is one of the most effective tools for the development of visible light active photocatalysts by generation of impurity levels in the bandgap. Extensive studies have been carried out for improving the photocatalytic activity of the photocatalysts towards water splitting reactions via doping with transitional metal ions and rare earth metal ions. For example, the electronic coupling between doping ions and TiO_2 leads to the introduction of an impurity energy level just below the conduction band, which can act as either an electron acceptor (Fig. 5a) or just above the valence band of TiO_2, acting as a donor level (Fig. 5b), which allows more visible light to be absorbed by TiO_2. This can be explained based on the band structure of TiO_2. Where the 3d, 4s, 4p orbitals of Ti contribute to the unoccupied conduction band, whereas 2p orbitals of O contribute to the filled valence band. Ti 3d orbitals dominate the lower position of conduction band [74, 85, 96].

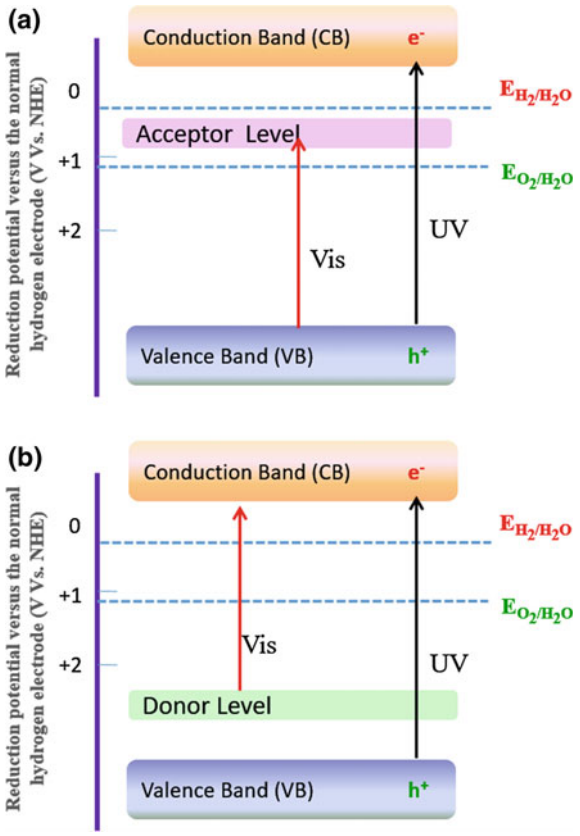

Fig. 5 Electronic coupling between doping metal ions and TiO_2 semiconductor

In addition to the introduction of an impurity level in the forbidden band, metal ion dopants can effectively separate the photogenerated electron-hole pairs by acting as a trapping center for photogenerated electrons, leading to high photocatalytic activity.

The electronic modification of the semiconductor surface via metal deposition has been reported by several authors [13, 28, 31, 39].

In an early study, photocatalytic water splitting by using Cr^{3+}-doped TiO_2 nanoparticles under illumination of visible light (400–550 nm) have been reported by Borgarello et al. [9]. They concluded that the transition of the photoexcited Cr^{3+} 3d electrons into the conduction band of TiO_2 is the reason for the observed enhancement in its visible light activity.

Liqiang et al. [59] reported that the addition of an appropriate amount of noble metals Ag and Pd to the ZnO surface greatly enhanced the photocatalytic activity of ZnO nanoparticles. Hu et al. [28] prepared a Ag/AgBr/TiO_2 photocatalyst under visible light irradiation. Deposition of noble metals such as Pd [101], Pt [93], Au [31], and Ag on TiO_2 surface has been reported in the literature [30, 60]. These metals greatly enhanced the photocatalytic activity by significantly minimizing the recombination rates of the photo-generated electrons (e^-) and holes (h^+).

Khan et al. [41] reported that Fe^{3+}-doped TiO_2 synthesized by hydrothermal method exhibited significantly enhanced its optical response under visible light through narrowing its bandgap energy. The authors demonstrated that the stoichiometric ratio of water splitting into H_2 and O_2 under visible light irradiation was found to be of 2:1, respectively.

However, several disadvantages have been reported for metal doping, such as thermal instability, high cost of ion-implantation apparatus required for doping metal-ions into semiconductors [95]. Besides, the partial blockage of surface sites available for photocatalytic activity caused by the metal ions doping into semiconductor [75].

Dholam et al. [17] found that Fe-doped TiO_2 generated higher H_2 rate compared to Cr-doped TiO_2 under illumination of visible light. They ascribed this enhancement to the fact that Fe ions can efficiently minimize the charge recombination by trapping both holes and electrons, whereas only one type of charge carrier can be trapped by Cr. It has been noted that co-doping with two metal ions exhibits higher water splitting than doping with single metal ion. Niishiro et al. [68] reported that the co-doping of TiO_2 with Ni^{2+} and Nb^{5+} produced more hydrogen than TiO_2 doped with Ni^{2+} alone under visible light irradiation ($\lambda > 420$ nm). They attributed the enhanced hydrogen production by the co-doping with two metal ions to the increase in the photocatalyst stability due to the charge balancing effect of the two different charged ions.

6.2 Doping with Nonmetal

Doping with nonmetal ion is another approach for extending photocatalytic activity of the photocatalyst into the visible region by narrowing its bandgap energy. Unlike metal ion doping, doping with nonmetal ion could hardly affect the CB band of

photocatalyst. Instead of forming donor levels in the forbidden band, nonmetal ion doping usually reconstructs the valence band and shifts its edge upward.

Doping with non-metallic elements, including sulphur [35, 70], nitrogen [5], fluorine [42, 56], boron [102], have been intensively carried out to improve the photocatalytic activity of nanophotocatalysts.

Early in 2002, Khan and co-workers [40] discovered that modification of n-TiO_2 by carbon synthesized via thermal oxidation of Ti metal sheet narrowed its bandgap energy from 3.2 to 2.32 eV and exhibited an efficiency of 8.35% for water splitting. Subsequently, further investigations have been stimulated for carbon modification of TiO_2 as visible light active photocatalysts for water splitting reactions ([87–90, 105].

Various studies have reported that doping of TiO_2 with non metal ions is more effective than metal ions towards the photocatalytic activity as they do not generate recombination centers produced by the existence of d-states deep in the band gap of TiO_2, in addition to the instability of the material doped with metal ions and the requirement of an expensive ion implantation facility [4, 5]. They attributed the band gap narrowing of TiO_2 resulting from the non metal doping to the mixing of p states of non metal dopants with the O 2p states of TiO_2 via interstitial or substitutional doping (Fig. 6).

Hoang et al. [27] reported that the nitrogen (N) modification of single crystalline TiO_2 nanowire arrays via nitridation process enhanced its visible light activity (extending to 520 nm) and narrowed its optical bandgap to be 2.4 eV. The N modified TiO_2 showed higher photocatalytic activities towards water splitting than unmodified TiO_2.

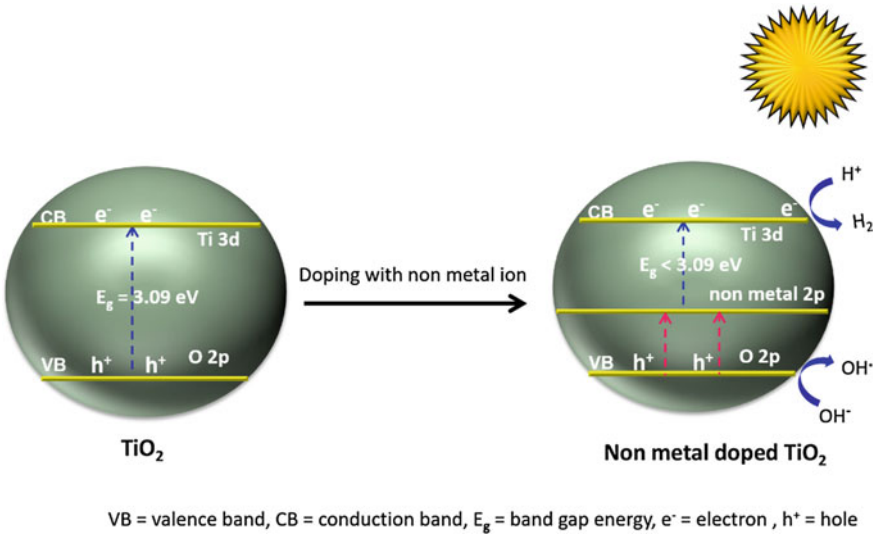

Fig. 6 Doping of TiO_2 with non metal ions

Modification of ZnO with nitrogen has been reported to play a main role of expanding its absorption to the visible region and enhancing its photocatalytic performance for water splitting [107, 116].

Similar to metal ions doping, co-doping with two non metal ions exhibits higher water splitting than doping with single non metal ion.

Luo et al. [61] reported that the activity of Br and Cl co-doped TiO_2 towards the H_2 production from water splitting is higher that of single doped TiO_2. Similarly, higher photocatalytic H_2 production rate was observed for co-doped of TiO_2 with carbon and sulfur compared to that of single doped TiO_2 [7]. B and N codoped TiO_2 showed enhanced water splitting efficiency under irradiation of visible light than that of N doped TiO_2, they ascribed this enhancement to the prolonged lifetime of the photogenerated charge carriers (holes and electrons) by B doping [55].

Several mechanisms have been proposed to elucidate the shift of absorption threshold to visible region and the photocatalytic activity of non-metal-doped photocatalysts. N doping of TiO_2 can increase photocatalytic activity by narrowing the TiO_2 bandgap by shift its photo-response into the visible region as a result of mixing of p states of nitrogen with 2p states of lattice oxygen and [19, 50]. Unlike metal-ion-doping, non-metallic-dopants replace oxygen vacancies in the lattice and are less likely to form recombination centers. N-doped TiO_2 hollow spheres had much higher photocatalytic activity under visible light irradiation than undoped TiO_2 [108]. Some studies have shown that the efficiency of non metal dopants in narrowing the band-gap is higher than the metal-dopants, however non-metal doping also has some disadvantages; studies have shown that the amount of a doped-non-metal component would decrease during the annealing process, thus decreasing visible light photoactivity [95].

6.3 Co-doping with Metal and Nonmetal

It is anticipated that the co-doping of photocatalyst with both metal and nonmetal atoms can also extend its visible light absorption. Recently co-doping has been identified as one of the ways to compensate the disadvantages of single metal and non-metal-ion-doped TiO_2, and was discussed by some researchers [62, 95, 112]. Co-doped TiO_2 with In and N showed higher H_2 production rate as compared single doped TiO_2 [78]. Doping with Cu metal atoms can effectively suppress the recombination of the photogenerated electron-hole pairs. In the meantime, carbon can enhance the photoresponse of the catalyst by narrowing its bandgap energy from 3.09 to 1.78 eV [38, 37], which can be attributed to the hybridization of the O 2*p* orbital with C 2*p* orbital. Selcuk and co-workers [86] investigated the co-doping of TiO_2 by N with different metals such as Pt, Fe, Ni, and Cr. The highest H_2 rate was obtained by Ni and N codoped TiO_2 under visible light irradiation.

6.4 Surface Sensitization with Dyes

Application of surface sensitization of semiconductors with dyes is another strategy for shifting its absorption threshold toward visible region. Furthermore, the electron–hole recombination could be inhibited due to the effective charge separation by the semiconductor/sensitizer interface. Since the work carried out by O'Regen and Gratzel in 1991 [71], this approach has been discussed for solar water splitting in different articles [10, 11, 48, 110]. Upon absorption of visible light, the adsorbed dye molecules on the semiconductor surface become excited and be able to inject electrons into the conduction band of the semiconductor, where the reduction reaction takes place. However, the dye-sensitizer molecules themselves are unable to oxidize water molecule to oxygen. Generally, in the absence of a sacrificial electron donor, dye molecules decompose through self-oxidation under photo-irradiation.

Efficient H_2 evolution from water under visible light irradiation was observed for platinized titanium oxide (Pt/TiO_2) nanoparticles sensitized by s $Ru(bpy)_3^{2+}$ or Eosin Y in the existence of triethanolamine or ethylenediaminetetraacetic acid acting as sacrificial electron donor [24, 44].

6.5 Coupling of Photocatalysts

Coupling of two semiconductors, having different energy levels for their band gaps, is an interesting approach that has been investigated to enhance the efficiency of the photocatalytic capability by expanding the energy range of photoexcitation into the visible light region and increasing the charge separation in the individual photoelectrodes [72]. In composite photocatalysts, the conduction band electrons from a small bandgap semiconductor photogenerated by the absorption of visible light can be injected to the CB of a large bandgap semiconductor, while the photogenerated holes remained in a small bandgap semiconductor, consequently, an efficient electron-hole separation can be accomplished. For successful coupling of semiconductors and for ensuring an effective migration of the charge carriers from one to another, the following conditions are necessary to be met: (1) the CB level of the wide bandgap semiconductor should be less negative than that of the narrow bandgap; (2) the CB level of the semiconductor with wide bandgap should be more negative than H_2O reduction potential and; (3) electron injection from narrow bandgap to the wide bandgap semiconductor should be fast and efficient.

Graphene oxide and carbon nanotubes (CNTs) coupling with TiO_2 have shown potential prolongation of electron-hole pairs by capturing the electron within their structure [12, 34, 51, 100]. The photocatalytic properties of TiO_2 composites with CdS [8], Al_2O_3 [14], SiO_2 [111], ZnO [98], ZnS [25], SnO_2 [114], Bi_2O_3 [103] have been studied. Although the experimental results showed that the coupling of semiconductors having suitable energy levels can attain an efficient photocatalyst

via better charge separation but their cost effectiveness for an industrial application remains as a challenging issue.

7 Conclusions

Utilization of two of our most abundant resources, sunlight and water, for the production of hydrogen via mimicking the natural photosynthesis process by the photocatalytic water splitting using a semiconductor photocatalyst is a fascinating way for the establishment of clean, sustainable and secure energy source.

The electronic structure and bandgap energy are the key parameters that decide the water splitting ability of the photocatalyst. The photocatalyst used for water splitting reaction should be capable to separate the photo-generated charge carriers. It is also essential for the separated charge carriers to reach the solid-liquid interface during their life time and to find suitable reaction partners, water molecules for holes and protons for electrons. Furthermore. The stability against photocorrosion and dissolution processes in aqueous environments is one of the necessary requirements that should be satisfied by the photocatalyst.

Various types of semiconductors have been reported to act as efficient photocatalysts to split water into H_2 and O_2 under illumination of UV light. However, the number of visible light active photocatalysts for water splitting is quite limited, due to their high bandgap energy.

Sincere efforts have been devoted for the enhancement of the efficiency of visible light active photocatalysts for water splitting thought narrowing its bandgap, shifting the absorption threshold toward visible region and increasing the charge carriers separation and migration. So approaching this target; several emerging strategies including doping of photocatalyst with metals and nonmetals, surface sensitization with dyes and coupling of photocatalysts have been extensively studied.

Further breakthroughs, efforts and studies are needed for large-scale hydrogen production from solar water splitting by using an efficient visible light active photocatalyst. Such an achievement will help in establishing clean, sustainable and secure energy source and solving environmental problems.

References

1. Abe R, Higashi M, Sayama K, Abe Y, Sugihara H (2006) Photocatalytic activity of R_3MO_7 and $R_2Ti_2O_7$ (R = Y, Gd, La; M = Nb, Ta) for water splitting into H_2 and O_2. J Phys Chem B 110:2219–2226. https://doi.org/10.1021/jp0552933
2. Akpan U, Hameed B (2009) Parameters affecting the photocatalytic degradation of dyes using TiO_2-based photocatalysts: a review. J Hazard Mater 170(2):520–529. https://doi.org/10.1016/j.jhazmat.2009.05.039

3. Arai N, Saito N, Nishiyama H, Inoue Y, Domen K, Sato K (2006) Overall water splitting by RuO_2-dispersed divalent-ion-doped GaN photocatalysts with d^{10} electronic configuration. Chem Lett 35:796–797. https://doi.org/10.1246/cl.2006.796
4. Asahi R, Morikawa T (2007) Nitrogen complex species and its chemical nature in TiO_2 for visible-light sensitized photocatalysis. Chem Phys 339:57–63. https://doi.org/10.1016/j.chemphys.2007.07.041
5. Asahi R, Morikawa T, Ohwaki T, Aoki K, Taga Y (2001) Visible-light photocatalysis in nitrogen-doped titanium oxides. Science 293:269–271. https://doi.org/10.1126/science.1061051
6. Ashokkumar M (1998) An overview on semiconductor particulate systems for photoproduction of hydrogen. Int J Hydrogen Energy 23:427–438. https://doi.org/10.1016/S0360-3199(97)00103-1
7. Bai HW, Kwan KSY, Liu ZY, Song X, Lee SS, Sun DD (2013) Facile synthesis of hierarchically meso/nanoporous s- and c-codoped TiO_2 and its high photocatalytic efficiency in H_2 generation. Appl Catal B 129:294–300. https://doi.org/10.1016/j.apcatb.2012.09.033
8. Bai S, Li H, Guan Y, Jiang S (2010) The enhanced photocatalytic activity of CdS/TiO_2 nanocomposites by controlling CdS dispersion on TiO_2 nanotubes. Appl Surf Sci 257:6406–6409. https://doi.org/10.1016/j.apsusc.2011.02.007
9. Borgarello E, Kiwi J, Gratzel M, Pelizzetti E, Visca M (1982) Visible light induced water cleavage in colloidal solutions of chromium-doped titanium dioxide particles. J Am Chem Soc 104:2996–3002. https://doi.org/10.1021/ja00375a010
10. Chen HM, Chen CK, Liu R, Zhang L, Zhang J, Wilkinson DP (2012) Nano-architecture and material designs for water splitting photoelectrodes. Chem Soc Rev 41:5654–5671. https://doi.org/10.1039/c2cs35019j
11. Chen X, Shen S, Guo L, Mao SS (2010) Semiconductor-based photocatalytic hydrogen generation. Chem Rev 110:6503–6570. https://doi.org/10.1021/cr1001645
12. Chen M-l, Zhang F-j, Oh W-C (2009) Synthesis, characterization, and photocatalytic analysis of CNT/TiO_2 composites derived from MWCNTs and titanium sources. New Carbon Mater 24(2009):159–166. https://doi.org/10.1016/S1872-5805(08)60045-1
13. Chiang K, Amal R, Tran T (2002) Photocatalytic degradation of cyanide using titanium dioxide modified with copper oxide. Adv Environ Res 6:471–485. https://doi.org/10.1016/S1093-0191(01)00074-0
14. Choi H, Stathatos E, Dionysiou DD (2006) Sol-gel preparation of mesoporous photocatalytic TiO_2 films and TiO_2/ Al_2O_3 composite membranes for environmental applications. Appl Catal B 63:60–67. https://doi.org/10.1016/j.apcatb.2005.09.012
15. Darwent JR, Mills A (1982) Photo-oxidation of water sensitized by WO_3 powder. J Chem Soc Faraday Trans 2:359–367. https://doi.org/10.1039/f29827800359
16. Darwent JR, Porter G (1981) Photochemical hydrogen production using cadmium sulphide suspensions in aerated water. J Chem Soc Chem Commun 4:145–146. https://doi.org/10.1039/c39810000145
17. Dholam R, Patel N, Adami M, Miotello A (2009) Hydrogen production by photocatalytic water-splitting using Cr- or Fe-doped TiO_2 composite thin films photocatalyst. Int J Hydrogen Energy 34:5337–5346. https://doi.org/10.1016/j.ijhydene.2009.05.011
18. Domen K, Naito S, Soma M, Onishi T, Tamaru K (1980) Photocatalytic decomposition of water vapour on an NiO–$SrTiO_3$ catalyst. J Chem Soc Chem Commun 12:543–544. https://doi.org/10.1039/C39800000543
19. Dong F, Wang H, Wu Z, Qiu J (2010) Marked enhancement of photocatalytic activity and photochemical stability of N-doped TiO_2 nanocrystals by Fe^{3+}/Fe^{2+} surface modification. J Colloid Interface Sci 343:200–208. https://doi.org/10.1016/j.jcis.2009.11.012
20. Ellis AB, Kaiser SW, Bolts JM, Wrighton MS (1977) Study of n-type semiconducting cadmium chalcogenide-based photoelectrochemical cells employing polychalcogenide electrolytes. J Am Chem Soc 99:2839–2848. https://doi.org/10.1021/ja00451a001
21. Erbs W, Desilvestro J, Borgarello E, Grätzel M (1984) Visible-light-induced oxygen generation from aqueous dispersions of tungsten(VI) oxide. J Phys Chem 88:4001–4006. https://doi.org/10.1021/j150662a028

22. Fujishima A, Honda K (1972) Electrochemical photolysis of water at a semiconductor electrode. Nature 238:37–38. https://doi.org/10.1038/238037a0
23. Hagfeldt A, Gratzel M (1995) Light-induced redox reactions in nanocrystalline systems. Chem Rev 95:4968. https://doi.org/10.1021/cr00033a003
24. Hashimoto K, Kawai T, Sakata T (1983) Hydrogen production with visible light by using dye-sensitized TiO_2 powder. Nouv J Chim 7:249–253
25. He T, Zhou Z, Xu W, Cao Y, Shi Z, Pan W-P (2010) Visible-light photocatalytic activity of semiconductor composites supported by electrospun fiber. Compos Sci Technol 70:1469–1475. https://doi.org/10.1016/j.compscitech.2010.05.001
26. Hitoki G, Ishikawa A, Kondo JN, Hara M, Domen K (2002) Ta_3N_5 as a Novel Visible Light-Driven Photocatalyst ($\lambda < 600$ nm). Chem Lett 31:736–737. https://doi.org/10.1246/cl.2002.736
27. Hoang S, Guo S, Hahn NT, Bard AJ, Mullins CB (2012) Visible light driven photoelectrochemical water oxidation on nitrogen-modified TiO_2 nanowires. Nano Lett 12:26–32. https://doi.org/10.1021/nl2028188
28. Hu C, Lan Y, Qu J, Hu X, Wang A (2006) Ag/AgBr/TiO_2 visible light photocatalyst for destruction of azodyes and bacteria. J Phys Chem B 110:4066–4072. https://doi.org/10.1021/jp0564400
29. Ikarashi K, Sato J, Kobayashi H, Saito N, Nishiyama H, Inous Y (2002) Photocatalysis for water decomposition by RuO_2-dispersed $ZnGa_2O_4$ with d^{10} configuration. J Phys Chem B 106:9048–9053. https://doi.org/10.1021/jp020539e
30. Iliev V, Tomova D, Bilyarska L, Eliyas A, Petrov L (2006) Photocatalytic properties of TiO_2 modified with platinum and silver nanoparticles in the degradation of oxalic acid in aqueous solution. Appl Catal B 63:266–271. https://doi.org/10.1016/j.apcatb.2005.10.014
31. Iliev V, Tomova D, Bilyarska L, Tyuliev G (2007) Influence of the size of gold nanoparticles deposited on TiO_2 upon the photocatalytic destruction of oxalic acid. J Mol Catal A Chem 263:32–38. https://doi.org/10.1016/j.molcata.2006.08.019
32. Inoue Y (2009) Photocatalytic water splitting by RuO_2-loaded metal oxides and nitrides with d^0- and d^{10}-related electronic configurations. Energy Environ Sci 2:364–386. https://doi.org/10.1039/b816677n
33. Ji F, Li C, Zhang J (2010) Hydrothermal synthesis of $Li_9Fe_3(P_2O_7)_3(PO_4)_2$ nanoparticles and their photocatalytic properties under visible-light illumination. ACS Appl Mater Interface 2:1674–1678. https://doi.org/10.1021/am100189m
34. Jiang G, Lin Z, Chen C, Zhu L, Chang Q, Wang N, Wei W, Tang H (2011) TiO_2 nanoparticles assembled on grapheme oxide nanosheets with high photocatalytic activity for removal of pollutants. Carbon 49:2693–2701. https://doi.org/10.1016/j.carbon.2011.02.059
35. Jo WK, Shin MH (2010) Applicability of a continuous-flow system inner-coated with S-doped titania for the photocatalysis of dimethyl sulfide at low concentrations. J Environ Manage 91:2059–2065. https://doi.org/10.1016/j.jenvman.2010.05.012
36. Kamat PV (2013) Energy outlook for planet earth. J Phys Chem Lett 4:1727–1729. https://doi.org/10.1021/jz400902s
37. Kavil YN, Shaban YA, Al Farawati RK, Orif MI, Zobidi M, Khan SU (2017) Photocatalytic conversion of CO_2 into methanol over Cu-C/TiO_2 nanoparticles under UV light and natural sunlight. J Photochem Photobiol A 347:244–253. https://doi.org/10.1016/j.jphotochem.2017.07.046
38. Kavil YN, Shaban YA, Al Farawati RK, Orif MI, Zobidi M, Khan SU (2018) Efficient photocatalytic reduction of CO_2 present in seawater into methanol over Cu/C-Co-doped TiO_2. Water Air Soil Pollut 229:236. https://doi.org/10.1007/s11270-018-3881-3
39. Keller V, Bernhardt P, Garin F (2003) Photocatalytic oxidation of butyl acetate in vapor phase on TiO_2, Pt/TiO_2 and WO_3/TiO_2 catalysts. J Catal 215:129–138. https://doi.org/10.1016/S0021-9517(03)00002-2
40. Khan SU, Al-Shahry M, Ingler WB Jr (2002) Efficient photochemical water splitting by a chemically modified n-TiO_2. Science 297(5590):2243–2245. https://doi.org/10.1126/science.1075035

41. Khan MA, Woo SI, Yang O-B (2008) Hydrothermally stabilized Fe(III) doped titania active under visible light for water splitting reaction. Int J Hydrogen Energy 33:5345–5351. https://doi.org/10.1016/j.ijhydene.2008.07.119
42. Kim J, Choi W, Park H (2010) Effects of TiO_2 surface fluorination on photocatalytic degradation of methylene blue and humic acid. Res Chem Intermed 36:127–140. https://doi.org/10.1007/s11164-010-0123-8
43. Kim J, Hwang DW, Kim HG, Bae SW, Ji SM, Lee JS (2002) Nickel-loaded $La_2Ti_2O_7$ as a bifunctional photocatalyst. Chem Commun 21:2488–2489. https://doi.org/10.1039/b208092c
44. Kiwi J, Graetzel M (1979) Projection, size factors, and reaction dynamics of colloidal redox catalysts mediating light induced hydrogen evolution from water. J Am Chem Soc 101:7214–7217. https://doi.org/10.1021/ja00518a015
45. Kudo A, Kato H, Tsuji I (2004) Strategies for the development of visible-light-driven photocatalysts for water splitting. Chem Lett 33:1534–1539. https://doi.org/10.1246/cl.2004.1534
46. Kudo A, Nagane A, Tsuji I, Kato H (2002) H_2 evolution from aqueous potassium sulfite solutions under visible light irradiation over a novel sulfide photocatalyst $NaInS_2$ with a layered structure. Chem Lett 31:882–883. https://doi.org/10.1246/cl.2002.882
47. Kudo A, Ueda K, Kato H, Mikami I (1998) Photocatalytic O_2 evolution under visible light irradiation on $BiVO_4$ in aqueous $AgNO_3$ solution. Catal Lett 53:229–230. https://doi.org/10.1023/A:1019034728816
48. Kumar SG, Devi LG (2011) Review on modified TiO_2 photocatalysis under UV/visible light: selected results and related mechanisms on interfacial charge carrier transfer dynamics. J Phys Chem A 115:13211–13241. https://doi.org/10.1021/jp204364a
49. Kurihara T, Okutomi H, Miseki Y, Kato H, Kudo A (2006) Highly efficient water splitting over $K_3Ta_3B_2O_{12}$ photocatalyst without loading cocatalyst. Chem Lett 35:274–275. https://doi.org/10.1246/cl.2006.274
50. Lai Y-K, Huang J-Y, Zhang H-F, Subramaniam V-P, Tang Y-X, Gong D-G, Sundar L, Sun L, Chen Z, Lin C-J (2010) Nitrogen-doped TiO_2 nanotube array films with enhanced photocatalytic activity under various light sources. J Hazard Mater 184:855–863. https://doi.org/10.1016/j.jhazmat.2010.08.121
51. Leary R, Westwood A (2011) Carbonaceous nanomaterials for the enhancement of TiO_2 photocatalysis. Carbon 49:741–772. https://doi.org/10.1016/j.carbon.2010.10.010
52. Lee Y, Nukumizu K, Watanabe T, Takata T, Hara M, Yoshimura M, Domen K (2006) Effect of 10 MPa ammonia treatment on the activity of visible light responsive Ta_3N_5 photocatalyst. Chem Lett 35:352–353. https://doi.org/10.1246/cl.2006.352
53. Lei Z, You W, Liu M, Zhou G, Takata T, Hara M, Domen K, Li C (2003) Photocatalytic water reduction under visible light on a novel $ZnIn_2S4$ catalyst synthesized by hydrothermal method. Chem Commun 2142–2143. https://doi.org/10.1039/b306813g
54. Lewis NS, Nocera DG (2006) Powering the planet: chemical challenges in solar energy utilization. Proc Natl Acad Sci USA 103:15729–15735. https://doi.org/10.1073/pnas.0603395103
55. Li Y, Ma G, Peng S, Lu G, Li S (2008) Boron and nitrogen co-doped titania with enhanced visible-light photocatalytic activity for hydrogen evolution. Appl Surf Sci 254:6831–6836. https://doi.org/10.1016/j.apsusc.2008.04.075
56. Li D, Ohashi N, Hishita S, Kolodiazhnyi T, Haneda H (2005) Origin of visible-light-driven photocatalysis: a comparative study on N/F-doped and N-F-codoped TiO_2 powders by means of experimental characterizations and theoretical calculations. J Solid State Chem 178:3293–3302. https://doi.org/10.1016/j.jssc.2005.08.008
57. Liao C-H, Huang C-W, Wu JCS (2012) Hydrogen production from semiconductor-based photocatalysis via water splitting. Catalysts 2:490–516. https://doi.org/10.3390/catal2040490
58. Linsebigler AL, Lu G, Yates JT (1995) Photocatalysis on TiO_2 surfaces: principles, mechanisms, and selected results. Chem Rev 95:735–758. https://doi.org/10.1021/cr00035a013
59. Liqiang J, Dejun W, Baiqi W, Shudan L, Baifu X, Honggang F, Jiazhong S (2006) Effects of noble metal modification on surface oxygen composition, charge separation and photocatalytic activity of ZnO nanoparticles. J Mol Catal A Chem 244:193–200. https://doi.org/10.1016/j.molcata.2005.09.020

60. Lu S-y, Wu D, Wang Q-l, Yan J, Buekens AG, Cen K-F (2011) Photocatalytic decomposition on nano-TiO_2: destruction of chloroaromatic compounds. Chemosphere 82:1215–1224. https://doi.org/10.1016/j.chemosphere.2010.12.034
61. Luo HM, Takata T, Lee YG, Zhao JF, Domen K, Yan YS (2004) Photocatalytic activity enhancing for titanium dioxide by co-doping with bromine and chlorine. Chem Mater 16:846–849. https://doi.org/10.1021/cm035090w
62. Ma Y, Zhang J, Tian B, Chen F, Wang L (2010) Synthesis and characterization of thermally stable SM, N Co-doped TiO_2 with highly visible light activity. J Hazard Mater 182:386–393. https://doi.org/10.1016/j.jhazmat.2010.06.045
63. Maeda K, Domen K (2007) New non-oxide photocatalysts designed for overall water splitting under visible light. J Phys Chem C 111:7851–7861. https://doi.org/10.1021/jp070911w
64. Matsumura M, Saho Y, Tsubomura H (1983) Photocatalytic hydrogen production from solutions of sulfite using platinized cadmium sulfide powder. J Phys Chem 87:3807–3808. https://doi.org/10.1021/j100243a005
65. NREL (1995) US Department of Energy, The Green Hydrogen report
66. Navarro RM, del Valle F, Villoria JA, Fierro JLG (2009) In: Serrano B, de Lasa H (eds). Elsevier Science Publishers
67. Ni M, Leung MKH, Leung DYC, Sumathy K (2007) A review and recent developments in photocatalytic watersplitting using TiO_2 for hydrogen production. Renew Sustain Energy Rev 11:401–425. https://doi.org/10.1016/j.rser.2005.01.009
68. Niishiro R, Kato H, Kudo A (2005) Nickel and either tantalum or niobium-codoped TiO_2 and SrTiO3 photocatalysts with visible-light response for H_2 or O_2 evolution from aqueous solutions. Phys Chem Chem Phys 7:2241–2245. https://doi.org/10.1039/b502147b
69. Ohmori T, Mametsuka H, Suzuki E (2000) Photocatalytic hydrogen evolution on InP suspension with inorganic sacrificial reducing agent. Int J Hydrogen Energy 25:953–955. https://doi.org/10.1016/S0360-3199(00)00014-8
70. Ohno T, Akiyoshi M, Umebayashi T, Asai K, Mitsui T, Matsumura M (2004) Preparation of S-doped TiO_2 photocatalysts and their photocatalytic activities under visible light. Appl Catal A 265:115–121. https://doi.org/10.1016/j.apcata.2004.01.007
71. O'Regan B, Gratzel M (1991) A low-cost, high-efficiency solar cell based on dye-sensitized colloidal TiO_2 films. Nature 353:737–740. https://doi.org/10.1038/353737a0
72. Di Paola A, Garcia-Lopez E, Marci G, Palmisano L (2012) A survey of photocatalytic materials for environmental remediation. J Hazard Mater 211–212:3–29. https://doi.org/10.1016/j.jhazmat.2011.11.050
73. Pleskov YV (1990) Solar energy conversion: a photo-electrochemical approach. Springer, Berlin
74. Raikar GN, Hardman PJ, Muryn CA, Vanderlaan G, Wincott PL, Thornton G (1991) Valence-band structure of TiO_2 along the Γ-$\sum$-M line. Solid State Commun 80:423–426. https://doi.org/10.1016/0038-1098(91)90719-C
75. Rauf MA, Meetani MA, Hisaindee S (2011) An overview on the photocatalytic degradation of azo dyes in the presence of TiO_2 doped with selective transition metals. Desalination 276:13–27. https://doi.org/10.1016/j.desal.2011.03.071
76. Reber JF, Meier K (1984) Photochemical production of hydrogen with zinc sulfide suspensions. J Phys Chem 88:5903–5913. https://doi.org/10.1021/j150668a032
77. Reber JF, Meier K (1986) Photochemical hydrogen production with platinized suspensions of cadmium sulfide and cadmium zinc sulfide modified by silver sulfide. J Phys Chem 90:824–834. https://doi.org/10.1021/j100277a024
78. Sasikala R, Shirole AR, Sudarsan V, Jagannath Sudakar C, Naik R, Rao R, Bharadwaj SR (2010) Enhanced photocatalytic activity of indium and nitrogen co-doped TiO_2–Pd nanocomposites for hydrogen generation. Appl Catal A 377:47–54. https://doi.org/10.1016/j.apcata.2010.01.039
79. Sato J, Kobayashi H, Ikarashi K, Saito N, Nishiyama H, Inoue YJ (2004) Photocatalytic activity for water decomposition of RuO_2-dispersed Zn_2GeO_4 with d^{10} configuration. J Phys Chem B 108:4369–4375. https://doi.org/10.1021/jp0373189

80. Sato J, Kobayashi H, Inoue Y (2003) Photocatalytic activity for water decomposition of indates with octahedrally coordinated d^{10} configuration. II. Roles of geometric and electronic structures. J Phys Chem B 107:7970–7975. https://doi.org/10.1021/jp030021q
81. Sato J, Saito S, Nishiyama H, Inoue Y (2002) Photocatalytic water decomposition by RuO_2-loaded antimonates, M_2Sb_2O=(M=Ca, Sr), $CaSb_2O_6$ and $NaSbO_3$, with d^{10} configuration. J Photochem Photobiol A 148:85–89. https://doi.org/10.1016/S1010-6030(02)00076-X
82. Sato S, White JM (1980) Photodecomposition of water over Pt/TiO_2 catalysts Chem. Phys Lett 72:83–86. https://doi.org/10.1016/0009-2614(80)80246-6
83. Sayama K, Yoshida R, Kusama H, Okabe K, Abe Y, Arakawa H (1997) Photocatalytic decomposition of water into H_2 and O_2 by a two-step photoexcitation reaction using a WO_3 suspension catalyst and an Fe^{3+}/Fe^{2+} redox system. Chem Phys Lett 277:387–391. https://doi.org/10.1016/S0009-2614(97)00903-2
84. Scaife DE (1980) Oxide semiconductors in photoelectrochemical conversion of solar energy. Sol Energy 25:41–54. https://doi.org/10.1016/0038-092X(80)90405-3
85. See AK, Bartynski RAJ (1992) Inverse photoemission study of the defective TiO_2 (110) surface. Vac Sci Technol A 10:2591. https://doi.org/10.1116/1.578105
86. Selcuk MZ, Boroglu MS, Boz I (2012) Hydrogen production by photocatalytic water-splitting using nitrogen and metal co-doped TiO_2 powder photocatalyst. React Kinet Mech Catal 106:313–324. https://doi.org/10.1007/s11144-012-0434-4
87. Shaban YA, Khan SUM (2007) Surface grooved visible light active carbon modified (CM)-n-TiO_2 thin films for efficient photoelectrochemical splitting of water. Chem Phys 339:73–85. https://doi.org/10.1016/j.chemphys.2007.07.019
88. Shaban YA, Khan SUM (2008) Visible light active carbon modified n-TiO_2 for efficient hydrogen production by photoelectrochemical splitting of water. Int J Hydrogen Energy 33:1118–1126. https://doi.org/10.1016/j.ijhydene.2007.11.026
89. Shaban YA, Khan SUM (2009) Carbon modified (CM)-n-TiO_2 thin films for efficient water splitting to H_2 and O_2 under xenon lamp light and natural sunlight illuminations. J Solid State Electrochem 13:1025–1036. https://doi.org/10.1007/s10008-009-0823-4
90. Shaban YA, Khan SUM (2010) Efficient photoelectrochemical splitting of water to H_2 and O_2 at nanocrystalline carbon modified (CM)-n-TiO_2 thin films. Solid State Phenom 162:179–201. https://doi.org/10.4028/www.scientific.net/SSP.162.179
91. Shaban YA, Khan SUM (2012) Photoresponse of visible light active CM -n-TiO_2, HM-n-TiO_2, CM-n-Fe_2O_3, and CM-p-WO_3 towards water splitting reaction. Int J Photoenergy 2012. https://doi.org/10.1155/2012/749135
92. Shibata M, Kudo A, Tanaka A, Domen K, Maruya K, Ohishi T (1987) Photocatalytic activities of layered Titanium compounds and their derivatives for H_2 evolution from aqueous methanol solution. Chem Lett 16:1017–1018. https://doi.org/10.1246/cl.1987.1017
93. Sun W, Zhang S, Liu Z, Wang C, Mao Z (2008) Studies on the enhanced photocatalytic hydrogen evolution over Pt/ PEG-modified TiO_2 photocatalysts. Int J Hydrogen Energy 33:1112–1117. https://doi.org/10.1016/j.ijhydene.2007.12.059
94. Takata T, Tanaka A, Hara M, Kondo JN, Domen K (1998) Recent progress of photocatalysts for overall water splitting. Catal Today 44:17–26. https://doi.org/10.1016/S0920-5861(98)00170-9
95. Teh CM, Mohamed AR (2010) Roles of titanium dioxide and ion-doped titanium dioxide on photocatalytic degradation of organic pollutants (phenolic compounds and dyes) in aqueous solutions: a review. J Alloy Compd 509:1648–1660. https://doi.org/10.1016/j.jallcom.2010.10.181
96. Thomas AG, Flavell WR, Mallick AK, Kumarasinghe AR, Tsoutsou D, Khan N, Chatwin C, Rayner S, Smith GC, Stockbauer RL, Warren S, Johal TK, Patel S, Holland D, Taleb A, Wiame F (2007) Comparison of the electronic structure of anatase and rutile TiO_2 single-crystal surfaces using resonant photoemission and X-ray absorption spectroscopy. Phys Rev B 75:035105. https://doi.org/10.1103/PhysRevB.75.035105
97. Tokunaga S, Kato H, Kudo A (2001) Selective preparation of monoclinic and tetragonal $BiVO_4$ with scheelite structure and their photocatalytic properties. Chem Mater 13:4624–4628. https://doi.org/10.1021/cm0103390

98. Wang J, Li J, Xie Y, Li C, Han G, Zhang L, Xu R, Zhang X (2010) Investigation on solar photocatalytic degradation of various dyes in the presence of Er^{3+}: $YAlO_3$/ZnO-TiO_2 composite. J Environ Manage 91:677–684. https://doi.org/10.1016/j.jenvman.2009.09.031
99. Wang X, Maeda K, Thomas A, Takanabe K, Xin G, Carlsson JM, Domen K, Antonietti M (2009) A metal-free polymeric photocatalyst for hydrogen production from water under visible light. Nat Mater 8:76–80. https://doi.org/10.1038/nmat2317
100. Wang F, Zhang K (2011) Reduced graphene oxide-TiO_2 nanocomposite with high photocatalystic activity for the degradation of rhodamine B. J Mol Catal A Chem 345:101–107. https://doi.org/10.1016/j.molcata.2011.05.026
101. Wu Z, Sheng Z, Liu Y, Wang H, Tang N, Wang J (2009) Characterization and activity of Pd-modified TiO_2 catalysts for photocatalytic oxidation of NO in gas phase. J Hazard Mater 164:542–548. https://doi.org/10.1016/j.jhazmat.2008.08.028
102. Xu J, Ao Y, Chen M, Fu D (2009) Low-temperature preparation of Boron-doped titania by hydrothermal method and its photocatalytic activity. J Alloy Compd 484:73–79. https://doi.org/10.1016/j.jallcom.2009.04.156
103. Xu J-j, Chen M-D, Fu D-g (2011) Preparation of bismuth oxide/titania composite particles and their photocatalytic activity to degradation of 4-chlorophenol. Trans Nonferrous Met Soc China 21:340–345. https://doi.org/10.1016/S1003-6326(11)60719-X
104. Xu Y, Schoonen MAA (2000) The absolute energy positions of conduction and valence bands of selected semiconducting minerals. Am Miner 85:543–556. https://doi.org/10.2138/am-2000-0416
105. Xu C, Shaban YA, Ingler Jr W B, Khan SUM (2007) Nanotube enhanced photoresponse of carbon modified (CM)-n-TiO_2 for efficient water splitting. Sol Energy Mater Sol C 91:938–943. https://doi.org/10.1016/j.solmat.2007.02.010
106. Yanagida T, Sakata Y, Imamura H (2004) Photocatalytic decomposition of H_2O into H_2 and O_2 over Ga_2O_3 loaded with NiO. Chem Lett 33:726–727. https://doi.org/10.1246/cl.2004.726
107. Yang X, Wolcott A, Wang G, Sobo A, Fitzmorris RC, Qian F, Zhang JZ, Li Y (2009) Nitrogen-doped ZnO nanowire arrays for photoelectrochemical water splitting. Nano Lett 9:2331–2336. https://doi.org/10.1021/nl900772q
108. Yanhui A, Jingjing X, Songhe Z, Degang F (2010) A one-pot method to prepare N-doped titania hollow spheres with high photocatalytic activity under visible light. Appl Surf Sci 256(2754):2758. https://doi.org/10.1016/j.apsusc.2009.11.023
109. Yeh TF, Syu JM, Cheng C, Chang TH, Teng HS (2010) Graphite oxide as a photocatalyst for hydrogen production from water. Adv Funct Mater 20:2255–2262. https://doi.org/10.1002/adfm.201000274
110. Youngblood WJ, Lee SA, Maeda K, Mallouk TE (2009) Visible light water splitting using dye-sensitized oxide semiconductors. Acc Chem Res 42:1966–1973. https://doi.org/10.1021/ar9002398
111. Yuan J, Hu H, Chen M, Shi J, Shangguan W (2008) Promotion effect of Al_2O_3-SiO_2 interlayer and Pt loading on TiO_2/nickel-foam photocatalyst for degrading gaseous acetaldehyde. Catal Today 139:140–145. https://doi.org/10.1016/j.cattod.2008.08.016
112. Zhang L, Li L, Mou Z, Li X (2012) Study on microstructure and catalytic performance of B, C, N Co-dopped TiO_2. Procedia Eng 27:552–556. https://doi.org/10.1016/j.proeng.2011.12.486
113. Zheng N, Bu X, Vu H, Feng P (2005) Open-framework chalcogenides as visible-light photocatalysts for hydrogen generation from water. Angew Chem Int Ed 44:5299–5303. https://doi.org/10.1002/anie.200500346
114. Zhou M, Yu J, Liu S, Zhai P, Jiang L (2008) Effects of calcination temperatures on photocatalytic activity of SnO_2/TiO_2 composite films prepared by an EPD method. J Hazard Mater 154:1141–1148. https://doi.org/10.1016/j.jhazmat.2007.11.021
115. Zhu J, Zäch M (2009) Nanostructured materials for photocatalytic hydrogen production. Curr Opin Colloid Interface Sci 14:260–269. https://doi.org/10.1016/j.cocis.2009.05.003
116. Zong X, Sun C, Yu H, Chen ZG, Xing Z, Ye D, Lu GQ, Li X, Wang L (2013) Activation of photocatalytic water oxidation on N-Doped ZnO bundle-like nanoparticles under visible light. J Phys Chem C 117:4937–4942. https://doi.org/10.1021/jp311729b

Oxygen Reduction Reaction

Rizwan Haider, Xianxia Yuan and Muhammad Bilal

Abstract Polymer electrolyte membrane fuel cells (PEMFCs) and metal air batteries are considered green and efficient electrochemical energy devices and both include reduction of oxygen at cathode during the working of device. Due to the sluggish reaction kinetics of ORR, it is considered the performance limiting factor and to cope with this issue scientists are trying to introduce low cost, highly durable and efficient electrocatalyst for cathode reaction. After the synthesis of catalyst material, different electrochemical techniques including Steady-state polarization, Cyclic voltammetry, Rotating disk electrode and Rotating ring disk electrode are used to check the performance and durability of ORR catalysts. In PEMFCs, water should be produced along with some heat by the 4-electron transfer reaction between oxygen, protons and the electrons. The reported ORR catalysts can be classified as platinum group metal catalyst, platinum group metal free catalyst and metal free catalysts. All the catalysts have their own pros and cons, while platinum supported carbon (Pt/C) is considered the state-of-the-art catalyst for both fuel cell and metal batteries.

Keywords Oxygen reduction reaction · Electrochemical techniques · ORR electrocatalysts

1 Introduction

Oxygen being a non-metal, belongs to sixth group of periodic table with atomic number 8. It is a strong oxidizing agent and gives oxides with other elements and compounds. Catalysis, biology, material dissolution and energy conversion are some important disciplines in which oxygen reduction reaction (ORR) plays a fundamental rule. Oxygen exist at room temperature in gaseous form and undergo reduction

R. Haider (✉) · X. Yuan
School of Chemistry and Chemical Engineering, Shanghai Electrochemical Energy Devices Research Center, Shanghai Jiao Tong University, Shanghai 200240, People's Republic of China
e-mail: haider38@sjtu.edu.cn

M. Bilal
School of Life Science and Food Engineering, Huaiyin Institute of Technology, Huai'an 223003, People's Republic of China

Inamuddin et al. (eds.), *Methods for Electrocatalysis*,
https://doi.org/10.1007/978-3-030-27161-9_15

Table 1 Electrode potential for O_2 reduction in different electrolytes

Type of electrolyte	Reaction equation	Electrode potential at standard condition (V)
Acidic aqueous	$O_2 + 4H^+ + 4e^- \rightarrow H_2O$	1.229
	$O_2 + 2H^+ + 2e^- \rightarrow H_2O_2$	0.70
	$H_2O_2 + 2H^+ + 2e^- \rightarrow 2H_2O$	1.76
Alkaline aqueous	$O_2 + H_2O + 4e^- \rightarrow 4OH^-$	0.401
	$O_2 + H_2O + 2e^- \rightarrow HO_2^- + OH^-$	−0.065
	$HO_2^- + H_2O + 4e^- \rightarrow 3OH^-$	0.867
Non-aqueous alkaline	$O_2 + e^- \rightarrow O_2^-$	Depends on the type of solvent
	$O_2^- + e^- \rightarrow O_2^{2-}$	

by accepting 1 electron in non-aqueous solutions and 2 or 4 electrons in aqueous solution. Successive one, two and four electron reductions of molecular oxygen gives the superoxide radical anion ($O_2^{-\cdot}$), H_2O_2, the hydroxyl radical ($OH^{\cdot}$) and water, respectively [1]. Table 1 is showing the thermodynamic electrode potential for O_2 reduction reaction with different electrolytes.

All of the above-mentioned electron transfer steps have their own importance. 4-electron transfer is important in fuel cells. 2-electron transfer is significant for H_2O_2 production while 1 electron transfer is important to understand the ORR mechanism. The ORR mechanism in fuel cells and batteries is very complicated as it involves different intermediates depending on the type and structure of electrodes, catalyst used and nature of electrolyte. On the other hand, during a corrosion reaction oxygen accepts one or more electrons from a metal in most cases to produce respective metal oxides [2].

ORR in metal-air batteries and fuel cells is in spotlight because of superior energy density and specific capacity of these energy storage devices when oxygen is reduced at cathode. Here, it would be worth mentioning that the word 'air' with a metal as named above, represents actually oxygen. In that particular case air containing oxygen is taken from environment. On the other hand, if pure oxygen is supplied by some other source, like oxygen cylinder or a chemical reaction, the batteries are termed as metal-oxygen batteries [3]. The ORR mechanism is similar for both metal-air and metal-oxygen batteries.

The kinetics of ORR reaction is sluggish, so an efficient and stable catalyst is always required to speed up the electrochemical reaction. To date Pt metal supported on carbon (Pt/C) is considered as contemporary ORR electrocatalyst with excellent performance and efficiency. Nonetheless the high cost and rare availability of Pt metal is motivation for researchers leading them to search for new ORR catalysts. Some examples of ORR electrocatalysts include carbon materials, metal oxides, noble metals and alloys, transition metal dichalcogenides (TMDCs) and chalcogenides, transition metal carbides (TMC) [4], phosphides [5] and nitrides [6].

During ORR, oxygen reaches to the catalyst active sites by mass transport diffusion where two reaction pathways are possible depending on the type of oxygen

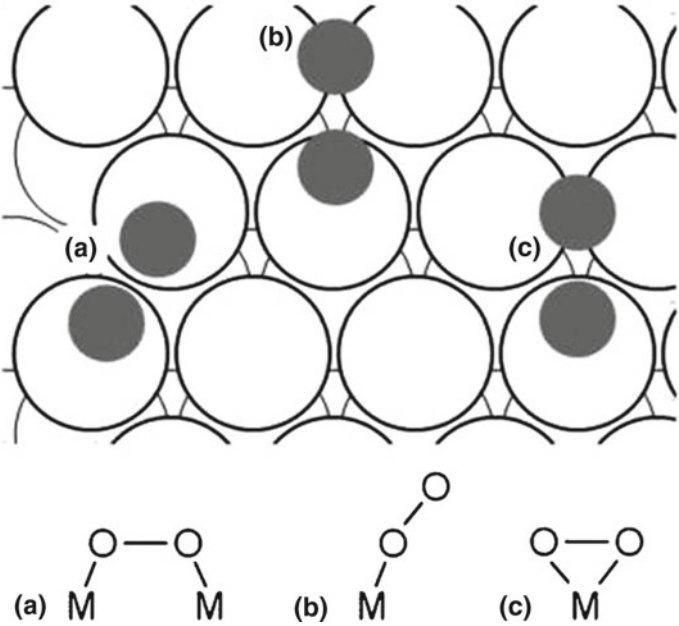

Fig. 1 Schematic diagram for molecular oxygen adsorption sites on the (111) face centered cubic transition metal electrocatalysts. The adsorption sites are labeled corresponding to the Yeager (**a**), Pauling (**b**) and Griffiths (**c**) models [7]

molecules chemisorption on the surface of catalyst. The oxygen adsorption may follow three different models (Fig. 1) depending upon the distance between electrocatalyst surface and oxygen molecules and the extent of proton solvation. First, Yeager model or two-site adsorption directly coverts adsorbed oxygen to water following 4-electron oxygen reduction mechanism. Second, end-on adsorption (Pauling model) lead towards peroxide production following 2-electron transfer—end-on adsorption may rearrange to single site adsorption yielding dual bond. Third is named as Griffiths model and it follows 4-electron pathway to produce water [7]. The mechanism involving direct conversion of oxygen to water is called direct pathway and follows 4-electron transfer. On the other hand, if oxygen is first converted to H_2O_2 following 2-electron pathway it is called peroxide pathway. Adsorbed MOMOH species are produced in the case of direct pathway and MOOH species are produced for peroxide pathway where M represents a transition metal. The general equations for their production are given below [8, 9].

$$2M + O_2 + e^- + H^+ \rightarrow MOMOH_{ads} \tag{1}$$

$$M + O_2 + e^- + H^+ \rightarrow MOOH_{ads} \tag{2}$$

The direct route mechanism occurs as follows

$$\mathrm{MOMOH_{ads}} \rightarrow \mathrm{MO_{ads}} + \mathrm{MOH_{ads}} \tag{3}$$

For a bimetallic electrocatalyst, Eqs. (1) and (3) can be rearranged as

$$\mathrm{M_1} + \mathrm{M_2} + \mathrm{O_2} + \mathrm{e^-} + \mathrm{H^+} \rightarrow \mathrm{M_1OM_2OH_{ads}} \tag{4}$$

$$\mathrm{M_1OM_2OH_{ads}} \rightarrow \mathrm{M_1O_{ads}} + \mathrm{M_2OH_{ads}} \tag{5}$$

For peroxide mechanism the second electron and proton transfer step may follow two steps. The two possibilities are: (1) formation of water and adsorbed oxygen atom as in Eq. 6 and/or (2) depending on the attacking site of proton on oxygen atom, a hydrogen peroxide intermediate may also be produced as in Eq. 7.

$$\mathrm{MOOH_{ads}} + \mathrm{M} + \mathrm{e^-} + \mathrm{H^+} \rightarrow \mathrm{MO_{ads}} + \mathrm{MOH_{2ads}} \tag{6}$$

$$\mathrm{MOOH_{ads}} + \mathrm{M} + \mathrm{e^-} + \mathrm{H^+} \rightarrow \mathrm{MOHOH_{ads}} \tag{7}$$

2 Oxygen Reduction Reaction Kinetics

The sluggish kinetics of ORR can be improved by keeping the reaction potential values close to the thermodynamic electrode potential which is also called the reversible electrode potential.

The current-overpotential relationship is given in Eq. 8 [10].

$$i_c = i^o_{O_2}\left(e^{\frac{n_{aO}\alpha_O F\eta_C}{RT}} - e^{\frac{n_{aO}(1-\alpha_O)F\eta_C}{RT}}\right) \tag{8}$$

Where, i_c is cathode current density for ORR, $i^o_{O_2}$ is exchange current density when oxygen is reduced at cathode, n_{ao} is electron number involved in the rate determining step at standard condition, a_o is transfer coefficient at standard conditions, η_c is ORR overpotential for cathode, F is Faraday constant, R is gas constant, and T is temperature (K). It is evident from the above equation that to achieve low overpotential leading to high current values and better performance, $(RT/\alpha_o n_{ao} F)$ should be small and exchange current density $i^o_{O_2}$ should large. Here, α_o and n_{ao} are intrinsic properties of material and depend on the nature of catalyst.

2.1 Tafel Slope

Tafel equation can be derived starting from the Butler-Volmer equation as given below

$$i = i^o\left(e^{\frac{\alpha F\eta_c}{RT}} - e^{\frac{(1-\alpha)F\eta_c}{RT}}\right) \tag{9}$$

Where, i is the net current and i^o is the exchange current. However at large negative overpotential value and minor backward reaction anodic current becomes zero and we have

$$i = i_c = i^o e^{-\alpha n_a F\eta/RT} \tag{10}$$

Where i_c is cathodic current, α is transfer coefficient, n_a is number of electrons involved in ORR, F is Faraday's constant, R and T have their usual significance. The above equation can be rearranged as

$$i_c = i^o \exp\left[-\frac{n_a \alpha F\eta}{RT}\right] \tag{11}$$

$$\log i_c = \log i^o - \frac{n_a \alpha F\eta}{2.303RT} \tag{12}$$

A more general form of potential current relationship can be written as

$$\eta = a + b\ \log i \tag{13}$$

Equation 13 is known as Tafel equation, where a and b are Tafel constants and their values are calculated experimentally. This equation can be used to get the Tafel slope by plotting η versus (log i). The calculated value of slope is termed as the Tafel slope. Tafel plots are useful for fitting the experimental data obtained during activation overpotential studies. Tafel slope only depends on α and n_a since all other terms are constant. Higher Tafel slope means a rapid rise in overpotential with lower current density. Hence, for low Tafel slope or large αn_a value, high current at low overpotential would be achieved during an electrochemical reaction. Two values of Tafel slope are reported for ORR on Pt/C, one at 60 mV/dec and other at 120 mV/dec contingent to the electrode potential range and nature of its material [11]. The Tafel slope for ORR mainly depends on electron transfer coefficient 'α' value and this value depends on the temperature. The α value increases linearly from 20 to 250 °C when ORR occurs on a Pt/C electrode. The relationship of α and T is given in Eq. 14 [11, 12]:

$$\alpha = \alpha^{\circ} T \tag{14}$$

Where α is ORR electron transfer coefficient, α^o is a constant with a value of 0.001678, and T is the temperature in Kelvin. Relative humidity (RH) is another major factor affecting transfer coefficient [10]. For PEMFCs paradigm, change of transfer coefficient for ORR, at 120 °C is related to RH as given in Eq. 15 [13]. In Eq. 15, RH_c is relative humidity of the cathode compartment.

$$\alpha = (0.001552 RH_c + 0.00139)T \tag{15}$$

2.2 Exchange Current Density

Second important kinetic parameter is exchange current density, which represents the rate of electrochemical reaction at equilibrium. Electrochemical reactions are reversible redox reactions and may occur as given in Eq. 16.

$$\mathrm{O} + n\mathrm{e}^- \leftrightarrow \mathrm{R} \tag{16}$$

Dynamic equilibrium is established in electrochemical reactions like all other reversible reactions. Exchange current density is defined as the net current density at equilibrium. At equilibrium, the value of exchange current density is always zero which is attributed to the equal but opposite amount of current flow during reverse and forward reaction [10]. The value of exchange current density governs the speed of reaction.

For an electrochemical reaction, electrode surface and nature of reaction are responsible for increase or decrease in exchange current density. For instance, the ORR exchange current density is many times lower than hydrogen oxidation reaction (HOR) for a Pt electrode. On the other hand, ORR bares low exchange current density for an Au electrode as compared to Pt. That is major reason why ORR kinetics is strongly dependent on catalyst or electrode material. In conclusion, exchange current density has variable values for different catalysts and electrode materials and a list of ORR exchange current densities for different materials is given in Table 2.

For fuel cell perception the ORR exchange current density is associated with the concentration (partial pressure, for gases) of reactant and area of electrode on which reaction is taking place. It is recommended to use intrinsic current density, as given in Eq. 17, during the lab experiments. The two major reasons for the above consideration are: (1) the actual geometric area of catalyst (Pt) is significantly larger than the electrochemical active surface area and (2) during a reaction involving gases, the partial pressure of oxygen is not exactly equal to 1 atm [12]:

$$i_{O_2}^{o-apparent} = (EPSA)_c i_{O_2}^o \left(\frac{P_{O_2}}{P_{O_2}^o} \right)^{\alpha_o} \tag{17}$$

Table 2 ORR exchange current densities on various electrode materials

Electrode material/catalyst	ORR exchange current density (A cm^{-2})	Electron transfer coefficiency	Electron transfer no. in rate determining step	Measurement conditions	Reference
Pt	2.8×10^{-7}	0.48	–	At Pt/Nafion interface at 30 °C	[14]
PtO/Pt	1.7×10^{-10}	0.46	–	At Pt/Nafion interface at 30 °C	[14]
FePc	1.3×10^{-7}	–	–	Acidic solution (pH = 1.3)	[15]
PtFe/C	2.15×10^{-7}	0.55	1	In 0.5 M H_2SO_4 at 60 °C	[16]
PtW_2C/C	4.7×10^{-7}	0.45	2	In 0.5 M H_2SO_4 at 25 °C	[17]
	5.0×10^{-5}	0.47	1		
Ru_xSe_y	2.33×10^{-8}	0.52	1	In 0.5 M H_2SO_4 at 25 °C	[18]
$Ru_xFe_ySe_z$	4.47×10^{-8}	0.51	1	In 0.5 M H_2SO_4 at 25 °C	[19]

Where, $i_{O_2}^{o-apparent}$ is apparent exchange current density, (EPSA)c is electroactive surface area of the cathode catalyst, $i_{O_2}^{o}$ is intrinsic exchange current density, $P_{O_2}^{o}$ is standard O_2 partial pressure, P_{O_2} is actual O_2 pressure, and α_o is transfer coefficient for ORR at standard conditions. As the factual state of ORR is not truly reflected by apparent exchange current density, henceforth exchange current density and intrinsic exchange current density will have a similar meaning in all references. Temperature is another factor affecting the ORR exchange current density and the relationship between temperature and exchange current density trails Arrhenius equation as given in Eq. 18.

$$i_{O_2}^{o} = I_{O_2}^{o} e^{-(E_a/RT)} \tag{18}$$

Where, $I_{O_2}^{o}$ is exchange current density, E_a is activation energy, while R and T have their typical nature. Various investigations have been reported, both in full and half-cell paradigm, explaining the temperature dependence of ORR with Pt metal electrode. Parthasarathy et al. [14] considered the Pt/Nafion interface and elaborated

the change in ORR kinetics at different temperature. Wakabayashi et al. [20] studied the effect of temperature on ORR kinetics in acidic solution at Pt electrode. Song et al. [12] performed ORR kinetics studies from 23 to 120 °C for PEMFCs and found that activation energy value is 57.3 kJ/mol for pure Pt metal and 28.3 kJ/mol for PtO/Pt surface. Depending on method used and nature of catalyst a broad range (21–83 kJ/mol) of activation energy values has been reported against ORR for both Tafel regions.

3 Electrochemical Techniques in Oxygen Reduction Reaction

ORR occurs in a series of reactions and mostly follows a complex mechanism. Hence, different electrochemical techniques along with other characterization techniques are used to study the mechanism of reaction. The general electrochemical methods employed to study oxygen reduction reaction catalysis include cyclic voltammetry (CV), steady-state polarization, rotating ring disk electrode (RRDE) and rotating disk electrode (RDE). A detailed explanation of these techniques is given in the below section.

3.1 Steady-State Polarization

This technique is based on potential polarization. In detail, the electrode surface potential is shifted away from equilibrium value heading towards a potential difference induced chemical reaction. In a simple elementary electrochemical reaction $O + ne^- \leftrightarrow R$, this potential polarization can be explained with the help of the Butler-Volmer equation as given in Eq. 19 [10]:

$$i = i^o\left(e^{\frac{\beta F \eta_c}{RT}} - e^{\frac{(1-\beta)F\eta_c}{RT}}\right) \tag{19}$$

Where, i^o is exchange current density, η_c is reactant (O) reduction overpotential, and β is symmetry factor. The symmetry factor is actually that fraction of overpotential which affects forward reaction. The above equation best describes an elementary reaction but mostly the electrochemical reactions involve multiple step and are not elementary. Either the reaction involves multiple electron transfer or a single electron transfer, it always undergoes many chemical and electron transfer steps leading to multiple elementary reaction. Certainly, there is a reaction rate value for each elementary step and it follows a separate rate equation along with Butler-Volmer equation for each electron transfer. It is well known that electrochemical current or rate of reaction is decided by considering slowest step but depending on their rate of

reaction, other reactions also interpose to the overall reaction rate. Due to the above facts it is very complex to determine the overall rate of reaction.

A chemical step may also be a rate determining step as in the case of ORR catalysis by carbon materials, where the movement of adsorbed superoxide might be the rate determining step. To conclude, the slowest or rate determining step is supposed to be a pseudo-elementary step transferring "n" electrons in a multiple electron transfer electrochemical reaction. To be specific, n can be 1 or 2 in the case of ORR depending on the potential range and the nature of catalyst being used. The current overpotential relationship for such type of pseudo-elementary step is given in Eq. 20 [2]:

$$i = i^{o}\left(e^{\frac{\alpha n F \eta_C}{RT}} - e^{\frac{(1-\alpha) n F \eta_C}{RT}}\right) \tag{20}$$

Where n is electron transfer number in the pseudo-elementary rate determining step, and α is transfer coefficient indicating the fraction of overpotential that activates the forward direction of the pseudo-elementary rate determining step. Steady-state polarization curves are used to display a relationship between current density and electrode potential. It can be recorded in two ways; (1) calculating a stable current density response against constant electrode potential or (2) recording the stable electrode potential response against constant current density. The evaluation criteria of polarization curve are application dependent. For fuel cells, high current density is always desired as it provides utmost power density and for ORR such current density can be achieved at lowest possible overpotential, thus for fuel cells it can be achieved at highest possible cell voltage. Figure 2 is displaying the steady-state polarization

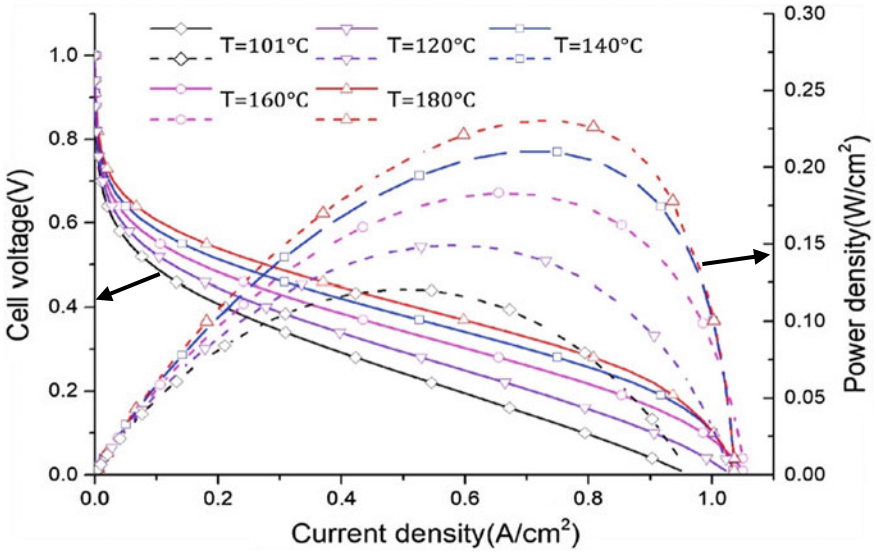

Fig. 2 Polarization curves for a HT-PEMFC with catalyst layer of 0.01 mm and proton exchange membrane thickness of 0.04 mm [21]

curves of a high temperature polymer electrolyte membrane fuel cell (HT-PEMFC) at different temperatures [21]. It is obvious that the cell performance is increasing with increasing temperature. Hence, it is concluded that PEMFC fuel cells perform better at high temperature as compared to low temperature. An overpotential versus (log *i*) plot or polarization curves fitting can be used to obtain Tafel slope or exchange current density.

A study reported low current density range i.e. <0.4 A/cm^2 and high current density range i.e. >0.4 A/cm^2 results showing different exchange current densities for fuel cell. For instance, in the case of ORR, an exchange current density value of 6.25×10^{-6} A/cm^2 has been reported for PtO/Pt surface at 80 °C, with current density values <0.4 A/cm^2. On the other hand, at current density values >0.4 A/cm^2, exchange current density of 5.26×10^{-6} A/cm^2 was reported using Pt metal as catalyst [12].

3.2 Cyclic Voltammetry

In electrochemistry, cyclic voltammetry (CV) may be considered as the most beneficial technique. In few minutes, it can give very useful qualitative information about the electrochemical reaction and catalyst. The catalytic activity and electrochemical response of catalyst depends on some electrochemical reactions. The principle of CV is not a focus of this chapter so we will simply explain how CV is applied to study the catalysis for ORR reaction in the presence of surface adsorbed catalysts. Figure 3 is displaying a cyclic voltammogram of Pt/C adsorbed on graphite electrode recorded in our lab using 0.1 M KOH solution as electrolyte. In the potential range of 0.2 to −0.8 V versus Ag/AgCl reference electrode, a very clear sharp wave can be observed and is attributed to O_2 reduction.

For surface adsorbed species, the electrochemical reaction mechanism can also be explained by the reaction involving change in redox peak potential with a variation in pH. Formal potential which is defined as the average of anodic and cathodic potential, is used to study such type of reactions. Hence, for an electrochemical reaction involving either OH^- or a proton, e.g.,

$$\mathrm{O} + m\mathrm{H}^+ + n\mathrm{e}^- \leftrightarrow \mathrm{R}$$

follows Eq. 21 for change in the pH versus formal potential;

$$E^f = E^0 - 2.303\frac{mRT}{nF}pH \tag{21}$$

where E^f is formal potential and E^o is Nernst potential [10]. The catalytic activity of a material is observed from the peak current and onset potential. For example, carbon-supported cobalt-polypyrrole catalyst (Co-PPy/C) shows different electrocatalytic activity in pyrolyzed and unpyrolysed form as shown in Fig. 4. In the plot five peaks

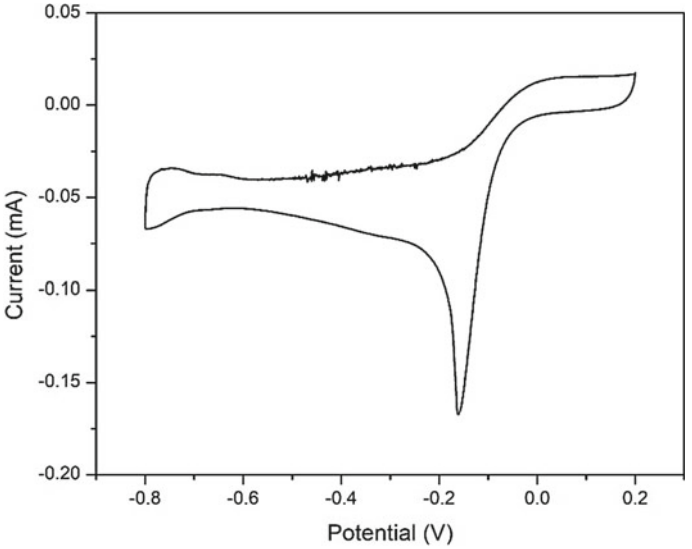

Fig. 3 Cyclic voltammogram of Pt/C adsorbed on a graphite electrode at 25 °C in 0.1 M KOH solution. Potential scan rate: 0.005 mV s^{-1}

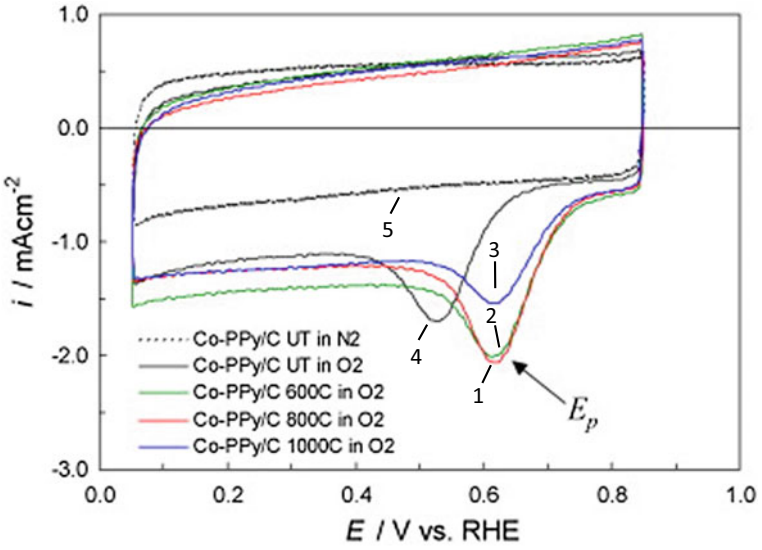

Fig. 4 Cyclic voltammograms for unpyrolyzed and pyrolyzed Co-PPy/C catalysts at 25 °C in 0.5 M H_2SO_4 under saturated N_2 and O_2, respectively. Potential scan rate: 50 mV s^{-1}. UT indicates the unpyrolyzed sample and 800C indicates the pyrolyzed sample at 800 °C. Co-PPy/C loading: 0.122 mg cm^{-2} [22]

are designated to different samples of Co-PPy/C. Sample 1, 2 and 3 are pyrolyzed at 800 °C, 600 °C and 1000 °C, respectively, while 4 and 5 are designated to unpyrolysed samples in O_2 and N_2 atmosphere, respectively. It should be noted that catalysis is taking place in 1, 2, 3 and 4 only because there is no oxygen present for sample 5. In comparison, the highest current density is achieved in 1 and onset potential of all the pyrolyzed samples is almost equal, about 350–400 mV earlier than the unpyrolysed sample in O_2 atmosphere (Peak 4) [22].

3.3 Rotating Disk Electrode

RDE is used as working electrode for electrochemical studies and is composed of a disk made of mostly glassy carbon or graphite surrounded by a thick layer of insulating polytetrafluoroethylene (PTFE). The other materials used to make RDE disk include, but not limited to, CdS, GaAs, Fe, Au, Cu, Ni, Pt, or Si [23]. It is used to limit the diffusion layer thickness. Equations used for RDEs are as follows [10]:

$$\frac{1}{I} = \frac{1}{I_k} + \frac{1}{I_D} = \frac{1}{I_k} + \frac{1}{B\omega^{1/2}} \tag{22}$$

Where I is disk current density, I_k is kinetic current density, I_D is diffusion limiting current density and ω is angular velocity of rotating disk ($\omega = 2\pi N$, where N is rotating speed in rpm). While B can be calculated using Eq. 23

$$B = 0.62nF(D_o)^{2/3}\upsilon^{-1/6}C_o \tag{23}$$

Where n is overall electron transfer number, D_o diffusion coefficient of O_2, ν is kinematic viscosity of electrolyte solution, and C_o is concentration of dissolved oxygen. I_k can be expressed as Eq. 24:

$$I_k = nFKC_o \tag{24}$$

Figure 5 is showing an example of RDE application in ORR including polarization curves and the Koutecky-Levich (K-L) plot for carbon-supported cobalt-polypyrrole catalyst (Co-PPy/C). These results are compared with theoretical plots for 4 and 2-electron process. The experimental data already reported in literature [26] was used for theoretical calculation of parameters to get the above plots. The K-L slope of unpyrolyzed Co-PPy/C resembles to the theoretical 2-electron process plots. On the other hand, pyrolyzed Co-PPy/C slops are well matched with theoretical 4-electron transfer reaction.

Along with the electrochemical factors, three non-electrochemical parameters are also required for RDE analysis. These parameters are temperature dependent and include O_2 solubility, electrolyte solution kinematic viscosity and O_2 diffusion coefficient. The values of these parameters also depend on the nature of electrolyte

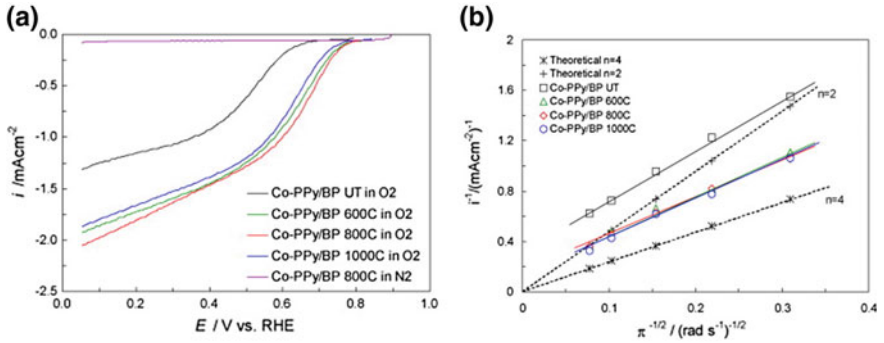

Fig. 5 **a** Polarization curves of unpyrolyzed and pyrolyzed Co-PPy/C catalysts at 25 °C in 0.5 M H_2SO_4 under saturated N_2 and O_2, respectively. Potential scan rate: 5 mV s^{-1}. Electrode rotation rate: 400 rpm. Co-PPy/C loading: 0.122 mg cm^{-2}. **b** Koutecky–Levich plots for the ORR on unpyrolyzed and pyrolyzed Co-PPy/C catalysts at 0.3 V versus RHE in 0.5 M H_2SO_4 under saturated O_2. The current densities were normalized to the geometric area. Co-PPy/C loading: 0.122 mg cm^{-2} [22]

used for ORR catalysis. Table 3 is showing the values of these parameters at different conditions.

Table 3 Non-electrochemical kinetic parameters for RDE data analysis

Experiment conditions (T,P electrolyte)	Diffusion coefficient of O_2 (cm^2 s^{-1})	Kinematic viscosity of the electrolyte solution (cm^2 s^{-1})	Solubility of O_2 (mol cm^{-3})	Reference
0.1 M $HClO_4$, 20 °C, 1 atm O_2	1.67×10^{-5}	–	1.38×10^{-6}	[20]
0.5 M H_2SO_4, 25 °C, 1 atm O_2	1.40×10^{-5}	0.010	1.10×10^{-6}	[19]
0.1 M KOH, 25 °C, 1 atm O_2	1.90×10^{-5}	–	1.20×10^{-6}	[14]
1 M NaOH, 25 °C, 1 atm O_2	1.65×10^{-5}	0.011	8.40×10^{-7}	[24]
0.1 M TBAP quinoline, 25 °C, 1 atm O_2	1.71×10^{-5}	0.033	1.49×10^{-6}	[25]

3.4 Rotating Ring Disk Electrode

The rotating ring disk electrode (RRDE) is a double working electrode and this technique is used to study the mechanism of ORR reaction. The intermediates formed on the disk of electrode during the ORR reaction are detected on the ring. On the disk, both 2-electron and 4-electron process may occur while H_2O_2 is oxidized to H_2O on the ring of RRDE [27].

The reduction current for 2-electron (I_{2e^-}) process is given by

$$I_{2e^-} = I_R/N \tag{25}$$

Where, I_{2e}^- is 2-electron ORR current on the disk electrode and N is collecting coefficiency of electrode. The disk current (I_D) can be calculated using Eq. 26:

$$I_D = I_{2e^-} + I_{4e^-} \tag{26}$$

Where, I_{4e}^- is 4-electron ORR current. Equation 26 can also be written as

$$\frac{I_D}{n_{e^-}} = \frac{I_{4e^-}}{4} + \frac{I_{2e^-}}{2} \tag{27}$$

Equation 27 can be rearranged to Eq. 28 and is used to calculate the number of electrons participating in ORR

$$n_{e^-} = \frac{4I_D}{I_D + I_R/N} \tag{28}$$

The $H_2O_2\%$ is estimated by Eq. 29.

$$H_2O_2\% = 200 \times \frac{I_R/N}{I_D + I_R/N} \tag{29}$$

Figure 6 is displaying the polarization curves, electron number (calculated using Eq. 28) and H_2O_2 percentage (calculated using Eq. 29) for ORR on polypyrrole based catalyst [28].

4 Electrocatalysts for Oxygen Reduction Reaction

Oxygen reduction reaction catalyst is considered performance limiting factor in both fuel cells and batteries, that is why ORR catalysts have been in spotlight since last two decades. The main problems associated with ORR catalysis include sluggish reaction kinetics, catalyst layer delamination, catalyst degradation and catalyst agglomeration or band formation. In the course of designing ORR catalyst attention should be

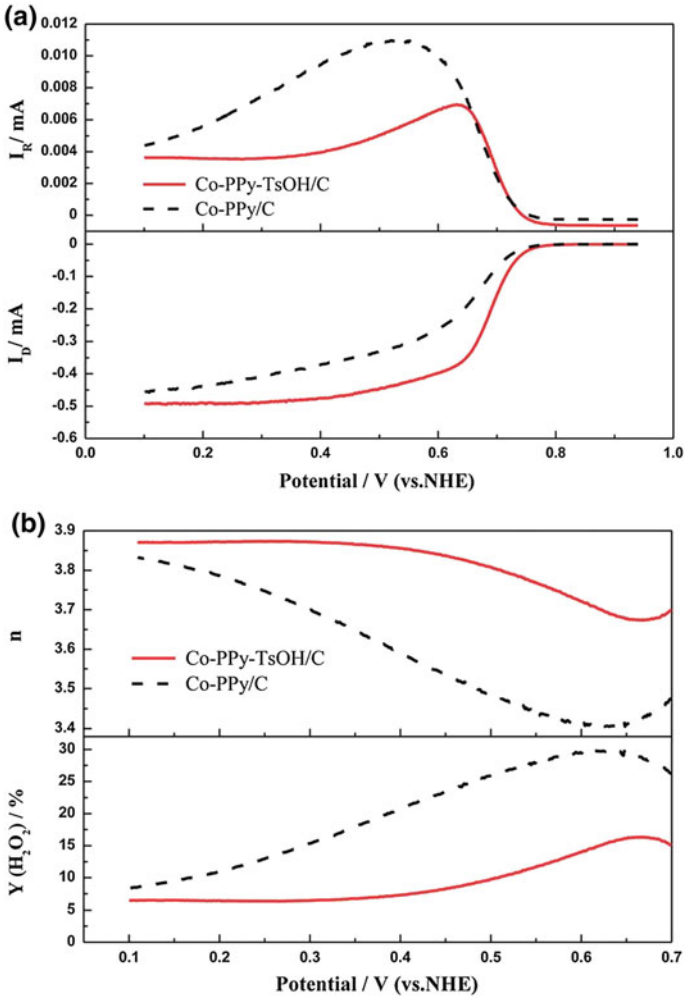

Fig. 6 RRDE voltammograms and the calculated values of transferred electron number (n) and yield of H_2O_2 (Y(H_2O_2)) during ORR. **a** Polarization curves of Co–PPy/C and Co–PPy–TsOH/C obtained with RRDE at room temperature in O_2 saturated 0.5 M H_2SO_4 with a potential scan rate of 5 mV s^{-1} and an electrode rotation rate of 900 rpm. **b** Calculated values of n and Y(H_2O_2) for Co–PPy/C and Co–PPy–TsOH/C catalyzed ORR

focused on high intrinsic activity and durability as well as low cost of material. For an effective catalyst, high activity can be achieved by structure engineering, like nanostructuring, alloying, intercalation, confinement of active elements or compounds in layered materials, shape engineering and implication of different type of catalyst supports. The other parameters mentioned above are the intrinsic properties of materials attributed to the nature of techniques for catalyst synthesis which depends on

the type and structure of catalyst. In the next section, we will have a look on some of the examples of electrocatalysts for ORR.

4.1 Pt-Based Catalyst for ORR

Pt metal-based catalysts have always been in focus for ORR owing to their excellent performance. The ORR on Pt surface usually follows 4 electron mechanism producing water in acidic solutions, while OH^- in alkaline solution along with a small amount of side reactions which are already discussed in detail in literature [29]. Here we will discuss some novel examples of Pt containing catalysts for ORR reaction. Usually Pt metal is dispersed on carbon supports and the contact is considered not very good, especially for high temperature applications. The other problem associated with this is non-homogeneous dispersion of Pt particles. A study reported [30] Pt-MoO_x interface on smooth MWCNT surface (Pt-MoO_x – MWCNT system) to overcome the above-mentioned problem. A polymer electrolyte membrane fuel cell fabricated by using 5% by weight MoO_x (Pt-MoO_x(5%) – MWCNT) as an additive and polybenzimidazole (PBI) membrane showed balanced Pt surface area leading to 9 times higher kinetic current calculated from K-L plots, as compared to Pt-MWCNT system. Similarly, some other studies reported enhanced performance with the addition of metal or metal oxide as an additive or alloy with Pt or Pt-group metals [31–33]. Different kinds of carbon support also aid in enhancing the performance of ORR reaction performance [34, 35]. Another problem associated with ORR catalysts is durability. High surface area (1037 m^2/g) 3D nanoporous carbon was used as a support to prepare a highly durable electrocatalyst (NanoPC/PyPBI/Pt) for ORR and compared with CB/PyPBI/P (Fig. 7) [36]. About 2.2 nm diameter Pt deposited on NanoPC carbon were wrapped in PyPBI layer. This system showed no loss of electrochemical active surface area (ECSA) even after 10,000 start/shutdown cycles (Fig. 8), which is excellent example of durable catalyst for ORR in PEMFC.

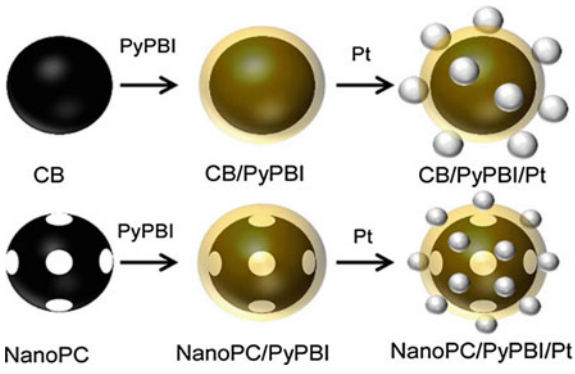

Fig. 7 Schematic illustration of preparation of CB/PyPBI/Pt and NanoPC/PyPBI/Pt electrocatalyst [36]

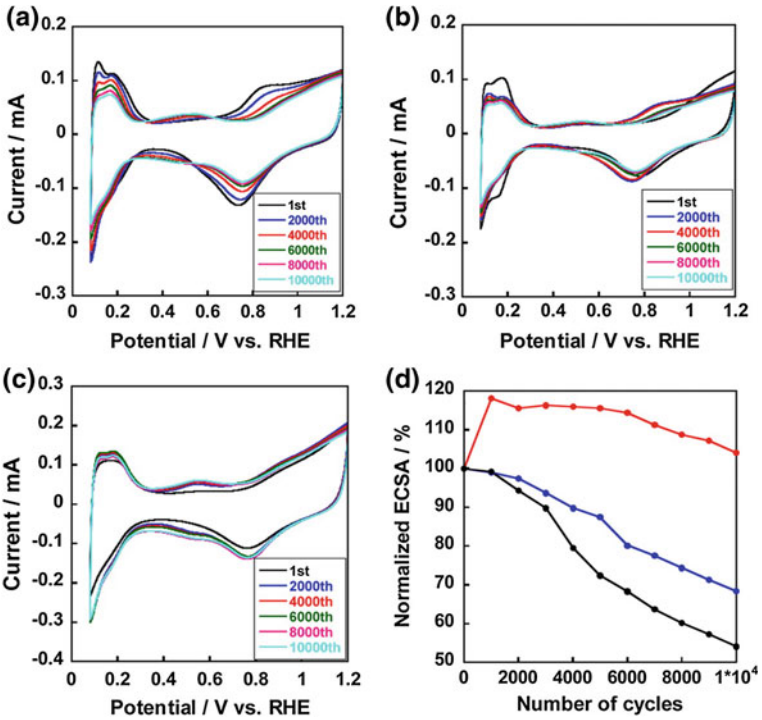

Fig. 8 CV curves of the **a** CB/Pt, **b** CB/PyPBI/Pt, and **c** NanoPC/PyPBI/Pt after 2000, 4000, 6000, 8000, and 10,000 potential cycles test. **d** Normalized ECSAs of CB/Pt (black line), CB/PyPBI/Pt (blue line) and NanoPC/PyPBI/Pt (red line) as a function of the number of potential cycles in the range of 1.0–1.5 V versus RHE [36]

It shows that the better engineering of carbon support helps to increase the durability of ORR catalyst.

A recent study reported that modification of MWCNTs with nitrogen containing compounds can increase the performance of Pt/MWCNT (40 wt%) electrocatalyst for ORR. RDE was used to perform the studies where 0.1 M $HClO_4$ was used as electrolyte. Melamine-formaldehyde resin was used as a precursor to introduce nitrogen (8.3 at.%) on MWCNT surface. The utilization ratio of Pt was increased (0.84) as compared to the Pt/CNT (0.29) leading to uplift in power density from 0.37 to 0.61 W cm^{-2} [37].

Platinum deposited poly(vinylpyrrolidone) (PVP) MWCNTs are reported as a highly durable ORR catalyst with a loss of only about 40% ECSA even after 150,000 cycles at 1.0–1.5 V versus RHE [38]. This performance is 15 times better than commercial Pt/C catalyst which shows about 50% ECSA loss just after 10,000 cycles. The device fabricated using this catalyst also showed 3.5 times high power density as compared to the commercially fabricated Pt/C containing device. Same group reported another MWCNTs based ORR catalyst containing phosphoric acid (PA)-doped platinum electrocatalyst supported on poly[2,20-(2,5-pyridine)-5,50-bibenzimidazole]

(para-PyPBI)-wrapped MWCNTs having performance comparable to commercial Pt/C [39]. A state-of-the-art ORR catalyst with outstanding performance was reported by the same group again showing durability for more than 400,000 fuel cell cycles and a power density of 252 mW/cm^2 at an operating temperature of 120 °C [40]. Synthesis route is shown in Fig. 9 while polarization curves and CV plots are displayed in Fig. 10.

From the above discussion, it is concluded that the problems associated with the Pt/C catalyst may be resolved by suitable modification of carbon support, use of additive and alloying Pt metal with other metals. Instead of all the above breakthroughs, still a PGM-free catalyst is required for ORR catalysis and wide spread applications of fuel cell and metal-air batteries.

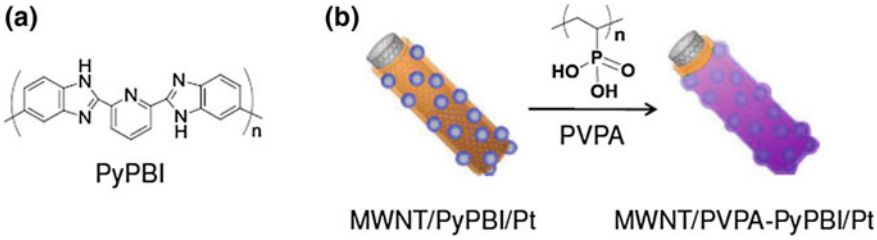

Fig. 9 **a** Chemical structure of PyPBI. **b** Schematic illustration of the preparation technique of the MWNT/PyPBI-PVPA/Pt [40]

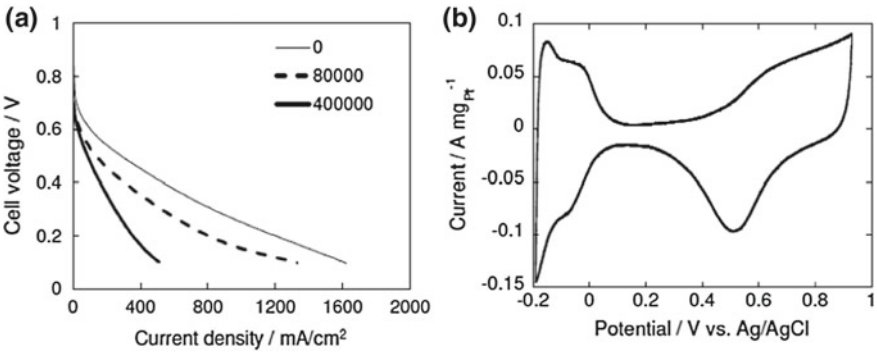

Fig. 10 **a** Polarization curves and durability test curves; **b** CV curve. The polarization curves were measured after every 1000 cycles of the potential sweep between 1.0 and 1.5 V. For convenience, only initial (thin solid line), after 80,000 cycles (bold dotted line) and after 400,000 cycles (bold solid line) were plotted. For PA-non-doped MEA, test was stopped at 8000 cycles [40]

4.2 Platinum Group Metal (PGM)-Free Catalysts

Owing to the scarcity and high price of Pt-group metals, Pt-group metal (PGM)-free catalysts have got special attention in the last decade. Numerous studies have been reported on PGM-free catalyst outperforming state of the art Pt/C and it would be worth mentioning that for the synthesis PGM-free catalyst mostly metals are co-doped with nitrogen. Low cost nitrogen and metal doped carbon materials (M-N/C) are the most prominent PGM-free electrocatalyst for ORR, where the metal is mostly Fe and/or Co. A recent study reported highly graphitic mesoporous Fe and nitrogen doped carbon materials (Fe-N/C) with a surface area of 800 m^2/g and an electrical conductivity of about 19 S/cm. The surface of prepared material was modified by post synthesis acid and thermal heat treatment. As synthesized materials showed more positive half-wave (0.87 V) and onset (1.04 V) potential values against reversible hydrogen electrode (RHE), leading to better ORR activity which was comparable with commercial 20% Pt/C catalyst [41]. Another study reported highly durable [42] mesoporous Fe-N/C. Liu et al. reported computational and experimental studies of Mn-N/C materials as better ORR catalysts [43] in acidic medium. It was demonstrated with the help of DFT calculation that the MnN_4 sites present in the material can catalyze the ORR reaction with much lower half wave potential (60 mV lower than Pt (111) and 80 mV lower than the eminent Fe-N/C ORR catalyst [44, 45]). This material also showed excellent potential cyclic stability, only losing 20 mV even after 10,000 cycles using oxygen saturated electrolyte at 0.6–1 V [43]. A comparison of reaction coordinates, in the form of free energy diagram, for MnN_4, FeN_4 and Pt (111) is given is Fig. 11. In M-N/C materials the main catalytic site is metal ion coordinated to pyridinic type nitrogen atom facilitating ORR catalysis as shown in Fig. 12. In an overall perspective, M-N/C are considered as a low-cost alternative for commercial Pt/C ORR catalyst.

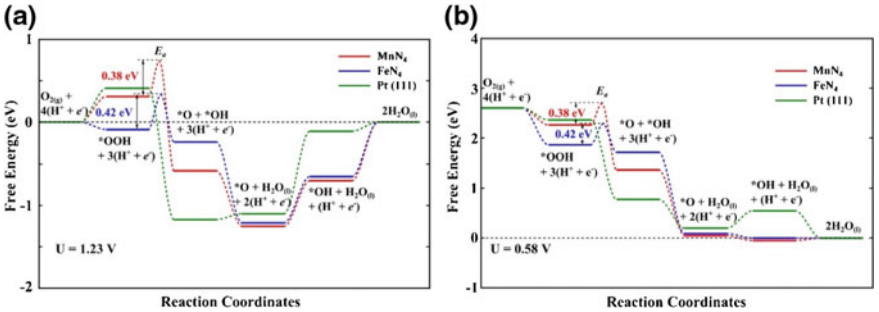

Fig. 11 Predicted free energy evolution diagrams for O_2 reduction through $4e^-$ associative pathway to form H_2O on MnN_4, FeN_4, and Pt (111) surface under electrode potential of **a** U = 1.23 V and **b** U = 0.58 V. The DFT calculations have included the explicit water solvation effect; the free energy calculations are performed at temperature of 300 K and in acid medium with pH value of 0 [43]

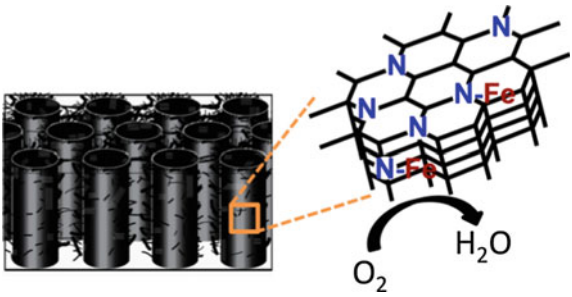

Fig. 12 Catalytic site in the case Fe-N/C ORR electrocatalyst [41]

Many other PGM-free ORR catalysts, apart from M-N/C, have also been reported. A recent research reported graphene coated Sn-doped C12A7 : e^- ($C_{12}A_{7-x}Sn_x$, where, $x = 0.2$ to 1) composite as an excellent ORR catalyst in alkaline medium. When $x = 1$, the calculated current density, onset potential, methanol resistance and long-term stability were comparable to commercial 20% Pt/C catalyst for ORR [46]. The only drawback of this material is that high temperature (1550 °C) is required to synthesize the material.

Some other examples of PGM-free ORR catalyst include cobalt based catalysts [47], porous carbon material [48] and carbon black [49]. Last two members shows excellent ORR activity when combined with suitable metals.

4.3 Metal-Free Electrocatalysts for ORR

Metal free ORR electrocatalyst have got researchers attention because of their better ORR activity and durability. Nitrogen-doped carbon including nitrogen-doped carbon nanotubes and nitrogen-doped graphene have been extensively studied during last few years [50]. The nitrogen is introduced using different precursors like Polypyrrole (PPy), ammonia, cyanamide, nitrogen gas, melamine, phthalocyanine and pyridine [28]. The oxygen reduction reaction on carbon is catalyzed by the strong interaction of surface carbon atoms [51]. Hydrophobicity control and homogeneous N-atoms distribution in the case of pyridine, as a precursor, is crucial to achieve an ORR catalyst with high activity and bottom up approach is recommended to achieve this target [50]. A schematic for synthesis of catalyst with high density of active sites is shown in Fig. 13.

A recent study reported synthesis of N-doped graphene (N-GP), where ammonia was used as a nitrogen precursor, and its use as ORR catalyst [52]. The results showed that exfoliation method, type of graphite precursor and electrolyte temperature has significant effect not only on the quality of product but on the catalytic properties also. Two major types of carbon materials are glassy carbon (GC) and graphite and they follow different mechanism for ORR catalysis. ORR on carbon normally follows first order kinetics with a Tafel slope of −120 mV for graphite and −60 mV for GC.

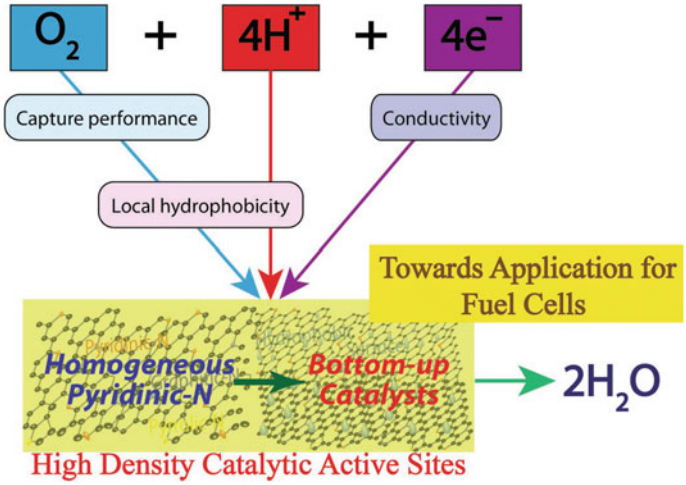

Fig. 13 Concept of electrocatalyst development with high-density catalytic active sites: schematic of different parameters to control the catalytic performance of a fuel cell ORR catalyst, displaying doped N as the ORR active center, the role of the catalyst surface hydrophobicity toward O_2 diffusion, the electronic state tuning of the catalyst, the conductivity of the electrolyte membrane for efficient H^+ ion transport, and the conductivity of the electrode for faster electron transfer

Different elementary steps are involved in the ORR mechanism for different carbons. The first step is adsorption followed by electron transfer, which finally results in the formation of superoxide (O_2^-). In the next step, disproportionation or reduction of superoxide is possible [53]. Some studies proposed a transformation between two different types of superoxides [51]. In the case of strong alkaline solution (pH > 10), two waves can be observed in the ORR curve; both of them can be attributed to the formation of O_2^- involving different carbon atoms on the same surface but away from each other [54].

In the study of ORR mechanism, the surface chemistry of carbon must be considered as it is believed to play a vital rule in oxygen reduction. Figure 14 is showing some important features of carbon surface [29].

Owing to all the above surface functional group, different carbon materials like graphite, glassy carbon, carbon nanotubes, heteroatom doped carbons, pre-treated carbon surfaces and graphene have been reported and explained in detail [29].

Core shell ZIF8@ZIF8 single crystal-based N-doped hierarchically porous carbon nanopolyhedras (CS-HPCNs) were reported to have greater number of graphitic and pyridinic nitrogen as compared to core less carbon nano cubes. Here, ZIF8 stands for zeolitic imidazolate framework with structure $Zn(mIM)_2$ and mIM is 2-methylimidazolate. When compared with commercial Pt/C catalyst, as prepared catalyst showed higher kinetic and limiting current density and comparable onset potential. The better ORR activity was ascribed to higher mesopore volume and surface area of material [55]. A main problem associated with the N-doped carbon is that their activity is comparatively lower than commercial Pt/C. This problem is

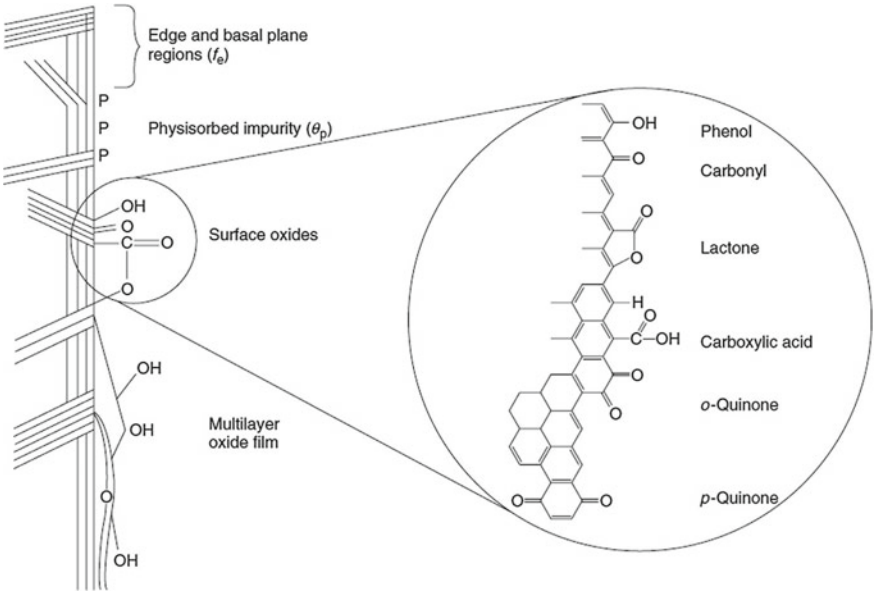

Fig. 14 Schematic showing some of the carbon surface features of relevance to electrochemistry, and details of some different possible oxygen-containing surface functional groups [29]

addressed by introducing binary and ternary-doped carbons like N,S,F doped [56, 57]; N,P doped [58]; N,S doped [59] carbon and N,P doped polymer [60]. Phenoxy-cyclophosphazenes (PCPZs) pyrolyzed on monodispersed silica spheres yielded high surface graphitized carbons with numerous N,P catalytic sites. N,P co-doped graphitized carbon (N,P-GC) showed bifunctional catalytic activity for ORR and oxygen evolution reaction (OER) [58]. As prepared catalyst with 30 nm SiO_2 particles as a support, showed ORR half wave potential of 0.85 V, which is comparable to commercial Pt/C. Figure 15 is showing results of different techniques for the above catalyst where 900, 1000 and 1100 is indicating the calcination temperature for different samples. Another study reported that introduction of binary and ternary dopant can enhance the distribution of active sites which eventually leads toward better ORR performance. This N, F and S doped graphene (FN_3SG) catalyst showed a half wave potential of 0.803 V and positive onset potential of 0.988 V versus RHE which is analogous to commercial Pt/C catalyst for ORR [56].

The activity and durability of metal-free ORR electrocatalyst, especially carbons can be increased by the introduction of nitrogen or other binary or ternary dopant as explained in the above examples. Instead of the numerous reports on metal-free ORR catalyst, development of carbon based metal-free electrocatalyst is still need of the day to introduce next generation metal air batteries and high performance fuel cells.

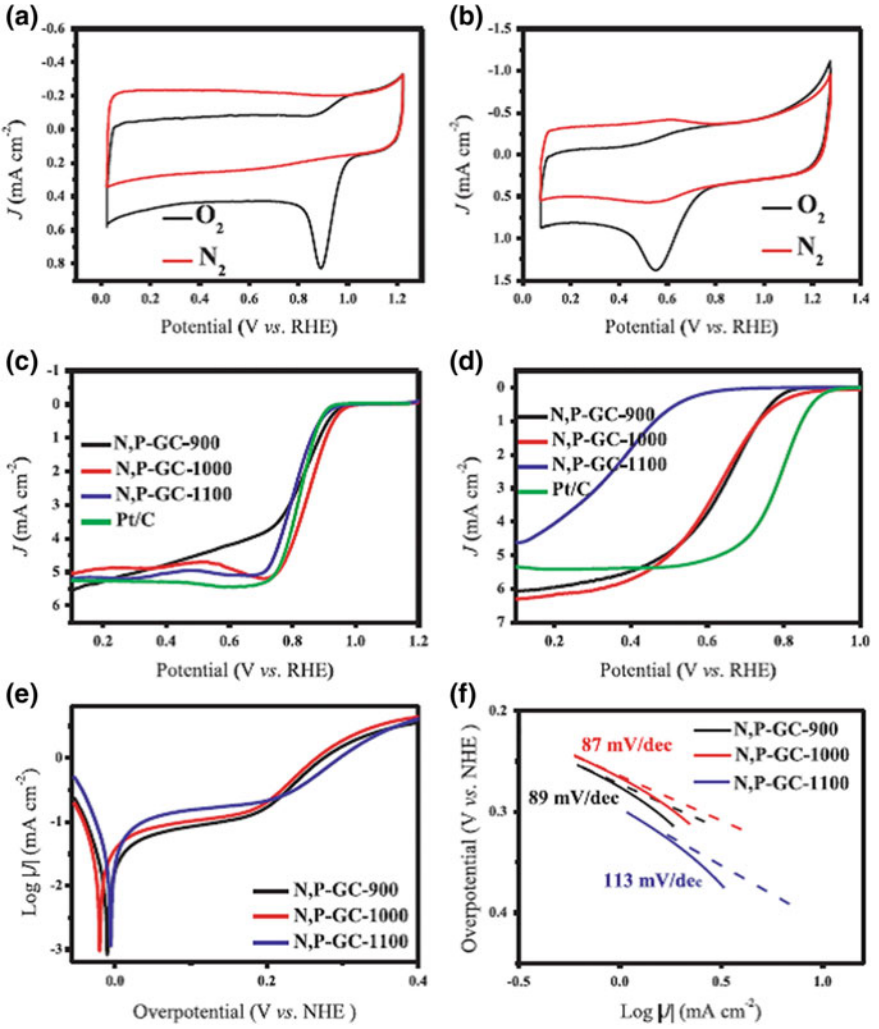

Fig. 15 CV curve of N, P-GC-1000 in 0.1 M KOH electrolytes (**a**) and 0.1 M $HClO_4$ (**b**); RDE polarization curves of N, P-GC hiring 30 nm SiO_2 under different calcining temperature in 0.1 M KOH (**c**) and in 0.1 M $HClO_4$ electrolytes. **d** The corresponding Tafel curves (**e**) and their slopes (**f**) in 0.1 M KOH [58]

References

1. Wood PM (1988) The potential diagram for oxygen at pH 7. Biochem J 253:287–289
2. Zhang J (2008) PEM fuel cell electrocatalysts and catalyst layers: fundamentals and applications. Springer
3. Radin MD, Siegel DJ (2015) In: Rechargeable batteries. Springer, pp 511–539
4. Zhang L, Zhang J, Wilkinson DP, Wang H (2006) Progress in preparation of non-noble electrocatalysts for PEM fuel cell reactions. J Power Sources 156:171–182

5. Hou X et al (2018) Low-cost nickel phosphide as an efficient bifunctional cathode catalyst for Li-O_2 batteries. J Electrochem Soc 165:A2904–A2908
6. Garden A, Abghoui Y, Skúlason E (2018) In: Alternative catalytic materials, pp 133–163
7. Mustain WE, Prakash J (2007) Kinetics and mechanism for the oxygen reduction reaction on polycrystalline cobalt–palladium electrocatalysts in acid media. J Power Sources 170:28–37
8. Wang Y, Balbuena PB (2004) Roles of proton and electric field in the electroreduction of O_2 on Pt (111) surfaces: results of an ab-initio molecular dynamics study. J Phys Chem B 108:4376–4384
9. Sidik RA, Anderson AB (2002) Density functional theory study of O_2 electroreduction when bonded to a Pt dual site. J Electroanal Chem 528:69–76
10. Bard AJ, Faulkner LR, Leddy J, Zoski CG (1980) Electrochemical methods: fundamentals and applications, vol 2. Wiley, New York
11. Damjanovic A (1993) Temperature dependence of symmetry factors and the significance of experimental activation energies. J Electroanal Chem 355:57–77
12. Song C et al (2007) PEM fuel cell reaction kinetics in the temperature range of 23–120 °C. Electrochim Acta 52:2552–2561
13. Zhang J et al (2008) PEM fuel cell relative humidity (RH) and its effect on performance at high temperatures. Electrochim Acta 53:5315–5321
14. Parthasarathy A, Srinivasan S, Appleby AJ, Martin CR (1992) Temperature dependence of the electrode kinetics of oxygen reduction at the platinum/Nafion® interface—a microelectrode investigation. J Electrochem Soc 139:2530–2537
15. Savy M, Andro P, Bernard C, Magner G (1973) Etude de la reduction de l'oxygene sur les phtalocyanines monomeres et polymeres—I. Principes fondamentaux, choix de l'ion central. Electrochimica Acta 18:191–197
16. Stassi A et al (2006) Electrocatalytic behaviour for oxygen reduction reaction of small nanostructured crystalline bimetallic Pt–M supported catalysts. J Appl Electrochem 36:1143–1149
17. Nie M, Shen PK, Wu M, Wei Z, Meng H (2006) A study of oxygen reduction on improved Pt-WC/C electrocatalysts. J Power Sources 162:173–176
18. González-Huerta R, Chávez-Carvayar J, Solorza-Feria O (2006) Electrocatalysis of oxygen reduction on carbon supported Ru-based catalysts in a polymer electrolyte fuel cell. J Power Sources 153:11–17
19. Gochi-Ponce Y, Alonso-Nunez G, Alonso-Vante N (2006) Synthesis and electrochemical characterization of a novel platinum chalcogenide electrocatalyst with an enhanced tolerance to methanol in the oxygen reduction reaction. Electrochem Commun 8:1487–1491
20. Wakabayashi N, Takeichi M, Itagaki M, Uchida H, Watanabe M (2005) Temperature-dependence of oxygen reduction activity at a platinum electrode in an acidic electrolyte solution investigated with a channel flow double electrode. J Electroanal Chem 574:339–346
21. Xia L et al (2018) Investigation of parameter effects on the performance of high-temperature PEM fuel cell. Int J Hydrogen Energy 43:23441–23449
22. Lee K et al (2009) Oxygen reduction reaction (ORR) catalyzed by carbon-supported cobalt polypyrrole (Co-PPy/C) electrocatalysts. Electrochim Acta 54:4704–4711
23. Denuault G, Sosna M, Williams K-J (2007) In: Handbook of electrochemistry. Elsevier, pp 431–469
24. Paliteiro C, Hamnett A, Goodenough JB (1987) The electroreduction of oxygen on pyrolytic graphite. J Electroanal Chem Interfacial Electrochem 233:147–159
25. Beyer W, von Sturm F (1972) Polarographic reduction of oxygen in the presence of phthalocyanine complexes. Angew Chem Int Ed Engl 11:140–141
26. Ocampo A, Castellanos R, Sebastian P (2002) Kinetic study of the oxygen reduction reaction on $Ru_y(CO)_n$ in acid medium with different concentrations of methanol. J New Mater Electrochem Syst 5:163–168
27. Antoine O, Durand R (2000) RRDE study of oxygen reduction on Pt nanoparticles inside Nafion®: H_2O_2 production in PEMFC cathode conditions. J Appl Electrochem 30:839–844
28. Yuan X, Ding X-L, Wang C-Y, Ma Z-F (2013) Use of polypyrrole in catalysts for low temperature fuel cells. Energy Environ Sci 6:1105–1124

29. Xing W, Yin G, Zhang J (2014) Rotating electrode methods and oxygen reduction electrocatalysts. Elsevier
30. Vellacheri R, Unni SM, Nahire S, Kharul UK, Kurungot S (2010) Pt–MoO_x-carbon nanotube redox couple based electrocatalyst as a potential partner with polybenzimidazole membrane for high temperature Polymer Electrolyte Membrane Fuel Cell applications. Electrochim Acta 55:2878–2887
31. Salvatore Aricò A et al (2010) Surface properties of Pt and PtCo electrocatalysts and their influence on the performance and degradation of high-temperature polymer electrolyte fuel cells. J Phys Chem C 114:15823–15836
32. You DJ et al (2012) Improvement of activity for oxygen reduction reaction by decoration of Ir on PdCu/C catalyst. Catal Today 185:138–142
33. Stassi A et al (2012) The effect of thermal treatment on structure and surface composition of PtCo electro-catalysts for application in PEMFCs operating under automotive conditions. J Power Sources 208:35–45
34. Sepp S et al (2016) Performance of polymer electrolyte membrane fuel cell single cells prepared using hierarchical microporous-mesoporous carbon supported Pt nanoparticles activated catalysts. Electrochim Acta 203:221–229
35. Jaouen F, Dodelet J-P (2007) Average turn-over frequency of O_2 electro-reduction for Fe/N/C and Co/N/C catalysts in PEFCs. Electrochim Acta 52:5975–5984
36. Yang Z, Moriguchi I, Nakashima N (2015) Durable Pt electrocatalyst supported on a 3D nanoporous carbon shows high performance in a high-temperature polymer electrolyte fuel cell. ACS Appl Mater Interfaces 7:9800–9806
37. Gribov E, Kuznetsov A, Golovin V, Krasnikov D, Kuznetsov V (2019) Effect of modification of multi-walled carbon nanotubes with nitrogen-containing polymers on the electrochemical performance of Pt/CNT catalysts in PEMFC. Mater Renew Sustain Energy 8:7
38. Yang Z, Nakashima N (2015) Poly (vinylpyrrolidone)-wrapped carbon nanotube-based fuel cell electrocatalyst shows high durability and performance under non-humidified operation. J Mater Chem A 3:23316–23322
39. Yang Z, Fujigaya T, Nakashima N (2015) A phosphoric acid-doped electrocatalyst supported on poly (para-pyridine benzimidazole)-wrapped carbon nanotubes shows a high durability and performance. J Mater Chem A 3:14318–14324
40. Fujigaya T, Berber MR, Nakashima N (2014) Design of highly durable electrocatalyst for high-temperature polymer electrolyte fuel cell. ECS Trans 64:159–169
41. Kim D et al (2018) Highly graphitic mesoporous Fe, N-doped carbon materials for oxygen reduction electrochemical catalysts. ACS Appl Mater Interfaces 10:25337–25349
42. Hu Y et al (2018) Immunity of the Fe-NC catalysts to electrolyte adsorption: phosphate but not perchloric anions. Appl Catal B 234:357–364
43. Liu K et al (2019) Mn- and N-doped carbon as promising catalysts for oxygen reduction reaction: theoretical prediction and experimental validation. Appl Catal B 243:195–203
44. Jiang R et al (2018) Ordered mesoporous FeN_x-doped carbon: a class of highly active and stable catalysts in acids, bases and polymer electrolyte membrane fuel cells. J Mater Chem A 6:3941–3953
45. Gokhale R et al (2018) Implementing PGM-free electrocatalysts in high-temperature polymer electrolyte membrane fuel cells. Electrochem Commun 93:91–94
46. Khan K et al (2018) Facile synthesis of tin-doped mayenite electride composite as a non-noble metal durable electrocatalyst for oxygen reduction reaction (ORR). Dalton Trans 47:13498–13506
47. Vengatesan S, Cho E, Oh I-H (2012) Development of non-precious oxygen reduction reaction catalyst for polymer electrolyte membrane fuel cells based on substituted cobalt porphyrins. Korean J Chem Eng 29:621–626
48. Li X, Liu L, Lee J-W, Popov BN (2008) Development of tellurium-modified carbon catalysts for oxygen reduction reaction in PEM fuel cells. J Power Sources 182:18–23
49. Nallathambi V, Lee J-W, Kumaraguru SP, Wu G, Popov BN (2008) Development of high performance carbon composite catalyst for oxygen reduction reaction in PEM Proton Exchange Membrane fuel cells. J Power Sources 183:34–42

50. Singh SK, Takeyasu K, Nakamura J (2019) Active sites and mechanism of oxygen reduction reaction electrocatalysis on nitrogen-doped carbon materials. Adv Mater 31:1804297
51. Yeager E (1986) Dioxygen electrocatalysis: mechanisms in relation to catalyst structure. J Mol Catal 38:5–25
52. Komba N, Wei Q, Zhang G, Rosei F, Sun S (2019) Controlled synthesis of graphene via electrochemical route and its use as efficient metal-free catalyst for oxygen reduction. Appl Catal B 243:373–380
53. Xu J, Huang W, McCreery RL (1996) Isotope and surface preparation effects on alkaline dioxygen reduction at carbon electrodes. J Electroanal Chem 410:235–242
54. Appleby A, Marie J (1979) Kinetics of oxygen reduction on carbon materials in alkaline solution. Electrochim Acta 24:195–202
55. Cao P et al (2019) Nitrogen-doped hierarchically porous carbon nanopolyhedras derived from core-shell ZIF-8@ ZIF-8 single crystals for enhanced oxygen reduction reaction. Catal Today 327:366–373
56. Li Y, Wen H, Yang J, Zhou Y, Cheng X (2019) Boosting oxygen reduction catalysis with N, F, and S tri-doped porous graphene: tertiary N-precursors regulates the constitutions of catalytic active sites. Carbon 142:1–12
57. Lv Y, Yang L, Cao D (2019) Sulfur, nitrogen and fluorine triple-doped metal-free carbon electrocatalysts for the oxygen reduction reaction. ChemElectroChem 6:741–747
58. Zhou Z, Chen A, Fan X, Kong A, Shan Y (2019) Hierarchical porous NP-coupled carbons as metal-free bifunctional electro-catalysts for oxygen conversion. Appl Surf Sci 464:380–387
59. Cazetta AL et al (2019) Metal-free ovalbumin-derived NS-co-doped nanoporous carbon materials as efficient electrocatalysts for oxygen reduction reaction. Appl Surf Sci 467:75–83
60. Lin X, Peng P, Guo J, Xiang Z (2019) Reaction milling for scalable synthesis of N, P-codoped covalent organic polymers for metal-free bifunctional electrocatalysts. Chem Eng J 358:427–434

History, Progress, and Development of Electrocatalysis

Amel Boudjemaa

Abstract This chapter reviews the history, the progress, development and achievement of electrocatalysis. We introduce some practical examples for electrochemical reactions as CO_2 reduction, hydrogen evolution and oxygen reduction reaction. Some examples of these anchored reaction using differents electrocatalysts cited metal oxide, carbon based material, alloy material, noble and precious metal, layered electrocatalytic materials, platinum-based electrocatalysts and electrocatalysts without Pt are cited.

Keywords Electrolysis · History · Progress · Development · Electrocatalyst · Electrocatalysis · Electrochemical energy conversion · CO_2 reduction reaction · Hydrogen evolution reaction · Oxygen oxidation reaction · Environment protection

1 Introduction

Recently, the International Energy Agency (IEA) reported that the energy supplied by fuels from fossil fuels energy source has been increased and reached 13,647 Mtoe in 2017. Based on the report of the International Energy Statistics, by 2050 annual energy consumption is envisaged to more than double and turn to the triple by the year 2100 [1]. So, the demand energy increased due to the development of human society leading and lead to the issues related to environmental pollution resulting a serious environmental degradation and global warming [2–5]. For this, we need to develop clean and sustainable technologies [6–8]. It is important to develop a new process for both the generation and storage of energy and protection of environment [9–13]. Renewable energy technologies depend on various main reactions, as well as oxidation/reduction reactions [14–16].

Grubb used the word electrocatalysis for the first time in 1963 in connection with the investigations of fuel cells [17]. However, the first interpretation of electrocatalysis process was introduced in 1935 by Horiuti and Polanyi [18] based on the upon

A. Boudjemaa (✉)
Centre de Recherche Scientifique et Technique en Analyses Physico-Chimiques (CRAPC), BP 384, Siège Ex-Pasna Zone Industrielle, Bou-Ismail, CP 42004, Tipaza, Algeria
e-mail: amel_boudjemaa@yahoo.fr; amel.boudjemaa@crapc.dz

Inamuddin et al. (eds.), *Methods for Electrocatalysis*,
https://doi.org/10.1007/978-3-030-27161-9_16

work of Gurney's analysis of 1931. Electrocatalysis is one of fields of catalysis that speeds up the rate of an electrochemical reaction occurring at the interface electrode/electrolyte [19]. Various applications such as electrodeposition, electropolymerization, electrosynthesis, electrochemical sensors, electrochemical capacitors, fuel cells, lithium ion batteries, solar cells, etc. [20–26]. To achieve these reactions, the development of electrocatalysts those are able to increase of reactions efficiency is required due to the various fields of catalysis [27]. On the other hand, electrocatalysis is not limited to heterogeneous catalysts where the catalyst can be used as immobilized on a conductive material or on a support. Due the electrocatalysis interdisciplinary, it is believed to play a central role of society through it inexpensive and environmentally friendly energy, fuels and chemicals production [28]. Over the past several decades, the progresses in the field of electrocatalysis have been motivated by both improvements in fundamental techniques and the technological imperative to develop enhanced low temperature electrocatalytic devices.

2 History of Electrocatalysis

2.1 Introduction

The history of electrocatalysis starts with electrochemistry history. It has seen a succession of several important stages during its evolution, often in correlation with the development of different branches of chemistry and physics. Indeed, it follows from the discovery of the principles of early magnetism XVI and XVII century and continues until the theories on conductivity and electric charge transport which has known many changes during its progress from first principles to complex theories. In the late 19th and 20th, the word electrochemistry used to describe electrical phenomena. In recent decades, electrochemistry has a huge field of research improves refining methods through electrolysis and electrophoresis, remove of contaminants, etc. In the period 1950s and 1960s, the role of electronic and geometric factors in the electrocatalysis using alloy electrocatalysts was the major contribution made by Bockris and coworkers [29].

2.2 History

In 1780, Luigi Galvani highlighted animal electricity by connecting two different metal plates (copper and iron) [30]. He caused the contraction of frog legs; his explanation was the existence of intrinsic electricity to the body of the frog. In 1786, Luigi Galvani fabricated the first battery without realizing it. Many years after, Alessandro Volta disproved this explanation in 1792 and demonstrated that the metals can produce electricity. He continued his experiments and published in

1800 his results which led him to design the first electric battery (which is a stack—hence the name of pile—of zinc and copper metal disks separated by a tissue or cardboard soaked in acid or salt water) [31]. The first batteries had a running time of about 20 min. The Volta battery is therefore the first independent source of electrical energy available. Therefore, the discovery of voltaic pile was in 1800 by Alessandro Volta. Meanwhile in Germany, Johann Wilhelm Ritter was studying electrolysis [32].

In early 1800s Humphry Davy, discovered the elements and improved the design of the voltaic pile. Michael Faraday highlighted in 1831 the principles of magnetic induction (creation of an electric current in a conductor placed in a magnetic field). He created the terms electrode, electrolyte, anode, cathode and ion. During the period 1833–1836, the laws of electrocatalysis revealed by Faraday were included [32]. Daniell cell was discovered in 1836 and attempted to eliminate the problem of hydrogen gas production of the Voltaic pile [32]. In 1859, Gaston Plante discovered a lead-acid battery, the oldest type of rechargeable battery currently used in motor vehicles [32].

Wilhelm Ostwald started his experimental work on electrochemistry in 1875. The first definition of catalyst was in 1894, the beginning of the catalysis field. Wilhelm Ostwald had his Nobel Laureate in 1909 (Nobelist in Chemistry, 1909). The year 1886 was established the process for the electrolytic production of aluminium. Nikola Tesla used of alternative current and he achieved to patent the results in 1888 [33, 32]. Gardner Cottrell introduced the Cottrell equation; the rules relation between electrode kinetics and mass transport [34, 32]. Edison Storage Battery was published in 1901 [35]. The theory of the electromotive force was developed in 1888 [36, 37]. Nernst's was the first researcher acknowledged the importance of ions in solution with his investigated in electrochemistry inspired by Arrhenius' dissociation theory. He explained the galvanic theory in 1889 [38].

Electrochemistry: Grundriss der technischen Elektrochemie auf theoretischer Grundlage book published in 1898 [39]. In 1898, the results of electrolytic oxidation and reduction were published [40]. Pierron illustrated that definite reduction products could result if the voltage at the cathode kept constant. After, the reduction of nitrobenzene at the cathode was elucidated. In 1910, the oil replaced water and the results were more precise [41]. In 1921, Jaroslav Heyrovský had a Nobel Prise in chemistry for his work about the elimination of the tedious weighing essential by previous analytical techniques [42]. In 1922, was the day of born of polarograph. After this, Masuzo Shikata builds the first instrument for the polarographic curves measurement [43]. In 1923, the year of the publication of the theory about how acids and bases behave using electrochemical basis [44]. The International Society of Electrochemistry (ISE) was created in 1949. Arne Tiselius was awarded a Nobel Prize in 1948 [45].

3 Progress and Development of Electrocatalysis

3.1 Electrochemical Energy Conversion

3.1.1 Introduction

The electrochemically catalytic conversion to value products is a promise way to produce green fuels. Recently, a main progress has been made in electrochemical energy conversion [46, 47]. Compared to the fossil energy, renewable energy is considered as the most powerful candidate due to its renewable and environmental friendly properties [48, 49]. The method of hydrogen generation via electrocatalysis is the electrocatalytic water splitting which has attracted most interest advantages [50, 51]. The key of the reaction is a catalyst that can be used as anode or cathode depend on the semiconductor type (n or p type) [52].

3.1.2 CO_2 Reduction Reaction (CO2RR)

Metal and Metal Oxide Electrode

The first studies on the electrocatalytic CO_2 reduction reaction (CO2RR) date back more than a century. CO2RR was reported for the first time in 1870, with a formic acid as the reaction product [53]. In an aqueous medium, the formation of formic acid is in competition with H_2, due to the reduction of water. Since the early 1900s and until 1980s, CO2RR has been studied on metal electrodes such as zinc, lead, copper and mercury, to convert CO_2 to formic acid [54]. In 1967, Haynes and Sawyer conducted a potentiostatic study on Au and Hg electrodes in DMSO electrolyte [55]. The resultants showed that CO and formate were the main products of CO2RR. In 1969, Paik and coauthors converted CO_2 on mercury electrode [56]. In 1970, Bewick et al. observed the formation of glycolic acid on Hg electrodes using a quaternary ammonium electrolyte [57]. Under similar operating conditions, Eggins et al. obtained oxalate on a mercury and graphite electrode, while glycolic acid observed on a lead electrode [58].

The electrocatalysis of CO2RR by transition metal complexes is more recent. Its origins date back to the 1970s, but the field has gained importance over the last thirty years [59]. In 1975, Aresta et al. have published a crystalline structure of CO_2 bound to a transition metal complex where they show $\eta 2$-bidentate bond involving carbon and oxygen atom, with significant structural curvature of CO_2 molecule [60]. From the beginning of 1980s, CO2RR had attracted more interest, because of the promising results, which estimated the possibility of applications on the industrial scale. In 1981, another important study published by Darensbourg et al. showed the interest of carbonyl anionic metal hydrides for CO2RR, HM $(CO)5-$ (M = Cr, Mo, or W) [61]. In the middle of 1980s, Frese and coauthors study the synthesis of

methanol by CO2RR on several metals and semiconductors such as Ru, Mo, GaAs and InP [62]. Promising results were obtained [63, 64].

In 1985, Hori et al. discover that metallic copper can converted CO_2 to hydrocarbons (methane, ethylene, etc.) with efficient reactivity [65, 66]. Since then, copper has remained the most studied metal for CO2RR, being the only one to give hydrocarbon products with yields higher than 50%. Excellent journals have been published in this area and several review articles have dealt with CO2RR [67, 68].

For example, Frese et al., discuss electrocatalytic reduction on solid electrodes [69]. Various kind of metal-based catalyses have been used as cathodes for the electrocatalytic CO2RR. Semiconductors [63], complexes [69], oxides [70] and alloys [71] have been studied in this field, but pure metals have been the most studied [54]. In 2008, Hori published a general review [54], in which he summarized the progress, focusing on the fundamental problems of CO2RR on metal electrodes and in particular on the electrocatalytic aspects.

Cokoja et al. publish a review presenting a global overview of homogeneous catalytic mechanisms for a large number of metal complexes used for CO2RR [70]. Other more recent journals summarize the catalytic activity of different transition metal complexes immobilized on electrodes [72]. They show that the efficiencies of modified electrodes depend on the nature of the complex, electrolyte, applied potential. Generally, in liquid medium, two major factors influence the selectivity of the products as well as the mechanisms of the electroreduction CO2RR. The first factor is related to the nature of the aqueous or organic solvent. While the second parameter was due to the nature of the catalyst used. This catalyst can be either dissolved in the case of homogeneous catalysis, or deposited on the working electrode or itself forming the electrode, it is in this case a heterogeneous catalysis.

For enhanced yields of CO2RR it was better to work in pH conditions where CO_2 was the majority. CO_2 dissolved in an aqueous medium leads to an acidic pH. In neutral electrolyte, where protons were not the majority, the faradic CO_2 conversion efficiencies were the highest, and it was in these electrolyte that most studies have been conducted.

Carbon Based Material

Eggins et al. investigated the electroreduction of HCO_3^- in a neutral aqueous medium on vitreous carbon (CV) [73]. The results confirmed that the decomposition of HCO_3^- in CO_2 is intermediate step for this reduction. Similarly, in a neutral medium and with Hg electrode, they showed that the $HCOO^-$ ion was the only the product with a faradic efficiency close to 100%. Schiffrin performed photoemission measurements for the study of the reduction of the $CO_2^{\cdot -}$ anion radical formed on Hg electrode [74]. The results showed that the CO_2 reduction potential did not depend on pH where the water provided the protons for forming the formate ion via $CO_2^{\cdot -}$. Hori and Suzuki confirmed the last hypothesis and demonstrated that the electrode potential was constant for pH ranging from 2 to 8 [74]. They explained that $CO_2^{\cdot -}$ free in solution, having a nucleophilic carbon, reacted with a proton of H_2O molecule to

form $HCO_2^{\cdot}$. H^+ will not bind to CO_2 de-oxygen since the pKa of $CO_2^{\cdot-}/HCO_2^{\cdot}$ pair was very low (pKa = 1.4) [75]. Then it is $HCO_2^{\cdot}$ which was reduced to $HCOO^{\cdot-}$.

In the field of CO2RR, the classification of metals made according to the reaction selectivity. There are two main pathways for the electroreduction of CO_2 in the presence of protons. The first one leads to the formation of CO and the other way gave a formate ion. Cu has an affinity for adsorbed CO, which allows it to reduce CO_2 beyond two electrons to methane and other hydrocarbons.

Alloy Materials

Christophe et al. were interested in Cu/Au alloys by varying the percentage of Au from 1 to 50% (Au1Cu99, Au10Cu90, Au20Cu80, Au50Cu50) [76]. The study indicated that CO formed increased with increasing amount of Au, while the CH_4 decreased. They also studied the activity of Cu in different crystal lattices. Among the alloys it was Au50Cu50 which had the highest faradic yield of gaseous product containing carbon (CO, CH_4 and various C2). Ishimaru et al. have studied the selective electroreduction (potential pulses) of CO_2 into C2 compounds (CH_3CHO, C_2H_5OH and C_2H_4) on different Cu/Ag alloys (87/13, 55/45, 28/72 and 13/87) [77]. The faradic efficiency of the compounds C2 depended on the atomic ratio in the various alloys as well as applied anodic and cathodic pulses. The maximum yield was 54.2% on Cu/Ag electrode (28/72) for anode pulses at −0.2 V/ENH and other cathodic at −1.8 V/ENH. It has been established that the formation of Cu oxide as well as the desorption of Ag under anodic polarization are the key factors for the selective CO2RR in C2 compounds on Cu/Ag alloy electrodes. Studies on Sb-Pb–Pt/GC alloys have also been presented in the literature [77]. The used alloys was not limited to the electrocatalytic CO2RR but was also involved in the chemical CO2RR (by adding a chemical reducer).

Komatsu and Kudo have studied the catalytic effect of several Raney-type alloys in order to form methane from the chemical CO2RR [78]. Addition of 0.2 g of Fe-Raney and 10 mmol of CsOH in 8 mL H_2O at 380 °C and 320 atm gave cesium formate with a yield of 32.9%. The addition of 0.05 g of Ru impregnated on carbon (Ru/C) modifies the selectivity of the reaction and the majority product becomes CH_4 with a faradic yield of 45.3% whereas cesium formate and H_2 are with 1.2 and 30% respectively. Despite all the improvements made to CO2RR on metal cathodes and metal alloys, the surge problem is not overcome. This situation conduced to find catalytic systems capable of improving the CO2RR in terms of reaction selectivity as well as energy by minimizing the reduction potential.

Gas Diffusion Electrodes

The application of the gas diffusion electrodes (GDE) began in 1987 with the experiments of Mahmood et al. for measurement of formic acid selectively in acid medium (pH = 2) [79]. GDEs were prepared from carbon black impregnated with different

metal salts. For lead-containing GDE, a faradic yield of 89% of formic acid was obtained. In this study, the use of indium and tin instead of lead showed a lower selectivity towards HCOOH, with CO as co-product. Hara et al., have worked with Pt impregnated GDE in an aqueous medium (0.5 M $KHCO_3$) and have shown that, at atmospheric pressure CO_2 was badly reduced whereas at high pressure (30 atm), CH_4 was obtained with a faradic efficiency 35% [80]. They also observed a high current density with a faradic yield of 43% methane at a CO_2 pressure of 50 atm.

The study of the comparative reactivity of Fe, Pd and Ag shows that the density of the maximum CO_2 reduction current to CO (3.05 A/cm^2) is reached for silver impregnated GDE [81]. Machunda et al., prepared modified GDE (electrodeposited) with tin and obtained formate with a faradic yield of 18% during the first 5 min of reaction, then this yield decreased to 12% after 1 h. They concluded that it was necessary to control the distribution of the material on the electrode in order to improve the reaction efficiency [79]. The same group was also interested in the microstructural changes of the surface of GDE after the use for CO_2 reduction. Lead has been electrodeposited on GDE. After exposure to CO_2 gas saturated with water vapor for 1 h, the particles were transformed into PbO_2 needles. In electroreduction, the maximum faradic yield attained was 65% in formic acid after 1500 s at −1.8 V/ENH. The initial current density reaches about 52 mA/cm^2, decreases to less than 46 mA/cm^2 within 500 s, and then stabilizes for 3500 s [82]. Tryk et al., have prepared GDE based on carbon fibers impregnated with Ni, Fe and Pd. Under atmospheric pressure of CO_2, the maximum current density obtained for the majority production of CO is 80 mA/cm^2 [83–85].

Other studies have been conducted with EDG using Cu as a catalyst. Ikeda et al., have shown that C_2H_4 and C_2H_5OH were the main products [86]. Whereas on GDE with copper particles with different sizes CH_4, C_2H_4, C_2H_5OH, CO and $HCOO^-$ were obtained. For the smallest particles, the selectivity for CO and hydrocarbons is highest. Cook et al. obtained CH_4 and C_2H_4 with a total faradic yield of 79% [87]. Furuya et al., studied the CO2RR on Ru and Pd-impregnated GDE and their Ru/Pd alloy (1/1) in aqueous electrolyte (0.5 M, $KHCO_3$). They obtained a faradic yield of 90% in formic acid on a GDE impregnated the alloy [88]. Ikeda et al. tested GDE loaded with CuO/ZnO = 3/7. At −1.32 V/ENH, ethanol was the main product (with an efficiency of 17% and a selectivity of 88%. The use of reduced Cu/ZnO = 3/7 GDE under H_2 showed a decrease in the formation of n-C_3H_7OH and C_2H_4 [89].

Schwarz et al. introduced Cu-based ceramics such as $La_{1.8}Sr_{0.2}CuO_4$, $Pr_{1.8}Sr_{0.2}CuO_4$ and $Gd_{1.8}Th_{0.2}CuO_4$ perovskites in GDE and conducted electroreduction experiments on CO_2 in KOH [90]. CH_3OH, C_2H_5OH and n-C_3H_7OH formed with an overall faradic efficiency of 40%. No catalytic activity was recorded in the absence of copper. More recently, Mignard et al., have studied the same catalyst supported on GDE but have obtained different products. Under identical operating conditions, CH_4, C_2H_4 and CO was the majority products. They suggested that this change in selectivity (from alcohols to hydrocarbons) might be due to the use of reagents and electrolytes from different suppliers, or a lack of electrolyte circulation in the system used [91].

3.1.3 Hydrogen Evolution Reaction (HER)

Noble and Precious Metal

Electrocatalysis was begun in 1920s by Bowden and Rideal, where a series of metals were elaborated for measurement of Hydrogen evolution reaction (HER) [92]. Pt-group metals, such as Pt, Ir, Pd, Rh, etc. exhibit a highest activities toward HER [93, 94]. Pt electrocatalyst could significantly lower the overpotential with the lowest Set off potential value of about (0.2–0.4 V) and the Tafel slope value is around 30 mV/decade [95]. In 1968s, the performances of electrode used as anode for chlorine evolution was patented by Beer [96]. RuO_2 was the active element in these catalysts. For the first time, Pt was not in the focus of the material choice and the result was more than excellent [97]. Pt was firstly used as cathodic and anodic electrode [98]. Pt was established to be the good electrode for HER with minimum overpotential. However, due to the scarcities and high cost of noble metal, the application of Pt-based electrocatalysts might be limited. Thus, the future development direction of highly activity electrocatalysts for HER is focused on the materials, which are cheap, and earth-abundant [99]. In the middle of 1970s, the materials without precious metals were improved and extended.

Precious metals are among the most active materials and it was discovered that these oxides are active even for cathodic processes [100, 101]. Generally, precious oxides as IrO_2 and RuO_2 are thermodynamically unstable in the conditions of H_2 evolution but they are very active and stable in reducing conditions. This behaviour is due to their electronic conductivity [102, 103]. In alkalis electrolyte, the cathodic electrocatalysts IrO_2, RuO_2 and Co_3O_4 were used for HER. IrO_2 has proved to be as active as RuO_2 and more active than Co_3O_4 [104]. Krstajic et al., studied the behaviour of RuO_2-doped Ni/Co_3O_4 electrodes [105, 106]. It is demonstrated that, less than 10 mol% RuO_2 in a Co_3O_4 matrix allows for the same electrocatalytic response as pure RuO_2. On the other hand, IrO_2 is even more active than RuO_2 for HER [107, 108].

Layered Electrocatalytic Materials

Recently, two-dimensional (2D) layered materials had attracted significant attention in the fundamental and application science due of their unique chemical and physical properties [109, 110]. Due to their anisotropic structure, chemical or mechanical processes, as well as the thin films, nanosheets, nanoribbons, nanoparticles and nanotubes [111], where they can obtained the ultrathin flakes.

Recently, molybdenum sulfides (MoS2) shown a good efficiency for the HER and will be one of the best electrocatalysts [112]. The electrocatalytic property of MoS2 for HER could stem from 1970s. In 1977, Jaegermann and Tributsch reported the electrochemical performance of MoS2 layer crystals [113]. However, the bulk MoS2

had a lower electrocatalytic activity. Consequently, few attentions had been attracted on this research topic. So during the past decades, the research progress is very slow [114].

In 2005, Hinnemann et al. examined the biomimetic electrocatalytic HER process for the Hydrogenase and Nitrogenase [115]. The results reported a good indicator of the electrocatalysts for HER and it will be applied to many material systems, ranged from metals to enzymes, including MoS2 [116]. After that, Chhowalla et al., reported that the elaboration of [(PY5Me2) MoS2]$^{2+}$ [117]. The use of the inorganic compound to mimic the sulfide-terminated edge sites of MoS2 was reported by Karunadasa et al. [116]. The authors verified once again that the active site of MoS2 was the disulfide-terminated edges supplied a way to prepare the powerful electrocatalytic molecular complexes. After the published work of Au supported MoS2, carbon paper supported MoS2 was reported by Chorkendorff and coworkers [118]. The value of Tafel slop is ~120 mV/dec. and the performance of MoS2 was promoted by the co-impregnation of cobalt. Compared with the bulk one, the performances of MoS2 had improved and it is still not a good enough to be regarded as a good electrocatalysts for HER.

In 2011, the elaboration of hybrids MoS2/Graphene was reported [111]. The as prepared catalysts exhibited great electrocatalytic activities for HER with the low potential value (~0.1 V) and Tafel slope (41 mV/dec). Another study of hybrids of MoSx with CNTs and other mesoporous carbons etc. were prepared and tested for HER [119–123]. In 2013, Chang et al., investigated the performance of the three-dimensional 3D MoSx@Graphene electrode [114].

The 3D MoSx@Graphene electrode had the highest electrocatalytic activities for HER at the temperature of 120 °C with the Tafel slop around 43 mV. Kibsgaard and co-authors described the method that controlled the surface structure of MoS2 [119]. Another route to improve the performance of MoS2 electrocatalyst for HER is to prepare MoS2 with a small particles size or with a few layers (or single layers). Wang and coworkers enhanced the electrocatalytic activities of MoS2 for HER by the ultrasonication of the bulk MoS2 [124]. Recently, it is reported that the layers of the MoS2 influenced on the reaction efficiency for HER where the few layer or single of MoS2 have the better performance [125, 126].

Recently, another kind of transition metal phosphides (TMPs), the first work was published in 2013 [127]. Since this date, various TMPs have been proven as promising electrocatalysts for HER, including CoP, Ni2P, MoP, Cu3P, FeP and Ni5P4 [128–133]. It was reported also, TMP nano arrays grew on 3D substrates show enhanced electrocatalytic activity [134–136].

3.1.4 Oxygen Reduction Reaction (ORR)

Oxygen reduction reaction (ORR) is a main reaction used in electrochemistry as well as environment, material and energy [137–140]. ORR is an essential reaction for proton exchange membrane fuel cells (PEMFC) [141]. Despite a many studies carried out for this reaction, the reaction mechanism and kinetics are still unclear, even on Pt-based catalysts that are the most used. At present, this is a big challenge

for electrochemists to design new electrocatalysts with low cost, high reactivity and selectivity, and a high stability in the electrolytic medium [142–144]. During the last twenty years, many review papers have been published for platinum (Pt), ruthenium (Ru) and cobalt-iron macrocycle materials [145–153]. The development of catalysts based on Ru or macrocycles of cobalt and/or iron are considered as an alternative for Pt-based materials due to their comparable activity of ORR through the tolerance to the presence of organic molecules [154–156].

Platinum-Based Electrocatalysts

Carbon-supported Pt is the most electrocatalyst used as cathode for PEMFC where Pt was a best electrocatalyst for ORR [157]. Pt modified transition metal was developed and improved their electrocatalytic reactivity [158]. Numerous studies have been reported in the literature for fuel cell applications [159–162].

United Technologies Corporation reported in 1980 the work on Pt alloys for ORR of phosphoric acid batteries (PAFC) [163]. In 1993, Mukerjee and Srinivasan study the Pt-alloy catalysts for PEMFCs [164]. The work reported that Pt-alloy illustrated a low current density range and a higher potential relative to Pt. Between 1995 and 1997, another work conducted on carbon-supported on Pt-M alloy (M = Fe, Mn, Ni, Ti, Cr and Cu) for PEMFC applications [137, 163]. Many studies have also been carried out on Pt-Co alloys [165–174], Pt-Ni [174], Pt–Fe [166], and Pt-Pd [167]. In all cases, the alloys have a better activity than Pt alone. This could be explained by an electron effect induced by the alloy [169] or by a surface area surface [52]. Alloys with Pt have also been reported using two metals [170]. Therefore, carbon-supported Pt/Cr/Cu alloys have a reactivity twice time better than Pt. They demonstrated also Pt-Cr-Cu based on metal oxides could improve the activity for ORR by a factor of six compared to Pt.

However, concerns may arise about the stability and durability of these alloys in long-term of utilization [137, 168]. The main factor hindering the implementation of PEMFC-type cells is the catalysts performance loss during reaction time. The catalysts degradation at the cathode is due to sintering of the particles [172], dissolution of the catalysts [175] and corrosion of the support [153, 158]. The electrocatalysts stability of Pt materials was investigated and reached more than 1000 h. While others works reported a poor stability of some materials after just a few hours of half-cell operation [176, 177]. The material performance related to the temperature, pressure and fuel flow [172]. In this context, durability tests in PEMFC showed a positive effect. In long-term tests, alloys such as Pt3Cr, Pt3Co and Pt3Ni showed negligible performance loss after operating periods ranging from 400 to 1200 h [164]. Colon-Mercado et al. studied Pt3Ni alloy supported on carbon [178]. The results show a better sintering resistance compared to Pt alone. Similarly, Gasteiger and co-authors reported that Pt_xCo_{1-x}/C compared with Pt/C demonstrated a good reactivity which was maintained after 1000 h of reaction [137].

Other studies on Pt-Co alloys [179–181] showed the same trend, after long tests, the activity of these alloys remained higher than Pt alone. Studies have therefore

focused on the development of catalysts that tolerate pollutants. Pt-Co has been studied for its tolerance against CO [182]. In 1964, Jasinski discovered the electroreactivity of nickel electrodes for ORR [183]. The reaction reactivity increased by electrode coating with cobalt phthalocyanine used as a new electrocatalyst replaces the expensive Pt-based electrode [184].

Electrocatalysts Without Pt

The research of catalysts based on noble or non noble metals for ORR was a challenge to develop the reaction reactivity [172]. Palladium (Pd) nanoparticles deposited on gold electrodes have been tested in KCl medium [185]. Pd nanoparticles were also deposited on carbon nanotubes and showed a diffusion controlled process [186]. Pd nanotiges deposited on carbon shows activity quite similar to Pt [187]. Silver (Ag) nanoparticles showed an activity in basic medium with a mechanism similar to Pt with high potential and a better tolerance to methanol [188].

Non-noble metals, such as copper are widely used and in particular, for this one it is possible to find a literature rich enough for its applications [172]. Ohno et al. studied the adsorption of oxygen on Cu (001) [189]. A similar study was conducted on Ni (100) [190]. Indeed, TiO_2 deposited on a Ti surface showed an activity for ORR [191]. Similarly, carbon-deposited Ta_2O_5 has a similar oxygen reduction potential compared to platinum [192]. Developments of electrocatalysts were also observed and developed [193]. The electroreactivity of these materials maybe due to the presence of a carbon carrier, a metal source, a nitrogen source, and a heat treatment temperature. In addition, the metal amount plays an important role for activity and stability.

Thus, tantalum was added to improve their activity which also reduced corrosion [194]. W2N/C had also developed [195]. Its activity is comparable in acidic medium and fuel cell test; moreover, it shows a good stability. On the other hand, its performances remain less than the commercial Pt/C. Over the last years, Ru (Ru-Se) materials were developed due to their activity for ORR and were considered a potential alternative to platinum catalysts [196–198].

Carbon Based Materials

Preliminary studies have demonstrated that carbon nanotubes (CNT) can be used as a support for the development of catalysts [199]. Thus, more studies that are detailed have shown that ORR on Pt deposited on Single Wall Carbon Nanotubes (SWCNTs) is improved compared to Pt/C [200]. It also appears that these CNT improve the durability of the electrocatalyst as well as its tolerance to CO [200]. Other studies focused on the modification of CNT by chemical treatment [201] or by nitrogen doping [202, 203]. A chemical treatment of CNT was developed for functionalized the material surface and also facilated the deposition of metal nanoparticles [201].

Microporous carbon supports and ordered hierarchical nanostructured carbon (OHNC) structures have been used as a support for high Pt nanoparticle loads [204, 205]. The uniform dispersion and the small particle size was lead to increase Pt activity and thus increasing PEMFC. Recently, it is observed that, the modification of the support with boron improves the durability of the catalysts by decreasing the corrosion phenomena [206]. Pt has recently been deposited on functionalized carbon nanofibers [207].

Rao et al. studied the carbon of the Sibunit family (Omsk, Russia) with different active surface and pore size values [208]. They have thus shown that the carbon support having the smallest active surface allowed to obtain a best specific activity. This type of carbon has been of great interest for both the cathode used in PEMFC cells and the anode of DMFC batteries [209, 208, 210]. Carbon and carbon nanofilaments has shown better corrosion stability compared to conventional carbon [211].

It has been demonstrated that carbon and nitrogen modified material show important ORR activity [212–216]. These results lead to the metallic active sites [215]. Another study demonstrated that, the lower amount of Fe and C was not a good choice [217].

Oxide-Based Materials

Early 1900s, the work on the electrochemical of cobalt oxide was carried out using anodic cobalt material [218, 219] mainly encouraged by the limitation of the corrosion phenomena. During the period 1950s and 1960s, the research focused on the of cobalt oxide materials evaluation through water oxidation performance [220, 221].

The high cost of Pt motivated research to investigate a non nobel metal [156, 222]. The attractive method is to using low cost material in their complex form. The complexes based on iron (Fe) and cobalt (Co) shown a highest activities but it was lower than Pt due to the lower stability. In the 1980s, Collman and Anson's work establish enhancements reactivity by using bis-cofacial cobalt porphyrins [223–225]. In 1964, Fe was used for ORR [226]. The works on the Fe based catalysts enhancement the ORR reactivity increased [222]. In 2011, the work on Fe based catalysts was reviewer in detail (Chen et al., [227, 228]. It is demonstrated that, under inert atmosphere the activity and the durability of Fe and Co based materials enhancement heating treatment [229–231].

References

1. U.S. Energy Information Administration. International energy statistics. U.S. Department of Energy, Washington, DC. www.eia.doe.gov
2. Dunn B, Kamath H, Tarascon JM (2011) Electrical energy storage for the grid: a battery of choices. Science 334:928–935. https://doi.org/10.1126/science.1212741
3. Alonso-Vante N (2003) In: Wieckowski A, Savinova ER, Constantinos VG (eds) Catalysis and electrocatalysis at nanoparticle surface. Basel, New York, p 931

4. Alonso-Vante N (2003) In: Vielstich W, Lamn A, Gasteiger H (eds) Handbook of fuel cells-fundamentals, technology and applications. Wiley, Chichester, UK, p 534
5. Vaona A (2016) The effect of renewable energy generation on import demand. Renew Energy 86:354–359. https://doi.org/10.1016/j.renene.2015.07.062
6. Kauder B, Potrafke N, Ursprung H (2018) Behavioral determinants of proclaimed support for environment protection policies. Eur J Polit Econ 54:26–41
7. Alonso-Vante N, Bogdanoff P, Tributsch H (2000) On the origin of the selectivity of oxygen reduction of ruthenium-containing electrocatalysts in methanol-containing electrolyte. J Catal 190:240–246. https://doi.org/10.1006/jcat.1999.2728
8. Alonso-Vante N, Borthen P, Fieber-Erdmann M, Strehblow HH, Holub-Krappe E (2000) In situ grazing incidence X-ray absorption study of ultra-thin Ru_xSe_y cluster-like electrocatalyst layers. Electrochim Acta 45:4227–4236. https://doi.org/10.1016/S0013-4686(00)00555-7
9. Friedlein JT, McLeod RR, Rivnay J (2018) Device physics of organic electrochemical transistors. Org Electron 63:398–414. https://doi.org/10.1016/j.orgel.2018.09.010
10. Lohse C (2018) Environmental impact by hydrogeothermal energy generation in low-enthalpy regions. Renew Energy 128:509–519. https://doi.org/10.1016/j.renene.2017.06.030
11. Petralia S, Sciuto EL, Messina MA, Scandurra A, Mirabella S, PrioloF ConociS (2018) Miniaturized and multi-purpose electrochemical sensing device based on thin Ni oxides. Sens Actuators B: Chem 263:10–19. https://doi.org/10.1016/j.snb.2018.02.114
12. Zhou M, Xu Y, Lei Y (2018) Heterogeneous nanostructure array for electrochemical energy conversion and storage. Nano Today 20:33–57. https://doi.org/10.1016/j.nantod.2018.04.002
13. Kudr J, Zitka O, Klimanek M, Vrba R, Adam V (2017) Microfluidic electrochemical devices for pollution analysis–A review. Sens Actuators B Chem 246:578–590
14. Dai L, Xue Y, Qu L, Choi H-J, Baek J-B (2015) Metal-free catalysts for oxygen reduction reaction. Chem Rev 115(11):4823–4892. https://doi.org/10.1021/cr5003563
15. Kuhl KP, Hatsukade T, Cave ER, Abram DN, Kibsgaard J, Jaramillo TF (2014) Electrocatalytic conversion of carbon dioxide to methane and methanol on transition metal surfaces. J Am Chem Soc 136(40):14107–14113. https://doi.org/10.1021/ja505791r
16. Pei Z, Gu J, Wang Y, Tang Z, Liu Z, Huang Y, Huang Y, Zhao J, Chen Z, Zhi C (2017) Component matters: paving the roadmap toward enhanced electrocatalytic performance of graphitic C3N4-based catalysts via atomic tuning. ACS Nano 11(6):6004–6014. https://doi.org/10.1021/acsnano.7b01908
17. Grubb WT (1963) In: 17th annual power sources conference, Atlantic City
18. Horiuti J, Polanyi M (1935) Grundlinieneiner Theorie der Protonübertragung. Acta Phys Chim USSR 2:505
19. Halder A, Zhang MW, Chi QJ (2016) Electrocatalytic applications of graphene–metal oxide nanohybrid materials. In: Advanced catalytic materials: photocatalysis and other current trends. InTech Open Access Publishers, pp 379–413 (chapter 14)
20. Banbur-Pawlowska S, Mech K, Kowalik R, Zabinski P (2016) Analysis of electrodeposition parameters influence on cobalt deposit roughness. Appl Surf Sci 388:805–808. https://doi.org/10.1016/j.apsusc.2016.04.005
21. Bizon N, Thounthong P (2018) Fuel economy using the global optimization of the Fuel Cell Hybrid Power Systems. Energy Convers Manag 173:665–678. https://doi.org/10.1016/j.enconman.2018.08.015
22. Gul T, Bischoff R, Permentier HP (2015) Electrosynthesis methods and approaches for the preparative production of metabolites from parent drugs. TrAC Trends Anal Chem 70:58–66. https://doi.org/10.1016/j.trac.2015.01.016
23. Lee JM, Jung KK, Ko JS (2016) Formation of nickel microcones by using an electrodeposition solution containing H3BO3. Curr Appl Phys 16:261–266. https://doi.org/10.1016/j.cap.2015.12.010
24. Liu X, Lillehoj PB (2017) Embroidered electrochemical sensors on gauze for rapid quantification of wound biomarkers. Biosens Bioelectron 98:189–194. https://doi.org/10.1016/j.bios.2017.06.053

25. Roghabadi FA, Ahmadi N, Ahmadi V, Carlo AD, Aghmiuni KO, Tehrani AS, Ghoreishi FS, Payandeh M, Fumani NMR (2018) Bulk heterojunction polymer solar cell and perovskite solar cell: concepts, materials, current status, and opto-electronic properties. Sol Energy 173:407–424. https://doi.org/10.1016/j.solener.2018.07.058
26. Zhao N, Fabre B, Bobadova-Parvanova P, Fronczek FR, Vicente MGH (2017) Synthesis and electropolymerization of a series of 2,2′-(ortho-carboranyl)bisthiophenes. J Organomet Chem 828:157–165. https://doi.org/10.1016/j.jorganchem.2016.11.029
27. Bandarenka AS, Koper MTM (2013) Structural and electronic effects in heterogeneous electrocatalysis: toward a rational design of electrocatalysts. J Catal 308:11–24. https://doi.org/10.1016/j.jcat.2013.05.006
28. Bonde J, Moses PG, Jaramillo TF, Norskov JK, Chorkendorff I (2008) Hydrogen evolution on nano-particulate transition metal sulfides. Faraday Discuss 140:219–231. https://doi.org/10.1039/B803857K
29. Bockris O'M, Srinivasan S (1969) Fuel Cells: their electrochemistry, McGraw-Hill, New York
30. Whittaker ET (1951) A history of the theories of ether and electricity, vol 1. Nelson, London, p 4. http://www.famousscientists.org/alessandro-volta/
31. Volta AGAA (1745–1827). Royal Netherlands Academy of Arts and Sciences. Retrieved 20 Jul 2015
32. Lefrou P, Fabry JC (2009) Poignet electrochemistry. The basics with examples. Springer, pp 2–6
33. Cheney M (2001) [1981] Tesla: man out of time
34. Bard AJ, Faulkner LR (2001) Electrochemical methods. Fundamentals and applications, 2nd edn. Wiley, New York
35. American Chemical Society. National Historic Chemical Landmarks. Thomas Edison, Chemist. http://www.acs.org/content/acs/en/education/whatischemistry/landmarks/thomas-edison.html
36. Nernst WZ (1888) Zur kinetik der in losung befindlichen korper. 1. Theori der diffusion. Z Phys Chem 2:613–637
37. Sur UK (2012) Recent Trend in Electrochemical Science and Technology, pp 1–303
38. Nernst W (1889) Sitzungsber preuss Akad Wiss 83–95; Nernst W (1889) Z Phys Chem 4:129–181
39. Haber F (1898) Grundriss der technischen Elektrochemie auf theoretischer Grundlage. http://books.google.com/books?id=ViVKAAAAMAAJ&oe=UTF-8
40. Cao A, Wieckowski J, Inukai N, Alonso-Vante (2006) Oxygen reduction reaction on ruthenium nanoparticles modified with selenium and sulfur. J. Electrochem. Soc. 153:A869–A874. https://doi.org/10.1149/1.2180709
41. Millikan RA [1868–1953] (1959) A biographical memoir by L. A. Du Bridge and Paul A. Epstein
42. The Nobel Prize in Chemistry 1959. Nobelprize.org. Nobel Media AB 2014. 2 Feb 2017
43. Shikata Masuzo (1925) Conception cells and electrolysis of sodium ethoxide solutions. Trans Faraday Soc 19:24. https://doi.org/10.1039/TF9241900721
44. Brock W (1993) The Norton history of chemistry. Norton, New York
45. Nobel Prize for Chemistry Prof. Arne Tiselius (1948). Nature 162:766. https://doi.org/10.1038/162766b0
46. Mao J, Wang Y, Zheng Z, Deng D (2018) The rise of two-dimensional MoS2 for catalysis. Front Phys 13:138118. https://doi.org/10.1007/s11467-018-0812-0
47. Xiong J, Di J, Li H (2018) Atomically thin 2D multinary nanosheets for energy-related photo. Adv Sci 5:180024. https://doi.org/10.1002/advs.201800244
48. Lin L, Zhou W, Gao R, Yao S, Zhang X, Xu W, Zheng S, Jiang Z, Yu Q, Li YW, Shi C, Wen XD, Ma D (2017) Low-temperature hydrogen production from water and methanol using Pt/α-MoC catalysts. Nature 544:80–83. https://doi.org/10.1038/nature21672
49. Zhang Y, Ji Q, Han GF, Ju J, Shi J, Ma D, Sun J, Zhang Y, Li M, Lang XY, Zhang Y, Liu Z (2014) Dendritic, transferable, strictly monolayer MoS2 flakes synthesized on SrTiO3 single crystals for efficient electrocatalytic applications. ACS Nano 8:8617–8624. https://doi.org/10.1021/nn503412w

50. Boudjemaa A, Popescu I, Juzsakova T, Kebir M, Helaili N, Bachari K, Marcu I-C (2016) M-substituted (M = Co, Ni and Cu) zinc ferrite photo-catalysts for hydrogen production by water photo-reduction. Int J Hydrogen Energy 41:11108–11118
51. Wang J, Cui W, Liu Q, Xing Z, Asiri AM, Sun X (2016) Recent progress in cobalt-based heterogeneous catalysts for electrochemical water splitting. Adv Mater 28:215–230. https://doi.org/10.1002/adma.201502696
52. Boudjemaa A, Bouarab R, Saadi S, BougueliaA Trari M (2009) Photo electrochemical H_2-generation over Spinel $FeCr_2O_4$ in X^{2-} solutions ($X^{2-} = S^{2-}$ and $SO_3{}^{2-}$. Appl Energy 86:1080–1086
53. Royer ME (1870) Réduction de l'acide carbonique en acide formique. Compt. Rend. 1870:731–732
54. Hori Y (2008) Electrochemical CO_2 reduction on metal electrodes. In: Modern aspects of electrochemistry. Springer, New York, pp 89–189. https://doi.org/10.1007/978-0-387-49489-0_3
55. Haynes LV, Sawyer DT (1967) Electrochemistry of carbon dioxide in dimethyl sulfoxide at gold and mercury electrodes. Anal Chem 39(3):332–338. https://doi.org/10.1021/ac60247a013
56. Paik W, Andersen TN, Eyring H (1969) Kinetic studies of the electrolytic reduction of carbon dioxide on the mercury electrode. Electrochim Acta 14(12):1217–1232
57. Bewick A, Greener GP (1970) The electroreduction of CO_2 to glycolate on a lead cathode. Tetrahedron Lett 11(5):391–394
58. Eggins BR, Ennis C, Mc Connell R, Spence M (1997) Improved yields of oxalate, glyoxylate and glycolate from the electrochemical reduction of carbon dioxide in methanol. J Appl Electrochem 27:706–712. https://doi.org/10.1023/A:1018444022321
59. Benson EE, Kubiak CP, Sathrum AJ, Smieja JM (2009) Electrocatalytic and homogeneous approaches to conversion of CO_2 to liquid fuels. Chem Soc Rev 38(1):89–99. https://doi.org/10.1039/B804323J
60. Aresta M, Nobile CF, Albano VG, Forni E, Manassero M (1975) New nickel–carbon dioxide complex: synthesis, properties, and crystallographic characterization of (carbon dioxide)-bis(tricyclohexylphosphine) nickel. J Chem Soc Chem Commun 15:636–637. https://doi.org/10.1039/C39750000636
61. Darensbourg DJ, Rokicki A, Darensbourg MY (1981) Facile reduction of carbon dioxide by anionic Group 6b metal hydrides. Chemistry relevant to catalysis of the water-gas shift reaction. J Am Chem Soc 103(11):3223–3224. https://doi.org/10.1021/ja00401a055
62. Frese KW, Jr Leach S (1985) Electrochemical reduction of carbon dioxide to methane, methanol, and CO on Ru electrodes. J Electrochem Soc 132(1):259–260. https://doi.org/10.1149/1.2113780
63. Canfield D, Frese KW Jr (1983) Reduction of carbon dioxide to methanol on n- and p-GaAs and p-InP. Effect of crystal face, electrolyte and current density. J Electrochem Soc 130(8):1772–1773. https://doi.org/10.1149/1.2120090
64. Summers DP, Leach S, Jr Frese (1986) The electrochemical reduction of aqueous carbon dioxide to methanol at molybdenum electrodes with low overpotentials. J Electroanal Chem Interfacial Electrochem 205(1–2):219–232
65. Hori Y, Suzuki S (1983) Electrolytic reduction of bicarbonate ion at a mercury electrode. J Electrochem Soc 130(12):2387–2390. https://doi.org/10.1149/1.2119593
66. Firmiano EGS, Cordeiro MAL, Rabelo AC, Dalmaschio CJ, Pinheiro AN, Pereira EC, Leite ER (2012) Graphene oxide as a highly selective substrate to synthesize a layered MoS2 hybrid electrocatalyst. Chem Commun 48(62):7687–7689. https://doi.org/10.1039/C2CC33397J
67. Hori Y, Kikuchi K, Murata A, Suzuki S (1986) production of methane and ethylene in electrochemical reduction of carbon dioxide at copper electrode in aqueous hydrogen carbonate solution. Chem Lett 15:897–898. https://doi.org/10.1246/cl.1986.897
68. Lim RJ, Xie M, SkJM Lee JM, Fisher A, Wang X, Lim KH (2014) A review on the electrochemical reduction of CO_2 in fuel cells, metal electrodes and molecular catalysts. Catal Today 233:169–180. https://doi.org/10.1016/j.cattod.2013.11.037

69. Frese KW Jr (1993) In: Sullivan BP, Krist K, Guard HE (eds) Electrochemical and electrocatalytic reactions of carbon dioxide. Elsevier, Amsterdam, London, New York, Tokyo, pp 145–216
70. Cokoja M, Bruckmeier C, Rieger B, Herrmann WA, Kühn FE (2011) Transformation of carbon dioxide with homogeneous transition metal catalysts: a molecular solution to a global challenge? (Angew. Chem. Int. Ed. 37/2011). Angew Chem Int Ed 50(37):8510–8537. https://doi.org/10.1002/anie.201104738
71. Ikeda S, Shiozaki S, Susuki J, Ito K, Noda H (1998) Electroreduction of CO_2 using Cu/Zn oxides loaded gas diffusion electrodes. In: Advances in chemical conversions for mitigating carbon dioxide, proceedings of the fourth international conference on carbon dioxide utilization, pp 225–230. https://doi.org/10.1016/s0167-2991(98)80748-9
72. Inglis J, MacLean BJ, Pryce MT, Vos JG (2012) Electrocatalytic pathways towards sustainable fuel production from water and CO_2. Coord Chem Rev 256(21–22):2571–2600. https://doi.org/10.1016/j.ccr.2012.05.002
73. Eggins BR, Bennett EM, McMullan EA (1996) Voltammetry of carbon dioxide. Part 2. Voltammetry in aqueous solutions on glassy carbon. J Electroanal Chem 408:165–171. https://doi.org/10.1016/0022-0728(96)04590-1
74. Schiffrin DJ (1973) Application of the photo-electrochemical effect to the study of the electrochemical properties of radicals: CO_2 and CH_3. Faraday Discuss Chem Soc 56:75–95. https://doi.org/10.1039/DC9735600075
75. Hori Y, Suzuki S (1982) Electrolytic reduction of carbon dioxide at mercury electrode in aqueous solution. Bull Chem Soc Jpn 55(3):660–665. https://doi.org/10.1246/bcsj.55.660
76. Christophe J, Doneux T, Buess-Herman C (2012) Electroreduction of carbon dioxide on copper-based electrodes: activity of copper single crystals and copper-gold alloys. Electrocatalysis 3(2):139–146. https://doi.org/10.1007/s12678-012-0095-0
77. Ishimaru S, Shiratsuchi R, Nogami G (2000) Pulsed electroreduction of CO_2 on Cu/Ag alloy electrodes. J Electrochem Soc 147(5):1864–1867. https://doi.org/10.1149/1.1393448
78. Kudo K, Komatsu K (1999) Selective formation of methane in reduction of CO_2 with water by Raney alloy catalyst. J Mol Catal A: Chem 145(1–2):257–264. https://doi.org/10.1016/S1381-1169(99)00014-X
79. Mahmood MN, Masheder D, Harty CJ (1987) Use of gas-diffusion electrodes for high-rate electrochemical reduction of carbon dioxide. I. Reduction at lead, indium- and tin-impregnated electrodes. J Appl Electrochem 17(6):1159–1170. https://doi.org/10.1007/BF01023599
80. Hara K, Sakata T (1997) Electrocatalytic formation of CH4 from CO_2 on a Pt gas diffusion electrode. J Electrochem Soc 144(2):539–545. https://doi.org/10.1149/1.1837445J
81. Hara K, Sakata T (1997) Large current density CO_2 reduction under high pressure using gas diffusion electrodes. Bull Chem Soc Jpn 70(3):571–576. https://doi.org/10.1246/bcsj.70.571
82. Machunda RL, Ju H, Lee J (2011) Electrocatalytic reduction of CO_2 gas at Sn based gas diffusion electrode. Curr Appl Phys 11(4):986–988. https://doi.org/10.1016/j.cap.2011.01.003
83. Machunda RL, Lee J, Lee J (2010) Microstructural surface changes of electrodeposited Pb on gas diffusion electrode during electroreduction of gas-phase CO_2. Surf Interface Anal 42(6–7):564–567. https://doi.org/10.1002/sia.3245
84. Tryk DA, Yamamoto T, Kokubun M, Hirota K, Hashimoto K, Okawa M, Fujishima A (2001) Recent developments in electrochemical and photoelectrochemical CO_2 reduction: involvement of the $(CO_2)^{2\cdot-}$ dimer radical anion. Appl Organomet Chem 15(2):113–120. https://doi.org/10.1002/1099-0739(200102)15:2%3c113::AID-AOC105%3e3.0.CO;2-1
85. Yamamoto T, Tryk DA, Hashimoto K, Fujishima A, Okawa M (2000) Electrochemical reduction of CO_2 in the micropores of activated carbon fibers. J Electrochem Soc 147(9):3393–3400. https://doi.org/10.1149/1.1393911
86. Ikeda S, Ito T, Azuma K, Ito K, Noda H (1995) Electrochemical mass reduction of carbondioxide using Cu-loaded gas-diffusion electrodes. 1. Preparation of electrode and reduction products. Denki Kagaku 63:303–309

87. Cook RL, MacDuff RC, Sammells AF (1988) On the electrochemical reduction of carbon dioxide at in situ electrodeposited copper. J Electrochem Soc 135(6):1320–1326. https://doi.org/10.1149/1.2095972
88. Furuya N, Yamazaki T, Shibata M (1997), High performance Ru Pd catalysts for CO_2 reduction at gas-diffusion electrodes. J Electroanal Chem 431(1):39–41. https://doi.org/10.1016/S0022-0728(97)00159-9
89. Ikeda S, Ito K, Noda H (2009) AIP Conf Proc 1136(1):108–113. https://doi.org/10.1063/v1136.frontmatter
90. Schwartz M, Cook RL, Kehoe VM, MacDuff RC, Patel J, Sammells AF (1993) Carbon dioxide reduction to alcohols using perovskite type electrocatalysts. J Electrochem Soc 140(3):614–618. https://doi.org/10.1149/1.2056131
91. Mignard D, Barik R C, Bharadwaj AS, Pritchard CL, Ragnoli M, Cecconi F, Miller H, Yellowlees LJ (2014) Revisiting strontium-doped lanthanum cuprate perovskite for the electrochemical reduction of CO_2. J CO_2 Utiliz 5:53–59. https://doi.org/10.1016/j.jcou.2013.12.006
92. Bowden FP, Rideal E (1928) The electrolytic behaviour of thin films. Part I. Hydrogeneral. Proc Roy Soc A120:59–79
93. Jaramillo TF, Jorgensen KP, Bonde J, Nielsen JH, Horch S, Chorkendorff I (2007) Identification of active edge sites for electrochemical H-2 evolution from MoS2 nanocatalysts. Science 317(5834):100–102. https://doi.org/10.1126/science.1141483
94. Norskov JK, Bligaard T, Logadottir A, Kitchin JR, Chen JG, Pandelov S, Norskov JK (2005) Trends in the exchange current for hydrogen evolution. J Electrochem Soc 152(3):J23–J26. https://doi.org/10.1149/1.1856988J
95. Huang X, Zeng ZY, Bao SY, Wang MF, Qi XY, Fan ZX, Zhang H (2013) Solution-phase epitaxial growth of noble metal nanostructures on dispersible single-layer molybdenum disulfide nanosheets. Nat Commun 4(4):1444. https://doi.org/10.1038/ncomms2472
96. Beer HBS (1968) African Pat. Act No. 1952, 59
97. Hine F, Tilak BV, Denton JM, Lisius JD (eds) (1989) Performances of electrodes for industrial electrochemical processes. Electrochemical Society, Pennington, NJ
98. Kita H (1966) Periodic variation of exchange current density of hydrogen electrode with atomic number and reaction mechanism. J Electrochem Soc 113:1095–1111
99. Walter MG, Warren EL, McKone JR, Boettcher SW, Mi, QX, Santori EA, Lewis NS (2010) Solar water splitting cells. Chem Rev 110(11):6446–6473. https://doi.org/10.1021/cr1002326
100. Hayfield PCS (1998) Development of the noble metal/oxide coated titanium electrode. Part II: The move from platinum/iridium to ruthemum oxide electrocatalysts. Platin Met Rev 42(2):46–55
101. Trasatti S (1994) In: Lipkowski J, Ross PN (eds) The electrochemistry of novel materials. VCH, New York
102. Boodts JCF, Trasatti S (1989) Hydrogen evolution on iridium oxide cathodes. J Appl Electrochem 19:255–262. https://doi.org/10.1007/BF01062309
103. Trasatti S (1991) Physical electrochemistry of ceramic oxides. Electrochim Acta 36:225–241. https://doi.org/10.1016/0013-4686(91)85244-2
104. Veggetti E, Kodintsev IM, Trasatti S (1992) Hydrogen evolution on oxide electrodes: Co_3O_4 in alkaline solution. J Electroanal Chem 339:255–268. https://doi.org/10.1016/0022-0728(92)80456-E
105. Krstajic N, Trasatti S (1995) Cathodic behavior of RuO_2 doped Ni/Co_3O_4 electrodes in alkaline solutions: surface characterization. J Electrochem Soc 142:2675–2681. https://doi.org/10.1149/1.2050073
106. Krstajic N, Trasatti S (1998) Cathodic behaviour of RuO_2-doped Ni/Co_3O_4 electrodes in alkaline solutions: hydrogen evolution. J Appl Electrochem 28:1291–1297. https://doi.org/10.1023/A:1003444110172
107. Chen L, Guay D, Lasia A (1996) Kinetics of the hydrogen evolution reaction on RuO_2 and IrO_2 oxide electrodes in H_2SO_4 solution: an AC impedance study. J Electrochem Soc 143:3576–3584. https://doi.org/10.1149/1.1837255

108. Kodintsev IM, Trasatti S (1994) Electrocatalysis of H_2 evolution on $RuO_2 + IrO_2$ mixed oxide electrodes. Electrochim Acta 39:1803–1808. https://doi.org/10.1016/0013-4686(94)85168-9
109. Geim AK, Novoselov KS (2007) The rise of graphene. Nat Mater 6(3):183–191. https://doi.org/10.1038/nmat1849
110. Wang TY, Liu L, Zhu ZW, Papakonstantinou P, Hu JB, Liu HY, Li MX (2013) Enhanced electrocatalytic activity for hydrogen evolution reaction from self-assembled monodispersed molybdenum sulfide nanoparticles on an Au electrode. Energy Environ Sci 6(2):625–633. https://doi.org/10.1039/C2EE23513G
111. Li YG, Wang HL, Xie LM, Liang YY, Hong GS, Dai HJ (2011) MoS2 nanoparticles grown on graphene: an advanced catalyst for the hydrogen evolution reaction. J Am Chem Soc 133(19):7296–7299. https://doi.org/10.1021/ja201269b
112. Tributsch H, Bennett JC (1977) Electrochemistry and photochemistry of MoS2 layer crystals. 1. J Electroanal Chem 81(1):97–111. https://doi.org/10.1016/S0022-0728(77)80363-X
113. Jaegermann W, Tributsch H (1988) Interfacial properties of semiconducting transition-metal chalcogenides. Prog Surf Sci 29(1–2):1–167. https://doi.org/10.1016/0079-6816(88)90015-9
114. Chang YH, Lin CT, Chen TY, Hsu C, Lee YH, Zhang WJ, Wei KH, Li LJ (2013) Highly efficient electrocatalytic hydrogen production by MoSx grown on graphene-protected 3D Ni foams. Adv Mater 25(5):756–760. https://doi.org/10.1002/adma.201202920
115. Hinnemann B, Moses PG, Bonde J, Jorgensen KP, Nielsen JH, Horch S, Chorkendorff I, Norskov JK (2005) Biornimetic hydrogen evolution: MoS2 nanoparticles as catalyst for hydrogen evolution. J Am Chem Soc 127(15):5308–5309. https://doi.org/10.1021/ja0504690
116. Karunadasa HI, Montalvo E, Sun YJ, Majda M, Long JR, Chang CJ (2012) A molecular MoS2 edge site mimic for catalytic hydrogen generation. Science 335(6069):698–702. https://doi.org/10.1126/science.1215868
117. Chhowalla M, Shin HS, Eda G, Li LJ, Loh KP, Zhang H (2013) The chemistry of two-dimensional layered transition metal dichalcogenide nanosheets. Nat Chem 5(4):263–275. https://doi.org/10.1038/nchem.1589
118. Bonde J, Moses PG, Jaramillo TF, Nørskov JK, Chorkendorff I (2009) Hydrogen evolution on nano-particulate transition metal sulfides. Faraday Discuss 140:219–231
119. Kibsgaard J, Chen ZB, Reinecke BN, Jaramillo TF (2012) Engineering the surface structure of MoS2 to preferentially expose active edge sites for electrocatalysis. Nat Mater 11(11):963–969. https://doi.org/10.1038/nmat3439
120. Lu Z, Zhang H, Zhu W, Yu X, Kuang Y, Chang Z, Lei X, Sun X (2013) In situ fabrication of porous MoS2 thin-films as high-performance catalysts for electrochemical hydrogen evolution. Chem Commun 49(68):7516–7518. https://doi.org/10.1039/C3CC44143A
121. Lukowski MA, Daniel AS, Meng F, Forticaux A, Li LS, Jin S (2013) Enhanced hydrogen evolution catalysis from chemically exfoliated metallic MoS2 nanosheets. J Am Chem Soc 135(28):10274–10277. https://doi.org/10.1021/ja404523s
122. Merki D, Vrubel H, Rovelli L, Fierro S, Hu X (2012) Fe, Co, and Ni ions promote the catalytic activity of amorphous molybdenum sulfide films for hydrogen evolution. Chem Sci 3(8):2515–2525. https://doi.org/10.1039/C2SC20539D
123. Yan Y, Ge X, Liu Z, Wang JY, Lee JM, Wang X (2013) Facile synthesis of low crystalline MoS2 nanosheet-coated CNTs for enhanced hydrogen evolution reaction. Nanoscale 5(17):7768–7771. https://doi.org/10.1039/C3NR02994H
124. Yu YF, Huang SY, Li YP, Steinmann SN, Yang WT, Cao LY (2014), Layer-dependent electrocatalysis of MoS2 for hydrogen evolution. Nano Lett 14(2):553–558. https://doi.org/10.1021/nl403620g
125. Popczun EJ, Read CG, Roske CW, Lewis NS, Schaak RE (2014) Highly active electrocatalysis of the hydrogen evolution reaction by cobalt phosphide nanoparticles. Angew Chem Int Ed 53:5427–5430. https://doi.org/10.1002/anie.201402646
126. Xu Y, Wu R, Zhang J, Shi Y, Zhang B (2013) Anion-exchange synthesis of nanoporous FeP nanosheets as electrocatalysts for hydrogen evolution reaction. Chem Commun 49:6656–6658. https://doi.org/10.1039/c3cc43107j

127. Hellstern TR, Benck JD, Kibsgaard J, Hahn C, Jaramillo TF (2016) Engineering cobalt phosphide (CoP) thin film catalysts for enhanced hydrogen evolution activity on silicon photocathodes. Adv Energy Mater 6:1501758. https://doi.org/10.1002/aenm.201501758
128. Callejas JF, McEnaney JM, Read CG, Crompton JC, Biacchi AJ, Popczun EJ, Gordon TR, Lewis NS, Schaak RE (2014) Electrocatalytic and photocatalytic hydrogen production from acidic and neutral-pH aqueous solutions using iron phosphide nanoparticles. ACS Nano 8:11101–11107. https://doi.org/10.1021/nn5048553
129. Jiang P, Liu Q, Liang Y, Tian J, Asiri AM, Sun X (2014) A cost-effective 3D hydrogen evolution cathode with high catalytic activity: FeP nanowire array as the active phase. Angew Chem Int Ed 53:12855–12859. https://doi.org/10.1002/anie.201406848
130. Kibsgaard J, Jaramillo TF (2014) Molybdenum phosphosulfide: an active, acid-stable, earth-abundant catalyst for the hydrogen evolution reaction. Angew Chem Int Ed 53:14433–14437. https://doi.org/10.1002/anie.201408222
131. Laursen AB, Patraju KR, Whitaker MJ, Retuerto M, Sarkar T, Yao N, Ramanujachary KV, Greenblatt M, Dismukes GC (2015) Nanocrystalline Ni5P4: a hydrogen evolution electrocatalyst of exceptional efficiency in both alkaline and acidic media. Energy Environ Sci 8:1027–1034. https://doi.org/10.1039/C4EE02940B
132. Popczun EJ, McKone JR, Read CG, Biacchi AJ, Wiltrout AM, Lewis NS, Schaak RE (2013) Nanostructured nickel phosphide as an electrocatalyst for the hydrogen evolution reaction. J Am Chem Soc 135:9267–9270. https://doi.org/10.1021/ja403440e Epub 2013 Jun 13
133. Tian J, Liu Q, Asiri AM, Sun X (2014) Self-supported nanoporous cobalt phosphide nanowire arrays: an efficient 3D hydrogen-evolving cathode over the wide range of pH 0–14. J Am Chem Soc 136:7587–7590. https://doi.org/10.1021/ja503372r
134. Liang Y, Liu Q, Asiri AM, Sun X, Luo Y (2014) Self-supported FeP nanorod arrays: a cost-effective 3D hydrogen evolution cathode with high catalytic activity. ACS Catal 4:4065–4069. https://doi.org/10.1021/cs501106g
135. Pu Z, Liu Q, Asiri AM, Sun X (2014) Tungsten phosphide nanorod arrays directly grown on carbon cloth: a highly efficient and stable hydrogen evolution cathode at all pH values, ACS Appl Mater Interfaces 6:21874–21879. https://doi.org/10.1021/am5060178
136. Tian J, Liu Q, Cheng N, Asiri AM, Sun X (2014) Self-supported Cu3P nanowire arrays as an integrated high-performance three-dimensional cathode for generating hydrogen from water. Angew Chem Int Ed 53:9577–9581. https://doi.org/10.1002/anie.201403842
137. Gasteiger HA, Kocha SS, Sompalli B, Wagner FT (2005) Activity benchmarks and requirements for Pt, Pt-alloy, and non-Pt oxygen reduction catalysts for PEMFCs. Appl Catal B 56:9–35. https://doi.org/10.1016/j.apcatb.2004.06.021
138. Gewirth AA, Thorum MS (2010) Electroreduction of dioxygen for fuel-cell applications: materials and challenges. Inorg Chem 49:3557–3566
139. Vielstich W, Lamm A, Gasteiger HA, Yokokawa H (2003) Handbook of fuel cells: fundamentals, technology and applications. Wiley, Chichester, England
140. Wagner FT, Lakshmanan B, Mathias MF (2010) Electrochemistry and the future of the automobile. J Phys Chem Lett 1:2204–2219. https://doi.org/10.1021/jz100553m
141. Costamagna P, Srinivasan S (2001) Quantum jumps in the PEMFC science and technology from the 1960s to the year 2000: Part II. Engineering, technology development and application aspects. J Power Sources 102:253–269. https://doi.org/10.1016/S0378-7753(01)00808-4
142. Brandon NP, Skinner S, Steele BCH (1993) Recent advances in materials for fuel cells. Annu Rev Mater Res 33(2003):183–213. https://doi.org/10.1146/annurev.matsci.33.022802.094122
143. Sealy C (2008) The problem with platinum. Mater Today 11:65–68. https://doi.org/10.1016/S1369-7021(08)70254-2
144. Steel BCH, Heinzel A (2001) Materials for fuel-cell technologies. Nature 414:345–352. https://doi.org/10.1038/35104620
145. Adzic R (1998) In: Lipkowski J, Ross PN (eds) Frontiers in electrocatalysis, vol 197. Wiley, New York

146. Appleby AJ (1993) Electrocatalysis of aqueous dioxygen reduction. J Electroanal Chem 357:117–179. https://doi.org/10.1016/0022-0728(93)80378-U
147. Bezerra CWB, Zhang L, Liu H, Lee K, Marques ALB, Marques EP, Wang H, Zhang J (2007) A review of heat-treatment effects on activity and stability of PEM fuel cell catalysts for oxygen reduction reaction. J Power Sources 173:891–908
148. Bezerra CWB, Zhang L, Lee K, Liu H, Marques ALB, Marques EP, Wang H, Zhang J (2008) A review of Fe–N/C and Co–N/C catalysts for the oxygen reduction reaction. Electrochim Acta 53:4937–4951. https://doi.org/10.1016/j.electacta.2008.02.012
149. Kiros Y (2007) Metal porphyrins for oxygen reduction in PEMFC. Int J Electrochem Sci 2:285–300
150. Lee JW, Popov B (2007) Ruthenium-based electrocatalysts for oxygen reduction—a review. J Solid State Electrochem 11:1355–1364. https://doi.org/10.1007/s10008-007-0307-3
151. Markovic NM, Ross PN (2000) New electrocatalysts for fuels cells from model surfaces to commercial catalysts. CATTECH 4:110–126. https://doi.org/10.1023/A:1011963731898
152. Spendelow JS, Wieckowski A (2007) Electrolysis of oxygen reduction and small alcohol oxidation in alkaline media. Phys Chem Chem Phys 9:2654–2675. https://doi.org/10.1039/B703315J
153. Yu X, Ye S (2007) Recent advances in activity and durability enhancement of Pt/C catalytic cathode in PEMFC: Part I. Physico-chemical and electronic interaction between Pt and carbon support, and activity enhancement of Pt/C catalyst. J. Power Sources 172:133–144. https://doi.org/10.1016/j.jpowsour.2007.07.049
154. Alonso-Vante N (2006) Carbonyl tailored electrocatalysts. Fuel Cells 6:182–189. https://doi.org/10.1002/fuce.200500245
155. Alonso Vante N, Tributsch H (1986) Energy conversion catalysis using semiconducting transition metal cluster compounds. Nature 323:431–432. https://doi.org/10.1038/323431a0
156. Gasteiger HA, Markovic NM (2009) Iron-based catalysts with improved oxygen reduction activity in polymer electrolyte fuel cells. Science 324:48–49. https://doi.org/10.1126/science.1172083
157. Appleby AJ (1979) In: Dudley R, O'Grady W, Srinivasan S (eds) The electrocatalysis of fuel cells reactions. The Electrochemical Society Softbound Proceedings Series PV 97-2, Princeton, NJ, p 23
158. Yu X, Ye S (2007) Recent advances in activity and durability enhancement of Pt/C catalytic cathode in PEMFC: Part II: Degradation mechanism and durability enhancement of carbon supported platinum catalyst. J Power Sources 172:145–154. https://doi.org/10.1016/j.jpowsour.2007.07.048
159. Ercelik M, Ozden A, Seker E, Colpan CO (2017) Characterization and performance evaluation of PtRu/CTiO_2 anode electrocatalyst for DMFC applications. Int J Hydrogen Energy 42:21518–21529. https://doi.org/10.1016/j.ijhydene.2016.12.020
160. Savadogo O, Beck P (1996) Five percent platinum-tungsten oxide-based electrocatalysts for phosphoric acid fuel cell cathodes. J Electrochem Soc 143:3842–3846. https://doi.org/10.1149/1.1837306
161. Tian XL, Wang L, Deng P, Chen Y, Xia BY (2017) Research advances in unsupported Pt-based catalysts for electrochemical methanol oxidation. J Energy Chem 26:1067–1076
162. Wang P, Shao Q, Huang X (2018) Updating Pt-based electrocatalysts for practical fuel cells. Joule 2:2514–2516. https://doi.org/10.1016/j.joule.2018.11.024
163. Thompsett D (2003) In: Vielstich W, Gasteiger HA (eds) Handbook of fuel cells-fundamentals, technology and applications, vol III. Wiley, New York, pp 467–480
164. Mukerjee S, Srinivasan S (1993) Enhanced electrocatalysis of oxygen reduction on platinum alloys in proton exchange membrane fuel cells. J Electroanal Chem 357(1–2):201–224. https://doi.org/10.1016/0022-0728(93)80380-z
165. Hwang BJ, Kumar SMS, Chen CH, Monalisa Cheng MY, Liu DG, Lee JF (2007) An Investigation of structure–catalytic activity relationship for Pt–Co/C bimetallic nanoparticles toward the oxygen reduction reaction. J Phys Chem C 111:15267–15276. https://doi.org/10.1021/jp072681r

166. Li W, Zhou W, Li H, Zhou Z, Zhou B, Sun G, Xin Q (2004) Nano-stuctured Pt–Fe/C as cathode catalyst in direct methanol fuel cell. Electrochim Acta 49:1045–1055. https://doi.org/10.1016/j.electacta.2003.10.015
167. Li H, Sun G, Li N, Sun S, Su D, Xin Q (2007) Design and preparation of highly active Pt–Pd/C catalyst for the oxygen reduction reaction. J Phys Chem C 111(15):5605–5617. https://doi.org/10.1021/jp067755y
168. Liu G, Zhang H, Zhai Y, Zhang Y, Xu D, Shao Z-g (2007) Pt4ZrO_2/C cathode catalyst for improved durability in high temperature PEMFC based on H_3PO_4 doped PBI. Electrochem Commun 9(1):135–141
169. Salgado JRC, Antolini E, Gonzalez ER (2004) Structure and activity of carbon-supported Pt–Co electrocatalysts for oxygen reduction. J Phys Chem B 108:17767–17774. https://doi.org/10.1021/jp0486649
170. Tamizhmani G, Capuano GA (1994) Improved electrocatalytic oxygen reduction performance of platinum ternary alloy-oxide in solid-polymer-electrolyte fuel cells. J Electrochem Soc 141:968–975. https://doi.org/10.1149/1.2054866J
171. Travitsky N, Ripenbein T, Golodnitsky D, Rosenberg Y, Burshtein L, Peled E (2006) Pt-, PtNi- and PtCo-supported catalysts for oxygen reduction in PEM fuel cells. J Power Sources 161:782–789. https://doi.org/10.1016/j.jpowsour.2006.05.035
172. Wilson MS, Garzon FH, Sickafus KE, Gottesfeld S (1993) Surface area loss of supported platinum in polymer electrolyte fuel cells. J Electrochem Soc 140:2872–2877. https://doi.org/10.1149/1.2220925
173. Zignani SC, Antolini E, Gonzalez ER (2008) Evaluation of the stability and durability of Pt and Pt-Co/C catalysts for polymer electrolyte membrane fuel cells. J Power Sources 182:83–90. https://doi.org/10.1016/j.jpowsour.2008.03.061
174. Zignani SC, Antolini E, Gonzalez ER (2009) Stability of Pt-Ni/C (1:1) and Pt/C electrocatalysts as cathode materials for polymer electrolyte fuel cells: effect of ageing tests. J Power Sources 191:344–350
175. Meyers J, Darling R (2002) In: 202nd meeting of the Electrochemical Society, Salt Lake City
176. Paulus UA, Wokaun A, Scherer GG, Schmidt TJ, Stamenkovic V, Radmilovic V, Markovic NM, Ross PN (2002) Oxygen reduction on carbon-supported Pt–Ni and Pt–Co alloy catalysts. J Phys Chem B 106:4181–4191. https://doi.org/10.1021/jp013442l
177. Schmidt TJ, Paulus UA, Gasteiger HA, Alonso-Vante N, Behm RJ (2000) Oxygen reduction on $Ru_{1.92}Mo_{0.08}SeO_4$, Ru/carbon, and Pt/carbon in pure and methanol-containing electrolytes. J Electrochem Soc 147:2620–2624. https://doi.org/10.1149/1.1393579
178. Colón-Mercado HR, Kim H, Popov BN (2004) Durability study of Pt3Ni1 catalysts as cathode in PEM fuel cells. Electrochem Commun 6:795–799. https://doi.org/10.1016/j.elecom.2004.05.028
179. Neyerlin KC, Srivastava R, Yu C, Strasser P (2009) Electrochemical activity and stability of dealloyed Pt–Cu and Pt–Cu–Co electrocatalysts for the oxygen reduction reaction (ORR). J Power Sources 186:261–267. https://doi.org/10.1016/j.jpowsour.2008.10.062
180. Prostailo L, Haug A (2005) In: 208th meeting of the Electrochemical Society, Los Angeles
181. Yu P, Pemberton M, Plasse P (2005) PtCo/C cathode catalyst for improved durability in PEMFCs. J Power Sources 144:11–20. https://doi.org/10.1016/j.jpowsour.2004.11.067
182. García G, Silva-Chong JA, Guillén-Villafuerte O, Rodríguez JL, González ER, Pastor E (2006) CO tolerant catalysts for PEM fuel cells: spectroelectrochemical studies. Catal Today 116:415–421. https://doi.org/10.1016/j.cattod.2006.05.069
183. Jasinski R (1964) New fuel cell cathode catalyst. Nature 201:1212–1213. https://doi.org/10.1038/20112
184. Oh H-S, Kim H (2012) The role of transition metals in non-precious nitrogen-modified carbon-based electrocatalysts for oxygen reduction reaction. J Power Sources 212:220–225. https://doi.org/10.1016/j.jpowsour.2012.03.098
185. Shen Y, Bi L, Liu B, Dong S, (2003) Simple preparation method of Pd nanoparticles on an Au electrode and its catalysis for dioxygen reduction. Electronic supplementary information (ESI) available: XRD pattern of an evaporated Au electrode and CVs for the reduction of O2

on a bare Au(111) electrode or a Pd-nanoparticle-film-modified electrode. See: http://www.rsc.org/suppdata/nj/b3/b300566f/. New J Chem 27 (6):938
186. Lin Y, Cui X, Ye X (2005) Electrocatalytic reactivity for oxygen reduction of palladium-modified carbon nanotubes synthesized in supercritical fluid. Electrochem Commun 7:267–274. https://doi.org/10.1016/j.elecom.2005.01.007
187. Xiao L, Zhuang L, Liu Y, Lu J, HcD Abruna (2008) Activating Pd by morphology tailoring for oxygen reduction. J Am Chem Soc 131:602–608. https://doi.org/10.1021/ja8063765
188. Demarconnay L, Coutanceau C, Léger JM (2004) Electroreduction of dioxygen (ORR) in alkaline medium on Ag/C and Pt/C nanostructured catalysts-effect of the presence of methanol. Electrochim Acta 49:4513–4521. https://doi.org/10.1016/j.electacta.2004.05.009
189. Ohno S, Yagyuu K, Nakatsuji K, Komori F (2004) Dissociation preference of oxygen molecules on an inhomogeneously strained Cu(001) surface. Surf Sci 554 (2–3):183–192
190. Lescop B, Jay JP, Fanjoux G (2004) Reduction of oxygen pre-treated Ni(111) by H_2 exposure: UPS and MIES studies compared with monte carlo simulations. Surf Sci 548:83–94. https://doi.org/10.1016/j.susc.2003.09.051
191. Mentus SV (2004) Oxygen reduction on anodically formed titanium dioxide. Electrochim Acta 50(1):27–32
192. Kim JY, Oh TK, Shin Y, Bonnett J, Weil KS (2010) A novel non-platinum group electrocatalyst for PEM fuel cell application. Int J Hydrogen Energy (in press). https://doi.org/10.1016/j.ijhydene.2010.05.016
193. Jaouen F, Dodelet JP (2007) Average turn-over frequency of O_2 electro-reduction for Fe/N/C and Co/N/C catalysts in PEFCs. Electrochim Acta 52:5975–5984. https://doi.org/10.1016/j.electacta.2007.03.045
194. Lee K, Ishihara A, Mitsushima S, Kamiya N, Ki Ota (2004) Stability and electrocatalytic activity for oxygen reduction in WC + Ta catalyst. Electrochim Acta 49:3479–3485. https://doi.org/10.1016/j.electacta.2004.03.018
195. Biddinger E, von Deak D, Ozkan U (2009) Nitrogen-containing carbon nanostructures as oxygen-reduction catalysts. Top Catal 52:1566–1574
196. Johnston CM, Cao D, Choi JH, Babu PK, Garzon F, Zelenay P (2011) Se-modified Ru nanoparticles as ORR catalysts—Part 1: synthesis and analysis by RRDE and in PEFCs. J Electroanal Chem 662:257–266. https://doi.org/10.1016/j.jelechem.2011.07.015
197. Maheswari S, Sridhar P, Pitchumani S (2012) Pd-RuSe/C as ORR specific catalyst in alkaline solution containing methanol. Fuel Cells 12:963–970. https://doi.org/10.1002/fuce.201200069
198. Zaikovskii VI, Nagabhushana KS, Kriventsov VV, Loponov KN, Cherepanova SV, Kvon RI, Bönnemann H, Kochubey DI, Savinova ER (2006) Synthesis and structural characterization of Se-modified carbon-supported ru nanoparticles for the oxygen reduction reaction. J Phys Chem B 110(13):6881–6890. https://doi.org/10.1021/jp056715b
199. Cui HF, Ye JS, Zhang WD, Wang J, Sheu FS (2005) Electrocatalytic reduction of oxygen by a platinum nanoparticles/carbon nanotube composite electrode. J Electroanal Chem 577:295–302. https://doi.org/10.1016/j.jelechem.2004.12.004
200. Kongkanand A, Kuwabata S, Girishkumar G, Kamat P (2006) Single-wall carbon nanotubes supported platinum nanoparticles with improved electrocatalytic activity for oxygen reduction. Langmuir 22:2392–2396. https://doi.org/10.1021/la052753a
201. Xing Y (2004) Synthesis electrochemical characterization of uniformly-dispersed high loading Pt nanoparticles on sonochemically-treated carbon nanotubes. J Phys Chem B 108:19255–19259. https://doi.org/10.1021/jp046697i
202. Vijayaraghavan G, Stevenson KJ (2007) Synergistic assembly of dendrimer-templated platinum catalysts on nitrogen-doped carbon nanotube electrodes for oxygen reduction. Langmuir 23:5279–5282. https://doi.org/10.1021/la0637263
203. Maldonado S, Stevenson KJ (2005) Influence of nitrogen doping on oxygen reduction electrocatalysis at carbon nanofiber electrodes. J Phys Chem B 109(10):4707–4716
204. Fang B, Kim JH, Kim M, Yu JS (2009) Ordered hierarchical nanostructured carbon as a highly efficient cathode catalyst support in proton exchange membrane fuel cell. Chem Mater 21:789–796. https://doi.org/10.1021/cm801467y

205. Lefèvre M, Dodelet JP (2008) Fe-based electrocatalysts made with microporous pristine carbon black supports for the reduction of oxygen in PEM fuel cells. Electrochim Acta 53:8269–8276. https://doi.org/10.1016/j.electacta.2008.06.050
206. Acharya CK, Li W, Liu Z, Kwon G, Heath Turner C, Lane AM, Nikles D, Klein T, Weaver M (2009) Effect of boron doping in the carbon support on platinum nanoparticles and carbon corrosion. J Power Sources 192:324–329. https://doi.org/10.1016/j.jpowsour.2009.03.020
207. Sebastián D, Calderón JC, González-Expósito JA, Pastor E, Martínez-Huerta MV, Suelves I, Moliner R, Lázaro MJ (2010) Int J Hydrogen Energy 35:9934–9942
208. Rao V, Simonov PA, Savinova ER, Plaksin GV, Cherepanova SV, Kryukova GN, Stimming U (2005) The influence of carbon support porosity on the activity of PtRu/Sibunit anode catalysts for methanol oxidation. J Power Sources 145(2):178–187
209. Lebedeva NP, Booij AS, Voropaev IN, Simonov PA, Romanenko AV (2009) Sibunit carbon-based cathodes for proton-exchange-membrane fuel cells. Fuel Cells 9:439–452. https://doi.org/10.1002/fuce.200800180
210. Kaiser J, Simonov PA, Zaikovskii VI, Hartnig C, Jörissen L, Savinova ER (2007) Influence of carbon support on the performance of platinum based oxygen reduction catalysts in a polymer electrolyte fuel cell. J Appl Electrochem 37(12):1429–1437
211. Cherstiouk V, Simonov AN, Moseva NS, Cherepanova SV, Simonov PA, Zaikovskii VI, Savinova ER (2010) Microstructure effects on the electrochemical corrosion of carbon materials and carbon-supported Pt catalysts. Electrochim Acta 28:8453–8460. https://doi.org/10.1016/j.electroca.2010.07.047
212. Biddinger EJ, Ozkan US (2010) Role of graphitic edge plane exposure in carbon nanostructures for oxygen reduction reaction. J Phys Chem C 114:15306–15314
213. Gong K, Du F, Xia Z, Durstock M, Dai L (2009) Nitrogen-doped carbon nanotube arrays with high electrocatalytic activity for oxygen reduction. Science 323:760–764
214. Maldonado S, Stevenson KJ (2004) Direct preparation of carbon nanofiber electrodes via pyrolysis of iron(II) phthalocyanine: electrocatalytic aspects for oxygen reduction. J Phys Chem B 108:11375–11383
215. Matter PH, Wang E, Arias M, Biddinger EJ, Ozkan US (2007) Oxygen reduction reaction activity and surface properties of nanostructured nitrogen-containing carbon. J Mol Catal A: Chem 264:73–81
216. Yu D, Nagelli E, Du F, Dai L (2010) Metal-free carbon nanomaterials become more active than metal catalysts and last longer. J Phys Chem Lett 1:2165–2173
217. Birry L, Zagal JH, Dodelet JP (2010) Does CO poison Fe-based catalysts for ORR? Electrochem Commun 12:628–631
218. Byers HG (1908) The passive state of metals. A review of the literature and theories and some experiments on cobalt, iron and nickel. J Am Chem Soc 30:1718–1742. https://doi.org/10.1021/ja01953a010
219. Byers HG, Thing CW (1919) Passivity of cobalt. J Am Chem Soc 41:1902–1908. https://doi.org/10.1021/ja02233a006
220. Hickling A, Hill S (1947) Oxygen overvoltage. Part I. The influence of electrode material, current density, and time in aqueous solution. Discuss Faraday Soc 1: 236. https://doi.org/10.1039/df9470100236
221. Suzuki O, Takahashi M, Fukunaga T, Kuboyama J (1968) US Pat. No. 3,399,966
222. Jaouen F, Proietti E, Lefèvre M, Chenitz R, Dodelet JP, Wu G, Chung HT, Johnston CM, Zelenay P (2011) Recent advances in non-precious metal catalysis for oxygen-reduction reaction in polymer electrolyte fuel cells. Energy Environ Sci 4:114–130
223. Collman JP, Denisevich P, Konai Y, Marrocco M, Koval C, Anson FC (1980) Electrode catalysis of the four-electron reduction of oxygen to water by dicobalt face-to-face porphyrins. J Am Chem Soc 102:6027–6036
224. Collman JP, Bencosme CS, Durand RR, Kreh RP, Anson FC (1983) Mixed-metal face-to-face porphyrin dimers. J Am Chem Soc 105:2699–2703
225. Durand RR, Bencosme CS, Collman JP, Anson FC (1983) Mechanistic aspects of the catalytic reduction of dioxygen by cofacial metalloporphyrins. J Am Chem Soc 105:2710–2718

226. Badger G, Jones R, Laslett R (1964) Porphyrins. VII. The synthesis of porphyrins by the Rothemund reaction. Aust J Chem 17:1028–1035
227. Chen Z, Cummins D, Reinecke BN, Clark E, Sunkara MK, Jaramillo TF (2011) Core-shell MoO_3-MoS_2 nanowires for hydrogen evolution: a functional design for electrocatalytic materials. Nano Lett 11(10):4168–4175. https://doi.org/10.1021/nl2020476
228. Chen Z, Higgins D, Yu A, Zhang L, Zhang J (2011) A review on non-precious metal electrocatalysts for PEM fuel cells. Energy Environ Sci 4:3167–3192
229. Alt H, Binder H, Sandstede G (1973) Mechanism of the electrocatalytic reduction of oxygen on metal chelates. J Catal 28:8–19
230. Bagotzky VS, Tarasevich MR, Radyushkina KA, Levina OA, Andrusyova SI (1977) Electrocatalysis of the oxygen reduction process on metal chelates in acid electrolyte. J Power Sources 2:233–240
231. Jahnke H, Schönborn M, Zimmermann G (1976) Organic dyestuffs as catalysts for fuel cells. In: Schäfer F, Gerischer H, Willig F, Meier H, Jahnke H, Schönborn M, Zimmermann G (eds) Physical and chemical applications of dyestuffs, vol 61. Springer, Berlin/Heidelberg, pp 133–181

Characterization of Electrocatalyst

Jayashree Swaminathan and Ashokkumar Meiyazhagan

Abstract In the process of developing a catalyst, understanding their structure and properties is considered essential as it is obligatory to improve their performance or to resolve a failure issue. Hence, the purpose of this invited chapter is to give a brief summary of various characterization tools specifically, X-ray Diffraction (XRD), Brunauer, Emmett, and Teller (BET) technique, Infrared Spectroscopy (IR), UV-visible spectroscopy, Electron microscopy, and Electrochemical techniques, where we discussed the principle, application, and challenges associated with the catalyst characterization. Also, in this chapter, we illustrated the analysis and interpretation of characterization data with an example for better understanding. These perceptive investigations of different characterization tools lead to the establishment of empirical relationships between various factors that govern catalytic activity.

Keywords XRD · Electrochemical characterization technique · UV-visible spectra · Catalyst · Cyclic voltammetry

1 Introduction

The fundamental understanding of an ideal catalyst is necessary for the design and development of new catalysts with prominent activity and selectivity. It also helps in understanding their fundamental nature, exploring its catalytic mechanism, which in turn aids to identify the catalytic activity descriptors. An in-depth and rigorous characterization of catalyst and careful analysis is indispensable since, the performance of the catalyst is related to their electronic state, atomic structure, chemical structure, composition, and surface topography [1, 3, 23, 53]. However, no one technique can offer all the information about a catalyst at a time. Hence, various characterization

J. Swaminathan (✉) · A. Meiyazhagan
Department of Materials Science & NanoEngineering, Rice University, Houston, TX 77005, USA
e-mail: jayashreesavithiri@gmail.com

A. Meiyazhagan
e-mail: ma37@rice.edu

Inamuddin et al. (eds.), *Methods for Electrocatalysis*,
https://doi.org/10.1007/978-3-030-27161-9_17

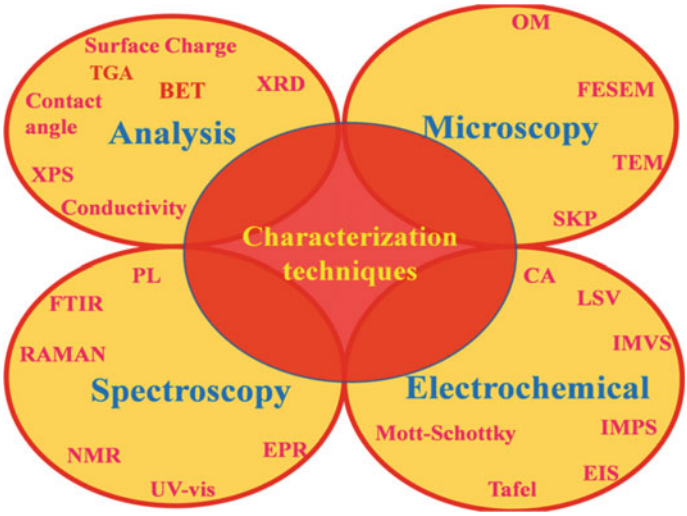

Fig. 1 Various characterization techniques available for analysis of catalysts

tools (as shown in Fig. 1) and comprehensive examination is mandatory for a complete understanding of the catalyst. The characterization tools allow either energetic photons, X-ray electrons, or ions to interact with material [30] and produce a wealth of information based on emitted, transmitted, or diffracted signals (as described in Fig. 2).

Techniques like XRD, Electron diffraction are widely used to identify the crystal structure of a catalyst. For understanding their chemical state (such as chemical bonding, composition, distribution, and degree), spectroscopies like XPS, XANES, ICP, AAS provide quantitative information and EPR contributes to a lesser extent. The functional group in the catalyst is predominantly probed by spectroscopies like IR, Raman, and NMR. A better understanding of internal porosity, the surface area can be obtained using BET. UV-vis spectroscopy is used to understand the optical behavior of catalyst. Spectroscopies like SEM, TEM, etc. can be used to recognize the size, shape, and microstructure of catalyst. Electrochemical techniques like linear sweep voltammetry, cyclic voltammetry, electrochemical impedance, chronoamperometry, chronopotentiometry can also be very informative in an insightful understanding of the electrocatalytic behavior of catalyst. The work function, catalytic active spots can be studied by SPM like SKP, SECM. These characterization tools are limitlessly extended like EELS, SIMS-ISS, Mossbauer spectroscopy. However, we limit our discussion to valuable characterization tools for conciseness. Since a fundamental understanding of a catalyst is essential, this chapter explains only the working principle of the characterization technique, and mostly focuses on the application, analysis, and interpretation of the data.

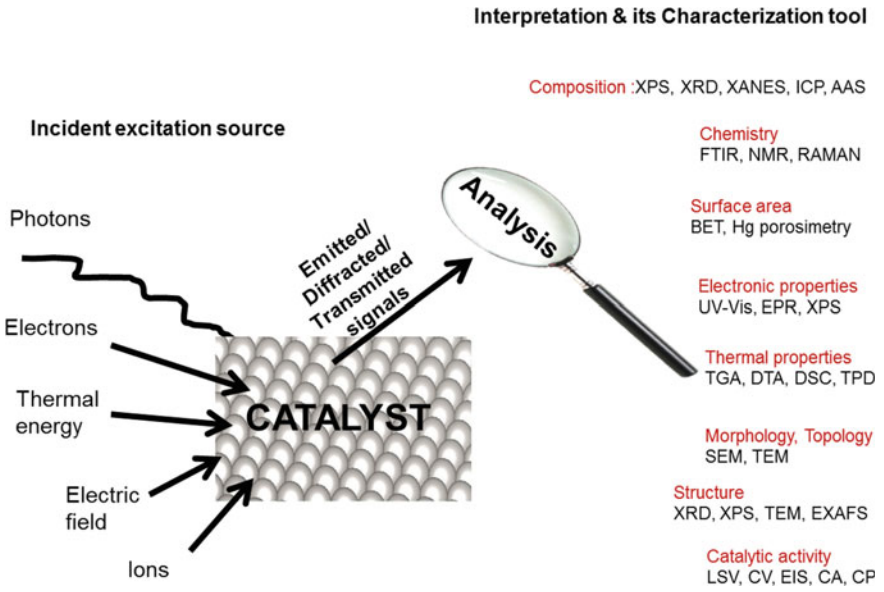

Fig. 2 Scheme representing the overall principle of different characterization techniques

2 X-Ray Diffraction (XRD)

XRD technique uses an X-ray beam to diffract atoms of the catalyst and discloses detailed information about its crystallographic structure based on Bragg's law of diffraction:

$$n\lambda = 2d \sin \theta$$

where n is order of reflection (any whole number), θ is the Bragg's angle (half-value of the diffraction angle from the catalyst), and λ is X-rays wavelength (usually Cu $K_\alpha = 1.54$ Å), and d is the lattice/interplanar spacing. Thus, diffraction peaks width carries information on dimensions of a catalyst particle. If the XRD peak width is very sharp, then the catalyst possesses micron-sized crystals; Nano-sized catalyst retains a broader XRD peak due to a large number of surface atoms diffracting X-rays. Debye-Scherrer equation is used to analyze the average crystallite size (D) of the spherical particle:

$$D = \frac{K\lambda}{\beta_{hkl}\cos\theta}$$

where K = shape factor (0.87–1.00) and β_{hkl} = full width at half maximum intensity.

Also, dislocation density in the catalyst is calculated with the expression [37]:

$$\delta = \frac{1}{D^2}$$

where δ, D is the dislocation density and crystallite size of the catalyst.

Besides, we can also estimate the lattice strain (ε) in the catalyst by analyzing the XRD peak shift and broadening using the Williamson-Hall (W-H) equation [48]:

$$\beta_{hkl} \cos \theta_{hkl} = \frac{K\lambda}{D} + 4\text{si}\varepsilon\text{n}\theta_{hkl}$$

However, for each diffraction peak, the instrumental broadening $(\beta_{hkl})_{Instrumental}$ is corrected using the relation:

$$\beta_{hkl} = \sqrt{(\beta_{hkl})^2_{Measured} - (\beta_{hkl})^2_{Instrumental}}$$

On plotting β cos θ/λ against sin θ/λ and linear fitting, the intercept and slope give the value of D and ε, respectively. Choudhury and Choudhury [9] has calculated the developed lattice strain in TiO_2 on annealing at different temperature (200, 450, 700, 950 °C) using the W-H method (Fig. 3). From the magnitude of lattice strain (Table 1), it is well understood that Ti200 possess the highest lattice strain while

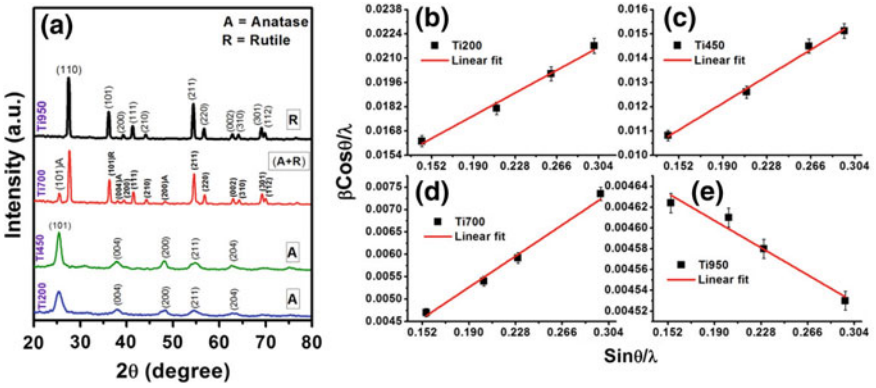

Fig. 3 XRD pattern and the corresponding W-H plot of TiO_2 at a different annealing temperature. Reproduced from Choudhury B; Copyright © 2013, Springer

Table 1 Magnitude of lattice strain obtained from W-H plot

Sample	Annealing temperature (°C)	Lattice strain
Ti200	200	0.0345
Ti450	450	0.0290
Ti700	700	0.0183
Ti950	900	−0.0006

Reproduced from Choudhury et al., Copyright © 2013, Springer

lowest strain is observed in Ti950. The high lattice strain in Ti200 could be due to enormous defects and atoms on the amorphous grain boundary, which leads stress and enforce a strain in the lattice. This effect is decreased, and phase transformation has been observed from anatase to rutile on annealing. Besides, positive (negative) strain indicates the crystal lattice is under tensile (compressive) forces. These strain-induced lattice distortions influence the catalytic behavior due to localization of carriers [2].

The developed intrinsic stress (σ) is calculated using the relation [20]:

$$\sigma = \frac{Y(a - a_0)}{2a_0\gamma}$$

Here, a, a_0 are the lattice constant obtained from XRD data and standard pattern, respectively. Whereas, Y and γ are Young's modulus and Poisson's ratio of catalyst, respectively.

Besides, a material with highly preferred orientation is called textured material and possesses high surface energy due to their high index planes (planes with a huge density of steps, kinks, and terraces). This textured material favors catalytic activity, and the extent of preferred crystallographic orientation of different crystalline planes is determined by calculating the intensity of the XRD spectrum using the following formula (Harris analysis [46]):

$$T_C(h_ik_il_i) = \frac{I(h_ik_il_i)}{I_0(h_ik_il_i)} \left\{ \frac{1}{N} \sum_{i=1}^{N} \frac{I(h_ik_il_i)}{I_0(h_ik_il_i)} \right\}^{-1}$$

For a given peak, $I(h_ik_il_i)$ is the integrated intensity ratios of diffraction peak $(h_ik_il_i)$ of a catalyst and $I_0(h_ik_il_i)$ is the integrated intensity available on a powder diffraction file (PDF) card; N is the number of diffraction peaks reflected in the XRD data and $T_C(h_ik_il_i)$ is the texture coefficient of the plane indexed by Miller indices $(h_ik_il_i)$.

Thus, XRD plays an active role in estimating the crystallite size, strain induced lattice distortion, and texture of the catalyst. Even though XRD gives quick and reliable information, this technique is suitable for catalyst with crystallinity. Amorphous phases (crystallites smaller than 50 Å) give either broad and weak diffraction lines or no diffraction.

3 Physical Surface Area Determination

Pore architecture of the catalyst controls the transport phenomenon and governs the accessibility of catalyst active sites. The presence of pores provides channels for facile migration of ions and by-product. Pores are classified into micropores, mesopores, and macropores depending on their size as:

1. Macropore (>50 nm)
2. Mesopore (2–50 nm)
3. Micropore (<2 nm).

Usually, Bulk diffusion occurs on a macroporous surface while Knudsen and molecular diffusion occur in the mesoporous and microporous surfaces, respectively. Besides, the presence of several pores determines the internal surface area (SA) of the catalyst. As SA symbolizes surface free energy, adsorption capacity and hence catalytic activity is enhanced if the material has a higher surface area (i.e., a large number of small pores). Conversely, if the pore size is too small, diffusional resistance persists and reaction by-products block the pores and hinder the activity. Thus, the quantitative determination of pore size, pore volume, and pore size distribution are essential in determining the activity of the catalyst.

The pore size is usually determined by understanding the physical adsorption of inert probing of gas molecules (N_2, O_2, CO_2, Ar, Krypton, He, Methane) on the solid catalyst surface. Typically, liquid N_2 (77 K) is exposed to the solid catalyst in a vacuum chamber, and the consequent adsorption (N_2 adsorbed) and desorption (N_2 removed) isotherms is evaluated over a broad range of relative pressures in order to determine the adsorbed gas molecules volume to form a monolayer on the catalyst. As each adsorbed N_2 molecule occupies only a cross-sectional area (16.2 $Å^2$), SA of catalyst can be quantitatively determined. Figure 4 shows the various stages of physical interaction of probing gas molecules on the catalyst surface. Initially, the microporous surface is filled by probing gas and forms a monolayer called "knee." On further increasing relative pressure of the gas, multilayer and capillary condensation occurs on catalyst surface. Thus, the distribution of micro, mesopore size in the catalyst can be quantified based on the gas adsorbed amount at different relative pressure.

Depending on the nature of adsorbed volume at various relative pressures, IUPAC classified the adsorption isotherm as Type I to Type VI as shown in Fig. 5 [40, 41]. As seen, all isotherms usually consist of three regions:

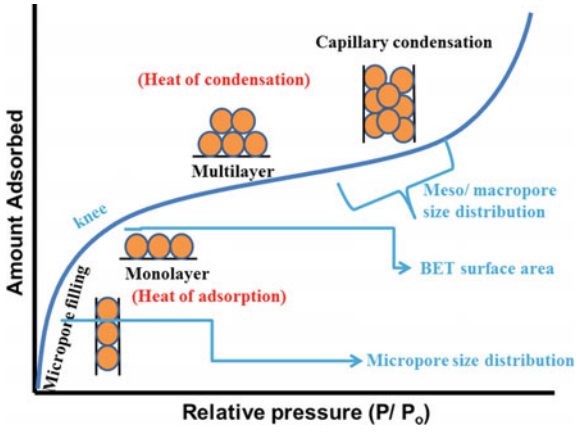

Fig. 4 Stages of physical interaction of probing gas molecules on the catalyst surface

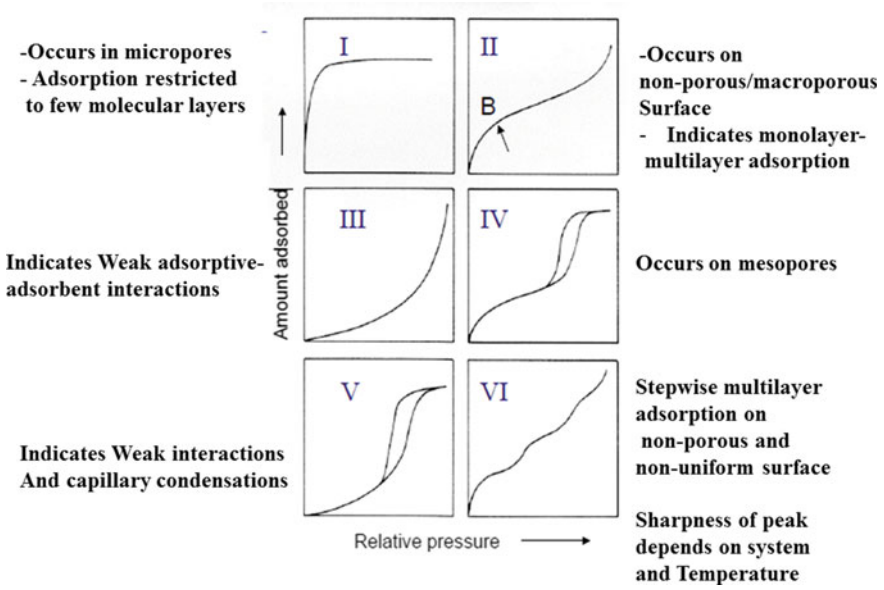

Fig. 5 IUPAC classification of adsorption isotherm. Copyright © IUPAC & De Gruyter, 2015

(i) Concave to the X-axis (at low pressure)
(ii) Linear (at intermediate pressure)
(iii) Convex to X-axis (at high pressure).

The surface area was determined in the region of pressure range where (i) $V(P_0 - P)$ increase with P/Po. (ii) Intercept should be positive (>0). It usually occurs at a low-pressure region (0.05 < P/Po < 3) for macro and mesoporous materials and represents the formation of a complete monolayer [4].

By analyzing the data with a suitable evaluation method as listed below, pore size, pore volume, the total surface area is determined.

(i) Barrett-Joyner-Halenda Method (BJH)
(ii) Dollimore Heal Method (DH)
(iii) Dubinin-Radushkevich Method (DR)
(iv) MP method (MP)
(v) t-plot
(vi) α plot
(vii) Dubinin-Astakhov Method (DA)
(viii) Saito-Foley Method (SF)
(ix) Frenkel-Halsey-Hill Method (FHH)
(x) Neimark-Kiselev Method (NK)
(xi) Horvath-Kawazoe Method (HK)
(xii) Oliver-Conklin
(xiii) Brunauer, Emmett, and Teller (BET).

Brunauer, Emmett, and Teller (BET) technique are one of the simple and broadly used methods to evaluate the surface area, pore size, pore volume, etc. [8]. The relation between N_2 volume adsorbed, and the volume adsorbed to cover a monolayer at a given partial pressure is given by the BET equation:

$$\frac{P}{V(P_0 - P)} = \frac{1}{V_m \mathrm{C}} + \frac{(C-1)P}{V_m C P_O}$$

where P = partial pressure of N_2, P_0 = saturation pressure at experimental temperature (vapor pressure of liquid N_2), V = volume adsorbed at P, V_m = volume adsorbed at monolayer coverage, C = a constant. Plotting $\frac{P}{V(P_0-P)}$ versus P/Po under proper pressure region gives the value of slope $(C-1)/V_m C$ and intercept $1/V_m C$, respectively. From the slope and intercept, the volume of the adsorbed monolayer (V_m) and C can be calculated. Similarly, the surface area S_t and specific surface area S are calculated by:

$$\text{Surface Area} = S_t = VmA_{cs}N;$$
$$\text{Specific surface area} = S = S_t/m$$

where A_x, N represents the cross-sectional area of an adsorbed molecule and Avagadro constant. M is the weight of the catalyst.

Besides, the pore volume and pore radius can be determined by:

$$\text{Volume of liquid in } N_2 \text{ pore} = V_{liq} = P_a V_{ads} V_m / RT$$

V_m—molar Volume of liquid adsorbed, V_{ads}—Volume of gas adsorbed at ambient temperature T and pressure P_a.

$$\text{Average pore radius} = r_p = 2V_{liq}/S$$

Also, the shape of the hysteresis loop (Type IV and V isotherm) provides various information about the nature of pores as shown in Fig. 6 [41]. However, the measured surface area from BET is not a real active surface area, and it is just a representative of the particular gas adsorbed/desorbed quantity. In other words, BET detects only the geometric SA but not the real active catalytic surface area. Also, the validity of BET results is questionable as the catalyst structure is not the same on all surfaces. The results may be a consequence of primary micropore filling or localized monolayer coverage. It is generally argued that BET analysis overestimates the microporous surface as there is a probability of enriched physical adsorption by micropore filling [43].

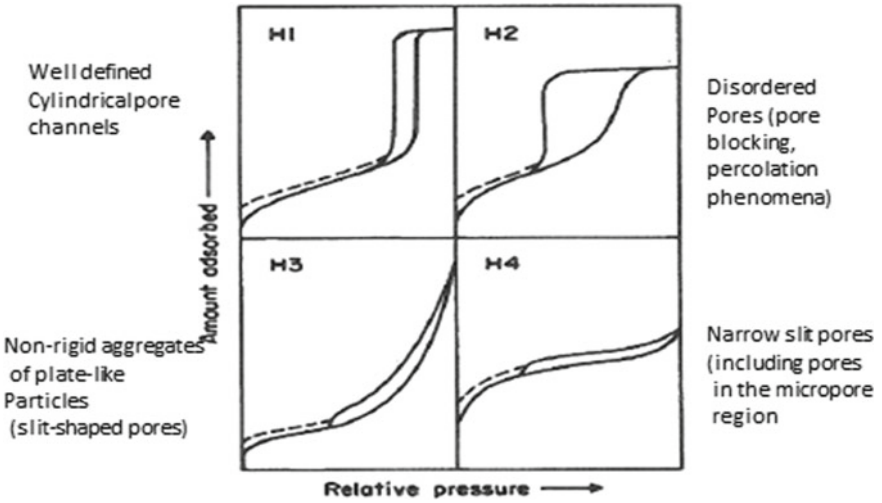

Fig. 6 Different types of a hysteresis loop. Copyright © IUPAC & De Gruyter, 2015

4 Infra-Red Spectroscopy (IR)

It is a well-known fact that the same material possesses different properties owing to the difference in their functional groups. Hence, analyzing the functional group of the catalyst helps us to identify their inherent properties. IR spectroscopy plays a substantial role in defining the structure and functional group of catalysts. It is based on the fact that material's absorption relies on their vibrational energy gap. i.e., these absorptions occur at resonant frequencies (frequency of the absorbed radiation corresponds to the vibration of an atom or frequency of the bond). Hence, absorption of catalyst at specific frequencies is a characteristic and fingerprint of their structure. The number of peaks is associated with the number of vibrational freedoms of the molecule and the peak intensity depends on the change of dipole moment and transition of energy levels. Besides, IR absorption is an indicator of bond strength. Mostly, light atoms and stronger bonds will vibrate at a high frequency (wavenumber).

IR spectroscopy is considered as a vital characterization tool to identify unsaturated sites through comparison of functional groups between the defective and pristine (non-defective) materials. For example, the different electrostatic environment of titanium oxide has been distinguished by their O–H stretch frequencies (Table 2). It is because of the conception that as oxygen vacancy in titania increases, Ti–O–Ti bond strength will decrease, and hence, the hydroxyl groups will be incorporated to compensate the coordinative unsaturated valence sites. But IR spectroscopy is considered as a useful tool only for the non-symmetrical molecule (changes in dipole moment). If the molecule is symmetrical, it is "IR in-active."

Table 2 Vibrational changes associated with the defect in titania

Molecular signature (cm^{-1})	Inference	Ref.
700	Symmetry stretching vibration of Ti–O bonds in TiO_4 tetrahedra	[45]
940	Non-bridging oxygen bonds in the Ti–O molecule	[54]
1688	Ti–$(OH)_2$ stretching vibrations of $H_2Ti(OH)_2$ molecule	[54]
3280	Internally bound O–H stretch	[15]
3488	OH group at the internal defect site	[42]
3400	Bridging OH group	[26]
3685–3700	Tetrahedral coordinated vacancies Ti^{4+}–OH	[45]
3640	Bridging OH gp $(Ti^{4+})_2$–OH	[38]
3687	Ti^{4+}–OH	[31]
3716	Ti^{3+}–OH^- (Octahedral vacancies)	[39]
3710	embedded terminal isolated titanol –OH groups	[45]
3672	Terminal titanol group	[11]

5 UV-vis Spectroscopy

UV-vis spectroscopy is one of the essential characterization tools for investigating photoelectrocatalyst as it quantifies the optical bandgap of the material. It is primarily an absorption/diffuse reflectance spectroscopy, which measures the attenuation of a light beam after it passes through the catalyst and reflects. The attenuation of the light beam is correlated to the inherent catalyst properties through Beer-Lambert's law [34]:

$$\text{Absorbance } A = a(\lambda) * b * c$$

where $a(\lambda)$ is the wavelength dependent absorptivity co-efficient; whereas b and c are the path length and concentration of the analyte, respectively. As energy levels of matter are quantized, light with a precise amount of energy is absorbed, and hence, electronic structure and optical behavior of the catalyst are evaluated.

If the material is transparent (clear and colorless solution), absorbance mode (measuring absorbance as a function of wavelength) is used. While diffuse reflectance DRS mode (measuring reflectance as a function of wavelength) should be used for highly scattered (optically rough film or powders) material. The Diffuse reflectance curve can be converted to an equivalent absorption [10, 29] curve using Kubelka Munk function (F(R)):

$$F(R) = \alpha = (1 - R)^2/2R$$

where α and s are the optical absorption coefficient and scattering coefficient, respectively. The relationship between α and energy band gap (E_g) of the catalyst is given by [27]:

$$\alpha h\upsilon = A(h\upsilon - E_g)^n$$

where A is a proportionality constant and n is an index related to specific electronic transition (n = 1/2 for direct allowed, 3 for in-direct forbidden transition, 2 for in-direct allowed and 3/2 for direct forbidden,). The material may have both direct and indirect transition or either one of the allowed transitions [13]. Tauc plot or Kubelka-Munk plot is used to evaluate the bandgap and determine which transition is feasible.

Typical Tauc plot has hυ on the abscissa and $(\alpha h\nu)^{1/n}$ on the ordinate, and 'n' value relies on the nature of the transition. The resultant plot has a distinct linear regime which pinpoints the absorption onset and extrapolation of the linear region to the abscissa affords E_g.

For DRS measurements, the equation can be written by Kubelka-Munk theory as

$$F(R) * h\upsilon = A(h\upsilon - E_g)^n$$

Kubelka-Munk plot [$(F(R).E)^n$ vs. E] is used to calculate E_g by linear extrapolation of the graph and assessing its abscissa on the x-axis intercept.

Besides, the shape of the spectrum represents the nature of the material. If the spectrum has steep and parallel absorption edges, then the material possesses narrow bandgap; however, the materials with a disorder or localized states will result in an absorption tail. This absorption tail is also called the Urbach tail, and it is due to delocalized electrons. The width of the Urbach tail (Urbach energy—E_u) is related to α as shown in the equation [14]:

$$\alpha = \alpha_0 \exp \frac{E}{E_u}$$

where α_0 is the constant and E, E_u are the photon and Urbach energy respectively.

Hence, E_u can be determined by plotting ln α against E and reciprocating the slope at the linear portion (below the optical bandgap). We can also draw ln[F(R)] versus E Since α is linearly related to F(R) by Kubelka-Munk theory.

For a typical analysis, Yaghoubi et al. [49] have calculated the optical bandgap and Urbach's tail of undoped, oxygen vacancy-rich titania using Kubelka-Munk plot. As TiO_2 is an indirect bandgap material, $(F(R).h\upsilon)^{0.5}$ versus E is plotted. As seen (Fig. 7), sample exhibit sub-bandgap absorption owing to presence of oxygen vacancy associated large Urbach tail (2.2 eV). This disorder induced midgap-states, which was supported by XPS and UPS characterization. The schematic illustrates the effect of localized energy states in TiO_2 for CO_2 photocatalysis.

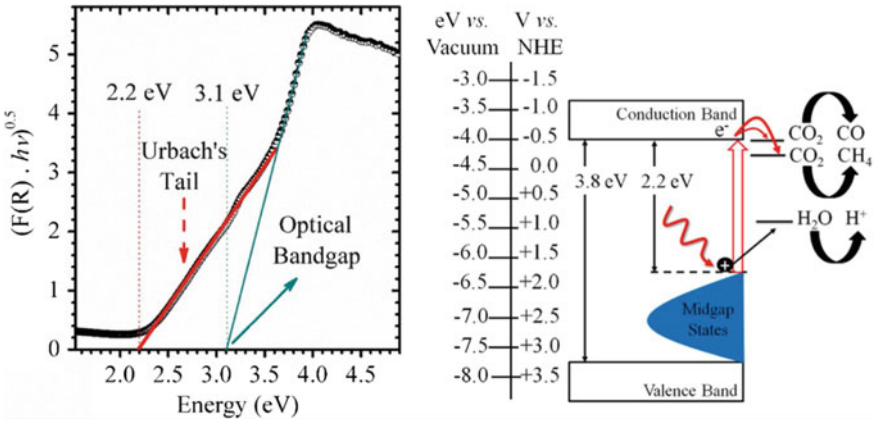

Fig. 7 Estimation of optical bandgap and Urbach tail of undoped, oxygen vacancy-rich titania using Kubelka-Munk function. Reproduced from Yaghoubi et al., Copyright © 2015, American Chemical Society

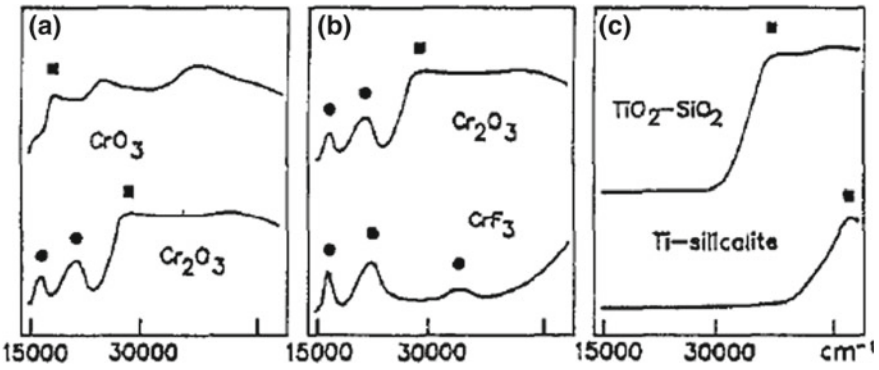

Fig. 8 Influence of change in oxidation state (**a**), ligand type (**b**), coordination number (**c**) on UV-vis spectra. Reproduced from Leofanti et al., Copyright © 1997, Elsevier

Besides optical bandgap and Urbach tail of the material, we could also infer the change in oxidation state, ligand type, and coordination number of the catalyst (Fig. 8) [52].

6 Electron Microscopy

A surface is a place of catalytic activity, and hence understanding the surface properties of catalyst is crucial. Electron microscopes like SEM, TEM, AES, ED provide a

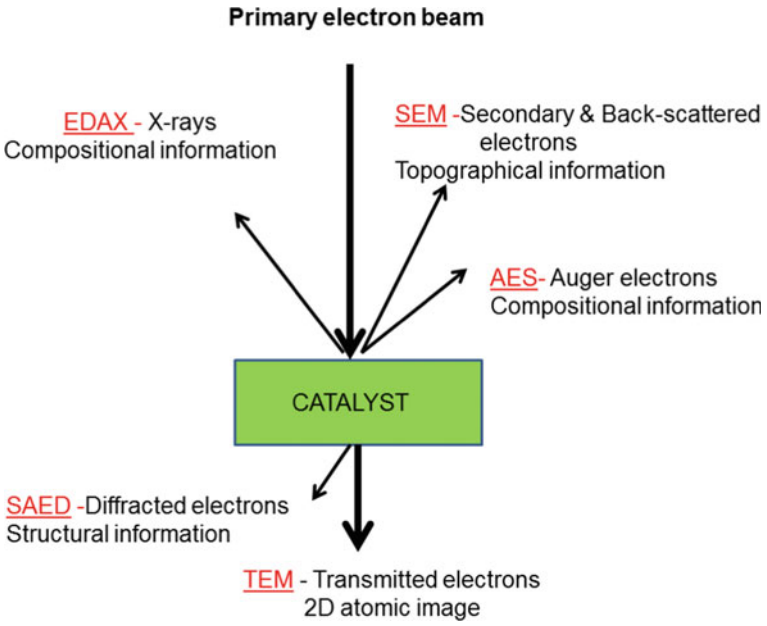

Fig. 9 Detectable signals when an electron beam interacts with the sample

treasure of information like surface morphology, size, shape, crystallography, chemical composition and, homogeneity of catalyst. These microscopes use an electron beam to interact with the samples and detect the scattered/diffracted/transmitted electrons (Fig. 9).

SEM analyzes secondary or back-scattered electrons while TEM analyze transmitted and diffracted electron from the sample. Secondary electrons could study the topographical information as it has low energies (10–50 eV). Since electrons are transmitted and diffracted in TEM, it offers valuable information on the crystallinity, morphology and stress-strain state of the sample. It even projects the information in sub-nanometer resolution 2D image [33, 44].

In the same way, selected part (typical ~10 nm) of an electron diffraction pattern facilitates us to detect crystallographic phases as in XRD. The single crystal particle shows spots while randomly oriented particles exhibit a ring pattern. Bradby et al. [7] has differentiated the amorphous and crystalline silicon after indentation by SAED pattern (Fig. 10). Even we can identify the distribution of amorphous and crystalline (or different crystalline) compounds and relative ratios of different crystalline faces through SAED analysis [47].

Emitted X-rays and Auger electrons are characteristic of an element which helps to determine the chemical composition of catalyst (EDX analysis and AES).

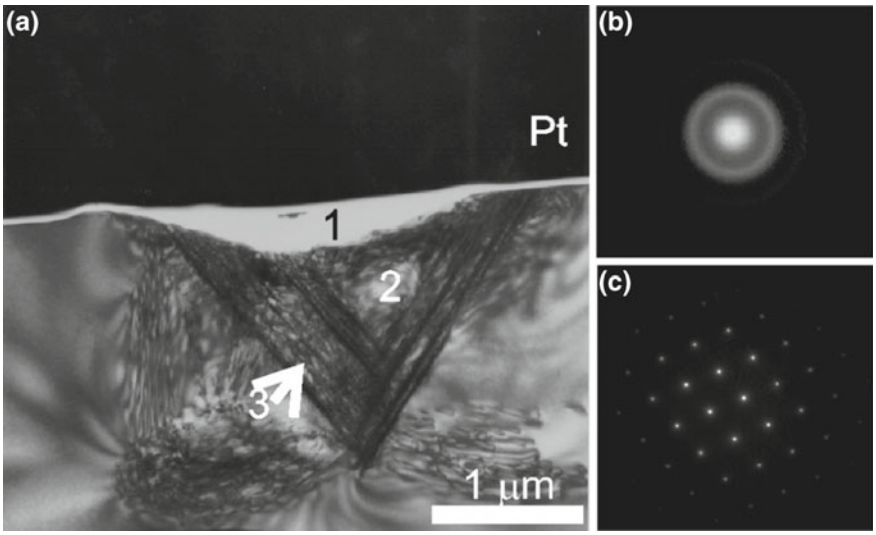

Fig. 10 **a** TEM image of silicon after indentation and the corresponding SAED pattern of **b** amorphous silicon from region 1 **c** crystalline silicon from region 2. Reproduced from Gorelik et al., Copyright © 2002, Springer Nature

7 Electrochemical Techniques

Electrocatalytic reactions are generally composed of several simple steps involving the transport of electrons, protons, and reactants/products. Hence, understanding the charge separation, mass transport, and charge transfer behavior of catalyst is essential. Electrochemical techniques like cyclic voltammetry, linear sweep voltammetry, impedance spectroscopy, chronoamperometry, chronopotentiometry play a vital role in monitoring the charge transfer kinetics, the rate constant, stability, and selectivity of the catalyst. It offers to appraise the real-time performance (activity) towards the desired electrochemical reactions. It is usually carried out using a three-electrode system with platinum as a counter electrode, and the catalyst is used as a working electrode. The reference electrode is based on the electrolyte (solution) pH (Hg/Hg_2SO_4 for acidic medium, Hg/HgO for alkaline and Ag/AgCl for neutral medium.

8 Linear Sweep Voltammetry (LSV)

In this method, the current of the working electrode (catalyst) is measured when its potential is swept linearly with time. Hence, the activity of a catalyst is gauged by both the onset potential (where the catalytic reaction starts) and the peak (or limiting) current. Higher activity of catalyst implies the catalyst has low onset potential and

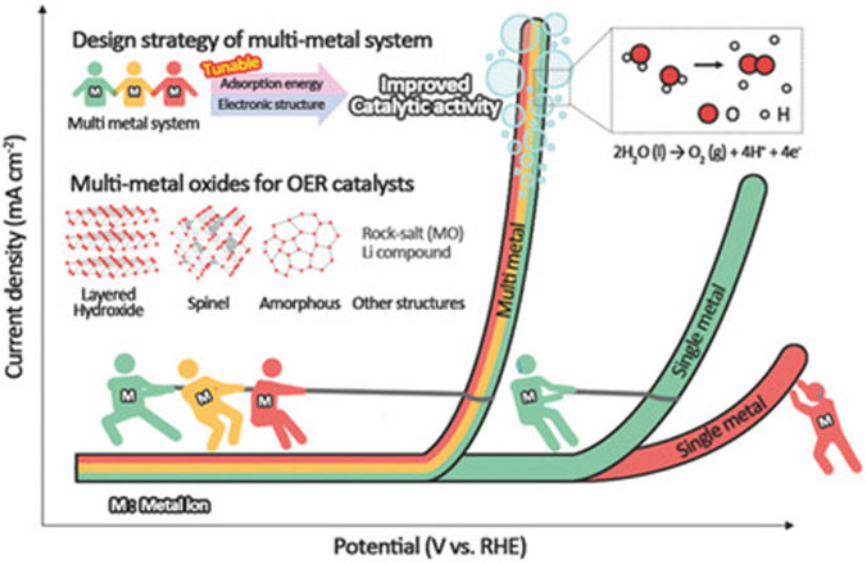

Fig. 11 LSV compares the OER catalytic activity of single metal and multi-metal system. Reproduced from Kim et al., Copyright © 2018, WILEY-VCH Verlag GmbH & Co. KGaA, Weinheim

higher peak current at lower overpotential. Figure 11 shows the improved catalytic activity of multi-metal system rather than single-metal composition for Oxygen Evolution Reaction (OER) by exhibiting low onset potential and higher peak current at lower overpotential [21].

Besides, the sudden increase in current after specific potential region infers formation of the inversion layer, and hence the conduction and valence band edge position is calculated based on the onset regime at cathodic and anodic regime, respectively. Yeh and Teng [50] has calculated the conduction band edge position of p-type GO based on the onset potential of the cathodic linear potential scan, as shown in Fig. 12.

Then, the energy positions in the electrochemical scale are converted to absolute value scale (AVS) using equation [51]:

$$E(\text{NHE}) = \text{E(RHE)} + 0.059\text{pH}$$
$$E(\text{NHE}) = -E(\text{AVS}) - 4.50$$

The obtained current density at a particular potential should be divided by the total mass of the catalyst in order to calculate its mass-specific activity, while area specific activity is calculated by current density divided by the total surface area of the catalyst. Higher specific activity signifies the effective use of catalyst.

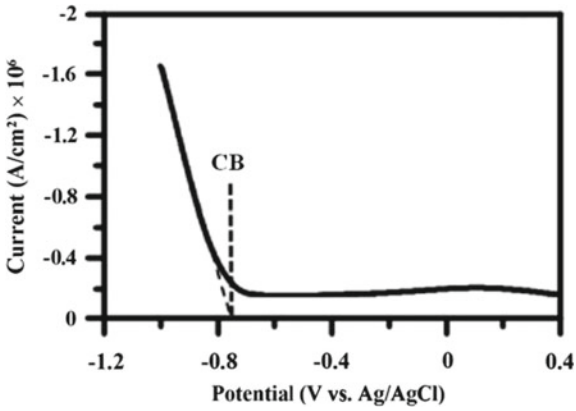

Fig. 12 Determination the conduction band (CB) edge position of the p-type GO specimens based on cathodic linear potential scan for at 5 mV/s. Reproduced from Yeh et al., Copyright © 2012, Electrochemical Society

9 Tafel Analysis

Tafel analysis is a powerful probe to determine the reaction kinetics and rate determining steps involved in electrocatalysis. It analyses the observed electric current behavior at high overpotential region ($|\eta| > 0.118/n$ V) to the applied potential, which affords the electrochemical reaction kinetics of the catalyst [5]. The Tafel equation is:

$$\eta = b \log(j/j_0)$$

where η, j, j_0 are the overpotential, current density, and exchange current density, respectively.

Hence by plotting log j and η, we can obtain two important catalytic descriptors—Tafel slope (b) and exchange current density (j_0). Tafel line extrapolation to the equilibrium potential (E_o) gives j_0 and the slope give 'b'.

Tafel slope depicts the efficiency of the catalyst, whereas j_0 accounts the intrinsic catalytic activity under equilibrium conditions ($\eta = 0$). Conventionally, experimentally observed Tafel slope is compared with the theoretically derived slope, and we can predict the reaction mechanism. For example, Hydrogen evolution reaction consists of three steps as follows:

$$\text{Volmer step}: \quad H_3O^+ + e^- + M \rightarrow M{-}H + H_2O$$
$$\text{Heyrovsky step}: \quad M{-}H + H_3Q^+ + e^- \rightarrow H_2 + H_2O + M$$
$$\text{Tafel step}: \quad 2M{-}H \rightarrow H_2 + 2M$$

where M is the catalytic surface empty site, each step influences the overall reaction rate, and if the rate determining steps are Volmer, Heyrovsky, and Tafel, then the observed Tafel slopes (as shown in Fig. 13) are 120, 40 and 30 mV dec^{-1}, respectively [36].

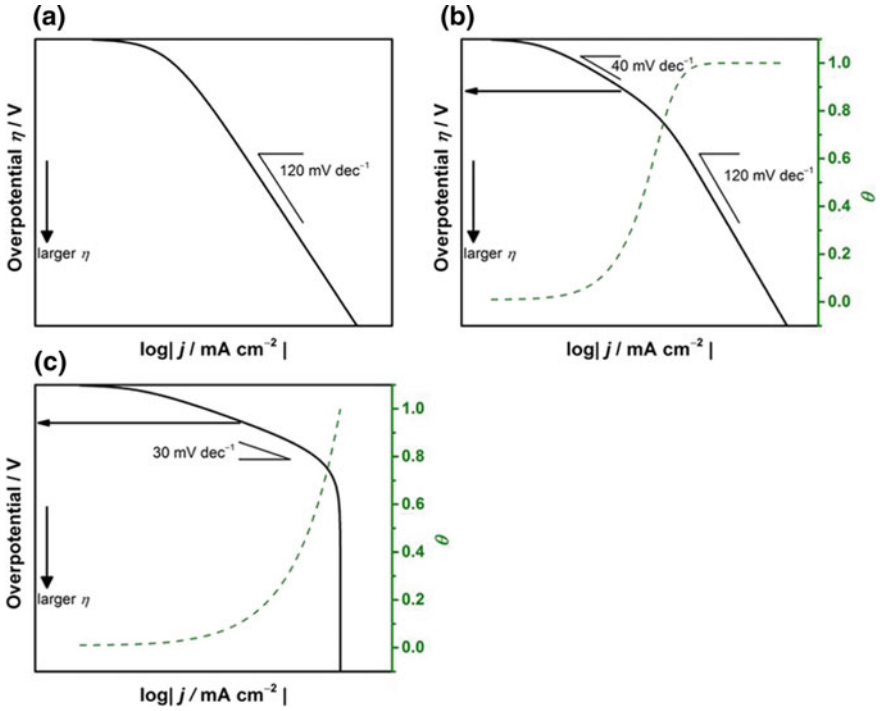

Fig. 13 Stimulated behavior of Tafel relation for hydrogen evolution reaction assuming Volmer, Heyrovsky, and Tafel as the rate determining steps. Reproduced from Shinagawa et al., Copyright © 2015, Nature

Nevertheless, potential dependent Tafel analyses often lead to misrepresentation of data if very small overpotential region is considered. This analysis is also viable only without mass transport and ohmic resistance losses.

10 Cyclic Voltammetry

Cyclic Voltammetry (CV) gives an 'electrochemical spectrum' of a catalyst. It indicates the potential at which catalytic reactions occur, and the resultant current predicts the reactivity of the catalyst. Integrating the acquired current with time under the entire anodic (or cathodic) peak area pertain the total charge of the oxidation (or reduction) process. From this charge, the total amount of the electrochemically active species which contribute towards catalysis reaction can be evaluated using Faraday's law. Hence, the efficiency of the catalyst is analyzed from the CV peak area. Besides, CV also plays an active role in understanding the reactivity of the catalyst. If the catalyst possesses reversible catalytic activity (both oxidation and a reduction reaction occurs), then its anodic and cathodic peak position does not change with scan rate

(υ) and their peak height is proportional to the square root of the scan rate based on the Cottrell equation:

$$I_p = 2.69 \times 10^5 \, AD^{1/2} \, v^{1/2} \, c$$

where I_p is the peak current (A), n is the number of electrons involved in the electrochemical process per reactant molecule, and A is the electrode area (cm^2), υ is the potential scan rate V s^{-1}, D is diffusion coefficient (cm^2 s^{-1}), C is concentration of reaction species (mol cm^{-3}). If the catalyst is not efficient to do both oxidation and reduction, the separation of the two peaks becomes larger than in the reversible case.

Also, the relationship between anodic/cathodic peak current and scan rate helps to identify whether the catalytic reaction is diffusion controlled or kinetically controlled. If the scan rate is directly proportional to $\upsilon^{1/2}$, then the reaction is diffusion controlled. If it linearly fits υ, then the reaction is kinetically controlled. Thus, the scan rate dependent CV response suggests the electron transfer step of the catalyst is diffusion controlled or kinetically controlled.

11 Electrochemical Active Surface Area (ECSA) from CV

As CV describes the whole electrochemical spectrum, it outlines both non-faradaic (charge storage) and Faradaic (charge transfer) behavior of the catalyst. Thus, measuring the double-layer charging capacitance (C_{DL}) from non-faradaic region helps us to calculate ECSA using the equation [28, 35]:

$$ECSA = C_{DI}/C_S$$

where C_s is the specific capacitance (capacitance of an atomically smooth planar catalyst surface) per unit area under identical electrolyte conditions. Typically, C_{DL} is measured in which no apparent Faradaic processes occur (~0.1 V potential window centered at the open-circuit potential (OCP) of the system). To measure C_{DL}, i_c is measured at multiple scan rates under a static CV as double-layer charging current is equal to the product of the scan rate (v) and the electrochemical double-layer capacitance ($i_c = v.\ C_{DL}$). A plot of i_c as a function of v yields a straight line with a slope equal to C_{DL}, which is used to calculate ECSA. For example, McCrory et al. [28] have calculated the electrochemically active surface area of NiO_x catalyst from CV based on the double-layer capacitance measurements in 1 M NaOH, as shown in Fig. 14. It was calculated to be 0.091 mF from the average of the absolute value of the slope of the linear fits to the data (Fig. 14b). Measuring the ECSA from CV and comparing it with the total surface area from BET discloses the actual active sites of the catalyst.

The CV is also used to measure the optical bandgap of the catalyst. As the removal of an electron from HOMO is an oxidation process and energy necessary to inject an electron to LUMO is the reduction process, the energy difference between the

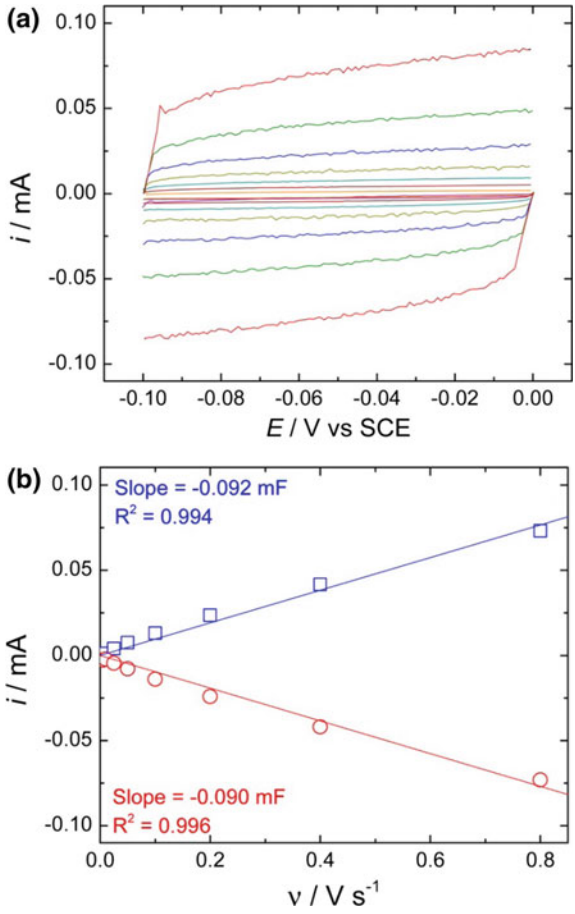

Fig. 14 **a** CV of NiOx at the scan rate: (purple line) 0.005, (orange line) 0.01, (dark redline) 0.025, (cyan line) 0.05, (brown line) 0.1, (blue line) 0.2, (green line) 0.4, and (red line) 0.8 V/s. **b** Measured cathodic (red open circle) and anodic (blue open square) charging currents at −0.05 V versus SCE as a function of scan rate. Reproduced from McCrory et al., Copyright © 2013, American Chemical Society

onset of oxidation and reduction reaction gives the quasi-particle bandgap. Haram et al. [17] calculated the quasi-particle gap (ε_{gap}^{qp}) of Q-CdTe, as a function of size from CV and compared with optical band gap (ε_{gap}^{qp}) from DFT calculations and UV-visible spectra (Fig. 15). Based on Fig. 15b and Table 3, we can infer that the optical bandgap obtained from CV is in good agreement with DFT calculations and UV-vis spectra.

However, this method of measuring band structure parameters is limited to semiconductors like CdS, CdSe [16, 24].

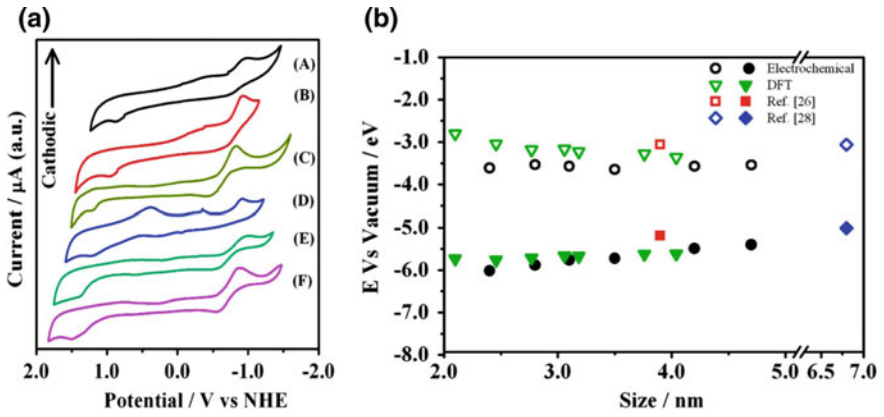

Fig. 15 **a** CV recorded on varied sizes of Q-CdTe (sample-A to sample-F). Scan rates were 100 mV s^{-1} for all the cases. **b** Comparing HOMO and LUMO positions obtained from DFT and CV. Reproduced from Haram et al., Copyright © 2011, American Chemical Society

Table 3 Band structure parameters of oleic acid capped Q-CdTe obtained from UV-vis spectroscopy and cyclic voltammetry

Sample ID	From UV-vis spectroscopy		From cyclic voltammetry		
	Average Q-dot size (nm)	Optical bandgap—ε_{gap}^{op} (eV)	Conduction band edge (e1) versus vacuum	Valence band edge (h1) versus vacuum	Quasi particle gap—ε_{gap}^{qp} (eV)
A	4.7	1.88	−3.54	−5.4	1.86
B	4.2	1.94	−3.56	−5.49	1.93
C	3.5	2.09	−3.65	−5.73	2.08
D	3.1	2.19	−3.57	−5.76	2.19
E	2.8	2.33	−3.53	−5.88	2.34
F	2.4	2.40	−3.61	−6.02	2.41

Reproduced from Haram et al., Copyright © 2011, American Chemical Society

12 Chronoamperometry/Chronopotentiometry

Excellent durability is a crucial requirement for the catalyst. Hence, the long term performance of the catalyst is studied by measuring the current at a constant voltage. This method is called Chronoamperometry while measuring the voltage at constant current is chronopotentiometry. It is better to fix a current density larger than 10 mA cm^2 (higher overpotential than onset potential) to avoid bubbling effect and study the catalytic stability for a more extended period (>400 h) [55].

In the case of photo-electrocatalysis, chronoamperometry is also used to separate the hole current (due to minority carriers) and steady state current. As light shines on

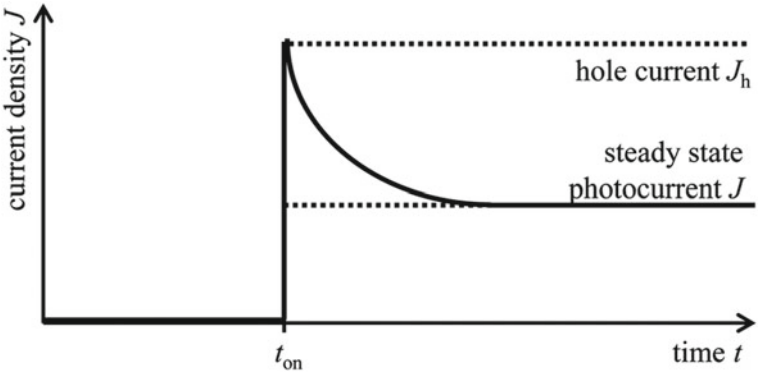

Fig. 16 Transient photocurrent response of a photoelectrode on illumination. Reproduced from Klotz et al., Copyright © 2017, Royal Society of Chemistry

the photo electrocatalyst, the electron-hole pair is generated, and holes move to the liquid junction (electrolyte). It accumulates there until a steady-state concentration is achieved at which point the rate of arrival of holes is exactly counterbalanced by interfacial charge-carrier transfer and recombination. This can be well seen in transient photocurrent response (CA) of a photo-electrode by a spike current followed by a steady state current on illumination (Fig. 16) [22].

Thus, integrating the area under the photocurrent spikes helps to estimate the extent of hole trapping at the semiconductor liquid junction. Hence, charge-transfer efficiency and recombination rate of photo-electro catalyst are evaluated. The charge transfer efficiency η_t is given by

$$\eta t = \frac{J}{J_h} = \frac{J_h + J_r}{J_h} = \frac{J}{J - J_r}$$

where J_h, J_r and J denote the current density of holes, electrons and steady state photocurrent, respectively.

Overall, this CA technique delivers integral response of the catalyst. It could not distinguishes different faradaic processes, which co-occur. It does not predict whether the performance is due to corrosion (degradation) or catalytic activity of the material. Convection (buildup of density gradients and environmental vibration) at a longer time will also affect the results.

13 Electrochemical Impedance Spectroscopy (EIS)

EIS uses alternating current (AC) signal (~10 mV) with a frequency vary from 1 to 1 MHz and offers a possibility to understand the separate role of ions and electrons in catalyst conductivity. As electrons move faster than ions, electronic transportation

is studied at lower frequency region while ionic transportation is studied at higher frequency region. Besides the applied small amplitude AC voltage does not perturb its equilibrium, and hence steady state of the system is studied.

There are many ways to plot the impedance data such as Nyquist plot (Z' vs. Z''), Bode plot (phase angle vs. frequency, $|Z|$ vs. frequency). All plots represent the same data in different forms, and the obtained plot is fitted with an equivalent circuit model based on the physicochemical properties of the catalyst [6]. Typical Nyquist plot of catalyst is shown in Fig. 17.

The solution resistance (R_S) and charge transfer resistance (R_{ct}) of the catalyst are obtained from the high and low-frequency intercept of the real axis in the Nyquist plot, respectively. If the distance between working and counter electrode is L (cm) and A (cm^2) is the cross-sectional area of the catalyst, then conductivity (σ) of the catalyst is determined by:

$$\sigma = \frac{L}{R_{ct} A}$$

The Warburg Impedance at the low-frequency region is associated with mass–transport resistance. If the catalyst exhibits only Warburg, then the conduction of catalyst occurs only by diffusion of ions. Relaxation time (τ) is estimated from the frequency (f) corresponding to $-Z''_{max}$ in the semicircle of the Nyquist plot using the equation ($\tau = 1/2\pi f$). Low τ represents the fast charge transfer characteristics. Besides, the Capacitance C at space charge layer is computed using Brugg's equation [$C = (R.Q)^{1/\alpha}/R$, where $\frac{1}{R} = \frac{1}{R_s} + \frac{1}{R_{ct}}$] [32].

AC conductivity (σ) is obtained using the relation [18]:

$$\sigma = \frac{Z'}{Z'^2 + Z''^2}$$

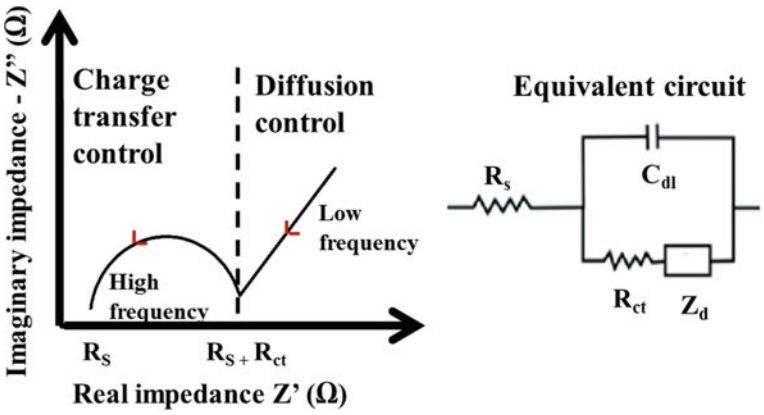

Fig. 17 Typical Nyquist plot of catalyst

where Z′ and Z″ represent the real and imaginary parts of Z, respectively. If it obeys universal power law [$\sigma(\omega) = \sigma(0) + B\omega^p$, where ω is the angular frequency ($2\pi f$), $\sigma(0)$ is the conductivity at low frequency, p is a constant between 0 and 1], the conductivity at plateau region (low frequency) is taken as a purely resistive DC conductivity (σ_{DC}) [12, 19].

Even though EIS supplies a wide variety of data, the major shortcoming of this spectroscopy is ambiguity in the selection of the equivalent circuit model. More than one equivalent circuit can be fitted easily, and so one should have prior knowledge or additional information from other techniques to model the right equivalent circuit.

14 Mott–Schottky Analysis

The Mott–Schottky technique is a powerful tool to understand the changes that occur in an electrochemical interface of the catalyst. The small-signal AC potential excitation is applied at fixed-frequency to an electrochemical cell as a function of DC bias and capacitance of the working electrode is measured using the relation $C = 1/\omega Z_{im}$. Then the plot of capacitance versus voltage gives Mott–Schottky Plot. The carrier density (N_D) and flat-band potential (E_{FB}) are measured using the Mott–Schottky equation:

$$N_D = \frac{2C^2}{e\varepsilon\varepsilon_0 A^2}\left[\left(\begin{array}{c} E \\ E_{FB} \end{array}\right) - \frac{K_B T}{e}\right]$$

where e is the elementary electron charge (1.6×10^{-19} C); ε_0 is the permittivity of vacuum (8.86×10^{-12} F m^{-1}); ε is the dielectric constant of sample E_{FB} is the built-in voltage (flat band potential); K_B is the Boltzmann constant (1.38×10^{-23} J K^{-1}); A is the surface area of the electrode and T is the temperature (298 K). The flat band potential (equivalent to Fermi level of the electrode before reaching equilibrium) is obtained from the extension of the linear part of Mott–Schottky plot and donor density are measured by frequency–dependent slope. If the slope of the M-S plot is positive, then the material is n-type or vice versa [32]. Lin et al. [25] have constructed the energy diagram and band alignment of p-InP and TiO_2 in solution (Fig. 18) with the measured E_{FB} and N_D (from M.S plot) and the optical band gap (from UV-vis absorption spectra).

15 Conclusion

As seen, characterization techniques are an invaluable tool to understand the electrocatalyst and contributed significantly to new insights in catalysis. It is also clear

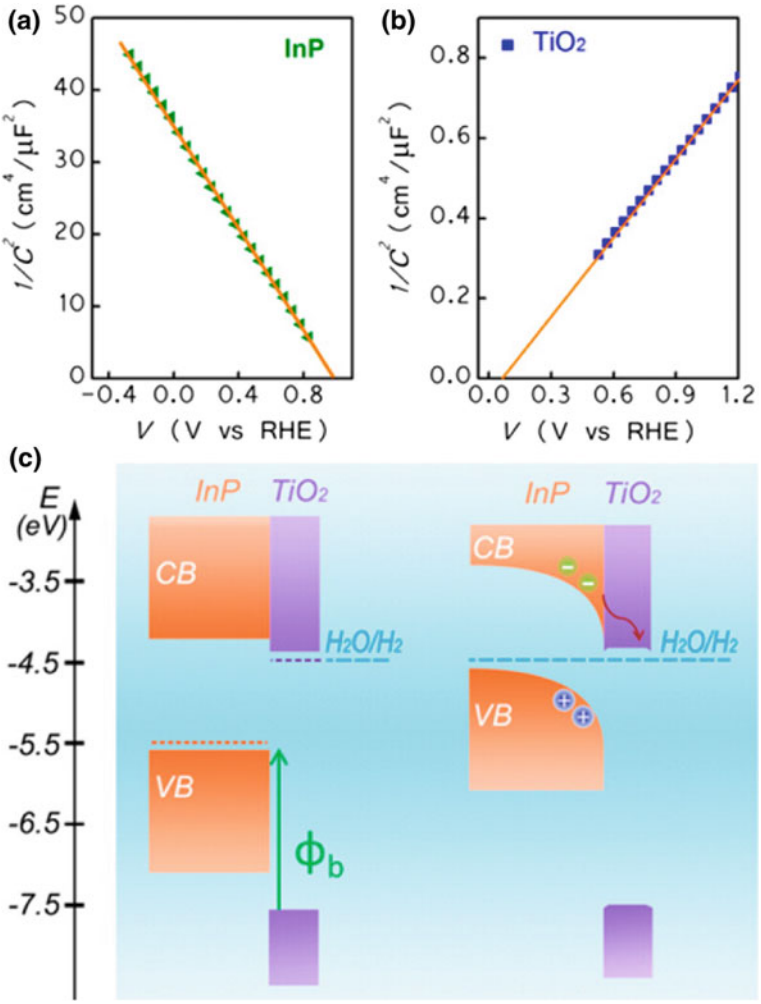

Fig. 18 Mott–Schottky plot of InP (**a**) TiO_2 (**b**) and its energy band diagram (**c**). Reproduced from Lin et al., Copyright © 2015, American Chemical Society

that no characterization technique is effortless and straightforward. Extensive experience and sound theoretical background in spectroscopy, material science, physical chemistry, and solid-state physics are inevitable for the conventional and meaningful interpretation of spectra of catalysts. Besides, interconnecting all characterization data is mandatory for a complete understanding of the behavior and property of a catalyst.

References

1. Acres BGJK (1980) The characterisation of catalysts. Platin Met Rev 24:14–25. https://doi.org/10.1207/S15327647JCD0204_5
2. Amakawa K, Sun L, Guo C et al (2013) How strain affects the reactivity of surface metal oxide catalysts. Angew Chem Int Ed 52:13553–13557. https://doi.org/10.1002/anie.201306620
3. Austermann RL, Denley DR, Hart DW, Himelfarb PB, Irwin RM, Narayana M, Szentirmay R, Tang SC, Yeates RC (1987) Catalyst characterization. Anal Chem 59:68R–102R. https://doi.org/10.1021/ac00139a005
4. Bae YS, Yazayd'n AÖ, Snurr RQ (2010) Evaluation of the BET method for determining surface areas of MOFs and zeolites that contain ultra-micropores. Langmuir 26:5475–5483. https://doi.org/10.1021/la100449z
5. Bard AJ, Faulkner LR (2004) Electrochemical methods. Fundamentals and applications
6. Barsoukov E, Ross MJ (2005) Impedance spectroscopy—theory, experiment, and applications
7. Bradby JE, Williams JS, Wong-Leung J, Swain MV, Munroe P (2000) Transmission electron microscopy observation of deformation microstructure under spherical indentation in silicon. Appl Phys Lett 77:3749–3751. https://doi.org/10.1063/1.1332110
8. Brunauer S, Emmett PH, Teller E (1938) Adsorption of gases in multimolecular layers. J Am Chem Soc 60:309–319. https://doi.org/10.1021/ja01269a023
9. Choudhury B, Choudhury A (2013) Local structure modification and phase transformation of TiO_2 nanoparticles initiated by oxygen defects, grain size, and annealing temperature. Int Nano Lett 3:1. https://doi.org/10.1186/2228-5326-3-55
10. Christy AA, Kvalheim OM, Velapoldi RA (1995) Quantitative analysis in diffuse reflectance spectrometry: a modified Kubelka-Munk equation. Vib Spectrosc 9:19–27. https://doi.org/10.1016/0924-2031(94)00065-O
11. Crocker M, Herold RHM, Wilson AE, et al (1996) H-1 NMR spectroscopy of titania—chemical shift assignments for hydroxy groups in crystalline and amorphous forms of TiO_2. J Chem Soc Trans 92:2791–2798
12. Dyre JC (1988) The random free-energy barrier model for ac conduction in disordered solids. J Appl Phys 64:2456. https://doi.org/10.1063/1.341681
13. Ebraheem S, El-Saied A (2013) Band gap determination from diffuse reflectance measurements of irradiated lead borate glass system doped with TiO_2 by using diffuse reflectance technique. Mater Sci Appl 04:324–329. https://doi.org/10.4236/msa.2013.45042
14. El-Denglawey A (2011) Characterization of As-Se-Tl films near infrared region. J Non Cryst Solids 357:1757–1763. https://doi.org/10.1016/j.jnoncrysol.2011.01.026
15. Fujishima A, Zhang X, Tryk DA (2008) TiO_2 photocatalysis and related surface phenomena. Surf Sci Rep 63:515–582. https://doi.org/10.1016/j.surfrep.2008.10.001
16. Haram SK, Quinn BM, Bard AJ (2001) Electrochemistry of CdS nanoparticles: a correlation between optical and electrochemical band gaps. J Am Chem Soc 123:8860–8861. https://doi.org/10.1021/ja0158206
17. Haram SK, Kshirsagar A, Gujarathi YD et al (2011) Quantum confinement in CdTe quantum dots: investigation through cyclic voltammetry supported by density functional theory (DFT). J Phys Chem C 115:6243–6249. https://doi.org/10.1021/jp111463f
18. Hernandes AC (2006) Thermoluminescence kinetic parameters of $Bi_4Ge_3O_{12}$ single crystals. Nucl Instrum Methods Phys Res Sect B: Beam Interact Mater At 250:390–395. https://doi.org/10.1016/j.nimb.2006.04.144
19. Jonscher AK (1990) The "universal" dielectric response. III. IEEE Electr Insul Mag 6. https://doi.org/10.1109/57.63055
20. Khan MAM, Kumar S, Ahamed M et al (2011) Structural and thermal studies of silver nanoparticles and electrical transport study of their thin films. Nanoscale Res Lett 6:1–8. https://doi.org/10.1186/1556-276X-6-434
21. Kim JS, Kim B, Kim H, Kang K (2018) Recent progress on multimetal oxide catalysts for the oxygen evolution reaction. Adv Energy Mater 8:1–26. https://doi.org/10.1002/aenm.201702774

22. Klotz D, Grave DA, Rothschild A (2017) Accurate determination of the charge transfer efficiency of photoanodes for solar water splitting. Phys Chem Chem Phys 19:20383–20392. https://doi.org/10.1039/c7cp02419c
23. Leofanti G, Tozzola G, Padovan M, Petrini G, Bordiga S, Zecchina A (1997) Catalyst characterization: characterization techniques. Catal Today 34:307–327. https://doi.org/10.1016/s0920-5861(96)00056-9
24. Leonat L, Sbârcea G, Brañzoi IV (2013) Cyclic voltammetry for energy levels estimation of organic materials. UPB Sci Bull Ser B Chem Mater Sci 75:111–118
25. Lin Y, Kapadia R, Yang J et al (2015) Role of TiO_2 surface passivation on improving the performance of P-InP photocathodes. J Phys Chem C 119:2308–2313. https://doi.org/10.1021/jp5107313
26. Liu L, Chen X (2014) Titanium dioxide nanomaterials: self-structural modifications. Chem Rev 114:9890–9918. https://doi.org/10.1021/cr400624r
27. López R, Gómez R (2012) Band-gap energy estimation from diffuse reflectance measurements on sol-gel and commercial TiO_2: a comparative study. J Sol-Gel Sci Technol 61:1–7. https://doi.org/10.1007/s10971-011-2582-9
28. McCrory CCL, Jung S, Peters JC, Jaramillo TF (2013) Benchmarking heterogeneous electrocatalysts for the oxygen evolution reaction. J Am Chem Soc 135:16977–16987. https://doi.org/10.1021/ja407115p
29. Miklavcic SJ, Yang L (2004) Framework for homogeneous and inhomogeneous optical media. J Opt Soc Am A Opt Image Sci Vis 21:1942–1952
30. Moulijn JA, Van Leeuwen PWNM, Van Santen RA (1993) Catalysis: an integrated approach to homogeneous, heterogeneous and industrial catalysis. Stud Surf Sci Catal 79:363–400. https://doi.org/10.1016/S0167-2991(08)63814-8
31. Mozia S, Tomaszewska M, Kosowska B et al (2004) Decomposition of nonionic surfactant on a nitrogen-doped photocatalyst under visible-light irradiation. Appl Catal B Environ 55:195–200. https://doi.org/10.1016/j.apcatb.2004.09.019
32. Pu P, Cachet H, Laidani N, Sutter EMM (2012) Influence of pH on surface states behavior in TiO_2 nanotubes
33. Sadan MB, Houben L, Enyashin AN et al (2008) Atom by atom: HRTEM insights into inorganic nanotubes and fullerene-like structures. Proc Natl Acad Sci 105:15643–15648. https://doi.org/10.1073/pnas.0805407105
34. Shah RS, Shah RR, Pawar RB, Gayakar PP (2015) UV-visible spectroscopy—a review. ISSN: 2249-6807
35. Shin S, Han HS, Kim JS et al (2015) A tree-like nanoporous WO_3 photoanode with enhanced charge transport efficiency for photoelectrochemical water oxidation. J Mater Chem A 3:12920–12926. https://doi.org/10.1039/c5ta00823a
36. Shinagawa T, Garcia-Esparza AT, Takanabe K (2015) Insight on Tafel slopes from a microkinetic analysis of aqueous electrocatalysis for energy conversion. Sci Rep 5:1–21. https://doi.org/10.1038/srep13801
37. Subbaiah YPV, Prathap P, Reddy KTR (2006) Structural, electrical and optical properties of ZnS films deposited by close-spaced evaporation. Appl Surf Sci 253:2409–2415. https://doi.org/10.1016/j.apsusc.2006.04.063
38. Suriye K, Lobo-Lapidus RJ, Yeagle GJ, et al (2008) Probing defect sites on TiO_2 with $[Re_3(CO)_{12}H_3]$: spectroscopic characterization of the surface species. Chem A Eur J 14:1402–1414. https://doi.org/10.1002/chem.200701514
39. Szczepankiewicz SH, Colussi AJ, Hoffmann MR (2002) Infrared spectra of photoinduced species on hydroxylated titania surfaces. J Phys Chem B 104:9842–9850. https://doi.org/10.1021/jp0007890
40. Thommes M, Kaneko K, Neimark AV et al (2015) Physisorption of gases, with special reference to the evaluation of surface area and pore size distribution (IUPAC technical report). Pure Appl Chem 87:1051–1069. https://doi.org/10.1515/pac-2014-1117
41. Union I, Pure OF, Chemistry A (1985) Reporting physisorption data for. Area 57:603–619

42. Usseglio S, Calza P, Damin A et al (2006) Tailoring the selectivity of Ti-based photocatalysts (TiO_2 and microporous ETS-10 and ETS-4) by playing with surface morphology and electronic structure. Chem Mater 18:3412–3424. https://doi.org/10.1021/cm052841g
43. Walton KS, Snurr RQ (2007) Applicability of the BET method for determining surface areas of microporous metal-organic frameworks. J Am Chem Soc 129:8552–8556. https://doi.org/10.1021/ja071174k
44. Wang ZL (2003) New developments in transmission electron microscopy for nanotechnology. Adv Mater 15:1497–1514. https://doi.org/10.1002/adma.200300384
45. Wang Z, Yang C, Lin T et al (2013) H-doped black titania with very high solar absorption and excellent photocatalysis enhanced by localized surface plasmon resonance. Adv Funct Mater 23:5444–5450. https://doi.org/10.1002/adfm.201300486
46. Wang Y, Tang W, Zhang L (2015) Crystalline size effects on texture coefficient, electrical and optical properties of sputter-deposited Ga-doped ZnO thin films. J Mater Sci Technol 31:175–181. https://doi.org/10.1016/j.jmst.2014.11.009
47. Williams DB (2009) Transmission electron microscopy: a textbook for materials science
48. Williamson G, Hall W (1953) X-ray line broadening from filed aluminium and wolfram. Acta Metall 1:22–31. https://doi.org/10.1016/0001-6160(53)90006-6
49. Yaghoubi H, Li Z, Chen Y et al (2015) Toward a visible light-driven photocatalyst: the effect of midgap-states-induced energy gap of undoped TiO_2 nanoparticles. ACS Catal 5:327–335. https://doi.org/10.1021/cs501539q
50. Yeh T-F, Teng H (2012) Graphite oxide with different oxygen contents as photocatalysts for hydrogen and oxygen evolution from water. ECS Trans 41:7–26. https://doi.org/10.1149/1.3703509
51. Yong X, Schoonen MAA (2000) The absolute energy positions of conduction and valence bands of selected semiconducting minerals. Am Mineral 85:543–556. https://doi.org/10.2138/am-2000-0416
52. Zecchina A, Petrini G, Padovan M et al (2002) Catalyst characterization: characterization techniques. Catal Today 34:307–327. https://doi.org/10.1016/s0920-5861(96)00056-9
53. Zhang J (2008) PEM fuel cell, catalyst and catalyst layer. https://doi.org/10.1007/978-1-84800-936-3
54. Zhou M, Dong J, Zhang L, Qin Q (2001) Reactions of group V metal atoms with water molecules. Matrix isolation FTIR and quantum chemical studies. J Am Chem Soc 123:135–141. https://doi.org/10.1021/ja003072z
55. Zou X, Zhang Y (2015) Noble metal-free hydrogen evolution catalysts for water splitting. Chem Soc Rev 44:5148–5180. https://doi.org/10.1039/C4CS00448E

Interface Chemistry of Platinum-Based Materials for Electrocatalytic Hydrogen Evolution in Alkaline Conditions

Yuhang Wu, Juming Yao and Junkuo Gao

Abstract Alkaline electrolyzed water hydrogen production technology is of great significance to the development of sustainable alternative energy. Although precious metal Pt is the best electrocatalyst for hydrogen evolution reaction (HER), its alkaline HER involves the two-step reaction of water dissociation and hydrogen recombination, which limits its development in alkaline electrolyzed water technology. Therefore, amount of interface chemistry of materials has been investigated to design catalysts with a large number of active sites and stability to improve the performance of alkaline HER. In this chapter, we summarize the interfacial chemical specificity of the Pt and Pt-based catalysts for controlling alkaline HER kinetics to boost the water dissociation step and hydrogen evolution efficiency. This is a guiding significance for the future of building renewable and sustainable energy systems.

Keywords HER · Alkaline · Interface · Water dissociation · Pt-based catalyst

1 Background and Brief Introduction

The consumption of non-renewable energy and the global environmental pollution are two major social and economic challenges in human society[1–7]. Therefore, the development of sustainable new clean energy is essential to solving increasingly serious energy crises and environmental problems [8–12]. As an efficient, renewable, pollution-free new energy source, hydrogen is considered to be the most potential energy in this century. Since H_2 is regarded as "Ultimate Energy" of human beings, which represents the strategic direction of energy [13–20]. Therefore, the large-scale preparation of hydrogen is a prerequisite for the successful application of hydrogen energy. Among them, electrocatalytic water splitting has become the most promising hydrogen production route thanks to the advantages of high efficiency, simple process and mature technology [21–26]. However, high-performance and high-yield acidic HER hydrogen production is limited due to its high requirements for equipment and

Y. Wu · J. Yao · J. Gao (✉)
Institute of Fiber Based New Energy Materials, College of Materials and Textiles, Zhejiang Sci-Tech University, Hangzhou 310018, People's Republic of China
e-mail: jkgao@zstu.edu.cn

Inamuddin et al. (eds.), *Methods for Electrocatalysis*,
https://doi.org/10.1007/978-3-030-27161-9_18

catalyst durability [27, 28]. Therefore, alkaline HER has been extensively studied due to its low requirements for equipment and high durability for catalysts [29–31]. Since alkaline HER requires a high overpotential, the development of superior electrocatalysts for alkaline HER is essential to significantly reduce the energy loss of the electrochemical devices [32–34]. Thus, the mechanism of alkaline HER was deeply studied to develop advanced catalysts. Alkaline HER is a multi-progress reaction which is divided into three elementary processes: Volmer step ($H_2O + e^- = H_{ad} + OH^-$), followed by the Heyrovsky step ($H_2O + H_{ad} + e^- \rightarrow H_2 + OH^-$) or the Tafel step ($2H_{ad} \rightarrow H_2$) [35–38]. Among the HER electrocatalysts, Platinum exhibits excellent catalytic performance with ultra-low overpotential, resulting from the optimal platinum hydrogen adsorbates (Pt–H_{ad}) on the surface of Pt during water dissociation process [39, 40]. Nevertheless, the kinetics of alkaline HER are still hindered by the insufficient oxyphilic surfaces for the cleavage of O–H bonds in H_2O [41–43]. Therefore, HER electrocatalysts in alkaline environment must feature both optimal H_{ad} adsorption and strong dissociation water adsorption to overcome the additional energy and recombine hydrogen. At present, single-component catalysts are difficult to satisfy the above requirements simultaneously [44]. Thus, the design of high efficiency alkaline HER catalysts have recently turned to Pt-based (Pt–M, Pt–MO and Pt–M(OH), M = Ni, Co and Cu) materials. Among the afore-mentioned various combination methods, Pt–$Ni(OH)_2$ has emerged to be a prominent HER catalysts [45, 46]. Ni hydroxyl shows a higher affinity for water, while platinum has a higher theoretical activity for efficient hydrogen recombination. Hence, researches have paid much attention in Pt–$Ni(OH)_2$ bimetallic heterostructure, including crystal facet [47], nanostructure [48], defect [49] and so on.

In this chapter we summarize the mechanism of HER in alkaline environment, especially the catalytic mechanism on the interface of platinum and platinum-based materials in recent literature. Subsequently, we further explain the synergistic effect between platinum and the catalytic components that promote water dissociation. Furthermore, some recent progress Pt-based heterostructure in alkaline environment are discussed, and some valuable opinions and prospects of this attractive field are concluded in the end.

2 HER Mechanism in Alkaline Condition

The mechanism of HER in electrolyzed water has been widely investigated in the last century. A standard potential of 1.23 V is required for electrolyzed water [50–52]. Yet, in order to overcome the extra resistance (such as contact resistance between catalysts and electrode, solution resistance) in the electrolyzer and the kinetic barrier inherent in the two half reactions, a higher potential must be applied to initiate the reaction in practical operation [53–56]. Recently, the working potential can be effectively reduced through designing the battery to minimize the resistance loss and the advanced electrocatalysts to reduce the kinetic barrier [57]. Thus, the design of advanced anode electrocatalysts to enhance HER performance will expand the

industrial field of electrolyzers [46, 58–61]. The electrocatalytic hydrogen evolution process is combined with two reaction processes, Volmer-Tafel or Volmer-Heyrovsky mechanisms, and it can be applied in both acidic and alkaline conditions. However, the instability of the catalysts and the high requirements of acidic media for industrial equipment limit the development of acidic HER [62, 63]. Therefore, it is crucial to develop excellent HER catalysts under alkaline conditions. In the process of water electrolysis, water adsorption on the surface of the catalyst is necessary and there is a net charge transfer at the interface when water is adsorbed on the metal surface [57]. As shown in Fig. 1, the process of reducing water molecules adsorbed on the interface of the metal catalyst to H_{ad} and OH^- species is carried out in the Volmer step. Subsequently, hydrogen will be produced though the Volmer-Tafel or Volmer-Heyrovsky mechanisms [64, 65]. In Volmer-Tafel mechanism, hydrogen molecule formed by the combination of two hydrolyzed adsorbed hydrogen atoms. In addition, the Volmer-Heyrovsky mechanism generates hydrogen by reacting between H_{ad} and additional water molecules [66].

Heterogeneous catalysts (such as platinum) have been observed to exhibit poor catalytic activity and lower exchange current density in alkaline condition compared to that in acidic condition [67], which indicates that the catalytic activity can be greatly influenced in different reaction pathways [68]. Meanwhile, HER always forms the intermediate H_{ad} in different reaction pathways. In acidic environment, the Volmer step only involves the reduction of protons to H_{ad}, thus indicating that the catalytic activity is closely related to the free energy (ΔG_H) of H_{ad} [39]. Whether the value of $\triangle G_H$ is positive or negative is not conducive to the catalytic release of H_2, and Pt owns the best HER performance according to the optimal ΔG_H ($\Delta G_H \approx 0$) [64, 69]. However, under alkaline conditions, the adsorption energy of the active water molecules and the desorption of the hydroxide are also critical in the Volmer step. If the adsorption energy of active water is low, H_{ad} may not be activated well. In contrast, if the desorption energy of hydroxide ions is too high, it will cause the loss of active sites and lead to poisoning effects [68]. In addition, the hydroxyl species (OH_{ad}) is

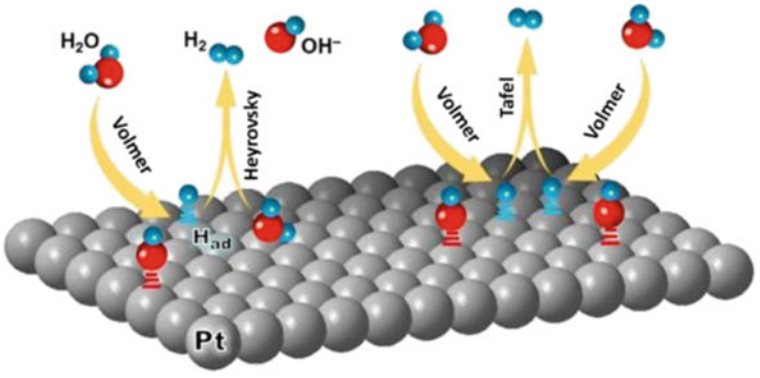

Fig. 1 The scheme of Volmer-Heyrovsky and Volmer-Tafel mechanisms on the Pt surface. Reproduced with permission from Wiley, Copyright, 2018 [57]

also adsorbed on the active site of the Pt interface, hindering the formation of H_{ad}, so as to reduce the efficiency of H_2 generation. Therefore, the design of heterogeneous alkaline HER catalysts with excellent activities should take into account the above parameters.

3 HER Electrocatalysis on Interface of Pt

In order to explore the slow kinetics of Pt in alkaline HER, lots of studies are focused on the interface of Pt. Markovic's group have demonstrated that the activity of alkaline HER on the Pt interface is closely related to the facet of Pt, and the adsorption strengths of H_{ad} and OH_{ad} depend on different Pt surfaces [64]. Meanwhile, the binding site of the adsorbed species determines the kinetics of alkaline HER as evidenced by the potentiodynamic and spectral experiments [70–72]. Two different H_{ad} binding conditions can be found on the Pt surface in the H_{ad} adsorption process: the underpotential deposition of H (H_{upd}) is generated at a positive potential relative to the hydrogen electrode, while the overpotential deposition of H (H_{opd}) takes place relatively reversible hydrogen electrode at a negative potential [57, 73]. Therefore, in order to maintain the physicochemical properties, above two species must bind at different sites of Pt surfaces.

The HER activity of Pt has been confirmed to increase in 0.1 M KOH solution as follows: Pt (111) < Pt (100) < Pt (110), which mainly due to structural sensitivity blockade of OH_{ad} and H_{upd} species on different faces of Pt [64]. Figure 2a is the cyclic voltammograms (CV) on different Pt surfaces which associated with OH_{ad} and H_{upd}. The charge value of H_{upd} is about 150 $\mu C\ cm^{-2}$, which is lower than that of OH_{ad} (about 220 $\mu C\ cm^{-2}$), and the separation occurs between the adsorption peak of OH_{ad} and the desorption peak of H_{upd} in the CV curve of Pt (111) surface. On the other hand, in the case of the CV for the Pt (100) and Pt (110) surfaces, the reversible OH_{ad} were generated in potential regions of $0.45 < V < 0.7$ and $0.35 < V < 0.65$ on the surfaces of Pt (100) and (110), respectively, so that the desorption peak of H_{upd} overlaps with the adsorption peak of OH_{ad}. All surfaces of Pt form irreversible OH_{ad} when the potential region of $V > 0.7$. It is supposed that the reversible OH_{ad} adsorbed on the surface of Pt during the forward sweep can be easily removed during the backward scans. The total charge value of H_{upd} is about 147 and 208 $\mu C\ cm^{-2}$ for Pt (100) and (110), respectively, higher than that of OH_{ad}. Thus, the increase in charge ratio for H_{upd}/OH_{ad} is consistent with the ordering of HER activity, which is Pt (111) < Pt (100) < Pt (110). To summarize, HER activity was significantly reduced due to more OH_{ad} attached to the interface of Pt (111) compared to the other two interfaces [57, 74]. Figure 2b shows that the top sites of Pt (110) is used for H_{ad} adsorption, causing H_2 recombination when H_{upd} is adsorbed on its surface grooves. As shown in Fig. 2c, the top sites of Pt (100) surface are easily occupied by the H_{upd}. However, when the potential is negative, some H_{upd} can be transferred to the groove sites, thus generating the adsorption sites of H_{ad}. On the interface of Pt (111), the Pt sites are highly occupied by H_{upd} due to the tightly packed alignment surface

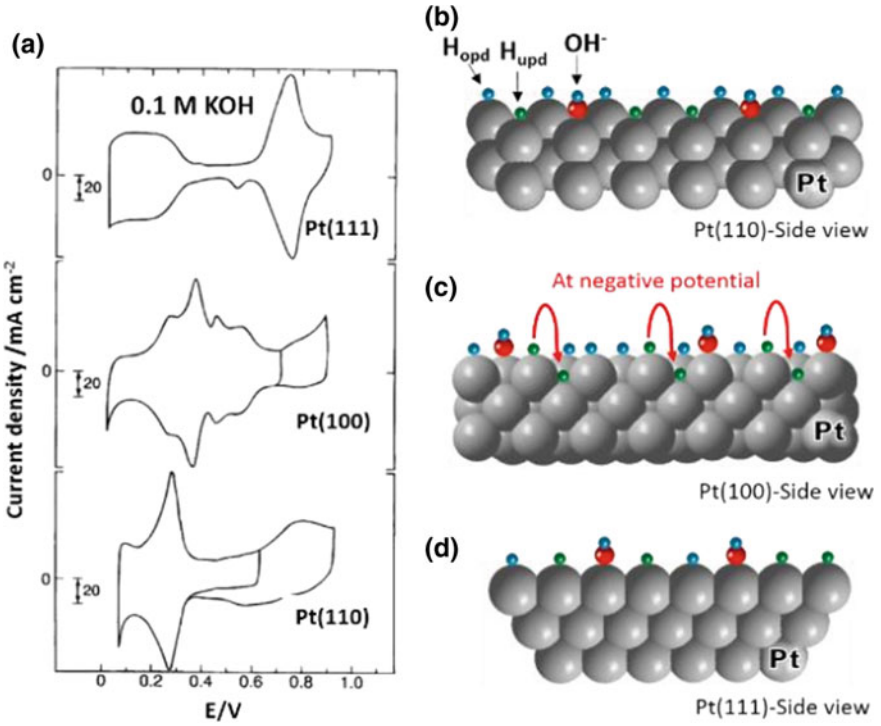

Fig. 2 **a** The cyclic voltammograms of Pt (hkl) in 0.1 M KOH at 1600 rpm with scan rate of 50 mV s^{-1} and the scheme of structure-dependent adsorption of different intermediates on the interface of Pt (hkl), **b** Pt (110), **c** Pt (100), and **d** Pt (111). Reproduced with permission from Wiley, Copyright, 2018 [57]

(Fig. 2d). Therefore, the HER mechanism on the interface of Pt is mainly depend on the competition between H_{ad} and two species (H_{upd} and OH_{ad}) for the Pt site.

4 HER Activity on the Interface of Pt-Based Materials

Metal Pt is considered to be one of the HER catalysts with the best performance in acidic conditions [75–77]. However, compared to acidic electrolytes, the HER kinetics of Pt under alkaline conditions is much slow, so that the electrocatalytic activity is reduced approximately two to three orders of magnitude. This is due to the different formation rates of H_{ad} on Pt interface in acid and alkaline environment, Pt is more favorable for the adsorption of hydronium ions in acidic media, but slower in alkaline solution due to water dissociation [70, 78]. Thus, many attempts have demonstrated that efficient H_2 production in alkaline electrolytes requires bifunctional active sites, including the improvement of water dissociation efficiency and the ability to adsorb

OH_{ad}. Thus, the introduction of water dissociation promoters further enhance the performance of alkaline HER to provide new opportunities [79–81].

4.1 Pt–M Nanocomposite for Alkaline HER

Lately, alloying non-precious transition metals (M = Ni, Co and Cu) with Pt has attracted extensive research interest owing to the electronic effects and chemical activity between Pt and transition metals [82, 83] (Table 1). The formation of Pt–M catalysts has triggered significant enhancement in HER activity and greatly reduced the usage of Pt under alkaline condition [84, 85].

Recently, Zhang and co-workers reported a carbon nano-flake arrays embedded with hollow Co-Pt bimetallic nanocluster, which grown on the carbon cloth [95]. Synergistic interaction between Co and Pt, open hollow structure provide large specific surface areas and abundant active sites, which significantly enhance HER performance. The DFT calculation results indicate the synergistic effect of excellent HER performance on Co-Pt, as shown in Fig. 3. When the active water molecules are adsorbed to the interface of Co-Pt, H_{ad} is more easily bound to the platinum atom while the OH^- group is bonded to the cobalt atom, Co promotes water dissociation to accelerate the formation of H_{ad} and produce H_2 on the Pt surface. Thus, the material exhibits excellent HER performance and extremely long durability of hydrogen release in alkaline condition. In addition, the amount of Pt is only controlled at 2.5 wt% and the overpotential reached 50 mV@10 mA cm^{-2}.

Table 1 Summary of HER activity of Pt–M alloy catalysts in alkaline environment

Electro-catalyst	Overpotential (mV vs. RHE)	Current density (mA cm^{-2})	Electrolyte	Refs.
Pt_3Ni_3 NWs/C-air	70	23	0.1 M KOH	[81]
PtCo–Co/TiM	70	46.5	1 M KOH	[86]
Pt–Ni nanocrystals	48	10	0.1 M KOH	[87]
PtNi–Ni NA/CC	38	10	0.1 M KOH	[88]
Pt–Ni(N) NWs	13	10	1 M KOH	[89]
PtNiCo nanohexapods	22	5	0.1 M KOH	[90]
hcp Pt–Ni excavated nano-multipods	65	10	0.1 M KOH	[91]
$Pt_{26}Cu_{74}$ NFs	18	10	0.5 M KOH	[92]
Pt–Cu DNFs	36	10	0.5 M KOH	[93]
Pt–Ni ASs	70	13.7	1 M KOH	[94]
Pt–Ni core-shell branched nanocages	104	10	0.1 M KOH	[59]

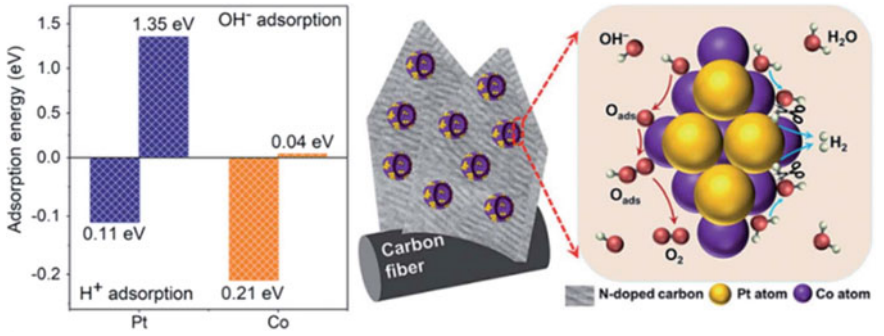

Fig. 3 The DFT calculation of the free energy for the adsorption of OH^- and H^+ on the surface of Co and Pt and the scheme of water dissociation on the interface of Pt–Co. Reproduced with permission from RSC, Copyright, 2018 [95]

Recently, Pt-based nanoframeworks (NFs) structures have been extensively studied thanks to their large surface area, 3D structure, and superior physical and chemical stability. Zhang and coworkers developed a simple solvothermal strategy for the preparation of monodisperse Pt–Cu dodecahedral nanoframes (Pt–Cu DNFs) [93]. The obtained Pt–Cu DNFs required an overpotential of just 36 mV@10 mA cm^{-2}, which was much smaller than that of Pt/C, Pt–Cu NPHs, and Pt black catalysts. It can be seen that doping an appropriate amount of Cu atoms can change the electronic structure, affecting the free energy of the adsorption for H* and OH intermediates. The introduction of Cu atoms also improves the efficiency of Pt significantly. Since the activity of Cu is so strong that it is more easily eroded in the electrolyte, Pt is prevented from being oxidized and exposed more active sites, thereby improving the durability of Pt–Cu DNFs.

Zhang et al. synthesized Pt–Ni bimetallic truncated octahedral nanocrystals through one-step solvothermal strategy [87]. The Pt–Ni nanocrystal structure had changed after introducing OH^-, which transformed into heterostructures with atomic segregation. As shown in Fig. 4a, Pt atoms are formed at lower oxidation-reduction potentials, and then promote the reduction of Ni^{2+}. After the introduction of OH^-, the Pt atoms are formed and migrated from surface to edge of the crystal and then accelerate the reduction of $Ni(OH)_2$. Meanwhile, the added OH^- can affect the reduction and migration of atoms, which can grow crystals by separating atoms. Figure 4b exhibits the catalytic mechanism of Pt–Ni electrocatalysts. Ni and Pt of heterostructures are two independent faces, which can effectively optimize the bond energy of H and OH, promoting water dissociation and hydrogen generation. Thus, tuning atomic distribution is beneficial to the adsorption of H and OH and enhance the HER catalytic activity under alkaline condition.

Furthermore, in order to understand the cause of the speed limit of HER on the atomic scale, Xie and coworkers adjusted the unfavorable orbital direction by N-induced orbital tuning to solve the problem of slow water dissociation [89]. N can effectively bind the active Ni sites and adjust its orbital orientation to enhance the

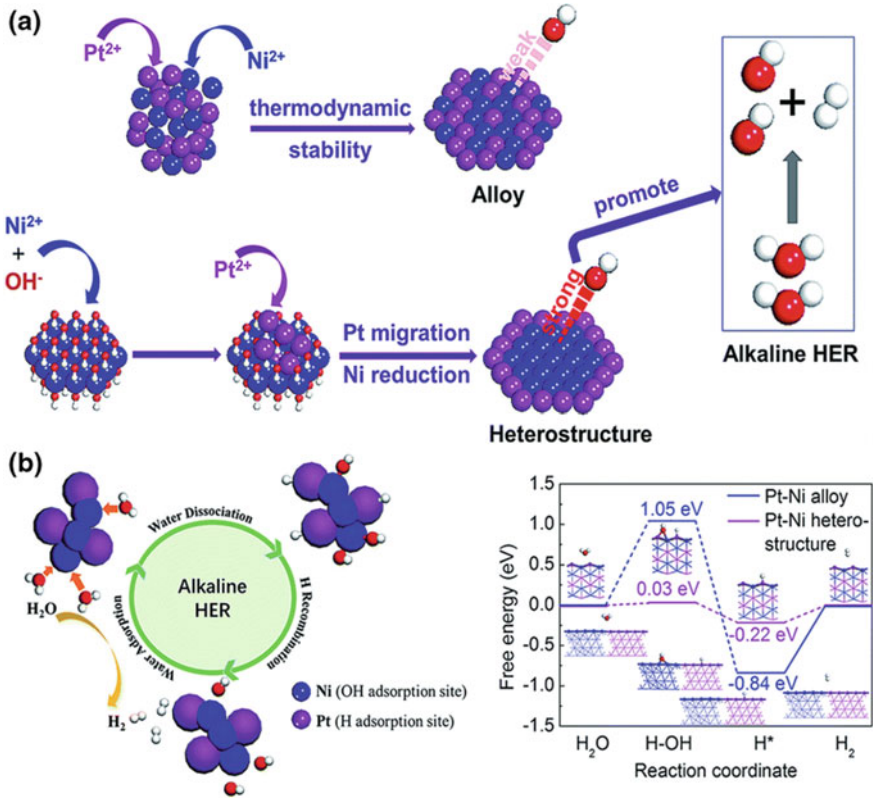

Fig. 4 **a** The growth process of Pt–Ni alloy and Pt–Ni heterostructure and their effect on atomic separation. **b** The alkaline HER mechanism scheme of the Pt–Ni electrocatalyst and the free energy of absorption on Pt–Ni alloy and Pt–Ni heterostructure. Reproduced with permission from RSC, Copyright, 2019 [87]

hydrolysis kinetics. Impressively, the overpotential of N modified Pt–Ni nanowires is clearly superior than commercial Pt/C, which is only 13 mV@10 mA cm^{-2}. The theoretical analysis proves that N doping can modulate the electronic structure around the Ni sites, so that the Ni sites in Pt–Ni generate the empty d_z^2 orbitals to adsorb water molecules as shown in Fig. 5. Meanwhile, the strategy can also be applied to improve HER performance of Pt-based alloys (such as Pt–Cu, Pt–Co and Pt–Ni) under alkaline condition.

4.2 Pt–MO Nanocomposite for Alkaline HER

It is well known that sluggish alkaline HER reaction kinetics result from the cleavage of H-OH chemical bonds and the desorption of hydrogen molecules [96]. One of the strategies to avoid the problem is to decorate Pt with metal oxides that enhance water

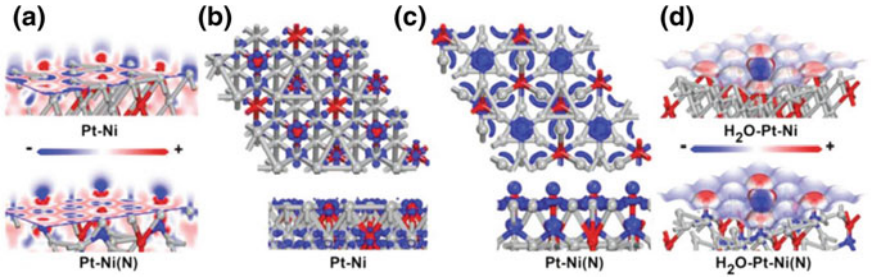

Fig. 5 **a** Electron density difference sections of Pt–Ni and Pt–Ni(N). **b**, **c** Top view and side view orbit above the Fermi level of Pt–Ni and Pt–Ni(N). **d** Surface electrostatic potential images for water adsorption on Pt–Ni and Pt–Ni(N). Reproduced with permission from Wiley, Copyright, 2019 [89]

dissociation, and nearby Pt can promote the recombination of H and the desorption of generated molecular H_2 [97]. Thus, various metal oxide decorative Pt composite materials have been extensively studied. Recently, Chen and co-workers reported a honeycomb-like Pt–NiO by nanoengineering strategy [98]. The porous NiO was supported on nickel foam as shell-core nanostructure by electrodeposition method, then decorated with fine Pt nanoparticles. The obtained Pt–NiO catalyst required an overpotential of only 34 mV@10 mA cm^{-2} and the calculated turnover frequency (TOF) was up to 532 A g_{pt}^{-1} with an ultra-low Pt content (0.1 mg cm^{-2}) at -0.05 V, which is higher than that of Pt/C. From the calculated free energy diagram (Fig. 6), it can be concluded that the water dissociation on the Pt interface requires a larger energy barrier. In contrary, the energy barrier requires for the hydrolysis of NiO/Pt surface is reduced more than 40%, which highlights the effect of NiO on promoting hydrolysis and is more favorable to produce hydrogen.

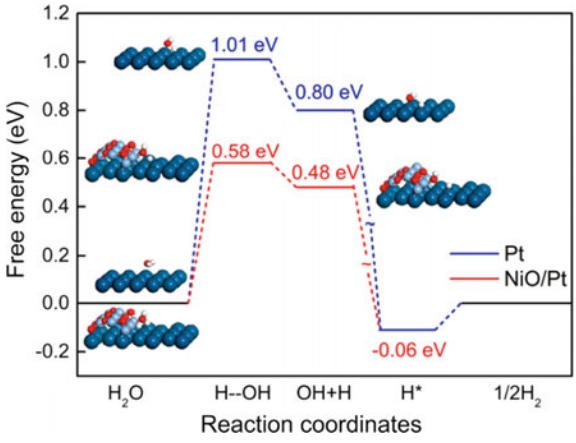

Fig. 6 DFT calculated the free energy of H_2O dissociation and H_2 desorption on the interface of Pt and NiO/Pt and the optimized structure of different reaction stages. Reproduced with permission from [98], Copyright, 2018, American Chemical Society

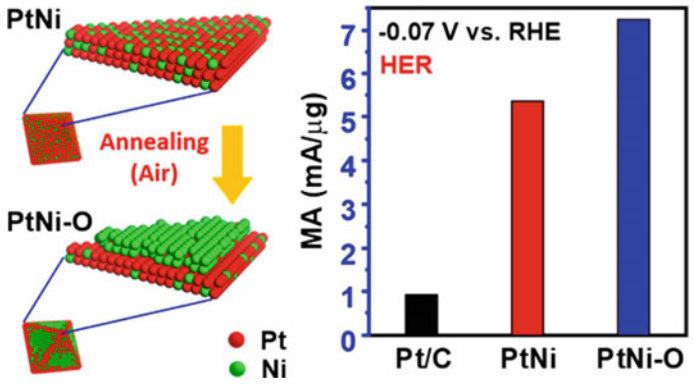

Fig. 7 Schematic diagram of calcination of PtNi/C to PtNi–O/C in air. Reproduced with permission from [99], Copyright, 2018, American Chemical Society

Zhao et al. presented a surface engineering strategy to develop a PtNi-O octahedron electrocatalyst, where the (111) facets are enriched with NiO [99]. The transformation process is showed in Fig. 7. Impressively, when the overpotential reaches 70 mV, the mass activity of Pt–NiO reaches up to 7.23 mA μg^{-1} and the alkaline overpotential is 39.8 mV@10 mA cm^{-2} with the Pt loading content of 5.1 μg_{pt} cm^{-2}. During the electrochemical reaction, the NiO at (111) facets transformed to $Ni(OH)_2$ and formed a $Ni(OH)_2$/Pt-like interfaces.

Except from the typical Pt–NiO system, the synergetic effects between Pt and other metal oxides were studied very recently. A versatile deposition strategy was developed to prepare Pt–Cu@Cu_xO nanowires by Tran and co-workers [100]. The ultra-fine Pt nanodots with a size of 2 nm completely cover Cu@Cu_xO nanowires, resulting in significant structural modulation. Meanwhile, the interaction between two metals can promote the charge transfer, leading to well-performance HER activity. The nanocatalyst showed the overpotential of 72 mV@10 mA cm^{-2} and a mass activity three times higher than that of Pt/C.

4.3 Pt–M(OH) Nanocomposite for Alkaline HER

Recently, $M(OH)_2$ modified Pt electrocatalysts are widely reported as high performance HER electrocatalysts. The enhanced catalytic performance can be attributed to the synergetic effect between H_2 combination on the interface of Pt atomic and water dissociation on M–OH interface. Among all the transition metals, Ni has the closest binding energy value on the interface of Pt, thus $Ni(OH)_2$ has been widely investigated while being modified with Pt and the advanced Pt-based $Ni(OH)_2$ are showed in Table 2.

Table 2 Summary of HER activity of Pt–$M(OH)_2$ catalysts in alkaline electrolytes

Electro-catalyst	Overpotential (mV vs. RHE)	Current density (mA cm^{-2})	Electrolyte	Refs.
Pt nanocrystals@2D-$Ni(OH)_2$ nanosheets	123	4.2	0.1 M KOH	[41]
PtO_2-Co(OH)F NA/TM	39	4	0.1 M KOH	[101]
Pt nanoparticle on $Ni(OH)_2$ nanospine	32	1.25	1.0 M NaOH	[58]
PtO_2–$Co(OH)_2$	65	10	1 M KOH	[102]
Pt nanowires on 2D-$Ni(OH)_2$ nanosheets	57.8	6.31	0.1 M KOH	[80]
β-$Ni(OH)_2$/Pt	92	10	0.1 M KOH	[103]
Pt–$Co(OH)_2$	32	10	1 M KOH	[104]
Pt/C with 10% $Ni(OH)_2$ nanoparticles	50	2.44 ± 0.7	0.1 M KOH	[46]
Pt_c/$Ni(OH)_2$ porous nanowires	32	10	0.1 M KOH	[105]
$Ni(OH)_2$–PtO_2 hybrid nanosheet array	31.4	4	0.1 M KOH	[106]
Pt-doped $Ni(OH)_2$	38	10	1 M KOH	[107]

Xie and co-workers reported a direct growth of $Ni(OH)_2$-PtO_2 nanosheet array on Ti mesh with an ultralow-Pt content (5.1 wt%) [106]. The obtained $Ni(OH)_2$-PtO_2 NS/Ti had a zero onset potential and only needed an small overpotential of 31.4 mV@4 mA cm^{-2}. Further research showed that the uniform dispersion and the small size of PtO_2 exposed more active sites, and the interfaces extremely promoted the water dissociation. The DFT suggested that the hybrid electrocatalyst had a much lower energy barrier, thus facilitate H_2O dissociation. Moreover, the optimal ΔG_H is close to zero (as shown in Fig. 8).

Records et al. developed a fascinating route to synthesize Pt–$Ni(OH)_2$ nanonetworks by using filamentous M13 bacteriophage as templates [108]. The virus has combined the advantages of nanoscopic proportions and the binding of cations by genetic engineering method. A facile synthesis technique like electroless deposition for the phage-templated bimetallic Pt–$Ni(OH)_2$ nanonetworks was presented to obtain bio-templated electrocatalysts for enhanced HER in alkaline environment. Through accurately optimize Pt loading, when the overpotential reached −70 mV versus RHE in 1 M KOH, the Pt–$Ni(OH)_2$ electrocatalyst exhibited the highest mass activity of −4.9 A mg_{Pt}^{-1} reported up to date. Such a bio-templated nanostructure with virus may offer a novel route for high-performance HER and other electrocatalytic energy conversion.

Jung et al. reported a simple and reliable strategy to synthesize crystalline hydroxide which was supported by Pt nanoparticles and harsh conditions like high pressure,

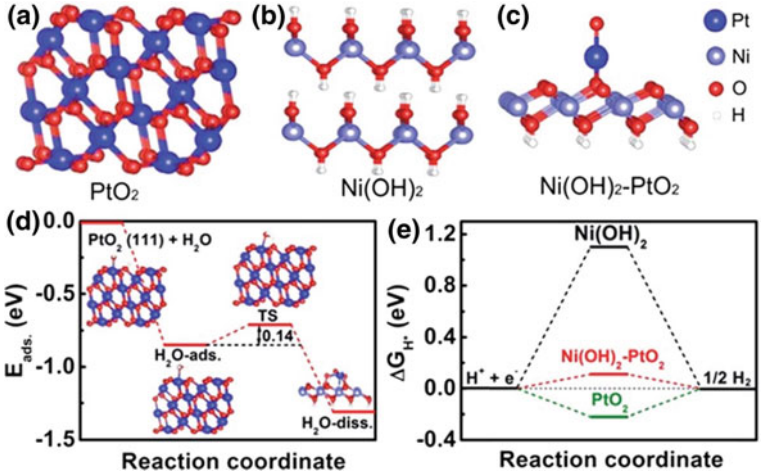

Fig. 8 The structure of PtO_2 (**a**), $Ni(OH)_2$ (**b**) and $Ni(OH)_2$–PtO_2 (**c**). **d** DFT calculated the free energy of water dissociation on the interface of $Ni(OH)_2$–PtO_2 and PtO_2. **e** DFT calculated ΔG_{H^*} for PtO_2, $Ni(OH)_2$ and $Ni(OH)_2$–PtO_2. Reproduced with permission from RSC, Copyright, 2018 [106]

long time and toxic solvent were prevented [79]. In the article, the $Ni(OH)_2$ nanoplate had a shape of hexagonal and good crystallinity. The size of Pt nanoparticles is about 3 nm and Pt nanoparticles were uniformly dispersed on the nanoplate without overlap.

The defective in nickel hydroxide also critical in the design of Pt–$Ni(OH)_2$ HER electrocatalysts. For instance, Wang and co-workers recently reported a electrocatalyst which was consisted with undercoordinated Pt and defective nickel hydroxide [49]. Surface uncoordinated Pt atoms can significantly reduce the potential of the critical step, thereby increasing the catalytic activity. Moreover, High indexed facets have high atomic steps density and ledges/kinks on catalysts surface. The DFT models suggested that the energy barrier required for hydrolysis can be largely reduced due to the synergy between uncoordinated Pt and defective in $Ni(OH)_2$ as shown in Fig. 9. The optimized catalysts showed 11 more times specific current density (0.51 mA cm^{-2}) and 7 more times (0.1 mA μg_{Pt}) mass current density than commercial Pt/C.

Moreover, the low coverage of Pt on the interface of Ni(OH) is the key to developing Pt–$M(OH)_2$ electrocatalysts for alkaline HER. Very recently, Sarabia et al. introduced $Ni(OH)_2$ on the surface of Pt (111) and thoroughly characterized the interface of $Ni(OH)_2$-Pt (111) in NaOH (0.1 M) [109]. The CO displacement experiment together with laser-induce temperature jump equipment help reveal the effect of $Ni(OH)_2$ on the interfacial region. The results illustrated that $Ni(OH)_2$ reduced the initial potential of hydroxide adsorption to a value lower than pure Pt (111). Furthermore, researchers found evidence for the shift of zero total charge potential shift and zero free charge potential/maximum entropy potential, which resulted in a less positive potential (as shown in Fig. 10).

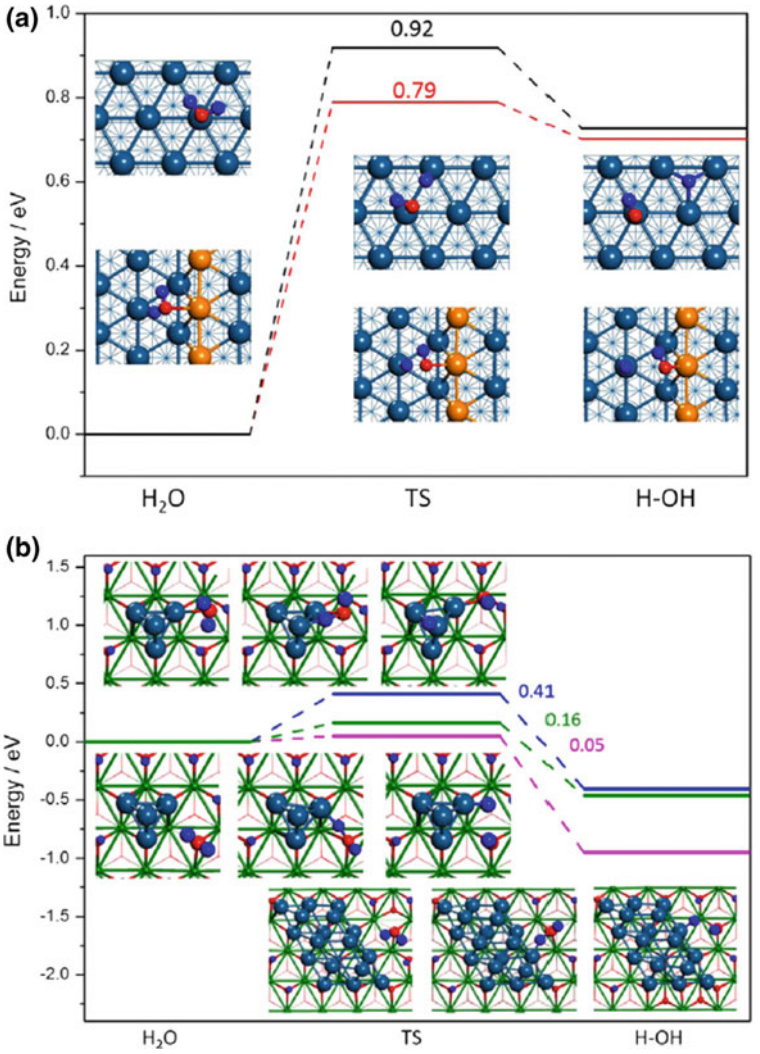

Fig. 9 The reaction energy diagram and corresponding structure for the Pt–$Ni(OH)_2$ HER electrocatalyst. Reproduced with permission from Elsevier, Copyright, 2018 [49]

4.4 Other Pt-Based Nanocomposites for Alkaline HER

In addition to the above alloying metals, metal oxides and hydroxides, there are other promoters that are combined with Pt for water dissociation, which are also being developed to promote alkaline HER (Table 3).

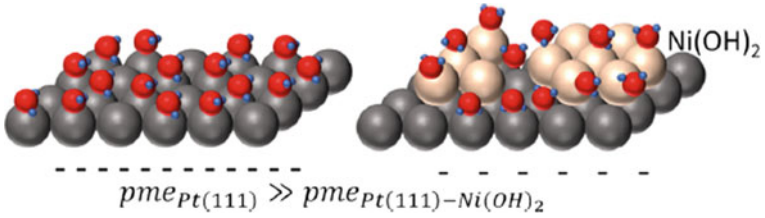

Fig. 10 Schematic illustration of the water dipoles on Pt(111)–$Ni(OH)_2$. Reproduced with permission from [109], Copyright, 2019, American Chemical Society

Table 3 Summary of HER activity of Pt-based other catalysts in alkaline electrolytes

Electro-catalyst	Overpotential (mV vs. RHE)	Current density (mA cm^{-2})	Electrolyte	Refs.
DR-MoS_2-Pt	200	169.8	1 M KOH	[110]
20 %Pt/$Ni(HCO_3)_2$	27	10	1 M KOH	[111]
Pt-CoS_2/CC hybrid	24	10	1 M KOH	[112]
Ni_3N/Pt	83	50	1 M KOH	[113]
Pt–TiN NAs	139	10	1 M KOH	[114]

Recently, Wang and co-workers synthesized Ni_3N nanosheets electrocatalyst loaded with platinum nanoparticles [113]. Due to the excellent metal conductivity and hydrogenated semiconductor surface of Ni_3N nanosheets, it not only facilitated electron transfer to promote reaction kinetics, but also possessed rich reactive sites to accelerate water dissociation and H_{ad} formation to recombine to produce H_2 on the surface of Pt. This strategy provides a good idea to maximize electrochemical performance by minimizing Pt in an alkaline environment. Meanwhile, the Ni_3N/Pt nanosheets exhibit excellent alkaline HER performance, the overpotential is 160 mV@200 mA cm^{-2}.

Recently, Lao and co-workers fabricated a unique hetero-structured nanomaterial which was constructed by platinum and nickel bicarbonate for accelerated HER under alkaline environment [111]. In this article, $Ni(HCO_3)_2$ was proved to have efficient water adsorption/dissociation ability for the first time. On the other hand, $Ni(HCO_3)_2$ can effectively prevent platinum nanoparticles from growing and agglomeration, thereby ensuring the utmost exposure of platinum. Figure 11 displayed a possible mechanism for advanced alkaline HER property of Pt/$Ni(HCO_3)_2$, where nickel bicarbonate served for water adsorption/dissociation while Pt atoms acted as HER active sites for H_{ad} adsorption and recombination during the Heyrovsky step or Tafel step. Owing to the strong interaction between two components, the specific heterostructure exhibited excellent HER catalytic activity.

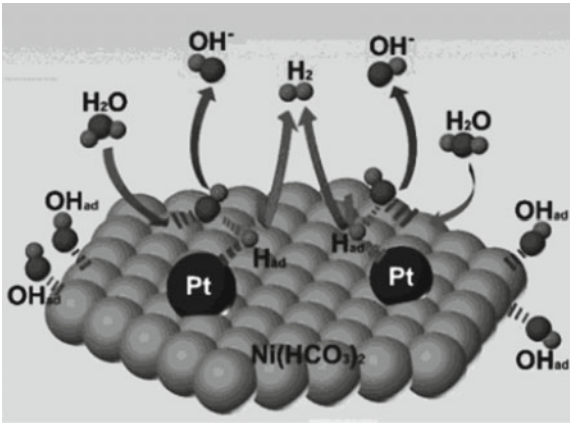

Fig. 11 An illustration for possible mechanism for advanced alkaline HER property of $Pt/Ni(HCO_3)_2$. Reproduced with permission from Wiley, Copyright, 2019 [111]

5 Conclusion and Perspective

Scientists have made many important advances and breakthroughs in the study of HER in Pt-based materials in alkaline environments. As promising strategies for designing alkaline HER catalysts to minimize the amount of Pt used, the mechanism in alkaline HER and the reaction kinetics on the Pt interface have been discussed in this chapter. In order to increase the alkaline HER activity, different amounts of catalysts are used to promote water adsorption. In addition, the authors also briefly summarize the recent research progress of Pt-based materials in alkaline HER. The adsorption behavior of the H_2O and OH^- on the interface of catalysts is improved by adjusting the electron catalytic structure of the metal, oxide, hydroxide and Pt interface, so that the alkaline HER activity is greatly improved.

In the future development of electrochemistry, in order to optimize the conversion of free energy into potential active materials and deepen the basic understanding of the interfacial chemistry between the catalyst and the Pt component, simple synthesis strategies should be exploited to minimize the content of Pt to reach industry standards and greatly reduce the energy consumption of hydrogen production.

References

1. You B, Sun Y (2018) Innovative strategies for electrocatalytic water splitting. Acc Chem Res 51(7):1571–1580
2. Haque F, Zavabeti A, Zhang BY, Datta RS, Yin Y, Yi Z, Wang Y, Mahmood N, Pillai N, Syed N, Khan H, Jannat A, Wang N, Medhekar N, Kalantar-zadeh K, Ou JZ (2019) Ordered intracrystalline pores in planar molybdenum oxide for enhanced alkaline hydrogen evolution. J Mater Chem A 7(1):257–268
3. Chow J, Kopp RJ, Portney PR (2003) Energy resources and global development. Science 302(5650):1528

4. Chu S, Majumdar A (2012) Opportunities and challenges for a sustainable energy future. Nature 488:294
5. Ager JW, Lapkin AA (2018) Chemical storage of renewable energy. Science 360(6390):707
6. Jia T, Dai Y, Wang R (2018) Refining energy sources in winemaking industry by using solar energy as alternatives for fossil fuels: a review and perspective. Renew Sust Energ Rev 88:278–296
7. Seh ZW, Kibsgaard J, Dickens CF, Chorkendorff I, Nørskov JK, Jaramillo TF (2017) Combining theory and experiment in electrocatalysis: insights into materials design. Science 355(6321):eaad4998
8. Turner JA (2004) Sustainable hydrogen production. Science 305(5686):972
9. Chu S, Cui Y, Liu N (2016) The path towards sustainable energy. Nat Mater 16:16–22
10. Suen N-T, Hung S-F, Quan Q, Zhang N, Xu Y-J, Chen HM (2017) Electrocatalysis for the oxygen evolution reaction: recent development and future perspectives. Chem Soc Rev 46(2):337–365
11. Lukatskaya MR, Dunn B, Gogotsi Y (2016) Multidimensional materials and device architectures for future hybrid energy storage. Nat Commun 7:12647
12. Momirlan M, Veziroglu TN (2005) The properties of hydrogen as fuel tomorrow in sustainable energy system for a cleaner planet. Int J Hydrogen Energy 30(7):795–802
13. Jiao Y, Zheng Y, Jaroniec M, Qiao SZ (2015) Design of electrocatalysts for oxygen- and hydrogen-involving energy conversion reactions. Chem Soc Rev 44(8):2060–2086
14. Daeneke T, Dahr N, Atkin P, Clark RM, Harrison CJ, Brkljača R, Pillai N, Zhang BY, Zavabeti A, Ippolito SJ, Berean KJ, Ou JZ, Strano MS, Kalantar-zadeh K (2017) Surface water dependent properties of sulfur-rich molybdenum sulfides: electrolyteless gas phase water splitting. ACS Nano 11(7):6782–6794
15. Roger I, Shipman MA, Symes MD (2017) Earth-abundant catalysts for electrochemical and photoelectrochemical water splitting. Nat Rev Chem 1:0003
16. Walter MG, Warren EL, McKone JR, Boettcher SW, Mi Q, Santori EA, Lewis NS (2010) Solar water splitting cells. Chem Rev 110(11):6446–6473
17. Stolarczyk JK, Bhattacharyya S, Polavarapu L, Feldmann J (2018) Challenges and prospects in solar water splitting and CO_2 reduction with inorganic and hybrid nanostructures. ACS Catal 8(4):3602–3635
18. Lu Q, Yu Y, Ma Q, Chen B, Zhang H (2016) 2d transition-metal-dichalcogenide-nanosheet-based composites for photocatalytic and electrocatalytic hydrogen evolution reactions. Adv Mater 28(10):1917–1933
19. Hosseini SE, Wahid MA (2016) Hydrogen production from renewable and sustainable energy resources: promising green energy carrier for clean development. Renew Sust Energ Rev 57:850–866
20. Gandía LM, Oroz R, Ursúa A, Sanchis P, Diéguez PM (2007) Renewable hydrogen production: performance of an alkaline water electrolyzer working under emulated wind conditions. Energy Fuels 21(3):1699–1706
21. Xu Y, Kraft M, Xu R (2016) Metal-free carbonaceous electrocatalysts and photocatalysts for water splitting. Chem Soc Rev 45(11):3039–3052
22. Duan J, Chen S, Zhao C (2017) Ultrathin metal-organic framework array for efficient electrocatalytic water splitting. Nat Commun 8:15341
23. Wang H, Lee H-W, Deng Y, Lu Z, Hsu P-C, Liu Y, Lin D, Cui Y (2015) Bifunctional non-noble metal oxide nanoparticle electrocatalysts through lithium-induced conversion for overall water splitting. Nat Commun 6:7261
24. Li J, Wang Y, Zhou T, Zhang H, Sun X, Tang J, Zhang L, Al-Enizi AM, Yang Z, Zheng G (2015) Nanoparticle superlattices as efficient bifunctional electrocatalysts for water splitting. J Am Chem Soc 137(45):14305–14312
25. Lu C, Tranca D, Zhang J, Rodríguez Hernández F, Su Y, Zhuang Z, Zhang F, Seifert G, Feng X (2017) Molybdenum carbide-embedded nitrogen-doped porous carbon nanosheets as electrocatalysts for water splitting in alkaline media. ACS Nano 11(4):3933–3942

26. Mueller-Langer F, Tzimas E, Kaltschmitt M, Peteves S (2007) Techno-economic assessment of hydrogen production processes for the hydrogen economy for the short and medium term. Int J Hydrogen Energy 32(16):3797–3810
27. Holladay JD, Hu J, King DL, Wang Y (2009) An overview of hydrogen production technologies. Catal Today 139(4):244–260
28. Safizadeh F, Ghali E, Houlachi G (2015) Electrocatalysis developments for hydrogen evolution reaction in alkaline solutions-a review. Int J Hydrogen Energy 40(1):256–274
29. Zeng K, Zhang D (2010) Recent progress in alkaline water electrolysis for hydrogen production and applications. Prog Energy Combust Sci 36(3):307–326
30. Hu W (2000) Electrocatalytic properties of new electrocatalysts for hydrogen evolution in alkaline water electrolysis. Int J Hydrogen Energy 25(2):111–118
31. Wang L, Li Y, Xia M, Li Z, Chen Z, Ma Z, Qin X, Shao G (2017) Ni nanoparticles supported on graphene layers: an excellent 3d electrode for hydrogen evolution reaction in alkaline solution. J Power Sources 347:220–228
32. Luo G-G, Zhang H-L, Tao Y-W, Wu Q-Y, Tian D, Zhang Q (2019) Recent progress in ligand-centered homogeneous electrocatalysts for hydrogen evolution reaction. Inorg Chem Front 6(2):343–354
33. Du H, Kong R-M, Guo X, Qu F, Li J (2018) Recent progress in transition metal phosphides with enhanced electrocatalysis for hydrogen evolution. Nanoscale 10(46):21617–21624
34. Yu P, Wang F, Shifa TA, Zhan X, Lou X, Xia F, He J (2019) Earth abundant materials beyond transition metal dichalcogenides: a focus on electrocatalyzing hydrogen evolution reaction. Nano Energy 58:244–276
35. Sheng W, Gasteiger HA, Shao-Horn Y (2010) Hydrogen oxidation and evolution reaction kinetics on platinum: acid vs alkaline electrolytes. J Electrochem Soc 157(11):B1529–B1536
36. Durst J, Siebel A, Simon C, Hasche F, Herranz J, Gasteiger HA (2014) New insights into the electrochemical hydrogen oxidation and evolution reaction mechanism. Energ Environ Sci 7(7):2255–2260
37. Danilovic N, Subbaraman R, Strmcnik D, Chang K-C, Paulikas AP, Stamenkovic VR, Markovic NM (2012) Enhancing the alkaline hydrogen evolution reaction activity through the bifunctionality of $Ni(OH)_2$/metal catalysts. Angew Chem Int Ed 51(50):12495–12498
38. de Chialvo MG, Chialvo A (1999) The Tafel-Heyrovsky route in the kinetic mechanism of the hydrogen evolution reaction. Electrochem Commun 1(9):379–382
39. Danilovic N, Subbaraman R, Strmcnik D, Stamenkovic V, Markovic N (2013) Electrocatalysis of the Her in acid and alkaline media. J Serb Chem Soc 78(12):2007–2015
40. Mahmood N, Yao Y, Zhang JW, Pan L, Zhang X, Zou JJ (2018) Electrocatalysts for hydrogen evolution in alkaline electrolytes: mechanisms, challenges, and prospective solutions. Adv Sci 5(2):1700464
41. Wang L, Zhu Y, Zeng Z, Lin C, Giroux M, Jiang L, Han Y, Greeley J, Wang C, Jin J (2017) Platinum-nickel hydroxide nanocomposites for electrocatalytic reduction of water. Nano Energy 31:456–461
42. Merte LR, Knudsen J, Grabow LC, Vang RT, Lægsgaard E, Mavrikakis M, Besenbacher F (2009) Correlating Stm contrast and atomic-scale structure by chemical modification: vacancy dislocation loops on FeO/Pt (111). Surf Sci 603(2):L15–L18
43. O'Brien JT, Williams ER (2012) Effects of ions on hydrogen-bonding water networks in large aqueous nanodrops. J Am Chem Soc 134(24):10228–10236
44. Sun F, Li Q, Xue H, Pang H (2019) Pristine transition-metal-based metal-organic frameworks for electrocatalysis. ChemElectroChem 6(5):1273–1299
45. Wang L, Lin C, Huang D, Chen J, Jiang L, Wang M, Chi L, Shi L, Jin J (2015) Optimizing the Volmer Step by single-layer nickel hydroxide nanosheets in hydrogen evolution reaction of platinum. ACS Catal 5(6):3801–3806
46. Wang G, Parrondo J, He C, Li Y, Ramani V (2017) $Pt/C/Ni(OH)_2$ bi-functional electrocatalyst for enhanced hydrogen evolution reaction activity under alkaline conditions. J Electrochem Soc 164(13):F1307–F1315

47. Xu X, Zhang X, Sun H, Yang Y, Dai X, Gao J, Li X, Zhang P, Wang H-H, Yu N-F, Sun S-G (2014) Synthesis of Pt–Ni alloy nanocrystals with high-index facets and enhanced electrocatalytic properties. Angew Chem Int Ed 126(46):12730–12735
48. Abbas SA, Iqbal MI, Kim S-H, Jung K-D (2017) Catalytic activity of urchin-like Ni nanoparticles prepared by solvothermal method for hydrogen evolution reaction in alkaline solution. Electrochim Acta 227:382–390
49. Wang Y, Zhuo H, Zhang X, Dai X, Yu K, Luan C, Yu L, Xiao Y, Li J, Wang M, Gao F (2018) Synergistic effect between undercoordinated platinum atoms and defective nickel hydroxide on enhanced hydrogen evolution reaction in alkaline solution. Nano Energy 48:590–599
50. Schalenbach M, Tjarks G, Carmo M, Lueke W, Mueller M, Stolten D (2016) Acidic or alkaline? Towards a new perspective on the efficiency of water electrolysis. J Electrochem Soc 163(11):F3197–F3208
51. Wrighton MS, Ellis AB, Wolczanski PT, Morse DL, Abrahamson HB, Ginley DS (1976) Strontium titanate photoelectrodes. Efficient photoassisted electrolysis of water at zero applied potential. J Am Chem Soc 98(10):2774–2779
52. Aricò A, Siracusano S, Briguglio N, Baglio V, Di Blasi A, Antonucci V (2013) Polymer electrolyte membrane water electrolysis: status of technologies and potential applications in combination with renewable power sources. J Appl Electrochem 43(2):107–118
53. Takenaka H, Torikai E, Kawami Y, Wakabayashi N (1982) Solid polymer electrolyte water electrolysis. Int J Hydrogen Energy 7(5):397–403
54. Hu S, Xiang C, Haussener S, Berger AD, Lewis NS (2013) An analysis of the optimal band gaps of light absorbers in integrated tandem photoelectrochemical water-splitting systems. Energ Environ Sci 6(10):2984–2993
55. Marini S, Salvi P, Nelli P, Pesenti R, Villa M, Berrettoni M, Zangari G, Kiros Y (2012) Advanced alkaline water electrolysis. Electrochim Acta 82:384–391
56. Greszler TA, Caulk D, Sinha P (2012) The impact of platinum loading on oxygen transport resistance. J Electrochem Soc 159(12):F831–F840
57. Ruqia B, Choi SI (2018) Pt and Pt-Ni$(OH)_2$ electrodes for the hydrogen evolution reaction in alkaline electrolytes and their nanoscaled electrocatalysts. Chemsuschem 11(16):2643–2653
58. Abbas SA, Kim S-H, Iqbal MI, Muhammad S, Yoon W-S, Jung K-D (2018) Synergistic effect of nano-Pt and Ni spine for Her in alkaline solution: hydrogen spillover from nano-Pt to Ni spine. Sci Rep 8(1):2986
59. Cao Z, Li H, Zhan C, Zhang J, Wang W, Xu B, Lu F, Jiang Y, Xie Z, Zheng L (2018) Monocrystalline platinum-nickel branched nanocages with enhanced catalytic performance towards the hydrogen evolution reaction. Nanoscale 10(11):5072–5077
60. Schmidt O, Gambhir A, Staffell I, Hawkes A, Nelson J, Few S (2017) Future cost and performance of water electrolysis: an expert elicitation study. Int J Hydrogen Energy 42(52):30470–30492
61. de Fátima Palhares DDA, Vieira LGM, Damasceno JJR (2018) Hydrogen production by a low-cost electrolyzer developed through the combination of alkaline water electrolysis and solar energy use. Int J Hydrogen Energy 43(9):4265–4275
62. Koper MT (2011) Thermodynamic theory of multi-electron transfer reactions: implications for electrocatalysis. J Electroanal Chem 660(2):254–260
63. de Chialvo MG, Chialvo A (1998) Kinetics of hydrogen evolution reaction with Frumkin adsorption: re-examination of the Volmer-Heyrovsky and Volmer-Tafel routes. Electrochim Acta 44(5):841–851
64. Markovića NM, Sarraf ST, Gasteiger HA, Ross PN (1996) Hydrogen electrochemistry on platinum low-index single-crystal surfaces in alkaline solution. J Chem Soc, Faraday Trans 92(20):3719–3725
65. Rheinländer PJ, Herranz J, Durst J, Gasteiger HA (2014) Kinetics of the hydrogen oxidation/evolution reaction on polycrystalline platinum in alkaline electrolyte reaction order with respect to hydrogen pressure. J Electrochem Soc 161(14):F1448–F1457
66. Barber J, Conway B (1999) Structural specificity of the kinetics of the hydrogen evolution reaction on the low-index surfaces of Pt single-crystal electrodes in 0.5 M dm^{-3} NaOH. J Electroanal Chem 461(1–2):80–89

67. Shen S, Zhao T, Xu J, Li Y (2010) Synthesis of PdNi catalysts for the oxidation of ethanol in alkaline direct ethanol fuel cells. J Power Sources 195(4):1001–1006
68. Gong M, Wang D-Y, Chen C-C, Hwang B-J, Dai H (2016) A mini review on nickel-based electrocatalysts for alkaline hydrogen evolution reaction. Nano Res 9(1):28–46
69. Nimlos MR, Chang CH, Curtis CJ, Miedaner A, Pilath HM, DuBois DL (2008) Calculated hydride donor abilities of five-coordinate transition metal hydrides [Hm (diphosphine)$_2$]$^+$(M = Ni, Pd, Pt) as a function of the bite angle and twist angle of diphosphine ligands. Organometallics 27(12):2715–2722
70. Strmcnik D, Lopes PP, Genorio B, Stamenkovic VR, Markovic NM (2016) Design principles for hydrogen evolution reaction catalyst materials. Nano Energy 29:29–36
71. Conway BE, Jerkiewicz G (2000) Relation of energies and coverages of underpotential and overpotential deposited H at Pt and other metals to the 'Volcano Curve' for cathodic H_2 evolution kinetics. Electrochim Acta 45(25):4075–4083
72. Subbaraman R, Tripkovic D, Strmcnik D, Chang K-C, Uchimura M, Paulikas AP, Stamenkovic V, Markovic NM (2011) Enhancing hydrogen evolution activity in water splitting by tailoring Li^+-$Ni(OH)_2$-Pt interfaces. Science 334(6060):1256–1260
73. Conway BE, Tilak BV (2002) Interfacial processes involving electrocatalytic evolution and oxidation of H_2, and the role of chemisorbed H. Electrochim Acta 47(22):3571–3594
74. Marković NM, Gasteiger HA, Ross PN (1996) Oxygen reduction on platinum low-index single-crystal surfaces in alkaline solution: rotating ring $Disk_{Pt(hkl)}$ studies. J Phys Chem 100(16):6715–6721
75. Bai S, Wang C, Deng M, Gong M, Bai Y, Jiang J, Xiong Y (2014) Surface polarization matters: enhancing the hydrogen-evolution reaction by shrinking Pt shells in Pt-Pd-Graphene stack structures. Angew Chem Int Ed 53(45):12120–12124
76. Li Q, Wu L, Wu G, Su D, Lv H, Zhang S, Zhu W, Casimir A, Zhu H, Mendoza-Garcia A, Sun S (2015) New approach to fully ordered Fct-FePt nanoparticles for much enhanced electrocatalysis in Acid. Nano Lett 15(4):2468–2473
77. Esposito DV, Hunt ST, Stottlemyer AL, Dobson KD, McCandless BE, Birkmire RW, Chen JG (2010) Low-cost hydrogen-evolution catalysts based on monolayer platinum on tungsten monocarbide substrates. Angew Chem Int Ed 49(51):9859–9862
78. van der Niet MJTC, Garcia-Araez N, Hernández J, Feliu JM, Koper MTM (2013) Water dissociation on well-defined platinum surfaces: the electrochemical perspective. Catal Today 202:105–113
79. Jung E, Park H-Y, Cho A, Jang JH, Park HS, Yu T (2018) Aqueous-phase synthesis of metal hydroxide nanoplates and platinum/nickel hydroxide hybrid nanostructures and their enhanced electrocatalytic properties. Appl Catal B-Environ 225:238–242
80. Yin H, Zhao S, Zhao K, Muqsit A, Tang H, Chang L, Zhao H, Gao Y, Tang Z (2015) Ultrathin platinum nanowires grown on single-layered nickel hydroxide with high hydrogen evolution activity. Nat Commun 6:6430
81. Wang P, Jiang K, Wang G, Yao J, Huang X (2016) Phase and interface engineering of platinum-nickel nanowires for efficient electrochemical hydrogen evolution. Angew Chem Int Ed 55(41):12859–12863
82. Wang L, Gao W, Liu Z, Zeng Z, Liu Y, Giroux M, Chi M, Wang G, Greeley J, Pan X, Wang C (2018) Core-shell nanostructured cobalt-platinum electrocatalysts with enhanced durability. ACS Catal 8(1):35–42
83. Zeng Y, Shao Z, Zhang H, Wang Z, Hong S, Yu H, Yi B (2017) Nanostructured ultrathin catalyst layer based on open-walled PtCo bimetallic nanotube arrays for proton exchange membrane fuel cells. Nano Energy 34:344–355
84. Xiong L, Kannan AM, Manthiram A (2002) Pt-M (M = Fe Co, Ni and Cu) electrocatalysts synthesized by an aqueous route for proton exchange membrane fuel cells. Electrochem Commun 4(11):898–903
85. Wang X, He Q, Song L, Jaroniec M, Zheng Y, Qiao S (2019) Breaking the volcano-plot limits for Pt-based electrocatalysts by selective tuning adsorption of multiple intermediates. J Mater Chem A 7(22):13635–13640

86. Wang Z, Ren X, Luo Y, Wang L, Cui G, Xie F, Wang H, Xie Y, Sun X (2018) An ultrafine platinum-cobalt alloy decorated cobalt nanowire array with superb activity toward alkaline hydrogen evolution. Nanoscale 10(26):12302–12307
87. Zhang C, Chen B, Mei D, Liang X (2019) The OH–driven synthesis of Pt-Ni nanocatalysts with atomic segregation for alkaline hydrogen evolution reaction. J Mater Chem A 7(10):5475–5481
88. Xie L, Liu Q, Shi X, Asiri AM, Luo Y, Sun X (2018) Superior alkaline hydrogen evolution electrocatalysis enabled by an ultrafine Ptni nanoparticle-decorated Ni nanoarray with ultralow Pt loading. Inorg Chem Front 5(6):1365–1369
89. Xie Y, Cai J, Wu Y, Zang Y, Zheng X, Ye J, Cui P, Niu S, Liu Y, Zhu J (2019) Boosting water dissociation kinetics on Pt-Ni nanowires by N-induced orbital tuning. Adv Mater 31(16):1807780
90. Oh A, Sa YJ, Hwang H, Baik H, Kim J, Kim B, Joo SH, Lee K (2016) Rational design of Pt-Ni-Co ternary alloy nanoframe crystals as highly efficient catalysts toward the alkaline hydrogen evolution reaction. Nanoscale 8(36):16379–16386
91. Cao Z, Chen Q, Zhang J, Li H, Jiang Y, Shen S, Fu G, Lu B-a, Xie Z, Zheng L (2017) Platinum-nickel alloy excavated nano-multipods with hexagonal close-packed structure and superior activity towards hydrogen evolution reaction. Nat Commun 8:15131
92. Huang X-Y, You L-X, Zhang X-F, Feng J-J, Zhang L, Wang A-J (2019) L-Proline assisted solvothermal preparation of Cu-Rich rhombic dodecahedral PtCu nanoframes as advanced electrocatalysts for oxygen reduction and hydrogen evolution reactions. Electrochim Acta 299:89–97
93. Zhang X-F, Wang A-J, Zhang L, Yuan J, Li Z, Feng J-J (2018) Solvothermal synthesis of monodisperse PtCu dodecahedral nanoframes with enhanced catalytic activity and durability for hydrogen evolution reaction. ACS Appl Energy Mater 1(9):5054–5061
94. Zhang Z, Liu G, Cui X, Chen B, Zhu Y, Gong Y, Saleem F, Xi S, Du Y, Borgna A (2018) Crystal phase and architecture engineering of Lotus-Thalamus-shaped Pt-Ni anisotropic superstructures for highly efficient electrochemical hydrogen evolution. Adv Mater 30(30):1801741
95. Zhang H, Liu Y, Wu H, Zhou W, Kou Z, Pennycook SJ, Xie J, Guan C, Wang J (2018) Open hollow Co-Pt clusters embedded in carbon nanoflake arrays for highly efficient alkaline water splitting. J Mater Chem A 6(41):20214–20223
96. Subbaraman R, Tripkovic D, Chang K-C, Strmcnik D, Paulikas AP, Hirunsit P, Chan M, Greeley J, Stamenkovic V, Markovic NM (2012) Trends in activity for the water electrolyser reactions on 3d M (Ni Co, Fe, Mn) Hydr(oxy)oxide catalysts. Nat Mater 11(6):550–557
97. Bruix A, Rodriguez JA, Ramírez PJ, Senanayake SD, Evans J, Park JB, Stacchiola D, Liu P, Hrbek J, Illas F (2012) A new type of strong metal-support interaction and the production of H_2 through the transformation of water on Pt/CeO_2 (111) and $Pt/CeO_x/TiO_2$ (110) catalysts. J Am Chem Soc 134(21):8968–8974
98. Chen Z-J, Cao G-X, Gan L-Y, Dai H, Xu N, Zang M-J, Dai H-B, Wu H, Wang P (2018) Highly dispersed platinum on Honeycomb-Like NiO@Ni film as a synergistic electrocatalyst for the hydrogen evolution reaction. ACS Catal 8(9):8866–8872
99. Zhao Z, Liu H, Gao W, Xue W, Liu Z, Huang J, Pan X, Huang Y (2018) Surface-engineered PtNi-O nanostructure with record-high performance for electrocatalytic hydrogen evolution reaction. J Am Chem Soc 140(29):9046–9050
100. Tran DT, Le HT, Luyen Doan TL, Kim NH, Lee JH (2019) Pt nanodots monolayer modified mesoporous $Cu@Cu_xO$ nanowires for improved overall water splitting reactivity. Nano Energy 59:216–228
101. Wang Z, Liu Z, Du G, Asiri AM, Wang L, Li X, Wang H, Sun X, Chen L, Zhang Q (2018) Ultrafine PtO_2 nanoparticles coupled with a Co(OH)F nanowire array for enhanced hydrogen evolution. Chem Commun 54(7):810–813
102. Wang Z, Ren X, Shi X, Asiri AM, Wang L, Li X, Sun X, Zhang Q, Wang H (2018) A platinum oxide decorated amorphous cobalt oxide hydroxide nanosheet array towards alkaline hydrogen evolution. J Mater Chem A 6(9):3864–3868

103. Yu X, Zhao J, Zheng L-R, Tong Y, Zhang M, Xu G, Li C, Ma J, Shi G (2018) Hydrogen evolution reaction in alkaline media: alpha- or beta-nickel hydroxide on the surface of platinum? ACS Energy Lett 3(1):237–244
104. Xing Z, Han C, Wang D, Li Q, Yang X (2017) Ultrafine Pt nanoparticle-decorated $Co(OH)_2$ nanosheet arrays with enhanced catalytic activity toward hydrogen evolution. ACS Catal 7(10):7131–7135
105. Yang H, Wang C, Hu F, Zhang Y, Lu H, Wang Q (2017) Atomic-scale Pt clusters decorated on porous A-$Ni(OH)_2$ nanowires as highly efficient electrocatalyst for hydrogen evolution reaction. Sci China Mater 60(11):1121–1128
106. Xie L, Ren X, Liu Q, Cui G, Ge R, Asiri AM, Sun X, Zhang Q, Chen L (2018) A $Ni(OH)_2$-PtO_2 hybrid nanosheet array with ultralow Pt loading toward efficient and durable alkaline hydrogen evolution. J Mater Chem A 6(5):1967–1970
107. Yuan G, Wen B, Hu Y, Zeng G, Zhang W, Wang L, Zhang X, Wang Q (2019) Aqueous substitution synthesis of platinum modified amorphous nickel hydroxide on nickel foam composite electrode for efficient and stable hydrogen evolution. Int J Hydrogen Energy 44(28):14258–14265
108. Records WC, Yoon Y, Ohmura JF, Chanut N, Belcher AM (2019) Virus-templated Pt-$Ni(OH)_2$ nanonetworks for enhanced electrocatalytic reduction of water. Nano Energy 58:167–174
109. Sarabia FJ, Sebastián-Pascual P, Koper MTM, Climent V, Feliu JM (2019) Effect of the interfacial water structure on the hydrogen evolution reaction on Pt (111) modified with different nickel hydroxide coverages in alkaline media. ACS Appl Mater Inter 11(1):613–623
110. Xie J, Gao L, Jiang H, Zhang X, Lei F, Hao P, Tang B, Xie Y (2019) Platinum nanocrystals decorated on defect-rich MoS_2 nanosheets for pH-universal hydrogen evolution reaction. Cryst Growth Des 19(1):60–65
111. Lao M, Rui K, Zhao G, Cui P, Zheng X, Dou SX, Sun W (2019) Platinum/Nickel bicarbonate heterostructures towards accelerated hydrogen evolution under alkaline conditions. Angew Chem Int Ed 58(16):5432–5437
112. Han X, Wu X, Deng Y, Liu J, Lu J, Zhong C, Hu W (2018) Ultrafine Pt nanoparticle-decorated Pyrite-type CoS_2 nanosheet arrays coated on carbon cloth as a bifunctional electrode for overall water splitting. Adv Energy Mater 8(24):1800935
113. Wang Y, Chen L, Yu X, Wang Y, Zheng G (2017) Superb alkaline hydrogen evolution and simultaneous electricity generation by Pt-decorated Ni_3N nanosheets. Adv Energy Mater 7(2):1601390
114. Wang C, Shi H, Liu H, Fu J, Wei D, Zeng W, Wan Q, Zhang G, Duan H (2018) Quasi-atomic-scale platinum anchored on porous titanium nitride nanorod arrays for highly efficient hydrogen evolution. Electrochim Acta 292:727–735